INVESTIGATING THE CHEMISTRY OF CATIONIC RHODIUM BISPHOSPHINE COMPLEXES: COMPARING REACTIVITY IN THE SOLID STATE WITH SOLUTION

Sebastian D. Pike

A thesis submitted in partial fulfilment of the requirements for the degree of Doctor of Philosophy at the University of Oxford.

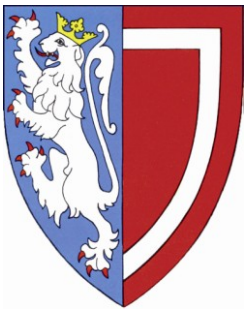

Balliol College

February 2014

The work presented in this thesis was carried out between January 2011 and February 2014, under the supervision of Professor. Andrew S. Weller. All of the work is my own unless otherwise indicated, and has not been submitted for any other degree at this or any other university.

Sebastian D. Pike

February 2014

ACKNOWLEDGEMENTS

I would like to thank Prof. Andrew Weller for being a fantastic supervisor throughout my DPhil. As well as giving me the opportunity to study in his research group, Andy has been incredibly supportive and helpful. Thanks also for the road-trips to Durham and St. Andrews, the many wonderful PV dinners and the sunny/rainy research days out!

The support and camaraderie of the other members of the Weller group has been spectacular during my time in the lab. In particular I would like to thank Dr. Adrian Chaplin for imposing "the ABC way" on all lab techniques, and also for his love of pink drinks, fondue and pouting; to Dr. Romaeo Dallanegra (Maeo) for running around and sorting just about everything in the lab and of course for his inspiring chest-hair and amaretto addiction; to Dr. Becky Pawley (Bex) and Dr. Laura Sewell (Sgt. Lozz) for the all the hugs, loving mockery and wonderful trips to the U.C.; to Indrek Pernik(s?), the pumpman himself, for his lunging techniques, turtle-necks, suspect undergarments and love of Sash & Enrique, but also his awesome friendship over the last 3 years; and to Heather Johnson (Hevs) for keeping all the messy boys in order inside the lab and also for trying to get into the Purple Turtle with a nectar card. Massive thanks also go to Dr. Miguel Huertos and to Dr. Rowan Young for all of the beers and for letting me sleep on the sofa during a fantastic conference in Lisbon. Thanks to Amit Kumar/no. 9 for his wonderful cooking and never-ending smile, and to Dr. Mark Chadwick for enduring one of the longest weekends in history with me at the Diamond light source and proof-reading my mega-chapter. Thanks to Dr. Tom Hooper for his round-about maneuvering, to Dr. Peng Ren for Chinese night and to all the Weller-group post-docs for their help and advice over the course of my project. I would also like to thank my two Part II students for being great fun to work with; to Mark Scott for being wonderfully laid-back and yet remarkably successful and to Gemma Adams for putting up with me being a useless supervisor whilst writing my thesis and for organizing a fun night at Magdalen. Thanks also to all the other part II students (Will – for his exhibitionism, Georgie – for keeping calm in a crisis, Molly – for always looking on the bright side of life, Tim – for absorbing hug attacks, Becky – for an excellent Christmas quiz, Rosie – for doing all of the sports & Lucy – for keeping me smiling during write-up) and to Dr. Amparo Prades, and Dr. Kiwi-Mike Jones who have brought so many fun moments to the group. Thanks to all of you who proof-read my thesis – I owe you all cake!

For X-ray Crystallography assistance and the 'Red Kite' conferences many thanks to Dr. Amber Thompson. For attempting to deal with horrendous crystallographic modulation gratitude goes to Dr Kirsten Christensen. For NMR advice (and disco tunes) thanks to Dr. Nick Rees. For SSNMR experiments huge thanks to the team at Durham (Dr. David Apperley and Fraser Markwell) and to lab-space donated by Dr. Phil Dyer and Prof. Paul Lowe, and assistance from Dr. Phil Schauer. For the powder X-ray crystallography experiment at Diamond additional thanks go to Dr. Michael Hart, Prof. Dermot O'Hare and Dr. Saul Moorhouse. Thanks also to Dr. Rob Jacobs for help and support with a range of experimental techniques including IR spectroscopy. Many thanks to our computational collaborators at Heriot-Watt university (Prof. Stuart Macgregor and Dr. Adrés Algarra).

Thanks go to Mr. Sharky, our inspirational group mascot, may he stay inflated for many years to come. I would also like to mention my toasted sandwich maker which has produced countless instant lunches essential for the writing-up process, and to Phil Collins for providing some sterling Friday afternoon entertainment.

I would like to thank all of my friends in Oxford for sharing the DPhil experience and wish them all well for the future.

I would finally like to thank my parents for wonderful, continual support and to Aoife for feeding me and putting up with grumpy, sleepy Seb during the write up process!

ABBREVIATIONS

Ar	Aryl	m/z	Mass to Charge Ratio
Ar^{Cl}	3,5-$C_6H_3Cl_2$	Me	Methyl
Ar^{F}	3,5-$C_6H_3(CF_3)_2$	MOF	Metal Organic Framework
BINAP	2,2'-bis(diphenylphosphino)-1,1'-binaphthyl	NBA	Norbornane
		NBD	Norbornadiene
Bu	*n*-Butyl	NBE	Norbornene
Cat.	Catalyst	NHC	*N*-heterocyclic carbene
COD	1,5-Cyclooctadiene	NMR	Nuclear Magnetic Resonance
Cp	Cyclopentadienyl	oep	Octaethylporphyrinato Dianion
Cp*	$[C_5Me_5]^-$	Ph	Phenyl
Cy	Cyclohexyl	PM RAIRS	Polarisation Modulation Reflection-Absorption Infrared Spectroscopy
Cyp	Cyclopentyl		
δ	Chemical Shift	PNC	Phthalocyanine-Derivative
d	Diameter	POCOP	1,3-[OP{$C_6H_2(CF_3)_3$-2,4,6}$_2$]$_2C_6H_3$
$dobdc^{4-}$	2,5-dioxido-1,4-benzenedicarboxylate	R	Alkyl
		σ-CAM	σ-Complex Assisted Metathesis
DPEPhos	Bis(2-diphenylphosphino-phenyl)ether	SC-SC	Single Crystal to Single Crystal
		SIPr	N,N'-(2,6-$^{i}Pr_2C_6H_3)_2C_3H_4N_2$
δν	Difference in Resonance Frequencies	SSNMR	Solid-State Nuclear Magnetic Resonance
ESI-MS	Electrospray Ionisation Mass Spectrometry	$t_{½}$	Half Life
		^{t}Bu	*tert*-Butyl
Et	Ethyl	TPP	Tetraphenylporphyrin
EXAFS	Extended X-Ray Absorption Fine Structure	triphos	Bis(diphenylphosphinoethyl) phenylphosphine
FWHM	Full Width Half Maximum	triphos*	1,1,1-tris(diphenylphosphino-methyl)ethane
^{i}Bu	*iso*-Butyl		
^{i}Pr	*iso*-Propyl	UV	Ultraviolet
IR	Infrared	WCA	Weakly Coordinating Anion
K_{eq}	Equilibrium constant	Xantphos	4,5-Bis(diphenylphosphino) -9,9-dimethylxanthene
KIE	Kinetic Isotope Effect		
M	mol dm^{-3}		

THESIS KEY

All chemical shifts (δ) are quoted in ppm. Data described within the text are enclosed in square brackets. Deuterated compounds labelled with d-. New compounds labelled **1-46**, previously reported compounds labelled in roman numerals.

Yellow, Amber, Orange, Vermilion, Red, Claret.

ABSTRACT

This thesis describes the synthesis and characterisation of a series of cationic rhodium *bis*-phosphine complexes. The reactivity of these new complexes in the solid-state and in solution is reported.

In **Chapter 2** the synthesis of a series of rhodium *bis*-phosphine diene complexes is presented and the reactions of these complexes with hydrogen in the solid-state are investigated. Several examples of zwitterionic complexes coordinating the $[BAr^F_4]^-$ anion are produced by hydrogenation. A rare example of a σ-alkane complex, $[Rh(^iBu_2PCH_2CH_2P^iBu_2)(\eta^2_{CH}\eta^2_{CH}\text{-NBA}][BAr^F_4]$, is also formed in the solid-state, by a single crystal to single crystal transition driven by hydrogen. This complex is crystallographically characterised and displays two short Rh···H−C σ-interactions. Deuteration studies indicate that the agostic complex $[Rh(^iBu_2PCH_2CH_2P^iBu_2)(\eta^2_{CC}\eta^2_{CH}\text{-NBE}][BAr^F_4]$ may form as a short lived intermediate prior to the formation of the σ-alkane complex. The temporal evolution of the solid-state hydrogenation reactions is monitored by powder X-ray diffraction methods.

In **Chapter 3** the C−X activation of various aryl halides using the $[Rh(^iBu_2PCH_2CH_2P^iBu_2)]^+$ fragment is reported. The 'ligand innocence' of the phosphine with respect to intramolecular C−H activation is also discussed. A rare example of C−X activation in the solid-state is presented, which shows the formation of an isomer that is not observed by analogous solution routes.

Chapter 4 investigates solid-state ligand exchange reactions using ethene, butadiene, CO and NH_3 gases. A solid-state transfer dehydrogenation reaction is reported within single crystals of $[Rh(^iBu_2PCH_2CH_2P^iBu_2)(C_2H_4)_2][BAr^F_4]$. H/D exchange of NH_3 can also occur in the solid state in the *bis*-ammonia complex $[Rh(^iBu_2PCH_2CH_2P^iBu_2)(NH_3)_2][BAr^F_4]$. A variety of rhodium complexes are tested as heterogeneous catalysts for the hydrogenation of ethene and the isomerisation of butene.

In **Chapter 5** the binding affinity of a variety of fluorinated arenes to rhodium *bis*-phosphine fragments is presented using ESI-MS methods. The dependence upon the arene substituents, phosphine substituents and phosphine bite angle are discussed.

CONTENTS

CHAPTER 1
INTRODUCTION

1.1. Overview

Organometallic chemistry is a well-documented area of research with a large variety of practical applications. Organometallic compounds are commonly used as catalysts for the production of commodity chemicals and polymers and also in natural product synthesis.[1, 2] The vast majority of research in the area has been undertaken in the solution phase, with studies in the solid-state often reserved only for structural analysis {e.g. X-ray crystallography and to a lesser extent solid-state nuclear magnetic resonance spectroscopy (SSNMR)}. In contrast to solution phase studies the catalytic abilities of organometallic compounds in the solid phase have been only briefly investigated.[3-6]

> *"Catalysis, involving organometallic complexes in the solid-state, is however an unexplored area of chemistry."* 1998 N. J Coville and L Cheng.[4]

In the 16 years since this review, only a few contributions have been added to this field, these will be discussed in detail later in the chapter.[6, 7]

Heterogeneous catalysis using the surfaces of metals or ionic platform materials is also a well researched area of chemistry with many industrial uses.[8-10] However the mechanism of the binding, catalytic steps and product release may be multifarious or difficult to understand when using such an extended material. There may also be a limited number of 'active sites' for catalysis.[11] In contrast, homogeneous catalysis tends to be a more defined process in which the mechanistic pathway can be more readily probed, and often utilises a single active metal centre which can be tuned with regard to reactivity by surrounding ligands.[1, 12] The greater degree of control using a single site catalyst can also allow for stereoselective or regiospecific reactivity to occur.[13, 14]

The active site of a heterogeneous catalyst may be mimicked by a well-defined homogeneous analogue. Study of such an analogue may allow further elucidation of the mechanistic pathways involved in reactivity. An example of such a process was the development of highly active selective

catalysts for the polymerisation of alkenes pioneered by Ziegler and Natta. Initially heterogeneous systems were employed using $TiCl_3$ crystallites with Et_2AlCl; this inspired the design of single site homogeneous catalysts using Group 4 metals with which the microstructure of a polymer could be carefully controlled.[2]

A more recent example of complementary homogeneous and heterogeneous research involves the study of molybdenum catalysts which can produce hydrogen from water. Nanoparticulate MoS_2 is an inexpensive solid material active for the electrochemical and photochemical generation of hydrogen from water.[11, 15, 16] It has been proposed that the active sites exist upon the edge of the nanoparticles, although the exact structure of these sites is not known. Long, Chang and co-workers have developed a homogeneous single site mimic for these edge sites, MoS_2(2,6-*bis*(1,1-*bis*(2-pyridyl)ethyl)pyridine), in which the triangular arrangement of the Mo-S_2 interaction is very similar to that found in the extended lattice of MoS_2 [Figure 1.1].[12] This molecular complex is active for the electrochemical generation of hydrogen from water and allows controlled investigation into the properties of the system. This is a good example of how heterogeneous catalysts inspire the design of single site homogeneous catalysts, which in turn lead to better understanding of the heterogeneous system.

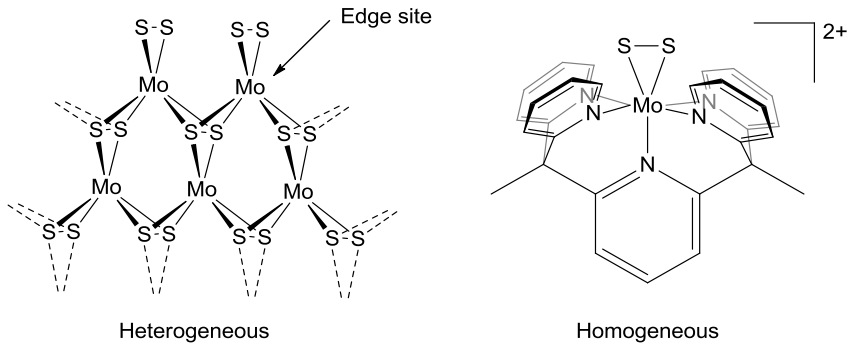

Figure 1.1. A heterogeneous catalyst and its molecular homogeneous mimic for use in catalytic electrochemical hydrogen production from water.

The use of discreet organometallic complexes in the solid-state as heterogeneous catalysts is an undeveloped field.[3, 4, 6] In theory, if using reagents in the gas phase, or dissolved in a solution that will not solvate the organometallic species, "heterogeneous" reactivity can occur. This could still incorporate the high degrees of selectivity and mechanistic control associated with single site "homogeneous" catalysis whilst using a solid-state catalyst. A further advantage of solid-state catalysis is the simple separation of products from catalyst, which may be important in the synthesis

of pharmaceutical products or in recycling expensive catalysts.[17, 18] Furthermore, working in solvent-free environments is considered environmentally friendly.

In addition, such a methodology potentially allows for the study of organometallic species in highly inert environments without the complications of unwanted reactivity with a solvent. Solid-state reactivity could allow for the isolation of otherwise unstable complexes, such as reactive intermediates.[19, 20]

In this thesis organometallic reactivity in the solid-state is investigated, in particular the reaction of complexes with gases such as H_2, ethene, NH_3 and CO. The isolation of highly unstable intermediates can be achieved (σ-alkane complexes) [Chapter 2] and simple catalytic processes are possible [Chapter 4]. Intramolecular rearrangements are also featured, including C–X activation [Chapter 3] and transfer dehydrocoupling [Chapter 4]. In addition comparative studies in the solution phase are reported. Furthermore the binding affinities of η^6-arene complexes, which are common throughout this thesis, are investigated by ESI-MS (electro-spray ionisation mass spectrometry) in the gas phase [Chapter 5].

1.2. Cationic Rhodium Phosphine Complexes

1.2.i. Rhodium in Organometallic Chemistry

Rhodium is used extensively in organometallic chemistry (as well as in motor-vehicle catalytic converters) despite its scarcity {and therefore its high price (~$1040 / troy ounce)[21]}. Due to its location in the periodic table it is ideal for catalytic processes: it has variable oxidation states (+1 and +3 are common); and can form stable 16 electron, square planar, neutral or cationic complexes capable of oxidative addition (*i.e.* bond activation). As a late transition metal it only requires a small number of ligands to reach electronic saturation, therefore steric crowding is unlikely to hinder reactivity. Importantly it is a second row transition metal, which tend to form intermediary strength bonds, allowing both capture and release of reagents in catalytic processes.[2] The lack of common paramagnetic oxidation states and its ability to form stable cationic species make it an attractive transition metal for research purposes since NMR spectroscopy and ESI Mass Spectrometry can be used for characterisation.

Perhaps the most famous example of a rhodium catalyst is Wilkinson's catalyst, $Rh(PPh_3)_3Cl$, which catalyses the hydrogenation of alkenes. The general mechanism involves dissociation of one PPh_3 ligand to form a low valent 14 electron complex with a 'vacant site', allowing subsequent oxidative addition of hydrogen; coordination and insertion of alkene; and reductive elimination of the desired alkane [Scheme 1.1].[1, 22]

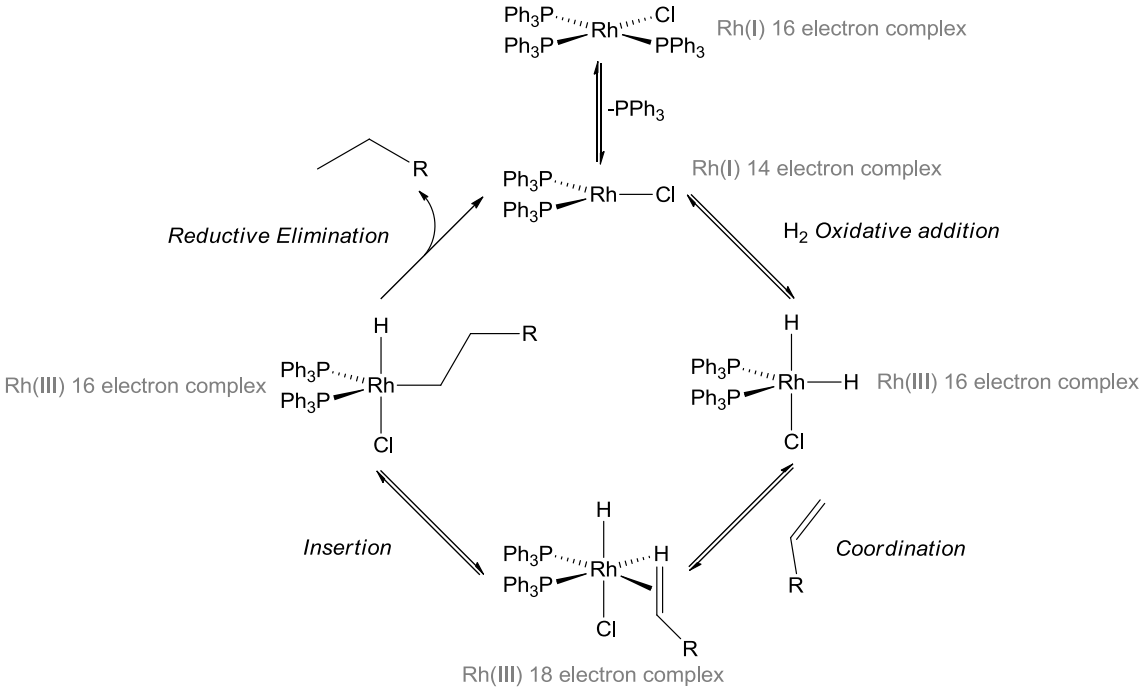

Scheme 1.1. Catalytic cycle for alkene hydrogenation using Wilkinson's catalyst.

The use of specific phosphines to determine both the steric and electronic environment of a rhodium catalyst has since been developed. The hydroformylation process which combines an alkene with CO and H_2 gases to form an aldehyde may form linear or branched products.[1] Studies found that using rhodium catalysts with chelating phosphines which exhibited wide bite angles (P-Rh-P angle, *vide infra*) could promote the production of the favoured linear product [Figure 1.2].[23]

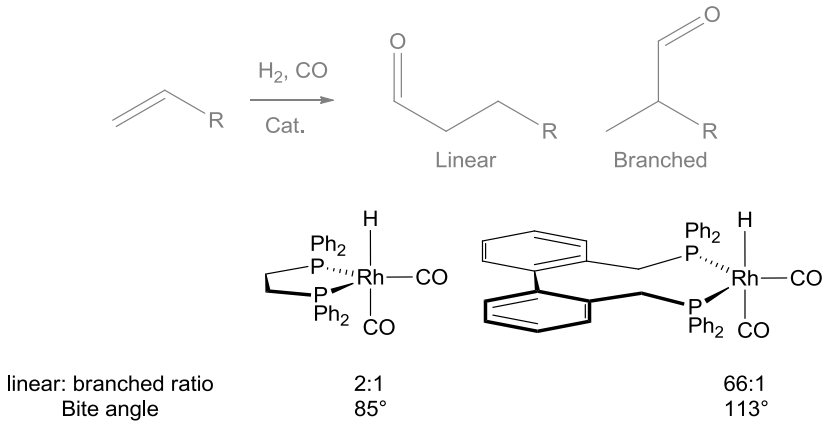

Figure 1.2. Catalysts used for hydroformylation with different phosphines. The P-Rh-P bite angle influences the selectivity of the reaction. General hydroformylation reaction shown in grey.

Catalysts can also be designed to influence the stereochemistry of the products they form. Noyori developed a {Rh(BINAP)} based catalyst for asymmetric amine isomerisation which allows an industrial synthesis of menthol (single enantiomer), one of the world's most utilised natural products, used in a wide variety of applications from toothpaste to pharmaceuticals [Scheme 1.2]. [24, 25]

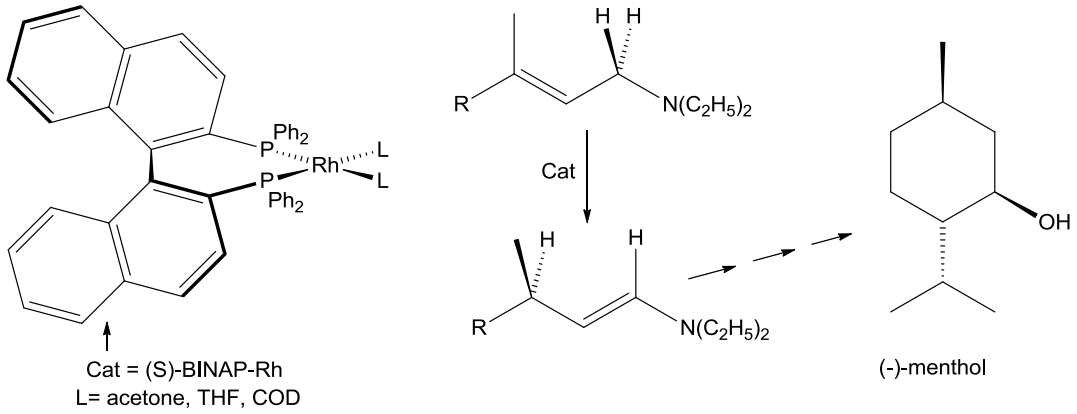

Scheme 1.2. Noyori's BINAP catalyst used for asymmetric amine isomerisation used in menthol synthesis.

1.2.ii. Phosphine Ligands

Rhodium phosphine complexes are used as catalysts in many different reactions - along with the aforementioned examples of hydrogenation and hydroformylation many other important transformations are promoted such as hydrosilation and hydroaminomethylation.[1, 26-30] Tertiary phosphines (PR_3) are useful two electron donors for formation of transition metal complexes. They

generally bind quite strongly, although monodentate phosphines can reversibly dissociate (as in Wilkinson's complex).[2, 22] As well as electronically stabilising a metal centre they also create a steric scaffold around the metal, allowing selective binding of different substrates. Phosphines are both σ-donors (P lone pair) and π-acceptors (P–C σ*) which allows a strong synergic interaction with a transition metal [Figure 1.3]. The amount of back bonding depends on the nature of the substituents (R) and has been directly measured by comparison of the IR stretching frequencies of CO bonds in $Ni(CO)_3(PR_3)$, where steric differences have little importance.[31] This study shows that alkyl substituents allow the least back bonding, whilst more electron withdrawing substituents such as arenes or OR groups allow for greater donation into the σ* bond. This effect is due to the position of the σ* orbital which becomes lower in energy and more accessible to the metal donor orbitals when more electronegative substituents are used.

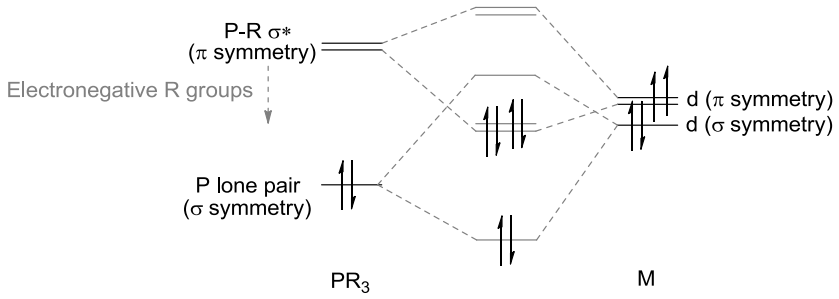

Figure 1.3. Simplified molecular diagram for the interaction of a phosphine with a transition metal.

The steric profile of a phosphine can be defined by a "cone angle" proposed by Tolman.[31] A cone encapsulating the metal and the entire phosphine (with a defined M−P bond length of 2.28 Å) can be used to compare the sterics of different phospines within the vicintiy of the metal centre [Figure 1.4].

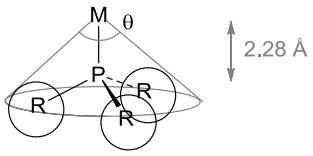

Figure 1.4. Tolman cone angle of a phosphine.

Nolan also introduced the concept of percent buried volume which describes the amount of a defined sphere surrounding the metal centre which is occupied by a ligand. This is particularly useful for

rationalising the steric effects of bulky *N*-heterocyclic carbene (NHC) ligands (which can act as alternatives to phosphine ligands).[32]

Chelating phosphines are commonly used and coordinate strongly, and typically irreversibly to a metal centre (due to the chelate effect). Bidentate, tridentate and tetradentate coordination modes are known.[2, 33, 34] Chelation supports a metal centre in a defined manner which may be advantageous for catalysis as long as the generation of a vacant site is not required. A tridentate phosphine complex (triphos)RhCl (triphos = $(Ph_2PCH_2CH_2)_2PPh$), which is an analogue of Wilkinson's catalyst, is not effective as a hydrogenation catalyst [Scheme 1.3]. Dissociation of one phosphorus donor is suppressed, due to the entropic and enthalpic advantages of the ligand binding strength through the chelate effect.[31, 35]

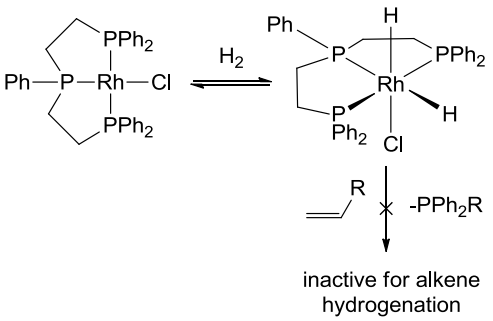

Scheme 1.3. Inactive catalyst for alkene hydrogenation due to its strongly bound chelating phosphine.

The length of the backbone connecting two phosphorus donors affects the 'bite angle' (θ) of the ligand which has a strong effect upon the electronics of an interaction with a metal centre [Figure 1.5].

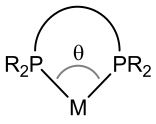

Figure 1.5. Bite angle (θ) of a chelating phosphine.

Small bite angle ($\theta \leq 90°$) chelating ligands have been shown to be both active and selective in catalysis.[36-39] In comparison to monodentate phosphines, they allow greater control of the available mechanistic pathways due to the locked *cis* positioning of the phosphines and also the lower probability of phosphine de-coordination. Chelating small bite angle bidentate phosphines with rhodium have a precedent for not forming stable dihydride species in monomeric $\{RhP_2\}^+$ species.[40, 41]

This may be explained by the ease of reductive elimination of H_2 from such species, which is related to bite angle. Dubois, Labinger, Bercaw and co-workers directly investigated the equilibrium between a range of $[RhP_2H_2]^+$ complexes (P_2 = bidentate phosphine) and their reductive elimination products, $[RhP_2]^+$. They found that chelating phosphines with large bite angles, small cone angles and electron donating substituents favoured the Rh(III) state (*i.e.* reductive elimination is disfavoured), with bite angle being the dominant factor [Scheme 1.4].[42] Tetrahedral distortion from a square-planar geometry is caused by large bite angles. This affects the molecular orbital overlap between the metal fragment and incoming H_2 such that the metal σ-acceptor orbital in RhP_2 drops in energy and the π-donor orbitals raise in energy. This favours oxidative addition of hydrogen, whilst in contrast small bite angles favour the square planar Rh(I) complex.

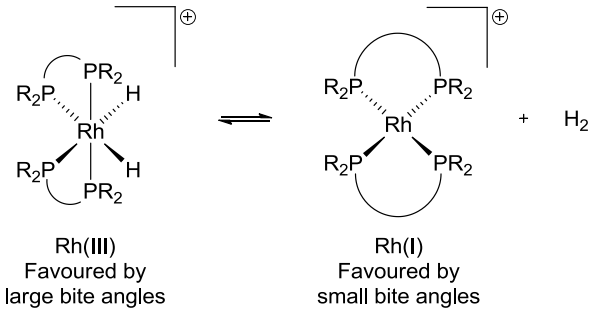

Scheme 1.4. Oxidative addition and reductive elimination of H_2 to $[RhP_2]^+$ in equilibrium. Oxidative addition favoured by large bite angles.

1.2.iii. Weakly Coordinating Anions

Cationic transition metal complexes tend to have more contracted metal d-orbitals and this can allow for greater control in reactivity - by avoiding unwanted oxidative addition with solvents such as CH_2Cl_2 for example.[43, 44] In order to use cationic species, non-coordinating anions are essential in order to make coordinatively unsaturated species. Whilst anions such as $[BF_4]^-$,[45] $[BPh_4]^-$,[46, 47] $[CF_3SO_3]^-$ [45] and $[PF_6]^-$ [45] are commonly used, all have been shown to be coordinating or reactive with low coordinate cationic partners.[48] In attempts to reduce their coordinating ability, complex anions have been designed such that the negative charge is delocalised across a large non nucleophilic and chemically inert area. Commonly used weakly coordinating anions are based upon $[BAr_4]^-$, $[Al(OR)_4]^-$ or carborane $[CB_{11}R'_{12}]^-$ structures (Ar = aryl, R = (fluoro)alkyl, R' = H, alkyl, halogen).

Borate anions such as $[BAr^F_4]^-$ (Ar^F = 3,5-$(CF_3)C_6H_3$) and $[B(C_6F_5)_4]^-$ are considered to be some of the best weakly coordinating anions with the fluorinated aryl groups reducing the coordinating ability of the arene rings.[49] However it is suggested that in $[BAr^F_4]^-$ steric crowding has a large part to play in the coordinating ability, as small cations can still coordinate to the arene ring. In fact, the arene ring has been observed to coordinate through η^3 and η^4 interactions to $[AgL_2]^+$ (L_2 = $C_6H_4I_2$ or 2,2'-bipy) and by η^6 interactions to cationic Rh and Ir complexes, such as $Rh(\eta^2\eta^2\text{-COD})\{\eta^6\text{-}Ar^F(BAr^F_3)\}$, $Rh\{P(Cyp_2)(\eta^2\text{-}C_5H_7)\}\{\eta^6\text{-}Ar^F(BAr^F_3)\}$ and $Ir(H)_2(PCyp_3)\{\eta^6\text{-}Ar^F(BAr^F_3)\}$ [Figure 1.6].[50-52]

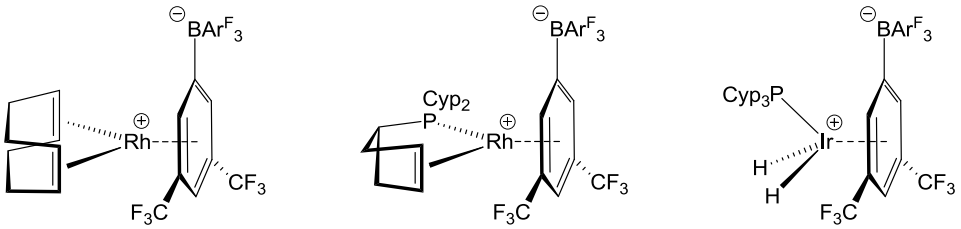

Figure 1.6. Examples of η^6 coordination of $[BAr^F_4]^-$ to $[RhL_2]^+$ and $[Ir(H)_2L]^+$ (L = phosphine or alkene) cations to form zwitterions.

Bulky borate anions are particularly suitable for stabilising 14 or 16 electron fragments because coordination in a formally η^2 or η^4 manner (as a 2 or 4 electron donor) is disfavoured. These coordination modes require the bending of bulky CF_3 groups away from their favoured in plane geometry.

Coordination of the $[B(C_6F_5)_4]^-$ anion is rare, but crystallographically characterised examples show M–F interactions with early transition metals or lanthanides e.g. $(Cp^*)_2Ti(\kappa^2_F\text{-}C_6F_5)B(C_6F_5)_3$ [Figure 1.7].[53]

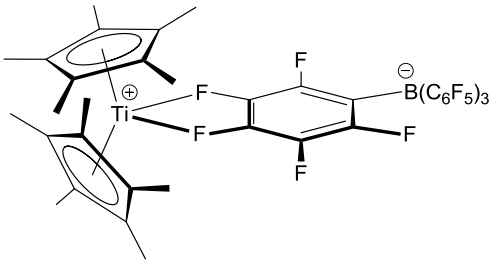

Figure 1.7. M–F coordination of $[B(C_6F_5)_4]^-$.

An alternative anion is $[BAr^{Cl}_4]^-$ (Ar^{Cl} = 3,5-$C_6Cl_2H_3$), which although more coordinating than $[BAr^{F}_4]^-$, often allows the formation of crystalline material suitable for X-ray diffraction analysis, which may otherwise prove problematic with $[BAr^{F}_4]^-$.[54-56]

Carborane anions such as $[CB_{11}H_{12}]^-$ are weakly coordinating, and partial halogenation to form $[CB_{11}H_6X_6]^-$ (X = Cl, Br) reduces their coordinating ability and increases their resistance to oxidation.[57, 58] The chlorinated carborane $[CB_{11}H_6Cl_6]^-$ [Figure 1.8] and its methylated analogue [1-H-$CB_{11}Me_5Cl_6]^-$ are considered to be two of the very weakest coordinating anions and have been used in conjuction with electrophilic cations such as $[SiR_3]^+$ and $[C_{60}]^+$; however, synthesis of the chlorinated carboranes can be challenging. The extremely non-nucleophilic [1-R-$CB_{11}F_{11}]^-$ (R= Me, Et) is thought to be the least coordinating of the carborane anions.[48, 59]

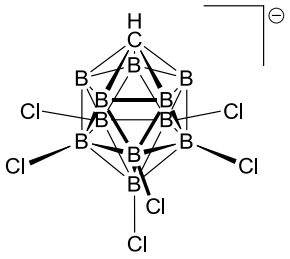

Figure 1.8. Weakly coordinating carborane anion $[CB_{11}H_6Cl_6]^-$.

The "Krossing anions" $[Al(OR^F)_4]^-$ {R^F = $CH(CF_3)_2$, $CMe(CF_3)_2$ and $C(CF_3)_2$} are stable, weakly coordinating anions [Figure 1.9].[60] Analysis of the coordination environments of Ag^+ cations in various solvents of crystallisation showed that $[Al(OC(CF_3)_3)_4]^-$ is at least as non coordinating as $[CB_{11}H_6Cl_6]^-$. The Ag^+ cations coordinate to the solvent ($C_2H_4Cl_2$) preferentially unless a very poorly coordinating solvent is chosen (such as 1,3-$C_6H_4(CF_3)_2$).[60]

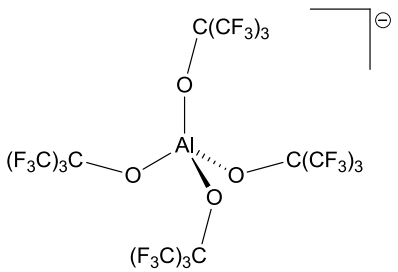

Figure 1.9. The weakly coordinating perfluorinated "Krossing anion".

A study into the relative coordinating abilities of $[BAr^F_4]^-$ and $[CB_{11}H_6Br_6]^-$ was undertaken by Weller and co-workers with the low coordinate $[Rh\{PCyp_2(\eta^2\text{-}C_5H_7)\}]^+$ (Cyp = C_5H_9) fragment.[51] The $[BAr^F_4]^-$ anion coordinates to the metal in an η^6 manner whilst the carborane coordinates in a κ^3 manner through three bromine atoms [Scheme 1.5]. $[NBu_4][BAr^F_4]$ was added to the carborane bound complex $Rh\{PCyp_2(\eta^2\text{-}C_5H_7)\}(\eta^3\text{-}CB_{11}H_6Br_6)$ and an equilibrium between the two anion bound rhodium complexes was established. This equilibrium was measured at different temperatures to establish the thermodynamics of the anion exchange by a van't Hoff plot. These data revealed that although the $[BAr^F_4]^-$ anion enthalpically binds more strongly than the carborane, its relative binding is entropically disfavoured. The entropy term is dominant at room temperature and so the carborane complex is observed as the major species. The chlorinated carborane $[CB_{11}H_6Cl_6]^-$ would not displace $[BAr^F_4]^-$ in the same system indicating its lesser coordinating ability.

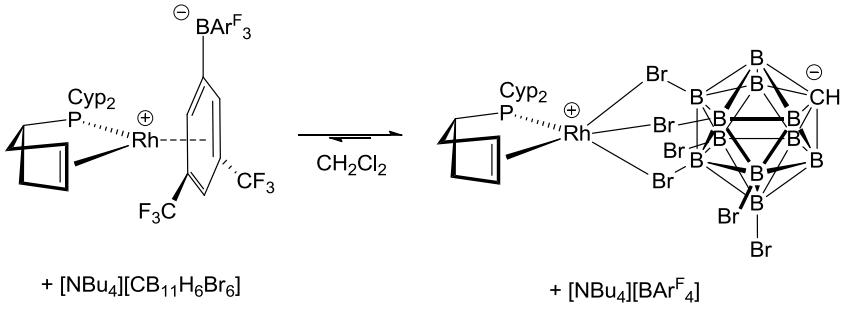

Scheme 1.5. Equilibrium between coordinated anion zwitterion complexes.

1.2.iv. Low Coordinate Complexes

Coordinatively unsaturated species are potentially highly reactive and are often proposed in catalytic cycles.[37, 61] Putative 'vacant sites' are often stabilised by weak interactions of various types. Coordinated solvent complexes often occur when acetone, acetonitrile or other coordinating solvents are used, although these can be highly fluxional in solution, constantly exchanging with other solvent molecules and allowing access to a transient 'vacant site'.[62] Similar effects can be seen by using a hemilabile ligand, e.g. DPEphos in which a pendant coordinating group can stabilise the metal centre but move away on the approach of an appropriate substrate.[63] When no lone pair or π interactions (e.g. C=C, arene) are possible, a metal may become stabilised by a σ-interaction - commonly this is a C–H agostic interaction.[64] Agostic interactions are often weak, demonstrated by the coupling constants of

the *trans* ligand to metal centre (if spin active, e.g. $^{31}P/^{103}Rh$),[65] and so can be thought of as 'vacant site'-like. True vacant sites are often stabilised by bulky ligands but may be difficult to experimentally confirm, especially when proposed in solution.[66, 67] Once a coordinatively unsaturated species has been prepared it will be highly reactive and care must be taken in its design so that it will not react with itself, for example by C–H activation - although this can be rapid and reversible leading to a 'masked vacant site'.[68] Activation or coordination of the counter-ion commonly occurs to yield a more stable species which is less reactive.[51, 69] Alternatively, dehydrogenation of an alkyl substituent can occur, yielding a C=C π bond which can coordinate to the metal.[70] Weller and co-workers have recently developed the $[Rh(P^iBu_3)_2][BAr^F_4]$ system; which although at first appears to be a 12 electron complex, is believed to exist with two delta agostic interactions from the ^{i}Bu groups (or anion interactions) in the solid-state. Whilst in solution (CH_2Cl_2), it is suggested that weak solvent or agostic interactions are likely.[64] This highly active species will even coordinate 1,2-$C_2H_4Cl_2$ (a poorly coordinating solvent) to form $[Rh(P^iBu_3)_2(\kappa^2_{Cl,Cl}\text{-}1,2\text{-}C_2H_4Cl_2)][BAr^F_4]$ [Scheme 1.6].[64]

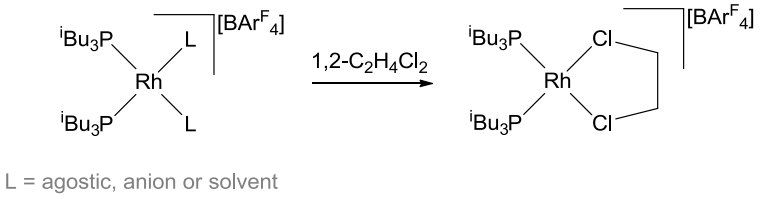

Scheme 1.6. A low coordinate complex likely to be stabilised by agostic interactions reacts to form an adduct with a poorly coordinating solvent 1,2-$C_2H_4Cl_2$.

C–H activation of agostically coordinated ^{i}Bu groups has been reported, resulting in a cyclometallated product. An example of this is the reductive elimination of C_6H_5OMe from $[Rh(P^iBu_3)(o\text{-}C_6H_4OMe)Br][BAr^F_4]$ *via* a σ-CAM mechanism [71] involving C–H activation of an agostic ^{i}Bu group [Scheme 1.7].[69] This lack of 'ligand innocence' is an unfortunate by-product of dealing with highly active species and should normally be avoided in order to design long-lived catalysts. It is noteworthy that other similar systems using P^iPr_3, PCy_3 and $PCyp_3$ all show similar or greater ligand-metal intramolecular reactivity than the P^iBu_3 system mentioned.[44, 52, 72, 73]

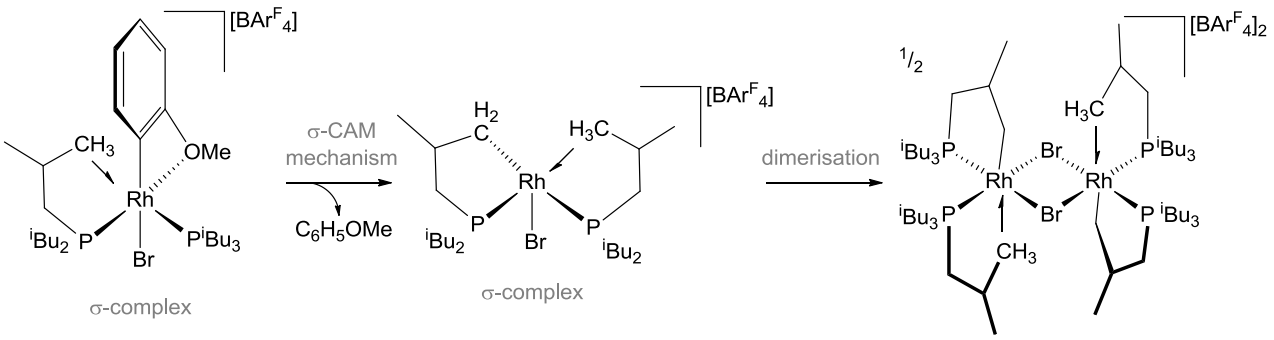

Scheme 1.7. Example of intramolecular ligand reactivity *via* C–H activation of ^{i}Bu group.[69]

Crystallographic examples of vacant sites have been reported, these include 14 electron complexes of cobalt, rhodium and iridium utilising bulky ligands to stabilise the 'vacant site' [Figure 1.10].[74-78]

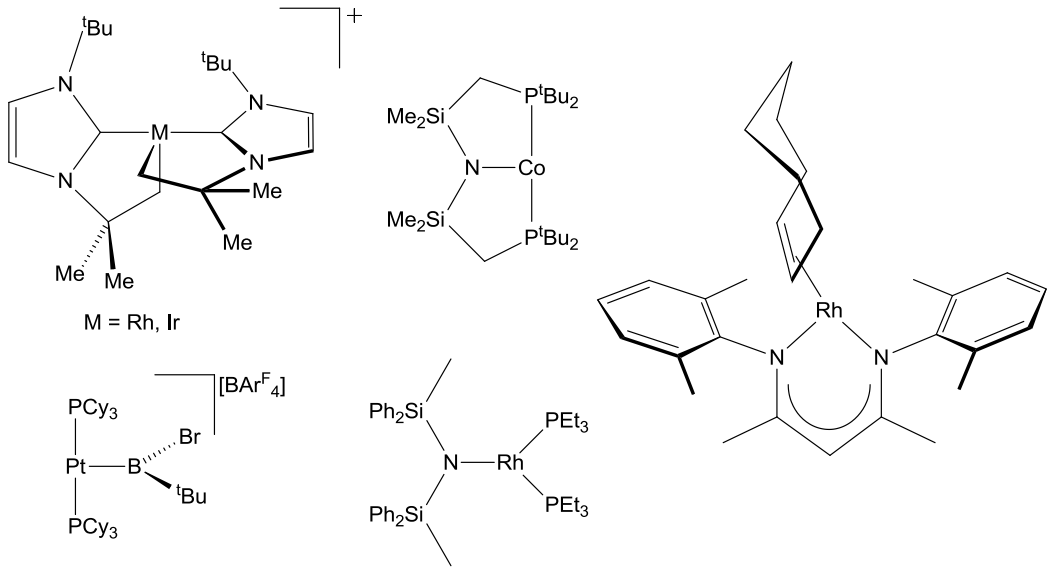

Figure 1.10. Crystallographic examples of cationic and neutral 14 electron complexes displaying a 'vacant site'.

By tuning complexes to become coordinatively unsaturated, perhaps by *in situ* generation of 'vacant sites' in the solid-state, reactive species could be synthesised which may show catalytic activity.[37, 61]

1.3. Solid-State Reactivity of Organometallic Complexes

1.3.i. Overview

A variety of organometallic reactions have been studied in the solid-state. The first examples originate in the 1960s when the oxidative addition of HCl gas to Vaska's complex, $IrCl(CO)(PPh_3)_2$, was observed in the solid-state to give a single isomeric product, (*trans*-chloro)-$Ir(H)Cl_2(CO)(PPh_3)$.[79] For reactivity to occur in the solid-state the reagents must be able to penetrate the solid structure and access the metal sites; this suggests that porosity within the extended solid structure will aid reaction.[6, 80] The idea of a "reaction cavity" was pioneered by Cohen and Schmidt, who proposed that reactions in the solid-state occur with the least amount of molecular movement possible.[81] There is, however, good evidence of limited molecular movement within the solid-state from X-ray diffraction studies, in particular the rotation of CH_3, CF_3 and C_5H_5 groups.[82] The constrained environments within a solid structure open up the possibilities of added reaction selectivity, potentially different from that observed in solution. For example, if a reaction cavity could be designed to be chiral then asymmetric reactivity may also be possible.[83] As solid-state reactions take place the products will replace the reagents. This generally occurs from the surface downwards, and Kaupp has proposed the idea of "phase rebuilding" where reaction direction is determined by crystallographic faces, and lattice reconstruction occurs over thousands of angstroms at a time.[84]

1.3.ii. Stoichiometric Reactions

Isomerisation reactions of organometallic complexes have been reported in the solid-state including racemisation (by thermal or photochemical excitation), ligand isomerisation, coordination isomerisation (at 4, 5, 6 and 7 coordinate complexes) and ligand linkage reactions (to create dimers or polymers).[4, 85, 86]

Decomposition reactions such as ligand dissociation, reductive elimination and decarbonylation reactions have also been studied with solid-state organometallic complexes [Scheme 1.8].[4, 87, 88]

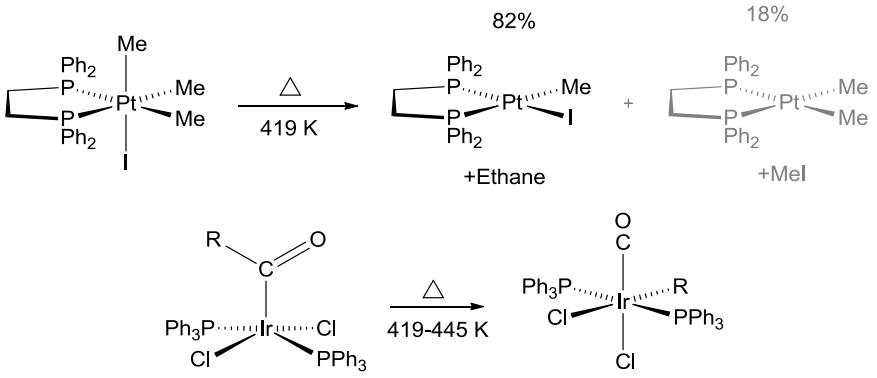

Scheme 1.8. Examples of reductive elimination and decarbonylation in solid-state complexes.

Stoichiometric reactions with gaseous reagents were extensively studied by Bianchini in the 1990s including the displacement of N_2 from [{κ^4-P($C_2H_4PPh_2)_3$}Co(N_2)][BPh_4] by various gases [Scheme 1.9].[89] It is proposed that small gaseous reagents can penetrate the crystal lattice of $[BPh_4]^-$ anions by dissolving in the hydrophobic regions formed by the tetraphos ligand backbone and anion phenyl groups.

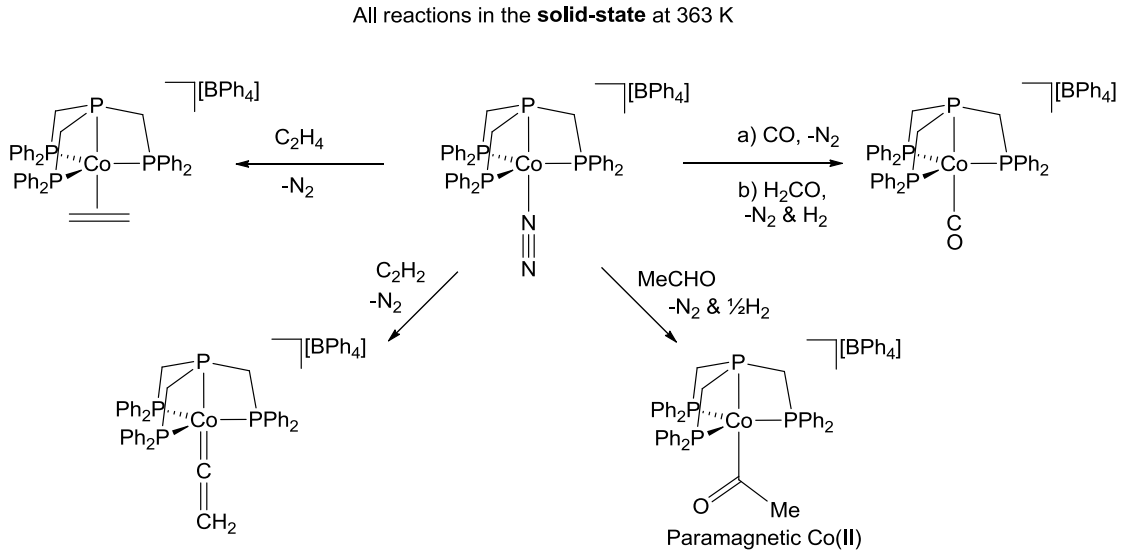

Scheme 1.9. Solid-state gas exchange reactions reported by Bianchini and co-workers

Oxidative addition of gases (HF, HCl, HBr, HI and H_2S) to Vaska type complexes ($IrX(CO)(PPh_3)_2$) (X = Cl, Br, I, SCN) have been reported alongside the reaction of I_2 to $Pt(acac)_2$.[4, 90]

Brammer and co-workers have shown the reaction of *trans*-[$CuCl_2$(n-Xpy)$_2$] (n=3,4 X=Cl,Br) with HCl gas to form (n-XpyH)$_2$[CuCl4] which requires breaking of two Cu−N bonds to form Cu−Cl

bonds and N−H bonds.[91-93] These reactions have been monitored by powder diffraction, displaying that microcrystalline products are formed. An in-situ powder diffraction study monitoring the progress of the gas-solid reaction and a subsequent phase change in the product {(4-ClpyH)$_2$[CuCl4] in this case} has been carried out at a synchrotron facility.[91]

Direct adduct formation with gases is common, sometimes with ligand displacement. Werner and co-workers report the addition of gases to chloride bridged dimer complexes indicating that dimeric species can be split apart in the solid phase [Scheme 1.10].[94]

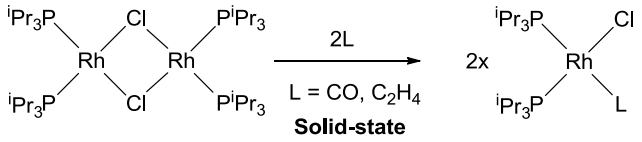

Scheme 1.10. Direct addition of gases to break up a dimeric complex.

The reversible addition of CO_2 to the rhodium and iridium complexes M(OH)(CO)(PPh_3)$_2$ was reported by Vaska and co-workers, although the nature of the M···CO_2 interaction was unclear.[95]

Aerobic oxidation of Cp*Co(^{i}PrIm)(CO) (^{i}PrIm = 1,3-di-isopropyl-imidazolin-2-ylidene) to form a carbonato complex Cp*Co(^{i}PrIm)($\kappa^2_{O,O}$-CO_3) was reported by Radius and co-workers This process occurs rapidly with air, both in solution and in the solid phase [Scheme 1.11].[96]

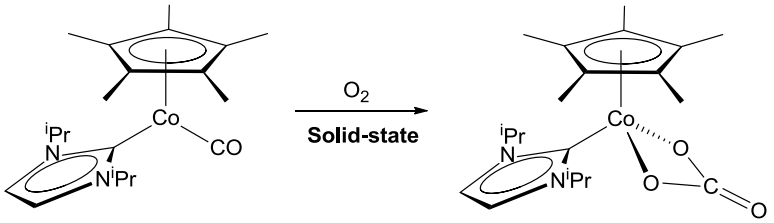

Scheme 1.11. Aerobic oxidation of a carbonyl complex to a carbonato complex.

Addition of olefins to a metal complex may result in olefin oligomerisation. In fact, Bianchini has shown that addition of C_2H_2 to Ir(triphos*)(C_2H_4)(H_2) {triphos* = (Ph_2PCH_2)$_3$$CCH_3$} leads to various products, including benzene and butadiene complexes [Scheme 1.12].[97, 98] Siedle and co-workers have shown trimerisation of C_2H_2 with [Ir(PPh_3)$_2$$H_2$]$_3$[$PW_{12}O_{40}$] forming a benzene complex, whilst C–H activation of propene with the same starting material forms an allyl complex [Scheme 1.12].[5]

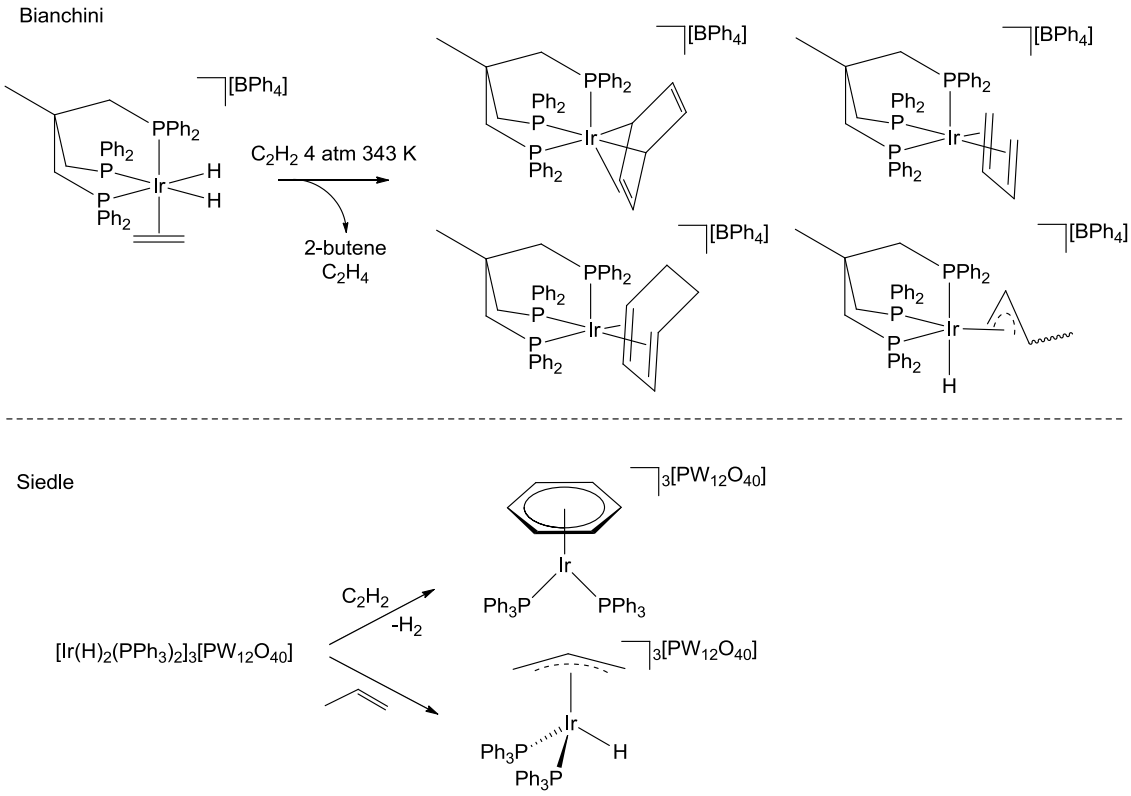

Scheme 1.12. Reaction of solid-state cationic iridium complexes with ethyne causes various C–C couplings. The C–H activation of propene to an iridium complex to form an iridium–allyl complex is also shown.

Reversible hydrogen addition to metal complexes warrants interest in the field of hydrogen storage materials. Weller and co-workers have reported the reversible addition of three molecules of hydrogen to $[(Ph_2PCH_2CH_2PPh_2)Rh\{\kappa^2_{P,C=C}PCyp_2(\eta^2\text{-}C_5H_7)\}][BAr^F_4]$ to form $[(Ph_2PCH_2CH_2PPh_2)Rh(PCyp_3)(H)_2(H_2)][BAr^F_4]$. In the solid phase the product loses two molecules of hydrogen under vacuum to form a red intermediate proposed to be $[(Ph_2PCH_2CH_2PPh_2)Rh(PCyp_3)][BAr^F_4]$, in which an agostic interaction is likely. This red intermediate then slowly loses H_2 to reform $[(Ph_2PCH_2CH_2PPh_2)Rh(\kappa^2_{P,C=C}PCyp_2(\eta^2\text{-}C_5H_7)][BAr^F_4]$. In solution, no red intermediate is seen, although decoordination of the dihydrogen ligand is observed initially before subsequent hydrogen loss [Scheme 1.13]. This system shows the possibility of catching intermediates in the solid phase, which would react or rearrange in the more mobile solution phase.

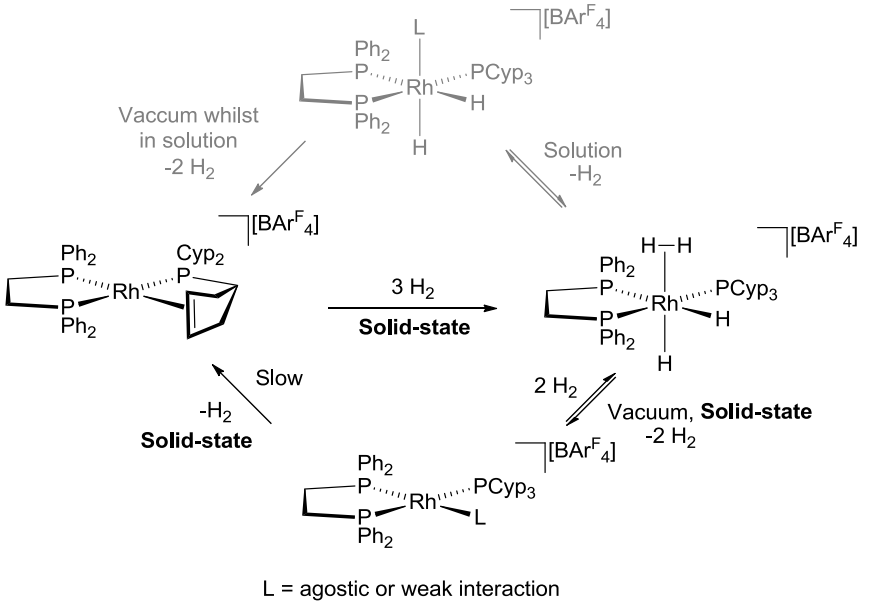

Scheme 1.13. Reversible addition of hydrogen to a rhodium complex in solution and the solid-state. A different intermediate upon hydrogen loss is identified in the solid-state reaction to the solution route.

Other examples of differing reactivity in solution and the solid-state have also been reported.[94, 99] Werner and co-workers display the formation of a monocarbonyl species in the solid-state by reaction with CO gas, whereas a dicarbonyl will form in the analogous solution phase reaction [Scheme 1.14].[94]

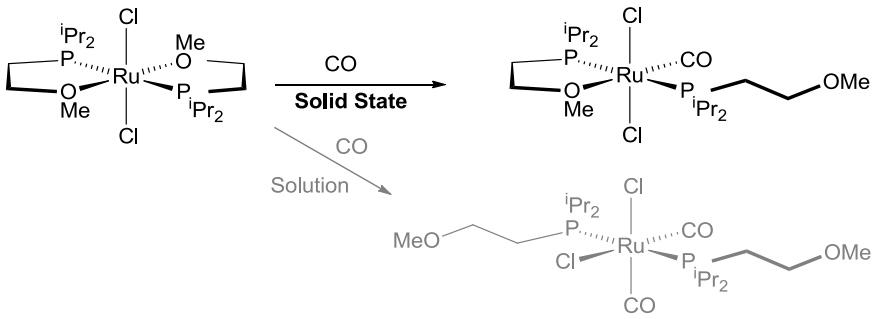

Scheme 1.14. Formation of a monocarbonyl complex in the solid phase whilst a dicarbonyl forms in solution.

The kinetics of solid-state reactions have proved difficult to measure due to their inherent complexity; as the reaction may take place at different rates upon the surface and within the interior of a crystalline material. Caulton and co-workers investigated the rates of addition of gases (CO, O_2, H_2, Cl_2, C_2H_2) to $Ru(CO)_2(P^tBu_2Me)_2$ and found that the fastest reactivity occurred when the product was most different in size or shape to the starting material. This suggests that changing molecular shape

induces strain in a crystalline material which will then undergo micro-cracking. Cracks will expose more of the interior of the crystal to the gaseous reagent and increase reaction rate. When little change in shape occurs the crystals may become "passivated" by a surface layer of the product, slowing further reactivity.

1.3.iii. Single Crystal to Single Crystal Transitions

A single crystal to single crystal (SC-SC) transition is one in which crystallinity is retained throughout a reaction, allowing the product to be characterised directly by single crystal X-ray crystallography.[7] For crystallinity to be retained, a very small structural reorganisation is required to avoid crystal cracking. It is also likely that crystal size will affect reaction time in SC-SC transitions (because of the surface area : volume ratio). Techniques to enable such transitions involve using bulky ligands or anions which may create a rigid porous structure in which smaller movements are possible.[6, 100]

SC-SC reactions present the best possibilities for added selectivity within a solid-state pocket, as the reaction cavity must remain well defined. The ability for selective catalysis using single crystals is discussed later (*Section 1.3.vi*).

If gaseous reagents require access to the interior of the crystal then empty or partially filled channels throughout the lattice may be necessary.[80] This is suggested by Brookhart and co-workers, who observe channels of disordered toluene throughout the crystalline lattice of (POCOP)IrL (POCOP = 1,3-[OP{$C_6H_2(CF_3)_3$-2,4,6}$_2$]$_2C_6H_3$, L = N_2, CO, NH_3, C_2H_4, $(H_2)(H)_2$, O_2).[6] They reported a series of SC-SC gas transfer reactions using this system [Scheme 1.15, Table 1.1-entry A]. Interestingly, the precursor (L = N_2) is stable under vacuum but readily reacts with more strongly binding gases, which suggests that an associative mechanism for gas exchange is operating within the interior of the crystal.

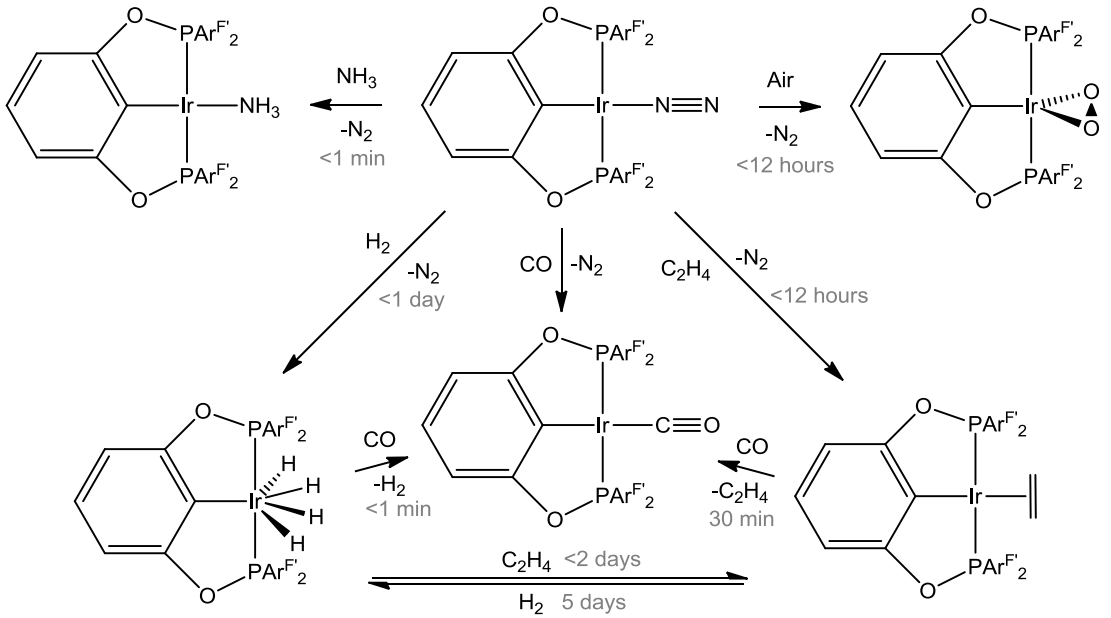

Scheme 1.15. Gas transfer SC-SC transitions. $Ar^{F'} = 2,4,6\text{-}C_6H_2(CF_3)_3$, all reactions at 298 K and 1-1.5 atm reagent gas, reaction time written in grey.

SC-SC transitions may be reversible. Van Koten and co-workers report the reversible addition of SO_2 to (NCN)PtCl (NCN = $C_6H_2(OH)\text{-}5(CH_2NMe_2)_2\text{-}1,3$). They proposed that this material could be used as a gas-triggered switch, with SO_2 uptake signalled either by colour change or by crystal expansion [Table1.1-entry B].[101]

SC-SC transitions may also be sequential. Crudden and co-workers present a double SC-SC gas exchange reaction using the (SIPr)RhCl(L) system (SIPr=N,N'-(2,6-$^{i}Pr_2C_6H_3)_2C_3H_4N_2$, L=$N_2$, O_2 or CO) [Scheme 1.16, Table1.1-entry C]. Firstly N_2 is replaced with O_2, and then O_2 is replaced with CO, without crystal degradation at either stage.[100]

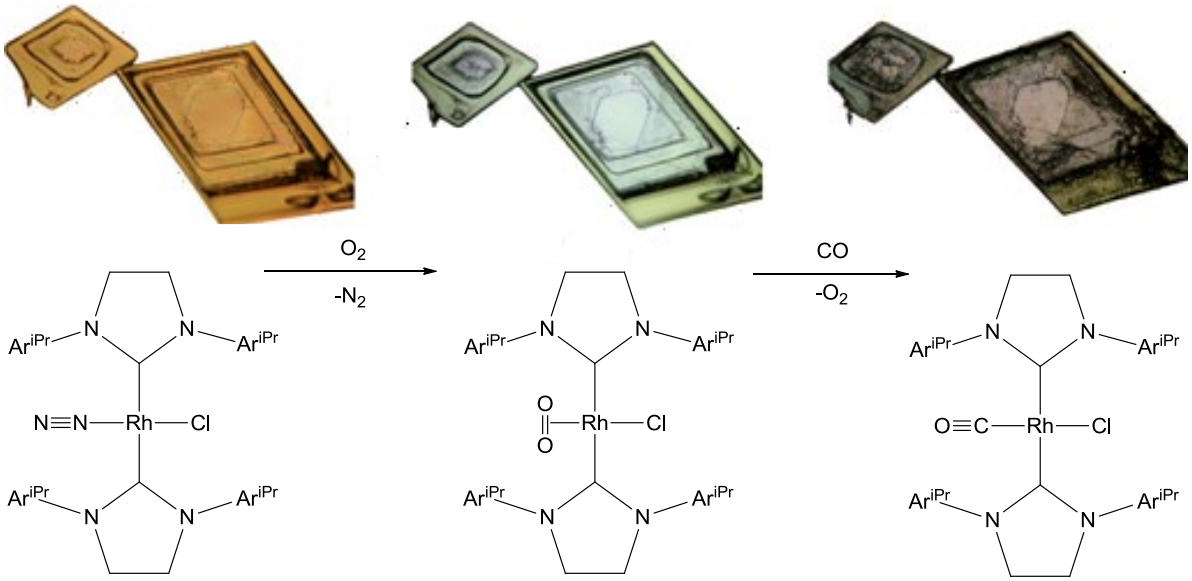

Scheme 1.16. Sequential SC-SC gas transfer transitions (Ar^{iPr} = 2,6-$^{i}Pr_2C_6H_3$).
Photograph reproduced from: John Wiley and Sons, Angewandte Chemie International Edition, Double Single-Crystal-to-Single-Crystal Transformation and Small-Molecule Activation in Rhodium NHC Complexes (License Number: 3306990921808).[100]

SC-SC transitions can also take place in a suspension of non-solvating liquid. McKeown and co-workers present SC-SC transitions upon $Fe(MeOH)_2$(phthalocyanine-derivative). Large interconnected voids (8 nm^3) run through this structure which allow liquid penetration, and the two complexed axial ligands can be reversibly displaced by the suspension medium (methanol, acetone or water) [Figure 1.11, Table1.1-entry D].[80]

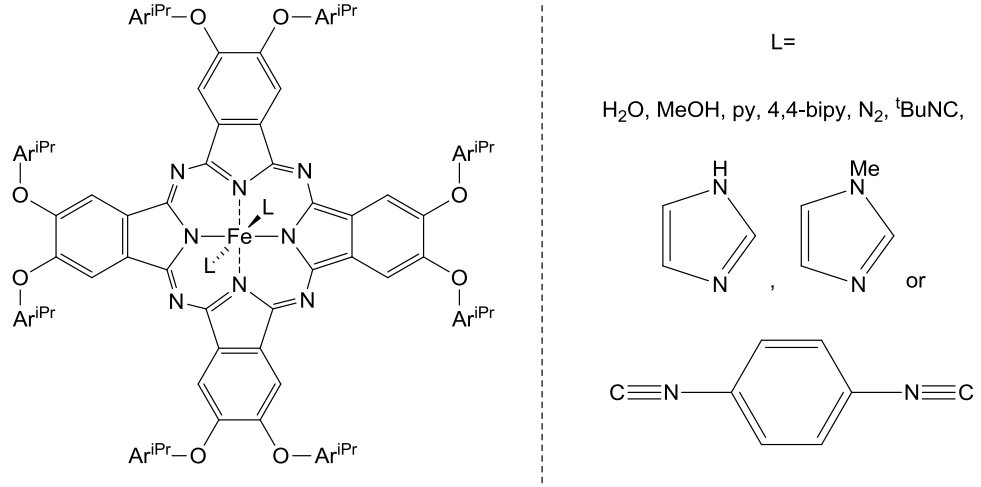

Figure 1.11. Porous phthalocyanine derivative complex (PNC[*c*L-Fe-*v*L]) which can undergo SC-SC ligand (L) exchanges as a solid immersed in organic solvents. (Ar^{iPr} = 2,6-$^{i}Pr_2C_6H_3$).

In the absence of added reagents, SC-SC transitions can occur in the form of a phase change. Balch and co-workers report a reversible phase change when acetone or dichloromethane vapour is passed over a crystal of β-$Au_2(\mu\text{-}Ph_2PCH_2CH_2PPh_2)_2I_2.(OCMe)_2$, even though no additional solvent incorporation is observed. The reverse reaction occurs if the crystal is left in air [Scheme 1.17, Table1.1-entry E].[102]

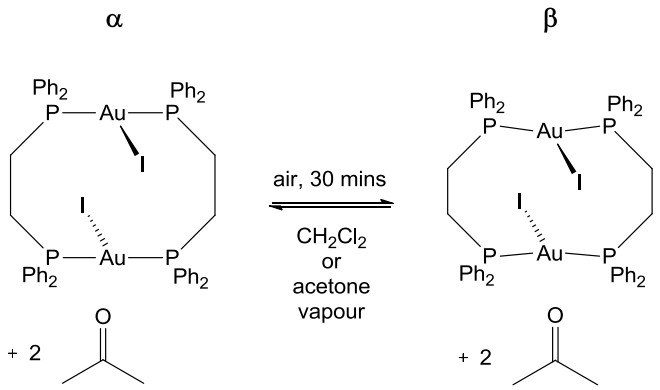

Scheme 1.17. Phase change SC-SC transition driven by drying in air and reversible by exposure to CH_2Cl_2 or acetone vapour. Au···Au distances: α; 3.6720(2) Å, β; 3.3955(2) Å.

Brill and Rheingold showed that the dimerisation of $CpCo(S_2C_6H_4)$ in the single crystal phase at room temperature could be reversed into a monomeric species upon warming to 423 K whilst still maintaining crystallinity [Scheme 1.18, Table1.1-entry F].[86] The dimeric species is thermodynamically favoured in the crystalline lattice at room temperature [computationally calculated $\Delta H_{(\text{dimerisation, 423-433 K})} = -18.9$ kJ/mol] but the monomer is thermodynamically favoured in solution, presumably due to a dominant entropy term.

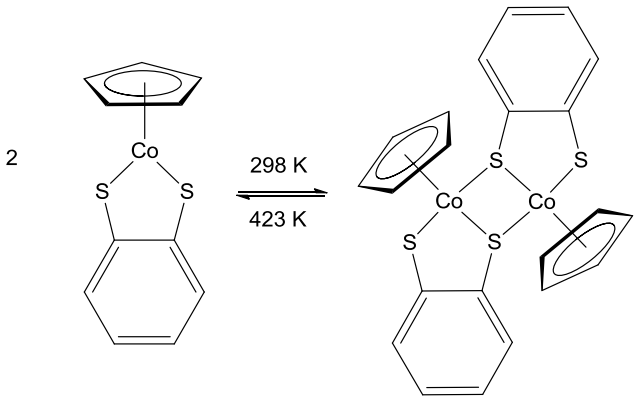

Scheme 1.18. Reversible dimerisation in a single crystal.

SC-SC reactions present possibilities for directly forming reactive complexes which may not be stable in solution. Addo and co-workers were able to crystallographically characterise biologically important porphyrin complexes which bind NO. Examples include (TPP)Fe(NO)(OC(=O)CF_3),[19] [(TPP)Fe(NO)(H_2O)][(TPP)Fe(H_2O)][OC(=O)CF_3]$_2$ [103] (TPP = tetraphenylporphyrin) and [(oep)Fe(NO)(S-2,6-($CF_3CONH)_2C_6H_3$)] [104] (oep = octaethylporphyrinato dianion) [Table1.1-entry G]. These complexes were formed by addition of NO gas to the unsaturated precursors in the solid-state. This transformation was not possible using solution crystallisation methods, as in solution a mixture of by-products form instead [Scheme 1.19].[19, 103, 104]

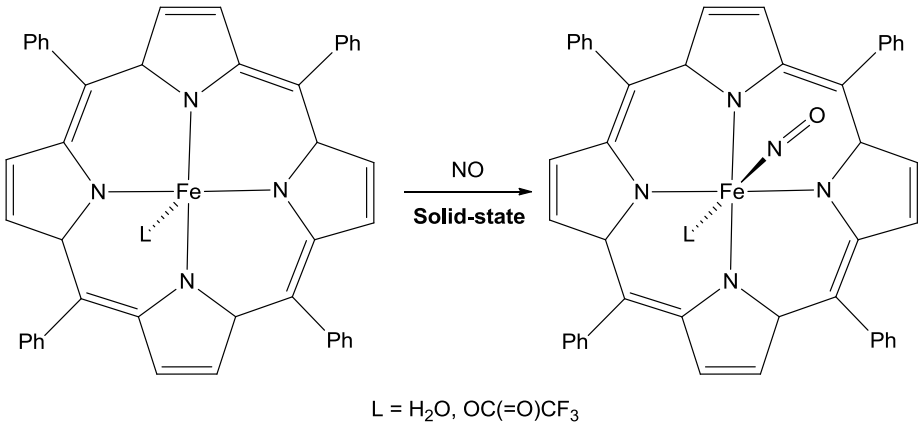

Scheme 1.19. Formation of biologically important (NO)-Fe-porphyrin complexes by SC-SC transitions.

Minimal structural changes are required to allow SC-SC transitions, with most examples showing less than 4% volume change (see Table 1.1). Examples of SC-SC transitions are displayed below with their respective crystallographic volume change (z = 1 equivalent) [Table 1.1]. McKeown and co-workers' large phthalocyanine-derivative complexes display large expansions when a bidentate ligand such as 4,4-bipy or CN(C_4H_6)NC displaces ^{t}BuNC and bridges two metal sites, but these transitions still amount to small percentage volume changes. Van Koten and co-workers' example of SO_2 uptake is exceptional because it involves a very large percentage volume change (15.7%) with expansion predominantly along one axis.

Entry *& corresponding author*	**Starting Complex Space Group, Volume (Å^3), (*z*)**	**Product Space Group, Volume (Å^3), (*z*)**	**Change in Volume (Å^3) *(and Percentage Change).* For *z = 1* Equivalent**
A *Brookhart*[6]	(POCOP)Ir(N_2) *P* −1, 3002.11(14), (*z = 2*)	(POCOP)Ir(O_2) *P* −1, 3046.3(10), (*z= 2*)	+22 *(+1.4%)*
		(POCOP)Ir(CO) *P* −1, 3000.1(2), (*z = 2*)	−1 *(−0.06%)*
		(POCOP)Ir(C_2H_4) *P* −1, 3020.6(2), (*z = 2*)	+9 *(+0.6%)*
		(POCOP)Ir($H)_2(H_2$) *P* −1, 2986.6(4), (*z = 2*)	−8 *(−0.6%)*
		(POCOP)Ir(NH_3) *P* −1, 3003.56(19), (*z = 2*)	+1 *(+0.04%)*
B *Van Koten*[101]	(NCN)PtCl *P* na2_1, 1346.0(4), (*z = 4*)	(NCN)PtCl(SO_2) *P* na2_1, 1557.5(4), (*z = 4*)	+53 *(+15.7%)* (contraction along **a** expansion along **c**)
C *Crudden*[100]	(SIPr)RhCl(N_2) *P* 2_12_12, 2855.15(8), (*z = 2*)	(SIPr)RhCl(O_2) *P* 2_12_12, 2852.13(12), (*z = 2*)	−3 *(−0.1%)*
	(SIPr)RhCl(O_2) *P* 2_12_12, 2852.13(12), (*z = 2*)	(SIPr)RhCl(CO) *P* 2_12_12, 2861.5(3), (*z = 2*)	+9 *(+0.4%)*
D *McKeown*[80]	PNC[*c*^{t}BuNC-Fe-*v*^{t}BuNC] *P* n-3n, 52348.5(7), (z=12)	PNC[*c*^{t}BuNC-Fe-*v*(py)$_{0.7}$(^{t}BuNC)$_{0.3}$] *P* n−3n, 52736(2), (z=12)	+32 *(+0.7%)*
		PNC[*c*MeOH-Fe-*v*Me($C_3N_2H_3$)] *P* n−3n, 52819.6(12), (z=12)	+39 *(+0.8%)*
		PNC[*v*^{t}BuNC-Fe-*c*(4,4-bipy)-Fe-*v*^{t}BuNC)] *P* n−3n, 54263.4(5), (z=12)	+160 *(+3.7%)*
		PNC[*v*N_2-Fe-*c*CN(C_6H_4)NC-Fe-*v*N_2)] *P* n−3n, 53204(5), (z=12)	+71 *(+1.6%)*
E *Balch*[102]	α-Au_2(μ-$Ph_2PCH_2CH_2$-$PPh_2)_2I_2$.$(OCMe)_2$ *P* 2$_1$/c, 2824.28(13) (*z = 2*)	β-Au_2(μ-$Ph_2PCH_2CH_2PPh_2)_2I_2$.$(OCMe)_2$ *P* −1, 1411.99(7) (*z = 1*)	−0.2 *(~0%)* (change in space group)
F *Brill & Rheingold*[86]	CpCo($S_2C_6H_4$) *P* 2$_1$/c, 2159.1(6), (*z = 8*)	[CpCo($S_2C_6H_4$)]$_2$ *P* 2$_1$/c, 1031.2(3), (*z = 2 (dimer)*)	−12 *(−4.5%)* (for *z=1* monomer, *z*= ½ dimer)
G *Addo*[19, 103, 104]	(TPP)Fe{OC(=O)CF_3} *P* −1, 2093.1(3), (*z = 2*)	(TPP)Fe(NO){OC(=O)CF_3} *P* −1, 2144(3), (*z = 2*)	+25 *(+2.4%)*
	[(TPP)Fe(H_2O)][OC(=O)CF_3] *P* −1, 1833.4(3), (*z = 2*)	[(TPP)Fe(NO)(H_2O)][(TPP)Fe(H_2O)] [OC(=O)$CF_3]_2$ *P* −1, 3818.2(16), (*z = 2*)	+38 *(+4.1%)* (for *z=1* starting material, *z*= ½ product)
	[(oep)Fe{S-2,6-($CF_3CONH)_2C_6H_3$}] *P* −1, 2266.3(6), (*z = 2*)	[(oep)Fe(NO){S-2,6-($CF_3CONH)_2C_6H_3$}] *P* −1, 2360(2), (*z = 2*)	+47 *(+4.1%)*

Table 1.1. Examples of SC-SC transitions and the crystallographic volume changes involved.

1.3.iv. Surface Immobilised Organometallic Complexes

An alternative to solid-state organometallic chemistry is surface-supported organometallic chemistry, in which a heterogeneous material such as silica, zeolites or even MgO acts as a support to which the organometallic moiety is bound.[105-109] The metal species can be bound directly to the surface *via* oxide linkages ("surface organometallic chemistry"), or a linking ligand can connect the support to the metal ("supported homogeneous catalysis").[106] The support itself is likely to interact with the organometallic species, either directly by acting as a hemi-labile ligand; or by trapping of the other ligands, such as phosphines - this may in some cases be detrimental to catalysis. Silica supports contain surface silanol and siloxane moieties which can be used to bind metal fragments, however they may also change the mode of operation of the catalyst.[107] Copéret suggests that as a result of the amorphous nature of silica, metal sites can exist in different environments due to the number and type of neighbouring siloxane bridges.[110] The surface silanol groups can be passivated by treatment with hexamethyldisilazane, coating the surface with inert $SiMe_3$ groups.[107] Thieuleux, Copéret and co-workers have reported a detailed study into the ligating effects of a silica surface by binding a Grubbs style catalyst to the surface with two different linkers, one rigid and the other flexible.[111] They found that the flexible linker allowed the surface to act as a hemi-labile ligand, stabilising the active 14 electron catalytic species. The rigid linker prevents this surface coordination, and therefore after phosphine dissociation (which is irreversible because the phosphine then binds to other surface sites), the low coordinate 14 electron complex is susceptible to decomposition [Scheme 1.20].

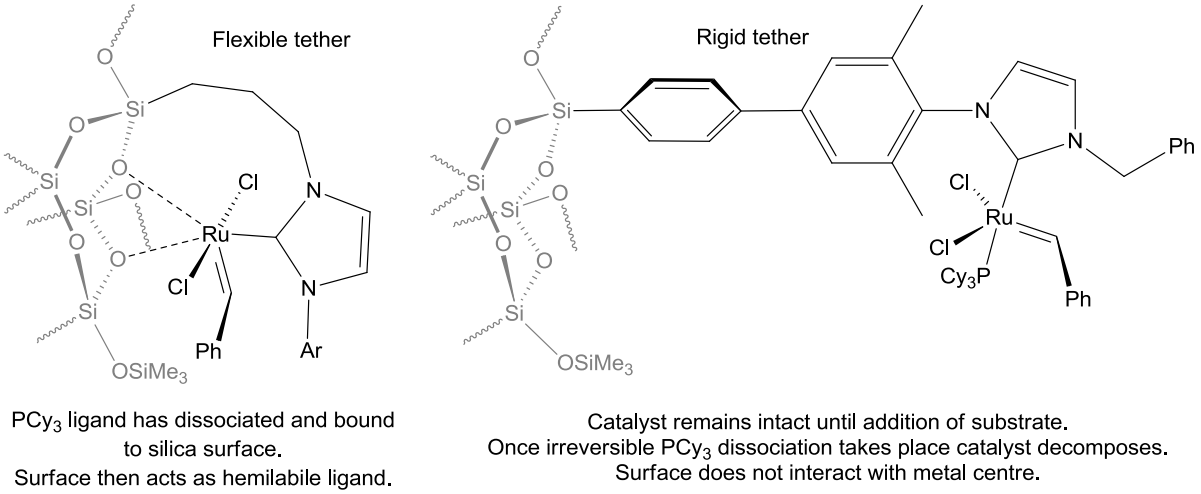

Scheme 1.20. Surface-supported Grubbs catalysts with flexible and rigid tethers.

As well as stabilising a catalyst, the surface may also act in a cooperative way by acting as an acidic site - this is suggested in the zeolite supported rhodium catalysed dimerisation of ethene reported by Gates and co-workers.[108]

Investigating the surface species can prove challenging and a number of methodologies have been employed including SSNMR, IR, EXAFS, and more specialised techniques such as dynamic nuclear polarisation surface enhanced NMR spectroscopy (DNP SENS), which can enhance the signal of surface species by one hundred fold.[111]

The concept of surface-supported catalysis within the cavities of porous materials has also been investigated, especially with the view of asymmetric synthesis [Figure 1.12].[112] Organometallic species have been attached inside porous silica structures in order to create an asymmetric reaction pocket. These structures have proved to be regioselective and enantioselective in allylic amination, hydrogenation and epoxidation reactions.[113]

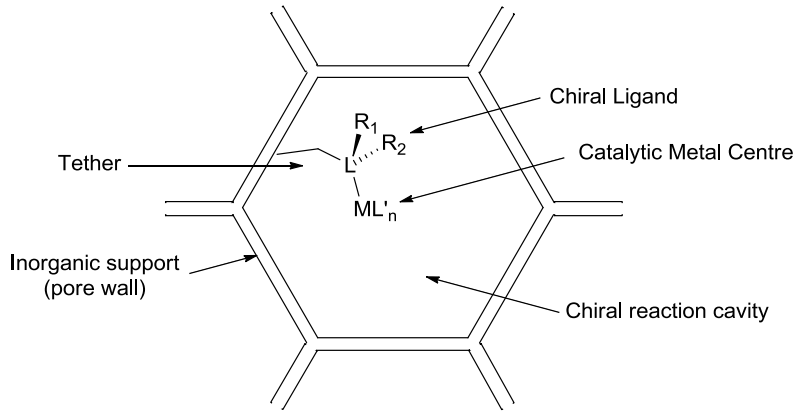

Figure 1.12. Representation of a chiral reaction cavity formed by connecting a chiral organometallic unit within a porous material.

1.3.v. Self Supported Transition Metal Catalysts

Along with the previously mentioned supported catalysts, recent efforts have been invested into the production of 'self supported' materials, including coordination polymers and metal organic frameworks (MOFs).[114]1-D, 2-D and 3-D metal-organic assemblies can be created - the metal atoms often act as the geometry enforcing linkage points, but are also envisaged as potential active sites for catalysis. It can be problematic to generate vacant sites around these metal centres, since the metal

will attempt to coordinate fully to the organic linkers in the formation of the structure. A further problem is the characterisation of the extended structure, which can sometimes be disordered or exist in varying forms. The advantages of such systems are their recyclability and the simple separation from reaction products. Recyclability is especially important for expensive chiral ligand systems and much interest lies in heterogenising organometallic fragments such as Ru-BINAP.[115, 116] Additional selectivity is also possible if the reaction takes place within porous materials, and several frameworks have been shown to act selectively only reacting with smaller reagents.[117, 118]

Early reports of self supported catalysts include the linkage polymers of $[RhCl(CO)(1,4\text{-}(CN)_2C_6H_4)]_n$ which would hydrogenate and isomerise 1-hexene by a heterogeneous mechanism, with no leaching of complexes into solution.[119] An active rhodium site was created by photolytic dissociation of the CO ligand. A similar system was formed with two bridging ligands per metal, enabling a well defined 3-D stacked layer structure to form. The surface and corner positions are likely to contain unsaturated metal centres which are catalytically active; however, the interior sites are proposed to be totally inactive.[120, 121]

Multidentate oxime, thio-urea, phosphine and NHC ligands have all been used to form frameworks with Pd for use in Suzuki-Miyaura C–C coupling reactions.[122-125] Karimi and co-workers report a coordination polymer of palladium with a linking bidentate NHC ligand, which is insoluble in water, allowing an environmentally-friendly, solvent-free C–C coupling reaction to take place [Scheme 1.21].[125] The authors utilise the mercury test, which probes for nanoparticle formation, and do not observe a loss in activity, however it is difficult to prove that nanoparticles are in no way involved for such systems.

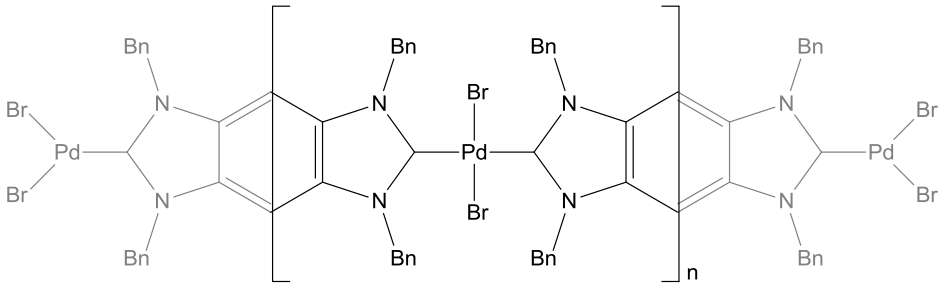

Scheme 1.21. A coordination polymer of Pd capable of catalysing heterogeneous Suzuki-Miyaura cross coupling in water.

More complex structures can also be formed with a mixture of metal sites. For instance copper, nickel or palladium porphyrin moieties can be included with rhodium-polycarboxylate linkages in which both metal sites may exhibit cooperative effects for hydrogenation reactions.[126, 127] The authors of this paper suggest the porphyrin group can bind the alkene whilst the rhodium will oxidatively cleave dihydrogen, and subsequent hydride transfer initates hydrogenation. Lin and co-workers produced a material based upon a chiral zirconium phosphonate structure with $(BINAP)Ru(Cl)_2(DPEN)_2$ (DPEN = 1,2-diphenylethylenediamine) incorporated.[128, 129] This can be used for heterogeneous enantioselective hydrogenation using methanol as the solvent. The precise structure of this material was not accurately determined [Figure 1.13].

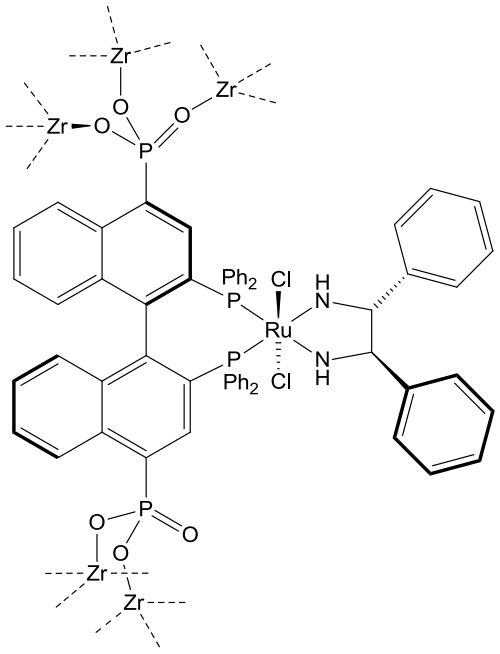

Figure 1.13. Self supported chiral catalyst for enantioselective hydrogenation reactions.

Ding and co-workers also report self-supported enantioselective catalysts for hydrogenation and sulfoxidation reactions.[130, 131] They report a continuous flow system using rhodium-phosphine incorporated frameworks, allowing highly efficient catalysis to operate over a long period of time.[115]

Kaskel and co-workers have recently reported the formation of a porous organometallic network based upon rhodium olefin coordination [Figure 1.14].[132] Whilst accurate structural determination has proved difficult, the framework appeared to be air-stable unlike its homogeneous analogue

$[Rh(NBD)_2][BF_4]$. The framework reacted with CO and also catalysed transfer hydrogenation reactions.

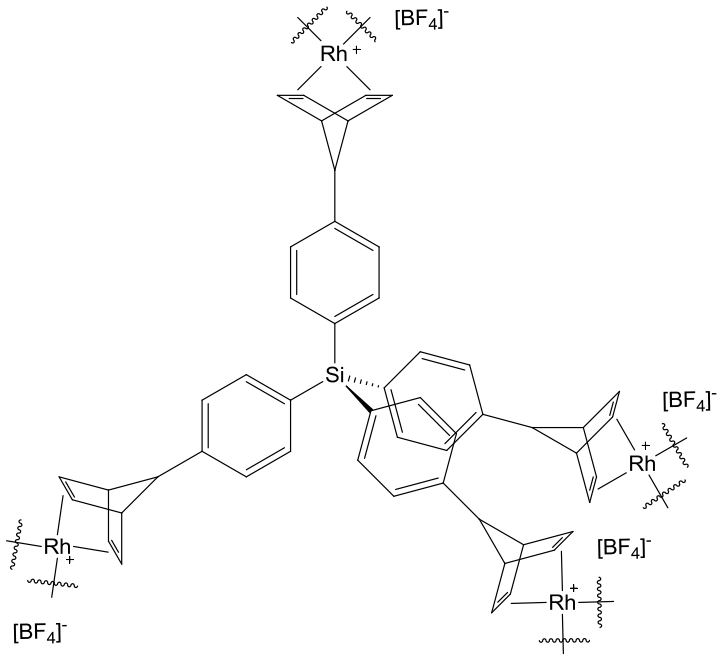

Figure 1.14. A representation of the structure of a porous organometallic framework based upon rhodium olefin coordination.

1.3.vi. Solid-State Organometallic Catalysis

Solid-state catalysis using organometallic complexes is a relatively undeveloped field. Bianchini and co-workers introduced the concept with simple ethene hydrogenation reactions using $[(triphos^*)Ir(H)_2(C_2H_4)][BPh_4]$ at 343 K.[3] The catalyst was active in the solid-state, presumably *via* hydride migration to form an $Ir–(C_2H_5)$ species which can react with H_2 to eliminate ethane. A flow reaction setup was constructed allowing the products to be analysed by GCMS. In solution the same species was not catalytically active because a dimeric bridging hydride species could rapidly form in the presence of H_2 and this was inactive for further reactions [Scheme 1.22]. In fact, some of the inactive dimeric species is also formed in the solid-state reaction (but appears to form at a slower rate than in solution), the amount of which increases with temperature. This highlights the ability of the solid-state to maintain reactive species by playing a role in protecting them from deactivation pathways that require structural reorganisation. The $[BPh_4]^-$ anions create a hydrophobic lattice structure ideal for allowing the passage of small hydrocarbon gases, however, access to the metal

centres may require some phosphine movement which could account for the elevated temperatures required.

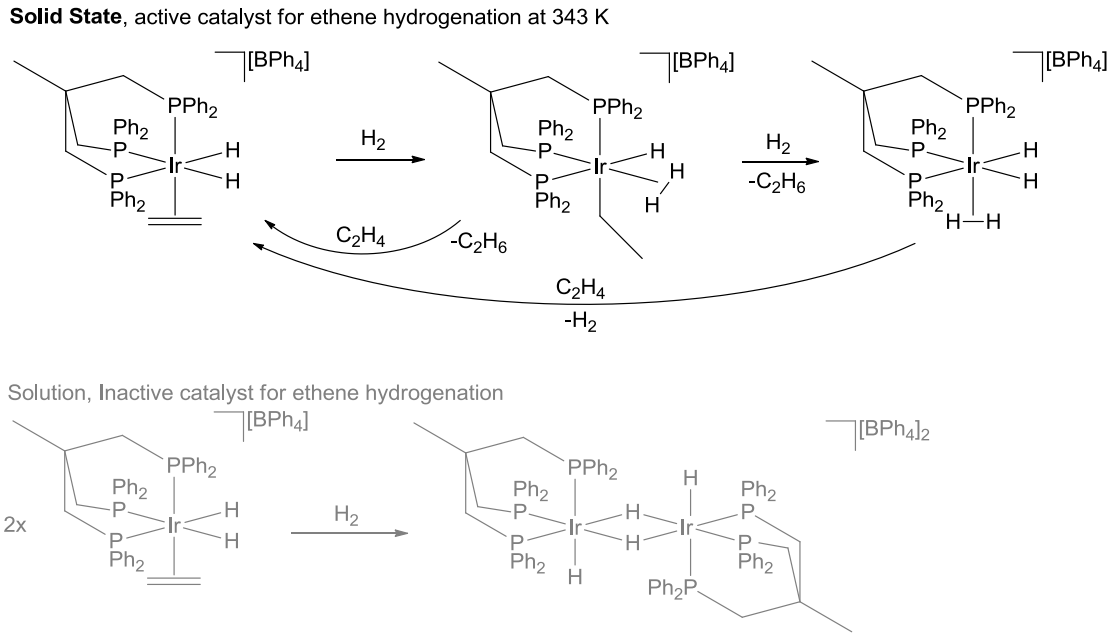

Scheme 1.22. Catalytic ethene hydrogenation in the solid-state which for this system is not possible in the solution phase (solution dimerisation shown in grey).

The trimerisation of ethyne to form benzene was also investigated by Bianchini and co-workers, who showed that an η^4-benzene complex acted as a precatalyst that is active at 373 K in the solid-state, with 4 atm ethyne (0.7 mol of benzene (mol of catalyst)$^{-1}$ hr^{-1}) [Scheme 1.23].[98]

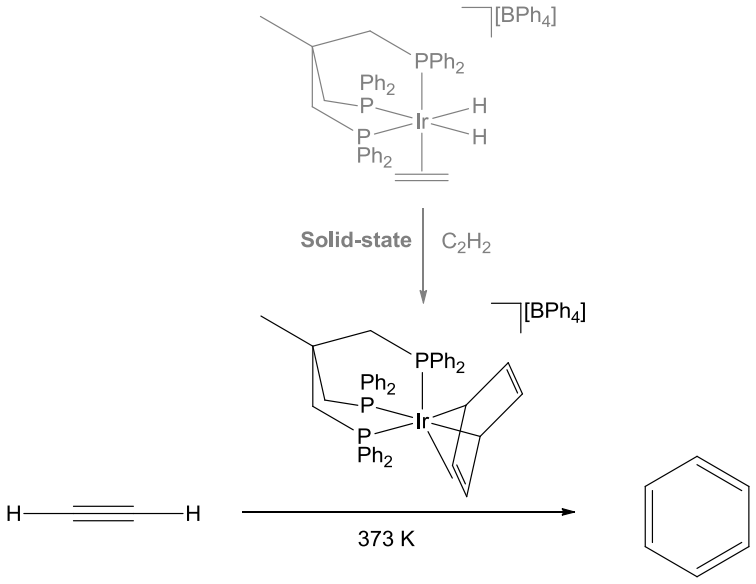

Scheme 1.23. Trimerisation of ethyne using a solid-state catalyst.

Siedle and co-workers reported room temperature catalytic activity of their iridium phosphine cations partnered with Keggin type trianions $[(Ir(PPh_3)_2H_2)]_3[PW_{12}O_{40}]$ [Scheme 1.24].[5] The hydrogenation of ethene, propene and 1-hexene are recorded. The isomerisation of 1-hexene to a mixture of *cis* and *trans* 2-hexenes and 3-hexenes is also reported, presumably *via* a reversible C–H activation accessing an allyl-iridium-hydride intermediate. The authors do not comment on the rates of reaction. Similarly to the findings of Bianchini, addition of excess ethyne forms benzene in catalytic quantities, with an iridium-benzene complex expected to act as the precatalyst, although the reaction is reported to be slow. They also report the catalytic dimerisation of CF_2=CFCl to *cis* and *trans* 1,2-dichlorohexafluorocyclobutane complexes.

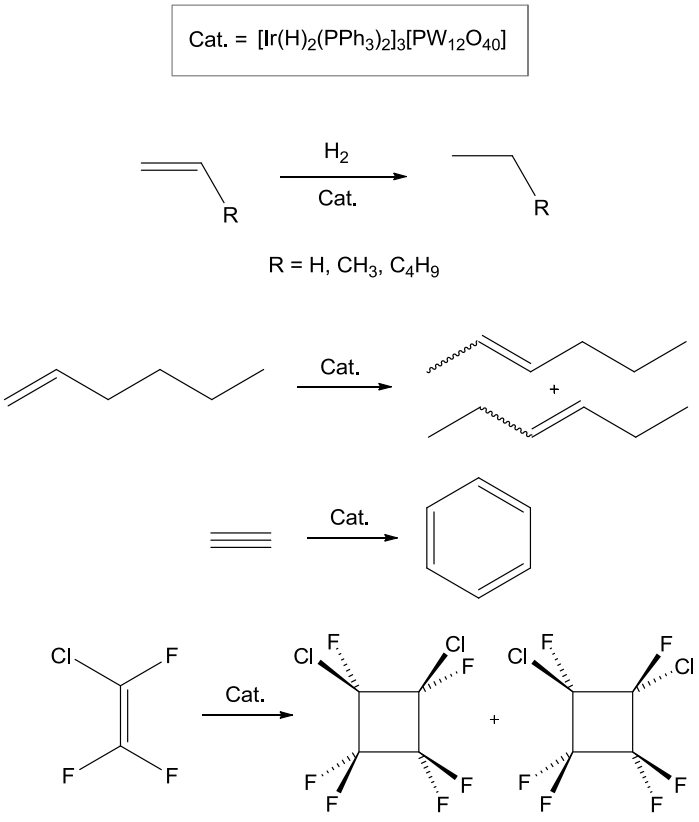

Scheme 1.24. Catalytic reactions using $[Ir(PPh_3)_2H_2]_3[PW_{12}O_{40}]$.

Limbach and co-workers have also reported the solid-state catalysed hydrogenation of ethene using Vaska's complex, $Ir(CO)Cl(PPh_3)_2$ [Scheme 1.25]. They followed the reaction by gas phase ^{1}H NMR spectroscopy and propose that due to hindered isomerisation in the solid-state, the resting species may be different to that in solution.[133]

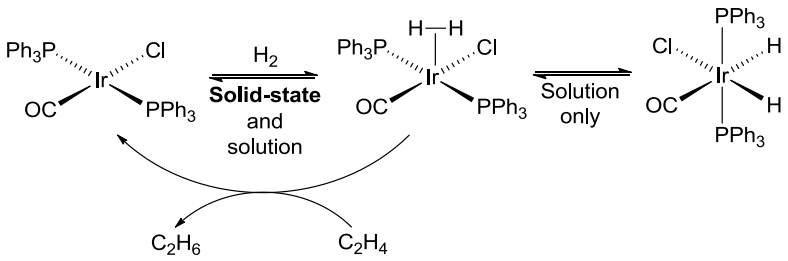

Scheme 1.25. Reaction of Vaska's complex with H_2 and ethene in the solid-state and solution.

Brookhart and co-workers have reported the hydrogenation of ethene using single crystals of (POCOP)Ir(N_2), also monitored by gas phase NMR spectroscopy.[6] At 298 K the reaction requires 5 hours to reach 95% but at 348 K 99% conversion occurs within 30 minutes. At this higher temperature the incorporated toluene is evaporated from the channels running through the crystals, and this is proposed to be responsible for the higher activity. Due to the colour of the crystals, they suggest (POCOP)Ir(C_2H_4) is the resting species. They also presented remarkable selective catalytic hydrogenation inside single crystals. They found that by passivating the surface sites of crystals of (POCOP)Ir(N_2) with a layer of (POCOP)Ir(CO), by an incomplete crystal to crystal transition (CO/N_2 gas exchange from crystal surface downwards), that they can selectively hydrogenate ethene in the presence of propene with a 25:1 preference at 348 K [Scheme 1.26].[6] They proposed that the porous crystals allow the smaller ethene and hydrogen molecules access to the active interior metal sites, whilst the larger propene molecules cannot penetrate the surface. In the absence of surface passivation upon the single crystals only a small selectivity is seen in favour of hydrogenation of ethene (1.8:1 ratio of ethane to propane produced at 298 K).

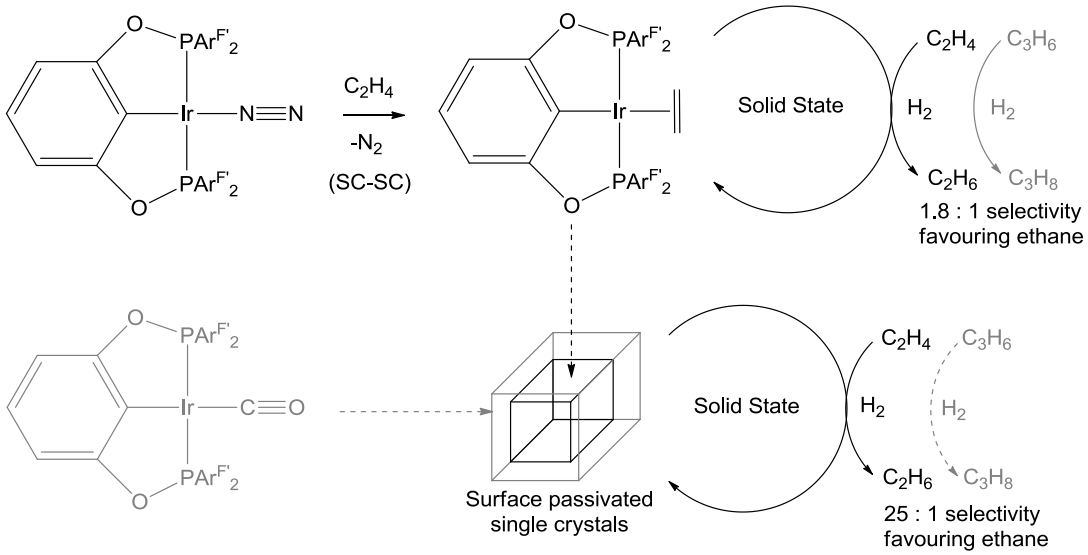

Scheme 1.26. Hydrogenation of ethene using single crystals, and the selective hydrogenation of ethene in the presence of propene using surface passivated single crystals.

Mul and co-workers have investigated the palladium catalysed CO/C_2H_4 co-polymerisation reaction which is operated under gas phase or slurry conditions in industry. The catalyst becomes incorporated into the growing polymer chain, and so its nature as a heterogeneous or homogeneous catalyst is not well defined. Mul and co-workers chose to investigate the mechanism by using microcrystalline ($Ph_2PCH_2CH_2CH_2PPh_2$)Pd(CH_3)(OTf) deposited onto a gold surface.[134] They were able to probe the first few turnovers of reaction using polarisation modulation reflection-absorption IR spectroscopy (PM RAIRS). In this situation the solid-state was the best model for understanding the mechanism of reaction in an industrial process [Scheme 1.27]. The findings suggest that ethene insertion into the Pd–acyl bond is actually CO-assisted. CO is able to displace the chelating ketone group more easily than ethene but can then exchange with ethene. This had not been previously revealed by solution studies [Scheme 1.27 (in grey)].

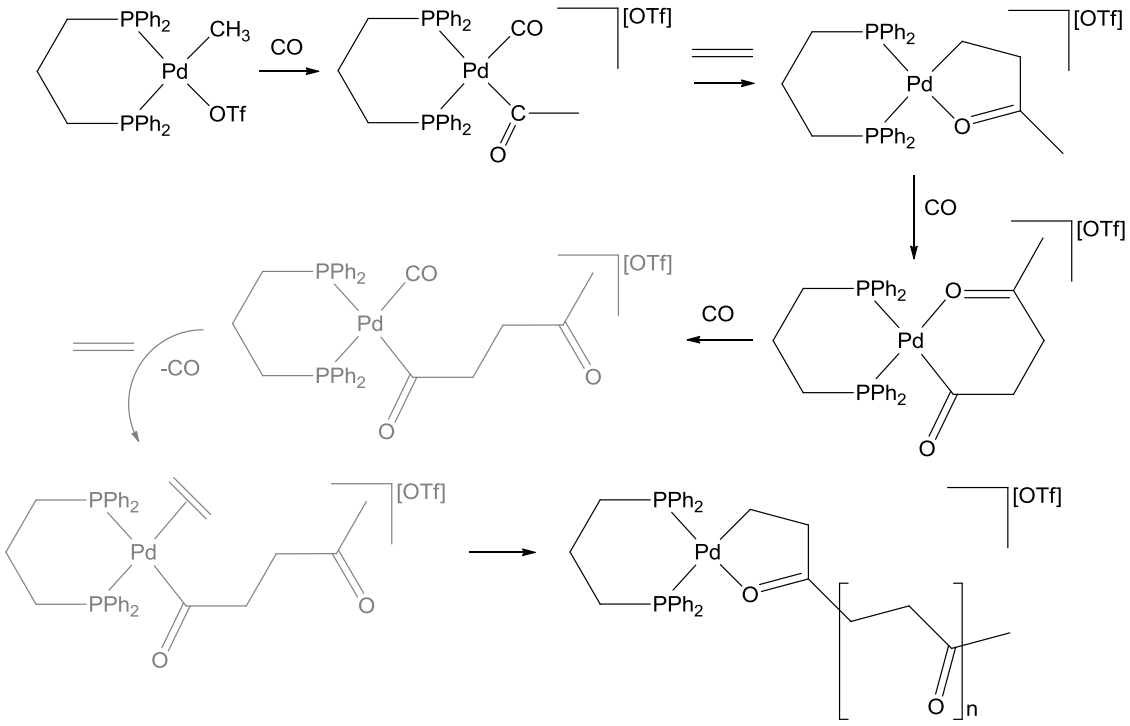

Scheme 1.27. First steps in the copolymerisation of CO and ethene using a palladium catalyst, detected in the solid-state using PM RAIRS (in black). Proposed catalytic propagation intermediates (in grey) displaying the assistance of CO for ethene insertion.

Dorta, Milstein and co-workers formed a variety of chiral crystalline organometallic complexes with either chiral phosphine ligands or chiral counterions.[135] Their idea was to investigate asymmetric reactivity with these solid-state complexes. Unfortunately this was not achieved in this instance and this interesting area is yet to be successfully developed.

1.4. Alkane σ-Complexes

1.4.i. σ-Complexes

Typically ligands bind to a metal through lone pairs or π-bonded electrons. However, when these regions of rich electron density are not available, then σ-interactions may form. A σ-complex contains a ligand that donates electron density from the σ bonding orbital of an X–Y bond into an empty orbital on a metal centre. Examples of σ-complexes include dihydrogen complexes (with typical M···H_2 interactions of 20 kcal/mol)[136-139] as well as σ-bound C–H,[137, 140] Si–H,[136, 137, 141-143] Al–H,[144] Ge–H,[136] Sn–H,[136] B–H,[138, 145, 146] P–H,[137] C–C[147, 148] and C–B[149] bonds. This interaction changes a 2

centre - 2 electron bond into a 3 centre - 2 electron bond.[150] Formally, 2 electrons are donated to the metal, however significant backbonding is also present from a π-symmetry metal orbital into the σ* orbital of the approaching bond. Such synergic bonding is important as pure Lewis acids, such as $AlMe_3$, are not known to coordinate to an X–Y σ-orbital to form σ-complexes.[2] In contrast, too much back donation will fully populate the σ* of the approaching bond and cause oxidative addition to occur with X–Y cleavage. This is closely related to the Dewar Chatt Duncanson model for the bonding of alkenes [Figure 1.15].[136, 151, 152]

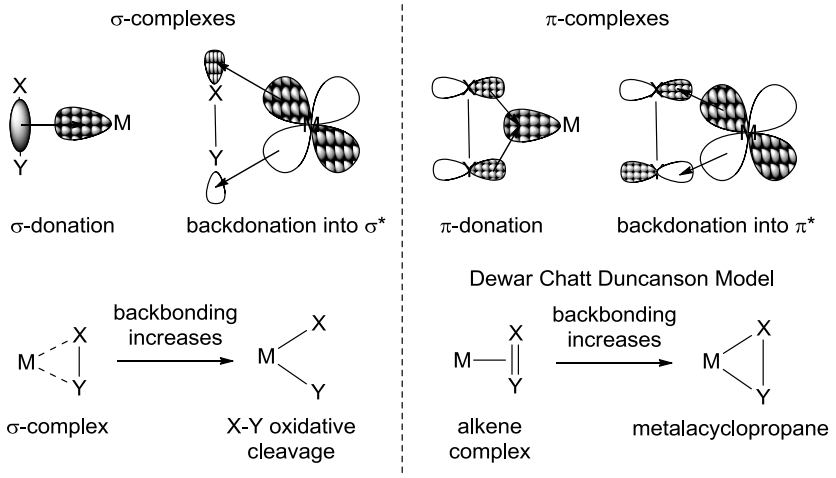

Figure 1.15. Bonding models for σ and π-complexes.

The donating bonds in σ-complexes are relatively non-polarised, since significant polarity would promote heterolytic bond cleavage of the donating group. Therefore the build-up of electron density is located along the internuclear region of the donating bond. This can make access to the σ-orbital difficult, especially in the case where multiple substituents are present (*i.e.* in C–C σ-complexes).[148] σ-X–H bonds utilise a spherical hydrogen 1s orbital, this, alongside the small size of the hydrogen atom, allows a close orbital interaction between the metal and the hydrogen end of the C–H bond. This often results in a tilted interaction, where the M–H distance is shorter than M–X. This is clearly shown in metal-borane (M···B–H) [Figure 1.16] and agostic (M···C–H) X-ray crystal structures (*N.B.* polarisation of (δ+)B–H(δ−) bonds also promotes this geometry).[64, 153]

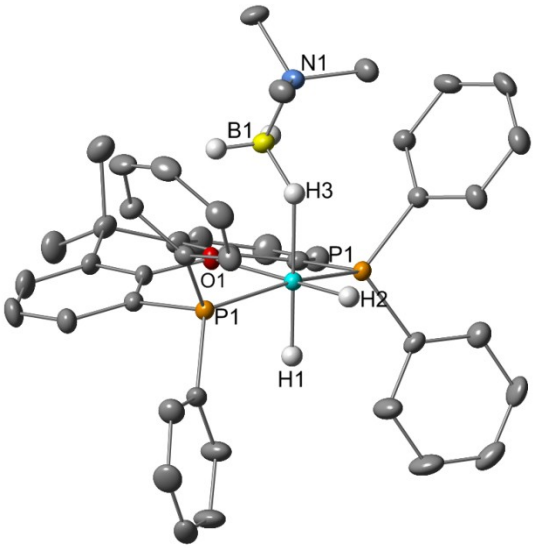

Figure 1.16. Typical tilted σ-interaction: Rh···B–H interaction in [Rh($\kappa^3_{P,O,P}$-Xantphos)$(H)_2$(η^1-$BH_3.NMe_3$)][BAr^F_4]. Only cation shown, displacement ellipsoid plot (30% probability), carbon bound hydrogens omitted for clarity. B–H hydrogen atoms located on fourier map.[153]

σ-complexes represent intermediates on the pathway to oxidative cleavage. In the case of dihydrogen, a clear spectrum of complexes varying from σ-complexes through to oxidatively added dihydride complexes exists, with some complexes displaying an equilibrium between these two extremes (so called "stretched dihydrogen complexes").[136, 139, 154] In the case of C–H bonds, the oxidative addition of C–H groups is a highly desirable reaction as a potential entrance into C–C bond forming reactions.[155, 156] C–H activation of alkanes is difficult due to the inert nature of the C–H bonds. High C–H bond strengths (90-104 kcal/mol), high pK_a values and low polarisability make functionalisation very challenging. [157] Therefore, study into precursory C–H σ-complexes may lead to mechanistic insight into these important oxidative cleavage reactions. Many examples of intramolecular M···C–H σ-interactions have been recorded, these are specifically termed agostic interactions [Figure 1.17].[140, 158] The tethered nature of an agostic interaction maintains a close M···C–H distance such that the interaction can occur without significant entropic penalty. Examples have shown that typical agostic M···H bond lengths generally fall between 1.8 and 2.4 Å and the M-H-C bond angle can vary from 90-140°.[140, 159-161]

Agostic interaction strengths of 8-15 kcal/mol have been estimated by dynamic NMR spectroscopy processes [162] and calorimetric studies [163] (*N.B.* these intramolecular interactions can be entropically stabilised by up to 10 kcal/mol in contrast to an intermolecular interaction).[139] These interactions can

act as latent vacant sites for catalysis,[164] and can sometimes undergo C–H oxidative addition, which may be reversible, forming a metallocycle.[69, 165] Agostic interactions displaying σ-donation should not be confused with anagostic interactions, which are electrostatic in nature. In anagostic interactions, electron density upon the metal can partially stabilise a δ+ hydrogen atom, in a similar way to a typical hydrogen bond [Figure 1.17]. Anagostic interactions differ from agostic interactions by a longer M–H distance (anagostic typically 2.3-2.9Å, compared to agostic 1.8-2.4 Å), and a more end-on binding mode (M-H-C angle: anagostic, 110-170°; agostic, 90-140°), due to a lesser interaction with the C–H carbon.[140, 152, 166] The NMR signal of a C–H proton is shifted upfield by an agostic interaction but downfield by an anagostic interaction.[167]

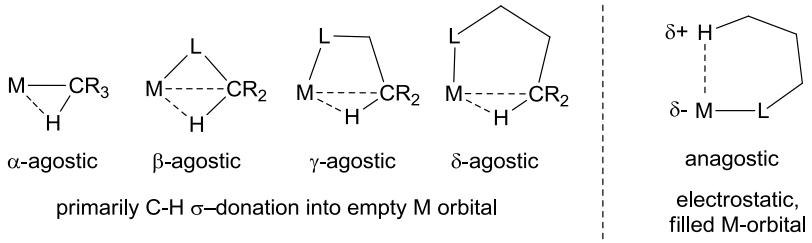

Figure 1.17. Agostic and anagostic interactions

The study of the coordination of unfunctionalised alkanes has been of great interest to organometallic chemists since the first suggestions of such an interaction in the 1970s.[168] Early computational studies suggested that a σ-alkane interaction could be as little as 5-12 kcal/mol.[169] Initial studies included photolysis of $Cr(CO)_6$ and $Fe(CO)_5$ isolated in low temperature matrixes; this generated a vacant site capable of coordinating weak ligands such as CH_4 [Scheme 1.28]. The new complex formed could be investigated by UV/visible spectroscopy and IR spectroscopy (which probe the e to a_1 electronic transition and CO vibrational modes respectively).[170, 171] This study suggests that the binding of CH_4 to the unsaturated $Cr(CO)_5$ unit is weaker than that of N_2 or H_2.

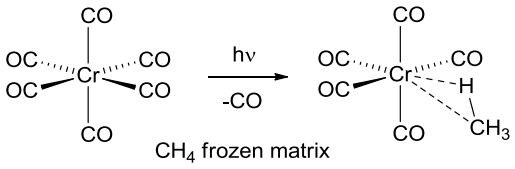

Scheme 1.28. Photolysis of $Cr(CO)_6$ in a frozen matrix of methane.

1.4.ii. Solution Phase Studies

Despite the apparent inert nature of alkanes, reactivity with metal centres has been discovered in the solution phase. C–H activation of an alkane requires a strong C–H σ-bond (380-450 kJ/mol) to be broken, but allows a strong M–H bond (300 kJ/mol) and a weaker M–C bond (210-340 kJ/mol) to form.[1] In the case of third row transition metals this process is favoured, however, it may be a more subtle balance for lighter transition metals.[171] There are now several examples of C–H activation of alkanes, such as the seminal C–H activation of cyclohexane observed by Bergman and co-workers, and independently by Graham and co-workers in 1982 [Scheme 1.29].[172-175]

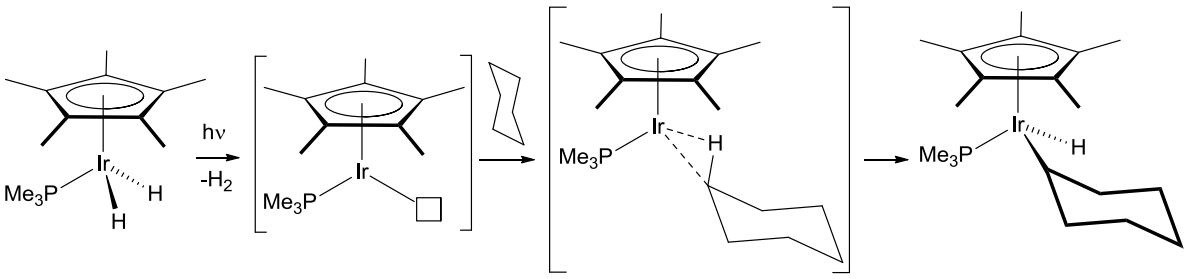

Scheme 1.29. C–H activation of cyclohexane by an unsaturated iridium complex. Intermediates in square brackets not observed.

This reactivity suggested the potential for activation of simple alkanes with long term goals of alkane upgrading and functionalisation. Key to these reactions are the σ-complex intermediates believed to occur prior to C–H activation. Typical metal-alkane interactions are reported as being less than 15 kcal/mol in binding strength, and so it is proposed that in many cases the formation of σ-alkane complexes may be the rate determining step in a C–H activation process, which often needs to occur *via* ligand dissociation [Scheme 1.30].[174, 176] With this in mind, it appears important to be able to optimise this coordination step if rapid catalytic processes are to be developed.

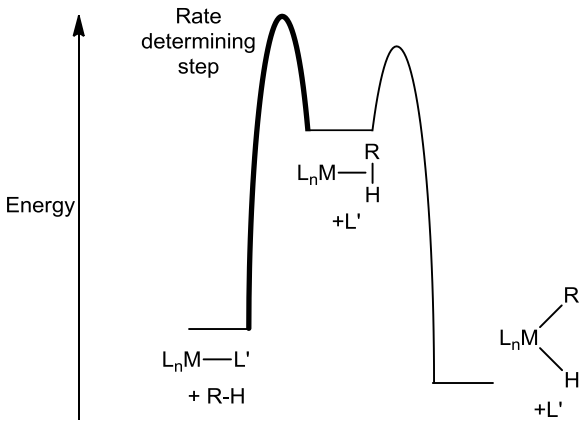

Scheme 1.30. Reaction profile for dissociation of ligand L' and coordination of alkane R–H prior to oxidative addition. Rate determining step of the total process is often the coordination of alkane.[174]

After the initial work in low temperature matrixes, photolysis of $Cr(CO)_6$ in alkane solvents was undertaken. This allowed the observation of pentane, cyclohexane and heptane complexes by visible spectroscopy.[177]

Alongside the initial spectroscopic data, further evidence of σ-alkane complexes in solution was obtained *via* a combination of isotope exchange and kinetic isotope effect experiments.[178, 179] H/D exchange in $Cp^*Rh(PMe_3)(^{13}CH_2CH_3)D$ at low temperatures only occurs upon the α carbon; with higher temperatures required to exchange the isotopically distinguishable α and β carbons presumably by a dissociative mechanism. These observations suggest a non-dissociative σ-complex assisted mechanism for the H/D exchange [Scheme 1.31].

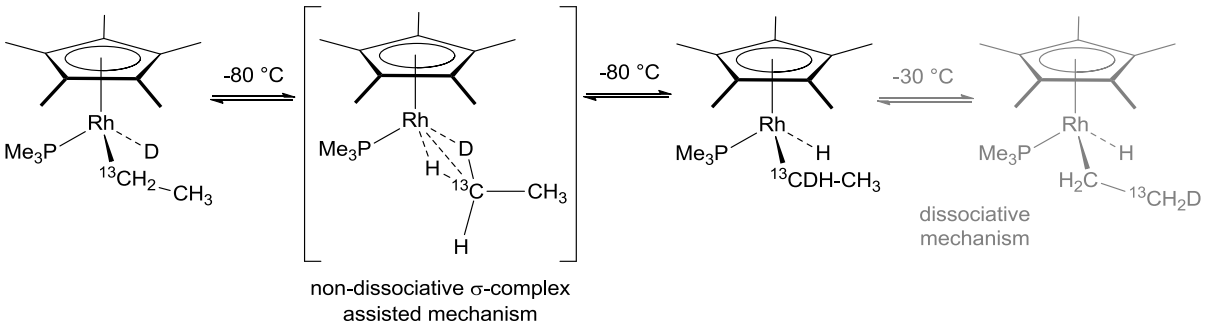

Scheme 1.31. Isotope exchanges occurring at different temperatures.

The reductive elimination of alkanes was also studied and displayed inverse kinetic isotope effects (KIE), k_H/k_D = 0.5 - 0.7 for $Cp^*M(PMe_3)(alkyl)H$ (M = Rh, Ir) and $Cp_2W(CH_3)H$.[178-181] Since a KIE is

expected to originate from a bond cleavage process, it is expected that the majority of the measured KIE occurs from the reductive coupling process, which converts the alkyl hydride complex to an intermediary σ-alkane complex (KIE_1), and that dissociation of the alkane from the σ-alkane complex has little effect. However, since conversion of alkyl hydride complex to σ-alkane complex is seen to be reversible, a second KIE must be considered for the reverse reaction (KIE_2). KIE_1 requires cleavage of a M–H/D bond and so is expected to be a normal KIE (greater than 1) (M–D bond is stabilised relative to the transition state). Likewise, KIE_2 requires cleavage of a C–H/D bond and again a normal KIE is expected, but one which will be larger than KIE_1, due to the greater strength of the C–H/D bond relative to the M–H/D bond. Therefore the equilibrium lies further to the right hand side for the deuterated system, in favour of the σ-alkane complex [Scheme 1.32]. The kinetic equilibrium isotope effect, which can be measured as the release of alkane, is the ratio of KIE_1 / KIE_2 which, since less than 1, is observed as an "inverse" isotope effect. In short, the inverse equilibrium isotope effect suggests an intermediary complex in the release of the alkane, *i.e.* a σ-alkane complex.

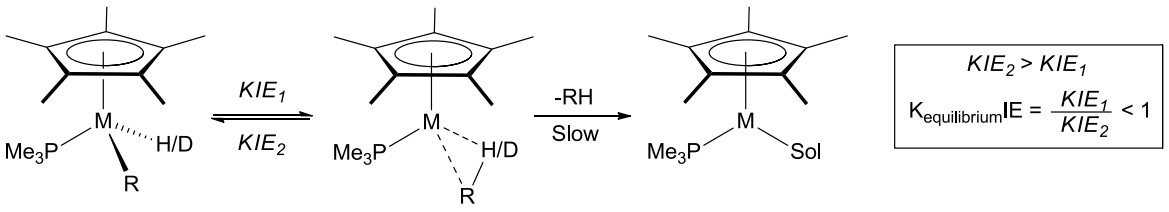

Scheme 1.32. Reductive elimination of alkane displays an inverse kinetic equilibrium isotope effect, indicating the presence of an intermediary σ-alkane complex.

The use of fast timescale IR spectroscopy (time resolved infra red, TRIR) alongside photolysis experiments led to a variety of new σ-alkane complexes in solution.[182] Bergman and co-workers indicated the formation of σ-alkane complexes in low temperature inert gas solutions doped with neopentane using flash photolysis upon $Cp^*Rh(CO)_2$ to form $Cp^*Rh(CO)(C(CH_3)_4)$.[183] George and co-workers followed up this work by forming $CpRe(CO)_2$(n-heptane) at room temperature, which they then compared to short lived analogues of other transition metals [Scheme 1.33].[184] They discovered a far slower rate of displacement of the heptane ligand by CO in the case of rhenium ($k_{298}=2x10^3$ s^{-1}) in comparison with earlier transition metals and manganese; this hinted towards longer lived σ-complexes using late transition metals. The binding energies of alkanes to $\{CpRe(CO)_2\}$ fragments were computationally calculated and varied from 9.2-13.1 kcal/mol.[169]

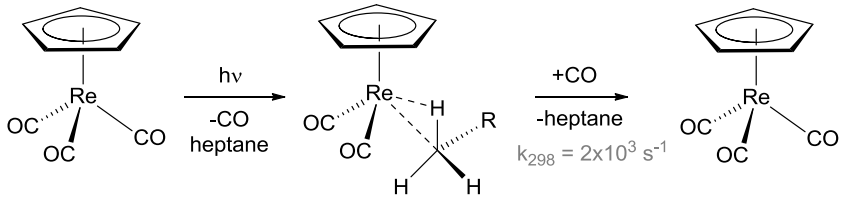

Scheme 1.33. Photolysis of $CpRe(CO)_3$ in heptane and rate of subsequent recombination of CO

Encouraged by the longevity of the rhenium alkane complexes, Ball and co-workers were able to produce NMR spectra of $CpRe(CO)_2$(cyclopentane) at 193 K by *in situ* photolysis of the $CpRe(CO)_3$ precursor in alkane solvents whilst inside an NMR spectrometer.[185] The back reaction with CO regenerated the tricarbonyl complex and so a maximum yield of 20% alkane complex was achieved under constant irradiation. A new upfield resonance at δ −2.3 was assigned as the average shift of the bound methylene group of cyclopentane; exchange between the two equivalent CH groups was expected [Scheme 1.34]. A ^{13}C NMR signal was recorded at δ −31.2 for the same complex corresponding to the M···C–H carbon.

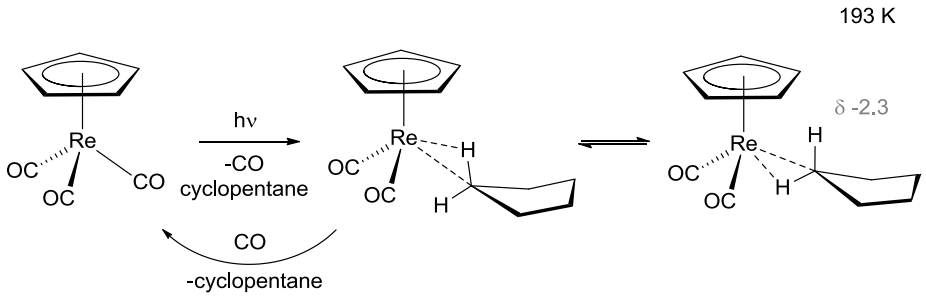

Scheme 1.34. Photolysis of $CpRe(CO)_3$ in cyclopentane to form a σ-complex which rapidly exchanges geminal C–H groups.

More recently, NMR experiments have been carried out on a variety of other σ-alkane complexes including $CpMn(CO)_2$(propane), $TpRe(CO)_2$(cyclopentane) (Tp = hydrotris(pyrazol-1-yl)borate) and $\{\kappa^3_{O,O,O}CpCo(PO(OEt)_2)_3\}Re(CO)_2$(cyclohexane) [Figure 1.18]. The upfield chemical shifts of these compounds ranged between δ −2 and −9 – note that these values correspond to the average chemical environment of the coordinating C–H groups, since exchange between geminal protons is rapid. In the case of cyclohexane, with a fixed chair configuration at 178 K, the axial C–H bond coordinates for the majority of the time, and a low chemical shift is recorded.[186-188]

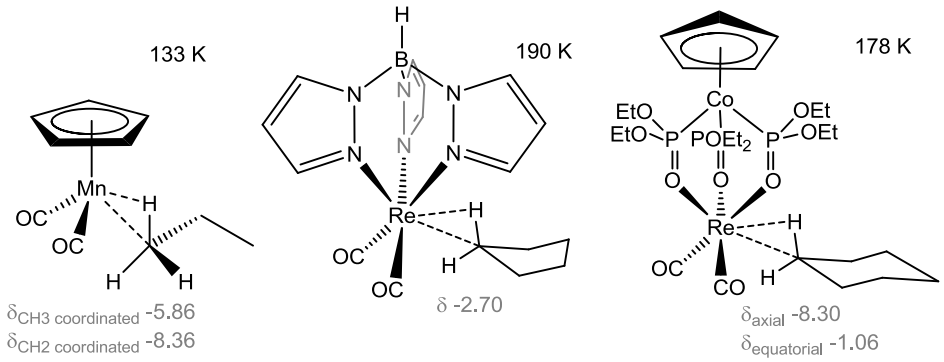

Figure 1.18. Various σ-alkane complexes characterised by NMR spectroscopy, highfield ^{1}H NMR resonances displayed in grey.

The characterisation of σ-methane and σ-ethane complexes proved to be the greatest challenge. George and co-workers analysed a variety of complexes of this kind, $Cp^*M(CO)_2(CH_4/C_2H_6)$ (M = Mn, Re), by TRIR spectroscopy, generated from the photolysis of $Cp^*M(CO)_3$ using supercritical methane/ethane as a solvent.[189, 190] They found these complexes to be shorter-lived than analogous heptane complexes and in rapid equilibrium with the appropriate alkyl hydride complexes.

It wasn't until 2009 that the characterisation of a methane complex was achieved by NMR spectroscopy by Brookhart and co-workers[191] The complex (PONOP)Rh($^{13}CH_3$) (PONOP = 2,6($^{t}Bu_2PO)_2C_5H_3N$) was protonated with $[H(OEt_2)_2][BAr^F{}_4]$ in $CDCl_2F$ at 163 K to form the σ-methane complex $[(PONOP)Rh(^{13}CH_4)][BAr^F{}_4]$ [Scheme 1.35(a)]. NMR spectroscopy revealed a broad proton resonance at δ −0.86 indicative of fast exchange of the four protons in methane. The ^{13}C NMR spectrum displayed a very high field quintet at δ −41.7, indicating a strong influence of the rhodium upon the electronic environment of methane. Warming the complex led to loss of methane and proposed formation of a solvent complex. The partially deuterated methane complex, $[(PONOP)Rh(CHD_3)][BAr^F{}_4]$, displays an isotope shift upon the upfield proton resonance to δ −1.02 [Scheme 1.35(b)]. The C–D bonds will be stabilised relative to the C–H bond in the non-σ-bound positions compared to the σ-bound environment, due to the shallower potential energy well of the σ-bound position. Therefore the C–H bond is coordinated to the metal for greater than a quarter of the time and the recorded chemical shift is closer to the true static bound C–H value.

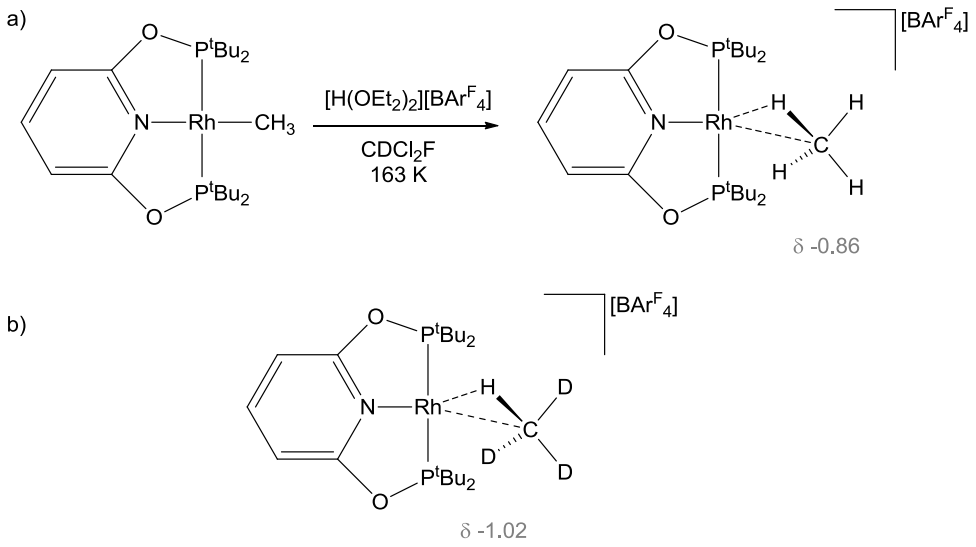

Scheme 1.35. a) Protonation of Rh–CH_3 complex to form a σ-methane complex at low temperature. b) preferred conformation of σ-d^3-methane complex, with C–H bond coordinated to rhodium. Recorded ^{1}H NMR chemical shifts of methane displayed in grey.

The related iridium complex [(PONOP)Ir(H)(CH_3)][BAr^F_4] exists as a long-lived (hours at 296 K) methyl hydride species rather than a σ-methane complex, indicating the propensity of third row transition metals for higher oxidation states.[192] Interestingly, reductive elimination of methane from this complex is accelerated by the addition of a σ-H_2 ligand in the sixth position, whilst addition of a different ligand such as CO slows the process (as would typically be expected) [Scheme 1.36].[2, 193] It is proposed that a σ-CAM mechanism [71] can take place in which [(PONOP)Ir(H)(CH_3)(σ-H_2)][BAr^F_4] is in equilibrium with [(PONOP)Ir(H)$_2$(σ-CH_4)][BAr^F_4], thus generating a methane ligand that can dissociate.

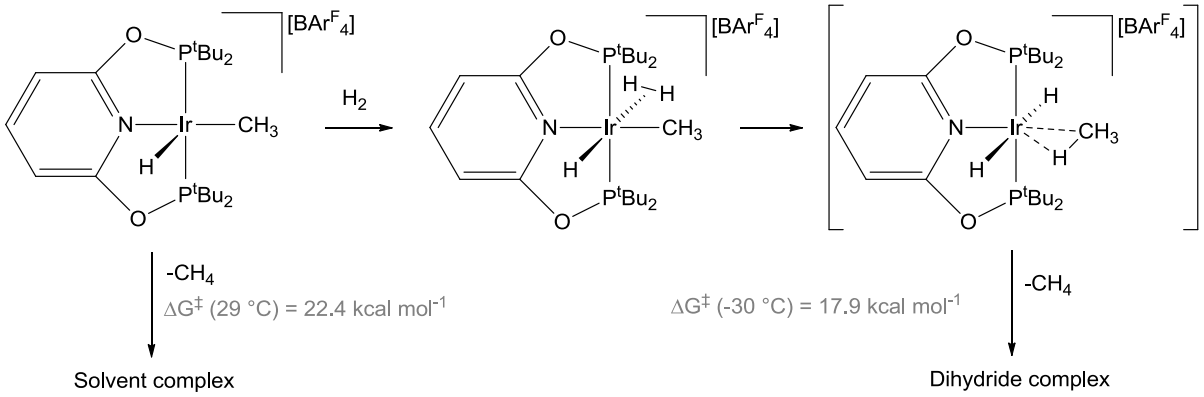

Scheme 1.36. Accelerated reductive elimination of methane from an iridium complex is observed by σ-complex assisted metathesis mechanism. Experimentally determined $\Delta G^{\ddagger}$ values displayed in grey.

Brookhart and co-workers have also recently reported the synthesis of a very unstable σ-ethane complex by protonation of (PONOP)Rh(C_2H_5) with [$H(OEt_2)_2$][BAr^F_4] in CD_2Cl_2 /$CDCl_2F$ at 123 K to form [(PONOP)Rh(η^2-C_2H_6)][BAr^F_4] [Scheme 1.37].[194] They propose a steric clash between the ethane and the pincer ligand weakens the interaction relative to the slightly more stable σ-methane complex [(PONOP)Rh($^{13}CH_4$)][BAr^F_4]. Low temperature NMR spectroscopic characterisation revealed $^{13}C\{^1H\}$ [δ −31.6] and $^1H_{(CH3\ average)}$ [δ −0.83] signals for the coordinated CH_3 group in [(PONOP)Rh(η^2-C_2H_6)][BAr^F_4]. Exchange of the two CH_3 groups in the coordinated ethane could be established by variable temperature NMR studies and a small barrier of 7.2(1) kcal/mol was established.

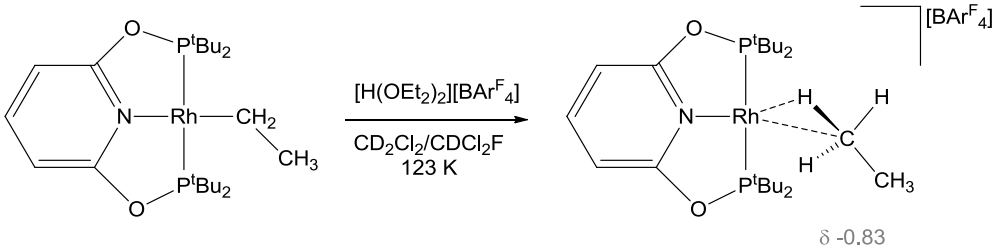

Scheme 1.37. Low temperature synthesis of [(PONOP)Rh(η^2-C_2H_6)][BAr^F_4]. Average chemical shift of coordinated CH_3 group shown in grey.

1.4.iii. Solid-State Studies

Before the start of this project only two solid-state structures with close metal-alkane interactions had been recorded.[195, 196] This is surely because of the short-lived nature of σ-alkane complexes which are often only observed at low temperatures, incompatible with the general slow techniques used in growing diffraction quality crystals.

Reed and co-workers utilised host/guest effects by creating a molecular hydrophobic cavity around an Fe(II) centre. They used a double A-frame porphyrin (H_2DAP) precursor which formed an iron complex which when recrystallised from fluorobenzene/heptane gave crystals of Fe(DAP).(n-heptane) suitable for X-ray crystallography [Figure 1.19].[195] The heptane sits within the cavity approaching the iron centre, but is crystallographically disordered over two positions such that only approximate bond length analysis is possible. Fe···C distances of 2.5 and 2.8 Å are estimated, consistent with agostic

interactions of iron [197] [*N.B.* sum of van der Waals radii Fe···C–H, 4.44 Å].[198, 199] The iron is displaced out of the porphyrin plane, an indication of 5-coordinate geometry which requires a σ-heptane interaction. The authors propose by computational analysis that the alkane interacts in an unsymmetrical bidentate manner through two geminal C–H bonds; however, the structure is poorly resolved.

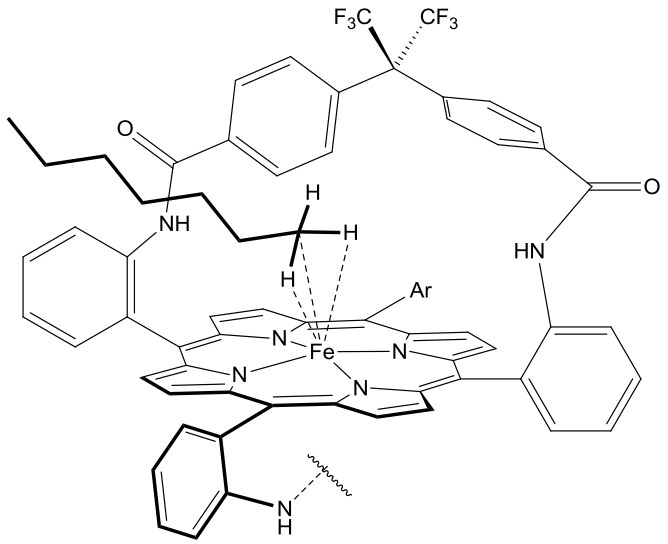

Figure 1.19. Iron porphyrin complex coordinating n-heptane in the solid-state.

Meyer and co-workers were able to add a series of alkanes (cyclopentane, cyclohexane, methylcyclopentane, methylcyclohexane and neohexane) to a coordinatively unsaturated uranium (III) complex [{$(ArO)_3tacn$}U] {$[(ArO)_3tacn]^{3-}$ = (3,5-^{t}Bu,2-$OC_6H_2)_3$*NNN*-$(CH_2NCH_2)_3$} to form σ-alkane adducts.[196] These were amenable to characterisation by X-ray crystallography. High-quality diffraction data were recorded for the bulkier alkanes indicating U···C bond lengths ranging between 3.731(8) (neohexane) and 3.864(7) (methylcyclohexane) [Figure 1.20]. The sum of van der Waals radii for U···$CH_2/_3$ is calculated by the authors as 3.9 Å,[198, 200] however in keeping with recently reported values of van der Waals radii, the value is calculated to be 4.71 Å.[199] The long interactions suggest only a small covalent interaction is probable in these structures. Stabilisation of the alkane may also come from hydrophobic interactions between the ligand ^{t}Bu groups and the alkane, with short contacts crystallographically observed.

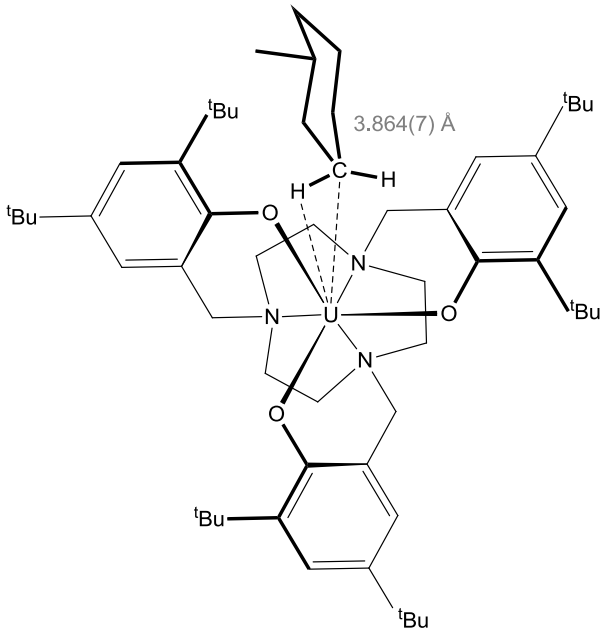

Figure 1.20. Uranium complex showing close interaction with an alkane. U–C distance shown in grey.

In recent attempts to separate small hydrocarbon gases through selective binding to metal organic frameworks (MOFs), Long and co-workers have been able to coordinate light alkanes to a variety of metals within the frameworks and characterise them by powder neutron diffraction.[201, 202] The frameworks M_2(dobdc) (M = Mn, Fe, Co, Ni, Zn; $dobdc^{4-}$ = 2,5-dioxido-1,4-benzenedicarboxylate) form an ordered structure with an open coordination site upon each metal. The uptake of ethene (1 bar, 318 K) approaches one molecule of ethene per metal centre (~100%), however, the uptake of alkanes under the same conditions is less than stoichiometric (propane ~ 85%, ethane ~75%, methane ~10%). The isosteric heats of adsorption were calculated for Fe_2(dobdc) giving values of −33, −25 and −20 kcal/mol for propane, ethane and methane respectively, consistent with the decreasing polarisability of the gases. The other metals all appear to bind the alkanes similarly. Structural determination of the frameworks was achieved by adding deuterated gases to the naked MOF at 300 K and cooling to 4 K for powder neutron diffraction experiments. Rietveld refinements were performed against the data to provide structural models. M–D distances of 2.59(2) (Fe···η^2-$_{D,D}$ d^6-ethane), 2.34(4) & 2.50(4) (Co···η^2-$_{D,D}$ d^6-ethane) and 2.18(1) & 2.86(2) (Fe··· η^2-$_{D,D}$ d^8-propane) were collected, with all interactions displaying a bidentate binding mode of two geminal C–D bonds [Figure 1.21].

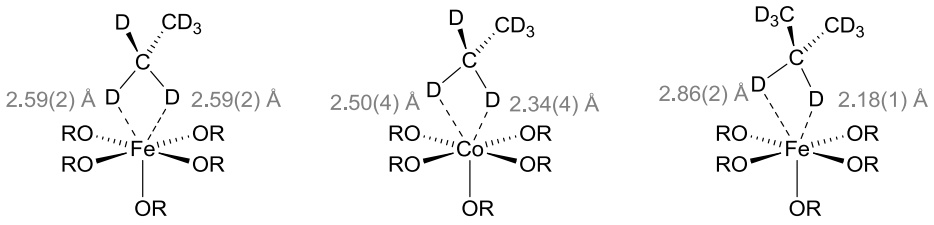

Figure 1.21. Deuterated ethane and propane adducts of M_2(dobdc) MOFs (M = Fe or Co). M–D bondlengths from neutron powder diffraction data analysis displayed in grey.

In 2013 a PhD thesis was published by Millard (Figueroa group, Uni. California) in which two cobalt σ-alkane complexes were presented (this work is yet to be published in a peer-reviewed journal).[203] A cobalt complex with a vacant site stabilised by bulky isocyanide ligands was formed $Co(SiMe_3)(CNAr^{Mes2})$ (Ar^{Mes2} = 2,6-(2,4,6-$Me_3C_6H_2$)C_6H_3). This was dissolved in alkane solvents (95% n-hexane or n-heptane, 5% benzene) to form solvent bound complexes. Crystalline material was produced after several days at 238 K which contained a dimeric complex bridged by an alkane, (μ2–(η2-H,C–(n–C_6H_{14}))[$Co(SiMe_3)(CNAr^{Mes2})_3$]2·(n–$C_6H_{14}$)·2($C_6H_6$) [Figure 1.22] or (μ2–(η2-H,C–(C_7H_{16}))[$Co(SiMe_3)(CNAr^{Mes2})_3$]2·(n–$C_7H_{16}$). In the n-hexane complex X-ray structure the bridging alkane was clearly resolved and even the hydrogen atoms could be resolved in the Fourier map. One C–H bond forms a close interaction with the cobalt centre, a short M···H distance 1.995(30) Å is recorded alongside a M···C distance of 2.718(3) Å, consistent with typical agostic interactions [*N.B.* sum of van der Waals radii Co···CH_3, 4.40 Å].[198, 199] The coordinated n-heptane molecule was slightly disordered in the solid-state structure of the n-heptane complex. In this case the short M···H distance was 1.982(30) Å and the M···C distances ranged 2.77-2.80 Å. Other co-crystallised solvents were present in both crystal structures but these did not form close interactions with the metal centres. Weak van der Waals interactions are predicted between the coordinated alkane and mesityl groups - these may help hold the alkane in place by host-guest interactions. It is noteworthy that the crystallographic pocket between the metal centres allows coordination of n-hexane or n-heptane, but no crystalline material of smaller or larger chain alkanes could be produced. This suggests that only a small size range of alkanes can be accommodated in a stable crystal lattice.

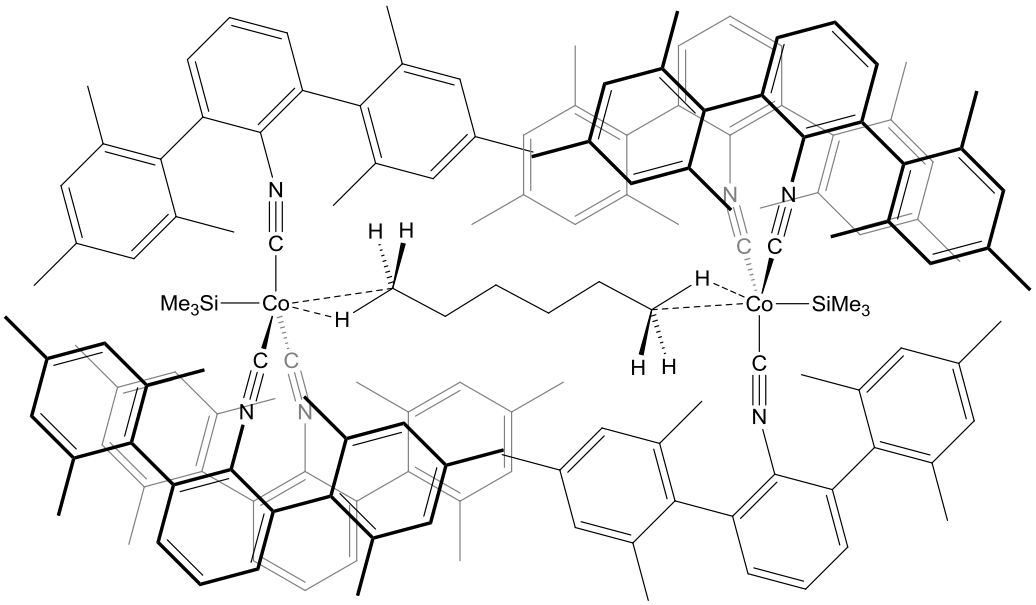

Figure 1.22. σ-n-hexane complex, with n-hexane bridging two cobalt centres.

Alkanes bound to two metals in a dinuclear complex were proposed by Bergman, and computational calculations suggested that a greater binding affinity of the alkane fragment was likely [9.3-20.5 kcal/mol] compared to the binding strength in a mononuclear complex [9.2-13.1 kcal/mol].[169]

In 2013 a series of potassium-alkane interactions were observed by Emslie and co-workers. These were described as weak electrostatic (cation induced dipole) interactions, once more stabilised by hydrophobic interactions between the alkane and hydrophobic ligand pocket (little covalency in contrast to the aforementioned σ-complexes).[204] A sterically hindered ligand ('XAT') coordinates to two potassium ions to form a complex $\{K_2(XAT)\}$ which once crystallised in the presence of hexane formed crystals of K_2(XAT)(n-hexane).toluene, with a K···C distance of 3.284(4) Å (consistent with face-on potassium-benzene interactions) [Figure 1.23] (*N.B.* sum of van der Waals radii for K and CH_2 = 4.73 Å).[198, 199]

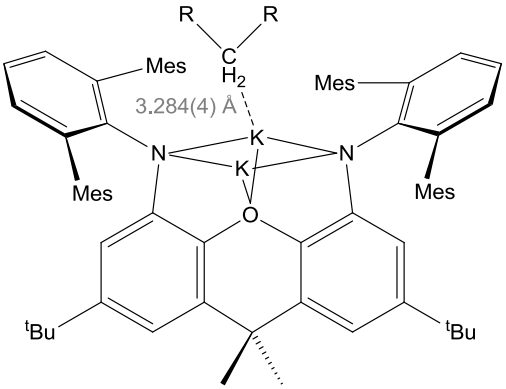

Figure 1.23. Potassium-alkane electrostatic interaction within a rigid hydrophobic pocket. K–C distance shown in grey.

1.4.iv. Chelating σ-complexes

In view of the relative abundance of agostic complexes with respect to σ-alkane complexes it appears that chelation is important in stabilising the σ-interaction, presumably through entropic preorganisation effects, but also potentially allowing a closer interaction with added enthalpic benefits. Whilst bidentate binding modes of alkanes have been discussed throughout this chapter, this generally refers to donation of multiple C–H bonds in a combined manner into a single site around a metal centre. There were no clear examples before this project of a chelating σ-alkane complex where two non-geminal C–H bonds donate into two sites around the same metal centre. Chelating borane and silane complexes (which are valence isoelectronic with a σ-alkane complex) have been crystallographically characterised. Shimoi and co-workers formed $Cr(CO)_4(\eta^4\text{-}B_2H_4.2PMe_3)$ and Weller and co-workers recently produced $(\kappa^2\text{-}_{P,P}Xantphos)Rh(\eta^4\text{-}B_2H_4.2NMe_3)$ [Figure 1.24]. Both complexes show two B–H interactions *cis* to each other, which can be considered η^4- coordination modes.[153, 205]

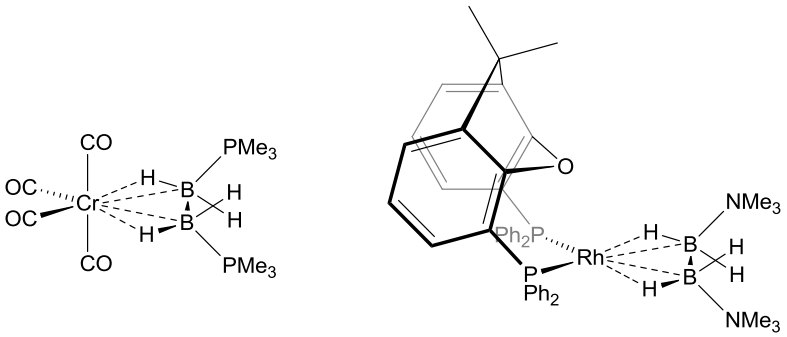

Figure 1.24. Chelating σ-borane ligands coordinating to transition metals.

Chelating silane complexes, in which two Si–H bonds coordinate to a ruthenium centre *trans* to each other, have been investigated by Sabo-etienne and co-workers [Figure 1.25]. [141]

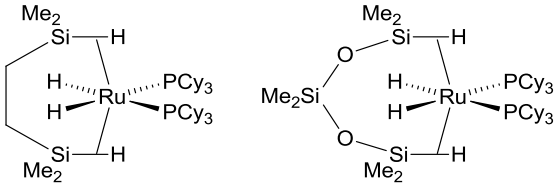

Figure 1.25. Chelating σ-silane ligands coordinating to *trans* sites upon ruthenium.

1.5. Summary

The solid-state differs from solution due to the lack of solvent interactions. Solvent molecules often stabilise reactive organometallic species by coordination, and in some cases can lead to unwanted side reactions, such as displacement of a weakly bound ligand. The generation of low valent species in the solid-state could be used to access complexes incorporating weak interactions (such as σ-interactions), since no stabilisation by solvent can occur.[20] Direct characterisation of solid-state reactions in the case of crystal to crystal transitions can be monitored by X-ray crystallography.[100] The crystal packing of cations and anions within the solid-state may be important in allowing both access to the active metal site, and also in controlling selectivity by defining a "reaction cavity".[6] Whilst a good number of examples of solid-state reactivity have been published with organometallic complexes, there are few reports of catalytic activity using organometallic species as heterogeneous catalysts.

In this project we will further explore organometallic chemistry in the solid-state and utilise the favourable properties (lack of competing solvent interactions, defined reaction cavities, encapsulation of reactive species) to characterise a series of meta-stable complexes, such as σ-alkane complexes. σ-alkane complexes are key intermediates in C-H activation and may also be present as short lived intermediates found in other common mechanisms such as hydrogenation reactions. Characterisation and rationalisation of the bonding modes within these σ-complexes is likely to be important in developing the functionalisation of readily available small alkanes such as methane.

We will present new transformations within solid-state organometallic complexes (such as C-Cl activation) which access products that are not formed by analogous solution routes, hence highlighting the differences between solution and solid-state reactivity and the ability to form otherwise unfavoured products.

Catalytic studies utilising solid-state organometallic complexes will act as proof of principle examples that organometallic complexes can act as active heterogeneous catalysts. Passivation of active surface sites is described by utilising a partial SC-SC in order to test whether catalytic reactions can take place within the interior of a crystal lattice.

The solid-state reactivity of a variety of coordinated small molecule (ethene, ammonia etc.) complexes is also examined in efforts to develop functionalisation of these small molecules via gas/solid reactions.

1.6. References

1. J. F. Hartwig, *OrganoTransition Metal Chemistry*, University Science Books, 2010.
2. R. H. Crabtree, *The Organometallic Chemistry Of The Transition Metals*, 4 edn., John Wiley & Sons, Inc., 2005.
3. C. Bianchini, E. Farnetti, M. Graziani, J. Kaspar and F. Vizza, *J. Am. Chem. Soc.*, 1993, **115**, 1753-1759.
4. N. J. Coville and L. Cheng, *J. Organomet. Chem.*, 1998, **571**, 149-169.
5. A. R. Siedle and R. A. Newmark, *Organometallics*, 1989, **8**, 1442-1450.
6. Z. Huang, P. S. White and M. Brookhart, *Nature*, 2010, **465**, 598-601.
7. M. E. van der Boom, *Angew. Chem. Int. Ed.*, 2011, **50**, 11846-11848.
8. M. Bowker, *Basis and Applications of Heterogeneous Catalysis*, OUP: New York, 1998.
9. L. E. Smart and E. A. Moore, *Solid state chemistry: an introduction*, 3 edn., CRC Press, 2005.
10. J. M. Thomas and W. J. Thomas, *Principles and practice of heterogeneous catalysis*, 3 edn., VCH publishers inc., 2005.
11. B. Hinnemann, P. G. Moses, J. Bonde, K. P. Jørgensen, J. H. Nielsen, S. Horch, I. Chorkendorff and J. K. Nørskov, *J. Am. Chem. Soc.*, 2005, **127**, 5308-5309.
12. H. I. Karunadasa, E. Montalvo, Y. J. Sun, M. Majda, J. R. Long and C. J. Chang, *Science*, 2012, **335**, 698-702.
13. J. Halpern, *Science*, 1982, **217**, 401-407.
14. C. Gonzalez-Rodriguez, R. J. Pawley, A. B. Chaplin, A. L. Thompson, A. S. Weller and M. C. Willis, *Angew. Chem. Int. Ed.*, 2011, **50**, 5134-5138.
15. T. F. Jaramillo, K. P. Jørgensen, J. Bonde, J. H. Nielsen, S. Horch and I. Chorkendorff, *Science*, 2007, **317**, 100-102.
16. Y. Li, H. Wang, L. Xie, Y. Liang, G. Hong and H. Dai, *J. Am. Chem. Soc.*, 2011, **133**, 7296-7299.
17. A. Tsoukala, L. Peeva, A. G. Livingston and H.-R. Bjørsvik, *Chem. Sus. Chem.*, 2011, **5**, 188-193.
18. J. Hagen, *Industrial catalysis : a practical approach*, Wiley-VCH, 1999.
19. N. Xu, L. E. Goodrich, N. Lehnert, D. R. Powell and G. B. Richter-Addo, *Angew. Chem. Int. Ed.*, 2013, **52**, 3896-3900.
20. T. M. Douglas and A. S. Weller, *New J. Chem.*, 2008, **32**, 966-969.
21. http://www.kitco.com/charts/rhodium.html, 2013.
22. J. A. Osborn, F. H. Jardine, J. F. Young and G. Wilkinson, *J. Chem. Soc. A: Inorganic, Physical, Theoretical*, 1966, 1711-1732.
23. C. P. Casey, G. T. Whiteker, M. G. Melville, L. M. Petrovich, J. A. Gavney and D. R. Powell, *J. Am. Chem. Soc.*, 1992, **114**, 5535-5543.
24. M. L. Crawley and B. M. Trost, *Applications of Transition Metal Catalysis in Drug Discovery and Development*, John Wiley & Sons, 2012.
25. R. Noyori, *Adv. Synth. Catal.*, 2003, **345**, 15-32.
26. A. J. Birch and D. H. Williamson, in *Organic Reactions*, John Wiley & Sons, Inc., 2004.
27. F. Denis, F. G. A. Stone and W. Robert, in *Adv. Organomet. Chem.*, Academic Press, 1979, vol. Volume 17, pp. 255-267.
28. D. Evans, J. A. Osborn and Wilkinso.G, *J. Chem. Soc. A - Inorganic, Physical & Theoretical*, 1968, 3133.
29. A. Evans and J. Tsuji, *Modern Rhodium-Catalysed Organic Reactions*, WILEY-VCH, 2005.
30. A. Seayad, M. Ahmed, H. Klein, R. Jackstell, T. Gross and M. Beller, *Science*, 2002, **297**, 1676-1678.
31. C. A. Tolman, *Chem. Rev.*, 1977, **77**, 313-348.
32. H. Clavier and S. P. Nolan, *Chem. Commun.*, 2010, **46**, 841-861.
33. C. M. Beck, S. E. Rathmill, Y. J. Park, J. Chen, R. H. Crabtree, L. M. Liable-Sands and A. L. Rheingold, *Organometallics*, 1999, **18**, 5311-5317.
34. M. M. T. Khan and A. E. Martell, *Inorg. Chem.*, 1974, **13**, 2961-2966.
35. T. E. Nappier, D. W. Meek, R. M. Kirchner and J. A. Ibers, *J. Am. Chem. Soc.*, 1973, **95**, 4194-4210.
36. I. Pernik, J. F. Hooper, A. B. Chaplin, A. S. Weller and M. C. Willis, *ACS Catalysis*, 2012, **2**, 2779-2786.
37. R. J. Pawley, G. L. Moxham, R. Dallanegra, A. B. Chaplin, S. K. Brayshaw, A. S. Weller and M. C. Willis, *Organometallics*, 2010, **29**, 1717-1728.
38. A. B. Chaplin, J. F. Hooper, A. S. Weller and M. C. Willis, *J. Am. Chem. Soc.*, 2012, **134**, 4885-4897.
39. M. J. Overett, K. Blann, A. Bollmann, R. de Villiers, J. T. Dixon, E. Killian, M. C. Maumela, H. Maumela, D. S. McGuinness, D. H. Morgan, A. Rucklidge and A. M. Z. Slawin, *J. Mol. Catal. A: Chem.*, 2008, **283**, 114-119.
40. I. D. Gridnev, N. Higashi, K. Asakura and T. Imamoto, *J. Am. Chem. Soc.*, 2000, **122**, 7183-7194.
41. J. Halpern, D. P. Riley, A. S. C. Chan and J. J. Pluth, *J. Am. Chem. Soc.*, 1977, **99**, 8055-8057.

42. A. D. Wilson, A. J. M. Miller, D. L. DuBois, J. A. Labinger and J. E. Bercaw, *Inorg. Chem.*, 2010, **49**, 3918-3926.
43. S. D. Pike, R. J. Pawley, A. B. Chaplin, A. L. Thompson, J. A. Hooper, M. C. Willis and A. S. Weller, *Eur. J. Inorg. Chem.*, 2011, 5558-5565.
44. T. M. Douglas, S. K. Brayshaw, R. Dallanegra, G. Kociok-Köhn, S. A. Macgregor, G. L. Moxham, A. S. Weller, T. Wondimagegn and P. Vadivelu, *Chem. Eur. J.*, 2008, **14**, 1004-1022.
45. W. Beck and K. Suenkel, *Chem. Rev.*, 1988, **88**, 1405-1421.
46. C. Bianchini, S. Moneti, M. Peruzzini and F. Vizza, *Inorg. Chem.*, 1997, **36**, 5818-5825.
47. K. Seppelt, *Angew. Chem. Int. Ed.*, 1993, **32**, 1025-1027.
48. I. Krossing and I. Raabe, *Angew. Chem. Int. Ed.*, 2004, **43**, 2066-2090.
49. V. Ryzhov, C.-N. Yang, S. J. Klippenstein and R. C. Dunbar, *Int. J. Mass spectrom.*, 1999, **185-187**, 913-923.
50. J. Powell, A. Lough and T. Saeed, *J. Chem. Soc. Dalton Trans.*, 1997, 4137-4138.
51. T. M. Douglas, E. Molinos, S. K. Brayshaw and A. S. Weller, *Organometallics*, 2006, **26**, 463-465.
52. S. v. Moret, R. Dallanegra, A. B. Chaplin, T. M. Douglas, R. M. Hiney and A. S. Weller, *Inorg. Chim. Acta*, 2010, **363**, 574-580.
53. M. W. Bouwkamp, P. H. M. Budzelaar, J. Gercama, I. Del Hierro Morales, J. de Wolf, A. Meetsma, S. I. Troyanov, J. H. Teuben and B. Hessen, *J. Am. Chem. Soc.*, 2005, **127**, 14310-14319.
54. A. B. Chaplin and A. S. Weller, *Eur. J. Inorg. Chem.*, 2010, 5124-5128.
55. J. Bauer, H. Braunschweig, A. Damme and K. Radacki, *Angew. Chem. Int. Ed.*, 2012, **51**, 10030-10033.
56. M. O'Neill, D. A. Addy, I. Riddlestone, M. Kelly, N. Phillips and S. Aldridge, *J. Am. Chem. Soc.*, 2011, **133**, 11500-11503.
57. T. Jelinek, J. Plesek, S. Hermanek and B. Stibr, *Czech Chem. Comm.*, 1986, **51**, 819-829.
58. C. A. Reed, *Acc. Chem. Res.*, 1998, **31**, 133-139.
59. D. Stasko and C. A. Reed, *J. Am. Chem. Soc.*, 2002, **124**, 1148-1149.
60. I. Krossing, *Chem. Eur. J.*, 2001, **7**, 490-502.
61. T. M. Boller, J. M. Murphy, M. Hapke, T. Ishiyama, N. Miyaura and J. F. Hartwig, *J. Am. Chem. Soc.*, 2005, **127**, 14263-14278.
62. S. H. Strauss, *Chem. Rev.*, 1993, **93**, 927-942.
63. G. L. Moxham, H. Randell-Sly, S. K. Brayshaw, A. S. Weller and M. C. Willis, *Chem. Eur. J.*, 2008, **14**, 8383-8397.
64. T. M. Douglas, A. B. Chaplin and A. S. Weller, *Organometallics*, 2008, **27**, 2918-2921.
65. J. H. Nelson, *Nuclear Magnetic Resonance Spectroscopy*, Pearson Education, Inc., 2003.
66. S. T. H. Willems, P. H. M. Budzelaar, N. N. P. Moonen, R. de Gelder, J. M. M. Smits and A. W. Gal, *Chem. Eur. J.*, 2002, **8**, 1310-1320.
67. A. Y. Verat, M. Pink, H. Fan, J. Tomaszewski and K. G. Caulton, *Organometallics*, 2007, **27**, 166-168.
68. M. Oliván, A. V. Marchenko, J. N. Coalter and K. G. Caulton, *J. Am. Chem. Soc.*, 1997, **119**, 8389-8390.
69. N. S. Townsend, A. B. Chaplin, M. A. Naser, A. L. Thompson, N. H. Rees, S. A. Macgregor and A. S. Weller, *Chem. Eur. J.*, 2010, **16**, 8376-8389.
70. T. M. Douglas, J. Le Notre, S. K. Brayshaw, C. G. Frost and A. S. Weller, *Chem. Commun.*, 2006, 3408-3410.
71. R. N. Perutz and S. Sabo-Etienne, *Angew. Chem. Int. Ed.*, 2007, **46**, 2578-2592.
72. A. B. Chaplin, A. I. Poblador-Bahamonde, H. A. Sparkes, J. A. K. Howard, S. A. Macgregor and A. S. Weller, *Chem. Commun.*, 2009, 244-246.
73. S. Hietkamp, D. J. Stufkens and K. Vrieze, *J. Organomet. Chem.*, 1978, **152**, 347-357.
74. N. M. Scott, R. Dorta, E. D. Stevens, A. Correa, L. Cavallo and S. P. Nolan, *J. Am. Chem. Soc.*, 2005, **127**, 3516-3526.
75. M. Ingleson, H. Fan, M. Pink, J. Tomaszewski and K. G. Caulton, *J. Am. Chem. Soc.*, 2006, **128**, 1804-1805.
76. P. Zhao, C. Krug and J. F. Hartwig, *J. Am. Chem. Soc.*, 2005, **127**, 12066-12073.
77. P. H. M. Budzelaar, N. N. P. Moonen, R. Gelder, J. M. M. Smits and A. W. Gal, *Eur. J. Inorg. Chem.*, 2000, 753-769.
78. H. Braunschweig, K. Radacki and K. Uttinger, *Chem. Eur. J.*, 2008, **14**, 7858-7866.
79. L. Vaska, *J. Am. Chem. Soc.*, 1966, **88**, 5325-5327.
80. C. G. Bezzu, M. Helliwell, J. E. Warren, D. R. Allan and N. B. McKeown, *Science*, 2010, **327**, 1627-1630.
81. M. D. Cohen and G. M. J. Schmidt, *J. Chem. Soc. (Resumed)*, 1964, 1996-2000.
82. D. Braga, *Chem. Rev.*, 1992, **92**, 633-665.
83. M. Sakamoto, *Chem. Eur. J.*, 1997, **3**, 684-689.

84. G. Kaupp_in:, J. L. Atwood, J. E. D. Davies, D. D. MacNicol and F. Votgle, *Comprehensive Supramolecular Chemistry*, Pergamon, New York, 1996.
85. N. J. Coville and D. C. Levendis, *Eur. J. Inorg. Chem.*, 2002, 3067-3078.
86. E. J. Miller, T. B. Brill, A. L. Rheingold and W. C. Fultz, *J. Am. Chem. Soc.*, 1983, **105**, 7580-7584.
87. K. I. Goldberg, J. Yan and E. M. Breitung, *J. Am. Chem. Soc.*, 1995, **117**, 6889-6896.
88. D. M. Blake, J. De Faller, Y. L. Chung and A. Winkelman, *J. Am. Chem. Soc.*, 1974, **96**, 5568-5569.
89. C. Bianchini, M. Peruzzini and F. Zanobini, *Organometallics*, 1991, **10**, 3415-3417.
90. P. M. Cook, L. F. Dahl, D. Hopgood and R. A. Jenkins, *J. Chem. Soc. Dalton Trans.*, 1973, 294-301.
91. I. J. Vitorica-Yrezabal, R. A. Sullivan, S. L. Purver, C. Curfs, C. C. Tang and L. Brammer, *CrystEngComm*, **13**, 3189-3196.
92. G. Minguez Espallargas, A. J. Florence, J. van de Streek and L. Brammer, *CrystEngComm*, **13**, 4400-4404.
93. G. Mínguez Espallargas, J. van de Streek, P. Fernandes, A. J. Florence, M. Brunelli, K. Shankland and L. Brammer, *Angew. Chem. Int. Ed.*, **49**, 8892-8896.
94. H. Werner, T. Rappert, M. Baum and A. Stark, *J. Organomet. Chem.*, 1993, **459**, 319-323.
95. B. R. Flynn and L. Vaska, *J. Chem. Soc., Chem. Commun.*, 1974, 703-704.
96. S. Durr, B. Zarzycki, D. Ertler, I. Ivanovic-Burmazovic and U. Radius, *Organometallics*, 2012, **31**, 1730-1742.
97. C. Bianchini, P. Frediani, M. Graziani, J. Kaspar, A. Meli, M. Peruzzini and F. Vizza, *Organometallics*, 1993, **12**, 2886-2887.
98. C. Bianchini, M. Graziani, J. Kaspar, A. Meli and F. Vizza, *Organometallics*, 1994, **13**, 1165-1173.
99. K. Osakada and H. Ishii, *Inorg. Chim. Acta*, 2004, **357**, 3007-3013.
100. O. V. Zenkina, E. C. Keske, R. Wang and C. M. Crudden, *Angew. Chem. Int. Ed.*, 2011, **50**, 8100-8104.
101. A. Martin, L. Martin, L. S. Anthony and K. Gerard van, *Nature*, 2000, **406**, 970-974.
102. S. H. Lim, M. M. Olmstead and A. L. Balch, *Chem. Sci.*, 2013, **4**, 311-318.
103. N. Xu, D. R. Powell and G. B. Richter-Addo, *Angew. Chem. Int. Ed.*, 2011, **50**, 9694-9696.
104. N. Xu, D. R. Powell, L. Cheng and G. B. Richter-Addo, *Chem. Commun.*, 2006, 2030-2032.
105. J. M. Basset, F. Lefebvre and C. Santini, *Coord. Chem. Rev.*, 1998, **178**, 1703-1723.
106. C. Copéret and J. M. Basset, *Adv. Synth. Catal.*, 2007, **349**, 78-92.
107. H. Staub, R. Guillet-Nicolas, N. Even, L. Kayser, F. Kleitz and F.-G. Fontaine, *Chem. Eur. J.*, 2011, **17**, 4254-4265.
108. P. Serna and B. C. Gates, *Angew. Chem. Int. Ed.*, 2011, **50**, 5528-5531.
109. V. A. Bhirud, J. O. Ehresmann, P. W. Kletnieks, J. F. Haw and B. C. Gates, *Langmuir*, 2005, **22**, 490-496.
110. D. Gajan and C. Coperet, *New J. Chem.*, 2011, **35**, 2403-2408.
111. M. K. Samantaray, J. Alauzun, D. Gajan, S. Kavitake, A. Mehdi, L. Veyre, M. Lelli, A. Lesage, L. Emsley, C. Copéret and C. Thieuleux, *J. Am. Chem. Soc.*, 2013, **135**, 3193-3199.
112. J. M. Thomas, T. Maschmeyer, B. F. G. Johnson and D. S. Shephard, *J. Mol. Catal. A: Chem.*, 1999, **141**, 139-144.
113. J. M. Thomas and R. Raja, *Acc. Chem. Res.*, 2008, **41**, 708-720.
114. Z. Wang, G. Chen and K. Ding, *Chem. Rev.*, 2008, **109**, 322-359.
115. L. Shi, X. Wang, C. A. Sandoval, Z. Wang, H. Li, J. Wu, L. Yu and K. Ding, *Chem. Eur. J.*, 2009, **15**, 9855-9867.
116. R. Noyori, T. Ohkuma, M. Kitamura, H. Takaya, N. Sayo, H. Kumobayashi and S. Akutagawa, *J. Am. Chem. Soc.*, 1987, **109**, 5856-5858.
117. M. Fujita, Y. J. Kwon, S. Washizu and K. Ogura, *J. Am. Chem. Soc.*, 1994, **116**, 1151-1152.
118. S. Horike, M. Dincă, K. Tamaki and J. R. Long, *J. Am. Chem. Soc.*, 2008, **130**, 5854-5855.
119. A. Efraty and I. Feinstein, *Inorg. Chem.*, 1982, **21**, 3115-3118.
120. I. Feinstein-Jaffe and A. Efraty, *J. Mol. Catal.*, 1987, **40**, 1-7.
121. S. A. Lawrence, P. A. Sermon and I. Feinstein-Jaffe, *J. Mol. Catal.*, 1989, **51**, 117-127.
122. Q.-P. Liu, Y.-C. Chen, Y. Wu, J. Zhu and J.-G. Deng, *Synlett*, 2006, **2006**, 1503-1506.
123. W. Chen, R. Li, Y. Wu, L.-S. Ding and Y.-C. Chen, *Synthesis*, 2006, **2006**, 3058-3062.
124. Y. M. A. Yamada, Y. Maeda and Y. Uozumi, *Org. Lett.*, 2006, **8**, 4259-4262.
125. B. Karimi and P. F. Akhavan, *Chem. Commun.*, 2009, 3750-3752.
126. W. Mori, T. Sato, T. Ohmura, C. Nozaki Kato and T. Takei, *J. Solid State Chem.*, 2005, **178**, 2555-2573.
127. T. Sato, W. Mori, C. N. Kato, E. Yanaoka, T. Kuribayashi, R. Ohtera and Y. Shiraishi, *J. Catal.*, 2005, **232**, 186-198.
128. A. Hu, H. L. Ngo and W. Lin, *Angew. Chem. Int. Ed.*, 2003, **42**, 6000-6003.
129. A. Hu, H. L. Ngo and W. Lin, *J. Am. Chem. Soc.*, 2003, **125**, 11490-11491.
130. X. Wang, X. Wang, H. Guo, Z. Wang and K. Ding, *Chem. Eur. J.*, 2005, **11**, 4078-4088.

131. K. Ding, Z. Wang, X. Wang, Y. Liang and X. Wang, *Chem. Eur. J.*, 2006, **12**, 5188-5197.
132. U. Stoeck, G. Nickerl, U. Burkhardt, I. Senkovska and S. Kaskel, *J. Am. Chem. Soc.*, 2012, **134**, 17335-17337.
133. J. Matthes, T. Pery, S. Gründemann, G. Buntkowsky, S. Sabo-Etienne, B. Chaudret and H.-H. Limbach, *J. Am. Chem. Soc.*, 2004, **126**, 8366-8367.
134. W. P. Mul, H. Oosterbeek, G. A. Beitel, G.-J. Kramer and E. Drent, *Angew. Chem. Int. Ed.*, 2000, **39**, 1848-1851.
135. R. Dorta, L. Shimon and D. Milstein, *J. Organomet. Chem.*, 2004, **689**, 751-758.
136. G. J. Kubas, *Metal Dihydrogen and σ-Bond Complexes - Structure, Theory, and Reactivity*, Kluwer Academic / Plenum Publishers, 2001.
137. R. H. Crabtree, *Angew. Chem. Int. Ed.*, 1993, **32**, 789-805.
138. G. Alcaraz, M. Grellier and S. Sabo-Etienne, *Acc. Chem. Res.*, 2009, **42**, 1640-1649.
139. G. J. Kubas, *J. Organomet. Chem.*, 2014, **751**, 33-49.
140. M. Brookhart, M. L. H. Green and G. Parkin, *Proc. Natl. Acad. Sci. U.S.A.*, 2007, **104**, 6908-6914.
141. F. Delpech, S. Sabo-Etienne, J.-C. Daran, B. Chaudret, K. Hussein, C. J. Marsden and J.-C. Barthelat, *J. Am. Chem. Soc.*, 1999, **121**, 6668-6682.
142. J. Yang, P. S. White, C. K. Schauer and M. Brookhart, *Angew. Chem. Int. Ed.*, 2008, **47**, 4141-4143.
143. X.-L. Luo, G. J. Kubas, C. J. Burns, J. C. Bryan and C. J. Unkefer, *J. Am. Chem. Soc.*, 1995, **117**, 1159-1160.
144. J. A. B. Abdalla, I. M. Riddlestone, R. Tirfoin, N. Phillips, J. I. Bates and S. Aldridge, *Chem. Commun.*, 2013, **49**, 5547-5549.
145. R. Dallanegra, A. B. Chaplin and A. S. Weller, *Angew. Chem. Int. Ed.*, 2009, **48**, 6875-6878.
146. C. Y. Tang, A. L. Thompson and S. Aldridge, *J. Am. Chem. Soc.*, 2010, **132**, 10578-10591.
147. M. Etienne and A. S. Weller, *Chem. Soc. Rev.*, 2014, **43**, 242-259.
148. A. B. Chaplin, J. C. Green and A. S. Weller, *J. Am. Chem. Soc.*, 2011, **133**, 13162-13168.
149. H. Braunschweig, P. Brenner, R. D. Dewhurst, I. Krummenacher, B. Pfaffinger and A. Vargas, *Nat. Commun.*, 2012, **3**, 6.
150. J. C. Green, M. L. H. Green and G. Parkin, *Chem. Commun.*, 2012, **48**, 11481-11503.
151. J. S. Dewar, *Bull. Soc. Chim. Fr.*, 1951, **18**, C71-C79.
152. J. Y. Saillard and R. Hoffmann, *J. Am. Chem. Soc.*, 1984, **106**, 2006-2026.
153. H. C. Johnson, C. L. McMullin, S. D. Pike, S. A. Macgregor and A. S. Weller, *Angew. Chem. Int. Ed.*, 2013, **52**, 9776-9780.
154. R. H. Crabtree, M. Lavin and L. Bonneviot, *J. Am. Chem. Soc.*, 1986, **108**, 4032-4037.
155. M. C. Willis, *Chem. Rev.*, 2010, **110**, 725-748.
156. P. B. Arockiam, C. Bruneau and P. H. Dixneuf, *Chem. Rev.*, 2012, **112**, 5879-5918.
157. R. G. Bergman, *Science*, 1984, **223**, 902-908.
158. M. Brookhart and M. L. H. Green, *J. Organomet. Chem.*, 1983, **250**, 395-408.
159. G. Parkin, *Acc. Chem. Res.*, 2009, **42**, 315-325.
160. M. Brookhart and M. L. H. Green, *J. Organomet. Chem.*, 1983, **250**, 395-408.
161. W. Baratta, C. Mealli, E. Herdtweck, A. Ienco, S. A. Mason and P. Rigo, *J. Am. Chem. Soc.*, 2004, **126**, 5549-5562.
162. P. M. Morse, M. D. Spencer, S. R. Wilson and G. S. Girolami, *Organometallics*, 1994, **13**, 1646-1655.
163. A. A. Gonzalez, K. Zhang, S. P. Nolan, R. Lopez de la Vega, S. L. Mukerjee, C. D. Hoff and G. J. Kubas, *Organometallics*, 1988, **7**, 2429-2435.
164. G. Kubas, *Catal. Lett.*, 2005, **104**, 79-101.
165. N. M. Scott, R. Dorta, E. D. Stevens, A. Correa, L. Cavallo and S. P. Nolan, *J. Am. Chem. Soc.*, 2005, **127**, 3516-3526.
166. W. I. Sundquist, D. P. Bancroft and S. J. Lippard, *J. Am. Chem. Soc.*, 1990, **112**, 1590-1596.
167. H. V. Huynh, L. R. Wong and P. S. Ng, *Organometallics*, 2008, **27**, 2231-2237.
168. R. J. Hodges, D. E. Webster and P. B. Wells, *J. Chem. Soc. A -Inorganic Physical & Theoretical*, 1971, 3230.
169. E. A. Cobar, R. Z. Khaliullin, R. G. Bergman and M. Head-Gordon, *Proc. Natl. Acad. Sci.* , 2007, **104**, 6963-6968.
170. R. N. Perutz and J. J. Turner, *J. Am. Chem. Soc.*, 1975, **97**, 4791-4800.
171. C. Hall and R. N. Perutz, *Chem. Rev.*, 1996, **96**, 3125-3146.
172. A. H. Janowicz and R. G. Bergman, *J. Am. Chem. Soc.*, 1982, **104**, 352-354.
173. S. E. Bromberg, H. Yang, M. C. Asplund, T. Lian, B. K. McNamara, K. T. Kotz, J. S. Yeston, M. Wilkens, H. Frei, R. G. Bergman and C. B. Harris, *Science*, 1997, **278**, 260-263.
174. P. J. Perez, *Alkane C-H Activation by Single-Site Metal Catalysis*, Springer, 2012.
175. J. K. Hoyano and W. A. G. Graham, *J. Am. Chem. Soc.*, 1982, **104**, 3723-3725.

176. G. S. Chen, J. A. Labinger and J. E. Bercaw, *Proc. Natl. Acad. Sci.* , 2007, **104**, 6915-6920.
177. J. M. Morse, G. H. Parker and T. J. Burkey, *Organometallics*, 1989, **8**, 2471-2474.
178. J. M. Buchanan, J. M. Stryker and R. G. Bergman, *J. Am. Chem. Soc.*, 1986, **108**, 1537-1550.
179. R. A. Periana and R. G. Bergman, *J. Am. Chem. Soc.*, 1986, **108**, 7332-7346.
180. R. M. Bullock, C. E. L. Headford, K. M. Hennessy, S. E. Kegley and J. R. Norton, *J. Am. Chem. Soc.*, 1989, **111**, 3897-3908.
181. W. D. Jones, *Acc. Chem. Res.*, 2003, **36**, 140-146.
182. A. J. Cowan and M. W. George, *Coord. Chem. Rev.*, 2008, **252**, 2504-2511.
183. A. A. Bengali, R. H. Schultz, C. B. Moore and R. G. Bergman, *J. Am. Chem. Soc.*, 1994, **116**, 9585-9589.
184. X.-Z. Sun, D. C. Grills, S. M. Nikiforov, M. Poliakoff and M. W. George, *J. Am. Chem. Soc.*, 1997, **119**, 7521-7525.
185. S. Geftakis and G. E. Ball, *J. Am. Chem. Soc.*, 1998, **120**, 9953-9954.
186. J. A. Calladine, S. B. Duckett, M. W. George, S. L. Matthews, R. N. Perutz, O. Torres and Q. V. Khuong, *J. Am. Chem. Soc.*, 2011, **133**, 2303-2310.
187. S. B. Duckett, M. W. George, O. S. Jina, S. L. Matthews, R. N. Perutz, X.-Z. Sun and K. Q. Vuong, *Chem. Commun.*, 2009, 1401-1403.
188. R. D. Young, A. F. Hill, W. Hillier and G. E. Ball, *J. Am. Chem. Soc.*, 2011, **133**, 13806-13809.
189. A. J. Cowan, P. Portius, H. K. Kawanami, O. S. Jina, D. C. Grills, X.-Z. Sun, J. McMaster and M. W. George, *Proc. Natl. Acad. Sci.* , 2007, **104**, 6933-6938.
190. B. Chan and G. E. Ball, *Journal of Chemical Theory and Computation*, 2013, **9**, 2199-2208.
191. W. H. Bernskoetter, C. K. Schauer, K. I. Goldberg and M. Brookhart, *Science*, 2009, **326**, 553-556.
192. W. H. Bernskoetter, S. K. Hanson, S. K. Buzak, Z. Davis, P. S. White, R. Swartz, K. I. Goldberg and M. Brookhart, *J. Am. Chem. Soc.*, 2009, **131**, 8603-8613.
193. J. Campos, S. Kundu, D. R. Pahls, M. Brookhart, E. Carmona and T. R. Cundari, *J. Am. Chem. Soc.*, 2013, **135**, 1217-1220.
194. M. D. Walter, P. S. White, C. K. Schauer and M. Brookhart, *J. Am. Chem. Soc.*, 2013, **135**, 15933-15947.
195. D. R. Evans, T. Drovetskaya, R. Bau, C. A. Reed and P. D. W. Boyd, *J. Am. Chem. Soc.*, 1997, **119**, 3633-3634.
196. I. Castro-Rodriguez, H. Nakai, P. Gantzel, L. N. Zakharov, A. L. Rheingold and K. Meyer, *J. Am. Chem. Soc.*, 2003, **125**, 15734-15735.
197. R. H. Crabtree, E. M. Holt, M. Lavin and S. M. Morehouse, *Inorg. Chem.*, 1985, **24**, 1986-1992.
198. L. Pauling, *The Nature of the Chemical Bond*, 3rd edn., Cornell University Press, 1960.
199. S. Alvarez, *Dalton Trans.*, 2013, **42**, 8617-8636.
200. J. E. Huheey, E. A. Keiter and R. L. Keiter, *Inorganic Chemistry: Principles of Structure and Reactivity*, 4th edn., Prentice Hall, 1993.
201. E. D. Bloch, W. L. Queen, R. Krishna, J. M. Zadrozny, C. M. Brown and J. R. Long, *Science*, 2012, **335**, 1606-1610.
202. S. J. Geier, J. A. Mason, E. D. Bloch, W. L. Queen, M. R. Hudson, C. M. Brown and J. R. Long, *Chem. Sci.*, 2013, **4**, 2054-2061.
203. M. D. Millard, Isolation of Four-Coordinate Iridium(I) Monohydrides and the X-ray Crystal Structure of a Cobalt Tris-Isocyanide Alkane sigma-Complex, PhD Thesis, University of San Diego, 2013.
204. N. R. Andreychuk and D. J. H. Emslie, *Angew. Chem. Int. Ed.*, 2013, **52**, 1696-1699.
205. M. Shimoi, K. Katoh and H. Ogino, *J. Chem. Soc., Chem. Commun.*, 1990, 811-812.

CHAPTER 2
SYNTHESIS AND CHARACTERISATION OF RHODIUM(I) σ-ALKANE COMPLEXES

2.1. Introduction

A detailed discussion of previously reported σ-alkane complexes is presented in *Section 1.4*.

Understanding the nature of σ-alkane complexes is key to the functionalisation of alkanes, as σ-alkane complexes are believed to act as precursors to C–H activation.[1-3] Activation of the C–H bonds of alkanes is difficult due to the high bond strengths (380-450 kJ/mol), high pK_a values and low polarisability of the bonds.[4, 5] Oxidative addition of a C–H bond forms a new M–H (300 kJ/mol) and M–C bond (210-340 kJ/mol), which may compensate for the breakup of the C–H bond.[5] Examples of the C–H activation of alkanes by organometallic species have been reported.[4, 6-9] A notable example of a homogeneous process which requires C–H activation of alkanes is transfer hydrogenation using iridium catalysts, reported by Goldman, Brookhart and co-workers [Scheme 2.1].[9, 10] By combining a dehydrogenation catalyst (iridium pincer complex)[11] with an alkene metathesis catalyst (Schrock-type molybdenum catalyst)[12] they can effectively promote metathesis of alkanes [Scheme 2.1].

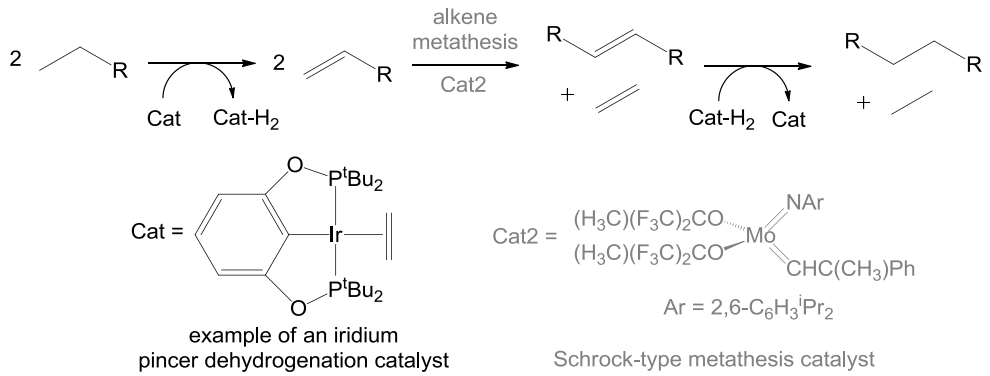

Scheme 2.1. Alkane metathesis by a tandem transfer dehydrogenation-alkene metathesis mechanism. Two different catalysts are used in this process.

The development of controlled, low energy functionalisation of alkanes is challenging, but promises valuable results such as the upgrading of short chain alkanes to form long chain hydrocarbons.

The route to the C–H activation of alkanes is believed to go *via* a σ-alkane complex. These complexes are reported to be weakly bound (typically < 15 kcal/mol)[13-16] and understanding the effects that stabilise a σ-interaction may be beneficial to designing future catalysts capable of C–H activation.

σ-alkane complexes have proved very difficult to characterise, especially in the solid-state by X-ray crystallography (*as outlined in Chapter 1*).[17-20] In particular it is noteworthy that no dependable general synthetic route to crystalline, ambient temperature stable σ-alkane complexes has been previously developed.

2.1.i. Design criteria for a general synthetic route to access σ-alkane complexes

In order to form stable σ-alkane complexes the entire system must be considered carefully. It is important to minimise any potential competing interactions since the σ-interaction (typically < 15 kcal/mol)[13-16] can easily be displaced by a stronger ligand.[21, 22] In many cases a solvent molecule will possess available areas of electron density for ligation to a metal centre, and may displace a σ-alkane interaction (e.g. 2-electron donors such as acetone and acetonitrile or 6-electron donors such as benzene or fluorobenzene) [Scheme 2.2]. Further difficulties may arise from reactivity with the solvent (CH_2Cl_2) or by poor solubility properties (pentane or C_6F_6). Over the timescales normally required for crystallisation (> 12 hours) solvent interactions are likely to hinder the formation of single crystals of a σ-alkane complex, by competing for the available sites upon the metal or initiating decomposition. It therefore appears that removal of the solvent all together may be beneficial for the production of reactive species.

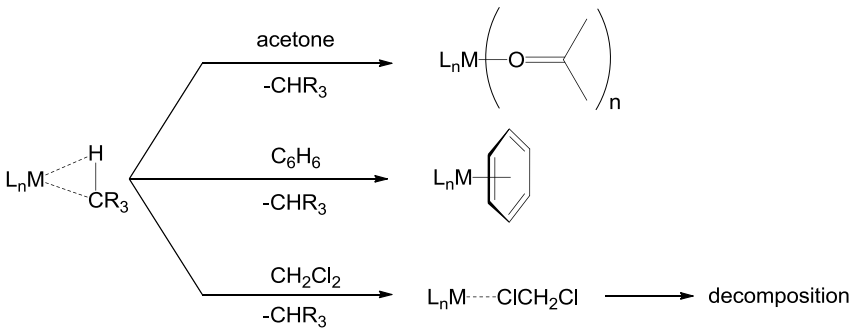

Scheme 2.2. Expected reactivity of a weakly bound σ-alkane complex upon solvation at ambient temperatures.

In order to synthesise a σ-alkane complex in the solid-state an alkane must be generated, and directed to the vicinity of a low coordinate metal centre. Hydrogenation of an alkene ligand is a well established reaction which has been reported with many transition metals, especially using homogeneous rhodium catalysts.[23-25] In solution the alkane generated by hydrogenation is usually assumed to rapidly leave the coordination sphere of the metal and is often dissolved well in solvent. In the solid-state it is possible that an alkane generated by hydrogenation of an alkene may remain within the vicinity of the metal and an interaction may occur [Scheme 2.3]. The parent alkene ligand should be chosen so that the hydrogenation reaction is fast allowing the direct formation of the alkane upon exposure to hydrogen. A slower reaction could allow alternative decomposition reactions to compete, diminishing the concentration of a σ-alkane complex. In the solid-state the metal centre must be capable of interacting with hydrogen, without requiring de-coordination of another ligand. 16 electron, square planar complexes are capable of this, as a dihydrogen molecule can approach the spatially available orbitals above the ML_4 plane and initiate hydrogenation.[26]

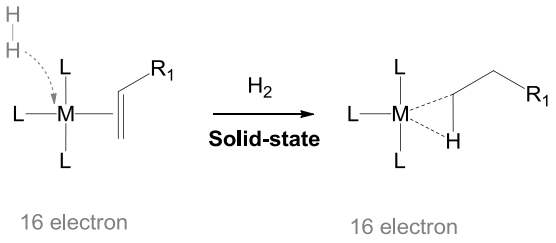

Scheme 2.3. Proposed hydrogenation of an alkene ligand in the solid-state to form a σ-alkane complex.

In order to retain a weakly coordinated alkane within the extended solid-state structure it is expected that the crystallinity of the material must remain intact. A single crystal to single crystal (SC-SC) transition driven by hydrogen gas is therefore desirable. To preserve crystallinity a well defined lattice structure is required to be maintained. This may be obtained through choice of sterically demanding ligands,[27, 28] or by choice of bulky counter-anions, which dominate the packing and encapsulate the cation in a defined cavity [Figure 2.1]. Upon reaction the cation must be able to rearrange without significant disruption of the unit cell. Counter-anions must be weakly coordinating since displacement of the alkane ligand by the anion is likely to occur otherwise. This would probably lead to the loss of crystallinity and decomposition of the σ-alkane complex.

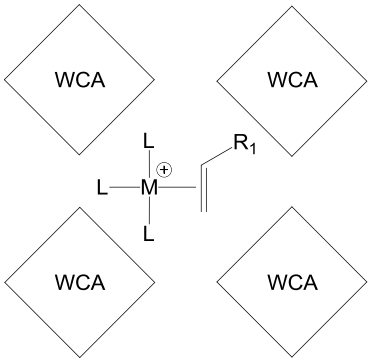

Figure 2.1. 2-D representation of a lattice structure dominated by anions in which the cation is enclosed in a defined cavity (WCA = weakly coordinating anion).

Reaction of organometallic complexes with hydrogen has the potential for forming σ-H_2 or hydride complexes and these interactions may directly displace a coordinated alkane complex (σ-H_2 complexes are more common than σ-C–H complexes).[29, 30] In order to favour σ-alkane coordination over a σ-H_2 interaction a chelating alkane might be preferable in which the chelate effect establishes an overall stronger metal-alkane interaction [Scheme 2.4]. Two vacant sites must be available after hydrogenation for the alkane to bind in a bidentate manner; suggesting two alkene ligands would be required in the precursor complex.

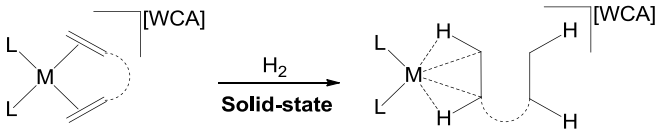

Scheme 2.4. Proposed formation of a chelating alkane ligand in the solid-state.

The alkene NBD (norbornadiene = C_7H_8) is commonly used in organometallic chemistry as it forms stable complexes which can be activated by hydrogenation of the diene, releasing NBA (norbornane = C_7H_{12}). Hydrogenation of NBD is generally rapid because of a favourable release of ring-strain as it becomes saturated.[23, 25, 31]

To avoid the formation of M(III) hydride species, which may displace σ-alkane ligands or disrupt crystallinity, the final product ideally would be a M(I) species. 4d metals have less extended atomic orbitals than 5d metals and further retraction of the atomic orbitals occurs in cationic species, these factors reduce the propensity for oxidative addition. For these reasons rhodium(I) appears a more likely candidate than iridium(I) and a cationic species is favoured. The ligand may also influence the

tendency of the complex to form Rh(III)-hydride species. Previous studies have indicated that smaller bite angle phosphines have a lower preference for forming higher oxidative state species relative to large bite angle phosphine ligands, at least when an equilibrium between oxidation states is established.[32] Therefore relatively small bite angle ligands are favoured for maintaining the original oxidation state [Scheme 2.5]. If a chelating phosphine ligand is chosen then non-coordinating substituents are necessary (such as alkyl groups with a low tendency for forming agostic interactions) as intramolecular interactions (*i.e.* coordination of the π-system of an arene group) could displace a σ-alkane interaction.

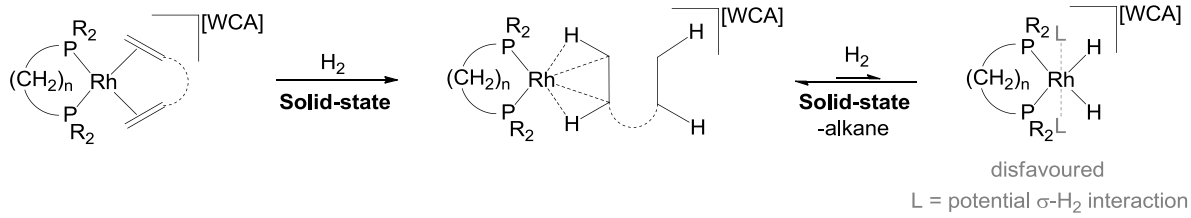

Scheme 2.5. Proposed solid-state hydrogenation reaction of target alkene complex (target complex: 16 electron square planar rhodium(I) with a small bite angle chelating phosphine (n = 1-3) and two alkene ligands supported by a WCA).

The criteria for a precursor for the potential formation of a σ-alkane complex are shown in Figure 2.2.

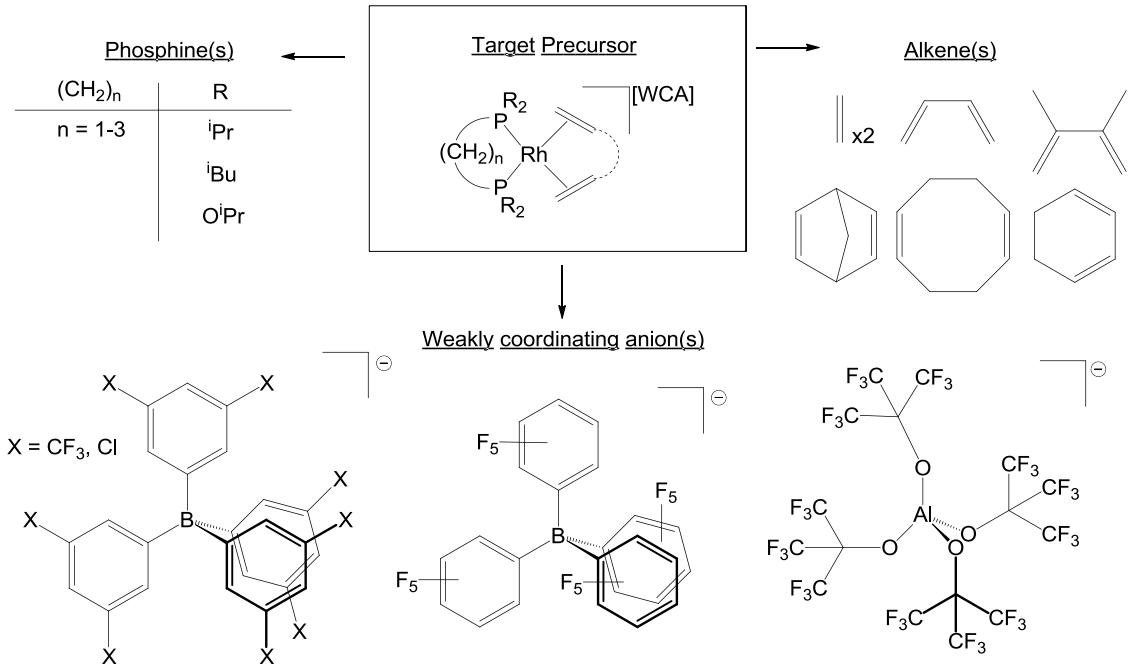

Figure 2.2. Set of possible components to form a target complex considering the criteria outlined.

2.1.ii. Hydrogenation of $[Rh(P^iBu_3)_2(\eta^2\eta^2\text{-NBD})][BAr^F_4]$

Rhodium complexes containing the monodentate phosphine P^iBu_3 have previously been reported.[33-36] It is noteworthy that clean crystalline complexes could often be generated with this phosphine when coupled with the $[BAr^F_4]^-$ anion; crystallinity is an important requirement for the characterisation of solid-state materials by single crystal X-ray crystallography. However it is noteworthy that low valent complexes containing P^iBu_3 are suggested to exhibit agostic interactions; these may compete with a potential σ-alkane interaction.[34, 35, 37]

Hydrogenation of previously reported orange $[Rh(P^iBu_3)_2(\eta^2\eta^2\text{-NBD})][BAr^F_4]$, **I**, in the solid-state rapidly (< 5 minutes) generates a previously reported (characterised in solution) off-white mixture of $[Rh(P^iBu_3)_2(H)_2(H_2)_n][BAr^F_4]$ (n = 1 or 2), **II**, $[Rh(P^iBu_3)_2(H)_2][BAr^F_4]$, **III**, and free norbornane (norbornane = NBA = C_7H_{12}) [Scheme 2.6 & Figure 2.3].[34, 38] Solvation of this off-white complex in CD_2Cl_2 at low temperature confirms its identity as **II** and **III** with hydride signals observed in the low temperature ^{1}H NMR spectrum [signals in agreement with reported data (at 180 K): **III**, δ −1.58 & −13.40; **II**, δ −21.14].[38] In **I** the phosphines occupy a *cis* geometry whereas in **II** and **III** the phosphines occupy *trans* positions. This structural rearrangement causes loss of crystallinity and **II/III** is generated in an amorphous form (crystalline samples of **I** lose definition and the ability to rotate polarised light). As previously reported, application of vacuum to a mixture of solid **II/III** initially forms pure **III**, and finally orange/brown $[Rh(P^iBu_3)_2][BAr^F_4]$, **IV**, after several hours [Scheme 2.6 & Figure 2.3]. **III** is stabilised by agostic interactions and the reported crystal structure details Rh···C agostic distances of 2.90(3) Å and 2.891(5) Å.[34, 38]

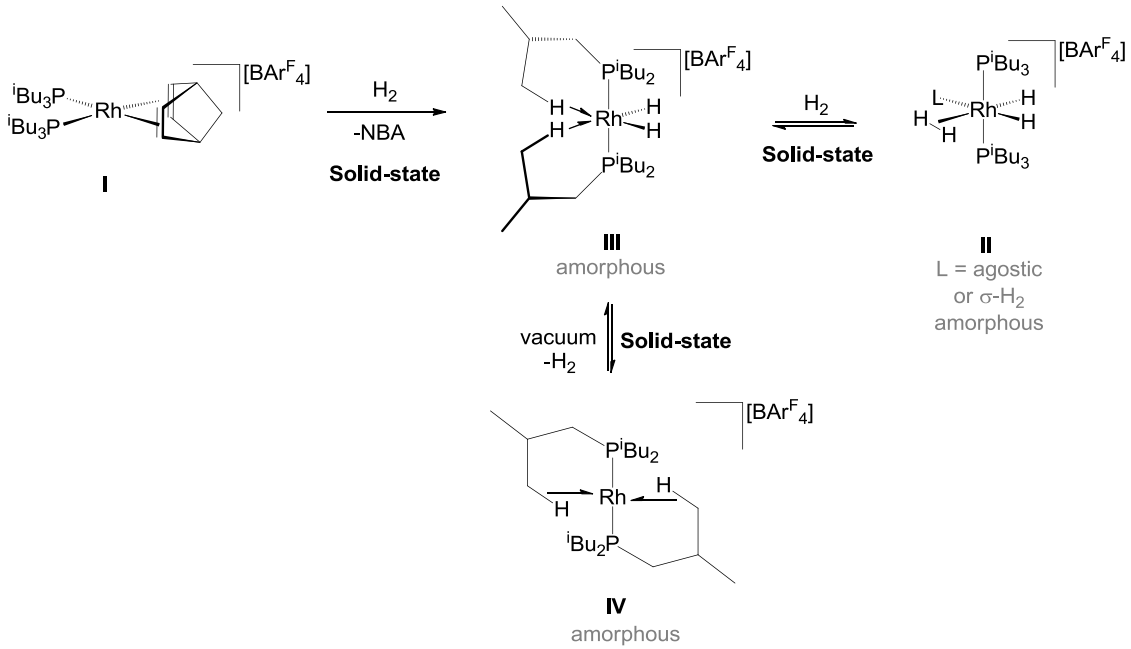

Scheme 2.6. Hydrogenation of **I** in the solid-state and the products which subsequently form under vacuum.

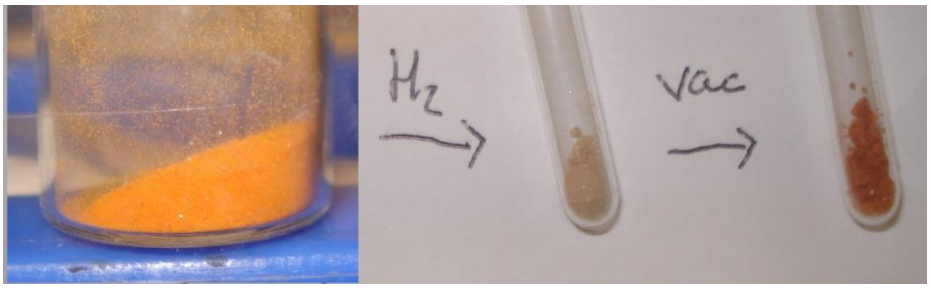

Figure 2.3. Colour changes observed upon hydrogenation of **I** and subsequent evacuation [**I**; orange, **II/III**; off-white, **IV**; orange/brown].

The independent mobility of monodentate P^iBu_3 phosphines around the coordination sphere of a metal may allow for the disruption of a crystal lattice and it appears that agostic interactions are able to form with this phosphine. By changing to a chelating phosphine the phosphorus atoms become locked into a *cis* position and a potential agostic interaction may be weakened by internal ring-strain. The phosphine $^iBu_2PCH_2CH_2P^iBu_2$ has been used to form complexes with molybdenum and the complex $Mo(^iBu_2PCH_2CH_2P^iBu_2)_2CO$ displays a weak agostic interaction with a long Mo···C distance [3.007(4) Å] [Figure 2.4].[37] The Mo···C agostic distance is at the limit of reported agostic interactions for molybdenum [1.8-3.0 Å] and the H-C-Mo angle is large [166°] for an agostic. This suggests that although agostic interactions are possible with this phosphine they may not be particularly stable.

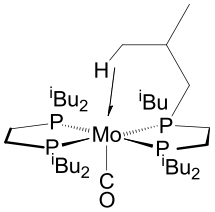

Figure 2.4. A molybdenum complex which exhibits an agostic interaction from chelating phosphine $^{i}Bu_2PCH_2CH_2P^{i}Bu_2$.

2.2. Hydrogenation of [Rh(^{i}Bu$_2$PCH$_2$CH$_2$P^{i}Bu$_2$)($\eta^2\eta^2$-NBD)][BAr$^F_4$]

Encouraged by the crystalline nature of complexes containing monodentate phosphine $P^{i}Bu_3$, which undergo a solid-state reaction with hydrogen, the chelating phosphine $^{i}Bu_2PCH_2CH_2P^{i}Bu_2$ was synthesised. The two carbon backbone of the phosphine ensures a small P-Rh-P bite angle (< 90°) will be defined upon coordination to a metal. There are no previous reports of $^{i}Bu_2PCH_2CH_2P^{i}Bu_2$ ligated to rhodium, with previous reports discussing coordination only to molybdenum and platinum.[37, 39-41]

2.2.i. Synthesis and characterisation of [Rh(^{i}Bu$_2$PCH$_2$CH$_2$P^{i}Bu$_2$)($\eta^2\eta^2$-NBD)][BAr$^F_4$]

[Rh(^{i}Bu$_2$PCH$_2$CH$_2$P^{i}Bu$_2$)($\eta^2\eta^2$-NBD)][BAr$^F_4$], **1**, was synthesised by the solvation of [RhCl(η^2,η^2-NBD)]$_2$ and $^{i}Bu_2PCH_2CH_2P^{i}Bu_2$ in C_6H_5F and subsequent addition of Na[BAr$^F_4$] [Scheme 2.7]. Separation of soluble by-products, likely to include [Rh(^{i}Bu$_2$PCH$_2$CH$_2$P^{i}Bu$_2$)$_2$][BAr$^F_4$], is facile because **1** mostly precipitates out of the C_6H_5F solution. Recrystallisation in CH_2Cl_2/pentane forms pure crystalline material of **1** in moderate yields (58%).

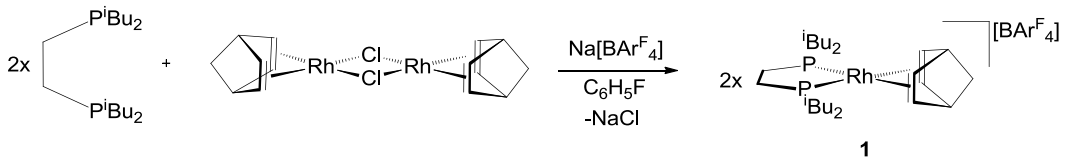

Scheme 2.7. Synthesis of **1**.

The ^{1}H NMR spectrum of **1** (CD_2Cl_2) displays three peaks for coordinated NBD [δ 1.78 (integral 2H), 4.09 (integral 2H) & 5.31 (integral 4H)]. The NBD alkene peak [$\delta_{(alkene)}$ 5.31] has been shifted upfield

compared to the signal of free NBD [free NBD ($CDCl_3$) $\delta_{(alkene)}$ 6.80], consistent with coordination to a metal centre, and falls within the range reported for NBD in previously published compounds such as $[Rh(Ph_2PCH_2CH_2PPh_2)(\eta^2\eta^2\text{-NBD})][BAr^F{}_4]$, **V** [$\delta_{(NBD)}$ (d_6-acetone) 1.82, 4.26 & 5.51],[42] and $[Rh(P^iBu_3)_2(\eta^2\eta^2\text{-NBD})][BAr^F{}_4]$, **I** [$\delta_{(NBD)}$ (CD_2Cl_2) 1.68, 3.97, 4.76].[34] The diastereotopic (^{i}Bu) CH_3 groups give two doublet signals in the ^{1}H NMR spectrum. The $^{31}P\{^1H\}$ NMR spectrum reveals a doublet signal [δ 50.0, J_{RhP} 158 Hz], the moderately large coupling constant being typical of Rh(I) complexes and similar to that reported for **I** [J_{RhP} 151 Hz],[34] and **V** [J_{RhP} 158 Hz].[42] The NBD alkene resonances are observed in the $^{13}C\{^1H\}$ NMR spectrum at 86.4 ppm. $^{31}P\{^1H\}$ and $^{13}C\{^1H\}$ SSNMR spectrum were also collected and these spectra match well with the solution phase spectra (*see Chapter 6, for full characterisation details*). It is however noteworthy that the solid-state ^{31}P resonance is broad [δ 48.5, FWHM 344 Hz], perhaps suggesting a small variation of phosphorus environments in the condensed phase.

Crystals of **1** can be grown from CH_2Cl_2/pentane or from C_6H_5F directly. An X-ray diffraction dataset was recorded and the solid-state structure was refined in collaboration with Dr. Amber Thompson (Chem. Crystallography, Uni. Oxford). The structure reveals the expected square planar geometry [Figure 2.5].

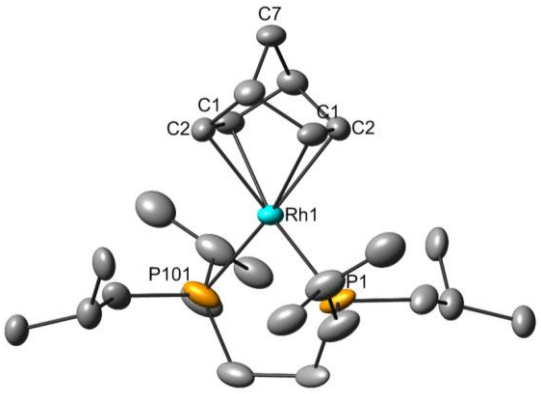

Figure 2.5. Displacement ellipsoid plot (30% probability) for the major cationic component of **1** in the solid-state. Hydrogen atoms omitted for clarity. Selected bond length (Å) and angle (º) data: Rh(1)–P(1), 2.250(4); Rh(1)–P(101), 2.290(4); Rh(1)–C(1), 2.232(6); Rh(1)–C(2), 2.218(6); C(1)–C(2), 1.363(1); P(1)-Rh(1)-P(101), 84.21(6); dihedral C(1)/C(2)/P(1)/P(101), −87.8(4).

The structure solves in the space group *C*2/c with the metal centre sitting upon a symmetry position so that only half the molecule need be modelled. The half phosphine fragment was disordered and was

modelled as a single whole molecule with 50% occupancy [Rh(1)–P(1), 2.250(4) Å; Rh(1)–P(101), 2.290(4) Å]. However close examination of the Fourier map revealed another minor peak ~2.3 Å from the rhodium corresponding to the phosphorus of a phosphine rotated by 90° (~10% occupancy). Repeated data collection revealed the same disorder proportions. Twinning was considered as a cause for this minor component but all sensible twin scale factors refined to zero, therefore it was treated as disorder and a minor disorder component was modelled. The cation, if viewed from above the NBD, fits tightly within a square and it is possible that this *pseudo* C_4 symmetry allows a fraction of cations rotated by 90° to fit into the same crystal lattice [Figure 2.6(a)]. Note also that the ^{i}Bu groups are flexible and can adjust to adopt different geometries; minor disorder of ^{i}Bu is often observed in solid-state structures. The extended lattice structure shows that each cation is surrounded by six $[BAr^{F}_{4}]^{-}$ anions in a *pseudo*-octahedral environment [Figure 2.6(b)]. This high symmetry environment may have only a slight preference for the orientation of the cation, allowing some alternate orientations which appear in the X-ray structure as disorder.

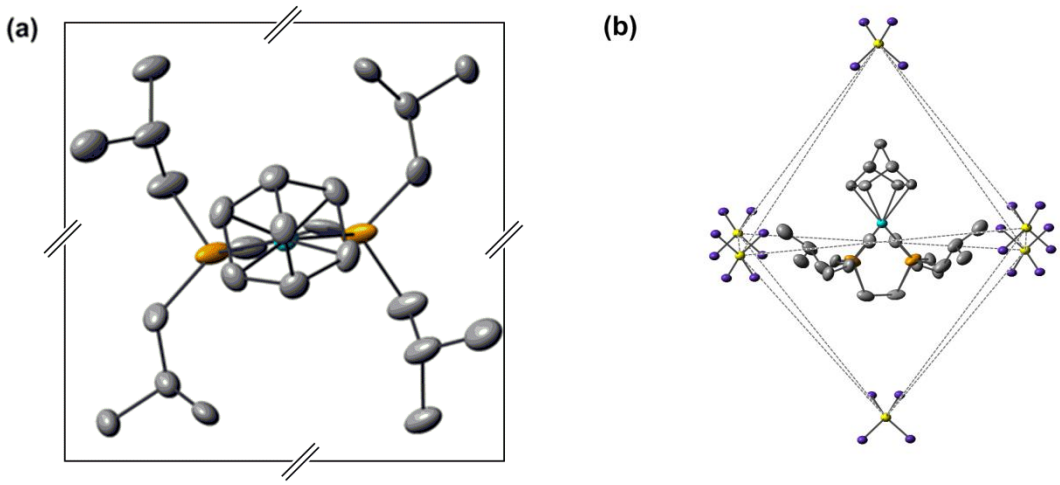

Figure 2.6. (a) Major disorder component of the cation of **1** viewed from above the NBD and enclosed within a square (close to *pseudo*-4-fold rotational symmetry), hydrogen atoms omitted for clarity. **(b)** Packing diagram of **1**; single cation enclosed within a *pseudo*-octahedron of anions, hydrogen atoms omitted and $[BAr^{F}_{4}]^{-}$ anions represented as BC_4 units (Ar^{F} groups omitted) for clarity.

The NBD C=C bond lengths in **1** are similar to the bond lengths recorded in the crystal structure of pure NBD suggesting that only a small amount of back donation from the metal into the C=C π^* orbital occurs [C=C bond length: **1**, 1.363(10) Å; pure NBD, 1.3359(14) Å & 1.3370(14) Å].[43]

2.2.ii. Hydrogenation of 1 in solution

1 is only sparingly soluble in C_6H_5F but dissolves well in 1,2-$C_6H_4F_2$. Exposure of **1** suspended in C_6H_5F or solvated in 1,2-$C_6H_4F_2$ to 1 atm H_2 results in a rapid (< 5 minutes) colour change from orange to yellow. The products formed are 18 electron, η^6-arene complexes $[Rh(^iBu_2PCH_2CH_2P^iBu_2)(\eta^6\text{-}C_6H_5F)][BAr^F{}_4]$, **2**, and $[Rh(^iBu_2PCH_2CH_2P^iBu_2)(\eta^6\text{-}1,2\text{-}C_6H_4F_2)][BAr^F{}_4]$, **3**, respectively [Scheme 2.8]. Both are characterised by NMR spectroscopy and ESI-MS, and are fully soluble in their parent fluorobenzene solvent.

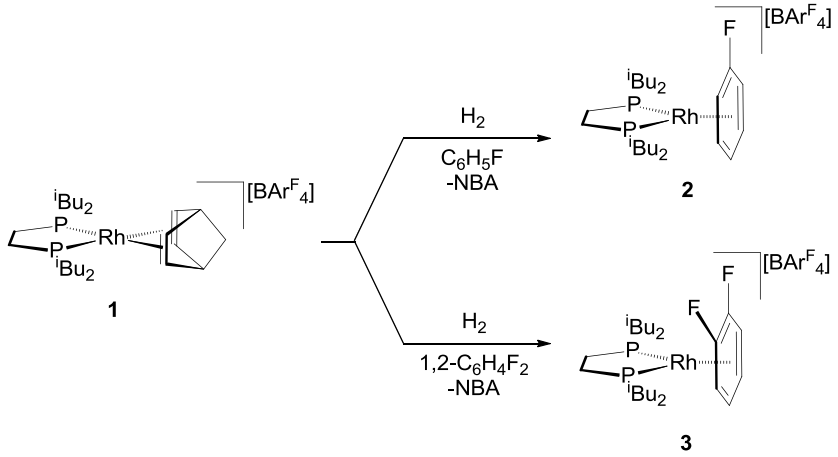

Scheme 2.8. Reaction of **1** with hydrogen in fluorobenzene solvents.

The ^{1}H NMR spectrum of **2** (C_6H_5F solvent) reveals three peaks for the coordinated C_6H_5F ligand which are observed upfield compared to those of the free C_6H_5F [**2**, $\delta_{(arene)}$ 5.47, 6.19 & 6.25; C_6H_5F, δ 6.92 & 7.11] This shift is consistent with coordination to a metal centre and is comparable with the reported data for other fluorobenzene complexes such as $[Rh(P^iBu_3)_2(\eta^6\text{-}C_6H_5F)[BAr^F{}_4]$, **VI** [$\delta_{(arene)}$ 5.49 & 6.22].[34, 44] A shift is also observed for the two ^{1}H NMR arene signals for **3** in comparison to the 1,2-$C_6H_4F_2$ solvent [**3**, $\delta_{(arene)}$ 6.18 & 6.83; 1,2-$C_6H_4F_2$, δ 7.00 & 7.07].

The $^{31}P\{^1H\}$ NMR spectrum of **2** [δ 74.5, J_{RhP} 206 Hz] and **3** [δ 74.7, J_{RhP} 204 Hz] in the parent fluorobenzene solvents are very similar, both displaying a doublet with a large rhodium-phosphorus coupling constant. Such a large coupling constant is indicative of a strong rhodium-phosphorus interaction, likely caused by a relatively weak *trans* interaction, as is often observed for η^6-arene complexes.[34, 44, 45]

Single crystals of both complexes were prepared for X-ray diffraction by layering the parent fluorobenzene solution with pentane. However the dataset recorded for **2** refined to give a highly disordered solid-state structure [tetragonal *P* −4 space group]. The ^{i}Bu groups were disordered fairly evenly over two distinct positions but, more problematically, there is a minor disorder component for the cation inverted (~14%), with a secondary rhodium position. The fluorine atom was also disordered over two symmetry related positions. The $[BAr^{F}_{4}]^{-}$ anions recreate a similar *pseudo*-octahedral geometry around the cation as observed for **1** [Figure 2.7(b)]. An approximate structure could be determined and is displayed as a ball and stick diagram in Figure 2.7(a).

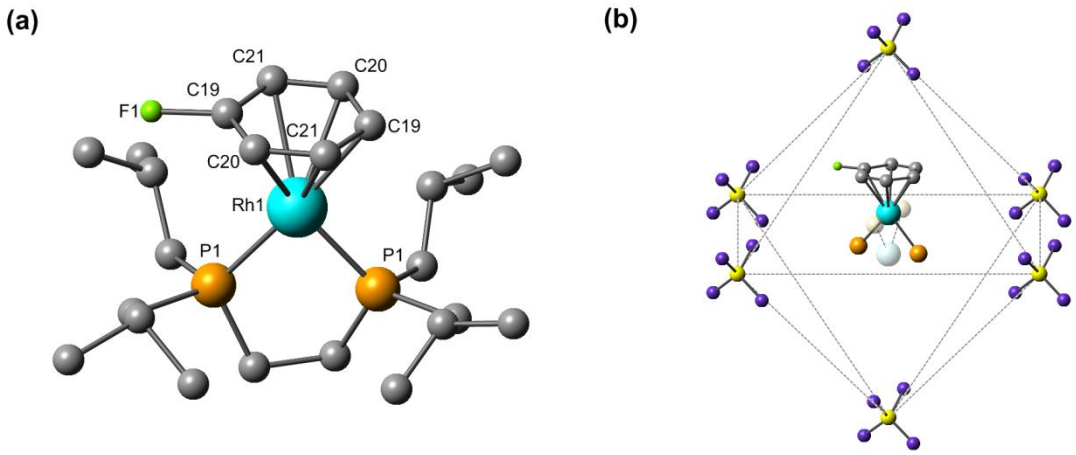

Figure 2.7. (a) Ball and stick diagram of the approximate solid-state structure of the major cationic disorder component of **2**. Hydrogen atoms omitted. **(b)** Approximate packing diagram of **2**; simplified cation $\{RhP_2(\eta^6\text{-}C_6H_5F)$ shown only$\}$ and minor disorder component overlaid (transparent $\{RhP_2\}$ fragment shown only) enclosed within a *pseudo*-octahedron of anions, hydrogen atoms omitted and $[BAr^{F}_{4}]^{-}$ anions represented as BC_4 units (Ar^{F} groups omitted) for clarity.

It therefore appears that in compounds **1** and **2** the cation may adopt alternative orientations within the anion-defined cavity although the effect is more pronounced in the structure of **2**.

A solid-state structure of **3** could be determined (solved by Dr. Adrian Chaplin; PDRA Weller Group) with greater accuracy than for **2**. Only very minor (~6%) rotated phosphine disorder components were observed and these were left unmodelled. The structure was solved in the tetragonal space group *P* −4 [Figure 2.8]. An octahedral arrangement of anions was again observed in the packing structure.

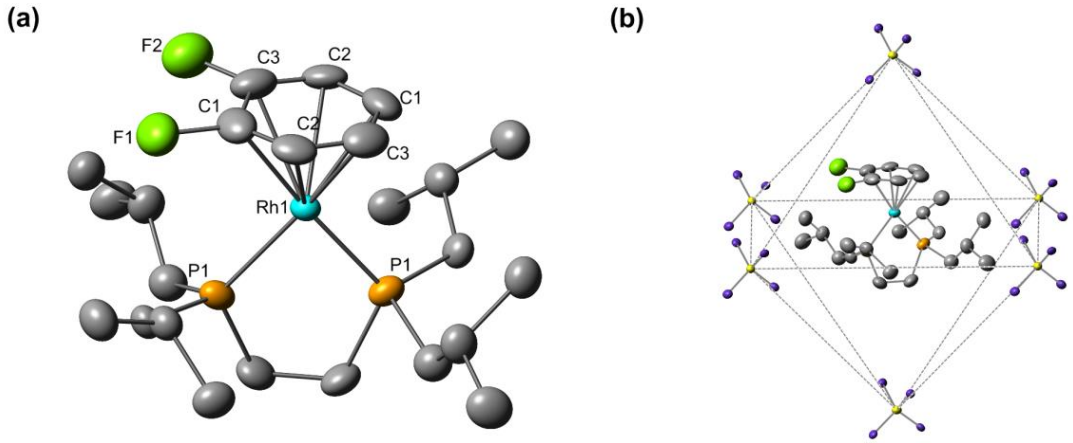

Figure 2.8. Displacement ellipsoid plots (30% probability) **(a)** the major cationic component of **3** in the solid-state. Hydrogen atoms omitted for clarity. **(b)** packing diagram of **3**, single cation enclosed within a *pseudo*-octahedron of anions, hydrogen atoms omitted and $[BAr^F{}_4]^-$ anions represented as BC_4 units (Ar^F groups omitted) for clarity. Selected bond length (Å) and angle (º) data: Rh(1)–P(1), 2.2416(19); Rh(1)–C(1), 2.276(9); Rh(1)–C(3), 2.336(10); P(1)-Rh(1)-P(101), 82.79(12).

Solid-state structures of η^6-1,2-$C_6H_4F_2$ complexes are rare with only the structure of analogous $[Rh(P^iBu_3)_2(\eta^6\text{-}1,2\text{-}C_6H_4F_2)][BAr^F{}_4]$, **VII**, reported with a transition metal [46] {other structures have been reported with indium and gallium (*bis* η^6-1,2-$C_6H_4F_2$ bent sandwich complexes)}.[47, 48] The Rh−$C_{(arene)}$ bond lengths are all similar [range 2.276(9)-2.336(10) Å] and are consistent with other η^6-arene complexes [**VI** Rh–$C_{(arene)}$ range, 2.266(15)-2.458(10) Å, **VII** Rh–$C_{(arene)}$ range, 2.313(5)-2.399(5) Å].[33, 34, 46] Chapter 5 explores the binding affinities of fluorobenzenes to rhodium complexes and shows 1,2-$C_6H_4F_2$ coordinates only weakly to a metal centre in the gas phase.

Hydrogenation of **1** in a non-coordinating solvent such as CH_2Cl_2 or suspended in C_6F_6 forms the yellow zwitterioinic complex $Rh(^iBu_2PCH_2CH_2P^iBu_2)\{\eta^6\text{-}C_6H_3(CF_3)_2\}BAr^F{}_3$, **4**, in which the anion is now coordinated to the metal centre [Scheme 2.9]. Decomposition of **4** occurs in CH_2Cl_2 over the course of ~1 hour but NMR analysis can be undertaken in C_6F_6 solvent, in which zwitterionic **4** is soluble. Neutral **4** is also partially soluble in pentane or hexane and once solvated can be crystallised by cooling such solutions to 277 K. **4** was characterised by NMR spectroscopy and by X-ray crystallography.

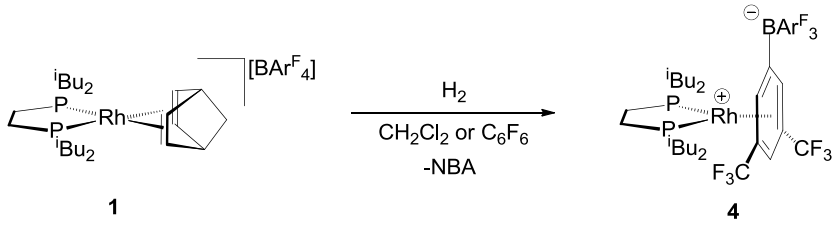

Scheme 2.9. Hydrogenation of **1** in a non coordinating solvent to form zwitterion **4**.

The ^{1}H NMR spectrum of **4** (C_6F_6 solvent) displays two doublet signals [δ 0.91 & 0.97] for the diastereotopic ^{i}Bu (CH_3) groups consistent with the other complexes described with this phosphine, however they are slightly shifted upfield relative to **1**. The coordinated anion displays a set of four peaks in the aryl region in a 2:1:3:6 relative ratio [δ 6.74, 7.36, 7.41 & 7.62] indicative of η^6-coordination of one arene group. The other three arene groups presumably undergo exchange by rotation around the B–C bond to the coordinated arene. This arrangement is confirmed by analysis of the ^{19}F NMR spectrum which reveals only two signals for the CF_3 groups, both similar to the signal of free $[BAr^F_4]^-$, with a 3:1 ratio [δ −67.43 & −64.93]. These ^{1}H and ^{19}F NMR spectra are very similar to the spectra of previously published coordinated $[BAr^F_4]^-$ complexes $Rh\{P(Cyp_2)(\eta^2\text{-}C_5H_7)\}\{\eta^6\text{-}Ar^F(BAr^F_3)\}$ and $Ir(H)_2(PCyp_3)\{\eta^6\text{-}Ar^F(BAr^F_3)\}$ (*see Section 1.2.iii*).[49, 50] The solution $^{31}P\{^{1}H\}$ NMR spectrum of **4** displays a doublet signal [δ 70.2, J_{RhP} 204 Hz] similar to that of **2** and **3**, a large coupling constant again being observed. The $^{31}P\{^{1}H\}$ SSNMR spectra reveals that there are four independent phosphorus environments in the solid-state. An X-ray crystal structure of **4** confirms two independent molecules are found in the solid-state and that each phosphorus environment is crystallographically distinct [Figure 2.9]. Single crystals were grown from a saturated pentane solution of **4** at 277 K. The solid-state structure shows a coordinated $[BAr^F_4]^-$ anion, with two independent molecules varying only by the position of the coordinated anion [torsion angles: P(1)P(2)Rh(1)C(51); 27.54(5)°, P(101)P(102)Rh(101)C(151); 47.49(6)°].[51]

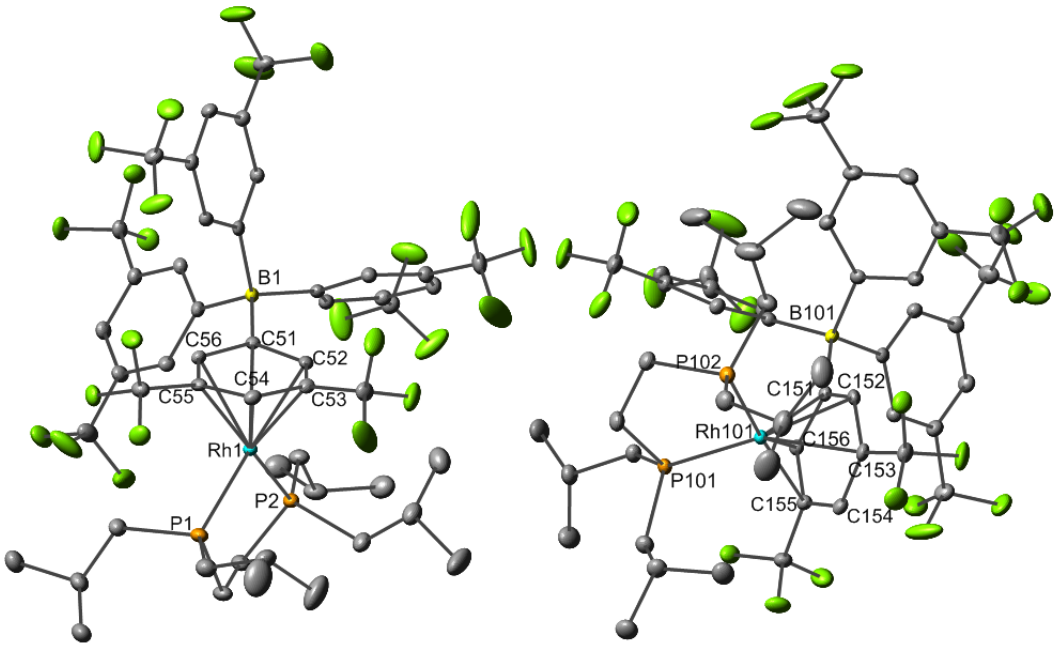

Figure 2.9. Displacement ellipsoid plot (30% probability) of complex **4** in the solid-state. Hydrogen atoms omitted for clarity. Selected bond length (Å) and angle (º) data: Rh(1)–P(1), 2.2429(6); Rh(1)–P(2), 2.2325(6); Rh(1)–C(19), 2.417(2); Rh(1)–C(24), 2.251(2); P(1)-Rh(1)-P(2), 85.23(2). Second molecule: Rh(101)–P(101), 2.2405(5); Rh(101)–P(102), 2.2491(5); Rh(101)–C(151), 2.4566(19); Rh(101)–C(155), 2.269(2); P(101)-Rh(101)-P(102), 83.63(2).

The Rh–$C_{(arene)}$ bond lengths vary from 2.251(2) Å to 2.4566(19) Å with the longest bonds to the carbons connected to the boron atoms. The bond lengths are roughly consistent with the previously published coordinated $[BAr^F_4]^-$ complexes [Rh(COD){η^6-$Ar^F(BAr^F_3)$}] Rh–$C_{(arene)}$ range: 2.251(5)-2.430(5) Å and Rh{$P(Cyp_2)(\eta^2$-$C_5H_7)$}{η^6-$Ar^F(BAr^F_3)$}] Rh–$C_{(arene)}$ range: 2.263(3)-2.426(3) Å].[49, 52] Previous reports locate the bonding/non-bonding boundary for Rh···C interactions in arene complexes at around 2.44-2.50 Å so it is debatable as to whether **4** should be defined as a η^5 or η^6 complex.[33, 53]

If **2** or **3** are dissolved in CH_2Cl_2 an equilibrium is established with **4** [Scheme 2.10]. The equilibrium lies in favour of the fluorobenzene complex for **2** but in favour of the zwitterion for **3**, indicating the respective binding affinities of the arenes relative to $[BAr^F_4]^-$. This topic is discussed in detail in *Chapter 5*.

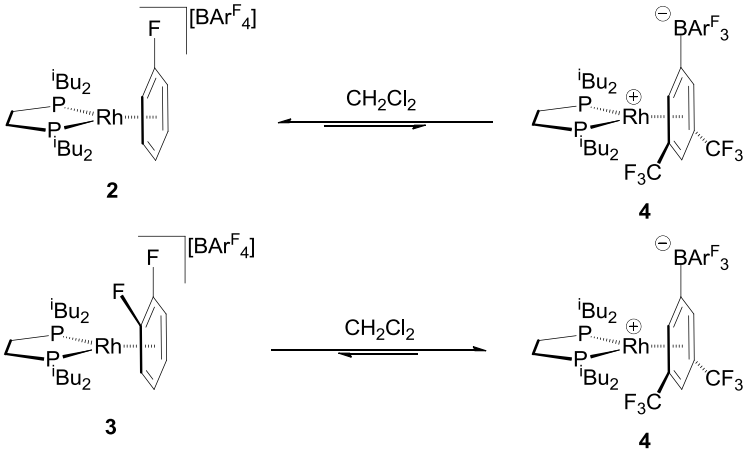

Scheme 2.10. Equilibria established in CH_2Cl_2.

2.2.iii. Hydrogenation of 1 in the solid-state

Exposure of a solid microcrystalline sample of orange **1** to 1 atm H_2 results in a rapid colour change (4 minutes) to a claret colour (complex **5**, *vide infra*) [Figure 2.10]. This material apparently remains stable under vacuum, argon or H_2 for several hours but eventually changes colour to yellow.

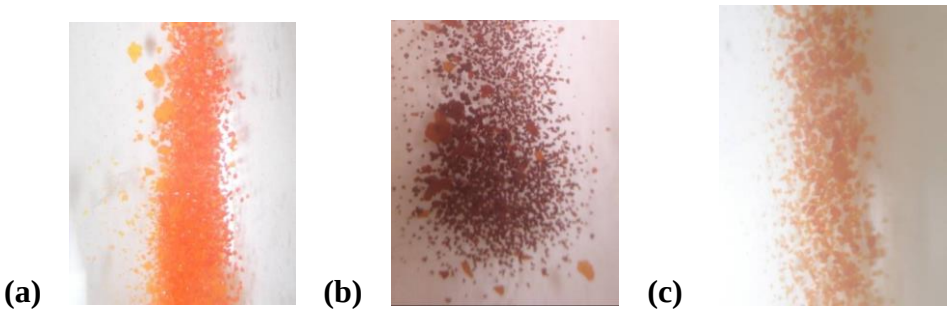

Figure 2.10. Colour changes observed upon exposure of crystalline **1 (a)** to hydrogen after 10 minutes **(b)** and 12 hours **(c)**.

Solvation of either the claret intermediate or yellow final product in CD_2Cl_2 indicates the formation of **4** in solution.

2.2.iv. The solid-state hydrogenation of 1 followed by SSNMR spectroscopy

SSNMR was required to probe the nature of the claret intermediate in the solid-state. SSNMR spectra were recorded at the EPSRC National Solid-State NMR service centre (Durham University, in collaboration with Dr. David Apperley). Samples of **1**, and **4** were analysed directly by SSNMR [Figure 2.11(a) & (d)]. To perform the hydrogenation reaction the rotor was filled with **1** and exposed to hydrogen (1 atm) with one end left open for 3.5 minutes at room temperature (the lid was later added within a glovebox). This process produced a $^{31}P\{^{1}H\}$ SSNMR spectrum with peaks assigned to the claret intermediate, which will be referred to as **5** (*vide infra*), alongside zwitterion **4** (with a small amount of unreacted **1**) [Figure 2.11(b)]. Over time (~15 minutes) the intermediate signal for **5** diminishes and the zwitterion grows to become the major species [Figure 2.11(c)]. It is noteworthy that the signal for **4** is very broad at first. We suggest that this is because the complex forms in an amorphous form [Figure 2.11(b)]. However gentle heating (~298 K) results in a phase change with recrystallisation to give a distinctive SSNMR spectrum consistent with previously prepared **4** [Figure 2.11(c) & (d)].

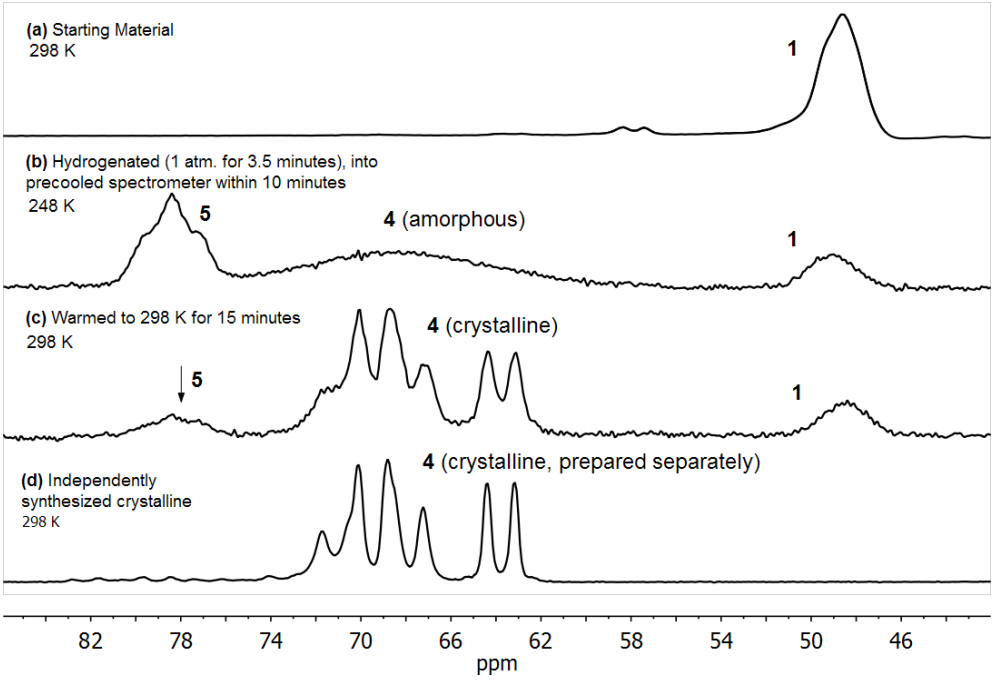

Figure 2.11. $^{31}P\{^{1}H\}$ SSNMR spectra before and after exposure to hydrogen, displaying the transitions which occur **1** to **5** to **4** (amorphous) and finally to **4** (microcrystalline).

Due to the experimental setup of the hydrogenation procedure there was a short time period at ambient temperature before the rotor was loaded into the pre-cooled probe, this resulted in the

observation of the final product **4** along with the intermediate **5** in the initial spectra [Figure 2.11(b)]. However, in all cases no longer than 12 minutes was needed from the start point of the hydrogenation procedure to recording the first spectrum.

The claret intermediate **5** was observed as a tightly coupled ABX system centred at δ 78.3 [δ 77.6, J_{RhP} ~ 194 ±10 Hz & δ 78.9, J_{RhP} ~ 191 ±10 Hz], the large coupling constant is indicative of a weakly bound ligand *trans* to phosphorus. This signal decayed rapidly at temperatures above 293 K, but appeared to remain stable at lower temperatures [≤253 K]. $^{13}C\{^{1}H\}$ SSNMR spectra of the hydrogenated material clearly showed the loss of the alkene NBD signals located at δ 86.6 and 87.4 consistent with the consumption of **1**. No other peaks were observed in the alkene region.

2.2.v. Crystallographic analysis of the SC-SC transition 1 to 5

In order to obtain more detailed structural information of complex **5** by X-ray crystallography single crystals of **1** were exposed to 1 atm hydrogen. A similar colour change to claret was observed and importantly the crystals maintained their ability to rotate polarised light (indicative of single crystallinity), although some cracking did occur. Therefore a SC-SC transition between **1** and **5** was proposed. Single crystals of **1** were exposed to 1 atm hydrogen for an optimised period of 11 minutes, as longer periods of reaction were found to encourage the partial formation of final product **4** and resulted in lower diffraction quality. A diffraction pattern of **5** was collected and the data refined in collaboration with Dr. Amber Thompson. A solid-state structure of **5** was revealed in which a NBA unit is observed to coordinate to the rhodium centre through two C–H σ-bonds, *i.e.* a square planar, 16 electron, rhodium(I) chelating σ-alkane complex [Figure 2.12].

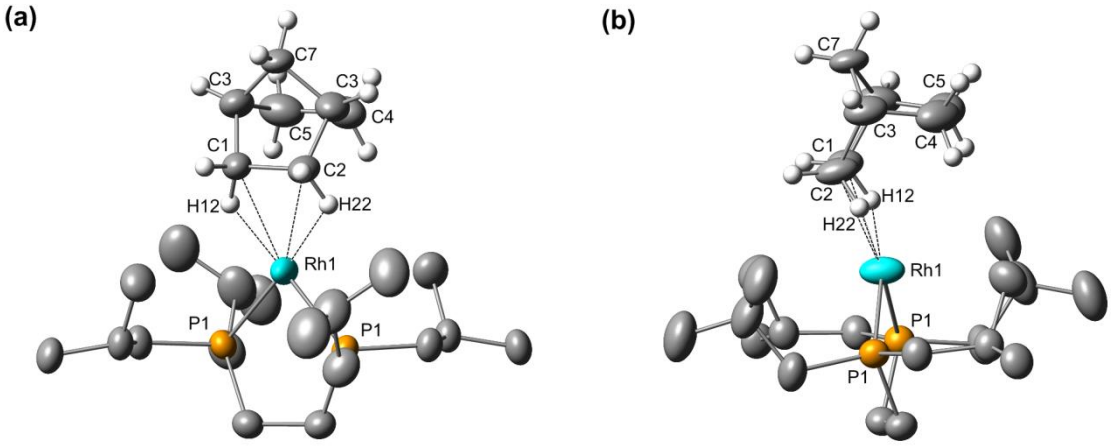

Figure 2.12. Displacement ellipsoid plot (30% probability) for the cationic component of **5** in the solid-state (one disorder component of NBA shown). All but NBA hydrogen atoms omitted for clarity (hydrogens in calculated positions). Two alternate views shown **(a)** and **(b)**. Selected bond length (Å) and angle (º) data: Rh(1)–P(1), 2.1875(13); Rh(1)–C(1), 2.494(10); Rh(1)–C(2), 2.480(11); C(1)–C(2), 1.557(15); C(4)–C(5), 1.51(2); P(1)-Rh(1)-P(1'), 84.16(7); dihedral C(1)/C(2)/P(1)/P(1'), −175.6(8).

The crystallographic procedure was repeated many times at collection temperatures ranging from 100-213 K, all experiments giving the same structure. A small amount (< 2%) of starting material (**1**, which is isomorphous) is retained in the highest quality X-ray structure, which was characterised by a peak of residual electron density near Rh(1) in the Fourier map. The residual peak was found to lie on the 2-fold axis, between the rhodium and the boron of the [BAr^F_4] anion. Its position and its distance to the boron atom [8.23(3) Å] was entirely consistent with the position of rhodium in the solid-state structure of **1** [Rh(1)–B(50), 8.200(8) Å]. Periods of crystal hydrogenation shorter than 11 minutes resulted in retention of greater amounts of **1** (e.g. 8 minutes hydrogenation, 20% **1** retention).

Small crystals of **5** changed color to yellow if left at ambient temperature for greater than 30 minutes. These gave no observable diffraction which is consistent with the transition to an amorphous form of **4**. Observing the crystals of **5** under a microscope over time showed a yellow amorphous exterior forming around the claret centre, suggesting the conversion to **4** occurred from the surface progressing inwards. This explains why crystals of **5** still diffracted in the presence of a small amount of **4**.

5, like **1**, solved in the monoclinic *C* 2/c space group with a very similar unit cell to **1** [Unit cell volumes (z = 4): **1**; 5957.62(19) $Å^3$, **5**; 6044.1(3) $Å^3$. SC-SC expansion = +22 $Å^3$ (for z = 1 equivalent), 1.5% volume increase] as expected for a SC-SC transition (*see Section 1.3.iii, Table1.1*

for comparisons).[27, 28, 54-56] The NBA was disordered equally over two symmetry related positions. The ~10% disorder (cation rotated ~90°) component located in the structure of **1** is greatly diminished in the structure of **5** (barely noticeable in the Fourier map). Perhaps there is sufficient flexibility in the crystal lattice to allow the disorder component to rotate under the internal pressure caused during the reaction. The NBA unit itself has moved significantly from the position of NBD in **1** (approximate 90° rotation), indicating that the ligands associated with the cation have the ability to rearrange within the well defined reaction cavity determined by the $[BAr^F_4]^-$ anions [Figure 2.13]. Presumably this change in geometry is driven by the alignment of the C–H bonds with the frontier molecular orbitals of the metal centre. The Rh···B distance (which is drawn through the NBA/NBD fragment) increases in the structure of **5** relative to **1**, most probably because the cation is pressed backwards by the expansion caused by hydrogenation and rotation of the NBA/NBD unit [Rh(1)···B(50) distances (drawn through NBA/NBD fragment): **1** 8.200(8) Å; **5** 9.13(1) Å]. The B···B *trans* octahedron distance {drawn through Rh(1) and NBA/NBD fragment} is also larger for **5** compared to **1** [B(50)···B(50) distances (drawn through Rh(1) and NBA/NBD fragment): **1** 17.062(10) Å; **5** 17.596(10) Å] indicating a minor change in packing geometry to accommodate the new cation.

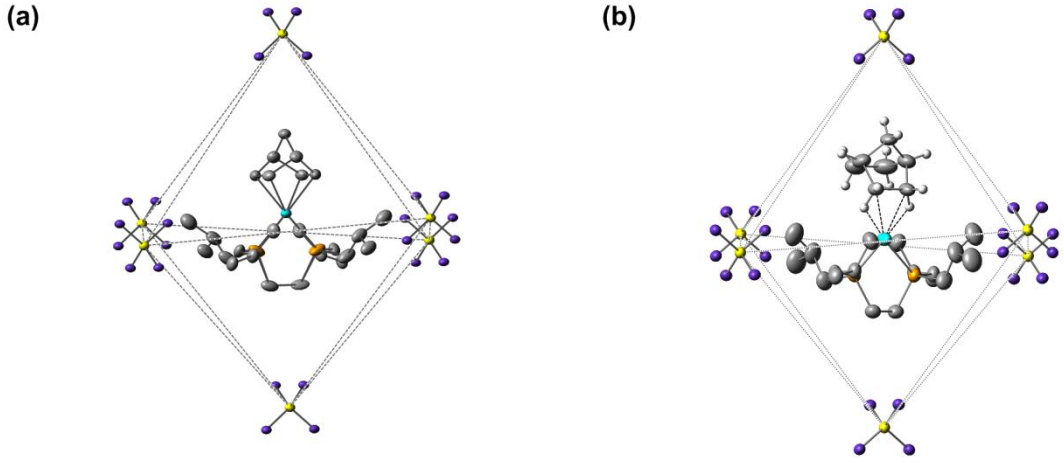

Figure 2.13. Packing diagrams of **1 (a)** and **5 (b)**; single cations enclosed within a *pseudo*-octahedron of anions, most hydrogen atoms omitted and $[BAr^F_4]^-$ anions represented as BC_4 units (aryl groups omitted) for clarity. The movement of the NBD/NBA unit can be observed, alongside the downwards movement of the $\{RhP_2\}$ fragment upon hydrogenation.

Inspection of the NBD/NBA fragments in the crystal structures of **1** and **5** reveals an apparent elongation of the C=C double bonds in **1** to C–C single bonds in **5** [**1**, C(1)–C(2), 1.363(10) Å; **5**, C(1)–C(2), 1.557(15) Å; C(4)–C(5), 1.51(2) Å] consistent with the hydrogenation reaction. The

hydrogen atoms of the organic fragment could not be located within the Fourier map and were placed in calculated positions. The Rh···C distances [Rh(1)–C(1), 2.494(10) Å; Rh(1)–C(2), 2.480(11) Å] are within the range reported for Rh–C distances for agostic interactions on rhodium [typically 2.4-3.0 Å][57] and are shorter than the Rh–C bond length in the recently reported cobalt-σ-hexane complex [2.718(3) Å][20] suggesting a significant σ-interaction is occurring in **5**. The sum of van der Waals radii for Rh and a CH_2 fragment is ~4.44 Å [58, 59] and so clearly the observed Rh···H–C distance is well within this distance. Analysis of the Rh–P bonds shows that those of **5** are shorter than those of **1** [**1**, Rh(1)–P(1), 2.250(4) Å; Rh(1)–P(101), 2.290(4) Å; **5**, Rh(1)–P(1), 2.1875(13)], however the bite angle remains almost identical. The bond length contraction is consistent with the comparative *trans* influence of alkene compared with σ-C–H interactions.

The C–H bonds that interact with the metal centre in **5** are located parallel to the plane of the square planar coordination structure, therefore any back-bonding interaction will take place from the d_{xy} orbital into the C–H σ* orbitals. Since only one d-orbital has the correct symmetry for back-donation the interaction must be shared across both C–H bonds. Therefore, this geometry predicts a small backbonding interaction to each C-H bond (which is confirmed by computational calculations, *vide infra*). This is particularly important with respect to C-H activation, since a large back-bonding interaction is required to cleave the C-H bond. In this geometry the alkane is more likely to remain intact rather than undergoing C-H activation.

Interestingly cooling **5** changes its colour from claret to orange, indicating the complex has thermochromic properties. This colour change appears to occur when the compound is cooled to 195 K or below. Accurate variable temperature UV-vis spectroscopy has not yet been undertaken to further understand this process.

2.2.vi. Computational investigation of the structure of σ-alkane complex 5

The structure of **5** was investigated by computational methods by Dr. Andrés Algarra and Prof. Stuart Macgregor (Heriot Watt University).[60] The computationally optimised structure reproduces the heavy atom positions of **5** well and hydrogen atom positions were also calculated. The Rh···C distance is calculated at 2.45 Å, which is close to the crystallographic value. A short Rh···H distance of 1.92 Å is

also calculated, which is similar (within 3σ error) to the crystallographic value generated from the recently reported cobalt-σ-hexane structure [Co···H; 1.995(30) Å]. The coordinating C–H bonds are calculated to become elongated by the σ-interaction in comparison with the non-coordinated geminal C–H bonds [C_a–H_a; 1.16 Å, C_b–H_b; 1.10 Å].[60] This is a consequence of partial population of the C–H σ* by back-donation from the metal, along with donation of C–H σ electron density to the metal. An atoms-in-molecule (AIM) study confirmed that two C–H interactions were indeed occurring. A curved bond path between Rh and H_a was calculated and is indicative of a 3-centre 2-electron interaction [Figure 2.14].

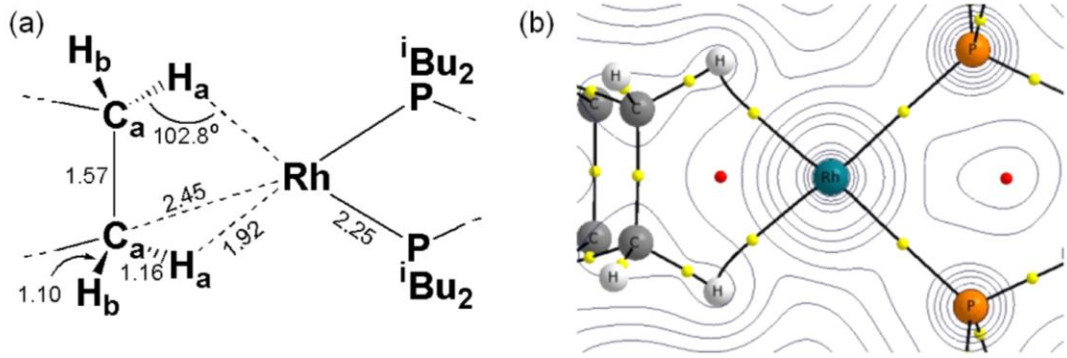

Figure 2.14. (a) Computed distances (Å) and angles (°) for **5**. **(b)** Contour plot of the total electron density in the Rh-H_a-H_a plane. Bond critical points shown in yellow, ring critical points in red (figure courtesy of Dr. Andrés Algarra and Prof. Stuart Macgregor). *Figure reproduced from: AAAS, Science, Synthesis and Characterisation of a Rhodium(I) σ-Alkane Complex in the Solid-State (License Number: 3310131484982).*[60]

A complementary natural bond order (NBO) analysis was also undertaken which showed that the main part of the σ-interaction in **5** is the σ-donation of the C_a–H_a bond into the metal centre. A lesser π-back-donation from the metal orbitals into the C_a–H_a σ* orbital is also computed. Second-order perturbation analysis reveals these interactions to be 20.3 and 8.9 kcal/mol respectively (in comparison the much stronger Rh···(C=C) bonding and back-bonding interactions in **1** are 62.3 and 42.7 kcal/mol respectively). Each σ-interaction [total 29.2 kcal/mol] is therefore roughly twice as strong as what might be typically expected for an agostic interaction (8-15 kcal/mol), indicating a remarkably strong combined σ-interaction occurs, which is in keeping with the short Rh···C distances.[29, 61, 62] It should, however, be noted that, in contrast to agostic interactions, loss of the alkane ligand from **5** is essentially irreversible and may be more entropically favoured. The NBO analysis also discounted for a significant Rh···(C–C) σ-interaction (total interaction ~0.8 kcal/mol).

Alternate geometries of the norbornane fragment were also investigated by computational methods but these all proved to be higher in energy than the conformation observed by experiment.

The $^{13}C\{^{1}H\}$ chemical shifts of the Rh···C–H interactions were calculated to lie at δ 31.2 & 33.3 by computational methods (although this value was dependent upon the calculation method [δ 25.8-35.2 range across all methods]). Two signals are predicted due to a slight asymmetry in the molecule, which is observed in the SSNMR spectra (tightly coupled ABX system). The signals for these interactions could not be definitely assigned in the SSNMR spectra collected, as they lie within the region of signals assigned to the ^{i}Bu groups of the phosphine. It is therefore likely that the resonances could be obscured. The ^{13}C NMR resonances associated with the agostic carbons of norbornene complexes **6** (*vide infra*) and the similar (2-Me-propenylnorbornyl)Pd(norbornene) are observed at δ 31.2 and 42.5 respectively.[63] In contrast the resonance for coordinated methane in [(PONOP)Rh($^{13}CH_4$)][BAr^F_4] is observed at δ −41.7, indicating a wide range of ^{13}C chemical shifts associated with the Rh···HC sigma interactions when directly interacting with a metal.[21]

2.2.vii. Solvation of σ-alkane complex 5 at low temperatures

Solution NMR spectra of **5** could not be captured even at very low temperatures. $CDCl_2F$ solvent was vacuum transferred onto a powdered crystalline sample of complex **5** kept frozen in liquid N_2. The frozen sample was quickly transferred into the NMR spectrometer, with a bright red solution observed as the solvent melted. ^{1}H NMR and $^{31}P\{^{1}H\}$ NMR spectra were recorded at 163 K. One equivalent of free NBA was seen immediately in the ^{1}H NMR spectrum, suggesting that complex **5** is not stable in solution at this temperature and that NBA dissociates readily. The resulting organometallic species shows several broad peaks assigned to the phosphine alkyl groups (δ 1-2.5). No peaks were observed between δ 0 and −10 where a σ-complex or agostic interaction would be expected.[21, 22, 64-66] There are also four small relatively sharp peaks {total integration approximately 0.6, and each ≤ 0.3 relative to the [BAr^F_4] peak (8H)} characteristic of hydrides located between −14 and −20 ppm (all apparent quartets, showing coupling to rhodium and phosphorus). These are tentatively assigned as C–H activated species that may occur as minor components of what is likely to be a highly active system, possibly metallacyclic products which form from an ^{i}Bu agostic intermediate.[35] These hydride peaks disappear once warmed to 253 K. No incorporation of deuterium into any component was observed

by exposing a fresh solution (**5** in $CDCl_2F$) to D_2 (1.3 atm) at 157 K °C for 2.5 hours (D_2 and $CDCl_2F$ removed by vacuum and ^2H NMR spectrum recorded in CH_2Cl_2 at 295 K).

The $^{31}P\{^1H\}$ NMR spectrum at 163 K showed a signal centred at δ 82.9 which we assign as a tightly coupled ABX system (J_{RhP} 135 and 140 Hz), however the identity of this species is unknown. A small amount of **4** also forms at this temperature. When warmed to 153 K, **4** grows in intensity to finally be the only species, as observed by the diagnostic pattern downfield in the ^1H NMR spectrum and the expected doublet in the $^{31}P\{^1H\}$ NMR spectrum.

We can only speculate on the species present at 163 K but computational calculations suggest that a *bis*-agostic species $[Rh(^iBu_2PCH_2CH_2P^iBu_2)][BAr^F_4]$ is close in energy to **5** [Scheme 2.11]. Such an agostic interaction could also lead to intramolecular C–H activation leading to a metallacyclic complex.[35] We cannot discount that this species could be a solvent–bound complex, and in fact an analogous $\{RhP_2\}^+$ fragment is suspected to coordinate CH_2Cl_2 at low temperatures (*see Section 2.6.vii*). No high field Rh···HC peak is located in the ^1H NMR spectrum, however other similar complexes which are suggested to exist with agostic or solvent interactions also show no diagnostic high–field signals e.g. $[Rh(P^iBu_3)_2][BAr^F_4]$.[34, 67]

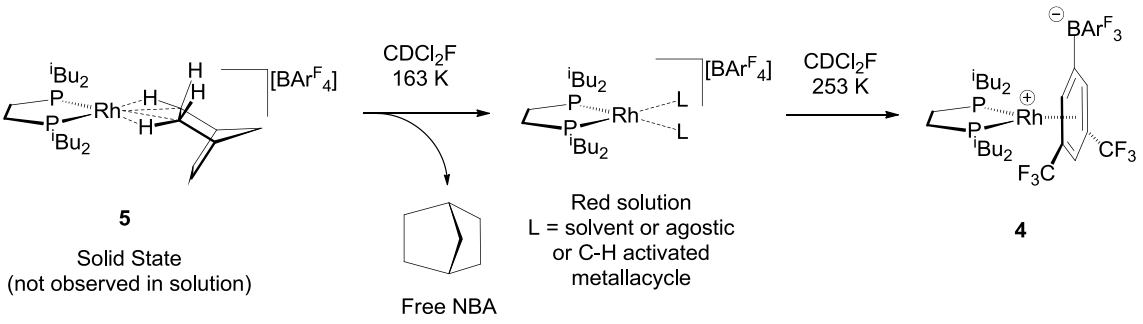

Scheme 2.11. Solvation of **5** in $CDCl_2F$ at 163 K and the possible products that occur upon loss of NBA.

2.2.viii. Deuteration of 1 in the solid-state and in solution

A powdered crystalline sample of **1** was exposed to a deuterium atmosphere in a high pressure NMR tube (1.3 atm for 3 minutes at 295 K), to presumably form d_4-**5** (observed by orange to claret colour change). Over time (~30 minutes) this product decomposes to form **4** and d_4-NBA. After evacuation

of the deuterium atmosphere and replacement with argon the products were solvated in C_6H_5F. A combination of ^1H, ^2H and $^{31}P\{^1H\}$ NMR spectra reveal evidence for the formation of d_4-NBA, as (*endo*-1,2 *exo*-4,5)d_4-NBA and **2** [Scheme 2.12].[68]

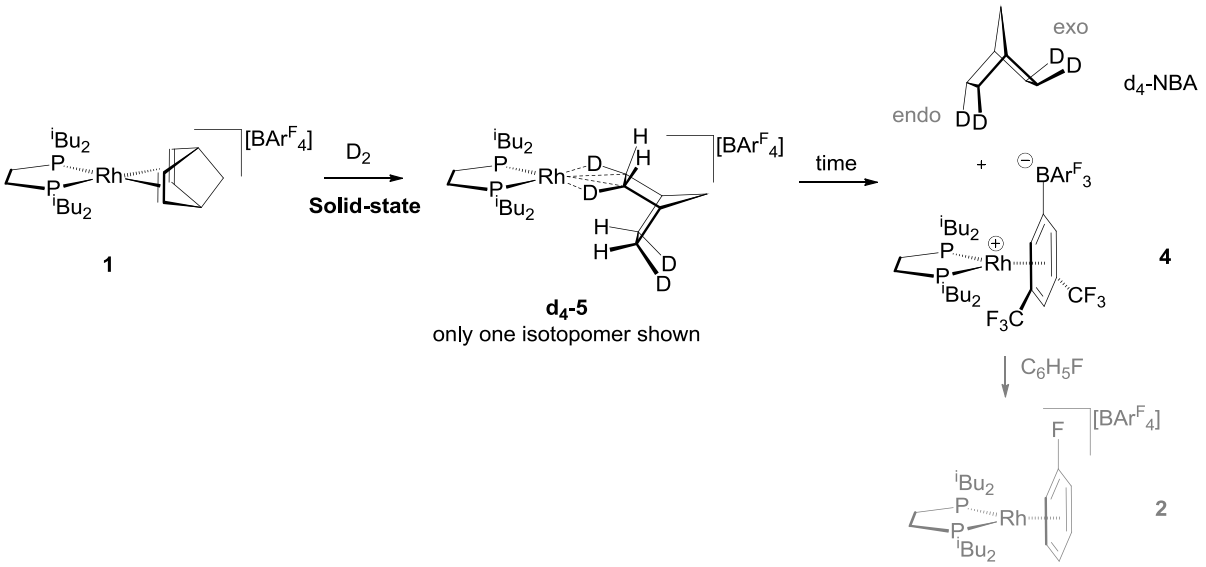

Scheme 2.12. Deuteration of **1** in the solid-state resulting in the production of (*endo*-1,2 *exo*-4,5)d_4-NBA and **4** (which forms **2** when solvated in C_6H_5F).

The ^2H NMR spectrum shows a 1 : 1 *exo* to *endo* ratio [Figure 2.15], consistent with a previous mechanistic study of the hydrogenation of NBD complexes in solution by Brown and co-workers.[69, 70]

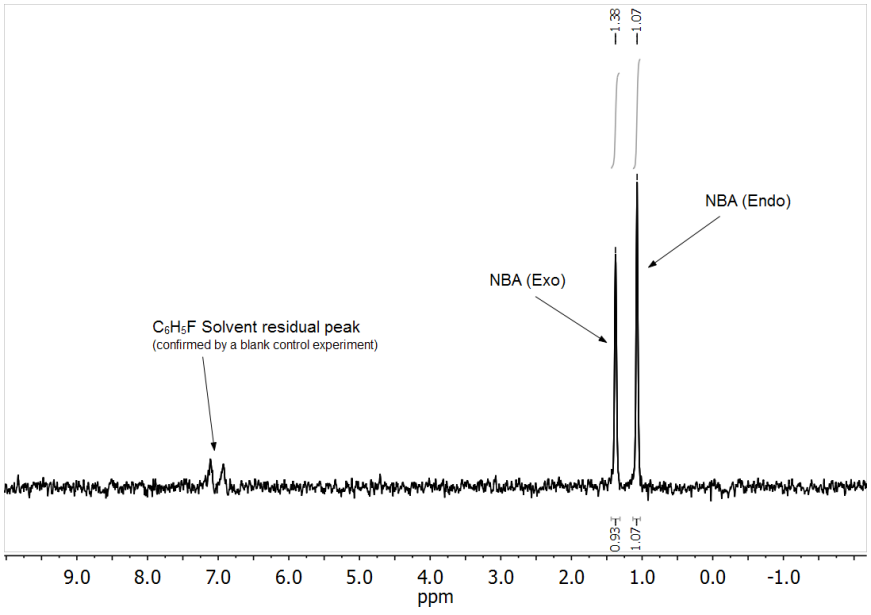

Figure 2.15. ^2H NMR spectrum (C_6H_5F solvent) showing d_4-NBA with effectively a 1:1 ratio of *endo* and *exo*-located deuterium.

Isolation of the final organometallic species (**2**, which forms upon solvation) by crystallisation, washing and subsequent solvation showed no retention of the ^{2}H signals in the ^{2}H NMR spectrum, showing that no H/D scrambling into the phosphine ligand has occured during the deuteration process. Direct addition of D_2 to **1** in a CH_2Cl_2 solution yielded the same two peaks in the ^{2}H NMR spectrum in a 1:1 ratio again assigned to (*endo*-1,2 *exo*-4,5)d_4-NBA.

Brown's deuteration study suggests that a d_2-NBE {(*endo*-1,2)$C_7H_8D_2$} (NBE = norbornene = C_7H_{10}) coordinated intemediate exists on the mechanistic pathway of hydrogenation of NBD complexes [Scheme 2.13]. Deuteration will occur to the face of an alkene which is coordinated to a metal, since the metal mediates the deuteride transfer. Therefore in order to direct deuterium onto the *exo* positions the ligand must move so that it coordinates its *exo* face to the metal, this is likely to occur due to stabilisation of the mono-alkene intermediate by an agostic interaction from a "bridge" C–H bond (*N.B.* the CH_2 protons of NBD are defined by Abraham as the bridge protons).[68]

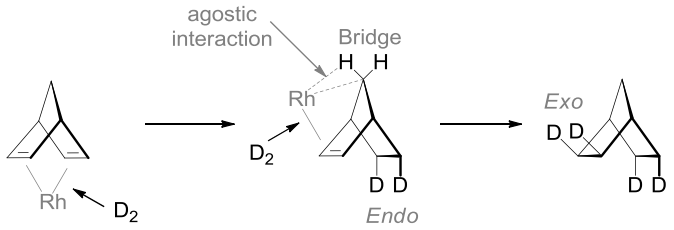

Scheme 2.13. Proposed metal-alkene geometries during the sequential hydrogenation of NBD in both the solid-state and in solution.

These results suggest that in both solution and the solid-state the NBE ligand, formed by initial addition of a single D_2 (or H_2), is likely to undergo rotation to form a complex with alkene and agostic interactions, [Rh(^{i}Bu$_2$PCH$_2$CH$_2$P^{i}Bu$_2$)($\eta^2_{cc}\eta^2_{CH}$-NBE)][BAr$^F_4$], **6**. This mobility within the solid-state is further supported by the second rotation of the NBA unit resulting in the observed solid-state geometry of **5** [Scheme 2.14].

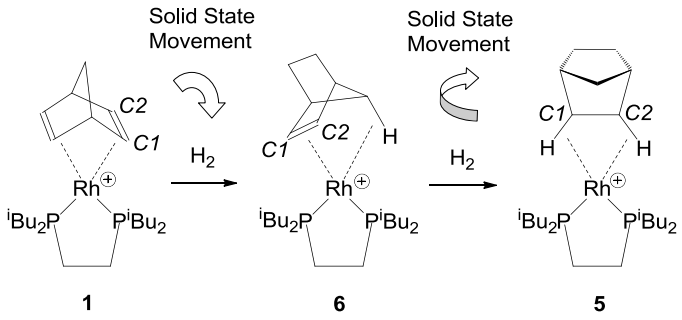

Scheme 2.14. Movement of the NBD/NBE/NBA fragment during solid-state hydrogenation. Dihedral angles (°) C1-C2-P-P: –87.8(4) (**1**), –87.9(10) (**6**), –175.6(8) (**5**). $[BAr^F_4]^-$ anions omitted for clarity.

Deuteration of **1** in the solid-state followed immediately by characterisation of the solid product by ^2H SSNMR spectroscopy only revealed a strong signal for the mobile d_4-NBA species and did not reveal any further information for **5**.

2.2.ix. Synthesis and characterisation of agostic complex 6

6 could be separately synthesised by reaction of **3** with an excess of NBE in CH_2Cl_2 [Scheme 2.15]. **6** is not stable in CH_2Cl_2 for prolonged periods at room temperature but can be recrystallised from CH_2Cl_2/pentane at 277 K.

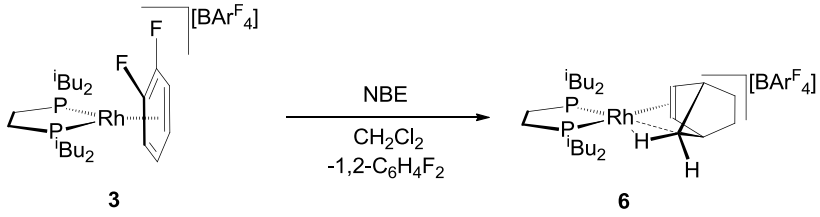

Scheme 2.15. Formation of **6.**

6 was characterised by solution NMR spectroscopy and in the solid-state by X-ray crystallography. The solution $^{31}P\{^1H\}$ NMR spectrum shows no sharp signals at room temperature but upon cooling to 225 K two doublet signals are observed in a 1:1 ratio. The doublets exhibit very different coupling constants indicative of different *trans* ligands to each phosphorus atom [δ 50.8, J_{RhP} 149 Hz & δ 79.4, J_{RhP} 210 Hz]. A coupling constant of 149 Hz is similar to that observed in **1**, *i.e.* phosphorus *trans* to an alkene ligand. The very large coupling constant in the second doublet indicates a very weakly bound ligand *trans* to phosphorus, likely in this case to be an agostic interaction. No J_{PP} coupling is

resolved in this low temperature spectrum. The lack of signal at room temperature suggests that a fluxional process is occurring and that the coalescence temperature for $^{31}P\{^{1}H\}$ NMR spectroscopy (202 MHz) is coincidentally around 295 K. Unfortunately **6** is too unstable to warm above room temperature, in order to locate the high temperature $^{31}P\{^{1}H\}$ NMR spectrum. The ^{1}H NMR spectrum was recorded at room temperature and reveals the averaged high temperature structure (*N.B.* $\delta\upsilon$ is greater for low temperature $^{31}P\{^{1}H\}$ NMR signals [$\delta\upsilon$ 5700 Hz] than for any set of low temperature ^{1}H NMR signals which become equivalent [^{i}Bu (CH_3) groups $\delta\upsilon$ 95 Hz]).[71] Two doublets are observed for the ^{i}Bu (CH_3) groups as expected for equivalent phosphorus environments. The NBE alkene ^{1}H NMR peaks are observed [δ 4.89] in a similar position to the analogous peaks in **1**. A slightly broadened ^{1}H NMR signal at high field [δ −3.66, FWHM 32 Hz] is observed with an integral equal to 1H, this is characterised as the signal from an agostic Rh···C–H interaction. Similar complexes with $\eta^2_{cc}\eta^2_{CH}$-NBE ligands display high field resonances between δ −0.9 and −10.2.[63, 72] The proton geminal to the agostically bound C–H is located at δ 1.45. At low temperature (185 K) the ^{1}H NMR spectrum of **6** displays four doublets for the ^{i}Bu (CH_3) groups indicating inequivalent phosphorus atoms and that the low temperature limit is achieved. The resonances for NBE are unchanged upon cooling, which is chemically sensible since there is only one binding mode for NBE which allows the agostic interaction. Any exchange mechanism would therefore retain the chemical environments of the NBE ligand. The mechanism of exchange is not clear but is likely to involve dissociation of the weakly held agostic interaction rotation of the alkene and re-coordination.

The $^{31}P\{^{1}H\}$ SSNMR spectrum of **6** was collected and reveals that two broad phosphorus signals are present [δ 55.7, FWHM 520 Hz & δ 75.7, FWHM 468 Hz]. This is consistent with the low temperature solution $^{31}P\{^{1}H\}$ NMR spectrum and suggests that the NBE unit is static or slow moving in the solid-state, the broad nature of the peaks suggests some mobility could be present. A peak for the "bridge" carbon was located in the $^{13}C\{^{1}H\}$ SSNMR spectrum at δ 31.4, this is in agreement with the solution $^{13}C\{^{1}H\}$ NMR signal [δ 31.6] and with the computationally calculated value [δ 38.9, courtesy of A. Algarra and S. Macgregor].[60]

Highly air sensitive crystals of **6** were generated and a solid-state structure was obtained which was consistent with previously reported $\eta^2_{cc}\eta^2_{CH}$-NBE complexes [Figure 2.16].[63, 72, 73] Similar to **1** the structure was solved in the monoclinic space group *C* 2/c (in collaboration with Dr. Amber

Thompson; Chem. Crystallography, Uni. Oxford) with the cation sitting upon a crystallographic two-fold rotor and only half the molecule refined. The NBE molecule is disordered over the 2-fold axis and so to enforce crystallographic symmetry constraints were placed upon the bridgehead carbons (C3) and two 'same distance' restraints were used (C3/3')–C(7) and (C3/3')–C(4/5).

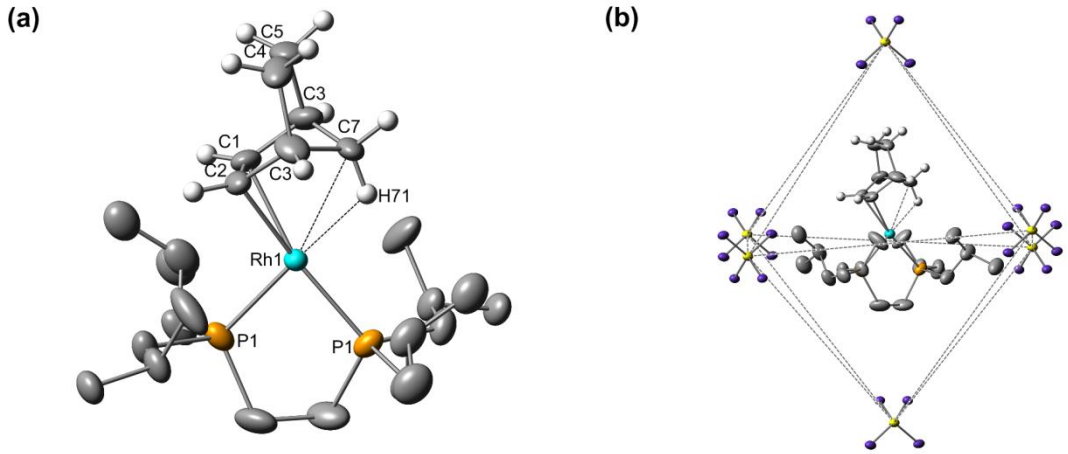

Figure 2.16. Displacement ellipsoid plots (30% probability) of **6** in the solid-state (one disorder component of NBE shown). All but NBE hydrogen atoms omitted for clarity. **(a)** Cationic component. **(b)** Packing diagrams; single cation enclosed within a *pseudo*-octahedron of anions, $[BAr^{F}_{4}]^{-}$ anions represented as BC_4 units (aryl groups omitted) for clarity. Selected bond length (Å) and angle (º) data: Rh(1)–P(1), 2.2261(15); Rh(1)–C(1), 2.214(13); Rh(1)–C(2), 2.169(12); Rh(1)–C(7), 2.576(14); C(1)–C(2), 1.29(2); C(4)–C(5), 1.48(3); P(1)-Rh(1)-P(1'), 83.90(10); dihedral C(1)/C(2)/P(1)/P(1'), −87.9(10).

The solid-state structure of **6** reveals coordination of the C=C bond to the metal centre in a similar manner to that observed in **1**, with the C=C bond lying perpendicular to the RhP_2 plane. The C=C bond length is short and clearly a double bond however the disorder present reduces the accuracy of bond length analysis for this structure [**6** C=C 1.29(2) Å, free NBE C=C 1.3344(55) Å, **1** C=C 1.363(10) Å]. An agostic interaction is present from the NBE "bridge" C–H bond, this structural motif being consistent with previously published NBE complexes.[63, 72, 73] The agostic Rh···C distance is longer than the Rh···C distances in **5** [**6**, Rh(1)···C(7) 2.576(14) Å; **5**, Rh···C 2.480(11) Å and 2.494(10) Å] but sits comfortably within the range of other agostic NBE complexes with rhodium, palladium and copper [2.53-2.85 Å][63, 72, 73] and is similar to the only other example containing rhodium [Rh({(2,6-MeC_6H_3)NCMe}$_2$CH)($\eta^2_{cc}\eta^2_{CH}$-NBE) Rh···C, 2.531(4) Å].[72] Due to the disorder of the NBE ligand in the solid-state structure of **6** the hydrogen atoms could not be located in the

Fourier map and were placed in calculated positions. No phosphine disorder was located in this structure.

The unit cell volume of **6** is very similar to that of **1** and **5** [Table 2.1] and the same packing structure is observed, with a *pseudo*-octahedron of $[BAr^F_4]^-$ anions [Figure 2.16(b)]. Inspection of the Rh(1)···B(50) distance (drawn through the NBE fragment) [8.802(7) Å] and the B···B *trans* octahedron distance (cutting through Rh and the NBE) [17.467(10) Å] shows that they fall between the analogous distances in **1** and **5**. This suggests that NBE requires more space than NBD but less than NBA, and is consistent with the access of an intermediate NBE complex (**6**) upon the SC-SC transition of **1** to **5**.

Complex	Unit cell volume (Å^3)	Rh(1)···B(50) distance (Å) (drawn through NBE fragment)	B···B *trans* octahedron distance (Å) (drawn through NBE fragment)
1	5957.62(18)	8.200(8)	17.062(10)
6	6008.93(15)	8.802(7)	17.467(10)
5	6044.1(3)	9.13(1)	17.596(10)

Table 2.1. Parameters showing the unit cell expansion upon hydrogenation of the NBD fragment (**1**) to NBE (**6**) and NBA (**5**).

Computational studies were undertaken upon **6** (courtesy of Dr. A. Algarra. S. Macgregor, Heriot-Watt Uni.).[60] These placed the agostic hydrogen 2.00 Å from the rhodium and described an extension of the C–H bond from 1.10 to 1.14 Å. A NBO analysis predicted a C–H σ-donation interaction of 15.6 kcal/mol with a metal to C–H σ* back-donation of 3.6 kcal/mol. These calculations suggest that the agostic interaction is weaker than the Rh···C–H interactions in **5**, this may be due to the restrained geometry which is enforced by the strong Rh···(C=C) interaction. The agostic interaction was further confirmed by an AIM study.

2.2.x. The solid-state hydrogenation of 6 followed by SSNMR spectroscopy

The solid-state hydrogenation of **6** could be followed by SSNMR by a similar method to that described in *Section 2.2.iv*. Powdered crystalline **6** was exposed to H_2 (1 atm 295 K, for 2 minutes) and then monitored by $^{31}P\{^1H\}$ SSNMR spectroscopy. The same sets of peaks were seen as for the hydrogenation of **1** (*i.e.* **5** and **4**). No residual **6** was observed after hydrogenation for 2 minutes

suggesting that **6** reacts faster with hydrogen at room temperature than **1**. This rapid reaction explains why no **6** is observed as an intermediate by SSNMR upon hydrogenation of **1**. The initial spectrum, recorded 7 minutes after the hydrogenation process begun, shows peaks assigned to the intermediate **5** and to the final product **4** (amorphous phase) [Figure 2.17(b)]. The $^{13}C\{^{1}H\}$ SSNMR spectrum showed total loss of the NBE alkene peak at δ 93.9 and no other peaks in the alkene region. Warming to 298 K resulted in the complete loss of **5** and the same amorphous to crystalline phase transition for **4** was observed as before.

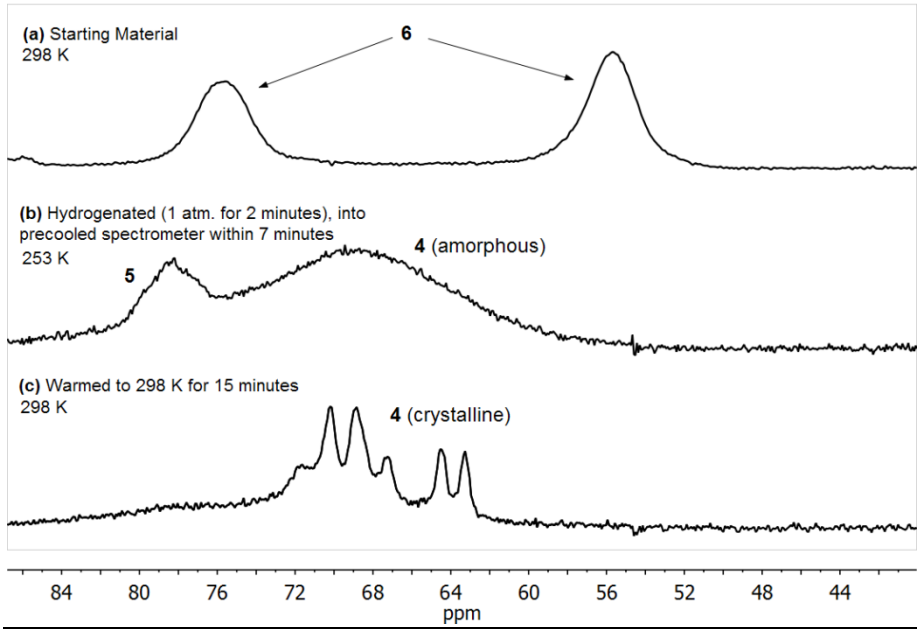

Figure 2.17. $^{31}P\{^{1}H\}$ SSNMR spectra displaying the transitions **6** to **5** to **4** (amorphous) and finally to **4** (crystalline).

2.2.xi. Deuteration of 6 in the solid-state and in solution

Addition of D_2 (1.3 atm) to a powdered sample of **6** for three minutes results in a colour change to claret (d_2-**5**). This converts into yellow amorphous **4** over 30 minutes with release of d_2-NBA. Dissolution of these amorphous products in C_6H_5F allows analysis by ^{2}H NMR spectroscopy, which reveals the deuterium to be located only in the *exo*-position of d_2-NBA ((*exo*-4,5)d_2-NBA) [Scheme 2.16]. Direct addition of D_2 to **6** in CH_2Cl_2 solution also formed the *exo* deuterated NBA product exclusively (alongside **4**). This is fully consistent with the mechanism proposed in *Section 2.2.viii* and the previously reported solution studies.[69]

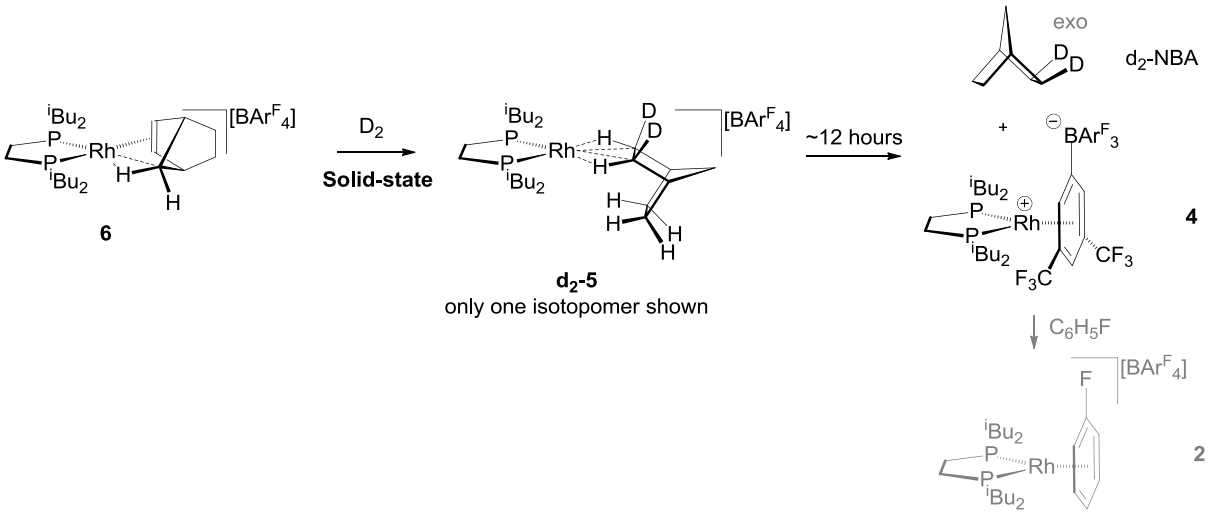

Scheme 2.16. Deuteration of **6** in the solid-state resulting in the production of (*exo*-4,5)d_4-NBA and **4** (which forms **2** when solvated in C_6H_5F).

2.2.xii. Comparison of the electron density maps generated from the X-ray diffraction datasets of 1, 5 and 6

The nature of the NBE and NBA disorder present in the crystal structures of **6** and **5** respectively requires careful analysis to be sure that the correct structures are derived. Examination of the electron density of the NBD/NBE/NBA fragment (in the X-ray diffraction datasets of **1**, **6** and **5**) using the modeling software MCE [74] clearly shows the difference between the structures [Figure 2.18]. Only one chemically sensible structure fits the electron density in each case. The position of the NBA bridge-head carbon can clearly be seen in an alternate position in **5**, after the NBA unit has undergone ~90° rotation relative to the position of NBD in **1**. A small residual electron density peak is observed between the rhodium and NBA in **5**, this is attributed to ~2% of unreacted starting material (**1**). Although 'same distance' restraints were necessary for the structure of **6**, the structures of **1** and **5** were refined without restraints to the coordinated NBD/NBA. This alongside the sensible organic bond lengths generated from structural refinement gives us confidence in our interpretation of the X-ray data. The electron density plots also support the proposed mobility of the NBD/NBE/NBA unit, with each orientation of the hydrocarbon inhabiting a similar volume of space.

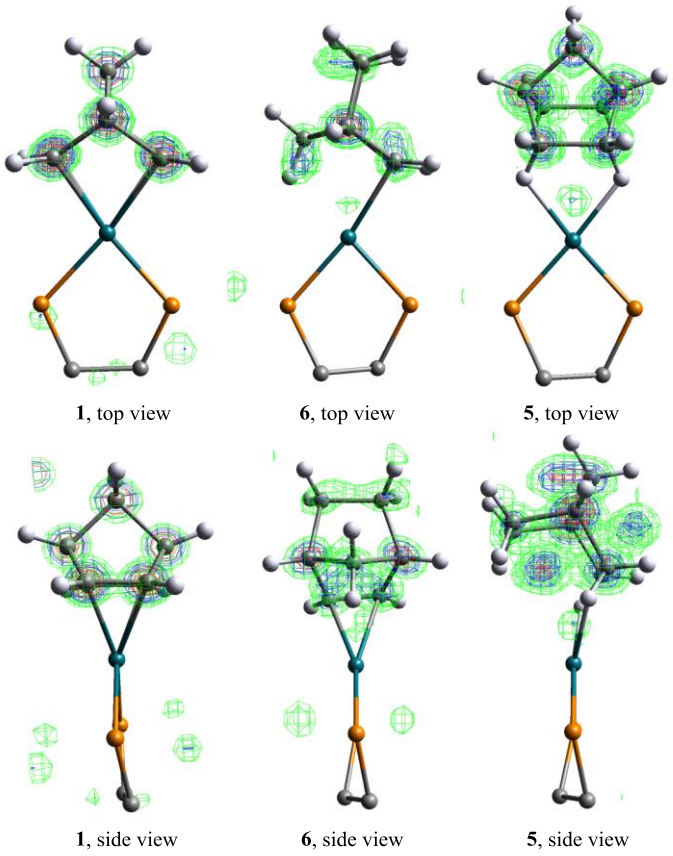

Figure 2.18. Sections of the difference Fourier maps for **1**, **6** and **5** (NBD, NBE and NBA) when the occupancies were set to zero, shown from left to right in two different orientations; contours drawn at 1, 2 and 3 electron levels with MCE.[74] Figure courtesy of Dr. Amber Thompson (Chem. Crystallography, Uni. Oxford). *Figure amended from: AAAS, Science, Synthesis and Characterisation of a Rhodium(I) σ-Alkane Complex in the Solid-State (License Number: 3310131484982).*[60]

2.2.xiii. Investigation of the phase change of 4 by *in situ* powder diffraction studies

The $^{31}P\{^{1}H\}$ SSNMR spectrum of **4** when generated by the solid-state hydrogenation of **1** or **6** suggests that it forms initially in an amorphous phase (< 298 K). However upon gentle heating (> 298 K) a phase change is observed by SSNMR. After heating the spectrum is consistent with microcrystalline material, being identical with samples of **4** independently made (crystallised by solution methods). The amorphous species (< 298 K) is attributed to the product formed on direct coordination of the $[BAr^{F}_{4}]^{-}$ anion after the loss of NBA from **5**. As the crystallinity of **5** collapses to give **4** there may be a variety of conformations in which the arene ring of the anion can coordinate, resulting in a broad (amorphous) peak in the SSNMR spectra. In order to probe this phase change

further and to gain more information upon the reaction of hydrogen with **1** an *in situ* powder X-ray diffraction study was undertaken at the Diamond Light Source (beam-line I12).

The powder X-ray diffraction experiment was undertaken in collaboration with Prof. Andrew S. Weller (University of Oxford), Dr. F. Mark Chadwick (PDRA, University of Oxford) and Dr. Michael Hart (Diamond) and also under the advice of Prof. Dermot O'Hare (University of Oxford). Prior to the main experiment preliminary diffraction data of **1** was collected at Diamond by Dr. Saul Moorhouse (University of Oxford).

A powdered sample of **1** with particle diameter (d) < 50 μm was used for the experiment. A H_2/He gas feed (10% H_2) was used for hydrogenation inside the experiment hutch [Figure 2.19]. Full experimental details are listed in *Section 6.1.vii*. Continual powder X-ray diffraction datasets were recorded (~10 s per diffraction experiment) with H_2/He added *in situ*. The 1-D powder X-ray diffraction patterns collected could be compared to the powder X-ray diffraction patterns simulated from the single crystal structures of **1**, **5** and **4** (using CrystalDiffract), this allowed for initial rationalisation of the data.

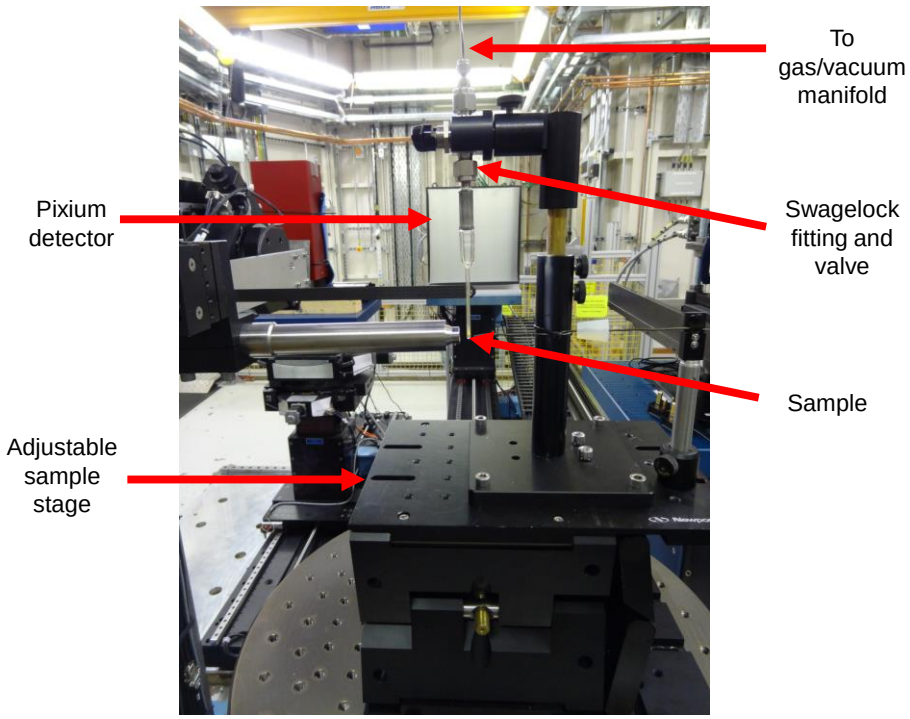

Figure 2.19. Experimental setup within the hutch at beam-line I12, Diamond light source.

The initial powder X-ray diffraction pattern was entirely consistent (by visual inspection) to that of the powder diffraction pattern simulated from the single crystal X-ray diffraction data of **1**. A Rietveld refinement was later undertaken by Dr. Frederick Mark Chadwick and a very close agreement between collected and calculated 1-D diffraction data was obtained (further refinements are currently in progress). The powder X-ray diffraction pattern appears spotty, which indicated the crystalline nature of the sample – as a number of small crystals are contributing to the circular diffraction pattern [Figure 2.20].

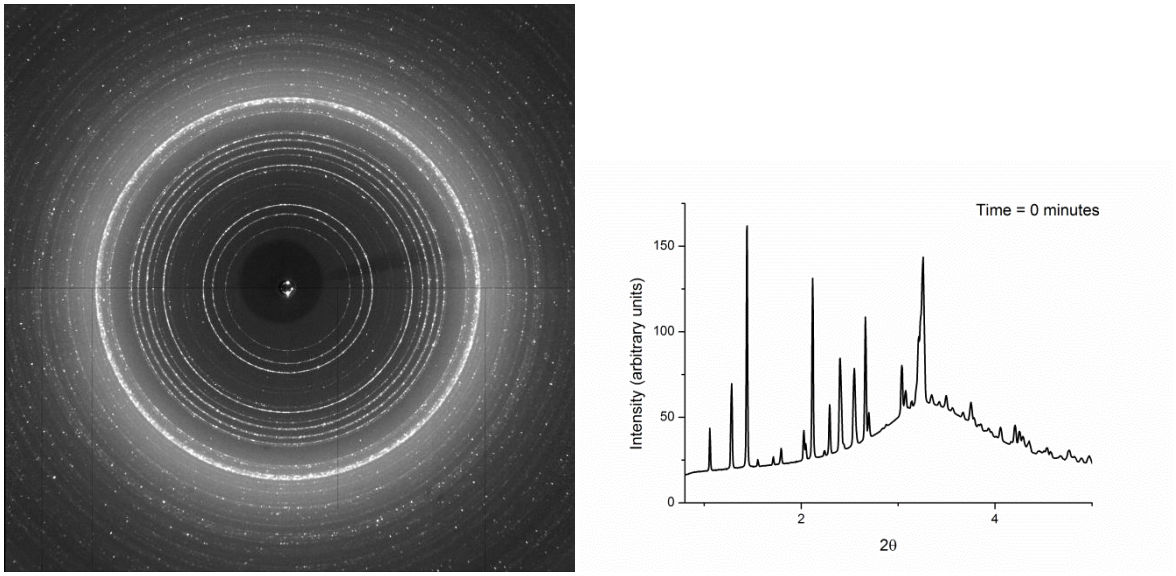

Figure 2.20. Initial powder diffraction pattern (with 1-D plot) collected (**1**) before hydrogen was added.

The powder X-ray diffraction pattern changes as **1** reacts with H_2, and after 5 minutes the pattern is visually comparable with that of the powder diffraction pattern simulated from the single crystal X-ray data of **5** [Figure 2.21]. Again a Rietveld refinement (by Dr. Chadwick) confirms the structure. The pattern is still spotty, indicating that crystallinity is maintained (*i.e.* a SC-SC transition has occured).

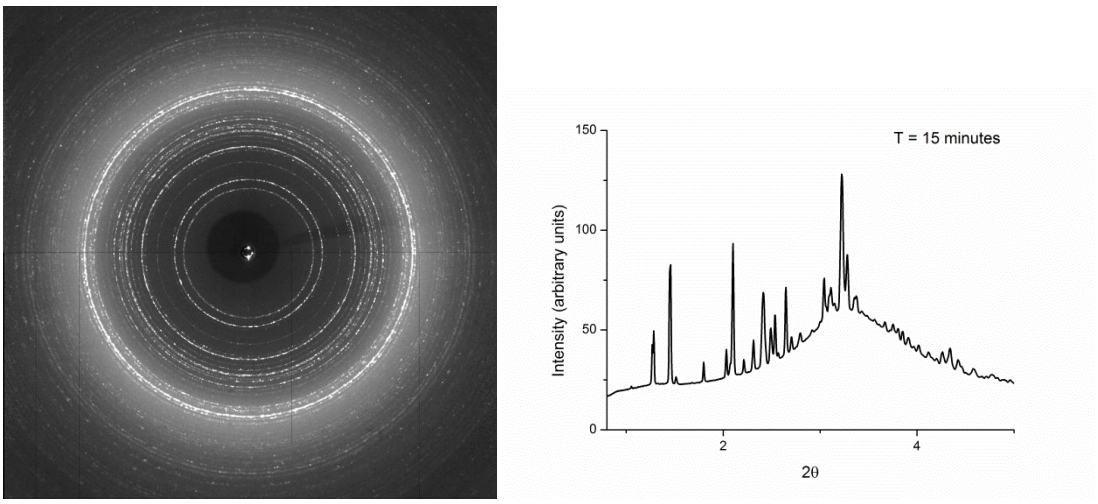

Figure 2.21. Powder diffraction of σ-alkane complex **5** formed *in situ* (with 1-D plot). Sample exposed to hydrogen for 15 minutes.

After 1 hour the diffraction pattern loses all definition and indicates the formation of an amorphous species. This is entirely consistent with the SSNMR spectroscopy data in which **4** originally forms in an amorphous phase [Figure 2.22]. No further change occurs at room temperature over 3.5 hours.

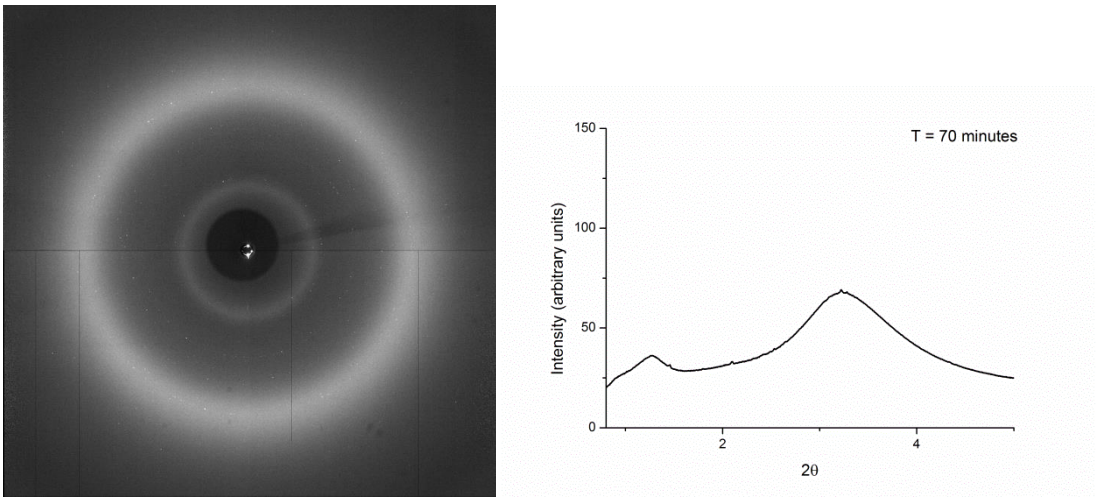

Figure 2.22. Powder X-ray diffraction pattern (with 1-D plot) of **4** in an amorphous form. Sample exposed to hydrogen for 70 minutes (before heating to 315 K).

The sample tube was then heated to 315 K for five minutes and a noticeable transformation occurred as the sample becomes slightly oily (no change was observed at 305 K). A powder X-ray diffraction dataset was then recorded on the beam-line and confirmed that a recrystallisation phase change had occurred. The pattern is now comprised of clean circles (without spots) indicating that a

microcrystalline material is present with very small crystal domains. The final pattern is visually comparable with the simulated powder pattern of **4** [Figure 2.23].

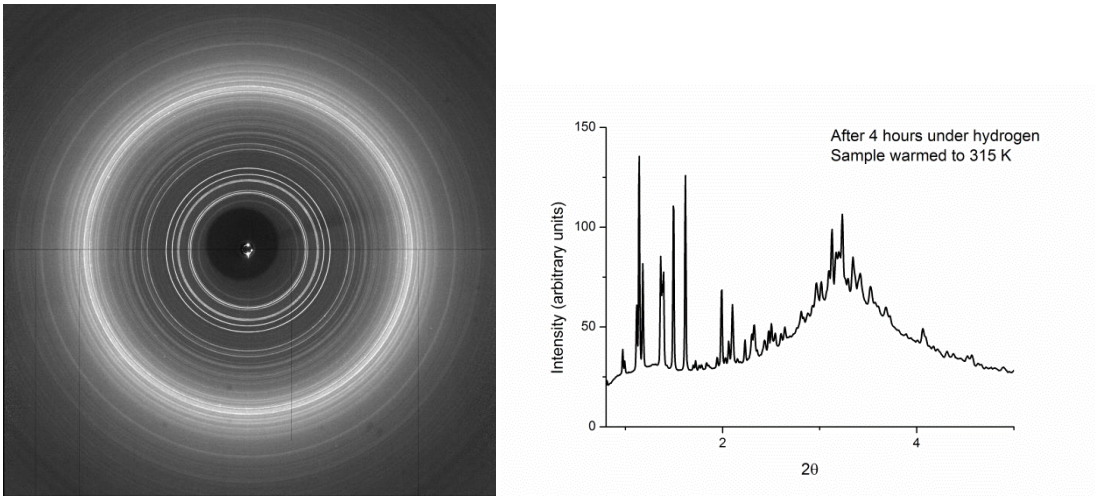

Figure 2.23. Powder X-ray diffraction pattern (with 1-D plot) of **4** in a microcrystalline form. Sample exposed to hydrogen for 4 hours and then subsequent heating to 315 K.

2.3. Hydrogenation of $[Rh(^{i}Bu_2PCH_2CH_2P^{i}Bu_2)(L_2)][BAr^{F}_4]$ (L_2 = alkenes or diene)

2.3.i. Overview

We have demonstrated that a σ-alkane intermediate will form upon addition of hydrogen across a coordinated alkene C=C bond in the solid phase, however the lifetime of such an intermediate will depend upon the local binding environment; both the strength of the σ-interaction and the surrounding steric environment. Taking the reaction of **1** with hydrogen as a basis point for similar alkene complexes it appears that the overall hydrogenation reaction may be broken down into two steps. Firstly the hydrogenation of a coordinated alkene will form an intermediate species which may be stabilised by a σ-alkane interaction (rate = k_1). Secondly loss of the alkane unit from the solid lattice is accompanied by coordination of the anion to rhodium (rate = k_2) [Figure 2.24]. In order to observe a σ-alkane intermediate as a major species the first step must occur more rapidly than the second step, *i.e.* $k_1 >> k_2$.

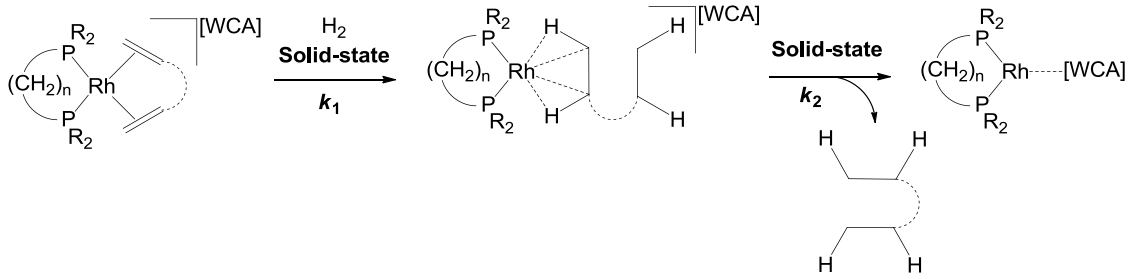

Figure 2.24. General reaction scheme for hydrogenation of cationic rhodium *bis*-alkene complexes.

Hydrogenation of NBD is rapid due to the release of ring-strain upon saturation.[23, 31] This ease of hydrogenation is useful in terms of solid-state hydrogenation because only one atmosphere of hydrogen is needed for rapid reaction (*i.e.* k_1 is fast). NBD is also a compact diene and allows the cation of **1** to fit well within the *pseudo*-octahedral cavity imposed by the surrounding $[BAr^F_4]^-$ anions. Following the success of the formation of σ-alkane complex **5**, and despite the seemingly ideal properties of NBD, various other alkene complexes were prepared and their solid-state reactions with H_2 monitored. The other alkenes tested were 1,5-cyclooctadiene (COD), 1,3-cyclohexadiene (C_6H_8), ethene, butadiene and 2,3-dimethyl-1,3-butadiene (2,3-$C_4H_4Me_2$) [Figure 2.25].

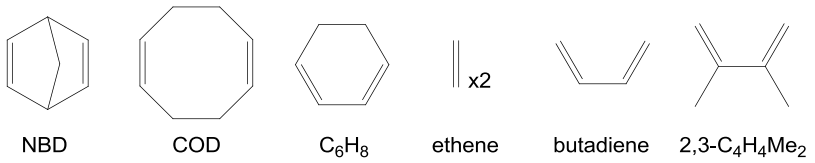

Figure 2.25. Alkenes used to form complexes $[Rh(^iBu_2PCH_2CH_2P^iBu_2)(L_2)][BAr^F_4]$ (L_2 = alkenes or diene)

2.3.ii. Synthesis and hydrogenation of $[Rh(^iBu_2PCH_2CH_2P^iBu_2)(\eta^2\eta^2\text{-COD})][BAr^F_4]$

$[Rh(^iBu_2PCH_2CH_2P^iBu_2)(\eta^2\eta^2\text{-COD})][BAr^F_4]$, **7**, was synthesised by addition of 1,5-cyclooctadiene to a 1,2-$C_6H_4F_2$ solution of **3** [Scheme 2.17]. Recrystallisation of the product in 1,2-$C_6H_4F_2$/pentane resulted in yellow crystalline material.

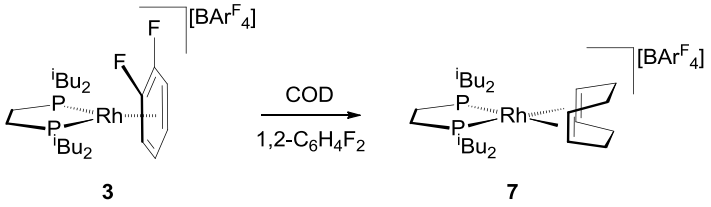

Scheme 2.17. Synthesis of **7**

The ^{1}H NMR spectrum (CD_2Cl_2) of **7** displays alkene resonances [δ 5.14] which are slightly upfield of the reported values for free COD [δ ($CDCl_3$) 5.58][75] consistent with coordination to a metal centre. The $^{31}P\{^{1}H\}$ NMR spectrum is comprised of a doublet peak [δ 50.3, J_{RhP} 150 Hz] which is similar to that observed for **1**. Despite the apparent visual quality of the crystalline material an accurate solid-state structure could not be determined by X-ray crystallography, possibly because of significant cation disorder.

7 reacts slowly with hydrogen at 1 atm in the solid-state, slow hydrogenation being typical of COD complexes.[23, 44] However **7** was shown to form **4** and free cyclooctane when exposed to 4 atm H_2 in the solid-state, with 87% conversion after one hour (characterised by solution NMR of the degassed product) [Scheme 2.18]. No strong colour changes were observed during the reaction [*see Section 2.3.vi.Figure 2.30*]. It appears that k_1 is slow for **7** and therefore k_2 may be competitive (to form **4**) – assuming that k_2 in this process may be similar to the rate for the transition from **5** to **4**. Consequently any intermediate species that forms in the hydrogenation reaction is not likely to form as a major species and is unlikely to be clearly observable by X-ray crystallography or SSNMR. Due to the slow hydrogenation reaction no SSNMR data was collected for this process.

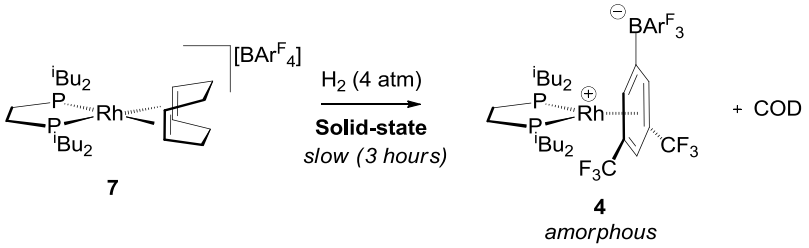

Scheme 2.18. Solid-state reaction of **7** with H_2

2.3.iii. Synthesis and hydrogenation of $[Rh(^{i}Bu_2PCH_2CH_2P^{i}Bu_2)(\eta^4\text{-}C_6H_8)][BAr^F{}_4]$

$[Rh(^{i}Bu_2PCH_2CH_2P^{i}Bu_2)(\eta^4\text{-}C_6H_8)][BAr^F{}_4]$, **8**, was synthesised by addition of excess cyclohexene to a solid sample **3** and solvation of the mixture in CH_2Cl_2. Upon solvation a colour change from yellow to deep red occurs. The red compound was recrystallised in CH_2Cl_2/pentane and characterised as **8** by NMR spectroscopy, ESI-MS and X-ray crystallography. During the reaction cyclohexene is reduced to cyclohexadiene, presumably by a transfer dehydrogenation reaction which releases one equivalent of cyclohexane [Scheme 2.19]. A similar reaction pathway has been previously reported by Weller and co-workers for the formation of $[Rh(PPh_3)_2(\eta^4\text{-}C_6H_8)][CB_{11}H_6Br_6]$ from the reaction of phenyl-bridged dimer $[Rh(PPh_3)_2]_2[CB_{11}H_6Br_6]_2$ with cyclohexene.[76]

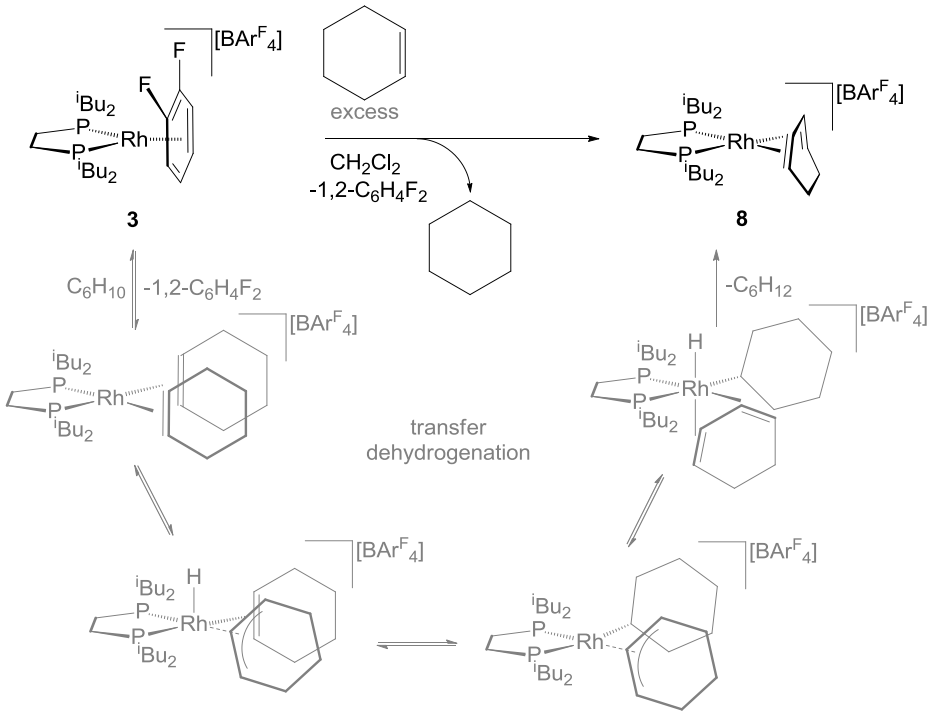

Scheme 2.19. Potential transfer dehydrogenation pathway for the formation of **8** as similarly proposed in previous reports.[76]

The ^{1}H NMR spectrum of **8** (CD_2Cl_2 solvent) displays two signals with integrals equal to 2H (relative to the 8H $[BAr^F{}_4]^-$ signal) within the range for alkene protons [δ 5.10, 5.31] confirming the presence of cyclohexadiene. The signals are upfield to the reported values of free cyclohexadiene [δ 5.84 (both coincident, $CDCl_3$)][75] indicative of coordination to a metal centre. The $^{31}P\{^1H\}$ NMR spectrum displays a doublet [δ 53.0, J_{RhP} 176 Hz] with a very similar J_{RhP} coupling constant to previously

reported C_6H_8 complex $[Rh(PPh_3)_2(\eta^4\text{-}C_6H_8)][CB_{11}H_6Br_6]$ [J_{RhP} 177 Hz]. A crystal structure of **8** was determined in which the cation was well ordered [space group *C*2/c] [Figure 2.26].

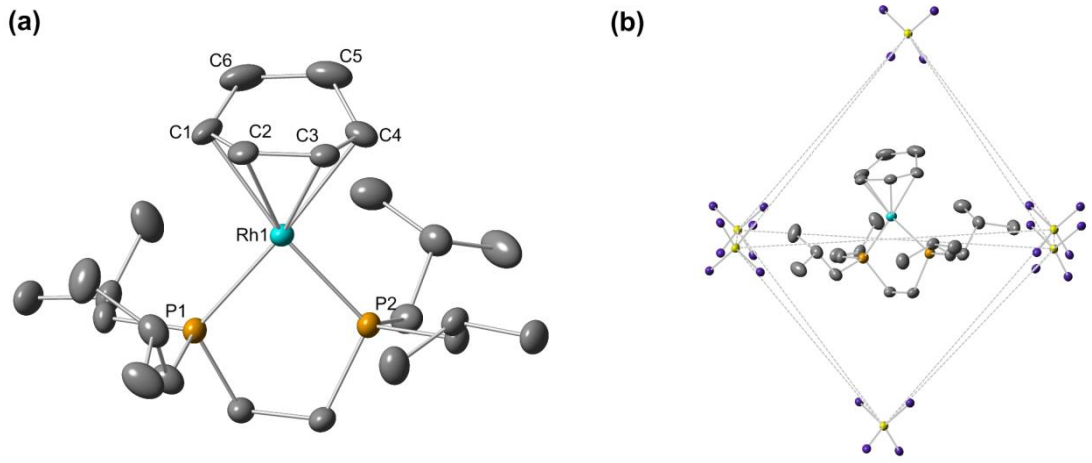

Figure 2.26. Displacement ellipsoid plots (30% probability) of **8** in the solid-state. Hydrogen atoms omitted for clarity. **(a)** Cationic component. **(b)** Packing diagram; single cation enclosed within a *pseudo*-octahedron of anions, $[BAr^F{}_4]^-$ anions represented as BC_4 units (aryl groups omitted) for clarity. Selected bond length (Å) and angle (º) data: Rh(1)–P(1), 2.2908(11); Rh(1)–P(2), 2.2879(11); Rh(1)−C(1), 2.261(4); Rh(1)–C(2), 2.164(4); Rh(1)–C(3), 2.154(4); Rh(1)–C(4), 2.273(4); C(1)–C(2), 1.388(7); C(2)–C(3), 1.431(6); C(3)–C(4), 1.376(6); P(1)-Rh(1)-P(2), 84.33(4).

The η^4-coordination mode of C_6H_8 is commonly found in the literature.[76-79] The Rh–C and C_6H_8 C–C bond lengths match well with the data collected for $[Rh(PPh_3)_2(\eta^4\text{-}C_6H_8)][CB_{11}H_6Br_6]$.[76]

A *pseudo*-octahedron of anions surrounding the cation is again observed. However, in this case the coordinated C_6H_8 invokes an asymmetry upon the cation so that it only occupies a single tilted position within the anion-defined cavity [Figure 2.26(b)]. The $^{31}P\{^1H\}$ SSNMR spectrum of **8** was collected and shows two distinct environments for the phosphorus atoms [δ 48.04, J_{RhP} 172 Hz & δ 52.95, J_{RhP} 165 Hz] further indicating the asymmetry in the solid-state [Figure 2.27(a)].

A powdered crystalline sample of **8** was hydrogenated in the solid-state, and showed a fast colour change (1 minute) from red to yellow [*see Section 2.3.vi.Figure 2.30*]. By $^{31}P\{^1H\}$ SSNMR it appears **8** adds H_2 rapidly to form **4** (amorphous form) and cyclohexane directly with no observable intermediates [Scheme 2.20 & Figure 2.27(b)] (although k_1 is fast, k_2 is also fast in this case). We speculate that the cyclohexane alkane unit, which is smaller than norbornane, may be able to escape the host-guest cavity more easily.

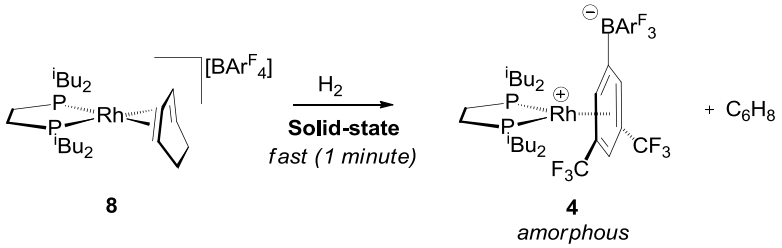

Scheme 2.20. Solid-state reaction of **8** with H_2.

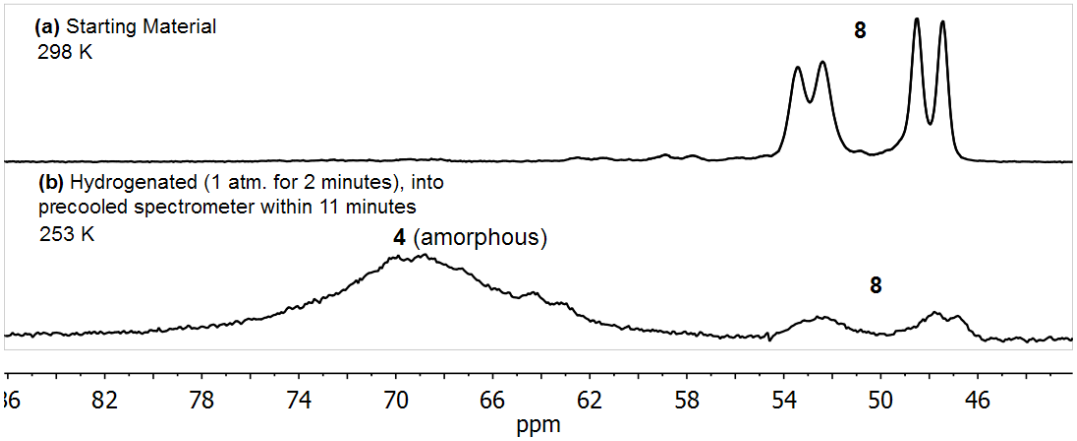

Figure 2.27. $^{31}P\{^{1}H\}$ SSNMR spectra displaying the transition of **8** to **4** by hydrogenation in the solid-state.

2.3.iv. Hydrogenation of [Rh(^{i}Bu$_2$PCH$_2$CH$_2$P^{i}Bu$_2$)(L$_2$)][BAr$^{F}_4$] {L$_2$ = (η^4-C$_4$H$_6$) or (C$_2$H$_4$)$_2$}

The synthesis and characterisation of compounds [Rh(^{i}Bu$_2$PCH$_2$CH$_2$P^{i}Bu$_2$)(η^4-C$_4$H$_6$)][BAr$^{F}_4$], **9**, and [Rh(^{i}Bu$_2$PCH$_2$CH$_2$P^{i}Bu$_2$)(C$_2$H$_4$)$_2$][BAr$^{F}_4$], **10**, will be discussed in detail in *Sections 4.2.ii and 4.2.iii* [Figure 2.28].

Figure 2.28. Complexes **9** and **10**.

Reaction of a powdered crystalline sample of **9** in the solid-state with H_2 (1 atm) shows a rapid colour change from claret to yellow (15 seconds) [*see Section 2.3.vi.Figure 2.30*]. Analysis of the headspace, of the sealed high-pressure NMR tube used for hydrogenation, by gas phase NMR directly after

hydrogenation shows the formation of butane gas [δ 0.94, 1.35]. Solvation of the product reveals **4** by $^{31}P\{^{1}H\}$ NMR spectroscopy [Scheme 2.21]. We expect the transition to be too fast for SSNMR analysis (both k_1 and k_2 are rapid) and thus did not pursue this further.

A powdered crystalline sample of **10** displayed a rapid (< 1 minute) red to yellow colour change under H_2 (1 atm) gas. A gas phase NMR spectrum of the headspace of the sealed NMR tube was undertaken (within five minutes). Alongside H_2, a peak corresponding to free ethane [δ 0.88] was observed suggesting that ethane is quickly ejected from the solid lattice after it is formed by hydrogenation. The remaining solid product was degassed and a solution NMR obtained indicating the expected formation of **4** as the final product [Scheme 2.21]. The loss of ethane (k_2) is expected to be too rapid for analysis of any intermediates by SSNMR (both k_1 and k_2 are rapid).

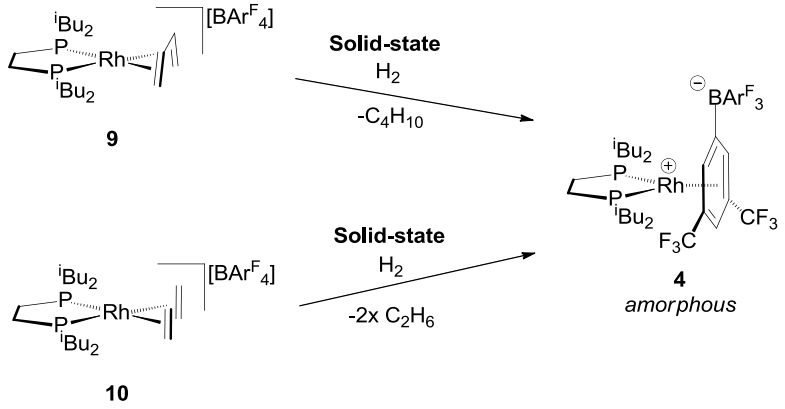

Scheme 2.21. Reaction of **9** and **10** with H_2 in the solid-state. Both reactions occur within 1 minute.

2.3.v. Synthesis and hydrogenation of [Rh(^{i}Bu$_2$PCH$_2$CH$_2$P^{i}Bu$_2$)(η^4-2,3-C$_4$H$_4$Me$_2$)][BAr$^F_4$]

[Rh(^{i}Bu$_2$PCH$_2$CH$_2$P^{i}Bu$_2$)(η^4-2,3-C$_4$H$_4$Me$_2$)][BAr$^F_4$] (2,3-C$_4$H$_4$Me$_2$ = 2,3-dimethyl-1,3-butadiene), **11**, was synthesised by the addition of 2,3-C$_4$H$_4$Me$_2$ to a solid sample of **3** followed by solvation of the mixture in CH_2Cl_2 [Scheme 2.22]. A colour change from yellow to red occurs upon solvation. The product, **11**, was recrystallised from CH_2Cl_2/pentane.

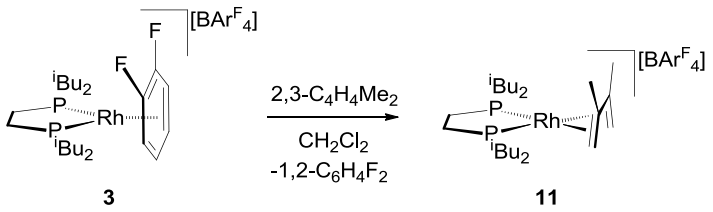

Scheme 2.22. Synthesis of **11.**

The ^{1}H NMR spectrum of **11** reveals two signals for the alkene protons [δ 2.64 and 4.04] and a three times bigger signal for the methyl groups [δ 2.12]. Both alkene peaks are positioned upfield of the reported value for free 2,3-$C_4H_4Me_2$ [δ 4.97 and 5.06] indicative of interaction of the alkene with the metal centre. The ^{i}Bu (CH_3) resonances are split into two sets by the presence of the η^4-2,3-$C_4H_4Me_2$ ligand. The ^{31}P{^{1}H} NMR spectrum displays a doublet [δ 53.2, J_{RhP} 167 Hz] with a J_{RhP} coupling constant less than **8** but greater than **1** and **7**.

An X-ray structure was determined for **11** revealing the expected structure [Figure 2.29]. The hydrogen atoms bonded to C(1) and C(4) could be located in the fourier map and are distorted away from the C(1-4) plane and the metal centre.

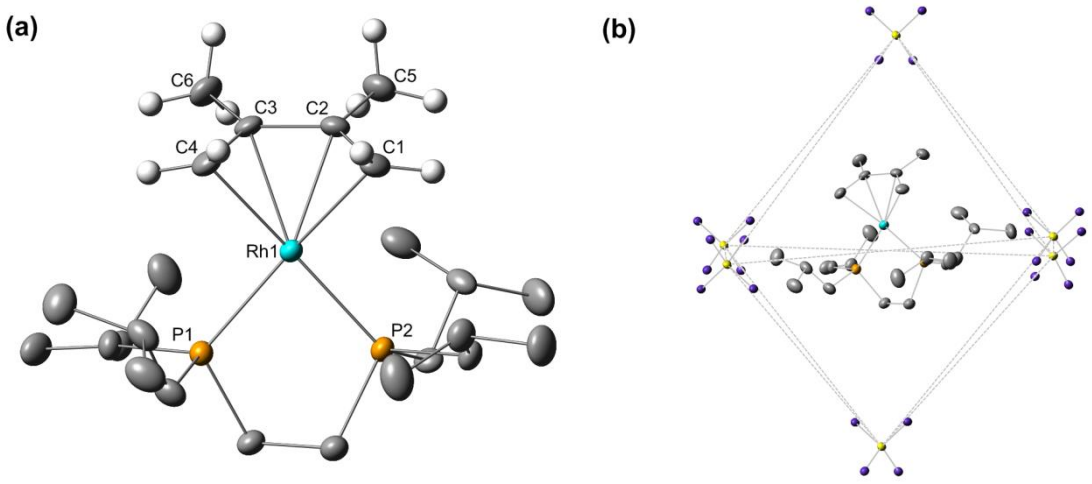

Figure 2.29. Displacement ellipsoid plots (30% probability) of **11** in the solid-state. All but 2,3-$C_4H_4Me_2$ hydrogen atoms omitted for clarity. **(a)** Cationic component. **(b)** Packing diagram; single cation enclosed within a *pseudo*-octahedron of anions, $[BAr^F_4]^-$ anions represented as BC_4 units (aryl groups omitted) for clarity. Selected bond length (Å) and angle (º) data: Rh(1)–P(1), 2.2944(11); Rh(1)–P(2), 2.2783(11); Rh(1)–C(1), 2.219(4); Rh(1)–C(2), 2.217(4); Rh(1)–C(3), 2.214(4); Rh(1)–C(4), 2.235(4); C(1)–C(2), 1.385(6); C(2)–C(3), 1.458(6); C(3)–C(4), 1.378(7); P(1)-Rh(1)-P(2), 83.76(4).

In general the bond lengths in the solid-state structure of **11** are consistent with those of **8** with both structures showing an η^4-coordination of the diene ligand. However a subtle difference is observed in the Rh–C bond distances of the two structures. In **11** all four carbons {C(1-4)} fall within a similar vicinity of the metal [2.214(4)-2.235(4) Å], whereas **8** shows a closer Rh–C distance for the central carbons [Rh(1)–C(2), 2.164(4) Å & Rh(1)–C(3) 2.154(4) Å] and longer distances for the outer two carbons [Rh(1)–C(1), 2.261(4) Å & Rh(1)–C(4) 2.273(4) Å] (*see Figure 2.26*). These differences are likely to be caused by the different steric requirements of C_6H_8 and 2,3-$C_4H_4Me_2$. The cation of **11** sits within a distorted-octahedral environment of anions similar to the packing structure of **8**. A similar structure to **11** as been previously reported for $Rh(P^iPr_3)(OSO_2CF_3)(\eta^4$-2,3-$C_4H_4Me_2)$ which shows the same geometry of the 2,3-$C_4H_4Me_2$ ligand.[80]

A powdered crystalline sample of **11** adds H_2 at a moderate rate. After 20 minutes under 1 atm H_2 a colour change from red to pink (likely a mixture of red and yellow complexes) had occurred and the solution NMR of the degassed product showed roughly 50% of the sample was now **4** (yellow) with the remainder starting material **11** (red). Similarly to **7** the slower reaction with hydrogen (k_1 is slow) reduces the possibility of isolating any short lived intermediates, because formation of **4** is likely to occur at a competitive rate (k_2). Due to the slow reaction with H_2 no solid-state NMR data was collected.

2.3.vi. Conclusions on the choice of appropriate alkene ligands

For the isolation of σ-alkane complexes by solid-state hydrogenation of alkene complexes it appears that NBD was a good initial choice. Rapid reaction of **1** with hydrogen at 1 atm allowed an opportunity to investigate the σ-alkane intermediate whilst it occurs as the major species. The NBA that is created also forms relatively strong σ-interactions. Displacement of NBA in **5** by the anion (to form **4**) is possibly retarded by the size of the NBA fragment which cannot escape from the crystal lattice easily. When other alkenes are used no σ-alkane intermediates are observed [Table 2.2 & Figure 2.30]. Small alkanes such as cyclohexane, butane and ethane are easily lost from the crystal lattice, possibly exiting *via* the porous structure (*see Section 2.8*) and allowing rapid transformation to **4**. COD and 2,3-$C_4H_4Me_2$ react with hydrogen slowly so that the secondary reaction to form **4** is now relatively rapid.

Complex	Alkene ligand	k_1 (% hydrogenation in 3 minutes*)	k_2	Intermediate detected
1	**NBD**	**Fast (100%)**	**Slow**	**Yes**
7	COD	Slow (5 %)	N/A	No
8	C_6H_8	Fast (100%)	Fast	No
9	ethene	Fast (100%)	Fast	No
10	butadiene	Fast (100%)	Fast	No
7	2,3-$C_4H_4Me_2$	N/A (50% after 20 minutes)	N/A	No

Table 2.2. Comparison of alkene complexes and their rates of hydrogenation.**Powdered sample, 3 minutes under 1 atm H_2, analysis by $^{31}P\{^1H\}$ NMR after solvation of products in C_6H_5F.*

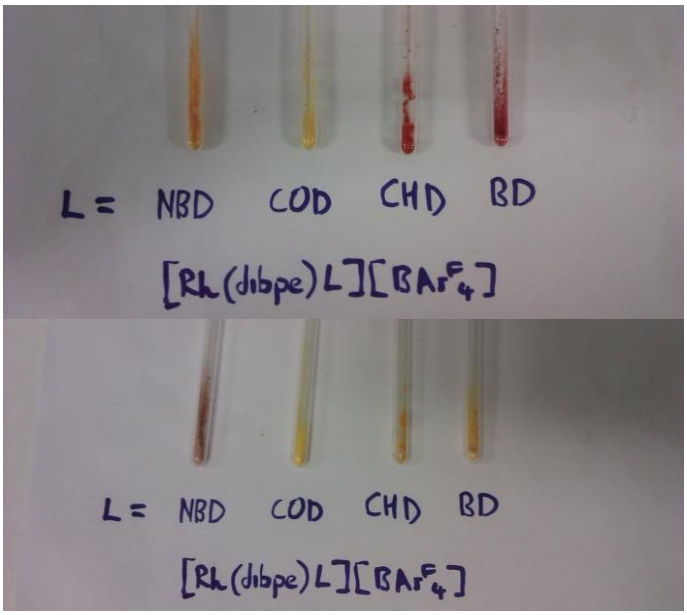

Figure 2.30. Colour changes of powdered crystalline samples of complexes (dibpe = $^{i}Bu_2PCH_2CH_2P^{i}Bu_2$) after exposure to 1 atm H_2 for 3 minutes (top: before, below: after 3 minutes). Only **1** ("NBD") forms a claret intermediate (**5**). **8** ("CHD") and **9** ("BD") form yellow **4** directly whilst **7** ("COD") does not react appreciably over this timescale.

2.4. Hydrogenation of [Rh($^{i}Bu_2PCH_2CH_2P^{i}Bu_2$)($\eta^2\eta^2$-NBD)][WCA] complexes

2.4.i. Overview

Once it was determined that NBD was the most suitable alkene precursor for the formation of a σ-alkane complex, attention was focussed towards the choice of weakly coordinating anion. The $[BAr^F_4]^-$ anion was originally chosen because of its poor coordinating ability, it also proved useful at forming a rigid crystalline lattice in which rearrangements to the cation could take place. However the

arene ring can coordinate to rhodium in an η^6-manner and displace a weakly coordinated ligand such as an alkane. The transition from **5** to **4** is an example of this.

In order to try and make a longer lived alkane complex a less coordinating anion is required. Since $[BAr^F_4]^-$ is considered one of the least coordinating anions [81] there are not many choices available. It is also important to consider that crystallinity is also an important characteristic for solid-state studies, and incorporation of co-crystallised solvent could prove problematic. We chose to target anions with a similar size and shape to $[BAr^F_4]^-$ such as $[B(C_6F_5)_4]^-$, $[BAr^{Cl}_4]^-$ and 'Krossing anions' $[Al(OC(CF_3)_3)_4]^-$ and $[Al(OCH(CF_3)_2)_4]^-$ [Figure 2.31]. Carborane anions were not investigated, as it was postulated that their smaller and more spherical shape may not form such well defined pockets enclosing the cation within the lattice, this may allow faster reorganisation to form an anion-coordinated species. Carborane anions are also known to coordinate to transition metal centres.[49, 81, 82]

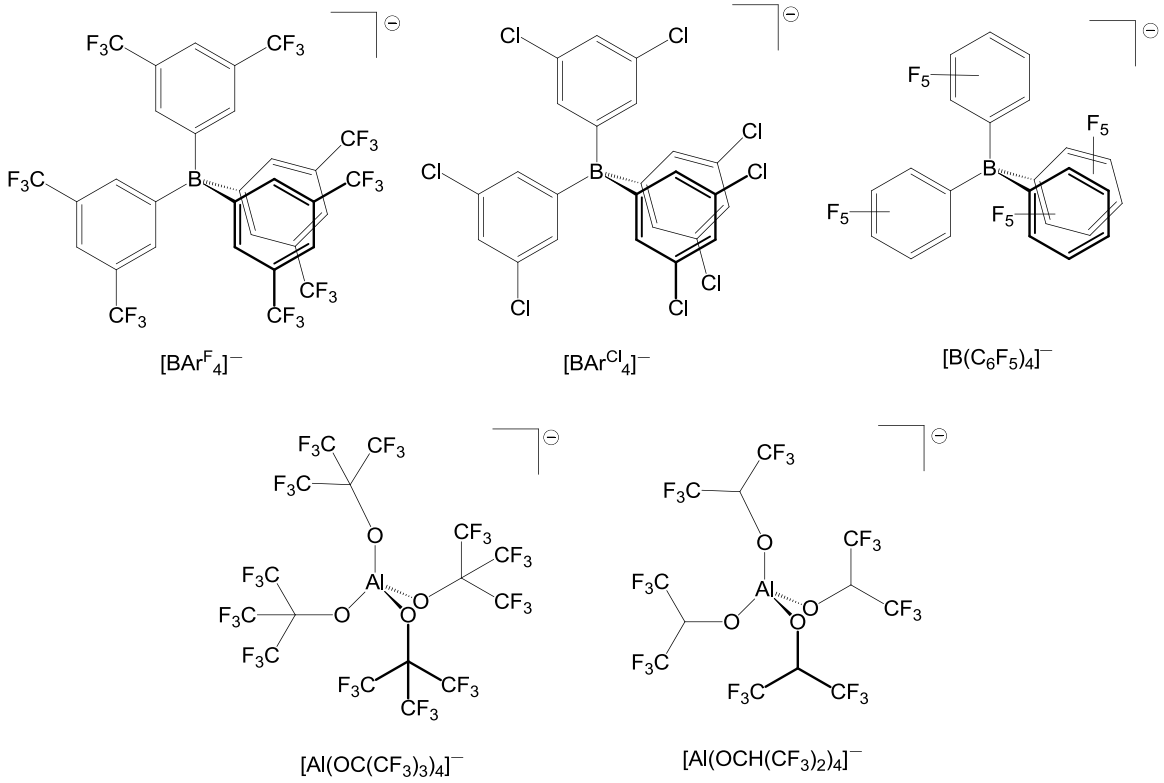

Figure 2.31. Weakly coordinating anions investigated.

Precursor complexes $[Rh(\eta^2\eta^2\text{-COD})_2][WCA]$ {$[WCA]^-$ = $[B(C_6F_5)_4]^-$, $[Al(OC(CF_3)_3)_4]^-$ and $[Al(OCH(CF_3)_2)_4]^-$} were synthesised following the preparation for the $[BAr^F_4]^-$ analogue.[83]

2.4.ii. Synthesis and hydrogenation of 1-[B(C$_6$F$_5$)$_4$] in solution

The anion [B(C$_6$F$_5$)$_4$]$^-$ appears an obvious replacement for [BAr$^F_4$]$^-$ since the greater amount of fluorine substituents on the aryl groups should make the arene bind less strongly (*see Chapter 5 for a more detailed discussion of* η^6*-arene binding affinities*).[84, 85] The synthesis of [Rh(^{i}Bu$_2$PCH$_2$CH$_2$P^{i}Bu$_2$)($\eta^2\eta^2$-COD)][B(C$_6$F$_5$)$_4$], was undertaken by adding ^{i}Bu$_2$PCH$_2$CH$_2$P^{i}Bu$_2$ to [Rh($\eta^2\eta^2$-COD)$_2$][B(C$_6$F$_5$)$_4$] [Scheme 2.23].[83] This product was then hydrogenated in C$_6$H$_5$F solution to form a solution of [Rh(^{i}Bu$_2$PCH$_2$CH$_2$P^{i}Bu$_2$)(η^6-C$_6$H$_5$F)][B(C$_6$F$_5$)$_4$]. Direct addition of NBD to this solution (once degassed) yields desired [Rh(^{i}Bu$_2$PCH$_2$CH$_2$P^{i}Bu$_2$)($\eta^2\eta^2$-NBD)][B(C$_6$F$_5$)$_4$], **1-[B(C$_6$F$_5$)$_4$]**. The ^{31}P{^{1}H} and ^{1}H NMR spectra (CD$_2$Cl$_2$) of **1-[B(C$_6$F$_5$)$_4$]** were fully consistent with the [BAr$^F_4$]$^-$ analogue **1** (except for the lack of protio anion signals) and the ^{19}F NMR spectrum revealed three signals in a 2:1:2 ratio representing the (C$_6$F$_5$) aryl groups upon the anion [δ −167.5, −163.7, −133.1] [Figure 2.32(a)].

Unfortunately crystalline material of **1-[B(C$_6$F$_5$)$_4$]** could not be formed; instead only oily solids could be prepared. These materials lack long range order and probably contain solvent molecules hence are not appropriate for crystalline solid-state reactions.

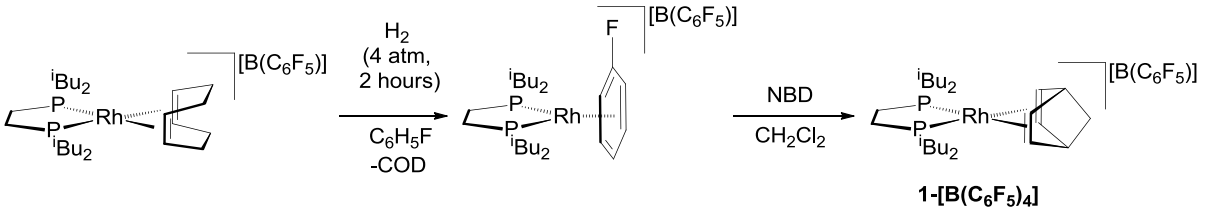

Scheme 2.23. Synthesis of **1-[B(C$_6$F$_5$)$_4$]**.

The hydrogenation of **1-[B(C$_6$F$_5$)$_4$]** was investigated in solution (CH$_2$Cl$_2$). A colour change from orange to yellow was observed upon addition of H$_2$ over three minutes. The ^{31}P{^{1}H} NMR spectrum shows the disappearance of **1-[B(C$_6$F$_5$)$_4$]** and the creation of two new doublet signals [δ 74, J_{RhP} 205 Hz & δ 67, J_{RhP} 195 Hz]. Both new signals contain large J_{RhP} coupling constants, which indicates that a weak *trans* ligand is opposite to phosphorus, as expected for a solvent or anion bound complex. The ^{19}F NMR spectrum displays multiple new peaks directly after hydrogenation indicating various fluorine environments, which presumably occurs due to anion interactions with the metal fragment (*N.B.* six or more new signals would be expected for an M···C$_6$F$_5$ coordinated complex) [Figure

2.32(b)]. The $[B(C_6F_5)_4]^-$ anion could coordinate to the metal centre by an η^6-interaction or perhaps through the fluorines (κ_{F2}) [Scheme 2.24]. The ^{1}H NMR shows that free NBA is now present. Rare examples of $[B(C_6F_5)_4]^-$ coordinated to a metal centre have been reported with early transition metals and lanthanides, coordination occurs through the fluorine atoms in these cases (*see Section 1.2.iii*). Structures containing late transition metals displaying η^6-coordination to C_6F_6 have also been reported, including $W(\eta^6\text{-}C_6F_6)_2$ and $Ni(^tBu_2PCH_2CH_2P^tBu_2)(\eta^2\text{-}C_6F_6)$.[86, 87]

30 minutes after addition of H_2 the $^{31}P\{^1H\}$ NMR signals become weak and the ^{19}F NMR spectrum returns to show only signals for the free anion [Figure 2.32(c) after 24 hours]. Decomposition of highly reactive species by reaction with H_2 and/or CH_2Cl_2 is expected and this may result in free anion. After 24 hours the $^{31}P\{^1H\}$ NMR shows a variety of new weak unidentified doublet signals, all of which have small (J_{RhP} < 150 Hz) coupling constants, suggestive of Rh(III) species.

A weakly bound zwitterionic complex was not isolated with this anion. The evidence of anion coordination, albeit to form a very unstable complex, suggests that, even if a crystalline solid of **1-[B(C$_6$F$_5$)$_4$]** could be formed, displacement of a σ-alkane ligand by the anion may still be possible.

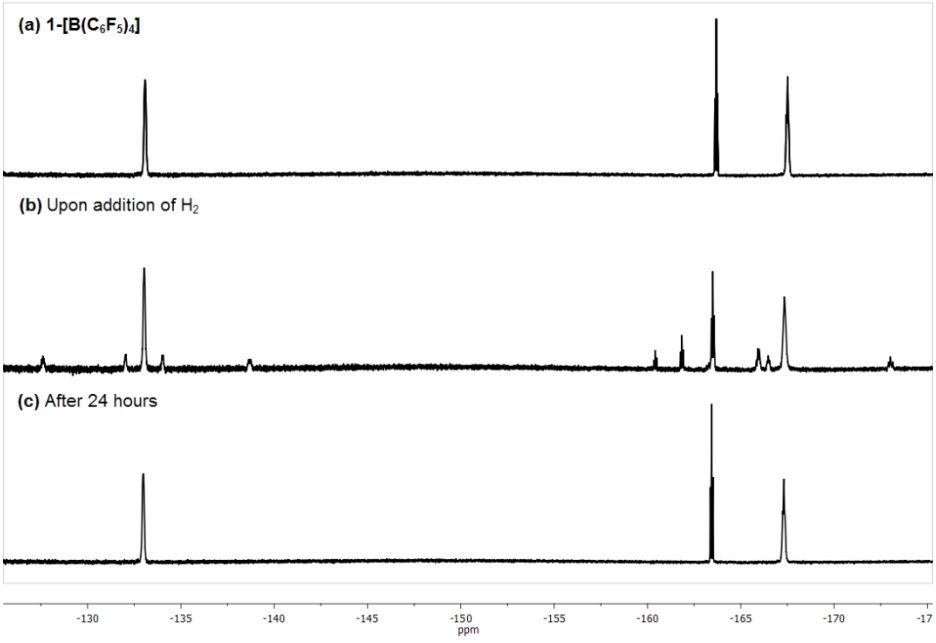

Figure 2.32. ^{19}F NMR spectra of **1-[B(C$_6$F$_5$)$_4$]** and the products of its reaction with hydrogen.

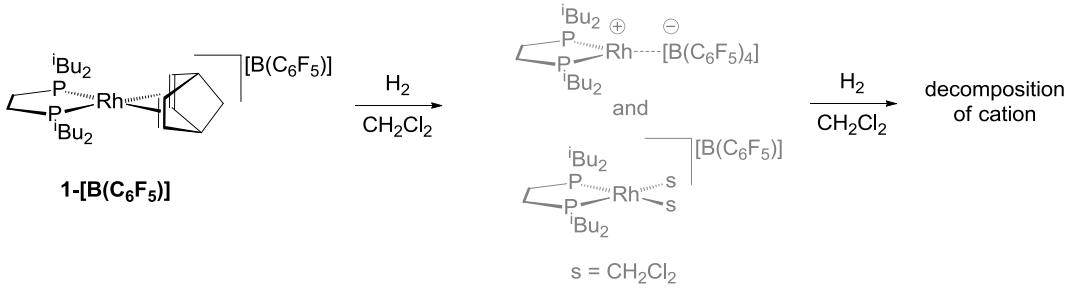

Scheme 2.24. Reaction of **1-[B(C$_6$F$_5$)$_4$]** with hydrogen in CH_2Cl_2 with proposed products shown in grey.

2.4.iii. Synthesis and hydrogenation of complexes containing 'Krossing anions'

The anions $[Al(OC(CF_3)_3)_4]^-$ and $[Al(OCH(CF_3)_2)_4]^-$, designed by Krossing,[88] were chosen as a suitable replacements for $[BAr^F{}_4]^-$ due to their extremely low coordinating properties. Using these anions made synthesis of suitable material far more challenging as it did not form crystalline material easily; instead typically forming oily products. It was possible, however, to form crystalline material of amber $[Rh(^iBu_2PCH_2CH_2P^iBu_2)(\eta^2\eta^2\text{-COD})][Al(OC(CF_3)_3)_4]$, **7-[Al(OC(CF$_3$)$_3$)$_4$]**, by addition of $^iBu_2PCH_2CH_2P^iBu_2$ to $[Rh(\eta^2\eta^2\text{-COD})_2][Al(OC(CF_3)_3)_4]$.[83] The NMR spectra of **7-[Al(OC(CF$_3$)$_3$)$_4$]** were fully consistent with those of $[BAr^F{}_4]^-$ analogue **7** although impurities were present in the bulk sample. ^{19}F NMR spectroscopy (CD_2Cl_2) revealed the resonance for free $[Al(OC(CF_3)_3)_4]^-$ as a singlet [δ −75.8].

A solid-state structure of **7-[Al(OC(CF$_3$)$_3$)$_4$]** was determined by X-ray crystallography [Figure 2.33]. This showed the cation sitting within a similar octahedral pocket as observed before with the $[BAr^F{}_4]^-$ anion [Figure 2.33(b)]. The octahedron of anions is somewhat stretched in comparison to the packing arrangements of $[BAr^F{}_4]^-$ anions in similar compounds [Al···Al$_{(\text{octahedron edges})}$ range 10.31(2)-14.02(2) Å *cf.* **1**, B···B$_{(\text{octahedron edges})}$ range 11.96(1)-13.35(1) Å]. Two ^{i}Bu groups of the cation penetrate the faces of the octahedron on the wider side. Whilst the anion is well ordered, the cation appears disordered and does not refine well. An approximate structure could be determined and reveals the expected connectivity.

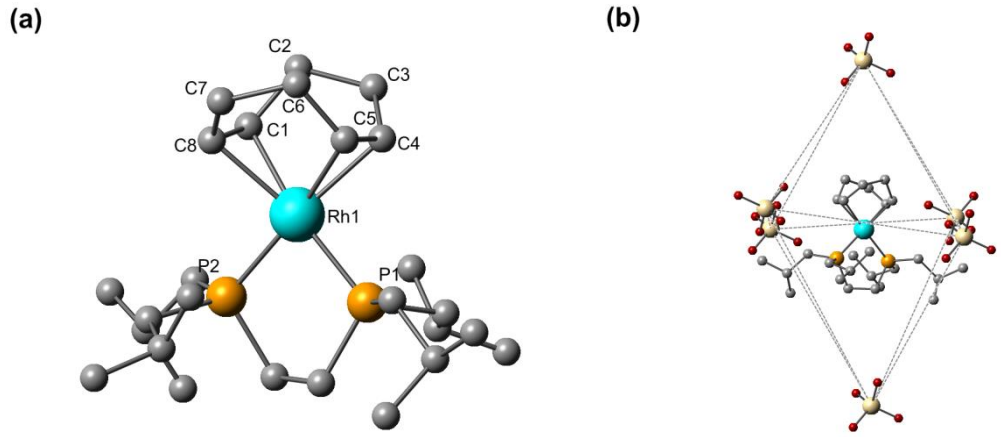

Figure 2.33. (a) Ball and stick diagram of the approximate solid-state structure of the major disorder component of **7-[Al(OC(CF$_3$)$_3$)$_4$]**. **(b)** Packing diagram of **7-[Al(OC(CF$_3$)$_3$)$_4$]**; cation enclosed within a *pseudo*-octahedron of anions, hydrogen atoms omitted and [Al(OC(CF$_3$)$_3$)$_4$]$^-$ anions represented as AlO$_4$ units {C(CF$_3$)$_3$ groups omitted} for clarity.

The COD ligand is expected to require a longer time to react with hydrogen (*i.e.* k_1 is slow),[23] however with less possibility of anion coordination (k_2 slow or may not occur) it was proposed that a long lived σ-alkane complex could still form. Unfortunately hydrogenation (1 atm) of amber single crystals of **7-[Al(OC(CF$_3$)$_3$)$_4$]** for one day yielded pale yellow crystals which gave no diffraction pattern by X-ray crystallography [Scheme 2.25]. Attempts to characterise this final species by solution NMR were inconclusive due to decomposition with solvent (CH_2Cl_2) or poor solubility (C_6F_6).

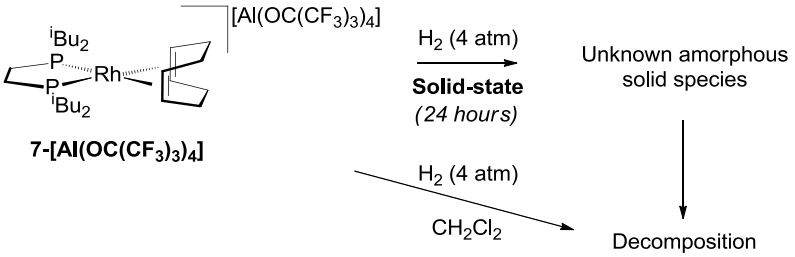

Scheme 2.25. Hydrogenation of **7-[Al(OC(CF$_3$)$_3$)$_4$]** in solution and the solid-state leading to uncharacterised species

The complex [Rh(^{i}Bu$_2$PCH$_2$CH$_2$P^{i}Bu$_2$)($\eta^2\eta^2$-NBD)][Al(OC(CF$_3$)$_3$)$_4$], **1-[Al(OC(CF$_3$)$_3$)$_4$]**, could not be synthesised as a crystalline solid although multiple synthetic routes were tried, however it could be analysed in solution. The best synthetic route was analogous to that of **1-[B(C$_6$F$_5$)$_4$]** but utilising the **[Al(OC(CF$_3$)$_3$)$_4$]$^-$** anion (*see Scheme 2.23*). The ^{31}P{^{1}H} and ^{1}H NMR spectra (CD_2Cl_2) of **1-**

[Al(OC(CF$_3$)$_3$)$_4$] were fully consistent with the [BAr$^F_4$]$^-$ analogue **1** (except for the lack of protio anion signals).

Hydrogenation of **1-[Al(OC(CF$_3$)$_3$)$_4$]** in various solvents was undertaken. In CD_2Cl_2 solvent a short-lived species was observed by $^{31}P\{^1H\}$ NMR spectroscopy with a large coupling constant [δ 75.7, J_{RhP} 210 Hz]. A similar weak $^{31}P\{^1H\}$ NMR signal was also observed in C_6F_6 solvent. Interestingly in C_6F_6 a set of two signals (6:4 ratio) were found in the $^{19}F\{^1H\}$ NMR spectrum in the region for the anion [δ (C_6F_6) −77.2 & −77.1], whereas a single peak had been observed before hydrogenation at approximately the same chemical shift. The ^1H NMR spectra in each case reveal signals consistent with free NBA. Therefore it appears that some interaction of the anion with a low coordinate metal centre may be possible, at least for a short time in a very weakly-coordinating solvent such as C_6F_6. The final cationic product in CD_2Cl_2 (under H_2) was characterised by ESI-MS as [{Rh(^{i}Bu$_2$PCH$_2$CH$_2$P^{i}Bu$_2$)}$_2$Cl$_3$H$_2$]$^+$ [calculated m/z = 949.25, found 949.23 with correct isotope pattern] [Scheme 2.26]. Decomposition products of this kind have been previously reported from CH_2Cl_2 solutions.[38] The difficulties involved with synthesis of clean material using the "Krossing anions" restricts us from commenting further on the products which form upon hydrogenation.

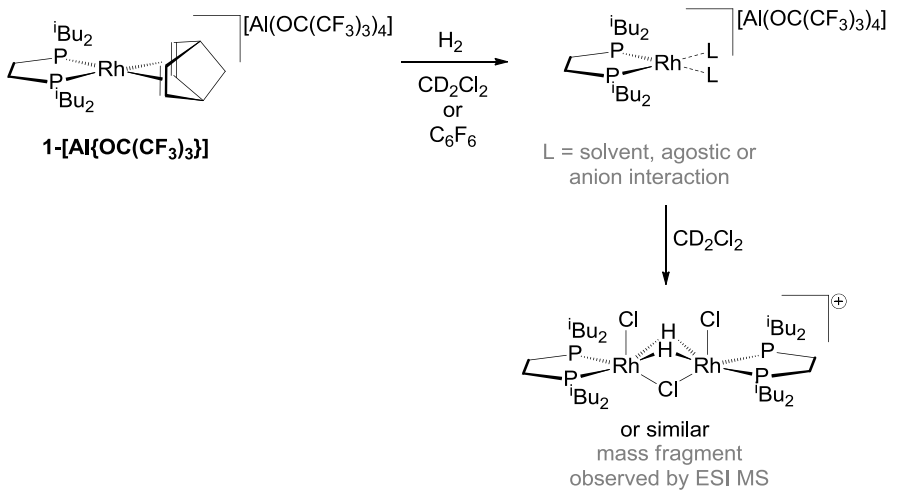

Scheme 2.26. Hydrogenation of **1-[Al(OC(CF$_3$)$_3$)$_4$]** in solution.

No other clean crystalline compounds were able to be formed using [Al(OC(CF$_3$)$_3$)$_4$]$^-$ or similar [Al(OCH(CF$_3$)$_2$)$_4$]$^-$ and these anions were not investigated further.

2.4.iv. Hydrogenation of 1-[BAr^{Cl}_4] in the solid-state

The anion $[BAr^{Cl}_4]^-$ is known to be more coordinating than $[BAr^{F}_4]^-$ [89] but $[Rh(^iBu_2PCH_2CH_2P^iBu_2)(\eta^2\eta^2\text{-NBD})][BAr^{Cl}_4]$, **1-[$BAr^{Cl}_4$]**, was synthesised for comparison with **1**. The synthesis and characterisation of **1-[BAr^{Cl}_4]** is discussed in detail in *Section 3.2.i*. Hydrogenation of orange **1-[BAr^{Cl}_4]** in the solid-state forms the yellow zwitterionic complex $Rh(^iBu_2PCH_2CH_2P^iBu_2)\{(\eta^6\text{-}C_6H_3Cl_2)BAr^{Cl}_3\}$, **12**. Although this reaction was rapid (< 10 minutes, k_1 and k_2 are both fast), no intermediates were observed by SSNMR [Scheme 2.27 & *see Section 3.2.ii*]. **12** is more stable in CH_2Cl_2 than the $[BAr^{F}_4]^-$ analogue **4**, indicating a more strongly bound anion. Perhaps a more stable zwitterionic final product allows a lower energy transition state for the displacement of any σ-alkane complex intermediates, reducing the lifetime of any intermediate.

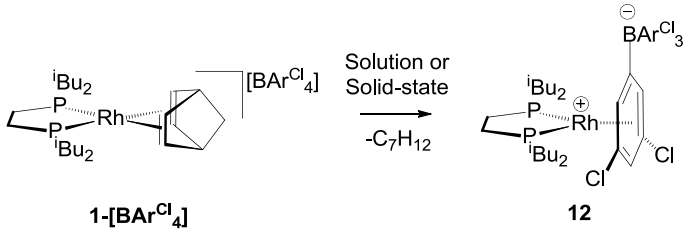

1-[BAr^{Cl}_4] **12**

Scheme 2.27. Reaction of **1-[BAr^{Cl}_4]** with H_2 in solution or in the solid-state.

2.4.v. Conclusions drawn from changing the weakly coordinating anion

The most important factor in studying solid-state reactivity of organometallic complexes is the ability to form clean crystalline products. Unfortunately utilisation of anions, other than $[BAr^{F}_4]^-$ and the more strongly coordinating $[BAr^{Cl}_4]^-$, mostly resulted in oily products which incorporate solvent molecules and lack crystallinity. However, the direct conversion of **1-[BAr^{Cl}_4]** into **12**, without observation of any intermediates, indicates that more strongly coordinating anions are likely to decrease the lifetime of any σ-alkane intermediates.

2.5. Hydrogenation of $[Rh(^{i}Pr_2PCH_2CH_2P^{i}Pr_2)(\eta^2\eta^2\text{-NBD})][BAr^F{}_4]$

2.5.i. Alternative *bis*-phosphine ligands

Having established that NBD is the most suitable alkene precursor for forming σ-alkane complexes and that $[BAr^F{}_4]^-$ is the best weakly-coordinating anion for forming crystalline materials a range of different chelating *bis*-phosphine complexes were synthesised in the hope of isolating a range of other potentially longer lived σ-alkane complexes. The chelate P_2 ligands utilised were phosphines $^{i}Pr_2P(CH_2)_nP^{i}Pr_2$ (n = 2 & 3) and phosphite $(^{i}PrO)_2PCH_2CH_2P(O^{i}Pr)_2$ [Figure 2.34]. These allow comparison with $^{i}Bu_2PCH_2CH_2P^{i}Bu_2$ by analysing the effects of changing substituent (sterics and electronics) and bite angle.

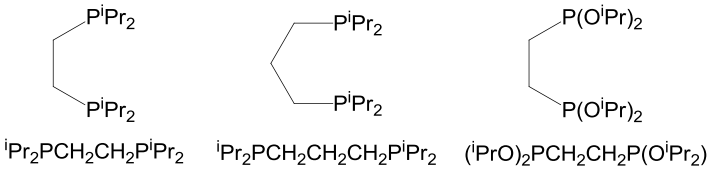

Figure 2.34. P_2 ligands explored.

2.5.ii. Synthesis of $[Rh(^{i}Pr_2PCH_2CH_2P^{i}Pr_2)(\eta^2\eta^2\text{-NBD})][BAr^F{}_4]$

By changing phosphine substituent from ^{i}Bu to ^{i}Pr a small steric change occurs. The ^{i}Pr group, although it contains less atoms than ^{i}Bu, has a greater steric influence close to the metal centre. $[Rh(^{i}Pr_2PCH_2CH_2P^{i}Pr_2)(\eta^2\eta^2\text{-NBD})][BAr^F{}_4]$, **13**, was synthesised by addition of NBD to previously reported $[Rh(^{i}Pr_2PCH_2CH_2P^{i}Pr_2)(\eta^6\text{-}C_6H_5F)][BAr^F{}_4]$, **VIII**, in CH_2Cl_2 [Figure 2.35].[44] A colour change from yellow to vermillion occurs on addition of NBD. Crystalline material is achieved by recrystallisation in CH_2Cl_2/pentane.

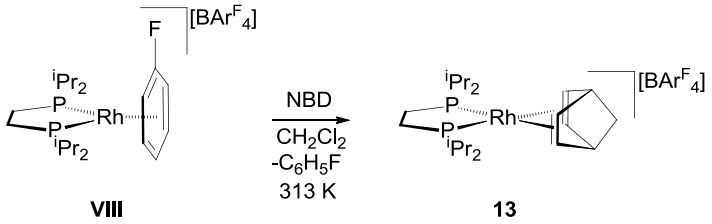

Figure 2.35. Synthesis of **13**.

The solution ^{1}H NMR spectrum of **13** displays NBD resonances [δ 1.84, 4.20, 5.62] similar to those in **1** [δ 1.78, 4.09, 5.31]. The ^{i}Pr groups are represented by multiplet signals [δ 1.19, 2.14] suggesting a diasterotopic relationship of the two methyl groups. The ^{31}P{^{1}H} NMR spectrum reveals a doublet signal [δ 78.1, J_{RhP} 155 Hz] with a J_{RhP} coupling constant similar to **1** [J_{RhP} 158 Hz]. A crystal structure of **13** was obtained [Figure 2.36(a)]. The cationic geometry, bond lengths and bite angle of **13** are very similar to those observed in the solid-state structure of **1**.

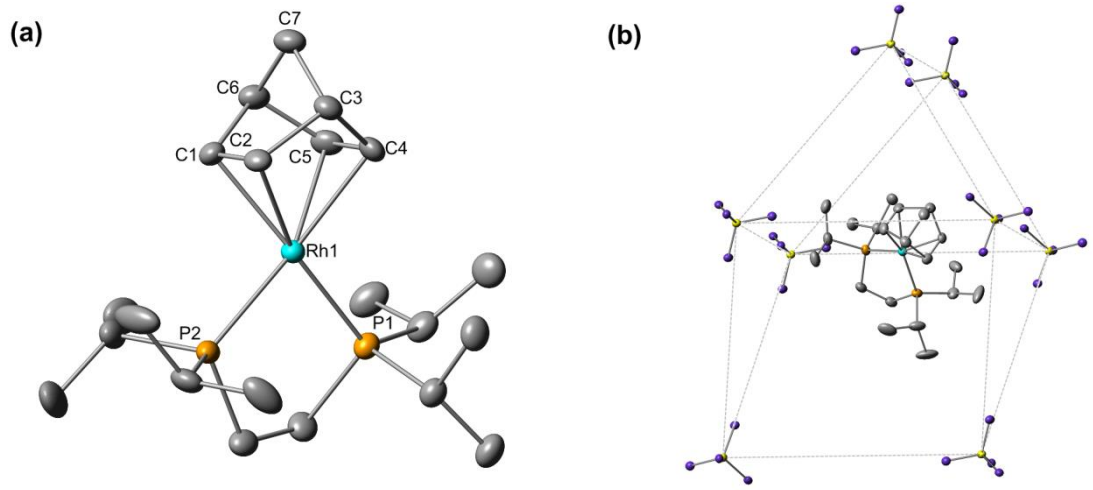

Figure 2.36. Displacement ellipsoid plots (30% probability) of **13** in the solid-state. Hydrogen atoms omitted for clarity. **(a)** Cationic component. **(b)** Packing diagram; single cation enclosed within a *pseudo*-gyrobifastigium of anions, $[BAr^{F}_{4}]^{-}$ anions represented as BC_4 units (aryl groups omitted) for clarity. Selected bond length (Å) and angle (º) data: Rh(1)–P(1), 2.2960(8); Rh(1)–P(2), 2.3016(8); Rh(1)–C(1), 2.214(3); Rh(1)–C(4), 2.230(3); C(1)–C(2), 1.370(4); C(4)–C(5), 1.362(5); P(1)-Rh(1)-P(2), 83.80(3).

By altering the alkyl substituents from ^{i}Bu (**1**) to ^{i}Pr (**13**) a small steric change occurs, inspection of the crystal packing geometry of **13** reveals that this small change is enough to cause a significant re-ordering of cations and anions in the solid-state relative to the packing structure of **1**. The cation in **13** sits in an asymmetrical pocket with a rough gyrobifastigium shape [Figure 2.36(b)] which is different to the octahedral cavity found in many of the complexes containing $^{i}Bu_2PCH_2CH_2P^{i}Bu_2$.

2.5.iii. The products of solid-state hydrogenation of 13

Solid-state hydrogenation of orange **13** results in a fairly rapid (5 minutes) colour change to an amorphous yellow product. This was characterised by solution NMR (C_6F_6 solvent) as anion bound complex $Rh(^{i}Pr_2PCH_2CH_2P^{i}Pr_2)\{\eta^{5}\text{-}C_6H_3(CF_3)_2\}BAr^{F}_{3}$, **14**, analogous to **4** [Scheme 2.28]. The same

transformation occurs rapidly in solution (CD_2Cl_2). After 1 day in CD_2Cl_2, under H_2 (1 atm) **14** has decomposed and some hydride peaks are visible in the ^1H NMR spectrum, the products of decomposition were not characterised.[90]

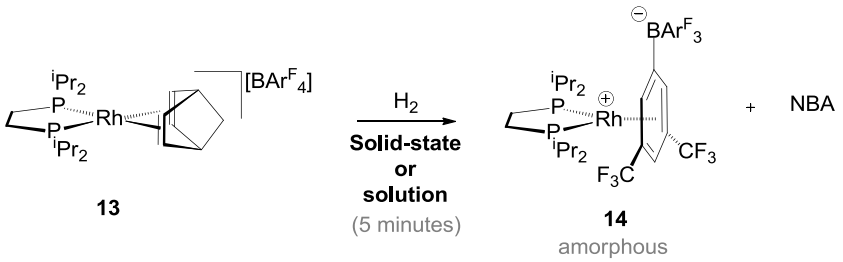

Scheme 2.28. Hydrogenation of **13** to form **14** in the solid-state or in solution.

Pure crystalline **14** can be synthesised by the solid-state hydrogenation of **13** followed by recrystallisation from C_6F_6/pentane at 277 K. A crystal structure was obtained showing a coordination mode similar to **4** [Figure 2.37].

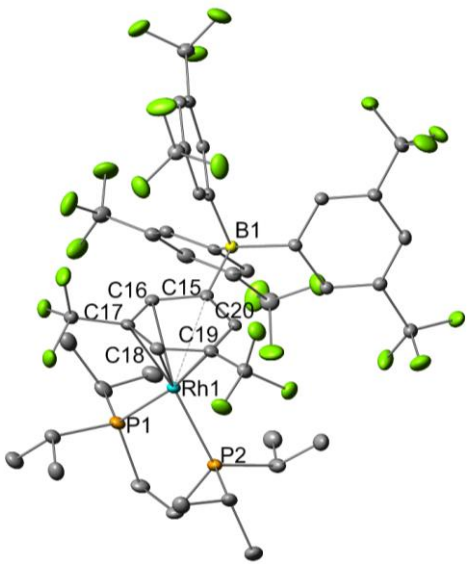

Figure 2.37. Displacement ellipsoid plot (30% probability) of complex **14** in the solid-state. Hydrogen atoms omitted for clarity. Selected bond length (Å) and angle (º) data: Rh(1)–P(1), 2.2616(7); Rh(1)–P(2), 2.2662(7); Rh(1)–C(15), 2.525(2); Rh(1)–C(17), 2.287(2); P(1)-Rh(1)-P(2), 84.14(3).

The Rh–P bond lengths and bite angle are similar to those observed in **4**, however the Rh–$C_{(arene)}$ bond distances are slightly longer [Rh–$C_{(arene)}$ average: **13**, 2.366(2) Å; **4**, 2.338(2) Å]. The Rh(1)–C(15) bond is particularly long [2.525(2) Å] suggesting the anion should be considered to coordinate in an η^5- manner.[33] The ^{i}Pr groups have a greater steric presence in close vicinity to the metal than ^{i}Bu

groups, and perhaps this forces the $[BAr^F_4]^-$ to coordinate at a slightly greater distance away. Similar to **4**, **13** decomposes in CH_2Cl_2 over approximately one hour.

The ^{1}H NMR spectrum of **14** in C_6F_6 displays the expected 1:2:3:6 ratio of peaks in the aryl region [δ 7.21, 7.22, 7.39, 7.50] consistent with coordination of one arene group and free rotation of the remaining three. These signals are similar to the aryl resonances of **4** in the same solvent [ratio 2:1:3:6; δ 6.74, 7.36, 7.41, 7.62] with the metal-coordinated arene signals upfield of the non-coordinated arene signals. The ^{31}P{^{1}H} NMR spectrum of **14** shows a doublet signal [δ 102.1, J_{RhP} 206 Hz] upfield of that observed for **13**, with a large coupling constant (there is a similar relationship between **1** and **4**). The ^{19}F NMR spectrum displays a 3:1 ratio of signals [δ −61.1 & −58.8] corresponding to the coordinated and non-coordinated arene-CF_3 groups.

Addition of D_2 to **13** in the solid-state forms **14** and d_4-NBA. Analysis of the d_4-NBA by ^{2}H NMR spectroscopy (C_6H_5F solvent) reveals two signals for the *exo* and *endo* positions of NBA, however unlike in the deuteration of **1** the *exo* & *endo* signals are not in a 1:1 ratio [Scheme 2.29(a)]. The *exo* peak is much smaller than the *endo* signal [~1:4 *exo*:*endo* ratio, major product (~60%) (*endo*-1,2,4,5)d_4-NBA], which suggests that access to an agostically stabilised NBE complex (after addition of one molecule of D_2) is not favoured in the solid-state.[69] This may hint towards a restricted mobility of the NBD/NBA unit within the crystalline lattice of **13**. If the deuteration experiment is repeated in solution (CH_2Cl_2) the *exo* to *endo* ratio is much closer to unity [~4:6 ratio, major product (~80%) (*endo*-1,2 *exo*-4,5)d_4-NBA] which suggests that without the constraints of a crystalline lattice an NBE fragment may have more room to rotate and form an agostically stabilised complex to which D_2 can add to the *exo* face [Scheme 2.29(b)].

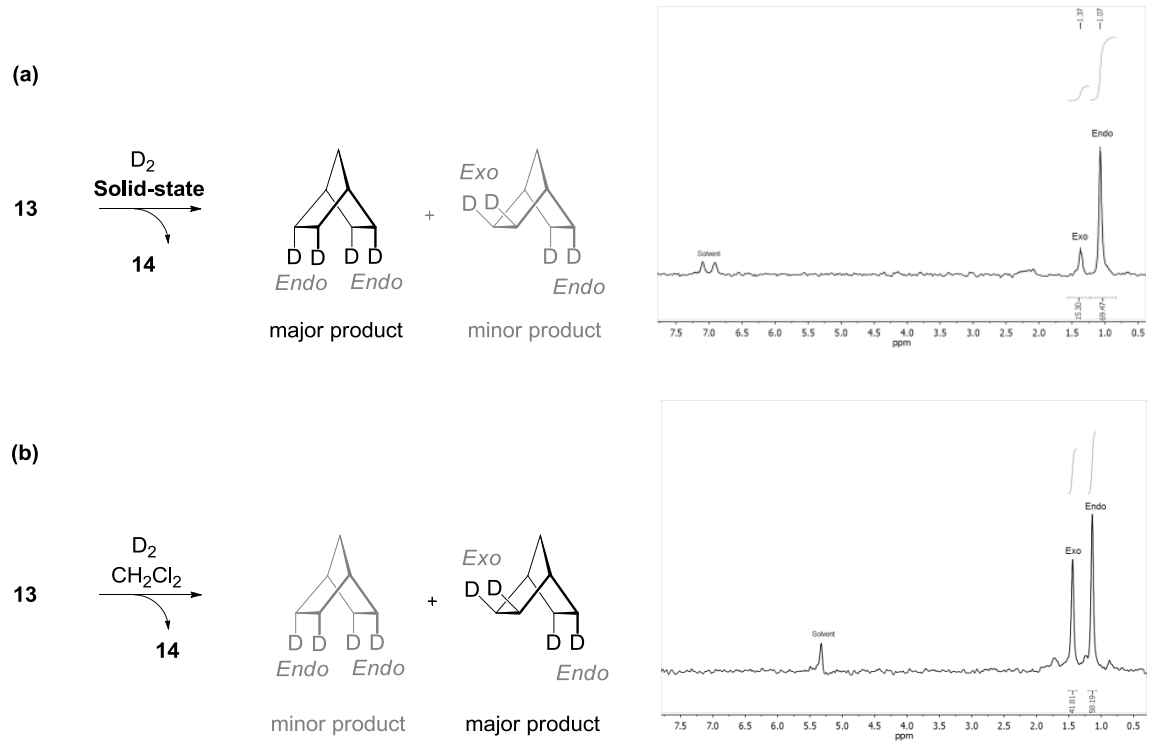

Scheme 2.29. Solid-state and solution deuteration of **13** forms two isotopomers of d_4-NBA alongside **14**. The ^{2}H NMR spectra of the products (after solvation of the solid-state reaction) are shown on the right hand side.

2.5.iv. The hydrogenation of 13 followed by SSNMR spectroscopy

A powdered crystalline sample of **13** was exposed to 1 atm H_2 for four minutes and the temporal evolution of the products followed by $^{31}P\{^1H\}$ SSNMR. The initial spectrum, recorded 11 minutes after the hydrogenation procedure started, reveals the formation of a short lived intermediate complex. A clear ABX system is observed [δ 112.8, J_{RhP} 193 Hz & δ 115.8, J_{RhP} 195 Hz], downfield of the starting material (analogous to the SSNMR spectrum of **5**). There is also a broad peak which is tentatively proposed as the amorphous anion bound species **14** (similar to aforementioned amorphous-**4**) [Figure 2.39(b)].

The intermediate complex decays rapidly at temperatures above 273 K (less than five minutes) [Figure 2.39(c)]. Whether this intermediate complex is a σ-alkane bound species [Figure 2.38] is difficult to accurately determine but it does appear similar to the SSNMR signal recorded for **5** [**5**: δ 77.6, J_{RhP} ~ 194 ±10 Hz & δ 78.9, J_{RhP} ~ 191 ±10 Hz]. A greater difference is observed in the phosphorus environments of the intermediate formed from **13** (compared to **5**). This allows for more

accurate analysis of the J_{RhP} coupling constants, and shows them to be large [J_{RhP} 193 & 195 Hz], which is expected when weak interactions occur in the *trans* positions.

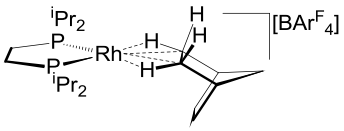

Figure 2.38. Possible structure for the short lived intermediate observed only by SSNMR after the hydrogenation of **13**.

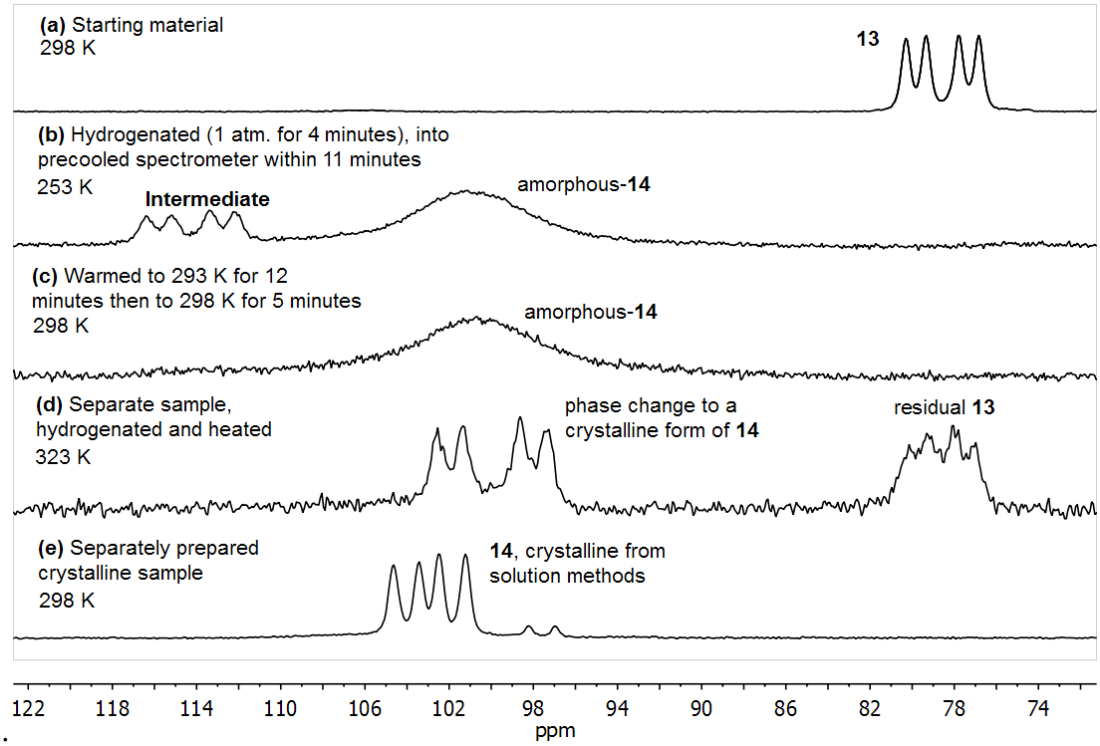

Figure 2.39. $^{31}P\{^{1}H\}$ SSNMR spectra displaying **13 (a)** and the products formed by hydrogenation **(b, c, d)** compared to separately synthesised **14 (e)**.

The broad peak of amorphous **14** undergoes a phase change recrystallisation at 323 K to give a double doublet signal [δ 98, J_{RhP} 195 Hz & δ 102, J_{RhP} 203 Hz] [Figure 2.39(d)]. The final product was characterised in solution (CD_2Cl_2 or C_6F_6) by NMR spectroscopy as **14**. However a separately prepared crystalline sample of **14** shows a set of sharp peaks (double doublet) in its SSNMR spectrum at slightly different chemical shifts [δ 102, J_{RhP} 202 Hz & δ 104, J_{RhP} 197 Hz] to that of the final product of the solid-state reaction [Figure 2.39(e)]. A minor peak is also observed in the spectrum which is consistent with the product formed from the solid-state reaction. The reasoning behind this is

unclear, perhaps different isomers of **14** form depending upon the route of synthesis (*N.B.* different molecular geometries were seen in the solid-state structure of analogous **4**). A sample of **13** was exposed to hydrogen for 1 hour and then heated at 323 K for 1 hour, upon solvation **14** was observed as expected, discounting a decomposition reaction at high temperature

2.6. Hydrogenation of [Rh(^{i}Pr$_2$PCH$_2$CH$_2$CH$_2$P^{i}Pr$_2$)($\eta^2\eta^2$-NBD)][BAr$^F_4$]

2.6.i. Synthesis and characterisation of [Rh(^{i}Pr$_2$PCH$_2$CH$_2$CH$_2$P^{i}Pr$_2$)($\eta^2\eta^2$-NBD)][BAr$^F_4$]

Increasing the bite angle of a chelating phosphine can influence both the steric and electronic parameters of a complex.[5, 32, 45] Whilst precursors for the synthesis of ^{i}Bu$_2$PCH$_2$CH$_2$CH$_2$P^{i}Bu$_2$ were not readily available, closely related ^{i}Pr$_2$PCH$_2$CH$_2$CH$_2$P^{i}Pr$_2$ was commercially available. Therefore the effect of a wider bite angle, in comparison to complexes containing ^{i}Pr$_2$PCH$_2$CH$_2$P^{i}Pr$_2$ (**13** and **14**), could be undertaken.

The initial synthesis of [Rh(^{i}Pr$_2$PCH$_2$CH$_2$CH$_2$P^{i}Pr$_2$)($\eta^2\eta^2$-NBD)][BAr$^F_4$], **15**, was carried out by Mark Scott (MChem student, Weller group).[91] Addition of NBD to a solid sample of previously reported [Rh(^{i}Pr$_2$PCH$_2$CH$_2$CH$_2$P^{i}Pr$_2$)(η^6-C$_6$H$_5$F)][BAr$^F_4$], **IX**,[44] followed by solvation of the mixture in CH_2Cl_2 generated orange **15**, which was recrystallised from CH_2Cl_2/pentane [Scheme 2.30].

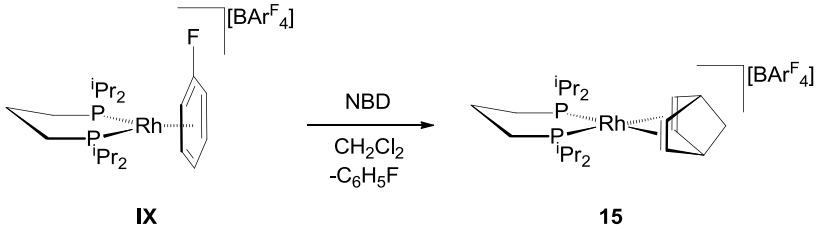

IX **15**

Scheme 2.30. Synthesis of **15**.

15 was characterised by NMR spectroscopy and ESI-MS in collaboration with Mark Scott. The ^{1}H NMR spectrum contains typical values for coordinated NBD [δ 1.77, 4.11 & 5.25] very similar to those of **1**. The ^{i}Pr CH$_3$ groups are split into two double-doublet signals [δ 1.15 & 1.31] indicative of a diastereomeric relationship and coupling to phosphorus as well as the C–H proton. The ^{31}P{^{1}H} NMR

spectrum displays a doublet [δ 22.3, J_{RhP} 148 Hz] with a coupling constant similar to that observed for **1**.

Orange crystals of **15** were grown from CH_2Cl_2/pentane and an X-ray diffraction pattern collected. Distinctive split diffraction spots were observed during collection and refinement revealed that a modulated structure was present.[92] The modulation was commensurate (the structure repeats over a period which is a small integer multiplied by one unit cell dimension) and the structure repeats every three molecules, therefore the structure could be accurately solved by using a large unit cell [**a**, 17.8334(5); **b**, 17.5483(4); **c**, 55.04605(15); *z* = 12; space group *C* 2/c]. Due to a symmetry element through the middle of the repeating unit 1.5 molecules are located in the asymmetric unit. The modulation is displayed as a slight tipping of the cation to and from a central orientation direction and is displayed in Figure 2.40. The modulation enforces three slightly different phosphorus environments in the crystalline phase.

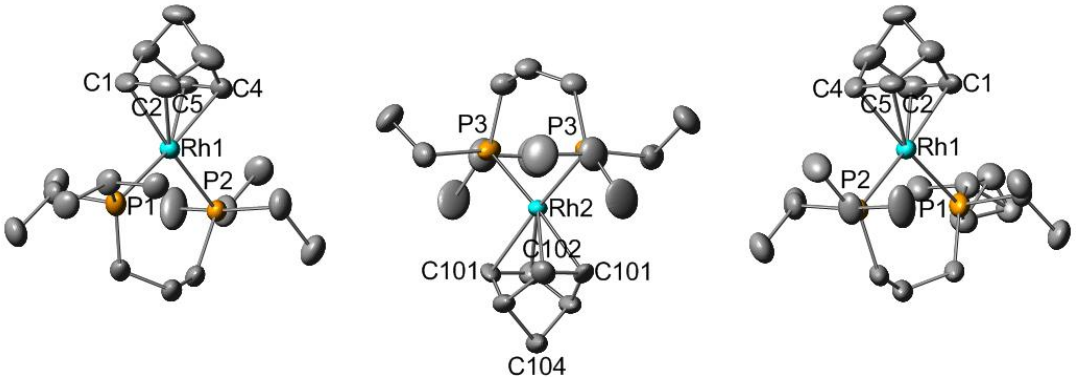

Figure 2.40. Displacement ellipsoid plot (30% probability) of **15** in the solid-state showing modulation repeating over three molecules. A symmetry plane runs through Rh(2) and C(104) in the central cation. Hydrogen atoms and anions omitted for clarity. Selected bond length (Å) and angle (º) data: Rh(1)–P(1), 2.310(3); Rh(1)–P(2), 2.321(3); Rh(1)–P(3), 2.316(3); Rh(1)–C(1-4)range 2.189(14)-2.209(11); Rh(2)–C(101) 2.223(11); Rh(2)–C(102) 2.203(13); C(1)–C(2), 1.36(2); C(4)–C(5), 1.337(18); C(101)–C(102), 1.384(19); P(1)-Rh(1)-P(2), 94.29(12); P(3)-Rh(1)-P(3'), 94.86(14).

The two independent molecules in the solid-state structure of **15** display similar bond lengths and angles. The structures are similar to **1** and **13** however the longer backbone in the phosphine in this case results in a larger bite angle [bite angle: **15**, 94.86(14)°; **1**, 84.21(6)°; **13**, 83.80(3)°].

Similar to **1**, but differing from the similar complex **13**, the $[BAr^F_4]^-$ anions form in an octahedral geometry around the cation [Figure 2.41]. This suggests that although ^{i}Pr groups may be smaller than ^{i}Bu groups the longer backbone in **13** produces a cation with similar steric demands to that of **1**.

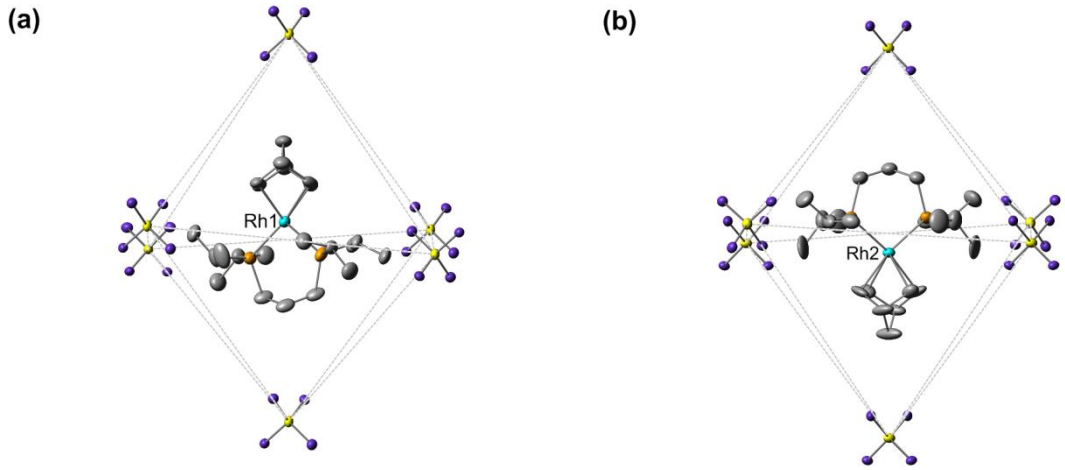

Figure 2.41. Packing diagrams of **15** in the solid-state; **(a)** around Rh(1), **(b)** around Rh(2). Displacement ellipsoid plots (30% probability), hydrogen atoms omitted for clarity, single cations enclosed within a *pseudo*-octahedron of anions, $[BAr^F{}_4]^-$ anions represented as BC_4 units (aryl groups omitted) for clarity.

2.6.ii. Hydrogenation of 15 in solution

The hydrogenation of **15** in solution (CH_2Cl_2) was performed by Mark Scott. A fast colour change was observed from orange to red upon addition of H_2. The red colour is short-lived (< 1 minute) and converts into a yellow solution. Some yellow precipitate forms after 3 hours. ESI-MS was undertaken upon the final solution and a peak corresponding to $[\{Rh(^iPr_2PCH_2CH_2CH_2P^iPr_2)\}_2H_3Cl_2]^+$ was found [m/z; calc 831.19, found 831.20], decomposition of similar low valent compounds in CH_2Cl_2 has been previously reported.[38] We propose that a short-lived solvent-bound red species $[Rh(^iPr_2PCH_2CH_2CH_2P^iPr_2)(CH_2Cl_2)_n][BAr^F{}_4]$ (n = 1 or 2), **16**, is forming (*see Section 2.6.vii*) before subsequent decomposition in CH_2Cl_2 [Scheme 2.31].

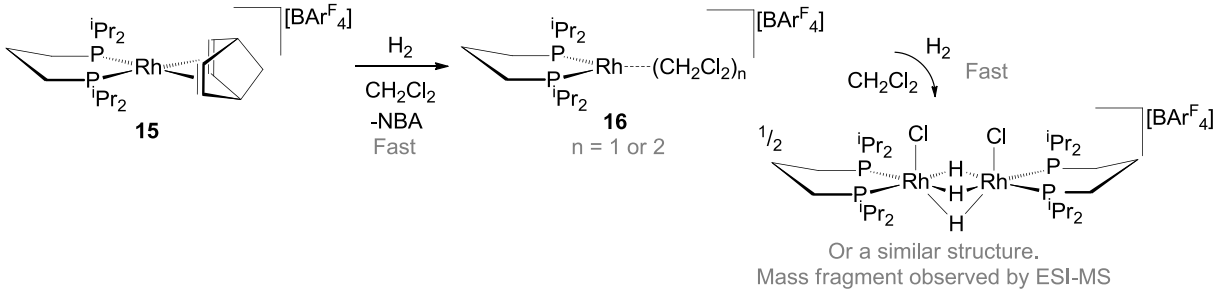

Scheme 2.31. Hydrogenation of **15** in solution, proposed to form a short-lived solvent-bound complex (**16**).

2.6.iii. Hydrogenation of 15 in the solid-state

Solid-state hydrogenation reactions were undertaken in collaboration with Mark Scott.[91] On addition of 1 atm of hydrogen to **15** in the solid-state a colour change from orange to claret occurs. This is consistent with the colour change seen upon hydrogenation of **1**. The claret species is proposed to be the σ-alkane complex [Rh(^{i}Pr$_2$PCH$_2$CH$_2$CH$_2$P^{i}Pr$_2$)(η^4-NBA)][BAr$^F_4$], **17** [Scheme 2.32]. If maintained under an atmosphere of H_2 a colour change to yellow occurs over the course of 2 hours. This final species was subsequently characterised by solid-state and solution NMR spectroscopy as a bridging hydride species [Rh(^{i}Pr$_2$PCH$_2$CH$_2$CH$_2$P^{i}Pr$_2$)(H)(μ-H)]$_2$[BAr$^F_4$]$_2$, **18** [Scheme 2.32]. If the hydrogen atmosphere is removed from claret **17** then the colour remains unchanged under argon for at least several hours. After longer time (~48 hours) periods a slightly more brown amorphous solid forms, it is likely that slow displacement of the σ-alkane ligand occurs with the formation of an anion coordinated species, Rh(^{i}Pr$_2$PCH$_2$CH$_2$P^{i}Pr$_2$)(η^4-C$_6$H$_3$(CF$_3$)$_2$)BAr$^F_3$, **19** (*vide infra*), similar to **4**.

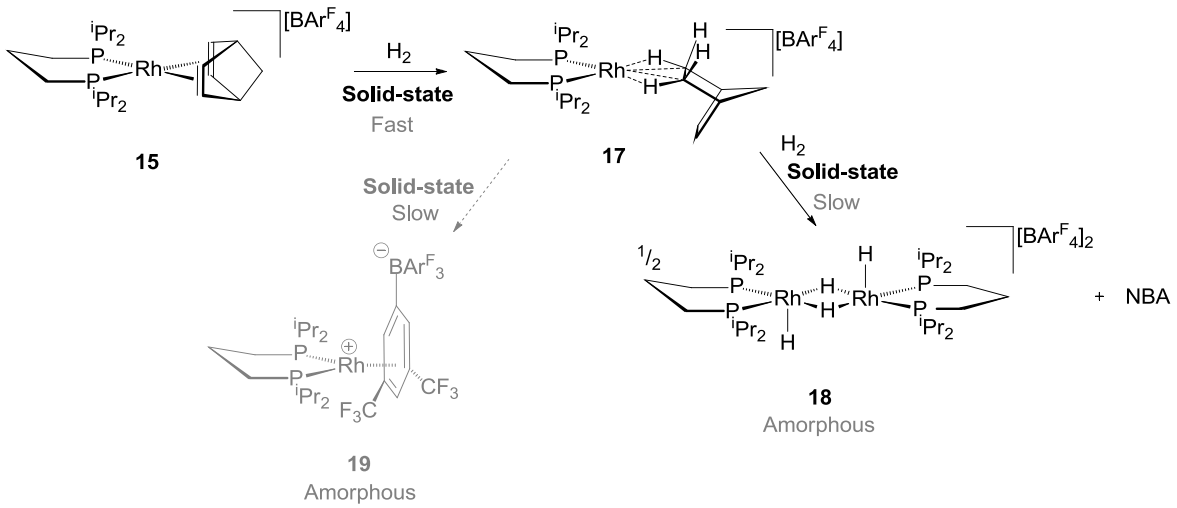

Scheme 2.32. Reaction of **15** with H_2 in the solid-state to form a proposed σ-alkane complex **17**, and the products that subsequently form over longer periods of time under H_2 (or argon; shown in grey).

Exposure of solid **15** to hydrogen for prolonged periods (over one hour) results in the gradual formation of **18** which is characterised by ESI-MS and by solution NMR spectroscopy. In CD_2Cl_2 a broad signal is observed in the $^{31}P\{^1H\}$ NMR spectrum [δ 59, FWHM 207 Hz] and hydride signals are observed in the ^1H NMR spectrum [major hydride signals (both broad) δ −6.9, FWHM 162 Hz; δ −23.0, FWHM 354 Hz]. In 1,2-$C_6H_4F_2$ a sharper doublet signal is observed in the $^{31}P\{^1H\}$ NMR spectrum [δ 61.5, J_{RhP} 103 Hz] showing a small J_{RhP} coupling constant typical of Rh(III) species. The

^{31}P signal is an unusual shape possibly a result of some second order coupling caused by hydrides or other phosphorus atoms found in a dimer. The hydrides are also observed as broad signals in the ^{1}H NMR spectrum when dissolved in 1,2-$C_6H_4F_2$ [δ −4.6, FWHM 124 Hz; δ −25.6, FWHM 132 Hz]. Whilst coupling constants could not be resolved from these broad hydride signals, high field hydrides are likely to indicate terminal hydrides (Rh–H), and signals located at less negative chemical shifts are more typical for bridging hydrides (Rh–H–Rh).[29, 38, 90] The recorded signals therefore suggest a structure in which hydrides are found in both terminal and bridging positions consistent with a bridging hydride dimeric species (which is in agreement with the ESI-MS data) [Scheme 2.32]. **18** is not stable in solution for prolonged periods at room temperature but microcrystalline material could be generated by layering a 1,2-$C_6H_4F_2$ solution with pentane at 277 K. These crystals were not suitable for X-ray diffraction, but elemental microanalysis was undertaken which was consistent with the proposed stoichiometry.

Further evidence of the hydride species was described by Mark Scott; **18** was dissolved in MeCN to form [Rh(^{i}Pr$_2$PCH$_2$CH$_2$CH$_2$P^{i}Pr$_2$)(MeCN)$_2$][BAr$^{F}_4$] and free hydrogen, which was observed in the ^{1}H NMR spectrum. These experiments are detailed in Mark Scott's Part II thesis.[91]

The formation of Rh(III) hydrides in the solid-state was not observed when using the smaller bite angle phosphines discussed earlier in this chapter and may be a direct consequence of the larger bite angle. Larger bite angles are proposed to favour higher oxidation states as described in *Section 1.2.ii*.[32]

Since coordinated [BAr$^{F}_4$]$^{-}$ complex **19** is not observed in solution (CH_2Cl_2 & C_6F_6), by room temperature NMR spectroscopy, alternative methods were necessary for characterisation. A freshly prepared solid sample of **17** was suspended in hexane. This caused a slight colour change from claret to brown, adding hexane may accelerate the loss of NBA (as NBA can dissolve in hexane) and enables the formation of **19**. **19** is partially soluble in hexane and its solubility was increased by heating the suspension to 313 K for one hour, followed by submersion of the flask in an ultrasound bath [Scheme 2.33]. This process forms a pale yellow solution which could be analysed by NMR spectroscopy, and also allowed the formation of small yellow crystals when left to cool to room temperature.

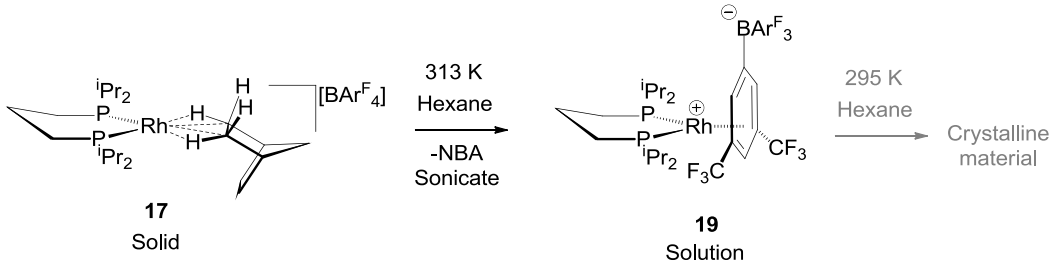

Scheme 2.33. Accelerated formation of **19** in pentane solution.

The $^{31}P\{^{1}H\}$ NMR spectrum of **19** (hexane solvent) shows a doublet [δ 41.5, J_{RhP} 196 Hz] with a typically large coupling constant similar to that of **4** and **14**. The ^{19}F NMR spectrum of **19** displays two signals in a 3:1 ratio [δ −63.3 & −60.3] suggesting coordination of one arene group of $[BAr^{F}_{4}]^{-}$ and free rotation of the other three. Unfortunately, without d_{14}-hexane available, the ^{1}H NMR spectrum of **19** was not obtained.

The X-ray structure of **19** was recorded and reveals the expected coordination of one arene group of the anion [Figure 2.42]. The Rh−C bond lengths are slightly longer than seen in **4** and **14** [bond length range: **19**, 2.313(3) - 2.552(2) Å; **4**, 2.2799(19) - 2.4470(19) Å; **14**, 2.287(2) - 2.525(2) Å]. The solid-state geometry of **19** shows that the arene could be considered to coordinate in an η^4 (or slipped η^6) manner, since two Rh–C distances are long [Rh(1)–C(20) 2.552(2) Å, Rh(1)–C(25) 2.486(3) Å]. This suggests the increase in both local bulk (from ^{i}Pr groups) and bite angle [bite angles: **4**, 83.63(2)° & 83.73(2)°; **14**, 84.14(3)°; **19**, 92.23(3)°] causes a greater steric presence for this phosphine, which may destabilise the anion bound zwitterionic complex **19**. This may explain why **19** is very unstable in CH_2Cl_2. The distance between the rhodium atom and the plane intersecting the six η^6-arene carbons was examined for anion bound complexes **4**, **14** and **19** and revealed that both of complexes with phosphines with ^{i}Pr substituents (**14** and **19**) had greater metal-arene separation than the complex with the ^{i}Bu phosphine (**4**) [Rh⋯arene plane (Å): **4**; 1.858 & 1.868; **14**, 1.920; **19**, 1.919]. An unstable anion-bound complex such as **19** may allow for a longer lived σ-alkane complex (**17**) because of a slow rate of displacement of the σ-alkane (k_2 is slow). However the longevity of **17** is difficult to determine and may be highly dependent on particle size.

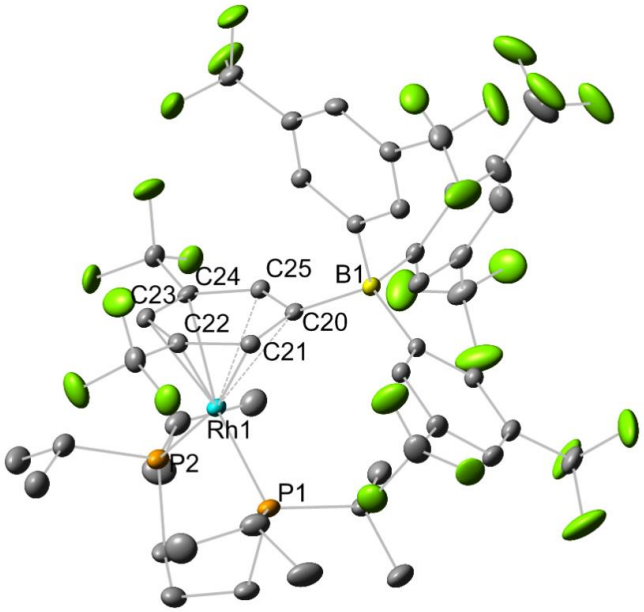

Figure 2.42. Displacement ellipsoid plot (30% probability) of complex **19** in the solid-state. Hydrogen atoms omitted for clarity. Selected bond length (Å) and angle (º) data: Rh(1)–P(1), 2.2746(7); Rh(1)–P(2), 2.2637(7); Rh(1)···C(20), 2.552(2); Rh(1)···C(25), 2.486(3); Rh(1)–C(22), 2.313(3); P(1)-Rh(1)-P(2), 92.23(3).

The Rh–P bond lengths are slightly shorter than those in **15** [**19**, 2.2637(7) & 2.2746(7); $\mathbf{15}_{(range)}$, 2.310(3) - 2.321(3)] indicating the weak *trans* effect of the arene ligand. The bite angle is also slightly smaller than those of **15** [**19**, 92.23(3); **15**, 94.29(12) & 94.86(14)] showing the flexibility of the phosphine.

2.6.iv. Hydrogenation of 15 followed by SSNMR spectroscopy

To gain clearer insight into the solid-state hydrogenation of **15** SSNMR studies were conducted {in collaboration with Mark Scott (Oxford) and Dr. David Apperley (Durham)}. Powdered crystalline **15** displays at least two overlapping phosphorus environments (~2:1 ratio of signals) in its $^{31}P\{^{1}H\}$ SSNMR spectrum [δ 21.4, J_{RhP} 141 Hz & δ ~19.3 (broad)], this is consistent with the modulated crystalline structure which exhibits three different phosphorus environments [Figure 2.43(a)]. The $^{13}C\{^{1}H\}$ SSNMR spectrum showed only weak peaks in the alkene region again a possible artifact of the different environments in the modulated structure.

A powdered crystalline sample of **15** was placed under an atmosphere of D_2 for 10 minutes and analysed by SSNMR directly. Two new species were initially observed in the $^{31}P\{^{1}H\}$ SSNMR, over

time the minor species grows at the expense of the initially major species [Figure 2.43(b) & (c)]. The initial major species is a doublet [δ 57.8, J_{RhP} 191 Hz] and is proposed to be the σ-alkane complex d_4-**17**. The signal is downfield of the starting material and exhibits a large coupling constant, both similar to **5**. The $^{13}C\{^1H\}$ SSNMR spectrum of d_4-**17** as the major species is fairly featureless but confirms the hydrogenation of alkenes by loss of peaks in this region of the spectrum. Whilst d_4-**17** appears stable at 233 K, at 298 K this species decays over the course of 30 minutes into a species exhibiting two doublets in the $^{31}P\{^1H\}$ SSNMR spectra [δ 39.6 and 43.7, both J_{RhP} 195 Hz] which is proposed to be **19** [**19** solution $^{31}P\{^1H\}$ NMR: δ 41.4, J_{RhP} 196 Hz]. The $^{13}C\{^1H\}$ SSNMR spectrum of this final species shows a variety of new peaks in the aromatic region corresponding to a change in the anion environment consistent with the formation of an anion bound zwitterionic complex (*i.e.* **19**).

SSNMR spectroscopy experiments show the decomposition of **5** into **4** over the course of less than 20 minutes at 298 K (*see Section 2.2.iv*). Therefore the fact that **17** is still visible by SSNMR after 60 minutes at the same temperature suggests a greater lifetime of this σ-alkane complex in the solid-state.

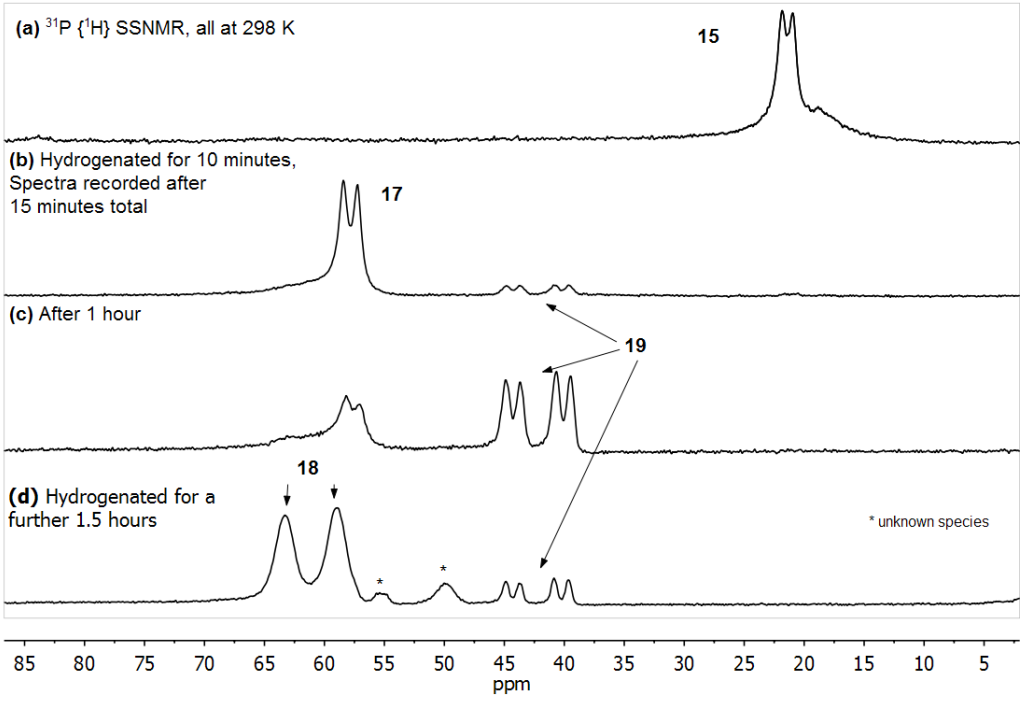

Figure 2.43. $^{31}P\{^1H\}$ SSNMR Spectra displaying the reaction of **15** with D_2 in the solid-state to form intermediate d_4-**17** which in time forms **19**. Subsequent deuteration forms dimeric deuteride species d_4-**18**.

Further evidence for species **17** and **19** comes from interpreting the $^{2}H\{^{1}H\}$ SSNMR spectra. ^{2}H SSNMR spectra can give an indication of the mobility of a chemical environment. A truly static environment will give a ^{2}H SSNMR spectrum with extensive spinning side bands which combine to form a Pake doublet shape (the doublet forms because ^{2}H is a quadrupolar nucleus).[93, 94] In contrast a mobile species (like a liquid) will give a single sharp signal. Whilst d_4-**17** is the major species (*i.e.* at the beginning of the SSNMR analysis), the major signal in the ^{2}H spectrum (233 – 298 K) is a broad peak with spinning side bands which centre about δ 0 [FWHM 290 Hz], most likely corresponding to d_4-**17** [Figure 2.44]. The presence of spinning side bands suggests the major signal comes from a close to static environment – *i.e.* part of the crystalline structure.[93, 95, 96] A minor sharp singlet at δ 1.2 [FWHM 41 Hz (from later experiments)] with no spinning sidebands is also present. A single peak, without sidebands, is indicative of a mobile species, such as a free solvent molecule. Therefore we propose that the small sharp peak at δ 1.2 is a small amount of free d_4-NBA [D_{endo} (δ 1.1) and D_{exo} (δ 1.4) signals overlapping] which is produced when d_4-**17** decomposes to form **19** (**19** is observed as a minor species in the $^{31}P\{^{1}H\}$ SSNMR at this point).

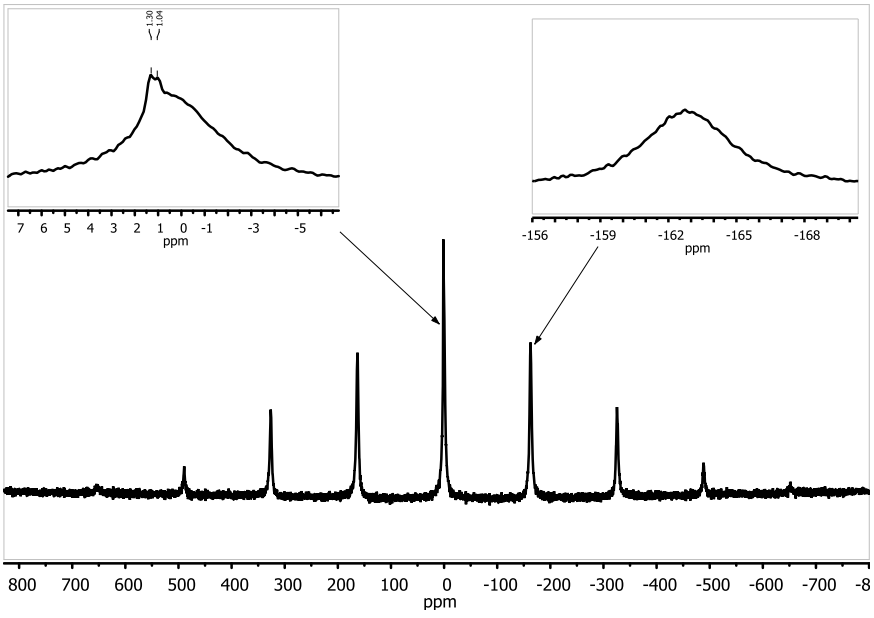

Figure 2.44. $^{2}H\{^{1}H\}$ SSNMR spectrum with d_4-**17** as the major product at 298 K, the broad peak corresponds to d_4-**17**, whilst the small sharp peak without spinning sidebands is a small amount of free d_4-NBA. Magnified regions of the spectrum show that the minor peak is only located in the central peak and does not exhibit side bands.

The breadth and position of the static ^{2}H SSNMR peak may be explained by the process of sequential deuteration of NBD, which leads to (*endo*-1,2 *exo*-4,5)d_4-NBA. Addition of D_2 to **15** followed by

solvation of the products in C_6H_5F reveals the formation of (*endo*-1,2 *exo*-4,5)d_4-NBA which was characterised by a 1 : 1 ratio of peaks in the ^{2}H NMR spectrum - (*endo*-1,2 *exo*-4,5)d_4-NBA also forms upon the deuteration of **1** (*see section 2.2.viii for details*). In the solid structure of **5** only the *endo* hydrogen positions of NBA coordinate to the metal, this is likely to also be the case in **17** (*vide infra*).

The breadth of the ^{2}H SSNMR peak for **17** is suggestive of some restricted molecular motion; slow site exchange of NBA between coordinated *endo* C–H groups is possible [Scheme 2.34].[97] The chemical shift of the broad peak is then likely to be an averaged value of the differing chemical environments. The *endo* deuteriums in free d_4-NBA are located at δ ~1.1, therefore, in order for the ^{2}H SSNMR peak to be observed at δ ~0, the metal-coordinated *endo* deuteriums are expected at approximately δ −1 [reported σ-alkane M···C–H ^{1}H NMR signals: δ 0 to −8].[68, 69] There must also be a signal for the *exo* deuteriums (which do not coordinate to the metal), this may also be broad due to site exchange and lie in approximately the same place as the *endo* signal. An isotope effect is expected to promote C–H coordination over C–D, hence the site exchange equilibrium may lie to one side [Scheme 2.34].[21, 98]

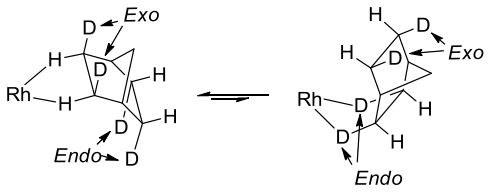

Scheme 2.34. Exchange process averaging the chemical shifts of the ^{2}H signals in d_4-**17**.

Once **19** has formed as the major species (298 K, 60 minutes) the sharp peak in the ^{2}H SSNMR spectrum corresponding to free NBA grows to become the major species [δ 1.2 (D_{endo} and D_{exo} peaks overlapping), FWHM 75 Hz (at ~50% free NBA)] and the broad peak with side-bands drops in intensity as this component diminishes [Figure 2.45].

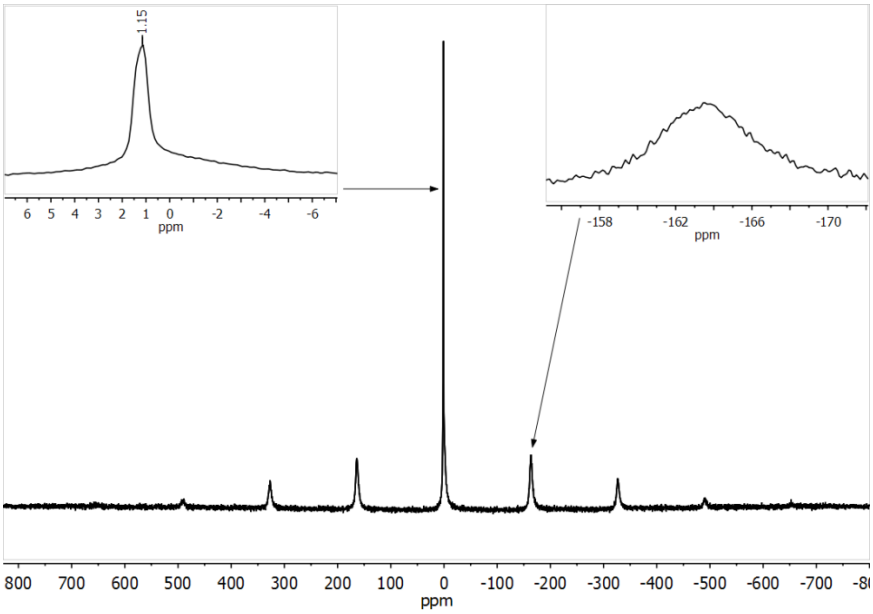

Figure 2.45. $^{2}H\{^{1}H\}$ SSNMR spectrum displaying roughly 50% free d_4-NBA, once **19** is proposed to have begun to form (~50% **19**, ~50% still **17** by integration of the $^{31}P\{^{1}H\}$ SSNMR spectra recoded directly afterwards). Central signal contains a sharp single line not present in the spinning sidebands indicative of mobile d_4-NBA.

If powdered crystalline **15** is exposed to D_2 for 2 hours and then degassed, two new broad peaks are observed in the $^{31}P\{^{1}H\}$ SSNMR spectra [δ 58.8 and 63.2], similar to the position of the solution signal of **18**, alongside some small unidentified signals [Figure 2.43(d)]. The $^{13}C\{^{1}H\}$ SSNMR spectrum displays a typical (non-coordinated) $[BAr^{F}_{4}]^{-}$ region. The ^{2}H SSNMR spectrum of directly prepared **18** displays a large sharp mobile peak for the free d_4-NBA released and also a smaller set of signals (with spinning sidebands) that corresponding to the deuterides of **18** [δ −5.1 & −25.8], these positions are similar to those observed in solution NMR spectrum of **18** and are consistent with bridging and terminal deuterides respectively.[29, 90]

2.6.v. Characterisation of 17 by X-ray crystallography

Single crystals of **15** were exposed to 1 atm H_2 for 40 minutes in order to try and form σ-alkane complex **17** by a SC-SC reaction. X-ray crystallography was undertaken on these samples both at Oxford University and at the Diamond Light Source (beam-line I19). The modulation seen in the crystalline phase of **15** is again present in the hydrogenated crystals however it now appears to have become incommensurate (structure does not repeat over a reasonable number of unit cells) and exists

in two directions (which may be a consequence of twinning), this makes refinement far more challenging. A low quality "averaged" structure was modelled which encouragingly shows the expected geometry of an NBA unit coordinating to rhodium through two *endo* C–H groups, similar to the geometry of the solid-state structure of **5** [Figure 2.46]. *Further more complex refinements are currently being undertaken by Dr Kirsten Christensen (Uni. Oxford).*

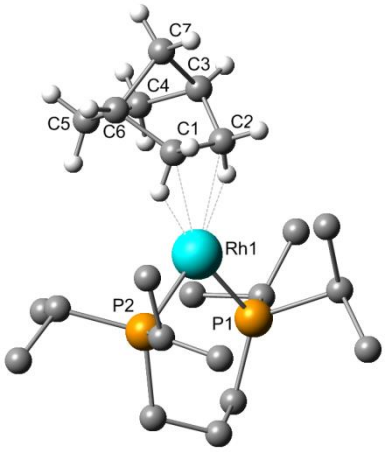

Figure 2.46. Ball and stick diagram of the averaged solid-state structure of the cation of **17**. Only NBA hydrogen atoms present. The dataset displayed incommensurate modulation; however this structure was refined from the data from central diffraction peaks only.

Whilst bond length analysis is not possible on such a low quality structure (R = 25%) approximate Rh(1)···C(1)/C(2) distances of 2.4-2.5 Å are long enough to suggest that σ-interactions may be present rather than coordination of an olefin. The NBA unit has rotated from its original position (as an NBD ligand), this is again consistent with the structure of **5** and supports the proposed connectivity displayed.

2.6.vi. Hydrogenation of 15 followed by powder X-ray diffraction techniques

The reaction of solid **15** (particle size: $d < 50$ μm) with H_2 was also followed using *in situ* powder X-ray diffraction at the Diamond light source using the procedure outlined in *Section 2.2.xiii*. The initial powder X-ray diffraction pattern is visually consistent with the powder X-ray diffraction pattern simulated from the single crystal structure of **15** [Figure 2.47] (accurate modelling of this pattern, which is hindered by the modulation present in **15**, is currently being investigated by Dr. Chadwick). The circular pattern is spotty, which is consistent with a crystalline powdered sample.

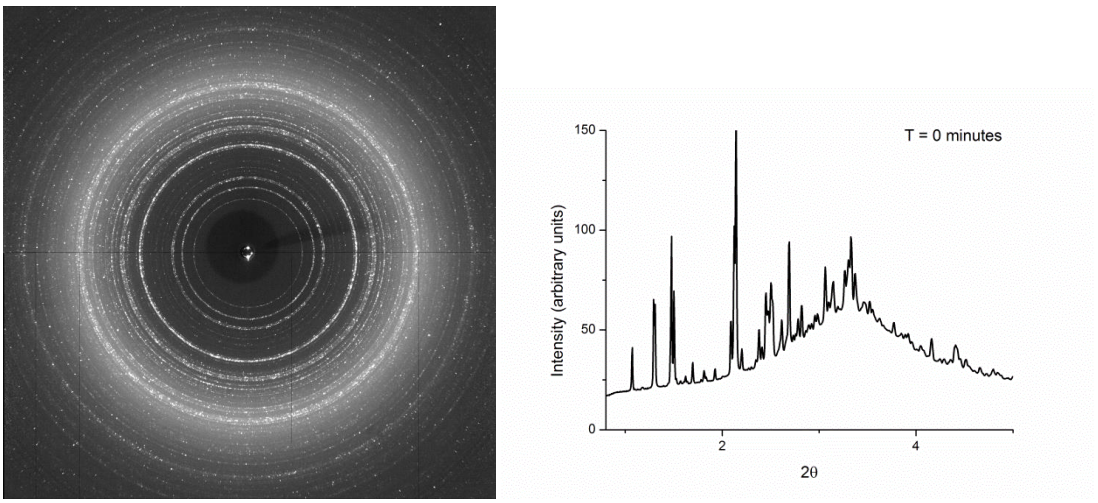

Figure 2.47. Powder diffraction pattern (with 1-D plot) of **15** before addition of hydrogen.

Over the course of 10 minutes under hydrogen the pattern changes and it is proposed that σ-alkane complex **17** has formed [Figure 2.48]. The sample was left under H_2 overnight with continual powder X-ray diffraction collection.

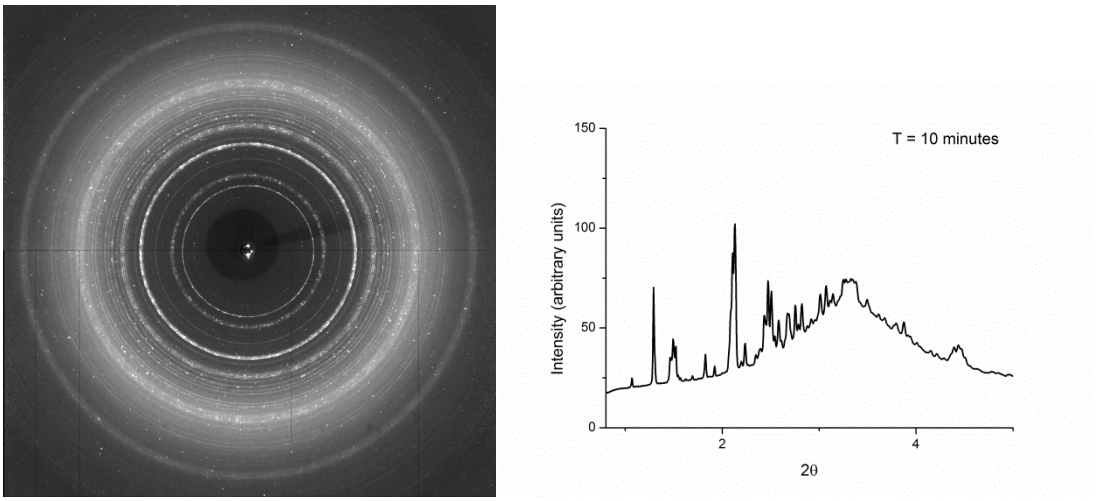

Figure 2.48. Powder diffraction pattern (with 1-D plot) collected 12 minutes after addition of hydrogen to **15**; σ-alkane complex **17** is proposed to have formed *in situ*.

After 1 hour the sample appears to become amorphous and the sample is likely to have formed **19** [Figure 2.49] (this is consistent with the behaviour of **5** which forms amorphous **4**). The $^{31}P\{^{1}H\}$ SSNMR spectrum of **19**, formed by a solid-state reaction, shows broad peaks; presumably indicating an initial amorphous phase.

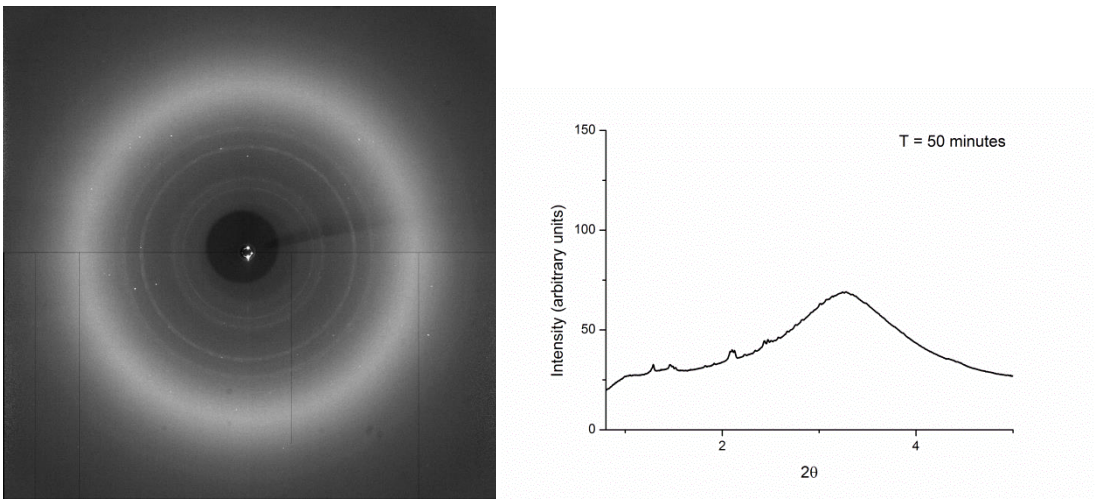

Figure 2.49. Powder diffraction pattern (with 1-D plot) collected 50 minutes after addition of hydrogen to **15**; an amorphous form of complex **19** is proposed to have formed *in situ*.

After 3 hours a set of new peaks grow in - this could be due to a recrystallisation phase change of **19**, similar to that observed with **4** (albeit upon heating), or it could be the slow formation of dimeric hydride species **18** [Figure 2.50]. The single crystal X-ray structure of **19** has been determined and a powder pattern simulation was compared to this final X-ray powder pattern. The patterns do not match which suggests that the final microcrystalline product is not **19**. It remains possible that the final product may be **18** (of which a single crystal structure has not been obtained for comparison).

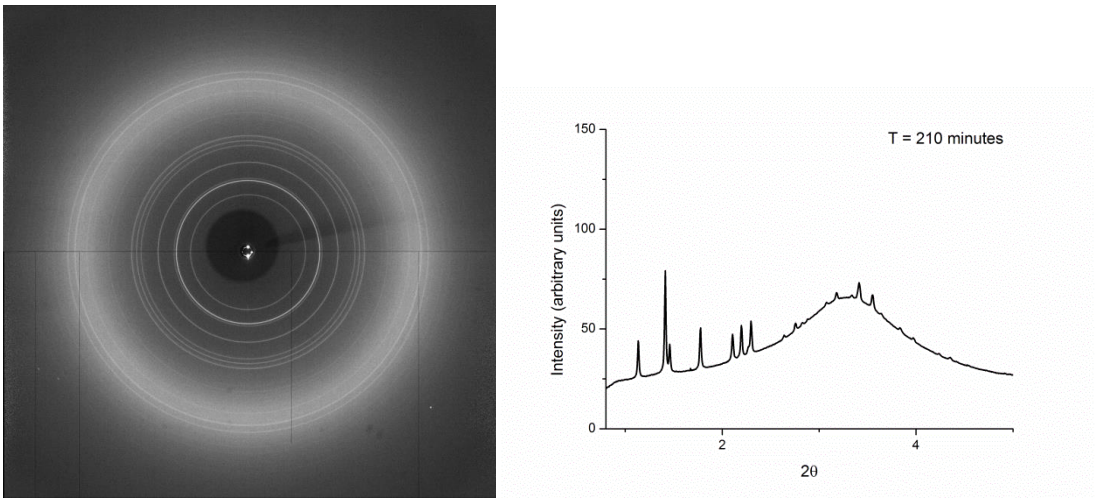

Figure 2.50. Powder diffraction pattern (with 1-D plot) collected 3.5 hours after addition of hydrogen. The dimeric hydride complex **18** may be forming after prolonged exposure to hydrogen.

It is difficult to accurately determine the longevity of the σ-alkane complexes **5** and **17**, but by analyzing the powder diffraction data under the same experimental conditions (particle size: $d < 50$

μm) it appears that the transition from σ-alkane complex to amorphous anion-bound complex (**4** or **19**) is about 45-60 minutes for both species. By SSNMR (room temperature, undefined particle size) decomposition to the anion bound complex was slightly slower for **17** (~1 hour) compared to **5** (~15 minutes). In the single crystalline phase **17** appears stable under hydrogen for longer than **5**, which allows collection of a diffraction pattern of the σ-complex after a longer period of hydrogenation (40 minutes to form **17**, *cf.* an optimised time of 11 minutes to form **5**). Overall it appears that **17** has a slightly greater lifetime at room temperature than **5** but that powdered samples of both (with the same particle diameter range) decompose into a $[BAr^F_4]^-$ coordinated complex within an hour. Larger crystals of **5** and **17** appear to have longer lifetimes.

2.6.vii. Solvation of 17 in CH_2Cl_2 and 1,2-$C_2H_4Cl_2$

Initial low temperature solution NMR studies were undertaken in collaboration with Mark Scott.[91] Solvation of freshly prepared **17** at low temperatures (below 195 K) in CH_2Cl_2 results in a red solution, which changes colour to yellow when warmed to room temperature. The red solution was prepared by distillation of CD_2Cl_2 onto a sample of **17** frozen in liquid N_2 allowing for direct analysis by ^1H and $^{31}P\{^1H\}$ NMR spectroscopy at low temperatures. The $^{31}P\{^1H\}$ NMR spectrum (188 K) displays a doublet [δ 51.01, J_{RhP} 199] with a large J_{RhP} coupling constant corresponding to a weakly bound ligand *trans* to phosphorus. The ^1H NMR spectrum indicated free NBA is present eliminating the possibility of **17** existing in solution and the ^{19}F NMR spectrum shows only one signal for $[BAr^F_4]^-$ suggesting an anion-coordinated complex (**19**) is not present either. Therefore a solvent complex, most likely $[Rh(^iPr_2PCH_2CH_2CH_2P^iPr_2)(CH_2Cl_2)_n][BAr^F_4]$, **16**, (n = 1 or 2) is proposed [Scheme 2.35]. CH_2Cl_2 complexes have been previously reported.[99, 100] For example solvation of previosuly reported low coordinate $[Rh(P^iBu_3)_2][BAr^F_4]$, **IV**, in CD_2Cl_2 results in a $^{31}P\{^1H\}$ NMR signal with a J_{RhP} coupling constant of 207 Hz, this may be a CH_2Cl_2-bound complex, although agostic interactions are also possible.[34, 38] At higher temperatures **16** is likely to decompose in CH_2Cl_2 forming Rh(III) complexes such as $[\{Rh(^iPr_2PCH_2CH_2CH_2P^iPr_2)\}_2H_3Cl_2)][BAr^F_4]$ which was observed by ESI-MS (by Mark Scott) [m/z: calc. 831.20, found 831.19 with the correct isotope pattern].[38, 82]

1,2-$C_2H_4Cl_2$ is a similar solvent to CH_2Cl_2 but is known to coordinate more readily to metal centres (although is still considered a poorly coordinating solvent).[34, 100] [Rh(^{i}Pr$_2$PCH$_2$CH$_2$CH$_2$P^{i}Pr$_2$)($\kappa^2_{Cl,Cl}$-1,2-$C_2H_4Cl_2$)][BAr$^F_4$], **20**, was prepared by either hydrogenation of a 1,2-$C_2H_4Cl_2$ solution of **15**, or by dissolving freshly prepared solid **17** in 1,2-$C_2H_4Cl_2$ [Scheme 2.35].

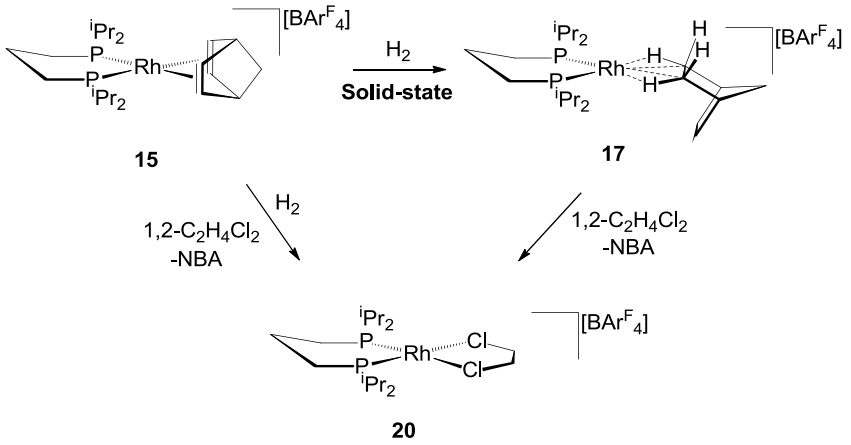

Scheme 2.35. Formation of **20**.

20 is an unstable red complex and displays a doublet in its $^{31}P\{^1H\}$ NMR spectrum (1,2-$C_2H_4Cl_2$ solvent) [δ 50.2, J_{RhP} 190] which is similar to that observed for **16**. Previously reported [Rh(P^{i}Bu$_3$)$_2$($\kappa^2_{Cl,Cl}$-1,2-$C_2H_4Cl_2$)][BAr$^F_4$], **X**, has a slightly higher coupling constant [δ 32.11, J_{RhP} 204] but acts as an example of 1,2-$C_2H_4Cl_2$ coordinating to rhodium. The ^{1}H NMR spectrum was collected in 1,2-$C_2H_4Cl_2$ at 240 K, however little information is obtained because the 1,2-$C_2H_4Cl_2$ ligand is likely to exchange rapidly with the solvent molecules and the protio solvent peak is large. A crystal structure of **20** was also obtained (tetragonal space group $P\,4_1\,2_1\,2$) and displays the 1,2-$C_2H_4Cl_2$ acting as a chelating ligand to the metal centre [Figure 2.51(a)]. The 1,2-$C_2H_4Cl_2$ ligand was slightly disordered over two similar positions but the rest of the cationic structure was well ordered. The anions define an octahedron surrounding the cation [Figure 2.51(b)].

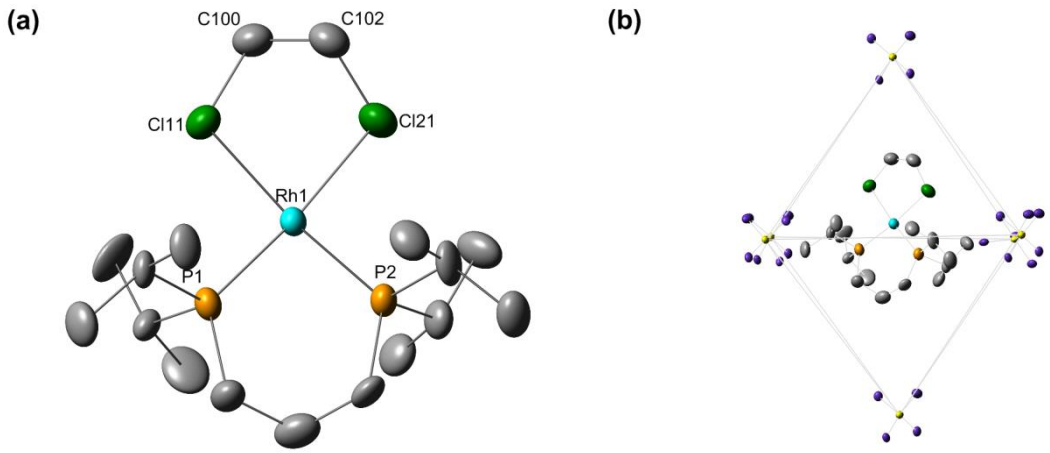

Figure 2.51. Displacement ellipsoid plots (30% probability) of the major disorder component of **20** in the solid-state. Hydrogen atoms omitted for clarity. **(a)** Cationic component. **(b)** Packing diagram; single cation enclosed within a *pseudo*-octahedron of anions, $[BAr^F_4]^-$ anions represented as BC_4 units (aryl groups omitted) for clarity. Selected bond length (Å) and angle (º) data: Rh(1)–P(1), 2.204(4); Rh(1)–P(2), 2.211(4); Rh(1)–Cl(11), 2.459(4); Rh(1)–Cl(21), 2.437(4); P(1)-Rh(1)-P(2), 93.77(15); Cl(11)-Rh(1)-Cl(21), 81.80(6).

The Rh–Cl bond lengths are entirely consistent with the similar structure **X** [Rh–Cl ring: **20** 2.437(4)-2.459(4) Å, **X** 2.4345(14)-2.458(9) Å].[34] A square planar geometry is adopted although the P-Rh-P bite angle is larger than the Cl-Rh-Cl angle indicative of the respective lengths of the ligand backbones. The Rh–P bond lengths [2.204(4) Å & 2.211(4) Å] are shorter than those observed in the solid-state structures of **15** [2.310(3) Å - 2.321(3) Å] or **19** [2.2637(7) Å & 2.2746(7) Å] a result of the weak *trans* influence of weakly coordinating 1,2-$C_2H_4Cl_2$.

The formation of solvent bound complexes **16** and **20**, without observation of **19**, indicates the relative instability of $[BAr^F_4]^-$ coordinated complex **19**. It is noteworthy that other stable η^6-arene complexes of this metal-phosphine fragment can be prepared, such as $[Rh(^iPr_2PCH_2CH_2CH_2P^iPr_2)(\eta^6\text{-}C_6H_5F)][BAr^F_4]$, **IX.**[44] Therefore it appears that a steric clash between the ^{i}Pr substituents and the bulky $[BAr^F_4]^-$ anion lessens the ability of the anion to coordinate relative to the smaller chlorinated solvent molecules.

2.7. Hydrogenation of $[Rh\{(O^iPr_2)PCH_2CH_2P(O^iPr_2)\}(\eta^2\eta^2\text{-NBD})][BAr^F{}_4]$

2.7.i. Synthesis of $[Rh\{(O^iPr_2)PCH_2CH_2P(O^iPr_2)\}(\eta^2\eta^2\text{-NBD})][BAr^F{}_4]$

The phosphite $(O^iPr_2)PCH_2CH_2P(O^iPr_2)$ is isosteric with phosphine $^iBu_2PCH_2CH_2P^iBu_2$ and so allows a comparison of electronic effects with little steric change. A phosphite should be less electron donating than a phosphine (and is a better π acceptor into its P-O σ* orbitals) so that a complexed metal may form tighter interactions with other coordinated ligands. Fryzuk and co-workers have previously used $(O^iPr_2)PCH_2CH_2P(O^iPr_2)$ in a variety of complexes, they also report the synthesis of the ligand.[101-105] However, there are no previously reported crystal structures of metals coordinated with $(O^iPr_2)PCH_2CH_2P(O^iPr_2)$ on the CSD.[106] Structures including related phosphite ligands, coordinated to Pt(II) complexes have been reported.[107]

$[Rh\{(O^iPr_2)PCH_2CH_2P(O^iPr_2)\}(\eta^2\eta^2\text{-NBD})][BAr^F{}_4]$, **21**, was formed by the solvation of $[(NBD)RhCl]_2$ with $(O^iPr_2)PCH_2CH_2P(O^iPr_2)$ in C_6H_5F and addition of $Na[BAr^F{}_4]$ [Scheme 2.36]. Recrystallisation can be achieved from CH_2Cl_2/pentane, an orange oily product forms initially but crystals slowly form from this oil. *N.B.* this synthetic route is not as effective as it was for **1** because **21** does not precipitate directly out of C_6H_5F.

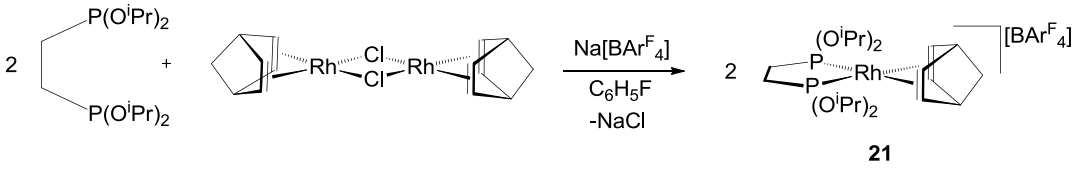

21

Scheme 2.36. Synthesis of **21.**

The ^1H NMR (CD_2Cl_2) spectrum of **21** shows typical resonances for coordinated NBD [δ 1.88, 4.17, 5.91] similar to those in **13** but slightly downfield of the resonances found in isostructural **1**. The (O^iPr) CH_3 groups are observed in the ^1H NMR spectrum as two sets of doublets [δ 1.29, 1.33] indicative of a diastereomeric relationship. The O^iPr methine resonance is located downfield at δ 4.42. The $^{31}P\{^1H\}$ NMR displays a doublet at a high chemical shift [δ 167.3, J_{RhP} 217] with a much larger J_{RhP} coupling constant than that observed in **1**. The chemical shift is consistent with a phosphite complex [102, 103, 105] in which the phosphorus atoms are more electron deficient than in a phosphine.

A crystal structure of **21** was obtained and refinement revealed a cation which is surrounded by the typical *pseudo*-octahedron of $[BAr^F_4]^-$ anions [Figure 2.52(b)]. The structure, which was solved in the space group *C* 2/c, was disordered. The rhodium sits on a symmetry axis and only half the molecule was modelled due to symmetry equivalence. The NBD ligand was disordered over the symmetry axis and is therefore equally disordered over two sites in close proximity to each other. Due to the overlapping nature of this disorder the bond lengths of the NBD fragment are not reliable. The phosphite ligand is also disordered. An approximate structure is shown in Figure 2.52, the geometry is consistent with the structure of isosteric **1**.

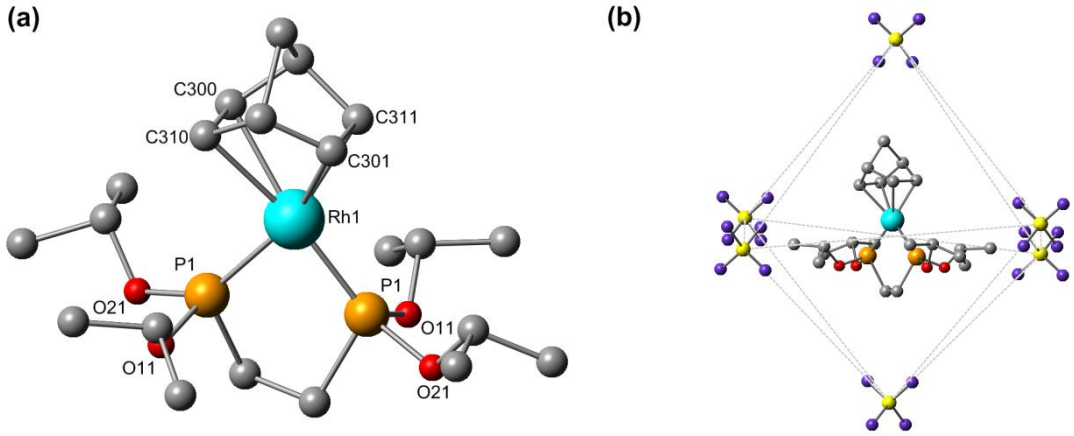

Figure 2.52. (a) Ball and stick diagram of the approximate solid-state structure of the major disorder cationic component of **21**. Hydrogen atoms omitted **(b)** Approximate packing diagram of **21**; enclosed within a *pseudo*-octahedron of anions, hydrogen atoms omitted and $[BAr^F_4]^-$ anions represented as BC_4 units (aryl groups omitted) for clarity.

2.7.ii. The product of the solid-state hydrogenation of 21

21 was exposed to H_2 (1 atm) in the solid-state and displayed a colour change from orange to yellow, the reaction occurred quickly with 100% hydrogenation within 3 minutes (by NMR spectroscopy analysis after solvation of final products). The final product of hydrogenation was confirmed as $Rh\{(O^iPr)_2PCH_2CH_2P(O^iPr)_2\}\{\eta^6\text{-}C_6H_3(CF_3)_2\}BAr^F_3$, **22**, (analogous to complexes **4**, **14** and **19**) by subsequent solution NMR spectroscopy [Scheme 2.37]. The same reaction occurs in solution (CH_2Cl_2), although **22** is unstable in this solvent and decomposes over ~1 hour to unidentified products.

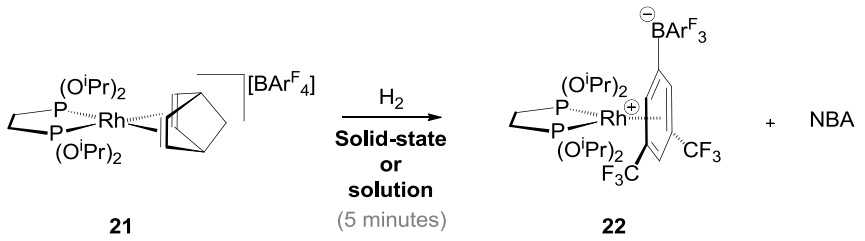

Scheme 2.37. Hydrogenation of **21** to produce **22** in the solid-state or in solution (CH_2Cl_2).

Zwitterionic-**22**, formed in the solid-state, can be recrystallised from pentane at 277 K. A crystal structure was obtained from the yellow crystals produced [Figure 2.53]. The structure was solved in the space group $P\,{-}1$ and two independent molecules were located in the asymmetric unit (similar to the structure of **4**). Both molecules have a very similar structural geometry but a slight difference in coordination geometry of the $[BAr^F_4]^-$ ligand is present [torsion angles: P(2)P(1)Rh(1)C(15), 134.3°; P(101)P(102)Rh(2)C(115), 131.3°]. Two disordered pentane molecules were also located in the crystal lattice.

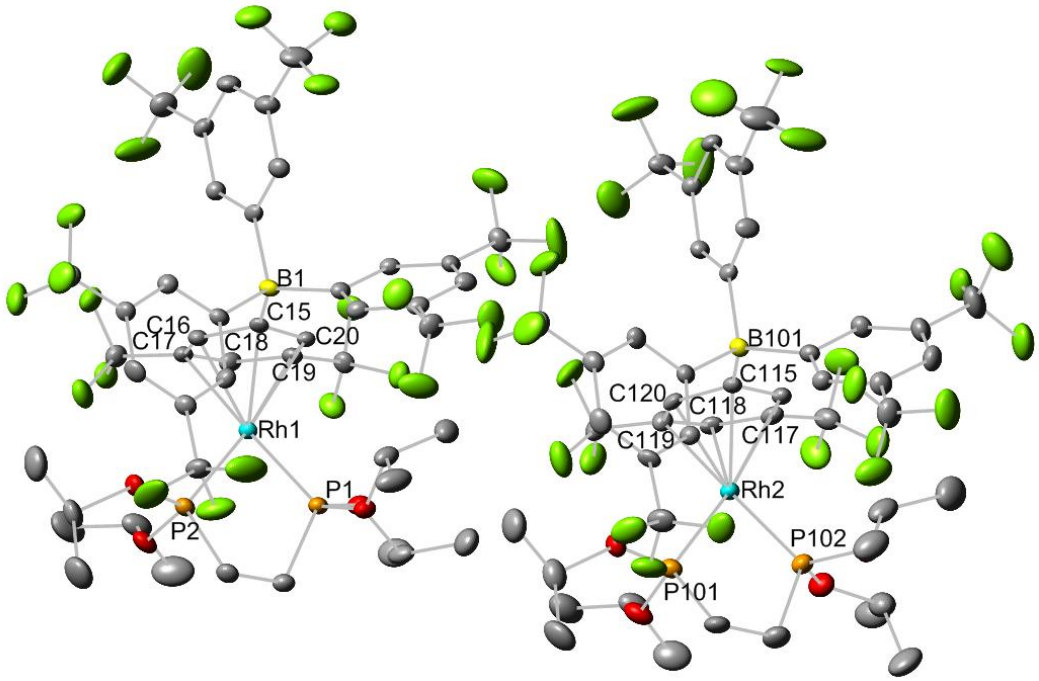

Figure 2.53. Displacement ellipsoid plot (30% probability) of complex **22** in the solid-state. Hydrogen atoms and co-crystallised pentane molecules omitted for clarity. Selected bond length (Å) and angle (º) data: Rh(1)–P(1), 2.2103(14); Rh(1)–P(2), 2.2075(14); Rh(1)–C(15), 2.456(5); Rh(1)–C(17), 2.296(5); P(1)-Rh(1)-P(2), 81.94(5). Second molecule: Rh(2)–P(101), 2.2018(15); Rh(2)–P(102), 2.2058(16); Rh(2)–C(115), 2.453(5); Rh(2)–C(119), 2.283(5); P(101)-Rh(2)-P(102), 82.28(6).

The Rh–$C_{(arene)}$ bond distances range from 2.283(5) Å to 2.456(5) Å with the longest distances to the carbons bonded to the boron centres [2.456(5) Å and 2.453(5) Å]. It is debatable as to whether the arene should be considered to be η^6 or η^5-coordinated in nature.[33] The Rh–C bonding range is similar to that observed for isosteric **4** [2.2799(19) - 2.4470(19) Å] and the distance between the rhodium atom and the plane intersecting the six η^6-arene carbons is also similar [Rh···η^6-plane (Å): **22**, 1.867 & 1.860; **4**, 1.858 & 1.868].

The $^{31}P\{^1H\}$ NMR spectrum of **22** displays a doublet [δ 176.7, J_{RhP} 265] downfield of the signal for **21** with a very high J_{RhP} coupling constant. This indicates a close interaction of the metal with the phosphite because of weak *trans* interactions (a similar increase in J_{RhP} coupling constant is seen for other η^6-arene complexes relative to the respective NBD complexes).

Addition of D_2 to **21** forms **22** and d_4-NBA. ^2H NMR spectroscopy was undertaken upon the products dissolved in C_6H_5F, this revealed two deuterium signals for the *endo* and *exo* positions of NBA.[68, 69] The signals were not of equal size and integration revealed a ~7:3 ratio of *endo* to *exo* signals (this is similar to the solid-state reaction of D_2 with **13** which also showed a greater proportion of deuterium in the *endo* sites of the d_4-NBA released). The ^2H NMR spectrum suggests a roughly equal proportion of (*endo*-1,2 *exo*-4,5)d_4-NBA and (*endo*-1,2,4,5)d_4-NBA are produced by this reaction [Scheme 2.38]. The deuteration experiment was repeated in solution and a similar ratio of peaks was observed with the *endo* signal clearly in majority. It may be possible that an agostically stabilised NBE complex is not very stable with the rhodium-phosphite fragment, or that re-organisation to form an NBE complex is slow in relation to hydrogenation. An independent attempted synthesis of an NBE complex with the phosphite system was unsuccessful.

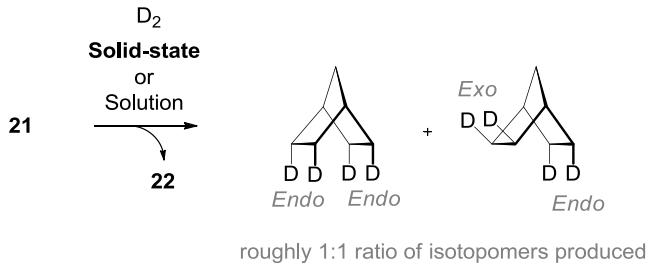

Scheme 2.38. Different isotopomers of d_4-NBA produced by deuteration of **21**.

2.7.iii. Hydrogenation of 21 followed by SSNMR spectroscopy

The reaction of **21** with H_2 in the solid-state to ultimately form **22** was followed by SSNMR spectroscopy [Figure 2.54]. The spectra do not indicate any σ-alkane complex or other intermediates. Rapid conversion from **21** to a presumably amorphous form of **22** was observed (k_1 and k_2 are fast).

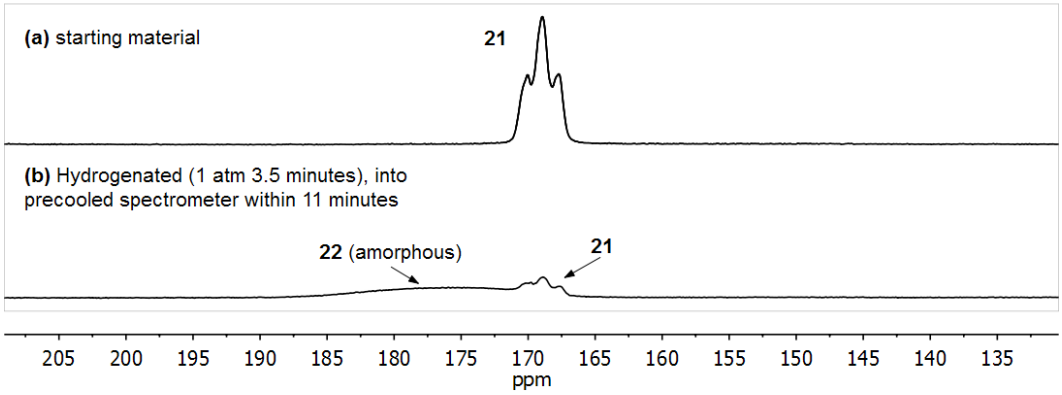

Figure 2.54. SSNMR spectra (at 298 K) of **21 (a)**, and the products (amorphous **22**) formed by hydrogenation in the solid-state **(b)**.

2.7.iv. Conclusions drawn from changing the phosphine ligand

A range of different chelating *bis*-phosphine rhodium diene complexes have been prepared and their reaction with hydrogen in the solid-state monitored. In some cases a σ-alkane complex is observed but only the wider bite angle complex **15** results in the ultimate formation of a Rh(III) hydride species [Scheme 2.39 & Table 2.3].

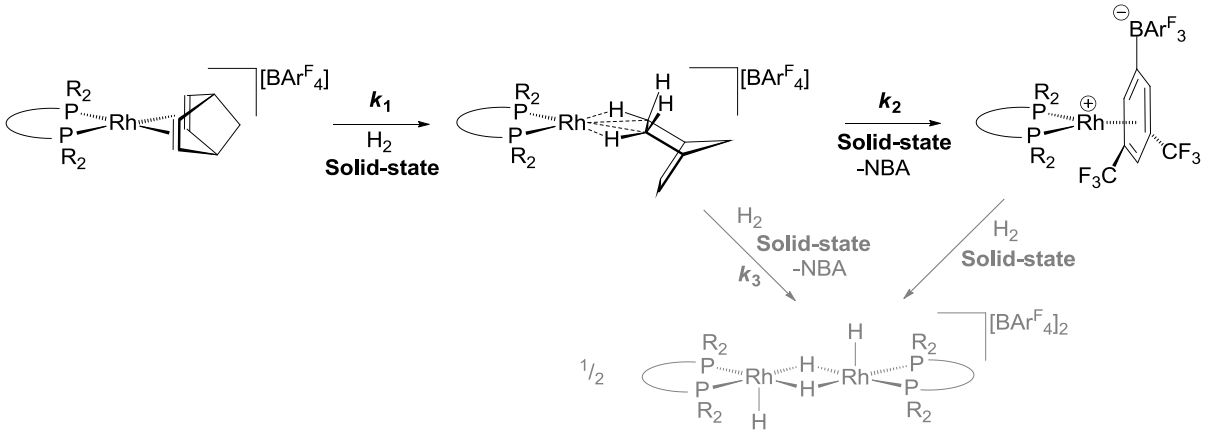

Scheme 2.39. Typical reaction scheme for the solid-state hydrogenation of [Rh(P_2)($\eta^2\eta^2$-NBD)][BAr$^F_4$] with hydrogen. The formation of a dimeric hydride species (shown in grey) after prolonged exposure to hydrogen only occurs for the wider bite angle P_2 ligand (^{i}Pr$_2$PCH$_2$CH$_2$CH$_2$P^{i}Pr$_2$).

Complex	P_2 ligand	k_1 (% hydrogenation in 3 minutes*)	k_2 (or k_3)	Intermediate detected
1	**^{i}Bu$_2$PCH$_2$CH$_2$P^{i}Bu$_2$**	**Fast (100%)**	**k_2 = Slow**	**Yes (5)**
13	**^{i}Pr$_2$PCH$_2$CH$_2$P^{i}Pr$_2$**	**Moderate (86%)**	**k_2 = Moderate**	**Yes (short lived)**
15	**^{i}Pr$_2$PCH$_2$CH$_2$CH$_2$P^{i}Pr$_2$**	**Fast (97%)**	**k_2 = Slow k_3 = Slow (forms hydride species under H_2)**	**Yes (17)**
21	(O^iPr)$_2$PCH$_2$CH$_2$P(O^iPr)	Fast (100%)	**k_2** =Fast	No

Table 2.3. Comparison of the rates of hydrogenation of [Rh(P_2)($\eta^2\eta^2$-NBD)][BAr$^F_4$] (P_2 = *bis*-phosphine), the formation of σ-alkane complex intermediates and rates of intermediate decomposition by reaction with the anion or H_2.

Whilst solid-state reorganisation effects are likely to be influential upon the longevity of the σ-alkane complexes, it is also possible that a more favourable interaction of the [BAr$^F_4$]$^-$ anion with the {RhP_2} fragment in the subsequent anion bound complex (which forms upon loss of alkane), may lower the transition state required to displace a σ-alkane fragment (k_2 becomes faster) [Figure 2.55].

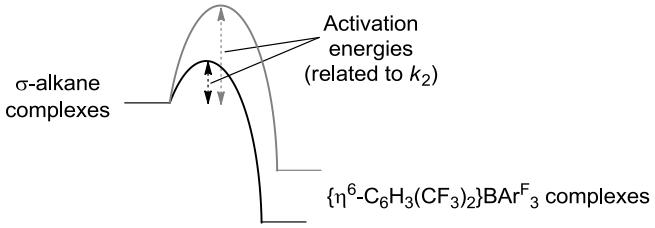

Figure 2.55. Proposed hypothesis relating the stability of the final η^6-anion bound complex with the transition state associated with the release of σ-alkane ligand.

Bulkier phosphine ligands, such as $^{i}Pr_2PCH_2CH_2CH_2P^{i}Pr_2$, may result in a less favourable interaction with the $[BAr^{F}_4]^-$ anion and therefore a higher energy route to loss of alkane. However, increasing the steric bulk of a phosphine by increasing the bite angle results in a greater possibility of forming Rh(III) hydride complexes – allowing an alternative decomposition pathway for loss of the σ-alkane ligand.

Analysis of the binding strengths of η^6-C_6H_5F (which binds in a similar manner to $[BAr^{F}_4]^-$) to the various $\{RhP_2\}^+$ fragments is undertaken in *Section 5.4*.

2.8. Analysis of crystal packing

A common theme of the solid-state structures of most of the complexes described in this chapter is the packing geometry which arranges six anions in an octahedron around the cation. This arrangement defines a cavity for the cation to occupy and may be responsible for the cation disorder found in some cases. To a rough approximation the anions $[BAr^{F}_4]^-$ and $[BAr^{Cl}_4]^-$ can be considered to wrap around the surface of a sphere with a radius of roughly 5 Å, this is shown in Figure 2.56 for **1** and **1-[BAr$^{Cl}_4$]** respectively.

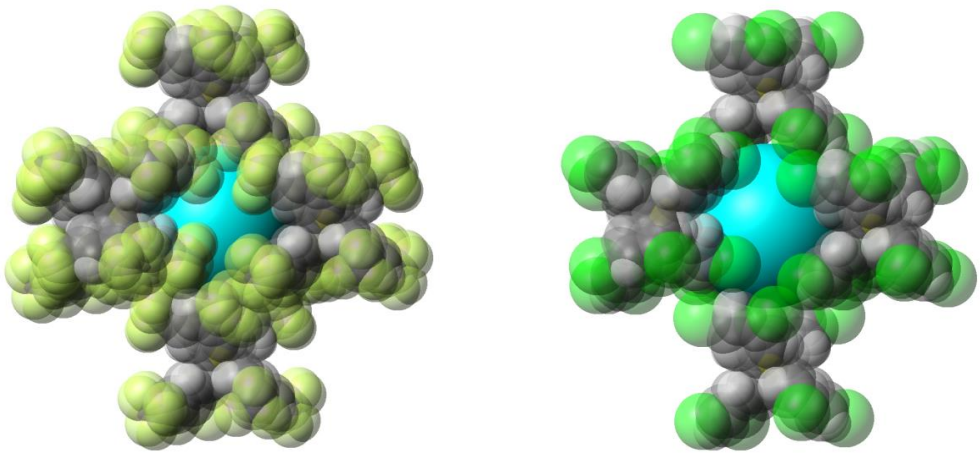

Figure 2.56. Space filling packing diagrams from structures of **1** and **1-[BAr$^{Cl}_4$]** showing an octahedron of (translucent) anions ($[BAr^{F}_4]^-$ and $[BAr^{Cl}_4]^-$) wrapping around a sphere which represents the cavity which a cation may occupy. Cation cavity (radius = 5 Å) (blue) centred upon centroid of six anions.

The size of this pocket appears to be fairly consistent across the structures and a comparison can be made from the average B···B distances which define the octahedron [Table 2.4].

Complex (Ligand, Anion)	Phosphine	Anion Packing arrangement	Average B···B distance (Å)
1 (NBD, $[BAr^{F}_{4}]^{-}$)	$^{i}Bu_2PCH_2CH_2P^{i}Bu_2$	Octahedron	12.86(1)
5 (NBA, $[BAr^{F}_{4}]^{-}$)			12.919(2)
8 (C_6H_8, $[BAr^{F}_{4}]^{-}$)			12.87(1)
11 ($C_4H_4Me_2$, $[BAr^{F}_{4}]^{-}$)			12.97(1)
7-[Al(OC(CF$_3$)$_3$)$_4$] (COD, $[Al\{OC(CF_3)_3\}]^{-}$)			12.86(2)
1-[BAr$^{Cl}_4$] (NBD, $[BAr^{Cl}_{4}]^{-}$)			12.33(1)
21 (NBD, $[BAr^{F}_{4}]^{-}$)	$(O^{i}Pr_2)PCH_2CH_2P(O^{i}Pr_2)$	Octahedron	12.94(1)
13 (NBD, $[BAr^{F}_{4}]^{-}$)	$^{i}Pr_2PCH_2CH_2P^{i}Pr_2$	Gyrobifastigium	11.53(1)
15 (NBD, $[BAr^{F}_{4}]^{-}$)	$^{i}Pr_2PCH_2CH_2CH_2P^{i}Pr_2$	Octahedron	12.69(2)

Table 2.4. Analysis of the crystal packing of solid-state structures of several selected compounds

The B···B distances are slightly smaller for the $[BAr^{Cl}_{4}]^{-}$ anion, probably since Cl is smaller than a CF_3 group, however the reduced bulk of this anion results in a similar size cavity to that formed from $[BAr^{F}_{4}]^{-}$. A much smaller average B···B distance is observed for **13** which exhibits a different packing structure; in this case eight anions pack around the cation. Interestingly, for this arrangement, the whole cation pocket is enclosed by anions except for one exposed face [Figure 2.57], whether this allows an exit route for NBA which shortens the lifetime of a σ-alkane complex in this system is uncertain.

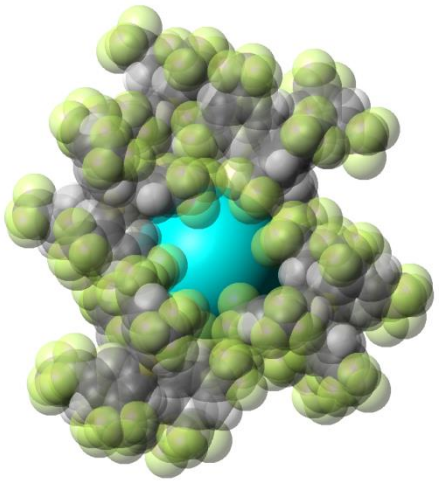

Figure 2.57. Space filling packing diagrams from structures of **13** showing a gyrobifastigium of (translucent) $[BAr^{F}_{4}]^{-}$ anions wrapping around a sphere which represents the cavity which a cation may occupy. Cation cavity (radius = 5 Å) (blue) centred upon centroid of six anions.

All the solid NBD complexes created react with hydrogen which suggests that the crystalline material is somewhat porous. Analysis of the crystal structures (full disorder models) using Crystal Explorer [108, 109] allowed the calculation of the percentage void volume inside these structures [approximate void percentage volume: **1**, 7%; **13**, 16%; **15**, 13%; **21**, 10%; **7-[Al(OC(CF$_3$)$_3$)$_4$]**, 16%; **1-[BAr$^{Cl}_4$]**, 11% (*N.B.* if the minor disorder component found in **1** is ignored then the percentage void volume is calculated at 10%)]. Although no well defined channels are visible, many of the voids appear interconnected. It is therefore imagined that hydrogen can penetrate these interconnected voids and access the metal centres within the crystalline lattice.

2.9. Conclusions

A set of complexes of the format [Rh(P_2)(L_2)][WCA] ($P2$ = chelating phosphine, L = alkene, WCA = weakly coordinating anion) were synthesised and their reactions with hydrogen in solution and the solid-state were investigated.

Reactions of crystalline NBD complexes with hydrogen in the solid-state can lead to SC-SC transitions (**1** to **5** and **15** to **17**) in which case a σ-alkane (NBA) complex is formed. In both cases evidence of an intermediate NBE complex, stabilised by an agostic interaction, is revealed by deuteration studies. The transition of NBD to NBE to NBA requires rotation of the hydrocarbon fragment at each step within the crystal lattice. The crystal packing of [BAr$^F_4$]$^-$ anions in these complexes define an octahedral environment surrounding the cation which may act as a pocket allowing cationic mobility, but also protecting the fragile σ-alkane species produced. In contrast, the σ-alkane complexes were not stable in solution. Analysis of the crystallographically characterised σ-alkane complex **5** reveals the alkane (NBA) to act as a chelating ligand in a Rh(I), 16 electron, square planar complex. Rh⋯C distances [2.480(11) & 2.494(10) Å] are located by X-ray crystallography are consistent with computational calculations, indicating two strong σ-interactions are present. The complex appears stable by SSNMR spectroscopy at 253 K.

The σ-alkane complexes (**5** and **17**) decompose over time to release NBA and form a zwitterionic species in which the [BAr$^F_4$]$^-$ anion coordinates to the metal centre through one of the arene rings (**4** and **19** respectively). Other [BAr$^F_4$]$^-$ complexes (**14** and **22**) have also been produced directly by

hydrogenation of NBD complexes (**13** and **21**). The stability of $[BAr^F_4]^-$ complexes could be related to the steric pressure between the phosphine substituents and the bulky anion. The Rh–$C_{(arene)}$ distances increase upon exchange of ^{i}Bu substituents with ^{i}Pr groups and further increase upon widening of the bite angle. This Rh–$C_{(arene)}$ extension alters the definition of the arene coordination geometry from η^6 to η^5 and finally to η^4. The lifetime of meta-stable σ-alkane complexes may depend on the stability of the final η^6-$[BAr^F_4]^-$ species, since there may be a link between final product stability and energy of the transition state.

Disorder (and modulation in **17**) in the crystalline phase make characterisation of these complexes by X-ray crystallography troublesome. However such problems may be inherent for a system which shows cationic mobility within the solid-state. Such mobility may be necessary to allow SC-SC transitions in which geometrical rearrangements occur.

Highlights of this chapter have been published in Science.[60]

2.10. References

1. J. A. Labinger and J. E. Bercaw, *Nature*, 2002, **417**, 507-514.
2. W. D. Jones, *Inorg. Chem.*, 2005, **44**, 4475-4484.
3. B. A. Arndtsen, R. G. Bergman, T. A. Mobley and T. H. Peterson, *Acc. Chem. Res.*, 1995, **28**, 154-162.
4. R. G. Bergman, *Science*, 1984, **223**, 902-908.
5. J. F. Hartwig, *OrganoTransition Metal Chemistry*, University Science Books, 2010.
6. A. H. Janowicz and R. G. Bergman, *J. Am. Chem. Soc.*, 1982, **104**, 352-354.
7. J. K. Hoyano and W. A. G. Graham, *J. Am. Chem. Soc.*, 1982, **104**, 3723-3725.
8. M. Kanzelberger, B. Singh, M. Czerw, K. Krogh-Jespersen and A. S. Goldman, *J. Am. Chem. Soc.*, 2000, **122**, 11017-11018.
9. R. Ahuja, B. Punji, M. Findlater, C. Supplee, W. Schinski, M. Brookhart and A. S. Goldman, *Nat. Chem.*, 2011, **3**, 167-171.
10. A. S. Goldman, A. H. Roy, Z. Huang, R. Ahuja, W. Schinski and M. Brookhart, *Science*, 2006, **312**, 257-261.
11. M. Gupta, C. Hagen, W. C. Kaska, R. E. Cramer and C. M. Jensen, *J. Am. Chem. Soc.*, 1997, **119**, 840-841.
12. R. R. Schrock, *Chem. Commun.*, 2005, 2773-2777.
13. X.-Z. Sun, D. C. Grills, S. M. Nikiforov, M. Poliakoff and M. W. George, *J. Am. Chem. Soc.*, 1997, **119**, 7521-7525.
14. C. E. Brown, Y. Ishikawa, P. A. Hackett and D. M. Rayner, *J. Am. Chem. Soc.*, 1990, **112**, 2530-2536.
15. J. M. Morse, G. H. Parker and T. J. Burkey, *Organometallics*, 1989, **8**, 2471-2474.
16. T. Jiao, G.-L. Leu, G. J. Farrell and T. J. Burkey, *J. Am. Chem. Soc.*, 2001, **123**, 4960-4965.
17. D. R. Evans, T. Drovetskaya, R. Bau, C. A. Reed and P. D. W. Boyd, *J. Am. Chem. Soc.*, 1997, **119**, 3633-3634.
18. I. Castro-Rodriguez, H. Nakai, P. Gantzel, L. N. Zakharov, A. L. Rheingold and K. Meyer, *J. Am. Chem. Soc.*, 2003, **125**, 15734-15735.
19. E. D. Bloch, W. L. Queen, R. Krishna, J. M. Zadrozny, C. M. Brown and J. R. Long, *Science*, 2012, **335**, 1606-1610.
20. M. D. Millard, Isolation of Four-Coordinate Iridium(I) Monohydrides and the X-ray Crystal Structure of a Cobalt Tris-Isocyanide Alkane sigma-Complex, PhD Thesis, University of San Diego, 2013.
21. W. H. Bernskoetter, C. K. Schauer, K. I. Goldberg and M. Brookhart, *Science*, 2009, **326**, 553-556.
22. S. Geftakis and G. E. Ball, *J. Am. Chem. Soc.*, 1998, **120**, 9953-9954.
23. J. R. Shapley, R. R. Schrock and J. A. Osborn, *J. Am. Chem. Soc.*, 1969, **91**, 2816-2817.
24. R. H. Crabtree, *The Organometallic Chemistry Of The Transition Metals*, 4 edn., John Wiley & Sons, Inc., 2005.
25. J. A. Osborn and R. R. Schrock, *J. Am. Chem. Soc.*, 1971, **93**, 2397-2407.

26. S. A. Macgregor, O. Eisenstein, M. K. Whittlesey and R. N. Perutz, *J. Chem. Soc. Dalton Trans.*, 1998, 291-300.
27. Z. Huang, P. S. White and M. Brookhart, *Nature*, 2010, **465**, 598-601.
28. O. V. Zenkina, E. C. Keske, R. Wang and C. M. Crudden, *Angew. Chem. Int. Ed.*, 2011, **50**, 8100-8104.
29. G. J. Kubas, *Metal Dihydrogen and σ-Bond Complexes - Structure, Theory, and Reactivity*, Kluwer Academic / Plenum Publishers, 2001.
30. R. H. Crabtree, *Angew. Chem. Int. Ed.*, 1993, **32**, 789-805.
31. F. Wang, M. J. Brunger and D. A. Winkler, *J. Phys. Chem. Solids*, 2004, **65**, 2041-2054.
32. A. D. Wilson, A. J. M. Miller, D. L. DuBois, J. A. Labinger and J. E. Bercaw, *Inorg. Chem.*, 2010, **49**, 3918-3926.
33. A. Woolf, A. B. Chaplin, J. E. McGrady, M. A. M. Alibadi, N. Rees, S. Draper, F. Murphy and A. S. Weller, *Eur. J. Inorg. Chem.*, 2011, 1614-1625.
34. T. M. Douglas, A. B. Chaplin and A. S. Weller, *Organometallics*, 2008, **27**, 2918-2921.
35. N. S. Townsend, A. B. Chaplin, M. A. Naser, A. L. Thompson, N. H. Rees, S. A. Macgregor and A. S. Weller, *Chem. Eur. J.*, 2010, **16**, 8376-8389.
36. S. D. Pike, Exploring New Hydroacylation Catlaysts Based on Rhodium Phosphine Systems, MChem Thesis, University of Oxford, 2010.
37. X.-L. Luo, G. J. Kubas, C. J. Burns, R. J. Butcher and J. C. Bryan, *Inorg. Chem.*, 1995, **34**, 6538-6545.
38. T. M. Douglas, Chemistry of Cationic Rhodium Alkyl Phosphine Complexes, DPhil Thesis, University of Oxford, 2009.
39. G. J. Kubas, R. R. Ryan and C. J. Unkefer, *J. Am. Chem. Soc.*, 1987, **109**, 8113-8115.
40. X.-L. Luo, G. J. Kubas, C. J. Burns, J. C. Bryan and C. J. Unkefer, *J. Am. Chem. Soc.*, 1995, **117**, 1159-1160.
41. Z. Anijang, J. Qiongzhong and Z. Liangfu, *Bopuxue Zazhi*, 1991, **8**, 215.
42. R. J. Pawley, G. L. Moxham, R. Dallanegra, A. B. Chaplin, S. K. Brayshaw, A. S. Weller and M. C. Willis, *Organometallics*, 2010, **29**, 1717-1728.
43. J. Benet-Buchholz, T. Haumann and R. Boese, *Chem. Commun.*, 1998, 2003-2004.
44. I. Pernik, J. F. Hooper, A. B. Chaplin, A. S. Weller and M. C. Willis, *ACS Catalysis*, 2012, **2**, 2779-2786.
45. R. Dallanegra, A. P. M. Robertson, A. B. Chaplin, I. Manners and A. S. Weller, *Chem. Commun.*, 2011, **47**, 3763-3765.
46. T. M. Douglas, A. B. Chaplin, A. S. Weller, X. Yang and M. B. Hall, *J. Am. Chem. Soc.*, 2009, **131**, 15440-15456.
47. S. Welsch, M. Bodensteiner, M. Dušek, M. Sierka and M. Scheer, *Chem. Eur. J.*, 2010, **16**, 13041-13045.
48. J. M. Slattery, A. Higelin, T. Bayer and I. Krossing, *Angew. Chem. Int. Ed.*, 2010, **49**, 3228-3231.
49. T. M. Douglas, E. Molinos, S. K. Brayshaw and A. S. Weller, *Organometallics*, 2006, **26**, 463-465.
50. S. v. Moret, R. Dallanegra, A. B. Chaplin, T. M. Douglas, R. M. Hiney and A. S. Weller, *Inorg. Chim. Acta*, 2010, **363**, 574-580.
51. A. Spek, *J. Appl. Crystallogr.*, 2003, **36**, 7-13.
52. J. Powell, A. Lough and T. Saeed, *J. Chem. Soc. Dalton Trans.*, 1997, 4137-4138.
53. P. Marcazzan, B. O. Patrick and B. R. James, *Organometallics*, 2003, **22**, 1177-1179.
54. N. Xu, L. E. Goodrich, N. Lehnert, D. R. Powell and G. B. Richter-Addo, *Angew. Chem. Int. Ed.*, 2013, **52**, 3896-3900.
55. A. Martin, L. Martin, L. S. Anthony and K. Gerard van, *Nature*, 2000, **406**, 970-974.
56. C. G. Bezzu, M. Helliwell, J. E. Warren, D. R. Allan and N. B. McKeown, *Science*, 2010, **327**, 1627-1630.
57. W. Baratta, C. Mealli, E. Herdtweck, A. Ienco, S. A. Mason and P. Rigo, *J. Am. Chem. Soc.*, 2004, **126**, 5549-5562.
58. L. Pauling, *The Nature of the Chemical Bond*, 3rd edn., Cornell University Press, 1960.
59. S. Alvarez, *Dalton Trans.*, 2013, **42**, 8617-8636.
60. S. D. Pike, A. L. Thompson, A. s. G. Algarra, D. C. Apperley, S. A. Macgregor and A. S. Weller, *Science*, 2012, **337**, 1648-1651.
61. P. M. Morse, M. D. Spencer, S. R. Wilson and G. S. Girolami, *Organometallics*, 1994, **13**, 1646-1655.
62. A. A. Gonzalez, K. Zhang, S. P. Nolan, R. Lopez de la Vega, S. L. Mukerjee, C. D. Hoff and G. J. Kubas, *Organometallics*, 1988, **7**, 2429-2435.
63. M. D. Walter, R. A. Moorhouse, S. A. Urbin, P. S. White and M. Brookhart, *J. Am. Chem. Soc.*, 2009, **131**, 9055-9069.
64. R. D. Young, A. F. Hill, W. Hillier and G. E. Ball, *J. Am. Chem. Soc.*, 2011, **133**, 13806-13809.
65. J. A. Calladine, S. B. Duckett, M. W. George, S. L. Matthews, R. N. Perutz, O. Torres and Q. V. Khuong, *J. Am. Chem. Soc.*, 2011, **133**, 2303-2310.
66. S. B. Duckett, M. W. George, O. S. Jina, S. L. Matthews, R. N. Perutz, X.-Z. Sun and K. Q. Vuong, *Chem. Commun.*, 2009, 1401-1403.
67. A. B. Chaplin, A. I. Poblador-Bahamonde, H. A. Sparkes, J. A. K. Howard, S. A. Macgregor and A. S. Weller, *Chem. Commun.*, 2009, 244-246.
68. R. J. Abraham and J. Fisher, *Magn. Reson. Chem.*, 1985, **23**, 856-861.
69. B. Nguyen and J. M. Brown, *Adv. Synth. Catal.*, 2009, **351**, 1333-1343.
70. R. R. Schrock and J. A. Osborn, *J. Am. Chem. Soc.*, 1976, **98**, 4450-4455.
71. J. A. Iggo, *NMR Spectroscopy in Inorganic Chemistry*, Oxford University Press, 1999.
72. P. H. M. Budzelaar, N. N. P. Moonen, R. Gelder, J. M. M. Smits and A. W. Gal, *Eur. J. Inorg. Chem.*, 2000, 753-769.
73. M. Pasquali, C. Floriani, A. Gaetani-Manfredotti and A. Chiesi-Villa, *J. Am. Chem. Soc.*, 1978, **100**, 4918-4919.
74. J. Rohlicek and M. Husak, *J. Appl. Crystallogr.*, 2007, **40**, 600-601.

75. http://sdbs.db.aist.go.jp, National Institute of Advanced Industrial Science and Technology, 2014.
76. A. Rifat, M. F. Mahon and A. S. Weller, *J. Organomet. Chem.*, 2003, **667**, 1-4.
77. P. H. M. Budzelaar, N. N. P. Moonen, R. de Gelder, J. M. M. Smits and A. W. Gal, *Chem. Eur. J.*, 2000, **6**, 2740-2747.
78. J. A. S. Howell, M. G. Palin, M.-C. Tirvengadum, D. Cunningham, P. McArdle, Z. Goldschmidt and H. E. Gottlieb, *J. Organomet. Chem.*, 1991, **413**, 269-286.
79. M. Crocker, M. Green, C. E. Morton, K. R. Nagle and A. G. Orpen, *J. Chem. Soc. Dalton Trans.*, 1985, 2145-2153.
80. M. Bosch, M. Laubender, B. Weberndörfer and H. Werner, *Chem. Eur. J.*, 1999, **5**, 2203-2211.
81. I. Krossing and I. Raabe, *Angew. Chem. Int. Ed.*, 2004, **43**, 2066-2090.
82. A. Rifat, N. J. Patmore, M. F. Mahon and A. S. Weller, *Organometallics*, 2002, **21**, 2856-2865.
83. B. Guzel, M. A. Omary, J. P. Fackler Jr and A. Akgerman, *Inorg. Chim. Acta*, 2001, **325**, 45-50.
84. V. Ryzhov, C.-N. Yang, S. J. Klippenstein and R. C. Dunbar, *Int. J. Mass spectrom.*, 1999, **185-187**, 913-923.
85. N. Hao and M. J. McGlinchey, *J. Organomet. Chem.*, 1978, **161**, 381-390.
86. J. J. Barker, A. G. Orpen, A. J. Seeley and P. L. Timms, *J. Chem. Soc. Dalton Trans.*, 1993, 3097-3102.
87. I. Bach, K.-R. Pörschke, R. Goddard, C. Kopiske, C. Krüger, A. Rufińska and K. Seevogel, *Organometallics*, 1996, **15**, 4959-4966.
88. I. Krossing, *Chem. Eur. J.*, 2001, **7**, 490-502.
89. A. B. Chaplin and A. S. Weller, *Eur. J. Inorg. Chem.*, 2010, 5124-5128.
90. I. R. Butler, W. R. Cullen, B. E. Mann and C. R. Nurse, *J. Organomet. Chem.*, 1985, **280**, c47-c50.
91. M. Scott, Exploring the synthesis of transition metal alkane complexes, MChem Thesis, University of Oxford, 2013.
92. R. Copley, BCA/CCG Intensive Training School in X-ray Structure Analysis, Durham, 2013.
93. T. Gutmann, I. del Rosal, B. Chaudret, R. Poteau, H.-H. Limbach and G. Buntkowsky, *Chem. Phys. Chem.*, 2013, **14**, 3026-3033.
94. M. A. Coutant, J. R. Sachleben and P. K. Dutta, *The Journal of Physical Chemistry B*, 2003, **107**, 11000-11007.
95. S. Macholl, J. Matthes, H.-H. Limbach, S. Sabo-Etienne, B. Chaudret and G. Buntkowsky, *Solid State Nucl. Magn. Reson.*, 2009, **36**, 137-143.
96. J. K. M. Sanders and B. K. Hunter, *Modern NMR Spectroscopy*, Oxford University Press, 1989.
97. M. D. Walter, P. S. White, C. K. Schauer and M. Brookhart, *J. Am. Chem. Soc.*, 2013, **135**, 15933-15947.
98. W. D. Jones, *Acc. Chem. Res.*, 2003, **36**, 140-146.
99. M. Gandelman, L. Konstantinovski, H. Rozenberg and D. Milstein, *Chem. Eur. J.*, 2003, **9**, 2595-2602.
100. G. L. Moxham, S. K. Brayshaw and A. S. Weller, *Dalton Trans.*, 2007, 1759-1761.
101. R. B. King and W. M. Rhee, *Inorg. Chem.*, 1978, **17**, 2961-2963.
102. M. D. Fryzuk, *Can. J. Chem.*, 1983, **61**, 1347-1351.
103. M. D. Fryzuk, *Organometallics*, 1982, **1**, 408-409.
104. M. D. Fryzuk, T. Jones and F. W. B. Einstein, *J. Chem. Soc., Chem. Commun.*, 1984, 1556-1558.
105. M. D. Fryzuk and W. E. Piers, *Organometallics*, 1990, **9**, 986-998.
106. http://webcsd.ccdc.cam.ac.uk/, 2014.
107. L. Dahlenburg, C. Becker, J. Höck and S. Mertel, *J. Organomet. Chem.*, 1998, **564**, 155-166.
108. S. K. Wolff, D. J. Grimwood, J. J. McKinnon, M. J. Turner, D. Jayatilaka and M. A. Spackman, *Crystal Explorer (v3.1)*, (2012) University of Western Australia.
109. M. J. Turner, J. J. McKinnon, D. Jayatilaka and M. A. Spackman, *CrystEngComm*, 2011, **13**, 1804-1813.

CHAPTER 3
C-X ACTIVATION OF ARYL HALIDES

3.1. Introduction

3.1.i. C–X activation of aryl halides in solution

The development of transition metal catalysed C–C coupling reactions has allowed for many new synthetic pathways for organic and pharmaceutical products.[1-4] The wide-scale application of these processes was recognised by the award of the Nobel Prize in Chemistry in 2010 to Heck, Negishi and Suzuki for their contributions to this field.[5-7] C–X (X = halogen) activation of aryl halides by oxidative addition is a key step in many coupling reactions [Scheme 3.1]. Relatively expensive aryl bromides or iodides are typically used in these processes, since C–X activation occurs readily [typical bond enthalpies (kJ/mol): C–I, 238; C–Br, 276; C–Cl, 338; C–F, 484].[8] Recent research however is focusing upon extending the scope of reactions to the (often cheaper) more readily available aryl chlorides.[1, 9, 10] C–X activation of aryl fluorides is rare, the strong C–F bond being difficult to activate, however notable examples exist.[11-15]

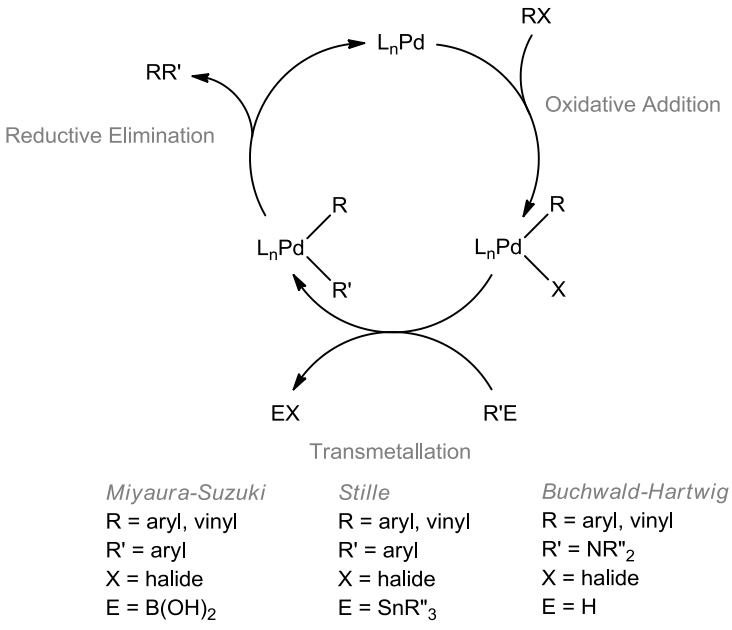

Scheme 3.1. C–C cross coupling reaction mechanism.

Typically palladium is the metal used in cross coupling reactions, although the use of rhodium and iridium complexes has been reported.[16-18] There are fewer examples of the C–X activation of aryl halides with group 9 metals compared to group 10 complexes.[19-21] The mechanism of C–X activation of aryl halides may be dependent on the particular aryl halide, but one-coordinate Pd(0) species have been postulated as reactive precursors to many transformations of this kind.[22] These species are formally 12 electron complexes, which become 14 electron Pd(II) species after oxidative addition of an aryl halide. Computational studies upon palladium phosphine complexes suggest initial coordination of the aryl halide may occur to an active metal species, in the form of an η^2- complex, this is then able to undergo oxidative cleavage [Scheme 3.2].[22]

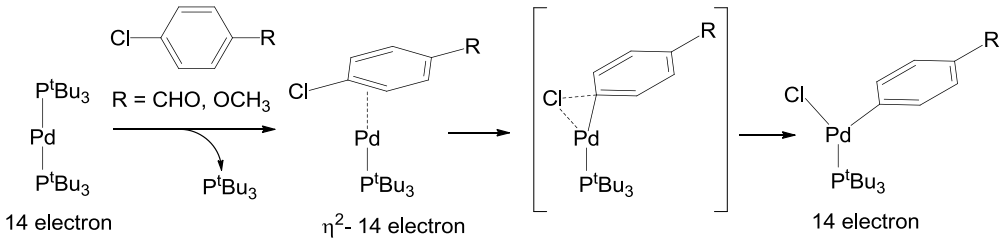

Scheme 3.2. Computationally proposed mechanism of C–Cl activation of chlorobenzene to a low coordinate Pd species.

3.1.ii. C–X activation of aryl halides using Rh*P*$_2$ complexes (*P* = phosphine)

Two-coordinate Rh(I) fragments such as $[RhP_2]^+$ (P = phosphine) are also formally 12 electron species capable of oxidative addition of aryl halides. Coordination of the aryl halide prior to oxidative cleavage has been reported in the form of an η^6-complex in this case [Scheme 3.3].[23]

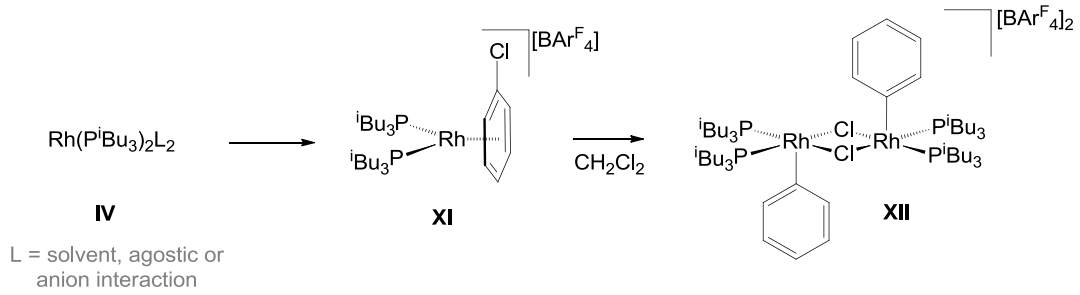

Scheme 3.3. Oxidative cleavage *via* an η^6-arene intermediate complex.

A study upon the C–X activation of aryl-halides with *ortho*-substituents to {Rh(P^iBu_3)$_2$} fragments has been reported by Weller and co-workers.[24] They show that after C–X activation a bulky aryl group can block dimerisation of the C–X activation products (which is observed for smaller aryl groups, see Scheme 3.3). The monomeric C–X activation species (**XIII**) contains a vacant site which is likely to be stabilised by an agostic interaction from an ^{i}Bu group. Subsequently C–H activation of the agostically coordinated C–H group can occur along with elimination of aryl–H by a σ-CAM mechanism.[25] The resulting product is a cyclometallated species which can dimerise (**XIV**) [Scheme 3.4].

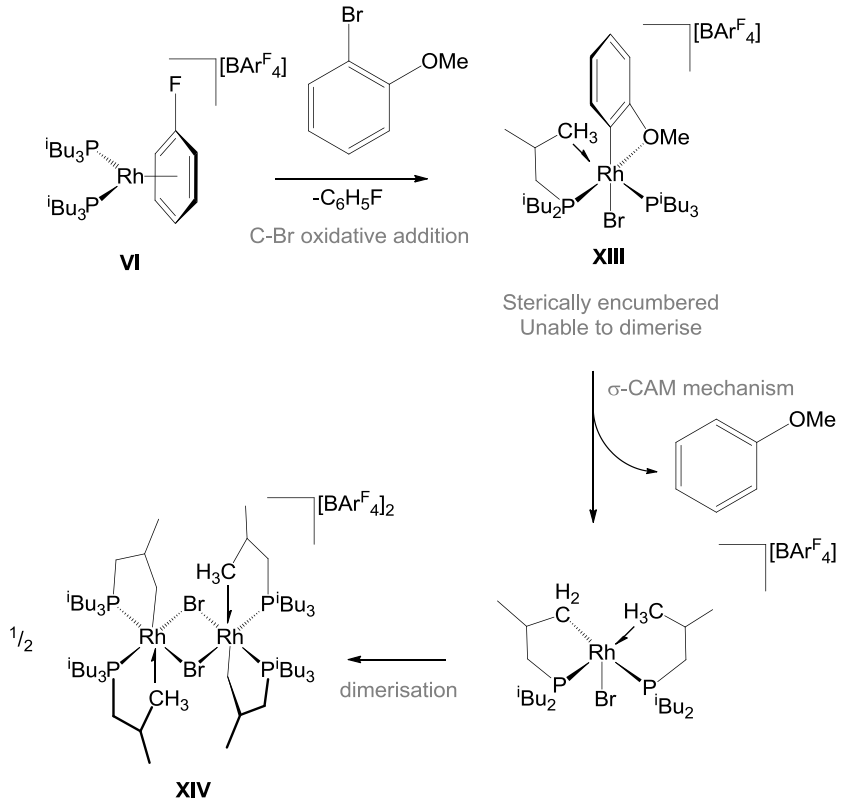

Scheme 3.4. Oxidative addition and subsequent cyclometallation previously reported.

The displayed lack of "ligand innocence" in the monodentate P^iBu_3 system would be detrimental in a catalytic process. Ideally a catalytic system should be resistant to side reactions which form by-products and deactivate the catalyst.

3.1.iii. Oxidative cleavage processes in the solid-state.

Oxidative cleavage processes using organometallic species in the solid-state is a relatively unexplored area of research with activation of dihydrogen probably the most commonly reported example.[26-29] Isolated examples of C–H,[28, 30] Si–H,[28] H–Cl,[31] Cl–Cl [30] and C–C [32] activation within the solid-state have also been reported.[29] Although C–X activation in the solid-state is very rare, van der Boom and co-workers have presented the C–Br activation of 4-(bromo-phenyl)-pyridin-4-yl-diazene by a platinum complex in solution and in the solid-state.[33] In solution, a first order kinetic profile is observed as expected for an intramolecular process [k = ~6.3 x 10^{-5} s^{-1} at 313 K], consistent with a rate determining step (C–X oxidative cleavage) occurring after initial coordination of the bromo-arene [Scheme 3.5]. The solid-state reaction reaches completion over 11 days at 347 K.

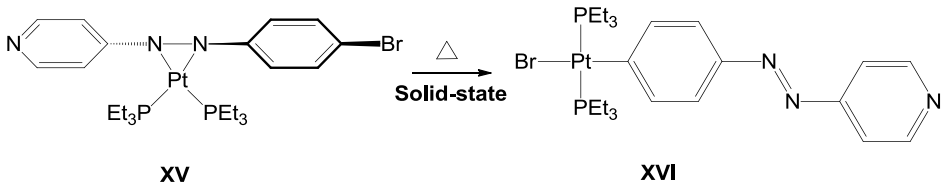

XV XVI

Scheme 3.5. C–Br activation in the solid-state.

Zhao recently reported an IR spectroscopic study upon the C–Cl activation of CH_3Cl by TiO_n and ZrO_n (n = 1 or 2) molecules in frozen argon matrices.[34] However, to the best of our knowledge, there are no previous examples of well defined chloro-arene activation in the solid-state. There are, however, heterogeneous cross coupling reactions that have been reported with metal organic frameworks that contain palladium complexes or self supported palladium catalysts, which must presumably operate through oxidative addition pathways.[11, 35]

3.1.iv. $[BAr^{Cl}_4]^-$ as a weakly coordinating anion.

The anion $[B(3,5\text{-}C_6H_3Cl_2)_4]^-$ $\{[BAr^{Cl}_4]^-\}$ has been previously reported as a weakly coordinating anion, suitable for partnering reactive cationic organometallic species [Figure 3.1].[36-38] Its utility is increased by desirable solubility properties and a lack of (CF_3) disorder in the solid-state (which is common for $[BAr^{F}_4]^-$). Recent reports have utilised $[BAr^{Cl}_4]^-$ as a counterion enabling the production of diffraction quality crystals in cases where $[BAr^{F}_4]^-$ was unsuitable for forming crystalline material.[39, 40]

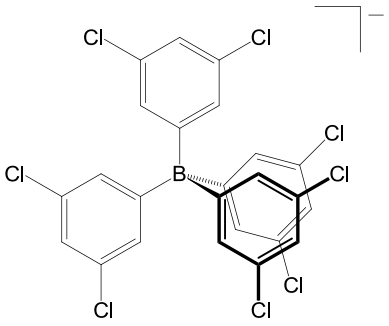

Figure 3.1. The $[BAr^{Cl}{}_4]^-$ anion.

$[BAr^{Cl}{}_4]^-$ has been previously observed to coordinate to a low valent rhodium(III) centre through the π system (η^6) of one arene ring (**XVIII**).[36] The anion will displace a weakly bound η^6-C_6H_5F ligand to form a zwitterionic complex when dissolved in CH_2Cl_2, whilst in C_6H_5F solution an equilibrium is observed in favour of the zwitterion [Scheme 3.6]. This demonstrates that $[BAr^{Cl}{}_4]^-$ is a stronger η^6-ligand for accessible metal centres than both $[BAr^{F}{}_4]^-$ and C_6H_5F. Since the coordinating ability of an arene is dependent upon its substituent groups, with electron withdrawing groups disfavouring coordination and anionic electron donating groups favouring coordination, it can be assumed a single fluorine has a greater destabilising effect than the combined substituents upon $[BAr^{Cl}{}_4]^-$.[41] *The binding affinities of arene ligands will be further discussed in Chapter 5*.

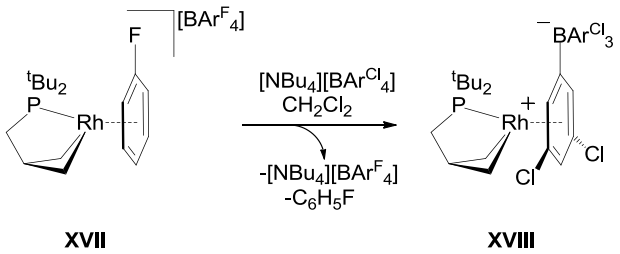

Scheme 3.6. Displacement of η^6-C_6H_5F ligand by $[BAr^{Cl}{}_4]^-$ in CH_2Cl_2 solvent. If dissolved in C_6H_5F an equilibrium between the two species is observed.

When η^6-coordination is not possible, *i.e.* in formally 14 or 16 electron complexes, $[BAr^{Cl}{}_4]^-$ is shown to act in a non-coordinating manner tolerating other weakly bound "ligands" such as agostic interactions (**XIX**) or truly vacant sites (**XX**) [Figure 3.2].[36, 37] To the best of our knowledge C–Cl activation of $[BAr^{Cl}{}_4]^-$ has not been reported before.

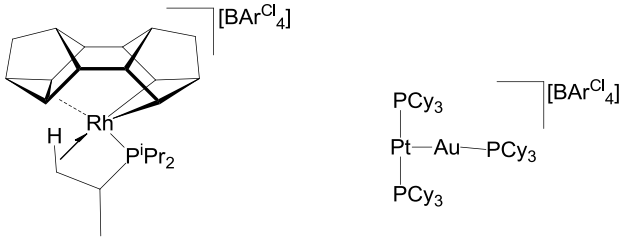

XIX **XX**

Figure 3.2. Low coordinate cations, which do not show covalent interactions to the $[BAr^{Cl}_4]^-$ anion in their solid-state structures.

3.2. C–Cl activation of the $[BAr^{Cl}_4]^-$ anion in solution and the solid-state

3.2.i. Synthesis and characterisation of precursor complexes

The complex $[Rh(^iBu_2PCH_2CH_2P^iBu_2)(\eta^2\eta^2\text{-NBD})][BAr^{Cl}_4]$, **1-[BAr$^{Cl}_4$]**, was synthesised in a similar fashion to **1** (*see Section 2.2.i*) with the exchange of $Na[BAr^{Cl}_4]$ for $Na[BAr^{F}_4]$ in the synthesis [Scheme 3.7].

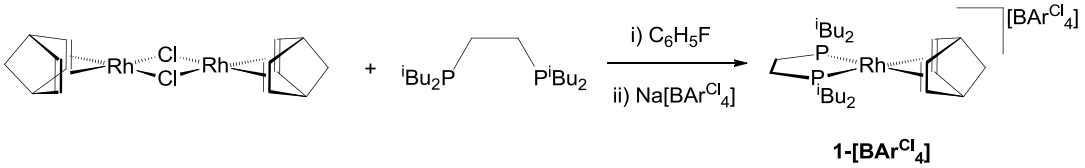

1-[BAr$^{Cl}_4$]

Scheme 3.7. Synthesis of **1-[BAr$^{Cl}_4$]**.

The ^1H and $^{31}P\{^1H\}$ NMR spectra were consistent with **1**. The $^{11}B\{^1H\}$ NMR spectrum contains a single peak [δ −6.9] as expected for the free $[BAr^{Cl}_4]^-$ anion. An X-ray crystal structure of **1-[BAr$^{Cl}_4$]** was obtained which shows that, despite a different counter-anion, the general extended structure is similar to **1**, with $[BAr^{Cl}_4]^-$ anions forming a *pseudo*-octahedron around the cation [Figure 3.3]. However on this occasion the structure solved in a triclinic space group and only limited cation disorder was located (^{i}Bu disorder only) in contrast to the more greatly disordered structure of **1**.

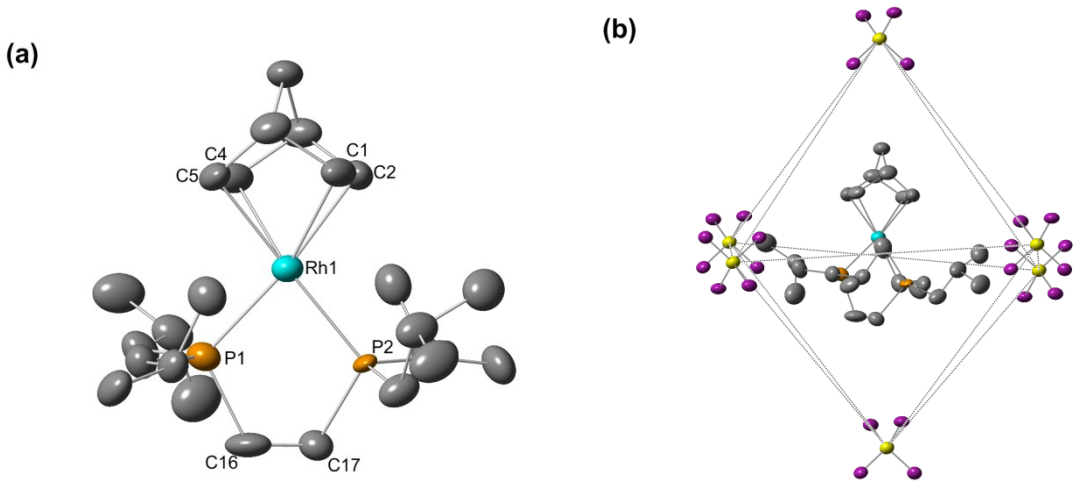

Figure 3.3. (a) Displacement ellipsoid plot (30% probability) for the major cationic component of **1-[BAr$^{Cl}_4$]** in the solid-state. Hydrogen atoms omitted for clarity. **(b)** Crystal packing diagram of **1-[BAr$^{Cl}_4$]** showing anions forming a *pseudo*-octahedron around the cation. [BAr$^{Cl}_4$]$^-$ anions represented as BC_4 units (aryl groups omitted) for clarity. Selected bond length (Å) and angle (º) data: Rh(1)–P(1), 2.2813(14); Rh(1)–P(2), 2.267(6); Rh(1)–C(1), 2.235(5); C(1)–C(2), 1.338(9); P(1)-Rh(1)-P(2), 82.68(14).

3.2.ii. Hydrogenation of 1-[BAr$^{Cl}_4$] in the solid-state and solution

A powdered crystalline sample of orange **1-[BAr$^{Cl}_4$]** was exposed to H_2 (1 atm), either in the solid-state or in a CH_2Cl_2 solution, to rapidly (< 10 minutes) give a yellow solid/solution of Rh(^{i}Bu$_2$PCH$_2$CH$_2$P^{i}Bu$_2$){(η^6-3,5-C$_6$H$_3$Cl$_2$)BAr$^{Cl}_3$}, **12**, with free NBA released [Scheme 3.8]. In the solid-state an orange to yellow colour change occurs within 10 minutes, with no visual evidence of a claret σ-alkane complex intermediate during the process. Previous reports show [BAr$^{Cl}_4$]$^-$ to bind more strongly to a Rh(I) centre than [BAr$^{F}_4$]$^-$, therefore it is likely that any form of σ-alkane complex intermediate is short-lived and easily displaced.[36] The solid-state reaction is not a SC-SC transition, as the product forms in an amorphous phase (*vide infra*). The product does, however, retain its powdery appearance, despite the loss of one equivalent of non-volatile NBA. This is in contrast to the formation of **4**, which has as a slightly oily appearance – presumably due to the free NBA released.

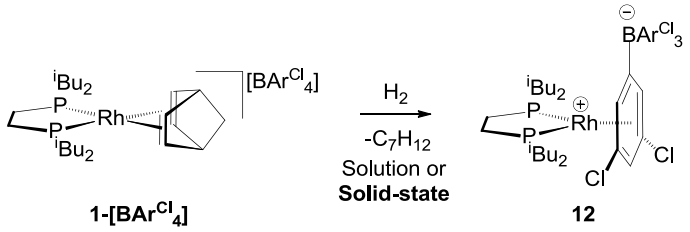

Scheme 3.8. Initial product of the hydrogenation of **1-[BAr$^{Cl}_4$]** in solution or the solid-state

12 has been characterised by solution and solid-state NMR spectroscopy. The solution (CD_2Cl_2) NMR data are consistent with a coordinated $[BAr^{Cl}_4]^-$ anion and are similar to **4**.[36] **12** does not appear to decompose in CD_2Cl_2, unlike **4**; this possibly suggests a more firmly held arene fragment. The $^{31}P\{^1H\}$ NMR spectrum displays a doublet with a large coupling constant [δ 67.8, J_{RhP} 202 Hz] typical of a Rh(I) η^6-coordinated arene complex (*see Sections 2.2.ii & 5.2.ii*). The ^1H NMR spectrum shows four signals for $[BAr^{Cl}_4]^-$ in a 6:3:2:1 ratio [δ 6.15-7.10] consistent with one η^6-coordinated arene and three arenes made equivalent by free rotation around C(19)–B(1) [Figure 3.4]. The $^{11}B\{^1H\}$ NMR spectrum contains one peak with a small shift upfield to that of free $[BAr^{Cl}_4]^-$ [**12**, δ −8.3; free $[BAr^{Cl}_4]^-$, δ −6.9], consistent with previously reported Rh{$\kappa_{P,C=C}$-P^{t}Bu$_2$CH$_2$CH(CH$_2$)$_2$}{(η^6-3,5-C$_6$H$_3$Cl$_2$)BAr$^{Cl}_3$}, **XVIII** [δ −7.6] (*see Scheme 3.6*).[36]

Hydrogenation of **1-[BAr$^{Cl}_4$]** in the solid-state was also followed by SSNMR spectroscopy with the assistance of Dr. David Apperley (at Durham University). A pure sample of **1-[BAr$^{Cl}_4$]** was characterised by SSNMR initially. In order to undertake the hydrogenation reaction the filled rotor was exposed to one atmosphere of hydrogen for 4.5 minutes with one end left open, and then after evacuation the rotor was capped within a glovebox. The $^{31}P\{^1H\}$ SSNMR spectra of the products displays a very broad signal [δ ~66, FWHM 1976 Hz] consistent with an amorphous form of **12** with a small amount of residual starting material [Figure 3.7(b)]. No evidence of any intermediate species was observed by SSNMR spectroscopy.

An X-ray crystal structure of **12** [Figure 3.4] was recorded by relatively rapid recrystallisation (~12 hours) of **12** from CH_2Cl_2-pentane. The structure displayed a geometry consistent with other coordinated $[BAr^{Cl}_4]^-$ and $[BAr^{F}_4]^-$ complexes such as **4**.[36, 42, 43] One arene ring coordinates through its π system in an approximate η^6- manner.

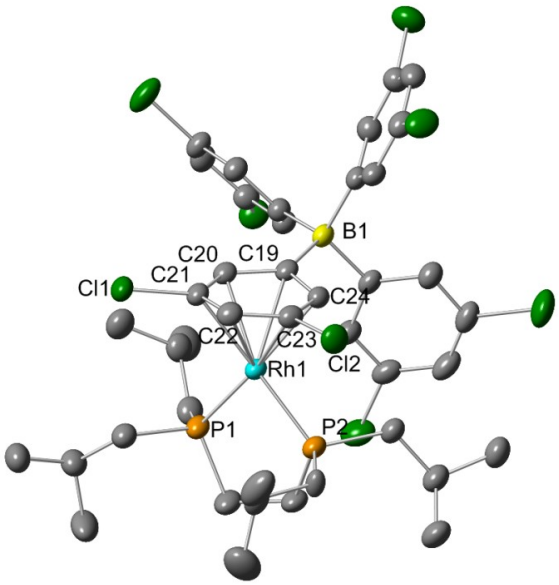

Figure 3.4. Displacement ellipsoid plot (30% probability) of complex **12** in the solid-state. Hydrogen atoms omitted for clarity. Selected bond length (Å) and angle (º) data: Rh(1)–P(1), 2.2429(6); Rh(1)–P(2), 2.2325(6); Rh(1)–C(19), 2.417(2); Rh(1)–C(24), 2.251(2); P(1)-Rh(1)-P(2), 85.23(2).

The Rh–C bond lengths vary from 2.417(2) Å to 2.251(2) Å with the longest Rh–C distances to C(19) and C(22) (1st and 4th ring positions relative to $BAr^{Cl}_3{}^-$). These bond lengths fall within the reported range for Rh–arene bonding interactions and therefore the complex can be considered to exhibit η^6-coordination to the anion. The Rh–$C_{(arene)}$ bond lengths are similar to those of η^6-$[BAr^F_4]^-$ coordinated complex, **4** [2.457(2) Å to 2.269(2) Å].

3.2.iii. C–Cl activation reaction and isomeric products

12 is the kinetic product from the hydrogenation of **1-[BAr^{Cl}_4]**, however over time (2 weeks) intramolecular C–Cl oxidative cleavage occurs to form a Rh(III) species which dimerises to form $[Rh(^iBu_2PCH_2CH_2P^iBu_2)\{C_6H_3Cl(BAr^{Cl}_3)\}Cl]_2$ **23**. This process occurs in solution (CH_2Cl_2) and in the solid-state. In solution a single isomer, **23-anti**, is observed which is only sparingly soluble in CH_2Cl_2; with single crystals slowly forming directly from the solution. A large amount of co-crystallised CH_2Cl_2 is present and the crystals rapidly crack up when removed from solution. A solid-state structure was determined from these crystals despite their inherent fragility. The geometry indicates C–Cl activation of the $[BAr^{Cl}_4]^-$ anion has occurred to form a Rh(III) dimeric species with bridging chlorides [Figure 3.5].

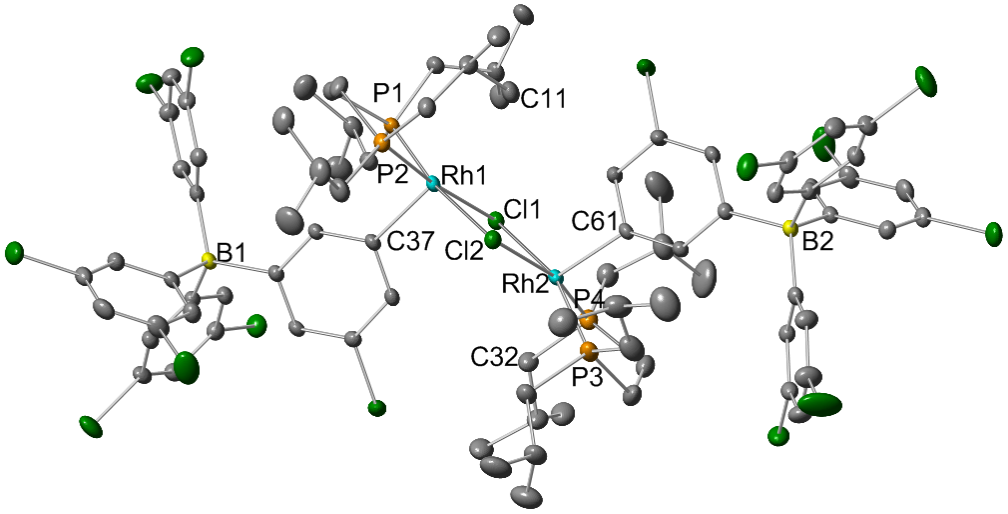

Figure 3.5. Displacement ellipsoid plot (30% probability) of complex **23-*anti*** in the solid-state. Hydrogen atoms omitted for clarity. Selected bond length (Å) and angle (º) data: Rh(1)–C(37), 2.030(3); Rh(2)–C(61), 2.020(3); Rh(1)–Cl(1), 2.4464(8); Rh(2)–Cl(1), 2.4796(9); Rh(1)–P(1), 2.2518(9); Rh(2)–P(4), 2.2239(11); Rh(1)···Rh(2), 3.7003(4). 87.52(4); P(1)-Rh(1)-P(2), 87.52(4); P(3)-Rh(1)-P(4), 84.69(4).

Each metal formally has 16 valence electrons with one 'vacant site' *trans* to the aryl group. The nearest Rh···C distances are long for a typical agostic interactions [Rh(1)–C(11): 3.149(5) Å (potential δ agostic); Rh(2)–C(32): 3.162(4) Å (potential γ agostic); typical agostic interactions Rh–C: 2.4-3.0 Å],[44] although it is noteworthy that P^{i}Bu group δ agostic interactions have been reported in the range 2.9-3.0 Å.[23, 45] Whilst a very weak interaction could be envisioned for Rh(1)···C(11)–H(111), the vacant site of Rh(2) is not geometrically aligned with its closest CH_2 group, suggesting that the structure is determined by packing efficiency rather than electronic effects.[46, 47] Dimeric structures similar to **23-*anti*** have been previously observed from the oxidative cleavage of aryl-halides.[23, 24, 48] The phosphorus, rhodium and chlorine atoms fall close to a plane with the aryl groups sitting roughly along the Rh-Rh vector, giving the molecule non-crystallographic C_{2h} symmetry. The two aryl groups are oriented symmetrically so that the bulky ($BAr^{Cl}{}_3^-$) groups point away from the centre of the molecule (*anti* to each other). This would appear to be the least sterically hindered structure. Solution NMR spectra of **23-*anti*** are consistent with the solid-state structure. Three ^{1}H resonances with integral equal to 1H are identified for the activated arene, the other arene groups appear equivalent by free rotation with 6:3 integral peaks observed. The ^{31}P{^{1}H} NMR spectrum displays a doublet [δ 88, J_{RhP} 140 Hz], with a far smaller coupling constant than **12** indicative of the transformation to a Rh(III)

species.[49] Whilst the phosphorus atoms appear equivalent by NMR spectroscopy their ^{i}Bu-CH_3 substituents are now split into two sets (four doublets in total) by the relative orientation of the aryl group sitting out of the plane. The $^{11}B\{^1H\}$ NMR spectrum (in CD_2Cl_2) contains a single peak [δ −6.65] which is similar to that of free $[BAr^{Cl}{}_4]^-$ [**1-[BAr^{Cl}$_4$]$^-$** (CD_2Cl_2) δ −6.95].

The C–Cl cleavage reaction also takes place in the solid-state. The products of this can be dissolved in CH_2Cl_2 and investigated immediately by solution NMR. The solid-state reaction product appears quite soluble in CH_2Cl_2 initially suggesting that clathration with the solvent is necessary to generate the insoluble species that forms slowly from solution. $^{31}P\{^1H\}$ NMR spectroscopy shows that a second isomer, **23-*syn***, is present from the solid-state route, comprising around 50% of the product [Figure 3.6]. The additional $^{31}P\{^1H\}$ NMR signals are two doublets [δ 86.9, J_{RhP} 139 Hz & δ 89.1, J_{RhP} 140 Hz], very similar in chemical shift and J_{RhP} coupling constant to that observed for **23-*anti***. The $^{11}B\{^1H\}$ NMR spectrum of the mixed isomers displays two peaks [δ −6.64 & −6.41] with a ~3:1 ratio. Considering ~50% of the product is **23-*anti*** [peak expected at δ ~ −6.65] this leaves a 1:1 ratio of peaks for the *syn* isomer. This indicates that asymmetry causes different environments at either end of the dimer, and we propose the structure in which one aryl group is rotated by 180° so that the bulky ($BAr^{Cl}{}_3^-$) group now points inwards.

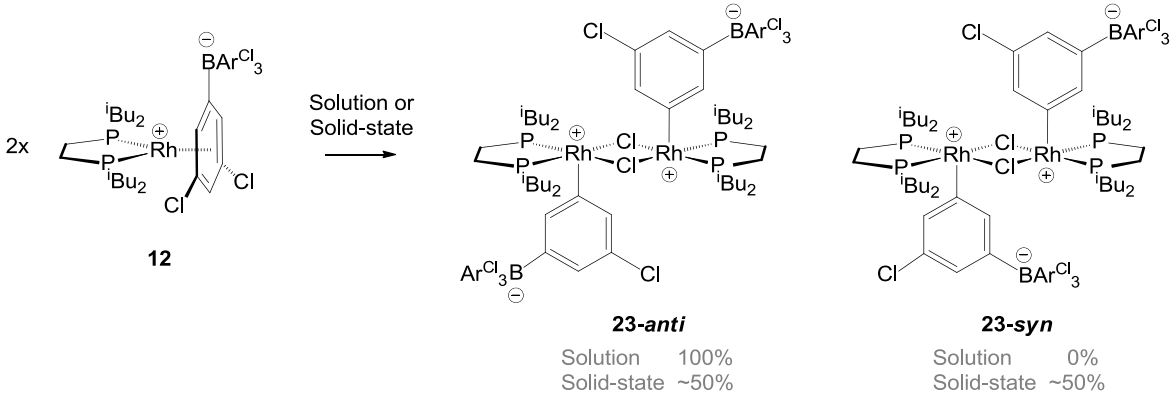

Figure 3.6. C–Cl activation of **12** and the two isomeric forms (*anti* and *syn*) of the product, **23**.

The ^1H NMR spectrum is consistent with this structure, with extra environments located for the rotated aryl group and eight ^{i}Bu signals located compared to the four observed in the anti isomer. No significant conversion between isomers is observed in solution at 298 K, therefore rotation around the Rh–aryl bond is clearly difficult. Dissolution and subsequent heating to 313 K of the ~1:1 mixture

formed by the solid-state reaction was undertaken and the $^{31}P\{^{1}H\}$ NMR and ^{1}H NMR spectra of this heated solution recorded. These spectra display **23-*anti*** as the dominant species demonstrating that the less sterically crowded *anti*-isomer is the thermodynamic product. These findings highlight solid-state reactivity as a method for accessing non-thermodynamic products which cannot be formed by solution methods, possibly due to the constrained nature of reactions within a solid-state environment.

The solid-state process was investigated by SSNMR at 313 K (in order to accelerate the reaction to occur over a reasonable timescale). This was undertaken after initial hydrogenation of **1-[BAr$^{Cl}_4$]** to form amorphous **12** (*Section 3.2.i*), and the final product **23** was again formed in an amorphous phase with a very broad $^{31}P\{^{1}H\}$ SSNMR signal [δ 88, FWHM 2804 Hz] [Figure 3.7(c)]. Solvation of this product confirmed the ~1:1 ratio of isomers.

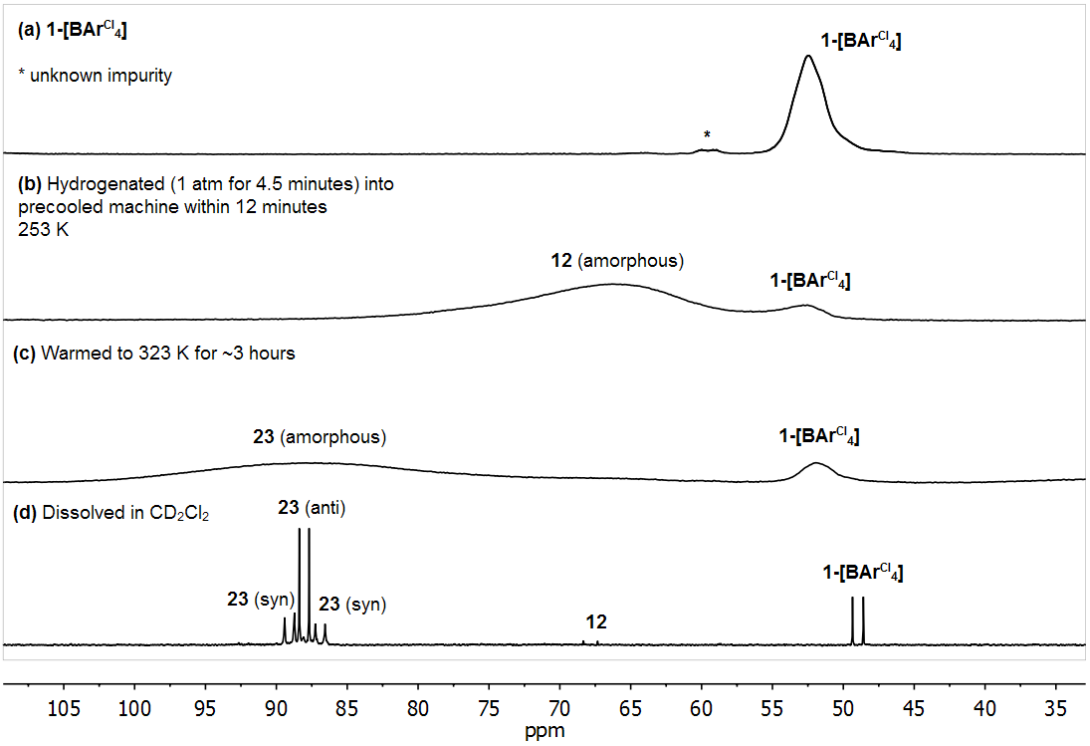

Figure 3.7. $^{31}P\{^{1}H\}$ solid-state NMR {**(a)**,**(b)** & **(c)**} and solution NMR **(d)** spectra of **1-[BAr$^{Cl}_4$]** and the products of its reaction with hydrogen (first at 253 K and then once warmed to 323 K for 3 hours, final solution spectra at ambient temperature).

23 is sparingly soluble in CH_2Cl_2 and partially precipitates out of solution (initial concentration ~ 0.01 M). Due to precipitation the total concentration of this species observed by $^{31}P\{^{1}H\}$ NMR spectroscopy decreases over time. **12** has good solubility in CH_2Cl_2 and, so unlike **23**, the concentration does not decrease due to precipitation. A sealed NMR capillary containing PPh_3 was

used as a standard to compare the changing concentrations of **12** over two weeks (approximately three half lives) by integration of the $^{31}P\{^{1}H\}$ NMR spectra. The consumption of **12** occurs with first order kinetics, as monitored by $^{31}P\{^{1}H\}$ NMR spectroscopy, which is consistent with intramolecular C–Cl activation acting as the rate determining step [Figure 3.8]. The reaction occurs slowly with a rate constant of $k = (2.8 \pm 0.1) \times 10^{-5}$ s^{-1} at 298 K. A possible mechanism could include initial arene ring slippage from η^6- to η^2-, allowing a vacant site for approach of the C–Cl bond [Scheme 3.9].[22, 23, 50] If this were the case the bulky $(BAr^{Cl}_3)^-$ group may promote ring slippage. A comparison with the less bulky chlorobenzene is reported in *Section 3.3.ii*.

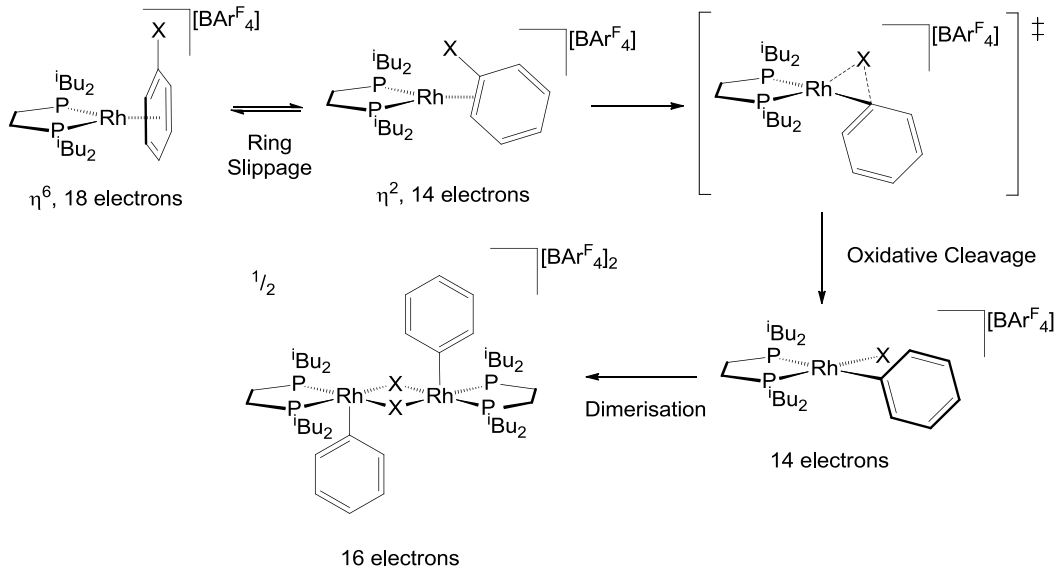

Scheme 3.9. Possible mechanism of C–X oxidative cleavage *via* ring slippage.

In order to investigate the kinetics for the solid-state transformation six high pressure NMR tubes each containing 5 mg of microcrystalline **1-[BAr$^{Cl}_4$]** were charged with 1 atm of H_2 for 90 minutes to form **12**. These were then degassed and kept under argon for various time periods (up to 2 weeks, approximately three half-lives) before monitoring by NMR spectroscopy directly (after solvation in CD_2Cl_2). The products of the solid-state reaction initially dissolved well in CH_2Cl_2. The yield of **23** (both isomers combined) was measured as a percentage of total $^{31}P\{^{1}H\}$ NMR signals observed; whilst this assumes complete solvation of all products it gives an approximate indication of the reaction rate. The reaction appears to again follow a first order kinetic profile, which occurs at the same rate within error, $k = (2.7 \pm 0.2) \times 10^{-5}$ s^{-1} at 298 K, in the solid-state as in solution [Figure 3.8].

The kinetics suggest that, in both the solid-state and in solution, intramolecular C–Cl activation is the rate determining step.

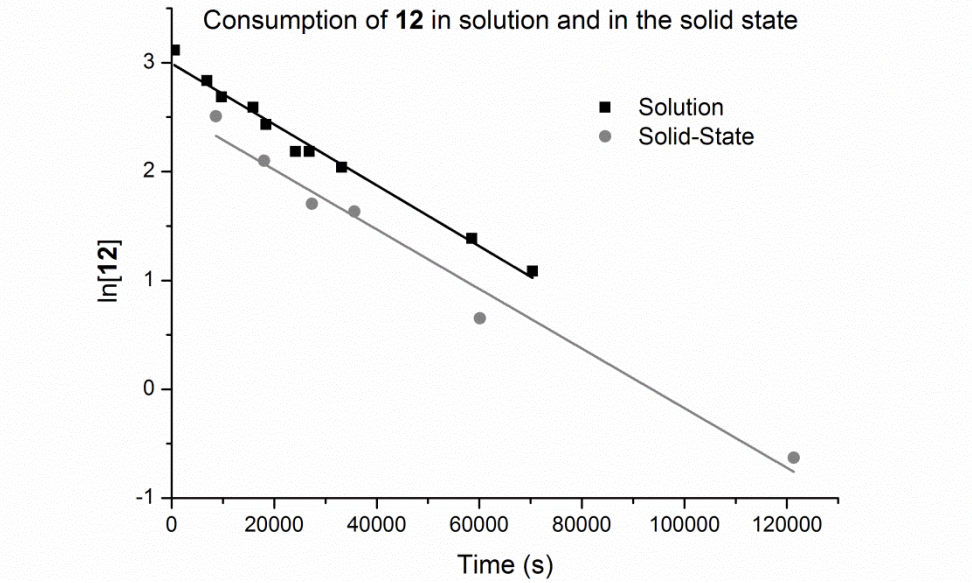

Figure 3.8. First order plot of the decay of **12**; ●, solid–state; ■, solution

3.3. C–X activation of halo-arenes in solution

3.3.i. Synthesis and characterisation of haloarene (C_6H_5X X = Cl, Br) complexes

In order to compare the oxidative cleavage of $[BAr^{Cl}{}_4]^-$ with that of simple aryl halides several η^6-halo-benzene complexes were synthesised: $[Rh(^iBu_2PCH_2CH_2P^iBu_2)(\eta^6\text{-}C_6H_5Cl)][BAr^F{}_4]$ **24** and $[Rh(^iBu_2PCH_2CH_2P^iBu_2)(\eta^6\text{-}C_6H_5Br)][BAr^F{}_4]$, **25**, alongside previously discussed η^6-C_6H_5F complex **2** (*see Section 2.2.i*).

24 was synthesised by dissolving **1** in a 1:1 mixture of C_6H_5Cl and CH_2Cl_2 solvent and placing the solution under hydrogen (1 atm) to produce the desired complex alongside one equivalent of free NBA in quantitative yields [Scheme 3.10].

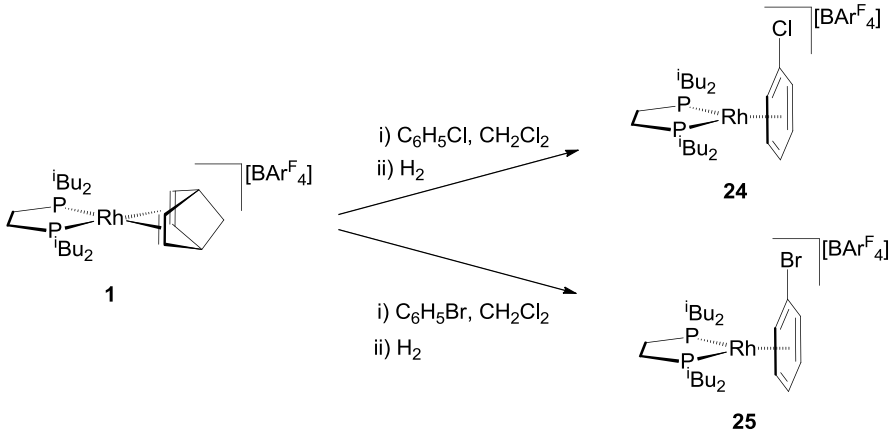

Scheme 3.10. Synthesis of **24** and **25**

NMR spectral analysis of **24** reveals a doublet with a large coupling constant in the $^{31}P\{^1H\}$ NMR spectrum [δ 73.2, J_{RhP} 201 Hz] consistent with other η^6-arene bound Rh(I) complexes such as **2** and $[Rh(P^iBu_3)_2(\eta^6\text{-}C_6H_5Cl)][BAr^F_4]$, **XI**. Three signals are observed for the coordinated arene in the ^1H NMR spectrum with the expected 2:2:1 ratio. These resonances are shifted upfield relative to free C_6H_5Cl consistent with coordination to a metal centre [23] [**24** $\delta_{(aryl)}$ (CD_2Cl_2): 6.15, 6.57, 6.75; C_6H_5Cl $\delta_{(aryl)}$ ($CDCl_3$): 7.14-7.43].[51] **24** appears stable in CH_2Cl_2 and single crystals could be grown by layering a solution with pentane. A solid-state structure was determined from these crystals (space group: *C* 2/c) which revealed significant cation disorder [Figure 3.9]. Whilst the chlorobenzene ligand appears to be locked into one position the phosphine can adopt two positions each with refined occupancy ~50%. The two structural models display the C(5)-Cl(1) vector approximately parallel or perpendicular to the plane of the phosphines [angle between Rh(1)-C(5)-Cl(1) plane and P(1)-Rh(1)-P(2) plane, 98.8° or P(3)-Rh(1)-P(4), 8.0°] indicating a close to 90° rotation of the phosphine differentiating the disorder components. The $[BAr^F_4]^-$ anions form a *pseudo*-octahedron around the cation. It appears the cation may adopt different geometries in the octahedral pocket formed by the surrounding anions. Whilst structural refinement gives the expected molecular geometries the cationic disorder is likely to reduce the accuracy of bond length and angle data and therefore a ball and stick diagram is presented.

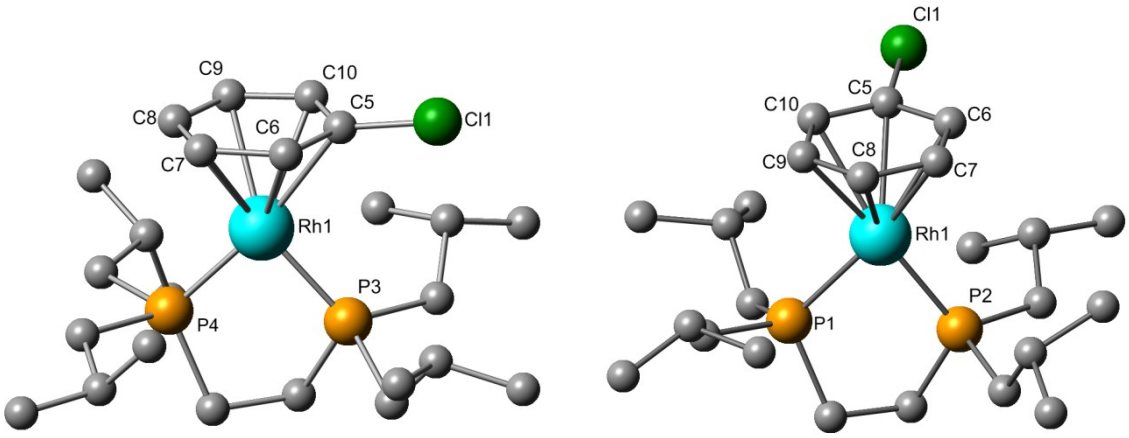

Figure 3.9. Ball and stick diagrams of the two disorder forms found in the solid-state structure of the cation of **24**. Hydrogen atoms omitted for clarity.

The bromobenzene analogue $[Rh(^{i}Bu_2PCH_2CH_2P^{i}Bu_2)(\eta^6\text{-}C_6H_5Br)][BAr^F{}_4]$, **25**, is synthesised by solvating **1** in CH_2Cl_2 with an excess of C_6H_5Br and then exposing the solution to hydrogen (1 atm) [Scheme 3.10]. However the initial product, **25**, has a short lifetime due to rapid C–Br activation (which as will be shown in *Section 3.3.ii* is a first order process, $t_{1/2}$ = 9.5 min). Because of this, only the $^{31}P\{^{1}H\}$ NMR spectrum was collected, which showed a doublet [δ 73.2, J_{RhP} 201 Hz] virtually identical to that of **24.**

3.3.ii. C–X activation reaction and products

24 remained stable in CH_2Cl_2 solution for two weeks and showed no C–Cl activation products. Heating to 313 K in solution (CH_2Cl_2) or to 323 K in the solid-state did not result in any observable C–Cl activation over three days. This is in contrast to the intramolecular C–Cl activation of chlorobenzene observed in the complex $[Rh(P^{i}Bu_3)_2(\eta^6\text{-}C_6H_5Cl)][BAr^F{}_4]$, **XI**, to form $[Rh(P^{i}Bu_3)_2(C_6H_5)(\mu\text{-}Cl)]_2[BAr^F{}_4]_2$, **XII**, [Scheme 3.11], which occurs with first order kinetics {k = (1.78 ± 0.05) x 10^{-4} s^{-1} at room temperature}.[23]

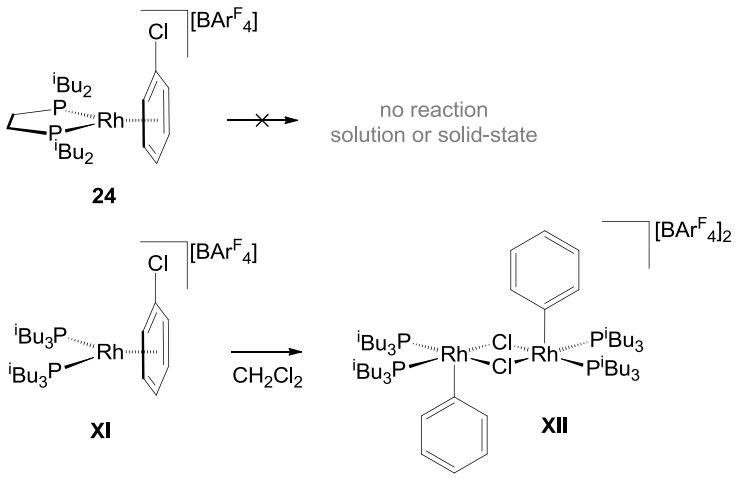

Scheme 3.11. 24 is stable to C–Cl activation whilst analogous **XI** reacts at room temperature in solution.

This difference in reactivity between the monodentate and chelating ^{i}Bu phosphine complexes may be connected to the effect of bite angle, which, in this case, may be both electronically and sterically influential. The solid-state structural P-Rh-P angle of the analogous complex $[Rh(P^{i}Bu_3)_2(\eta^6\text{-}C_6H_5F)][BAr^F{}_4]$, **VI**, is 95.31(5)° whilst for the major cationic solid-state disorder component of **24** the bite angle is approximately 86.5(2)°. Smaller bite angles have been shown to favour Rh(I) species whilst larger bite angles have a greater tendency to form Rh(III) complexes at least when in equilibrium between the two oxidation states (*see Section 1.2.ii*).[50, 52, 53]

Fluorobenzene complex **2** is also resistant to C–X activation as would be expected due to the strong C–F bond [typical bond enthalpies (kJ/mol): C–I, 238; C–Br, 276; C–Cl, 338; C–F, 484].[8]

The weaker C–Br bond in the bromobenzene analogue **25** undergoes C–Br oxidative cleavage rapidly (*vide infra* for kinetics) with subsequent dimerisation to form $[Rh(^{i}Bu_2PCH_2CH_2P^{i}Bu_2)(C_6H_5)Br]_2[BAr^F{}_4]_2$, **26** [Scheme 3.12].

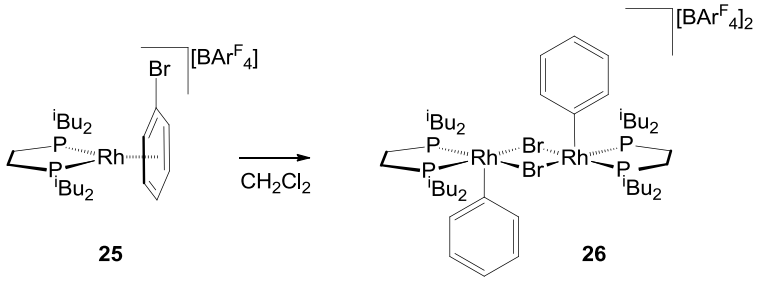

Scheme 3.12. C–Br activation of **25** in solution.

26 forms as the sole product of C–Br activation of **25** in less than five hours. Single crystals of **26** could be grown from CH_2Cl_2/pentane. The solid-state structure displays a geometry similar to **23** with phosphorous, rhodium and bromine atoms falling near to a plane and phenyl groups pointing outwards whilst sitting along the Rh-Rh vector. The complex has approximate non-crystallographic C_{2h} symmetry [Figure 3.10]. Each metal centre has formally 16 valence electrons with a vacant site *trans* to the phenyl group. Long Rh···C distances [Rh(1)–C(23): 3.391(6) Å] suggest that agostic interactions are not present.[54] This structure is wholly consistent with previously reported dimeric complexes that form from C–Br activation of aryl bromides.[24, 48]

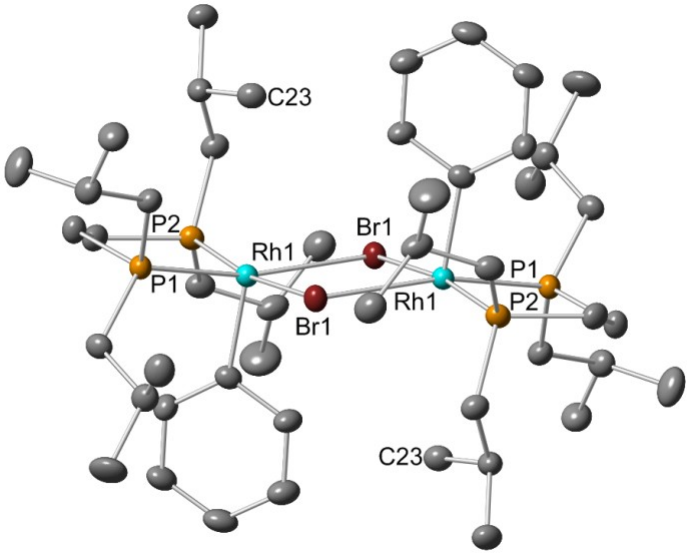

Figure 3.10. Displacement ellipsoid plot (30% probability) of complex **26** in the solid-state. Hydrogen atoms and anions omitted for clarity. Selected bond length (Å) data: Rh(1)–C(1), 2.024(6); Rh(1)–Br(1), 2.5979(7); Rh(1)–P(1), 2.2658(16); Rh(1)–P(2), 2.2508(16); Rh(1)···Rh(1), 3.921(4); P(1)-Rh(1)-P(2), 87.23(6).

The ^{1}H NMR spectrum of **26** displays two sets of signals for the ^{i}Bu (CH_3) groups (four doublets in total) consistent with the solid-state structure. The $^{31}P\{^1H\}$ NMR spectrum contains one doublet [δ 91.8, J_{RhP} 137 Hz] with a small coupling constant similar to **23**. ESI-MS of **26** generated a signal for $[\{Rh(^iBu_2PCH_2CH_2P^iBu_2)(C_6H_5)Br\}_2X]^+$ (X = Br^-, OH^-) rather than the expected dication. It is presumed that the doubly charged cation coordinates an anion during the ESI-MS experiment, probably from entrainment in the sample loop.

The reaction of **25** to **26**, *via* C–Br oxidative cleavage, was monitored over time by $^{31}P\{^1H\}$ NMR spectroscopy in solution (CH_2Cl_2), as a percentage of the total $^{31}P\{^1H\}$ NMR signal (only **25** and **26**

observed). No precipitation of **26** was observed, in contrast to **23**, as the $[BAr^{F}_{4}]^{-}$ anion generally forms more soluble complexes than for those of $[BAr^{Cl}_{4}]^{-}$.[36] The consumption of **25** followed first order kinetics with respect to **25** with a rate that is essentially independent of bromobenzene concentration; this being consistent with intramolecular C–Br activation acting as the rate determining step [Figure 3.11].[23] If a pre-equilibrium between **25** and **4** were to exist it appears to be strongly in favour of **25** such that changing the concentration of bromobenzene has a negligible effect upon the rate (no **4** is observed in the $^{31}P\{^{1}H\}$ NMR spectra). The rate constants of $k = (1.22 \pm 0.05) \times 10^{-3}$ s^{-1} (10 equivalents bromobenzene) and $k = (1.07 \pm 0.04) \times 10^{-3}$ s^{-1} (1 equivalent bromobenzene) were found at 298 K. The rate is essentially the same in both experiments suggesting a zero-order dependence upon the concentration of bromobenzene. This oxidative cleavage process is much faster than that of **12** to **23**.

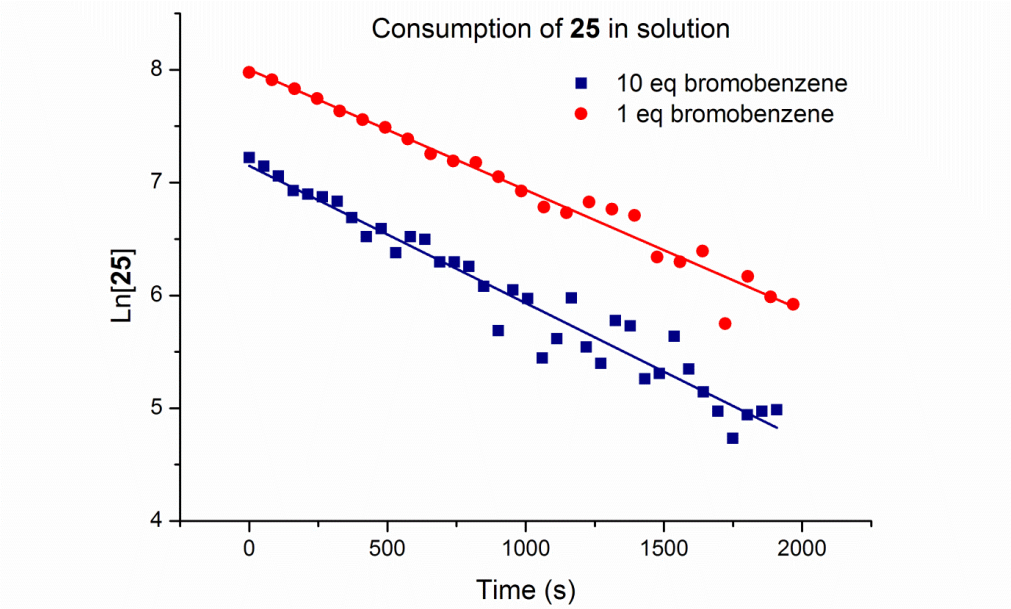

Figure 3.11. Plots of Ln([**25**]) vs time demonstrating C–Br activation is a first order process. Two experiments were undertaken with excess and with one equivalent of bromobenzene.

3.3.iii. C–Br activation of bulky aryl bromides

Bulky aryl bromides were also investigated to see if *ortho* substituents would have an effect upon the oxidative cleavage process. Cyclometallation of the ^{i}Bu groups upon $\{Rh(P^{i}Bu_{3})\}$ fragments has been reported after initial C–X activation of *ortho*-substituted aryl-halides.[24] This cyclometallation of the

ligand results in deactivation of the catalyst (*see Section 3.1.ii*). The "ligand innocence" of the chelating phosphine $^{i}Bu_2PCH_2CH_2P^{i}Bu_2$ is tested by oxidative cleavage reactions with bulky *ortho*-substituted aryl halides. The C–Br activation of *ortho*-bromotoluene, *ortho*-bromoanisole and 2-bromomesitylene was attempted [Figure 3.12].

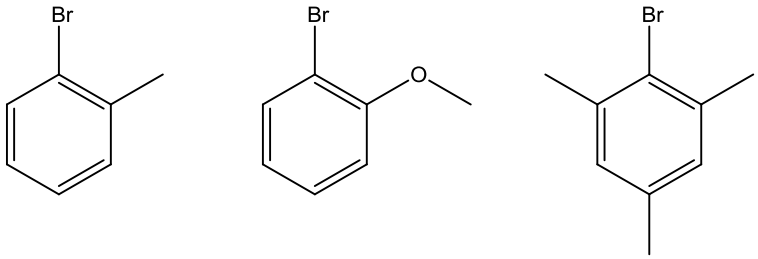

Figure 3.12. Sterically demanding aryl bromides.

Hydrogenation of **1** in CH_2Cl_2 in the presence of 20 equivalents of the bromo-arene directly produced new species characterised as η^6-complexes: $[Rh(^{i}Bu_2PCH_2CH_2P^{i}Bu_2)(\eta^6\text{-}o\text{-}C_6H_4MeBr)][BAr^F{}_4]$, **27**, $[Rh(^{i}Bu_2PCH_2CH_2P^{i}Bu_2)(\eta^6\text{-}o\text{-}C_6H_4(OMe)Br)][BAr^F{}_4]$, **28**, and $[Rh(^{i}Bu_2PCH_2CH_2P^{i}Bu_2)(\eta^6\text{-}1,3,5\text{-}(Me)_3C_6H_2Br)][BAr^F{}_4]$, **29**. The $^{31}P\{^{1}H\}$ NMR spectra of all three complexes display doublets with large coupling constants similar to **2**, **24** and **25** [**27**, δ 72.5 J_{RhP} 201 Hz; **28**, δ 73.4 J_{RhP} 202 Hz; **29**, δ 71.0 J_{RhP} 202 Hz]. The ^{19}F NMR spectra confirmed free $[BAr^F{}_4]^-$ anions, discounting any formation of anion coordinated complex **4**.

27 and **28** undergo C–Br activation rapidly to generate the dimeric products $[Rh(^{i}Bu_2PCH_2CH_2P^{i}Bu_2)(o\text{-}C_6H_4Me)Br]_2[BAr^F{}_4]_2$ **30**, and $[Rh(^{i}Bu_2PCH_2CH_2P^{i}Bu_2)(o\text{-}C_6H_4(OMe))Br]_2[BAr^F{}_4]_2$ **31** respectively, which were both characterised by ^{1}H and $^{31}P\{^{1}H\}$ NMR spectroscopy (**31** was further characterised by X-ray crystallography). Both reactions appear to form dimeric species directly, which are stable in CH_2Cl_2, and no evidence of subsequent reactivity resulting in cyclometallation (with loss of toluene or anisole) is observed over the duration of one week [Scheme 3.13].

Complex **29** is stable in CH_2Cl_2, even when heated to 313 K for two days, and does not undergo C–Br activation. We speculate that the methyl groups on both sides of the bromine block access to the C–Br bond.

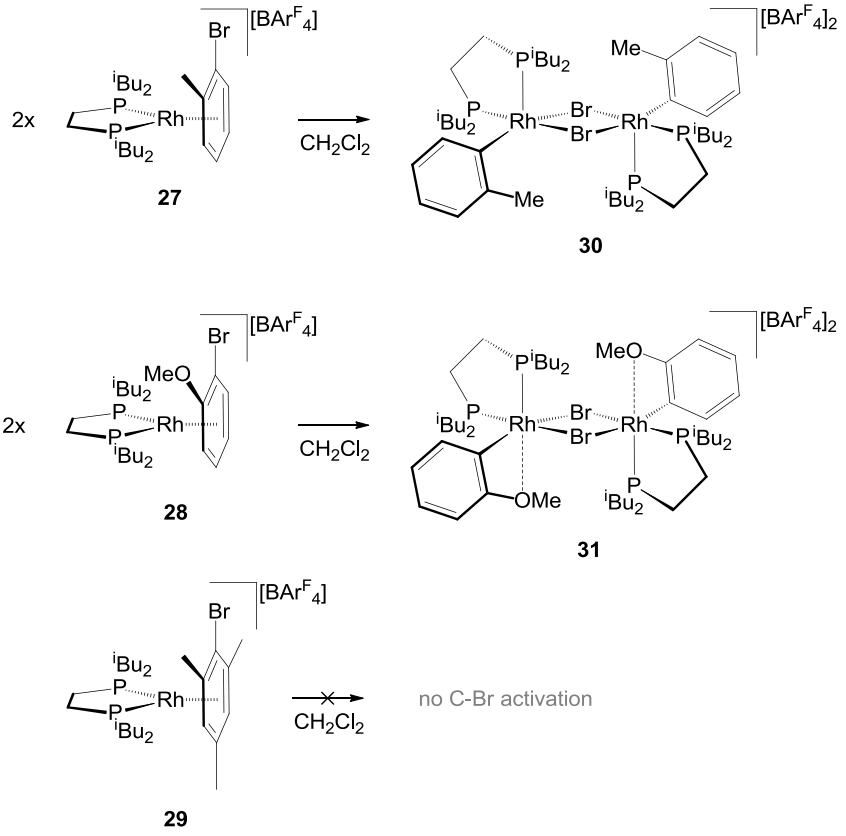

Scheme 3.13. Coordination of sterically demanding aryl bromides and subsequent C–Br activation with dimerisation.

The solid-state structure of **29** is a good model for the η^6-compounds that occur prior to C–Br activation (**25**, **27** and **28**), which have not been isolated due to their ability to undergo C–Br cleavage. **29** crystallises with a large unit cell containing 24 molecules, with three in the asymmetric unit. All three independent cations show very similar geometries. The arene coordinates in a regular η^6-coordination mode with approximate Rh–$C_{(arene)}$ distances ranging from 2.26(1)-2.39(1) Å across the three independent cations; there appears little rationale governing which points of the arene have the longest and shortest bonds. A minor disorder component is observed in two of the cations, in which the phosphine has rotated by ~90° (similar disorder observed for **24**), and the anions also exhibited rotational disorder of some CF_3 groups. All the disorder was left unmodelled because of the large amount of atoms present in the structure which meant refinement was very slow due to limited computing power, hence an approximate ball and stick structure is presented (R = 12.4%) [Figure 3.13].

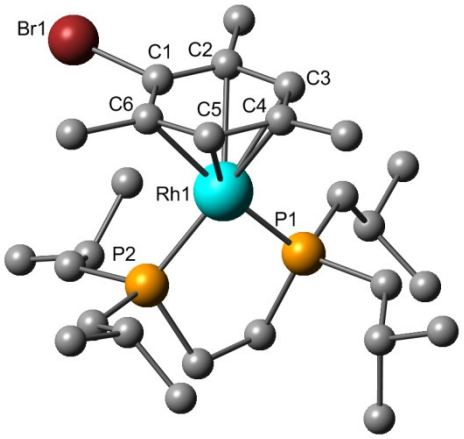

Figure 3.13. Ball and stick diagram of the structure of one cation of **29** in the solid-state (major disorder component, minor components not modeled). Only one independent cation shown, hydrogen atoms and anions omitted for clarity.

The NMR spectra of **29** are consistent with other η^6-arene complexes. In the ^{1}H NMR spectrum a single signal is observed for the two arene protons which is shifted upfield relative to the analogous resonance for the free arene [$\delta_{(arene)}$ **29** (CD_2Cl_2), 6.13; 1,3,5-MeC_6H_2Br ($CDCl_3$), 6.86]. The $^{31}P\{^1H\}$ NMR spectrum also reveals a single doublet resonance which indicates the equivalence of phosphorus atoms in solution upon the NMR timescale, which is in contrast to the solid-state structure, suggesting that rotation or libration of the coordinated arene can occur in solution.

The C–Br activation product **30** was isolated and characterised by NMR spectroscopy. The $^{31}P\{^1H\}$ NMR spectrum displays a broad resonance [δ 95, FWHM 310 Hz] at room temperature indicative of fluxional behaviour. At 193 K the phosphorus resonance splits into two broad resonances [δ 74.5, FWHM 366 Hz & δ 113.4 FWHM 387 Hz], suggesting an asymmetric structure, as the complex approaches the low temperature limit of fluxionality observed by NMR spectroscopy. The ^{1}H NMR spectrum at room temperature shows two sets of signals for the ^{i}Bu (CH_3) groups (four doublet signals in total, two are coincident), as observed for **26**, and consistent with phosphorus atoms made equivalent by a fluxional process. Four signals for the aromatic protons are observed (two coincident) [δ 6.71, 6.83, 7.12] and a slightly broadened signal for the tolyl (CH_3) is recorded which is slightly upfield of the analogous resonance for free *ortho*-bromotoluene [**30**, δ_{CH3} (CD_2Cl_2) 2.17; o-C_6H_4BrMe, δ_{CH3} ($CDCl_3$), 2.37].[51] No evidence of any agostic interactions are present in the high field region of the ^{1}H NMR spectrum. At 193 K the ^{1}H NMR spectrum is very broad and offers little extra

information. Unfortunately single crystals of **30** could not be formed; however considering the similarities in NMR spectra the structure is likely to be similar to that of **31**, as discussed below.

A solid-state structure (collection and refinement by Dr. Adrian B. Chaplin, PDRA Weller group) of **31** was collected and showed an alternate geometry to that of **26** [Figure 3.14]. The phosphorus atoms are now located in different environments in and out of the plane containing the rhodium and bromine atoms. The bulky *ortho*-anisole group takes the second position in the rhodium-bromine plane with the OMe group positioned below the metal centre, possibly allowing a weak Rh···O interaction, which would then formally allow an 18 valence electron structure. The structure thus adopts approximate C_i symmetry. The atom separation for Rh(1)···O(1) is 2.480(4) Å which is long for a Rh–O bond (typically 2.10-2.31 Å).[24, 39, 55]

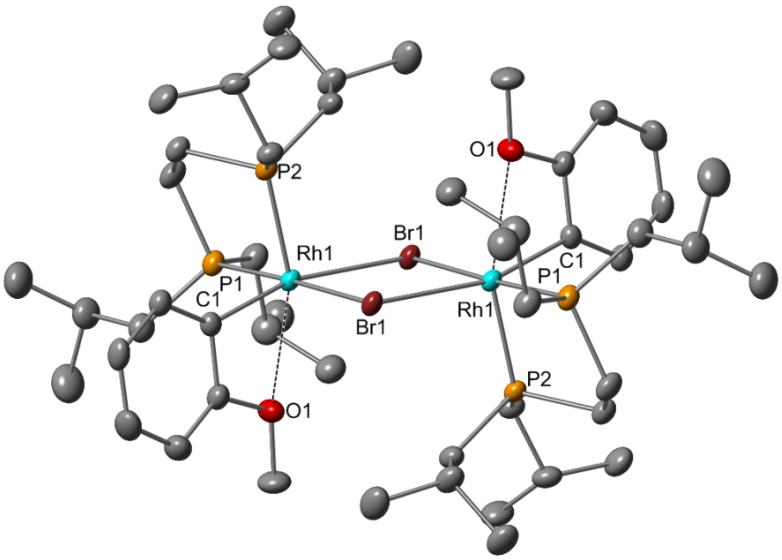

Figure 3.14. Displacement ellipsoid plot (30% probability) of complex **31** in the solid-state. Hydrogen atoms and anions omitted for clarity. Selected bond length (Å) and angle (°) data: Rh(1)–C(1), 2.021(5); Rh(1)–Br(1), 2.5701(6) & 2.5930(6); Rh(1)–P(1), 2.2768(13); Rh(1)–P(2), 2.2044(13); Rh(1)–O(1), 2.480(4); Rh(1)···Rh(1), 3.861; P(1)-Rh(1)-P(2), 86.49(5).

The $^{31}P\{^{1}H\}$ NMR spectrum of **31** is very broad [δ ~87, FWHM 3765 Hz] at room temperature, indicative of fluxionality. Low temperature $^{31}P\{^{1}H\}$ NMR spectroscopy reveals two phosphorus environments at 238 K [δ 77, J_{RhP} 123 Hz & δ 102, J_{RhP} 152 Hz] with different coupling constants, indicating the *trans* effect of the respective *trans* ligand (Br vs weakly bound OMe). The Rh(1)–P(2) bond [2.2044(13) Å], which is *trans* to the OMe group, is slightly shorter than the Rh(1)–P(1) bond length [2.2768(13) Å] [Figure 3.15].[56] The ^{1}H NMR spectrum at room temperature is similar to that of

30 with two sets of ^{i}Bu (CH_3) signals observed (four doublets in total). However at lower temperatures splitting occurs with at least three sets of signals in the ^{i}Bu (CH_3) region. This indicates the fluxional process is slowing so that the low temperature structure on the ^{1}H NMR timescale is becoming observable. Four sets of signals would be expected since there would be two phosphorus environments each with two sets of diastereotopic pairs of ^{i}Bu (CH_3) groups in the low temperature structure. If the weakly bound OMe group acts in a hemilabile manner in solution to form a five coordinate metal centre, the exchange process is likely to occur by a Berry-*pseudo*rotation process.[50]

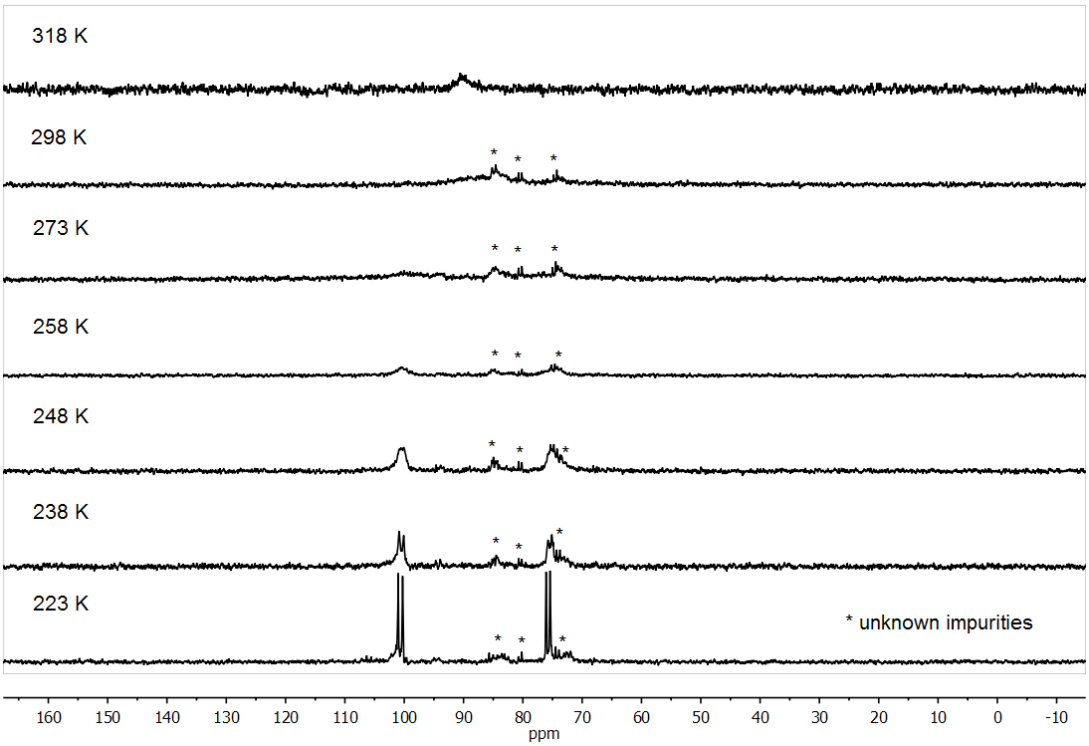

Figure 3.15. Variable temperature $^{31}P\{^{1}H\}$ NMR spectra of **31** (in CD_2Cl_2).

Variable temperature $^{31}P\{^{1}H\}$ NMR spectroscopy upon **31** allowed an Eyring plot to be generated by line-shape analysis of the spectra (modelled using gNMR software), with coalescence occurring at ~298 K [Figure 3.15, Figure 3.16].[57] The enthalpy and entropy of activation for the fluxional process can be determined [$\Delta H^{\ddagger}$ = (44.2 ±1.8) kJ/mol, $\Delta S^{\ddagger}$ = (−12.3 ±6.7) J K^{-1} mol^{-1}]. The small negative entropy of activation discounts a dissociative process for the fluxionality, suggesting the dimer remains intact.[58] The thermodynamic data allow calculation of the free energy of activation [$\Delta G^{\ddagger}_{(298)}$ = (47.9 ±3.8) kJ/mol] which is consistent with the approximate coalescence temperature formula which gives $\Delta G^{\ddagger}_{(298)}$ ~ 49.9 kJ/mol.[57]

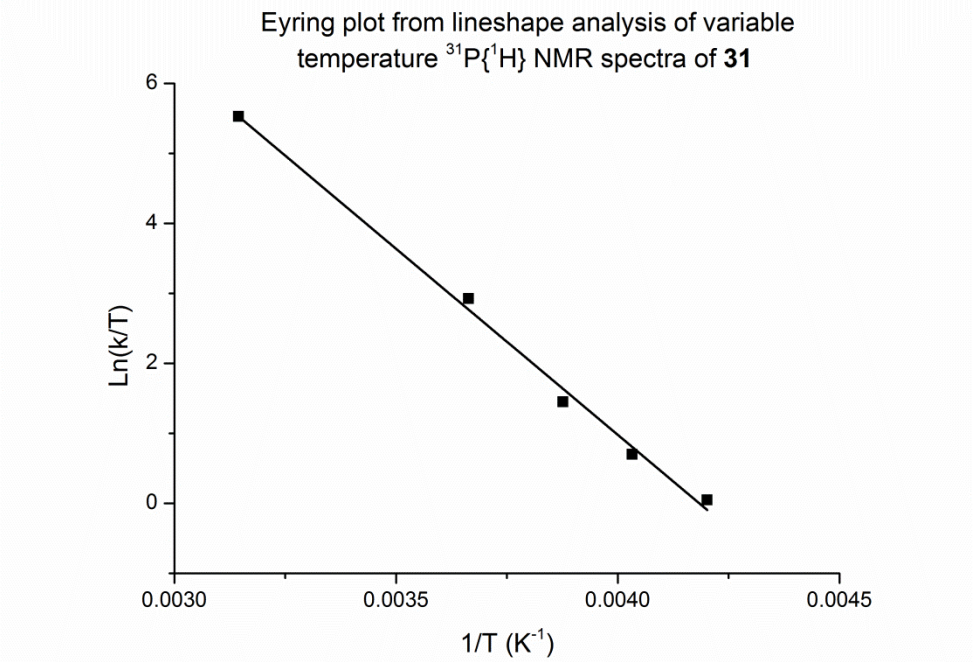

Figure 3.16. Eyring Plot for **31**.

Variable temperature $^{31}P\{^{1}H\}$ NMR spectroscopy of **30** shows that coalescence occurs at a lower temperature (243 K) than for **31** and the low temperature limit is not reached within the liquid range of CH_2Cl_2, therefore line-shape analysis was not attempted. The approximate coalescence temperature formula gives $\Delta G^{\ddagger}_{(243)} \sim 39.3$ kJ/mol for **30** which is considerably lower than the analogous calculated free energy of activation for the exchange in **31** at 243 K ($\Delta G^{\ddagger}_{(243)}$ = (47.2 ±3.4) kJ/mol).[57] We speculate that the weak Rh···O interaction may be influential in stabilising the structure of **31** with respect to fluxionality.

The kinetics of the C–Br activation of *ortho*-bromotoluene and *ortho*-bromoanisole were monitored by $^{31}P\{^{1}H\}$ NMR spectroscopy. The consumption of the starting materials **27** and **28** were recorded over time. A sealed capillary containing a solution of PPh_3 was used as a standard because the fluxional products (**30** and **31**) exhibit broad NMR signals which do not give accurate integral values for comparison [Figure 3.17]. Both reactions take place with first order kinetic profiles. Consumption of **27** occurs with a rate constant $k = (2.86 \pm 0.03) \times 10^{-4}$ s^{-1} at 298 K whilst the decay of **28** is faster and displays a rate constant $k = (1.10 \pm 0.03) \times 10^{-3}$ s^{-1} at 298 K which is very similar to the reaction of **25** to **26** ($k = (1.220 \pm 0.05) \times 10^{-3}$ s^{-1}).

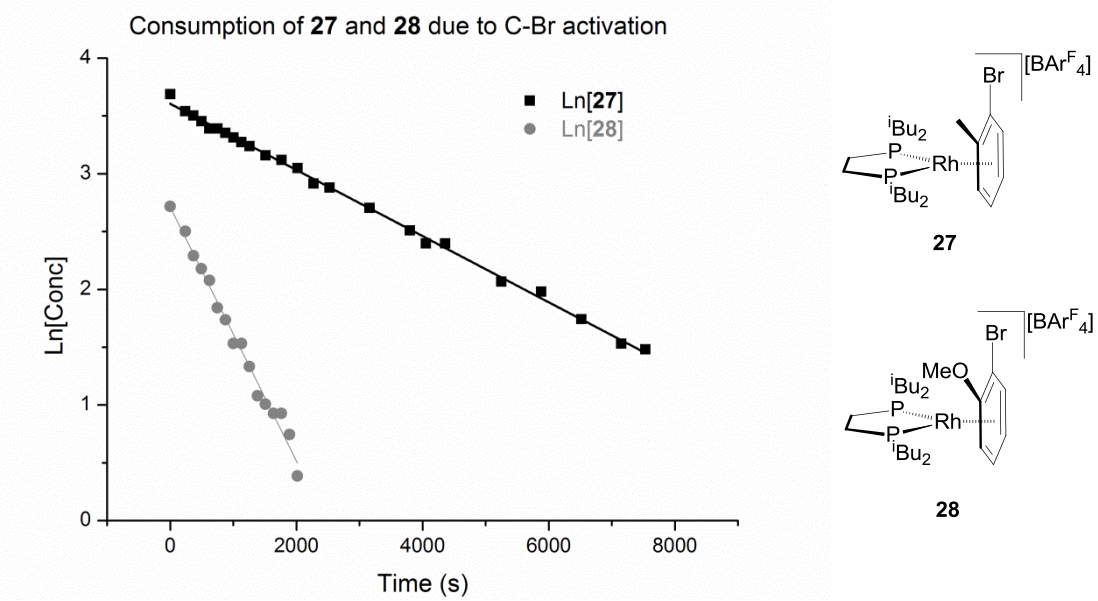

Figure 3.17. First order kinetic plot of the decay of **27** (■) and **28** (●)

Considering the rates of these reactions it seems that *ortho* substituents hinder C–Br activation - addition of an *ortho*-methyl group slows C–Br activation and addition of two *ortho*-methyl groups (in 2-bromomesitylene) shuts down reactivity all together. However these groups do not accurately model a large $(BAr^{Cl}_3)^-$ group which may have a greater steric (as well as a significant electronic) influence upon the C–Cl activation reaction **12** to **23** (*i.e.* by promoting η^6- to η^2- slippage). The addition of an *ortho*-methoxy group does not greatly affect the rate of reaction (*cf.* C_6H_5Br), possibly due to a trade-off between steric and electronic effects, or by stabilisation of the transition state by interaction of the methoxy group with the metal centre. Interaction of the OMe group with a rhodium complex has been reported in the monomeric complex $[Rh(P^iBu_3)_2(\kappa^2_{C,O}\text{-}C_6H_4OMe)Br][BAr^F_4]$, **XYIII** (*see Scheme 3.4).*[24]

The stable dimeric oxidative cleavage products **30** and **31** suggest that intramolecular C–H activation of an ^{i}Bu group to form a metallacyclic complex is not occurring with the chelating phosphine $^iBu_2PCH_2CH_2P^iBu_2$. This is consistent with the lack of agostic interactions observed in these compounds when a vacant site is present; perhaps the small bite angle restricts the ^{i}Bu groups from bending towards the metal and discourages interactions of this kind.[45] The lack of stable agostic interactions for this phosphine is also likely to allow for the stability of σ-alkane complex **5**.

3.4. Conclusions

The $[BAr^{Cl}_4]^-$ anion, whilst proven to be a very useful, non-coordinating anion, especially for achieving crystalline material, does exhibit coordinating ability to a low coordinate transition metal centre and can subsequently react by oxidative cleavage of a C–Cl bond. It has been determined that intramolecular oxidative cleavage processes of this type occur with first order kinetics. The $[BAr^{Cl}_4]^-$ anion appears to be more susceptible to C–X activation than C_6H_5Cl. This is possibly due to steric effects, which may promote η^6- to η^2- ring slippage that may be required prior to C–Cl oxidative cleavage. The weaker C–Br bond is readily activated. Bulky bromo-arenes do not promote subsequent cyclometallation in these compounds.[24] This is probably due to the chelating phosphine used, which, due to its small size, allows the formation of dimeric species; a process that stabilises the product of oxidative cleavage. The small bite angle of the phosphine may also prevent the close approach of its ^{i}Bu substituents for agostic interactions – which could in turn lead to C–H activation. This is consistent with the formation of **5**, in which the σ-alkane ligand would surely be displaced by agostic interactions if these were favourable. The lack of cyclometallation reactivity is noteworthy since 'ligand innocence' is a requirement for successful high turnover catalytic processes.

The C–Cl activation of $[BAr^{Cl}_4]^-$ also occurs in the solid-state, with a similar rate of reaction to that in solution. Considering this, and the first order kinetics observed in both the solid-state and in solution, it is possible that a similar rate determining step is occurring in both phases. This is likely to be an intramolecular C–Cl activation process. The solid-state reaction also accesses a non-thermodynamic isomeric product, highlighting the spatial restrictions that occur in a solid-state reaction.

Highlights of this chapter have been published in Dalton Transactions.[59]

3.5. References

1. A. F. Littke and G. C. Fu, *J. Org. Chem.*, 1999, **64**, 10-11.
2. A. Suzuki, *J. Organomet. Chem.*, 1999, **576**, 147-168.
3. B. H. Yang and S. L. Buchwald, *J. Organomet. Chem.*, 1999, **576**, 125-146.
4. J. F. Hartwig, *Acc. Chem. Res.*, 1998, **31**, 852-860.
5. R. F. Heck and J. P. Nolley, *J. Org. Chem.*, 1972, **37**, 2320-2322.
6. N. Miyaura and A. Suzuki, *J. Chem. Soc., Chem. Commun.*, 1979, 866-867.
7. A. O. King, N. Okukado and E. Negishi, *J. Chem. Soc., Chem. Commun.*, 1977, 683-684.
8. J. G. Stark and H. G. Wallace, *Chemistry Data Book*, 2nd edn., Hodder Murray, 1982.
9. A. F. Littke and G. C. Fu, *Angew. Chem. Int. Ed.*, 1998, **37**, 3387-3388.

10. A. F. Littke and G. C. Fu, *Angew. Chem. Int. Ed.*, 2002, **41**, 4176-4211.
11. B. Karimi and P. F. Akhavan, *Chem. Commun.*, 2009, 3750-3752.
12. Y. M. Kim and S. Yu, *J. Am. Chem. Soc.*, 2003, **125**, 1696-1697.
13. A. Nova, S. Erhardt, N. A. Jasim, R. N. Perutz, S. A. Macgregor, J. E. McGrady and A. C. Whitwood, *J. Am. Chem. Soc.*, 2008, **130**, 15499-15511.
14. H. Torrens, *Coord. Chem. Rev.*, 2005, **249**, 1957-1985.
15. T. Braun and R. N. Perutz, *Chem. Commun.*, 2002, 2749-2757.
16. L. Zhang and J. Wu, *Adv. Synth. Catal.*, 2008, **350**, 2409-2413.
17. J. C. Lewis, A. M. Berman, R. G. Bergman and J. A. Ellman, *J. Am. Chem. Soc.*, 2008, **130**, 2493-2500.
18. K. Ueura, T. Satoh and M. Miura, *Org. Lett.*, 2005, **7**, 2229-2231.
19. V. V. Grushin and H. Alper, *Chem. Rev.*, 1994, **94**, 1047-1062.
20. J. Ito, T. Miyakawa and H. Nishiyama, *Organometallics*, 2008, **27**, 3312-3315.
21. C. Douvris and C. A. Reed, *Organometallics*, 2008, **27**, 807-810.
22. M. r. Ahlquist and P.-O. Norrby, *Organometallics*, 2007, **26**, 550-553.
23. T. M. Douglas, A. B. Chaplin and A. S. Weller, *Organometallics*, 2008, **27**, 2918-2921.
24. N. S. Townsend, A. B. Chaplin, M. A. Naser, A. L. Thompson, N. H. Rees, S. A. Macgregor and A. S. Weller, *Chem. Eur. J.*, 2010, **16**, 8376-8389.
25. R. N. Perutz and S. Sabo-Etienne, *Angew. Chem. Int. Ed.*, 2007, **46**, 2578-2592.
26. T. M. Douglas and A. S. Weller, *New J. Chem.*, 2008, **32**, 966-969.
27. T. Kappen, J. J. Bour, P. P. J. Schlebos, A. M. Roelofsen, J. G. M. Vanderlinden, J. J. Steggerda, M. A. Aubart, D. A. Krogstad, M. F. J. Schoondergang and L. H. Pignolet, *Inorg. Chem.*, 1993, **32**, 1074-1075.
28. A. R. Siedle and R. A. Newmark, *Organometallics*, 1989, **8**, 1442-1450.
29. N. J. Coville and L. Cheng, *J. Organomet. Chem.*, 1998, **571**, 149-169.
30. M. Oliván, A. V. Marchenko, J. N. Coalter and K. G. Caulton, *J. Am. Chem. Soc.*, 1997, **119**, 8389-8390.
31. M. C. Ball and J. M. Pope, *J. Chem. Soc. Dalton Trans.*, 1973, 1802-1804.
32. A. B. Chaplin, J. C. Green and A. S. Weller, *J. Am. Chem. Soc.*, 2011, **133**, 13162-13168.
33. O. Zenkina, M. Altman, G. Leitus, L. J. W. Shimon, R. Cohen and M. E. van der Boom, *Organometallics*, 2007, **26**, 4528-4534.
34. Y. Zhao, *The Journal of Physical Chemistry A*, 2013, **117**, 5664-5674.
35. D. Saha, R. Sen, T. Maity and S. Koner, *Langmuir*, 2013, **29**, 3140-3151.
36. A. B. Chaplin and A. S. Weller, *Eur. J. Inorg. Chem.*, 2010, 5124-5128.
37. J. Bauer, H. Braunschweig, A. Damme and K. Radacki, *Angew. Chem. Int. Ed.*, 2012, **51**, 10030-10033.
38. M. O'Neill, D. A. Addy, I. Riddlestone, M. Kelly, N. Phillips and S. Aldridge, *J. Am. Chem. Soc.*, 2011, **133**, 11500-11503.
39. S. D. Pike, R. J. Pawley, A. B. Chaplin, A. L. Thompson, J. A. Hooper, M. C. Willis and A. S. Weller, *Eur. J. Inorg. Chem.*, 2011, 5558-5565.
40. H. C. Johnson, A. P. M. Robertson, A. B. Chaplin, L. J. Sewell, A. L. Thompson, M. F. Haddow, I. Manners and A. S. Weller, *J. Am. Chem. Soc.*, 2011, **133**, 11076-11079.
41. V. Ryzhov, C.-N. Yang, S. J. Klippenstein and R. C. Dunbar, *Int. J. Mass spectrom.*, 1999, **185-187**, 913-923.
42. S. v. Moret, R. Dallanegra, A. B. Chaplin, T. M. Douglas, R. M. Hiney and A. S. Weller, *Inorg. Chim. Acta*, 2010, **363**, 574-580.
43. J. Powell, A. Lough and T. Saeed, *J. Chem. Soc. Dalton Trans.*, 1997, 4137-4138.
44. W. Baratta, C. Mealli, E. Herdtweck, A. Ienco, S. A. Mason and P. Rigo, *J. Am. Chem. Soc.*, 2004, **126**, 5549-5562.
45. X.-L. Luo, G. J. Kubas, C. J. Burns, R. J. Butcher and J. C. Bryan, *Inorg. Chem.*, 1995, **34**, 6538-6545.
46. E. Clot, O. Eisenstein, T. Dubé, J. W. Faller and R. H. Crabtree, *Organometallics*, 2002, **21**, 575-580.
47. J. N. Coalter, J. C. Huffman, W. E. Streib and K. G. Caulton, *Inorg. Chem.*, 2000, **39**, 3757-3764.
48. S. T. H. Willems, P. H. M. Budzelaar, N. N. P. Moonen, R. de Gelder, J. M. M. Smits and A. W. Gal, *Chem. Eur. J.*, 2002, **8**, 1310-1320.
49. P. S. Pregosin and R. W. Kunz, *^{31}P and ^{13}C NMR of Transition Metal Phosphine Complexes*, Springer-Verlag, 1979.
50. J. F. Hartwig, *OrganoTransition Metal Chemistry*, University Science Books, 2010.
51. http://sdbs.db.aist.go.jp, National Institute of Advanced Industrial Science and Technology, 2014.
52. A. D. Wilson, A. J. M. Miller, D. L. DuBois, J. A. Labinger and J. E. Bercaw, *Inorg. Chem.*, 2010, **49**, 3918-3926.
53. J. M. Brown and P. J. Guiry, *Inorg. Chim. Acta*, 1994, **220**, 249-259.
54. M. Brookhart, M. L. H. Green and G. Parkin, *Proc. Natl. Acad. Sci. U.S.A.*, 2007, **104**, 6908-6914.
55. R. J. Pawley, G. L. Moxham, R. Dallanegra, A. B. Chaplin, S. K. Brayshaw, A. S. Weller and M. C. Willis, *Organometallics*, 2010, **29**, 1717-1728.
56. J. H. Nelson, *Nuclear Magnetic Resonance Spectroscopy*, Pearson Education, Inc., 2003.
57. J. A. Iggo, *NMR Spectroscopy in Inorganic Chemistry*, Oxford University Press, 1999.
58. J. Liu, C. Jacob, K. J. Sheridan, F. Al-Mosule, B. T. Heaton, J. A. Iggo, M. Matthews, J. Pelletier, R. Whyman, J. F. Bickley and A. Steiner, *Dalton Trans.*, 2010, **39**, 7921-7935.
59. S. D. Pike and A. S. Weller, *Dalton Trans.*, 2013, **42**, 12832-12835.

CHAPTER 4
SOLID-STATE REACTIVITY WITH GASES

4.1. Introduction

4.1.i. Abundant gaseous reagents

Gaseous reagents derived from fossil fuel reserves can be used by the chemical industry as basic building blocks. Methane is a highly abundant natural product and typically is converted to syngas (CO and H_2) by controlled combustion and then coupled into longer chain hydrocarbons by the Fischer-Tropsch process.[1] Typically the Fischer-Tropsch process uses heterogeneous catalysts (ruthenium or cobalt metals, or iron oxide/carbide) and employs temperatures in the range of 423-573 K with elevated pressures. Unsaturated alkenes (ethene, propene, butenes and butadiene) are commonly used as synthetic building blocks because their C=C bonds can be functionalised. Alkenes can be produced by high-temperature cracking of longer chain hydrocarbons found in fossil fuels.[2, 3] Manipulation of abundant feedstock hydrocarbons often requires high energy input (e.g. cracking and Fischer Tropsch) and the development of low energy processes driven by transition metal catalysts would be hugely beneficial.

Recent technical advancements in hydraulic fracturing have allowed access to a vast reserve of shale gas around the world, especially in North America and China. Shale gas contains small hydrocarbons (such as methane) in large quantities. This will make utilisation of methane even more desirable in the future. Ethane is also abundant in shale gas and industrial plants for the conversion of ethane to ethene by cracking methods are planned to be built in the USA over the next 4 years.[4] These developments likely allow ethene to be used as a very cheap chemical feedstock in the future. Already ethene is produced in quantities greater than any other organic compound (141 million tonnes were produced in 2011).[5] Ethene is used for polymerisation, the production of fine chemicals and the production of ethanol.

A variety of reactions of gases with solid-state organometallic complexes have been reported including SC-SC transitions involving gas exchange.[6-8] *This topic is covered in more detail in Sections 1.3.ii & 1.3.iii*.

4.1.ii. Oligomerisation of gaseous alkenes

Polymerisation of short chain alkenes is useful in the production of plastic materials.[9] Oligomerisation reactions are also useful to upgrade short hydrocarbon units into longer trimers or tetramers, which are often useful feedstocks for chemical industry.[9] The tetramerisation of ethene to form 1-octene by $[Cr\{(Ph_2P)_2N^iPr\}]^+$ based catalysts is a useful reaction developed by Sasol [Scheme 4.1].[10-13] The cationic catalyst requires combination with a very weakly coordinating anion, such as $[Al(OC(CF_3)_3)_4]^-$, as more strongly coordinating anions promote the trimerisation which forms 1-hexene instead.[13] The mechanism for ethene oligomerisation is believed to occur *via* coordination of two ethene molecules to chromium (**XXIa**) which can then reductively couple, forming a metallacyclic complex (**XXIb**).[11, 14] The metallacycle can then grow by insertion of further ethene molecules (**XXIc** &**XXId**), before reductive elimination of a longer chain linear alkene.

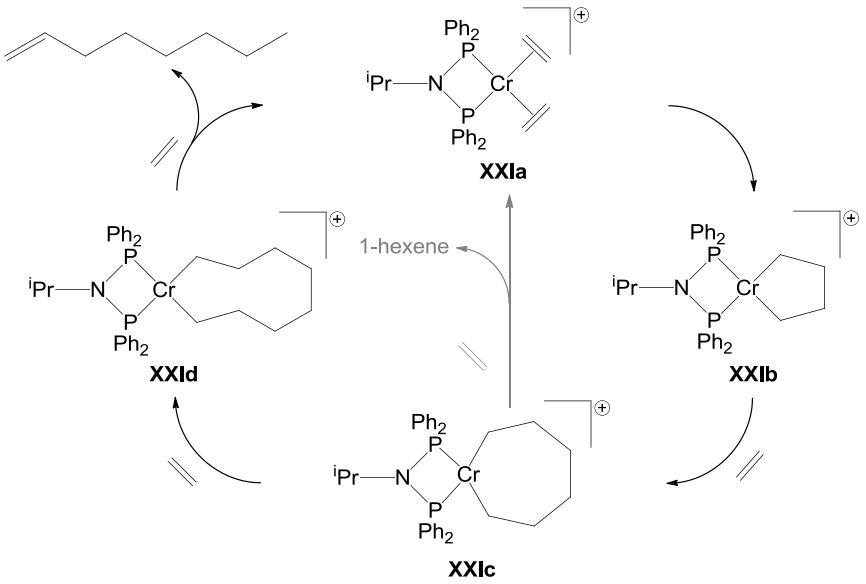

Scheme 4.1. Reported mechanism for the tetramerisation of ethene to form 1-octene using chromium catalysts coordinated to small bite angle chelating *bis*-phosphine ligands.[11] The side reaction to form 1-hexene is shown in grey.

4.1.iii. Activation of ammonia

N–H activation of ammonia is difficult due to the ability of ammonia to bind through its lone pair, which typically results in stable complexes that do not undergo further N–H reactivity. A rare example of N–H activation of ammonia has been demonstrated by Hartwig and co-workers using an

electron rich iridium pincer complex to form Ir($\kappa^3_{P,C,P}$-(^{t}Bu$_2$PCH$_2$CH$_2$)$_2$CH)(NH$_2$)(H), **XXIII** [Scheme 4.2(a)].[15] N–H activation was also observed by Turculet and co-workers using a similar iridium pincer complex to form Ir($\kappa^3_{P,Si,P}$-(2-Cy$_2$PC$_6$H$_4$)$_2$SiMe)(NH$_2$)(H), **XXV** [Scheme 4.2(b)].[16]

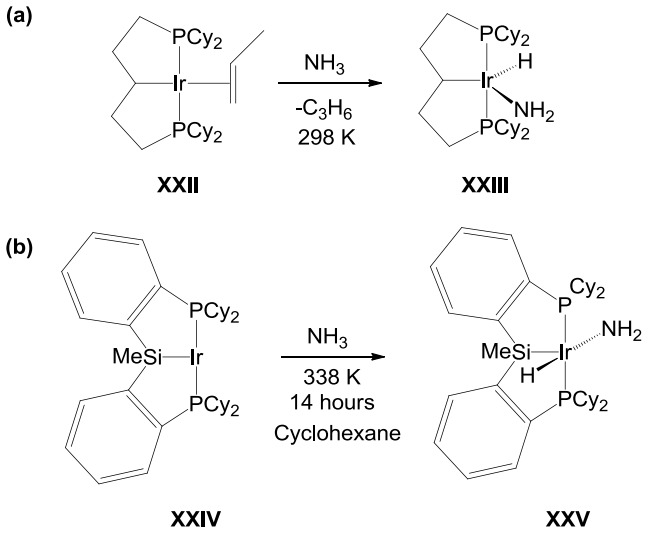

Scheme 4.2. N–H activation of ammonia using iridium pincer complexes; **(a)** Hartwig,[15] **(b)** Turculet.[16]

Access to amido complexes by reaction of methoxy complexes with ammonia has been demonstrated by Oro and co-workers.[17] In these reactions bridging [OMe]$^-$ ligands are protonated, presumably by NH$_3$, to leave bridging [NH$_2$]$^-$ units taking their place [Scheme 4.3]. The authors proposed that this transformation occurs *via* metal mediated N–H activation of ammonia.

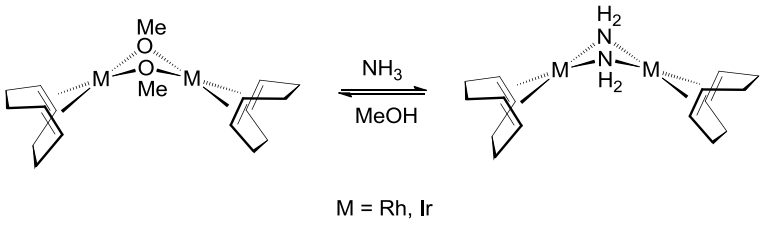

Scheme 4.3. Synthesis of amido-bridged complexes using ammonia.

Many simple reactions such hydroamination (addition of an N–H bond across a C=C bond), have not been realised using ammonia.[18, 19] Another problem with ammonia chemistry is the enhanced reactivity of many of the amine products, this makes controlled selective reactivity difficult.

Selective formation of primary amines from ammonia has been achieved by hydroaminomethylation using a biphasic system which utilises the different solubility properties of ammonia and the primary alkyl-amine product formed. Herwig, Beller and coworkers use a combination of water soluble rhodium and iridium catalysts to achieve the transformation (reaction carried out at 403 K and 120 bar syngas) [Scheme 4.4].

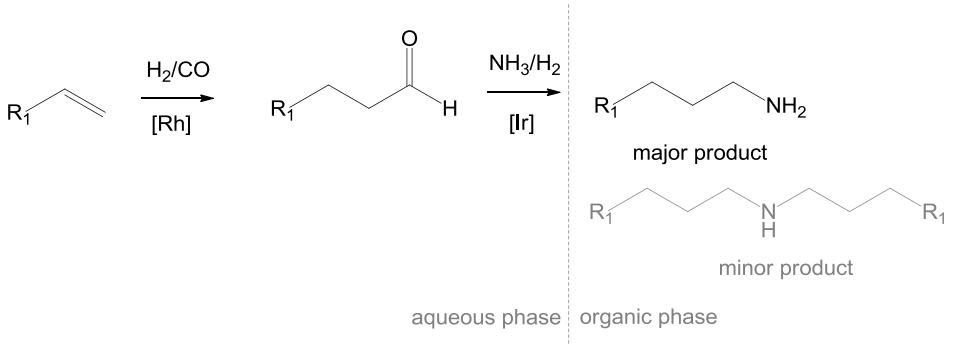

Scheme 4.4. Hydroaminomethylation using biphasic conditions to selectively produce the primary amine product.

Some other useful processes, such as catalytic allylic amination, have been developed using ammonia. The use of chiral ligands such as BINAP can allow the catalytic allylic amination reaction to become enantioselective [Scheme 4.5].[20]

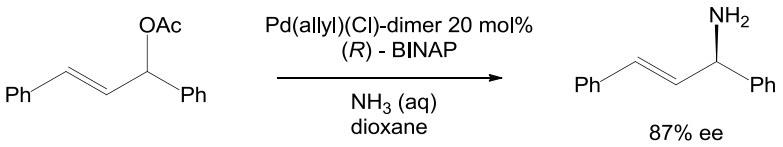

Scheme 4.5. Stereoselective catalytic allylic amination using an assymetric catalyst.

4.2. Synthesis and characterisation of rhodium complexes by solid/gas reactivity

Complexes **3** and **5** contain weakly bound ligands (η^6-$C_6H_4F_2$ & η^4-NBA respectively), which should be easily displaced, they are therefore useful precursors for synthesis of new compounds by solution (**3**) and solid-state (**5**) routes.

4.2.i. [Rh(^{i}Bu$_2$PCH$_2$CH$_2$P^{i}Bu$_2$)(CO)$_2$][BAr$^{F}_4$]

Addition of CO gas to a 1,2-$C_6H_4F_2$ solution of **3** forms the bright yellow carbonyl complex [Rh(^{i}Bu$_2$PCH$_2$CH$_2$P^{i}Bu$_2$)(CO)$_2$][BAr$^{F}_4$] **32** [Scheme 4.6]. Microcrystalline solid samples of freshly prepared **5** and **6** also react with CO gas to form slightly oily yellow solids (with displacement of oily NBA or NBE respectively and therefore not SC-SC transformations). These products were also characterised as **32** upon solvation in CD_2Cl_2 [Scheme 4.6].

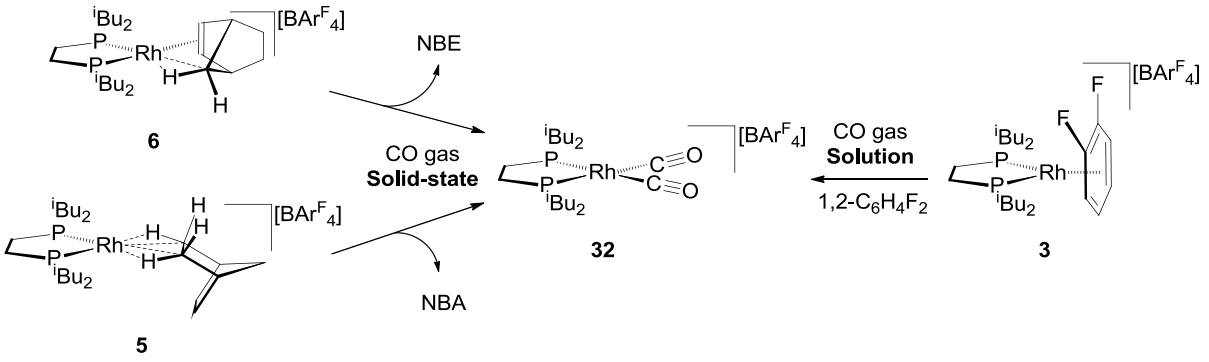

Scheme 4.6. Formation of carbonyl complex **32** in solution and the solid-state

The $^{31}P\{^{1}H\}$ NMR spectrum of **32** contains a doublet [δ 56.1, J_{RhP} 116 Hz] with a coupling constant which is small for a Rh(I) complex. This indicates that substantial electron donation from the strongly bound CO ligands (*trans* to phosphorus) to the metal centre is occurring. The analogous complex [*cis*-Rh(P^{i}Bu$_3$)$_2$(CO)$_2$][BAr$^{F}_4$] **XXVI** also exhibits a similar small coupling constant in its $^{31}P\{^{1}H\}$ NMR spectrum [J_{RhP} 115 Hz].[21]

CO binds strongly to transition metals utilising both σ donation and π back donation to form a stable complex.[22] The CO stretching frequencies in the IR spectra of **32** [Solution (CH_2Cl_2); 2093.4 and 2049.1 cm^{-1}, Solid-state; 2099.0 and 2056.9 cm^{-1}] confirm both the *cis* relationship (approximate C_{2v} symmetry) and back-bonding interaction. The CO stretches are located at lower energy than for free CO gas [free CO bond stretch: 2143 cm^{-1}], the reduction in stretching frequency is typical of a cationic transition metal carbonyl complex.[23] The back-bonding interaction appears weaker in **32** than in **XXVI** (**XXVI** Solution (CH_2Cl_2); 2015.5 & 1988.3 cm^{-1}) possibly indicating that optimal π-orbital overlap is restricted due to the small bite angle phosphine [Figure 4.1].[21]

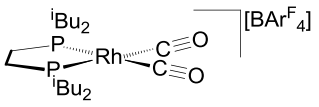

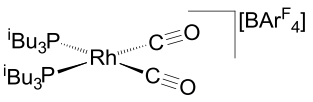

	32	**XXVI**
CO stretch (cm^{-1}):	2093.4 & 2049.1	2015.5 & 1988.3
J_{RhP} (Hz):	116	115
Bite angle(°)	83.2	estimated ~95*

Figure 4.1. Comparison of rhodium *bis*-phosphine *bis*-carbonyl complexes.*Bite angle estimated to be consistent with the reported solid-state structure of [*cis*-Rh(P^iBu_3)$_2$(η^6-C_6H_5F)$_2$][BAr^F_4].[24]

A solid-state structure of **32** was determined by X-ray crystallography. The structure was solved in the monoclinic *C* 2 space group [unit cell: **a**, 19.2382(17) Å; **b**, 16.0729(5) Å; **c**, 13.6017(12) Å, **β**, 134.960(16)°; volume, 2976.0(9) $Å^3$] [Figure 4.2(a)]. Whilst the anions refined well, the cation was disordered over two positions. One position is inverted with respect to the other and the RhP_2 planes intersect at 90° [Figure 4.2(c)]. Each disorder component was modelled at 50% occupancy, but could be reliably refined [R = 6.6%]. Both rhodium positions fall upon a symmetry axis so that only half of each cationic disorder component need be modelled. The ^{i}Bu groups of both disorder components overlap and so similarity restraints were used to maintain sensible geometries. The calculated solid-state CO bond lengths for **32** are slightly shorter [calculated 1.056(14) Å & 1.067(14) Å] than for free CO molecules [C≡O 1.12 Å].[25] This is in contrast to the IR spectra of **32** and related *cis*-{$Rh(CO)_2(P)_2$} (*P* = phosphine) complexes which predict an extension of the CO bond length.[26-29] We therefore present an approximate solid-state structure of **32** and suggest that accurate discussion of bond lengths and angles is not appropriate for this disordered structure. The anions form a *pseudo*-octahedral geometry around the cation in the packing structure similar to the structure of **1** [Figure 4.2(b)].

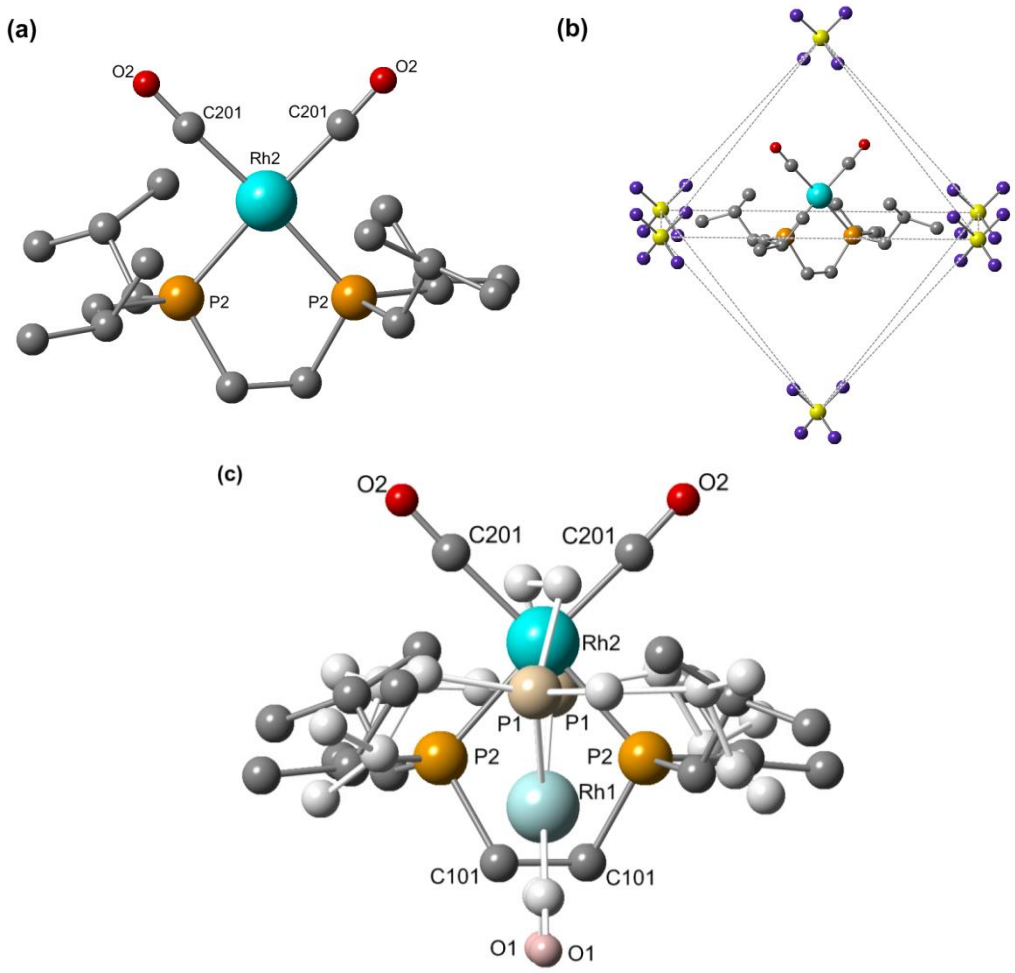

Figure 4.2. (a) Ball and stick diagram for one disorder component of the cation of **32** in the solid-state. Hydrogen atoms and anion omitted for clarity. **(b)** Crystal packing diagram of **32** showing anions forming a *pseudo*-octahedron around the cation. Anion represented by BC_4 units (aryl groups omitted) and hydrogens omitted for clarity. **(c)** Ball and stick disorder diagram displaying both disorder components of the cation overlaid, with the atoms and bonds of the second component paled. Hydrogen atoms and anion omitted for clarity.

4.2.ii. [Rh(^{i}Bu$_2$PCH$_2$CH$_2$P^{i}Bu$_2$)(η^4-C$_4$H$_6$)$_2$][BAr$^F{}_4$]

The dark claret butadiene complex [Rh(^{i}Bu$_2$PCH$_2$CH$_2$P^{i}Bu$_2$)(η^4-1,3-C$_4$H$_6$)][BAr$^F{}_4$] **9** can be synthesised by addition of 1,3-butadiene gas to a 1,2-C$_6$H$_4$F$_2$ solution of **3** or a freshly prepared solid sample of **5** (in which case an oily amorphous product forms alongside NBA, *i.e.* not a SC-SC transition) [Scheme 4.7]. Both reaction routes are rapid (colour change occurs within one minute). Recrystallisation is achieved in 1,2-C$_6$H$_4$F$_2$/pentane under an atmosphere of butadiene. Although **9** is stable when solvated in 1,2-C$_6$H$_4$F$_2$ under argon, application of a vacuum to the solution drives the back reaction to re-form **3**. In contrast, the complex is vacuum stable in the solid-state.

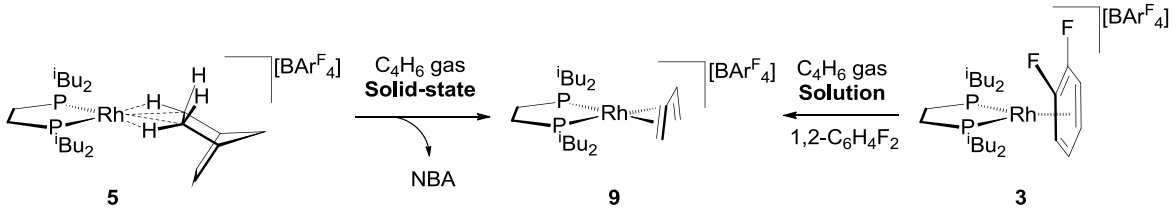

Scheme 4.7. Synthesis of **9** in solution and the solid-state.

A solid sample of anion-bound complex **4** reacts only very slowly with 1,3-butadiene gas with approximately 8% conversion to **9** over four days (by analysis of the $^{31}P\{^1H\}$ NMR spectrum of the products once solvated).

1,3-butadiene is a commonly used ligand in organometallic chemistry and rhodium phosphine complexes coordinated to 1,3-butadiene have been previously reported.[30] The ^1H NMR spectrum (CD_2Cl_2) of **9** reveals three peaks [δ 2.85, 4.27 & 5.44] attributed to the diene, which occur upfield in comparison to the ^1H NMR signals of free 1,3-C_4H_6 [δ (CCl_4) 5.03, 5.14 & 6.27],[31] indicative of interaction with a metal centre. The $^{31}P\{^1H\}$ NMR spectrum shows a doublet [δ 54.6, J_{RhP} 170 Hz]. ESI-MS and elemental micro-analysis confirm the composition of the complex. Both the ^1H and $^{31}P\{^1H\}$ NMR spectra are similar to those of previously reported analogous complex [Rh(^{i}Pr$_2$PCH$_2$CH$_2$CH$_2$P^{i}Pr$_2$)(η^4-1,3-C_4H_6)$_2$][CF_3SO_3] [^1H NMR spectrum (1,3-butadiene signals), δ 2.75, 4.34, 5.50; $^{31}P\{^1H\}$ NMR spectrum, δ 30.0, J_{RhP} 165 Hz].[30]

X-ray crystallographic analysis of dark claret single crystals of **9** revealed significant cation disorder within a well defined octahedron of [BAr$^F_4$]$^-$ anions [Figure 4.3]. The structure could be refined in the monoclinic *C* 2 space group with a unit cell which is very similar to that of **32** [unit cell **9**: **a**, 19.0002(4) Å; **b**, 16.61810(10) Å; **c**, 13.4375(3) Å; **β**, 135.006(4)°; volume, 2999.8(2) Å^3]. The cation is disordered over four positions, two of which are inverted with respect to the other two [Figure 4.3(c) & (d)]. Two rhodium positions are located both upon a symmetry axis so that only half of the cationic disorder components need be modelled. The RhP_2 planes are approximately parallel or intersect at 90 [angles between RhP_2 planes (°): 0 (±3) or 90 (±4)]. Whilst the two rhodium positions refine to 50% occupancy each, the four phosphine (& butadiene) positions are split into groups with refined occupancies of 35%, 34%, 16% and 15%. Due to the extended overlapping disorder only an approximate solution can be obtained using similarity restraints to maintain sensible geometries for

the ^{i}Bu, butadiene and phosphine backbone groups. The ^{i}Bu and butadiene groups of the two smallest disorder component could not be resolved. The $[BAr^{F}_{4}]^{-}$ anions form an octahedron around the disordered cation [Figure 4.3(b)]. The extensive disorder may be present because the cation is approximately spherical and sits within a high symmetry pocket.

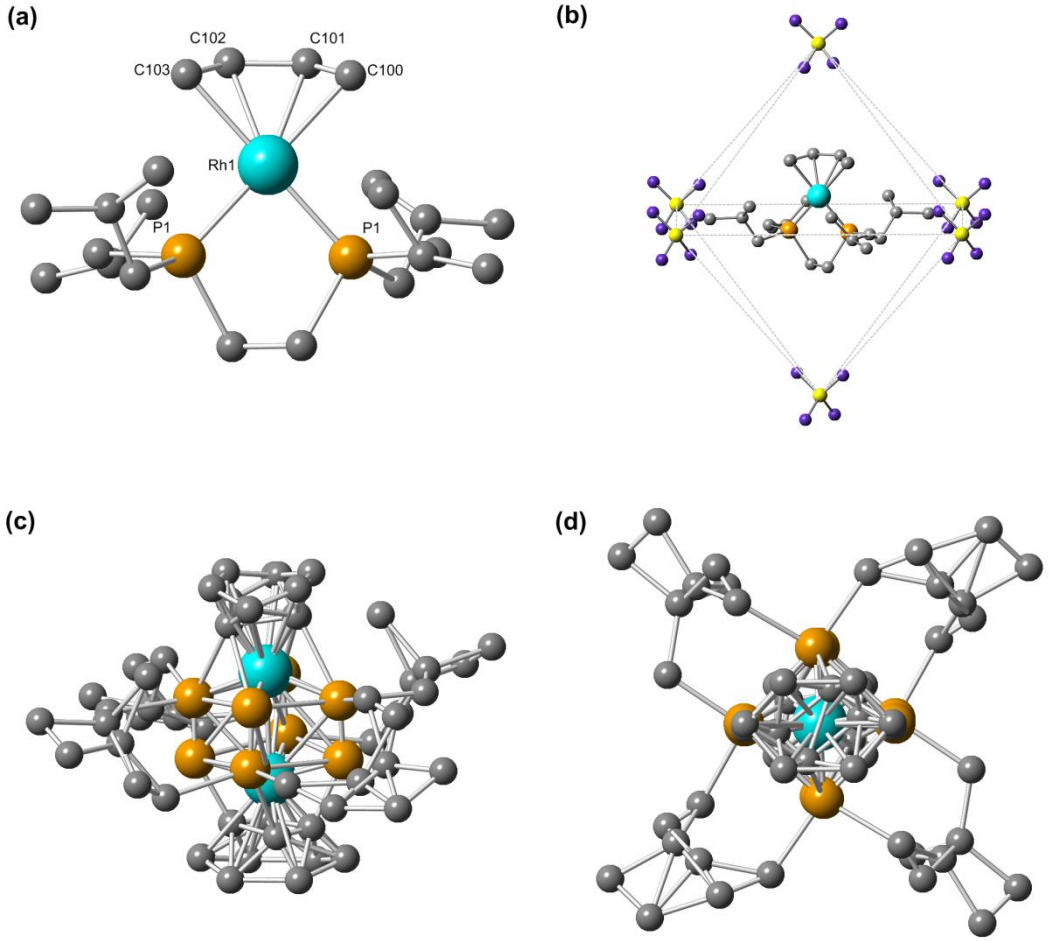

Figure 4.3. (a) Ball and stick diagram for one disorder component of the cation of **9** in the solid-state. Hydrogen atoms and anion omitted for clarity. **(b)** Crystal packing diagram of **9** showing anions forming a *pseudo*-octahedron around the cation. Anion represented by BC_4 units (aryl groups omitted) and hydrogens omitted for clarity. **(c & d)** Ball and stick disorder diagrams displaying the four disorder components of the cation overlaid (*N.B.* ^{i}Bu and butadiene groups of two smallest disorder components could not be resolved). Hydrogen atoms and anion omitted for clarity.

4.2.iii. $[Rh(^{i}Bu_2PCH_2CH_2P^{i}Bu_2)(\eta^2\text{-}C_2H_4)_2][BAr^{F}_{4}]$

Addition of ethene gas to freshly prepared solid **5** forms a red oily compound assigned as $[Rh(^{i}Bu_2PCH_2CH_2P^{i}Bu_2)(\eta^2\text{-}C_2H_4)_2][BAr^{F}_{4}]$, **10**, [Scheme 4.8]. Pure crystalline material can be

generated by recrystallising the resulting red oily product in CH_2Cl_2/pentane whilst continually keeping the flask under 1 atm of ethene. The complex is not stable in solution (CH_2Cl_2) or suspended in pentane at room temperature in the absence of an ethene atmosphere, as decomposition to **4** occurs [Scheme 4.8]. However solid **10** is stable to vacuum, confirmed by elemental micro-analysis of a crystalline sample, indicating a greater stability in the solid-state.

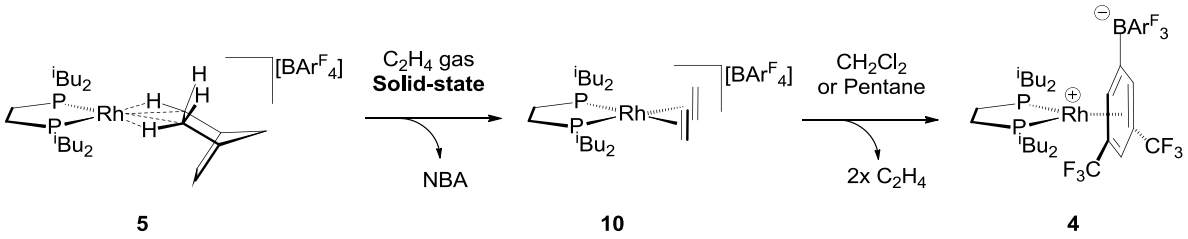

5 **10** **4**

Scheme 4.8. Formation of **10** in the solid-state and decomposition in solution.

10 can only be characterised in solution when under an ethene atmosphere or at low temperatures. The ^{1}H NMR spectrum at 240 K (achieved by distillation of CD_2Cl_2 onto a frozen sample of **10**) reveals a sharp signal for coordinated ethene [δ 3.98, FWHM 7 Hz]. If this sample is warmed the coordinated ethene signal broadens but also loses intensity as **10** decomposes to form **4**. The $^{31}P\{^{1}H\}$ NMR spectrum at 240 K contains a doublet signal [δ 54.7, J_{RhP} 144 Hz] alongside a minor peak corresponding to **4**, upon warming this minor peak becomes the major signal. The J_{RhP} coupling constant of **10** is similar to **1**, as a similar $\eta^2\eta^2$-coordination mode is in place. At room temperature under four atmospheres of ethene the doublet signal assigned to **10** is observed as the only species in the $^{31}P\{^{1}H\}$ NMR spectrum. The ^{1}H spectrum recorded under four atmospheres of ethene includes a broad signal for ethene at the chemical shift expected for dissolved free ethene [δ 5.31, FWHM 49 Hz] and no separate peak is observed for coordinated ethene, this suggests rapid exchange between coordinated and free ethene is occurring under these conditions.

X-ray diffraction analysis of high quality vermillion single crystals of **10** generated a solid-state structure which shows significant cation disorder. The structure solved in the *C* 2/c space group with a unit cell which has similar **a** and **b** axes to those of **32** and **10** but a different **c** axis and **β** angle [Unit cell: **a**, 19.1357(2) Å; **b**, 16.3613(2) Å; **c**, 38.2121(5) Å; **β**, 91.7612(9)°; volume, 11958.0(2) $Å^3$]. The phosphine is disordered over two positions with an approximate 2:1 ratio of occupancies. In order to maintain a square planar arrangement the ethene ligands are also disordered. The structure was refined

using restraints to make the disorder components behave similarly to each other, the final R-factor was < 12%. Unfortunately the disorder restricts accurate bond length analysis and an approximate ball and stick diagram is presented in Figure 4.4(a). The P(1)-Rh(1)-P(2) and P(3)-Rh(1)-P(4) planes are roughly perpendicular [angle between planes: 81°]. The ethene ligands sit near to perpendicular to the RhP_2 plane rather than in a planar geometry [angle between planes: P(1)-Rh(1)-P(2) and C(28)-Rh(1)-C(29)/C(30)-Rh(1)-C(31): 111°/ 122°] The ethene ligands sit slightly twisted rather than exactly perpendicular to the RhP_2 plane, this geometry has been previously reported by Budzelaar and co-workers and is expected to allow the ethene hydrogens to avoid steric clashes [Figure 4.4(c)].[32] The anions define an octahedral environment around the cation [Figure 4.4(b)].

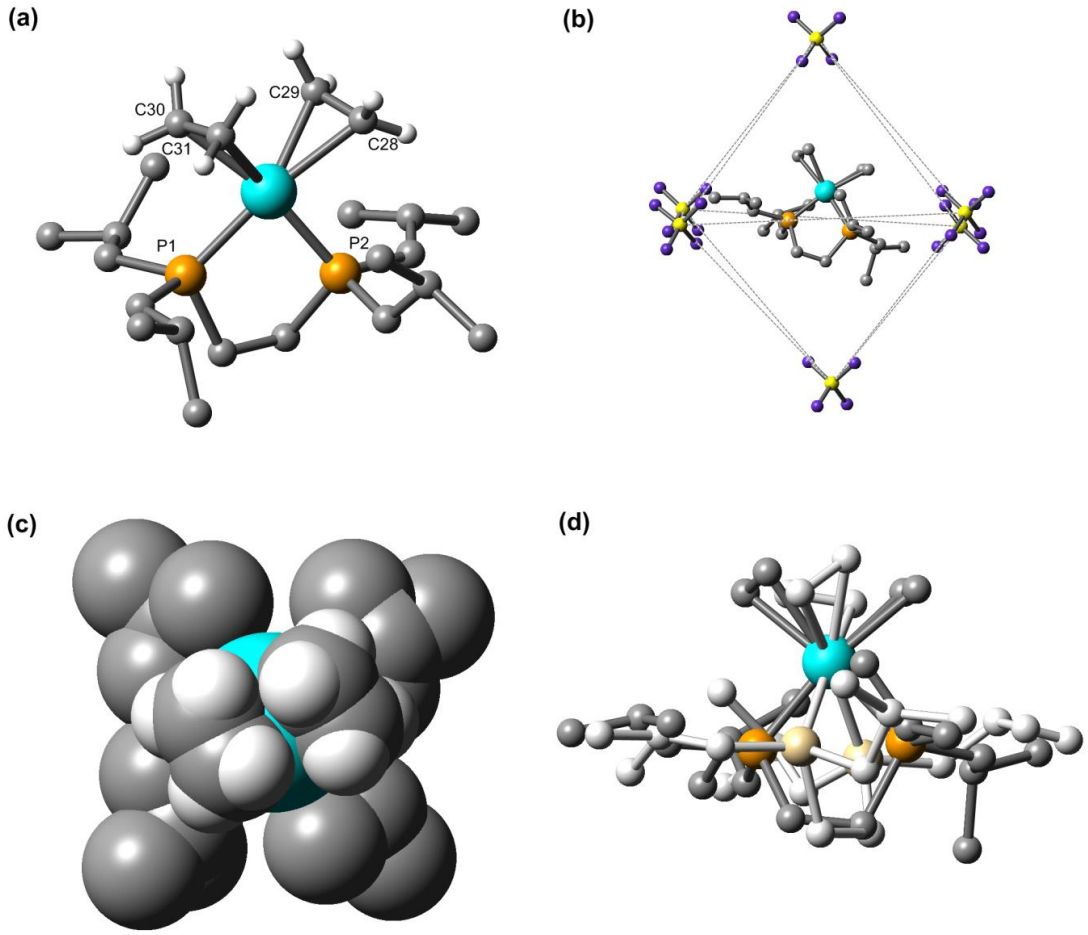

Figure 4.4. (a) Ball and stick diagram of the solid-state structure of the major disorder component of **10**, all but ethene hydrogens omitted. **(b)** Packing diagram of **10** with minor disorder component overlaid (transparent) enclosed within a *pseudo*-octahedron of anions, hydrogen atoms omitted and $[BAr^F{}_4]^-$ anions represented as BC_4 units (Ar^F groups omitted) for clarity. **(c)** Space filling diagram showing the cation of **10** from above the ethene ligands, only ethene hydrogen atoms shown. **(d)** Disorder diagram showing both cationic disorder components, hydrogen atoms and anions omitted for clarity (minor disorder component in pale colours).

Ethene gas does not react with **6** and **4** in the solid-state as confirmed by a lack of colour change and subsequent solution NMR spectroscopy analysis. However, in solution **6** & **4** both convert to orange **10** if maintained under an atmosphere of ethene.

Microcrystalline samples of **10** change colour from vermillion to claret over several weeks, solvation of this claret species indicated the formation of butadiene complex **9** in the solid-state by a reductive dehydrocoupling reaction (*see Section 4.4*).

4.2.iv. $[Rh(^{i}Bu_2PCH_2CH_2P^{i}Bu_2)(NH_3)_2][BAr^{F}_4]$

The ammonia complex $[Rh(^{i}Bu_2PCH_2CH_2P^{i}Bu_2)(NH_3)_2][BAr^{F}_4]$ **33** can be synthesised by the addition of a mixture of H_2 (~4 atm) and NH_3 (1 atm) gases to solid **1** [Scheme 4.9]. Freshly prepared **5** is also a suitable precursor and reacts with NH_3 gas to form **33** although some **4** can be formed as a by-product by this method. Direct solution methods (1,2-$C_6H_4F_2$) were unsuccessful for the synthesis of **33** (decomposition of the organometallic species occurs instead).

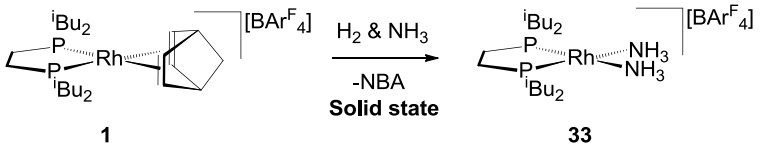

Scheme 4.9. Solid-state synthesis of ammonia complex **33**

The $^{31}P\{^{1}H\}$ NMR spectrum of **33** solvated in 1,2-$C_6H_4F_2$ displays a doublet [δ 65.5, J_{RhP} 177 Hz] with a relatively large coupling constant. This spectral data is very similar to data collected by Leitner, Brown and Brunner [δ (MeOH) 76, J_{RhP} 176 Hz] who proposed a cation of the form $[Rh(Ph_2PCH_2CH_2PPh_2)(NH_3)_2]^{+}$ which they formed by addition of $[HCO_2][NH_4]$ to $[Rh(Ph_2PCH_2CH_2PPh_2)(MeOH_2)_2]$.[33] **33** is not stable in CH_2Cl_2 and reacts to cleanly form an unidentified product with a different $^{31}P\{^{1}H\}$ NMR signal with a much smaller J_{RhP} coupling constant [δ 59.9, J_{RhP} 121 Hz]. This is possibly due to a reaction which forms a Rh(III) species. An unidentified white species also precipitates from CH_2Cl_2 solutions, possibly $[NH_4]Cl$.

33 was therefore characterised in 1,2-$C_6H_4F_2$, the ^{1}H NMR spectrum contains a sharp peak [δ 1.93] assigned to the coordinated ammine ligands. The chemical shift of ammine ligands is dependent upon

hydrogen-bonding interactions with solvent or anion {[$Pt(PPh_3)_2(NH_3)_2$][X]$_2$: $\delta_{(NH3)}$ ($CDCl_3$) 3.15 ([X]$^-$ = [PF_6]$^-$), 4.28 ([X]$^-$ = [NO_3]$^-$); [$Pt(Ph_2PCH_2CH_2PPh_2)(NH_3)_2$][$PF_6$]$_2$: $\delta_{(NH3)}$ (d_6–acetone) 4.6}.[34] In the case of **33** with a weakly coordinating anion and weakly coordinating solvent the chemical shift observed is upfield of other reported values.

ESI-MS experiments were unsuccessful in determining the cation but the composition was confirmed by C, H and N elemental micro-analysis.

33 can be recrystallised in 1,2-$C_6H_4F_2$/pentane solutions and single crystals were formed, which were suitable for X-ray diffraction. The solid-state structure is solved in the *C* 2/c space group and is well ordered, in contrast to the disordered structures of **9**, **10** and **32**. The [BAr^F_4]$^-$ anions do not form a well defined octahedron around the cation in **33**, instead a distorted octahedron of [BAr^F_4]$^-$ anions is found [Figure 4.5(b)]. This structure may be influenced by hydrogen bonding between the ammine ligands and CF_3 groups upon the anion. Fairly short H···F distances are located in the lattice structure [N(1)···F(190), 3.295(8) Å (H···F, 2.51 Å)].[35] Examples of hydrogen bonding in the crystal structures of ammonia complexes have been recorded, often between N–H and an oxygen atom acceptor. Reported N···O values for related systems vary from 2.84-3.19 Å (H···O, 2.00-2.37 Å).[34, 36]

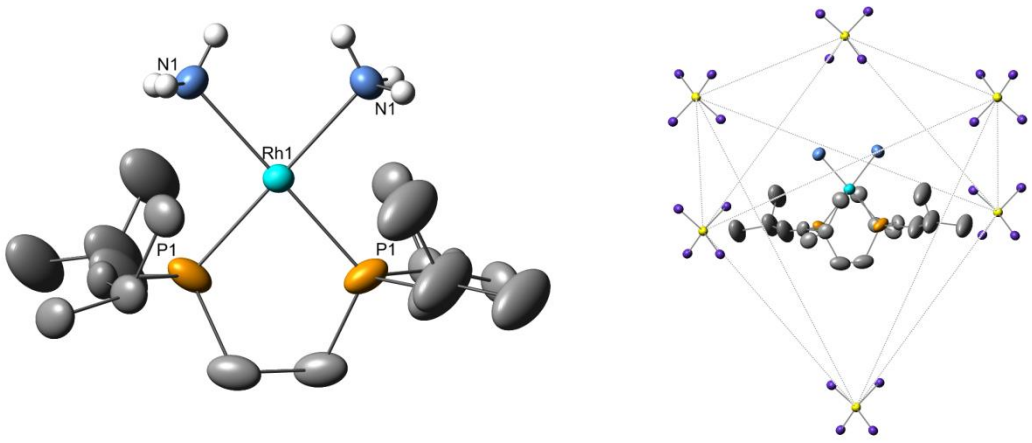

Figure 4.5. (a) Displacement ellipsoid plot (30% probability) for the cation of **33** in the solid-state. Hydrogen atoms except those on ammine ligands and anion omitted for clarity. **(b)** Crystal packing diagram of **33**, anion represented by BC_4 units (aryl groups omitted) and hydrogen atoms omitted for clarity. Selected bond length (Å) and angle (º) data: Rh(1)–P(1), 2.2028(14); Rh(1)–N(1), 2.181(4); P(1)–Rh(1)–P(1'), 84.07(6); N(1)-Rh(1)-N(1'), 84.79(16).

Related square planar rhodium(I) complexes containing ammine ligands have been structurally charactersied such as [$Rh(PPh_3)_3NH_3$][ClO_4], **XXVII** [37] and [Rh(COD)$(NH_3)_2$][PF_6] **XXVIII**, [36]

although none structurally characterised with chelating phosphine ligands. A square planar Pt(II) complex $[Pt(PPh_3)_2(NH_3)_2][NO_3]_2$, **XXIX**, with two ammine ligands has also been reported.[34] The Rh–N bond length of **33** [2.181(4) Å] is similar to reported ammonia complexes [**XXVII**, 2.14(1) Å; **XXVIII**, 2.12(1) Å].[36, 37]

4.3. Solid/Gas ligand exchange reactions

9 is a useful precursor compound because, similar to **1**, hydrogenation will release an inert alkane fragment and a reactive metal site. However, unlike NBA, the released butane is a gas and so by application of vacuum no alkane impurities are left in the product, allowing solvent-less synthesis of pure compounds and the possibility of SC-SC transitions.

The reaction of **9** with hydrogen in the absence of another reagent forms pure **4** with loss of crystallinity (*see Section 2.3.iv*). However if CO is mixed with H_2 and added to **9** then **32** is produced in an amorphous form (determined amorphous by visual inspection of the solid) [Scheme 4.10]. The reaction is rapid and butane is observed in the gas phase NMR spectra of the headspace [δ 0.94 & 1.35].

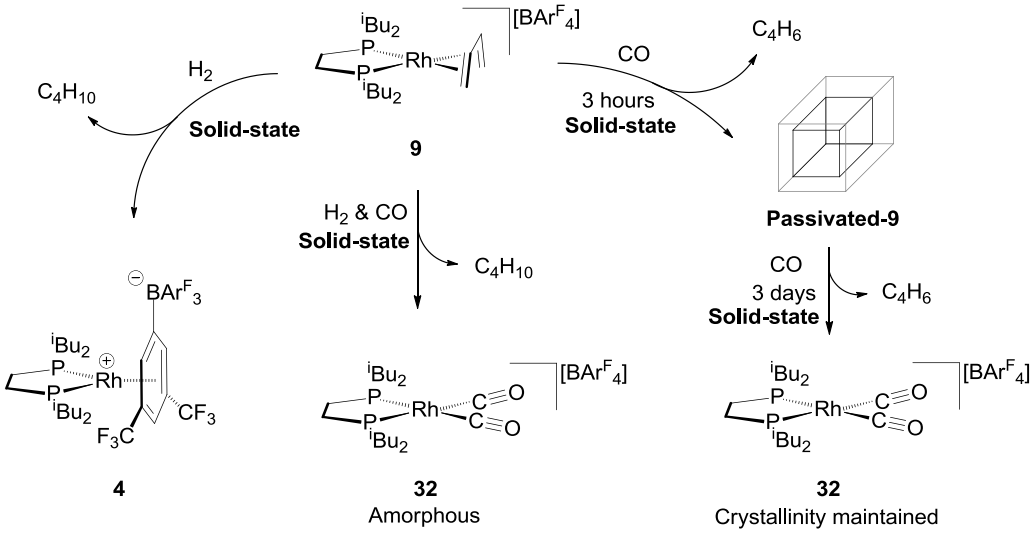

Scheme 4.10. Reactivity of **9** with H_2 and CO in the solid-state

In order to maintain crystallinity more gentle reaction conditions are required. Addition of CO gas to solid **9** in an NMR tube results in a claret to yellow colour change as butadiene is displaced directly

without the need for hydrogenation. Gas phase NMR spectroscopy of the headspace of the NMR tube reveals free butadiene gas [δ 4.98, 5.11 & 6.34].[38] Dark claret crystals of **9** were exposed to 1 atm of CO gas for 3 days to produce bright yellow crystals of **32**, which appear intact when viewed under a microscope [Scheme 4.10 & Scheme 4.11]. The crystals also retain their properties of rotating polarised light, which often indicates single crystallinity. A unit cell was collected for a yellow crystal which had been under an atmosphere of CO for one week. The unit cell dimensions [**a**, 19.238(5) Å; **b**, 16.047(2) Å; **c**, 13.590(4) Å; **β**, 134.99(5)°] resemble the unit cell of **32** [Table 4.1], unfortunately the dataset was not able to be solved, possibly due to the disorder which would likely be present (*see solid-state structure of* ***9***).

Complex	**a** (Å)	**b** (Å)	**c** (Å)	**β** (°)	Volume (Å^3)
9	19.0002(4)	16.61810(10)	13.4375(3)	135.006(4)	2999.8(2)
32	19.2382(17)	16.0729(5)	13.6017(12)	134.960(16)	2976.0(9)
9 + CO to form **32**	19.238(5)	16.047(2)	13.590(4)	134.99(5)	2967.2(9)

Table 4.1. Unit cell dimensions of **9**, **32** and the product of the reaction of a single crystal of **9** with CO gas.

The unit cells of **9** and **32** are very similar and a percentage volume change of −0.8% would be required upon transition between them, well within the range of previously reported SC-SC transitions (*see Section 1.3.iii, Table 1.1*). It is noteworthy that for a SC-SC transition to occur not only must CO penetrate the crystal lattice but the bulkier butadiene gas must be able to escape. This suggests porosity within the crystalline network. Brookhart suggests disordered channels of co-crystallised solvent are responsible for the porosity in his examples of SC-SC transitions, however in our case no co-crystallised solvent is present.[7] Analysis of the approximate solid-state structure of **9** (full disorder model) using CrystalExplorer [39, 40] shows that a series of voids are present in the unit cell, many of which are interconnected. The percentage void volume is calculated to be 7% (using full disorder model). The structure of **32** was also similarly analysed and showed a percentage void volume of 8% (using full disorder model). This suggests that, upon a SC-SC transition from **9** to **32**, the internal void-space is not greatly affected.

The packing structure of anions around the cations in both **9** and **32** are very similar suggesting that the crystal lattice defined by the anions does not require very much change upon transition between the two complexes [Figure 4.6 & Table 4.2].

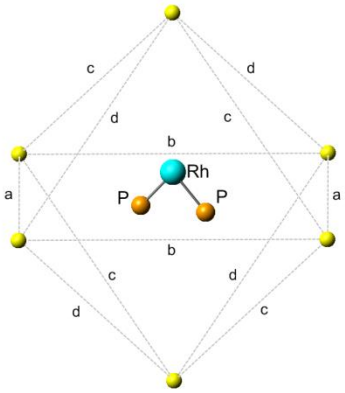

Figure 4.6. Diagram displaying the edges of the octahedron formed by the boron atoms of $[BAr^{F}_{4}]^{-}$ anions surrounding the cations in **9** and **32**. The major disorder component of the cation adopts the RhP_2 position shown.

Complex	a (Å)	b (Å)	c (Å)	d (Å)
9	13.435(3)	13.44(5)	12.621(5)	12.622(29)
32	13.61(22)	13.602(1)	12.54(12)	12.534(6)
% change	+1.3%	+1.2%	−0.6%	−0.7%

Table 4.2. B···B distances around the packing structure defined octahedrons of **9** and **32**.

The highly disordered solid-state structure of **9** suggests that the cation can adopt multiple positions within the surrounding octahedral cage of anions. Cation mobility inside the crystalline lattice has been discussed in *Section 2.2.viii* and similar flexibility of the cation is envisaged here within a defined anion lattice structure.

The **9** to **32** SC-SC transition begins from the surface of a crystal downwards and a clear yellow coating around the edges of the crystals is observed after 3 hours under one atm of CO gas. The depth of the yellow layer appears uniform across all faces and along all cracks of each crystal and independent of the overall size of the crystal [Scheme 4.11]. This observation is consistent with Kaupp's concept of "phase rebuilding" in solid-state transitions in which the crystal faces determine the direction of reaction.[41]

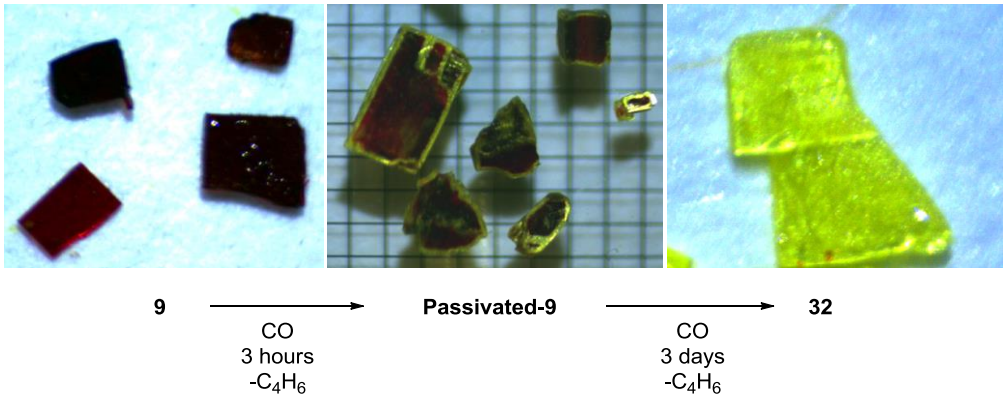

Scheme 4.11. Microscope pictures of single crystals of **9**, **Passivated-9** and **32**

The gas transfer reaction can be stopped by evacuation of the headspace before full conversion, this results in crystals with yellow **32** faces and a claret interior of **9** [Figure 4.7]. Since the CO complex is expected to be stable to further reactions this presents an interesting opportunity for exploring reactivity of the interior of a crystal. Brookhart and co-workers also used single crystals coated in a layer of carbonyl complex and termed these "passivated crystals", crystals of **9** with an outside layer of **32** will therefore be called **Passivated-9**.[7]

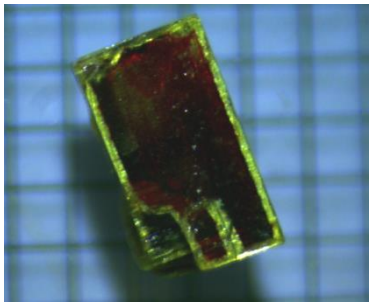

Figure 4.7. A microscope photo of a single crystal of **Passivated-9** after reaction with CO gas after 3 hours, the gradations in the background are 0.5 mm and allow approximate measurement of the depth of the **32** layer (0.075 mm). *N.B.* the top and bottom faces of the crystal are also coated in a thin yellow layer, however this is transparent enough for the red interior to be viewed from above.

A sample of **Passivated-9** was ground down and analysed by $^{31}P\{^{1}H\}$ SSNMR spectroscopy. In comparison to the SSNMR spectra of pure **32** and **9** this confirmed that a mixture of **32** and **9** was present in **Passivated-9** (approximate 1:1 ratio of complexes, but variable crystal sizes used).

Addition of H_2 gas to **Passivated-9** results in conversion of the interior of the crystal to **4** whilst the exterior **32** layer remains unchanged (by colour change and subsequent solution $^{31}P\{^{1}H\}$ NMR spectroscopy), however, this transition degrades the crystallinity of the sample. The crystals appear to

explode like popcorn kernels when viewed under the microscope as internal reorganisation is required to form **4**. However, defined crystalline domains of **32** are maintained [Figure 4.8].

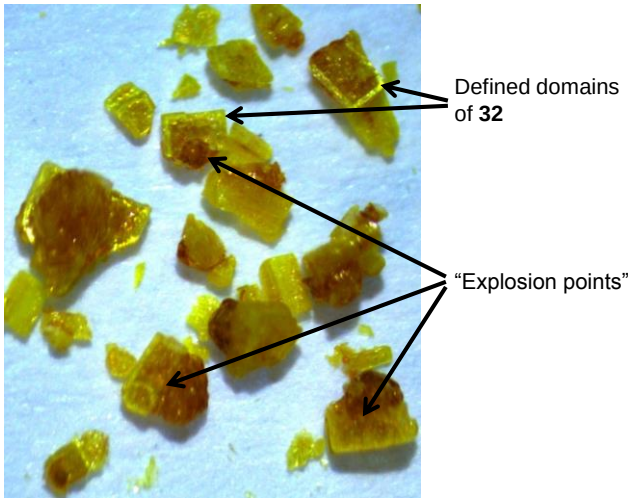

Figure 4.8. Crystals of **Passivated-9** after exposure to H_2 gas. Note the "explosions" which occur through one face of a crystal during loss of crystallinity, and also the defined yellow domains of **32** which are unaffected by the reaction (clear examples marked with arrows).

10 also reacts with CO gas to form **32** [Scheme 4.12]. This ligand displacement reaction occurs more rapidly with **10** than with **9**. Vermillion single crystals of **10** completely change colour to yellow in ~3 hours, perhaps as a function of the lower binding affinity of ethene compared to butadiene. These crystals also maintain their ability to rotate polarised light and diffract with a single pattern. Unfortunately, X-ray diffraction datasets of the products of this transition could not be solved, probably due to disorder within the final structure. It is noteworthy that the solid-state structure of **10** (space group *C* 2/c) is of lower symmetry than those of **9** and **32** (space group *C* 2); therefore a greater structural reorganisation may be required for a SC-SC transition from **10** to **32** to occur. Clear interconnected voids run through the structure of **10** (as calculated in Crystal Explorer)[39, 40] and the percentage void volume is calculated to be 9%.

9 also reacts with NH_3 gas to form **33** with the release of butadiene gas (observed by gas phase NMR spectroscopy of the headspace) [Scheme 4.12]. However in this case the product is observed to be in an amorphous form without the ability to rotate polarised light. This is likely to be caused by the formation of H···F hydrogen bonding interactions in **33** which distort the lattice structure and destroy the crystallinity. SC-SC transitions commonly occur only when the change in dimensions of the unit cell is small (*see Section 1.3.iii*). For the transition of **9** to **33** the percentage volume change required

is −2.7% (using half the unit cell volume for **33** in order to keep *z* consistent). Whilst this falls within the range of reported SC-SC transitions, the distribution of the anions which allow hydrogen bonding must require substantial molecular rearrangement. The reaction takes place rapidly and small crystals change colour entirely within one hour, the fast reactivity may be because the crystal loses definition and its surface area greatly increases as it becomes amorphous and full of micro-cracks. This concept was previously reported by Caulton and co-workers (*see Section 1.3.i*).[42]

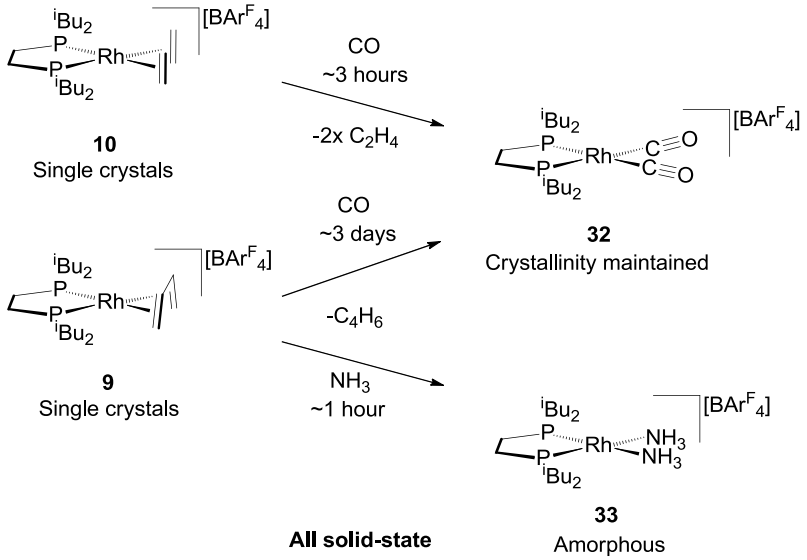

Scheme 4.12. Gas transfer reactions in the solid-state.

4.4. Dehydrocoupling of ethene in the solid-state

Microcrystalline samples of vermillion **10** slowly change colour to claret over several weeks. When this final product is solvated in 1,2-$C_6H_4F_2$ **9** is observed in the $^{31}P\{^1H\}$ NMR spectrum (and confirmed by ESI-MS) alongside **3** (which would form if **10** is dissolved in 1,2-$C_6H_4F_2$) [Scheme 4.13]. A batch of microcrystalline **10** was kept inside the glove-box and samples were dissolved periodically for NMR spectroscopy analysis, this showed a gradual increase in the amount of **9** present, approaching 50% conversion after 7 weeks [Figure 4.9]. The data collected suggests an induction period may occur, however, the low accuracy of integration of the $^{31}P\{^1H\}$ NMR spectra especially close to the baseline restricts accurate analysis. A sample kept for four months revealed 53% conversion to **9** (alongside **3** in 1,2-$C_6H_4F_2$ solution) suggesting that ~50% is the maximum yield of conversion.

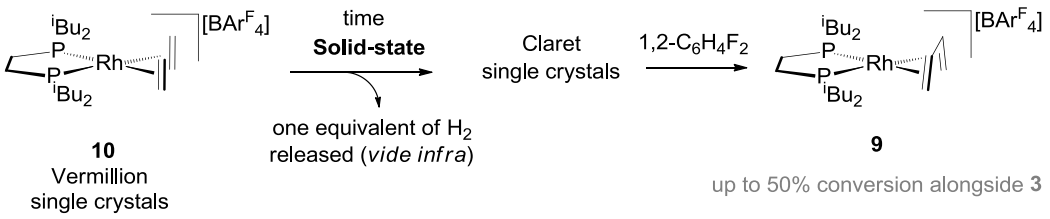

Scheme 4.13. Dehydrocoupling reaction in the solid-state. Upon solvation of the products in 1,2-$C_6H_4F_2$ **9** (up to 50%) and solvent coordinated complex **3** are observed.

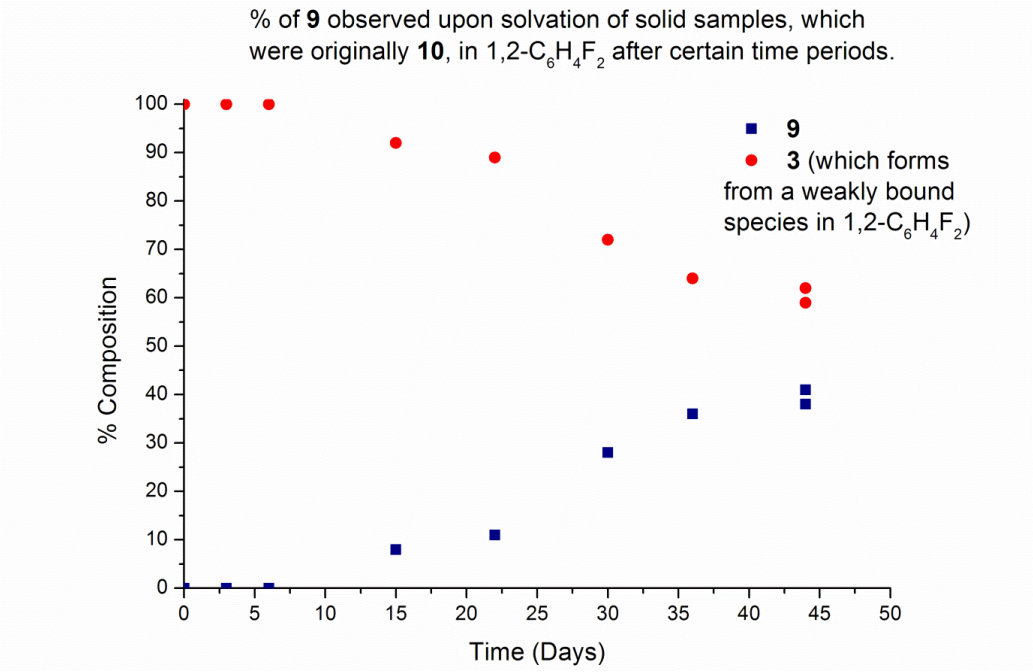

Figure 4.9. Gradual formation of **9** from a solid sample of **10** as measured by integral of the $^{31}P\{^{1}H\}$ NMR signals of the products which form upon solvation in 1,2-$C_6H_4F_2$.

Single crystals of **10** also change colour to dark claret without apparent loss of crystallinity (by inspection using a microscope). A single X-ray diffraction pattern can be collected; however, the disordered nature of the solid-state structures of both **9** and **10** would make solving an X-ray diffraction experiment upon a crystal containing a mixture of both unfeasible.

A sealed sample of **10** releases ethane over several weeks (observed by gas phase NMR spectroscopy). The conversion of **10** to **9** must release one equivalent of hydrogen and it has been determined that **10** reacts readily with H_2 in the solid-state to produce ethane gas (*see Section 2.3.iv*). It appears that whilst one molecule of **10** converts to **9**, a second molecule of **10** acts as a sacrificial hydrogen acceptor and releases one ethane molecule. This may explain why the reaction appears to only reach 50%. Interestingly crystallinity is retained during this process which suggests that the

hydrogen accepting molecules of **10** do not fully react with hydrogen to form amorphous-**4**, but, in fact, maintain their position in the crystalline lattice, possibly forming a 14 electron, 3 coordinate species $[Rh(^{i}Bu_2PCH_2CH_2P^{i}Bu_2)(\eta^2\text{-}C_2H_4)][BAr^F{}_4]$, in which only one ethene ligand is retained [Scheme 4.14].

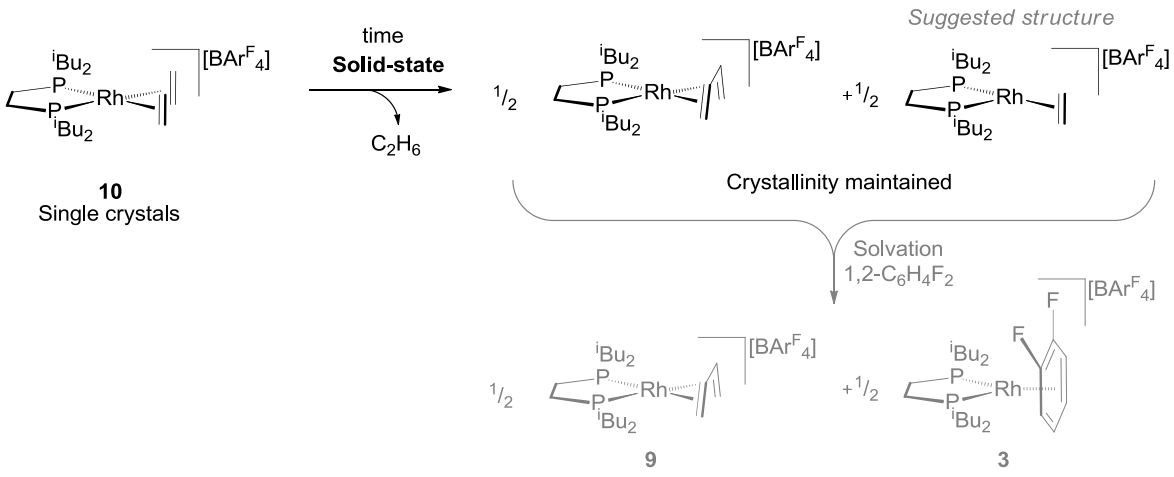

Scheme 4.14. Possible mixed crystalline product formed from **10** after loss of ethane in the solid-state.

The process appears to be a transfer dehydrocoupling reaction, in which three ethene ligands combine to give one butadiene ligand and one molecule of free ethane [Scheme 4.16]. Precedent for the coupling of ethene molecules by rhodium and iridium complexes has been reported with $Tp^{Me2}M(C_2H_4)_2$ complexes (Tp^{Me2} = tris(3,5-dimethyl-1-pyrazol-1-yl, M = Rh, Ir).[43-45] The first step of such a reaction is likely to operate by C–H activation of one ethene molecule (to form a vinyl hydride complex, **10-a** in Scheme 4.16). The insertion of the second ethene ligand into the Rh−H bond is expected to be more favoured than insertion into the Rh−vinyl bond. This would form an ethyl vinyl complex (**10-b** in Scheme 4.16) and previous reports of such complexes with rhodium have been reported.[43, 44]

Mechanistic studies upon the reaction of $Tp^{Me2}Ir(C_2H_4)_2$, which eventually converts to crotyl hydride complex $Tp^{Me2}Ir(H)(C_4H_7)$, suggest that after initial formation of an ethyl vinyl complex, $Tp^{Me2}Ir(C_2H_3)(C_2H_5)$, an α-H abstraction occurs to form an ethyl vinylidene hydride complex [Scheme 4.15].[45] Insertion of the carbene into the Ir−ethyl bond can then occur and subsequent β-H elimination and redistribution of the hydride allows the isomerisation to an (allylic) crotyl hydride

species [Scheme 4.15]. In this reaction the final crotyl hydride complex does not convert into a butadiene complex, perhaps because of the fact that iridium favours a higher oxidation state.

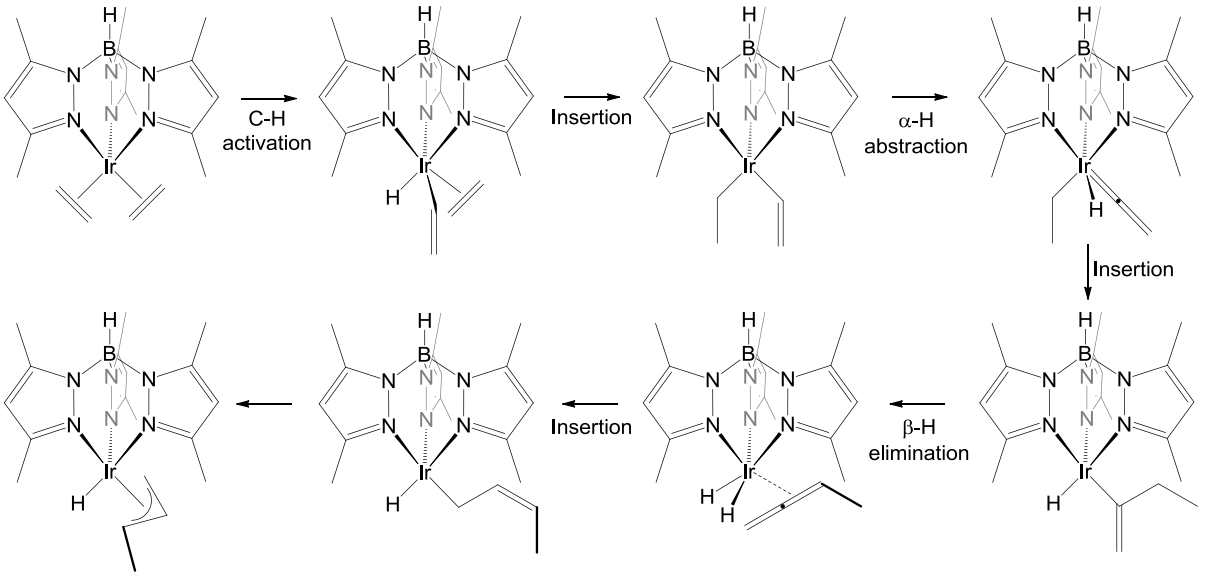

Scheme 4.15. Reported mechanism for coupling of two ethene ligands to form a stable crotyl hydride complex.

In the reaction of **10** to form **9** the mechanism may follow a similar route to that shown in Scheme 4.15. The resulting crotyl hydride complex, **10-e** [Scheme 4.16], could undergo another β-H elimination to generate a butadiene di-hydride complex **10-d**, this may reductively eliminate H_2 and generate **9**. Alternatively **10-d** may also be generated by reductive elimination of ethyl vinyl complex **10-b** to form a butene complex, **10-c**, (*vide infra* for attempted isolation of this species) followed by C-H activation and β-H elimination. The H_2 molecule which is released can then be absorbed by an ethene ligand on a second cation of **10**, and ethane is released from the system.

In comparison to the iridium system displayed in Scheme 4.15, which favours an Ir(III) octahedral geometry, the product of the rearrangement of **10** is likely to favour a Rh(I) square planar geometry and this may account for the formation of the butadiene complex **9**.

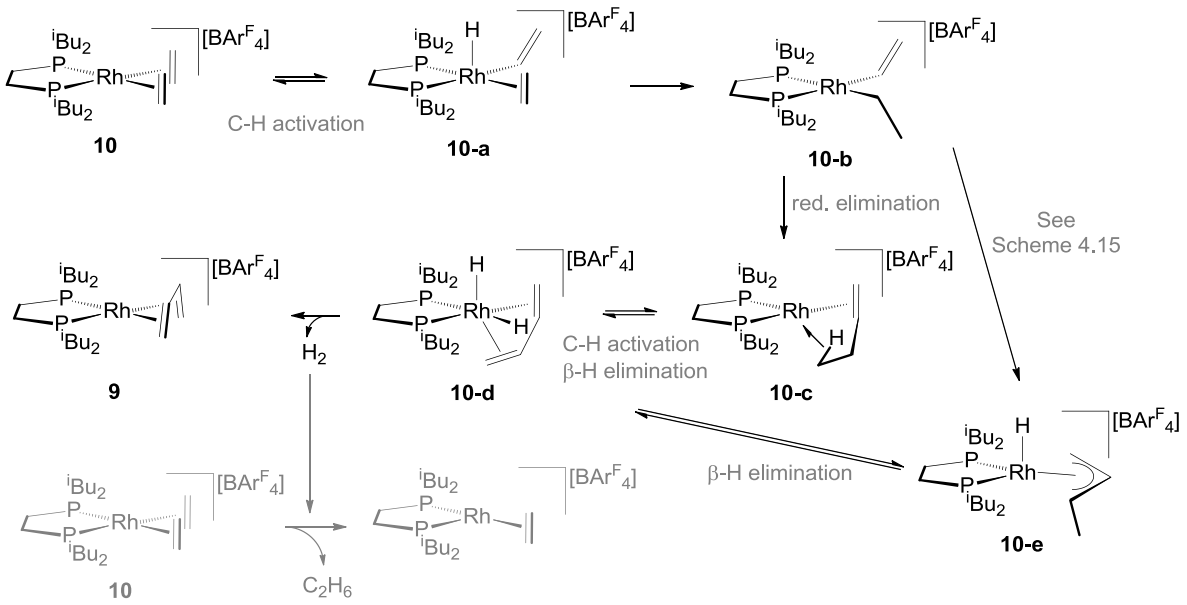

Scheme 4.16. Potential mechanisms for reductive dehydrocoupling of ethene to butadiene. Sacrificial hydrogenation of one ethene ligand shown in grey.

The thermodynamics of a transfer dehydrogenation reaction can be approximated by using the gas phase enthalpies of formation of the hydrocarbon species (this does not account for the energy involved with complexation to the metal centre) [Scheme 4.17]. Using data from the NIST Chemistry Web-book [46] the enthalpy of reaction for three ethene molecules converting into butadiene and ethane is exothermic [$\Delta_r H° = -132.2(\pm 2.59)$ kJ/mol]. This release of energy may compensate for the loss of one (ethene) ligand in alternate molecules.

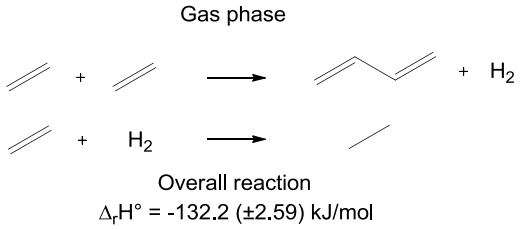

Scheme 4.17. Hypothetical gas phase reaction. Calculation using reported enthalpies of formation.

Evidence for the presence of low coordinate complex $[Rh(^{i}Bu_2PCH_2CH_2P^{i}Bu_2)(\eta^2\text{-}C_2H_4)][BAr^F{}_4]$ is found by solvation of a solid-sample sample of **10** that has been kept for two months and turned claret in colour. CD_2Cl_2 was distilled onto the sample whist it was cooled in liquid nitrogen and the frozen sample loaded into a NMR machine at 200 K before it melted. The $^{31}P\{^{1}H\}$ NMR spectrum at 200 K reveals **9** to be the major product, but less than 50% of the total integral (although due to potentially

incomplete solubility at low temperature integral values were not reliable), alongside signals for starting material **10** and its decomposition product – anion-bound **4**. Two other previously unobserved signals are also noted which couple to each other by a ^{31}P-^{31}P COSY experiment (at 200 K). The new signals are doublets of doublets [δ 47.0, J_{RhP} 162 Hz, J_{PP} 28 Hz & δ 71.4, J_{RhP} 186 Hz, J_{PP} 28 hz] with a combined integral similar to that of the signal for **9** [Figure 4.10]. The signals have different J_{RhP} coupling constants indicating an asymmetrical species with different *trans* effects influencing each phosphorus atom. These two doublet of doublet signals are lost upon warming to 250 K (as **4** grows in) indicating a very unstable species. Upon warming to room temperature decomposition of **10** (and some **4**) has occurred in CD_2Cl_2, but signals for **9** and **4** remain. Some small unidentified peaks are located in the alkene region of the low temperature ^1H NMR spectrum; however, accurate characterisation of these signals was not possible due to the mixture of species in the spectrum.

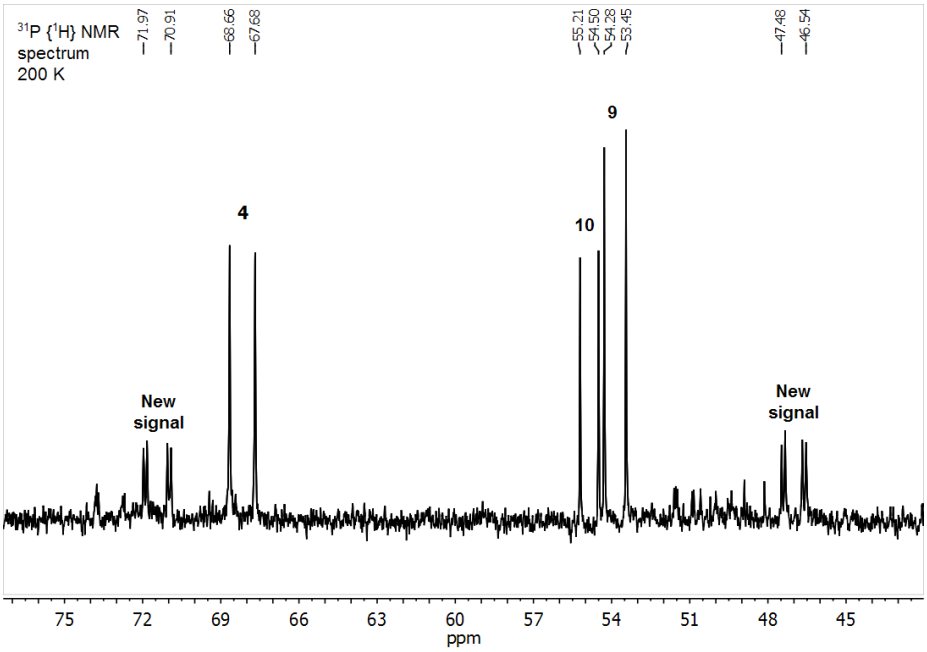

Figure 4.10. Low temperature $^{31}P\{^1H\}$ NMR spectrum (CD_2Cl_2, 200 K) of a solid sample of **10** which had been allowed to undergo internal reductive dehydrogenation over two months.

Budzelaar and co-workers have previously reported a three coordinate rhodium complex with a bidentate β-diiminate ligand and one alkene ligand, **XXX** [Figure 4.11].[32] In this molecule only one bulky cyclooctene molecule can fit around the metal centre and a roughly T-shaped geometry is observed [N-Rh-alkene$_{(C=C\ centroid)}$ 112°]. No agostic interaction is observed to the vacant site in this case.

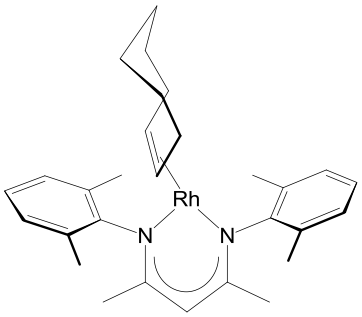

xxx

Figure 4.11. A previously structurally characterised three coordinate T-shaped rhodium complex containing one alkene ligand.

Coupling of ethene molecules has previously been observed in the solid-state reactions of $Tp^{Me2}M(C_2H_4)_2$ at elevated temperatures {M = Rh (333 K), Ir (373 K)}.[44, 45] In both cases a crotyl hydride species is produced, $Tp^{Me2}M(H)(C_4H_7)$, which is stable in solution. The rhodium crotyl hydride complex will, however, undergo photochemically driven loss of H_2 in solution to form a butadiene complex.[44] $Tp^{Me2}Rh(C_2H_4)_2$ does undergo slow dehydrocoupling to form a butadiene complex alongside the release of ethane in solution (with various side products also observed), with a greater yield of butadiene complex if excess ethene is present.[44]

The conversion of ethene into butadiene and ethane can be conducted catalytically using $Ti(Cp^*)_2(C_2H_4)$ dissolved in benzene or toluene, under a pressure of ethene (≤4 atm).[47] However, the rate of this reaction is extremely slow, with only 2 turnovers a year reported at 298 K. This reaction, which involves an electron rich metal centre, is expected to progress via a Ti(IV) metallacycle similar to the initial step in Scheme 4.1. Subsequent β-H eliminations and insertion of a new ethene ligand into a resulting Ti−H bond allow catalytic release of butadiene and ethane.

4.5. Attempted isolation of a butene complex

When **3** is dissolved in CH_2Cl_2 (*N.B.* an equilibrium of **3** and **4** initially forms) and exposed to one atmosphere of 1-butene gas a reaction occurs which can be monitored by $^{31}P\{^1H\}$ NMR spectroscopy. Initially a new signal is observed alongside signals for **3** and **4** [Figure 4.12]. The new signal is a slightly broad doublet [δ 66.6, J_{RhP} 190 Hz] with a large coupling constant indicative of a weakly

bound ligand, possibly a (fluxional) butene bound complex $[Rh(^{i}Bu_2PCH_2CH_2P^{i}Bu_2)(C_4H_8)_n][BAr^{F}_4]$ (n = 1 or 2) **34**.

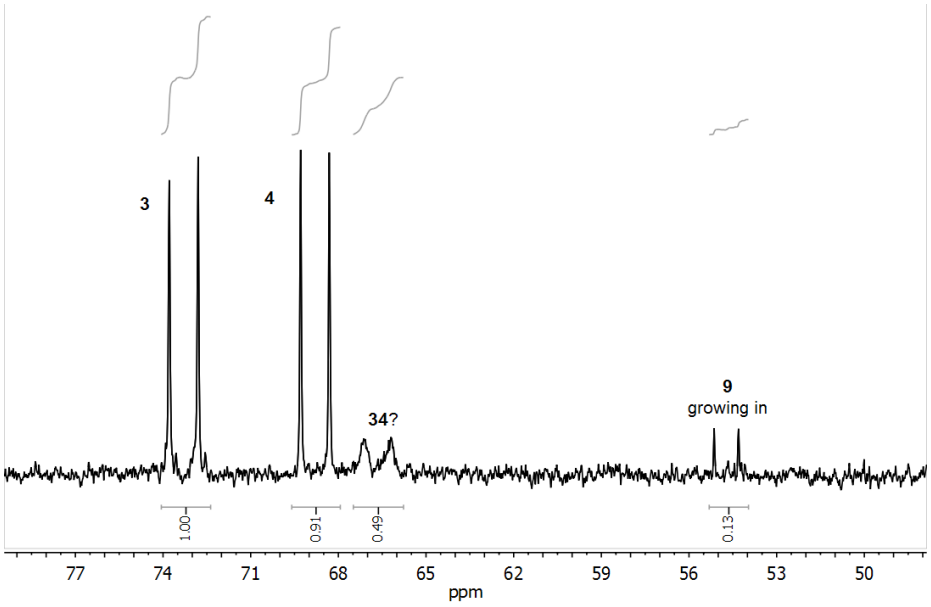

Figure 4.12. $^{31}P\{^{1}H\}$ NMR spectrum of **3** dissolved in CD_2Cl_2 under an atmosphere of 1-butene after 40 minutes.

Over several hours the signal at δ 66.6 decays and **9** is observed to grow in. A transfer dehydrogenation reaction is likely to be occurring to form the butadiene complex and one equivalent of free butane gas. A proposed mechanism is detailed in Scheme 4.18. ^{1}H NMR spectroscopy reveals isomerisation of 1-butene to 2-butenes also occurs (*see Section 4.7.ii*), therefore any coordinated 1-butene is also likely to convert to 2-butene (although whether *cis* or *trans* 2-butene is preferred is uncertain).

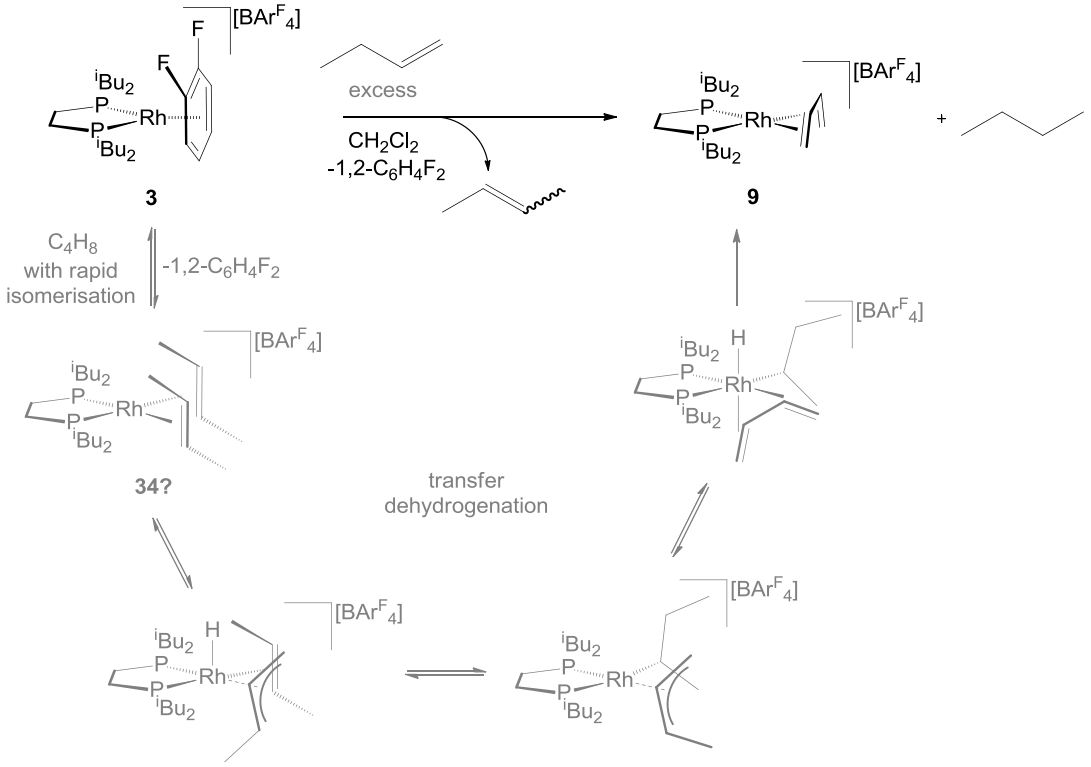

Scheme 4.18. Formation of **9** by transfer dehydrogenation of butene (to form coordinated-butadiene and free butane). Proposed mechanism in grey.

1-Butene reacts with freshly prepared solid **5** to give an orange/brown oily product which may be a butene complex (**34**). Under an atmosphere of 1-butene this orange/brown product turns into claret **9** (major product, 89% by $^{31}P\{^{1}H\}$ NMR spectroscopy, after 24 hours, alongside **4**) [Scheme 4.19]. Gas phase NMR spectroscopy of the headspace reveals isomerisation of 1-butene [δ 0.96, 2.02, 4.90, 5.85] to 2-butene [δ 1.56 & 5.43] has occurred (*see Section 4.7.ii*) and a small amount of butane is present from transfer dehydrogenation.

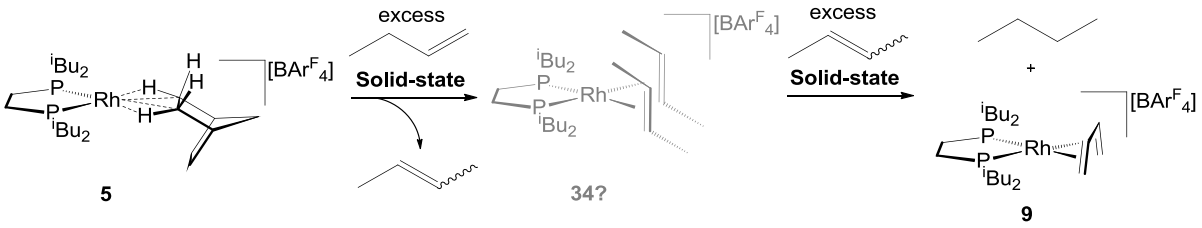

Scheme 4.19. Formation of an uncharacterised butene complex and subsequent transfer dehydrogenation to give **9** and butane (in presence of butene gas).

The thermodynamics of a transfer dehydrogenation reaction can be approximated by using the gas phase enthalpies of formations of the hydrocarbon species (this does not account for the energy

involved with complexation to the metal centre) [Scheme 4.20]. Using data from the NIST Chemistry Web-book [46] the enthalpy of reaction for two *trans*-2-butene molecules converting into butadiene and butane is slightly endothermic, although close to thermo-neutral [$\Delta_rH°$ = +4.8 (±3.46) kJ/mol]. Therefore the reaction is likely to be driven by the favourable interaction of butadiene with the rhodium centre (and also entropically favoured release of butane).

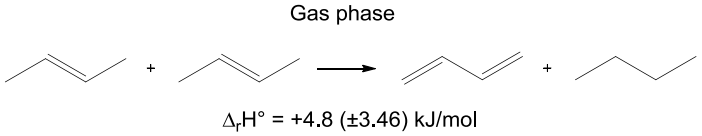

Scheme 4.20. Hypothetical gas phase reaction. Calculation using reported enthalpies of formation.

The orange/brown oily product formed from the reaction of **5** and 1-butene can be recrystallised in CH_2Cl_2/pentane at 277 K if the flask is continuously kept under 1 atm of butene, small vermillion crystals are produced (within 18 hours), however solvation of these at 200 K in CD_2Cl_2 results in a $^{31}P\{^1H\}$ NMR spectrum containing signals for **9** and **4** only. The crystals appeared to have darker interiors, perhaps because some dark claret **9** begins to form in the interior of the crystal. Microcrystalline samples of **34** change colour from orange to claret over several weeks, solvation of this claret species further indicated **9** is forming in the solid-state.

A freshly prepared sample of **5** was reacted with 1-butene gas for two hours to form an orange/brown product (**34**), the headspace was evacuated and the sample sealed under an argon atmosphere. After two weeks the sample had turned to a claret colour and the headspace was analysed by gas phase NMR spectroscopy. This revealed free butane gas had been released indicating that transfer dehydrogenation occurs in the solid-state without the need for an atmopshere of butene [Scheme 4.21]. After eight weeks the claret solid product was dissolved in 1,2-$C_6H_4F_2$ solvent (after evacuation of the headspace), $^{31}P\{^1H\}$ NMR spectroscopy revealed that ~60% of the product was now **9** with the remainder forming **3** (by displacement of a weakly bound ligand, possibly from residual **34**). This possibly suggests that two equivalents of butene are bound in **34**, of which one acts as a hydrogen acceptor in the dehydrogenation process.

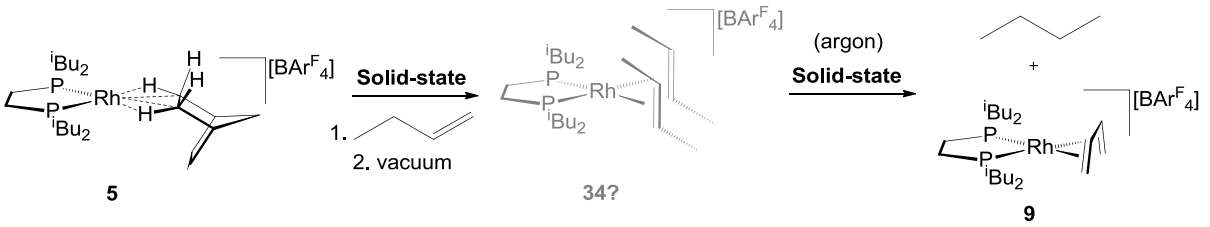

Scheme 4.21. Formation of an uncharacterised butene complex and subsequent solid-state transfer dehydrogenation to give **9** and butane (with no excess butene present).

Low temperature (200 K) ^{1}H and $^{31}P\{^{1}H\}$ NMR spectroscopy was not able to locate new signals for **34**. However the appearance of 2-butenes in the low temperature ^{1}H NMR spectra, alongside anion bound complex **4**, suggests that **34** may decompose in solution even at these low temperatures.

4.6. H/D exchange of ligated ammonia

A microcrystalline sample of **33** reacts with D_2 in the solid-state or solution (1,2-$C_6H_4F_2$) to form **d_6-33** (22 hours under D_2) indicating H/D exchange is occurring upon the ammine ligands.

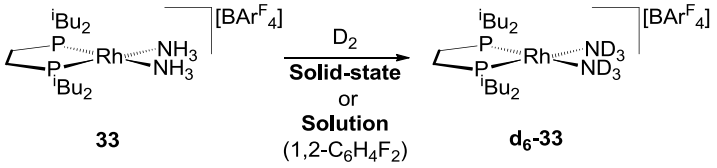

Scheme 4.22. H/D exchange occurring in the ammine ligands of **33**

H/D exchange of ammonia has been previous reported in solution and within frozen argon matrices using Ir(Cp*)$(H)_4$, however, in this case a bound ammonia complex (Ir(Cp*)$(H)_2NH_3$) was only implied by low temperature (10 K) IR spectroscopy.[48]

A solid sample of **33** which had been placed under D_2 for 22 hours was degassed and solvated solvated in 1,2-$C_6H_4F_2$. The ^{1}H NMR spectrum of this sample revealed that the protio ammine signal observed for **33** had been lost [δ 1.93] [Figure 4.13]. The ^{2}H NMR spectra contains a signal corresponding to the ND_3 ligands [δ 1.94]. H/D exchange is also similarly observed in a 1,2-$C_6H_4F_2$ solution if **33** is exposed to D_2.

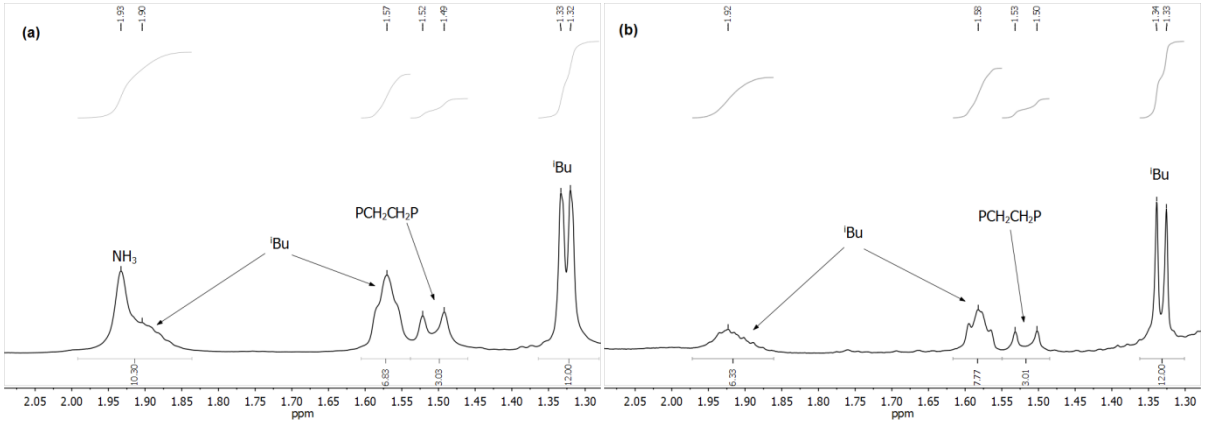

Figure 4.13. Section of the ^{1}H NMR spectrum of **33 (a)** before and **(b)** after deuteration (**d_6-33**), showing loss of the sharp NH_3 signal after H/D exchange has occurred.

A sample of **33** was sealed under D_2 for 24 hours to form **d_6-33**. A gas phase ^{1}H NMR spectrum of the headspace shows a broad signal consistent with the formation of HD (a control experiment confirmed that the D_2 gas feed did not contain a strong signal of HD). This sample was then evacuated and the **d_6-33** product was exposed to 1 atm NH_3. Within 20 minutes a signal for deuterated-ammonia was observed in the ^{2}H gas phase NMR spectrum [δ 0.12], suggesting that exchange of NH_3 and ND_3 ligands may occur or that an H/D exchange mechanism is possible between the gas phase and ligated ammonia molecules [Scheme 4.23]. Gas phase NMR spectroscopy (which often gives broad peaks) does not resolve any J_{HD} coupling in the gaseous species and unfortunately **33** is not suitable for ESI-MS.

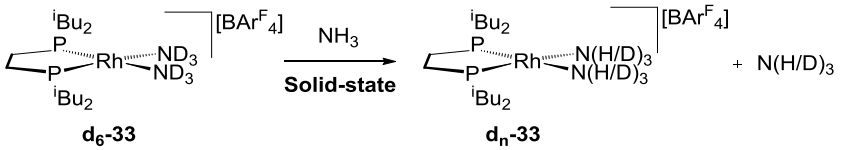

Scheme 4.23. Scrambling of deuterium upon exposure of **d_6-33** and NH_3. Although determination of whether NH_3 and ND_3 remain distinct or form $NH_{3-n}D_n$ is unclear by gas phase NMR spectroscopy.

Addition of 1 atm NH_3 and 4 atm D_2 to a sample of **33** resulted in the scrambling of deuterium into the gas phase and ligated ammonia molecules (by gas phase and solution ^{2}H NMR spectroscopy respectively), although protio signals for ammonia were also observed in the gas phase and solid product. HD was also observed in the headspace.

The mechanism of H/D exchange in **33** may occur *via* a reversible N–H activation pathway [Scheme 4.24(a)] or *via* an ammonium intermediate [Scheme 4.24(b)]. Computational calculations are currently being undertaken by Prof. Stuart Macgregor and co-workers at Heriot-Watt University to obtain further insight into the mechanism.

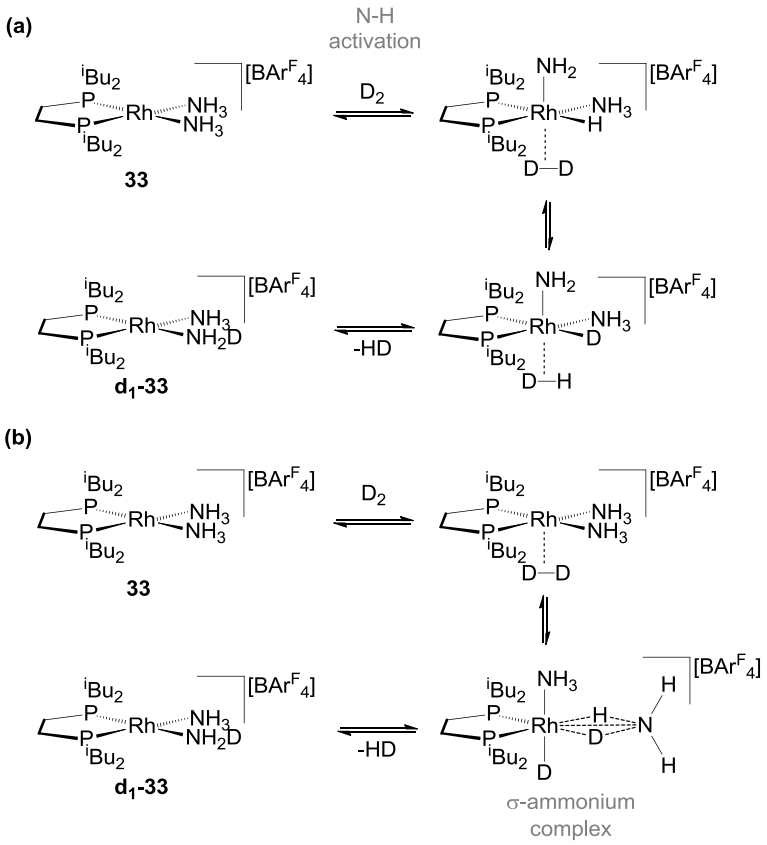

Scheme 4.24. Two possible mechanisms for solid-state H/D exchange

4.7. Gas phase reactions catalysed by solid-state organometallic complexes

Catalysis using solid-state organometallic compounds is a poorly developed area of chemistry (*see Section 1.3.vi*). With little precedent, research into this area is challenging. A series of catalytic transformations using organometallic complexes is presented in this section, however the exact conditions (gas pressure, particle size *etc.*) could not be controlled exactly with the apparatus available at this time. The results should therefore be considered comparative if not quantitative.

4.7.i. Hydrogenation of ethene

The hydrogenation of ethene is a simple reaction which can be monitored in the gas phase if catalysed by a heterogeneous species [Figure 4.14]. Gas phase NMR spectroscopy can be used to measure the reaction *in situ*, as the conversion of ethene to ethane is very clear in the gas phase spectrum (*N.B.* the T_1 times of ethene and ethane are similar in the gas phase, *see Section 6.1.iii*).[49]

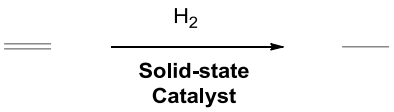

Figure 4.14. Hydrogenation of ethene

A high pressure NMR tube [volume ~2 ml] was charged with (3 ± 0.3) mg (2.2×10^{-3} mmol for **1**) of powdered microcrystalline catalyst (ground down with a spatula in the glove-box) and placed under ~1 atm ethene. The tube was then frozen at 77 K, freezing the ethene, and H_2 added in at 1 atm. When warmed to room temperature this gives partial pressures of roughly 1 atm ethene (~0.08 mmol) to 3.9 atm H_2 (~0.31 mmol). Once warmed the reaction was monitored immediately by gas phase ^{1}H NMR spectroscopy and the formation of ethane gas was observed [Figure 4.15]. If every molecule of catalyst was equally able to catalyse the reaction to completion a turnover number of ~40 would be expected. It is however more likely that the surface molecules undergo many more turnovers than molecules buried within the crystalline lattice due to mass transport effects.

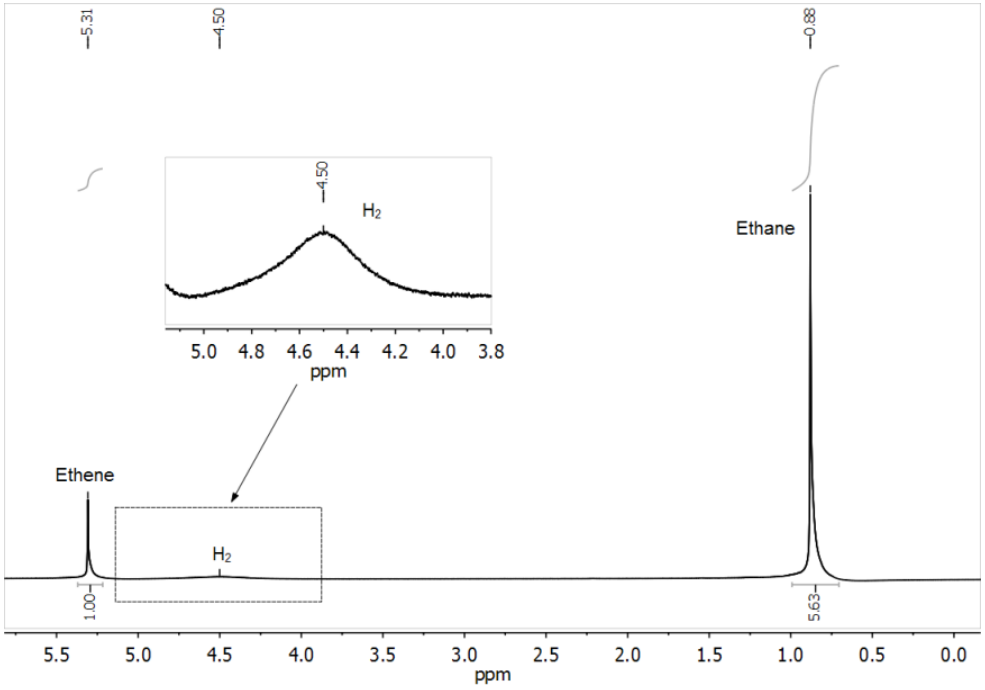

Figure 4.15. Gas phase NMR spectrum showing the hydrogenation of ethene in progress (using 3 mg of powdered solid **1** as a catalyst). NMR spectrum taken directly after addition of gas (time = 60 s). *N.B.* chemical shifts are referenced relative to reported gas phase data.[38]

A variety of potential solid-state catalysts were tested (**1**, **3**, **4**, **5**, **9**, **10**, **32** and **33** [Figure 4.16]) and the progress of reaction is displayed in Figure 4.17. All complexes tested catalysed the hydrogenation of ethene to completion, however, the timescales required varied dramatically.

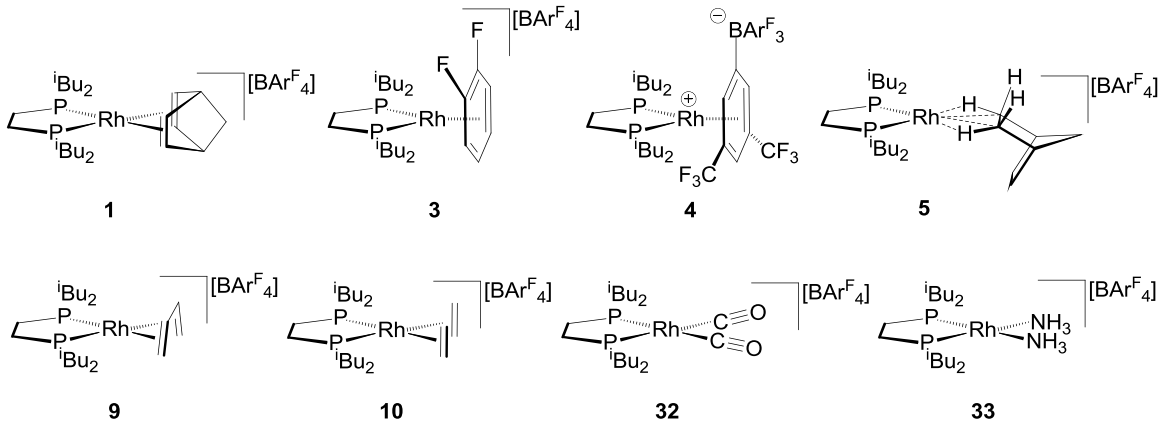

Figure 4.16. Selection of solid-state complexes tested as catalysis.

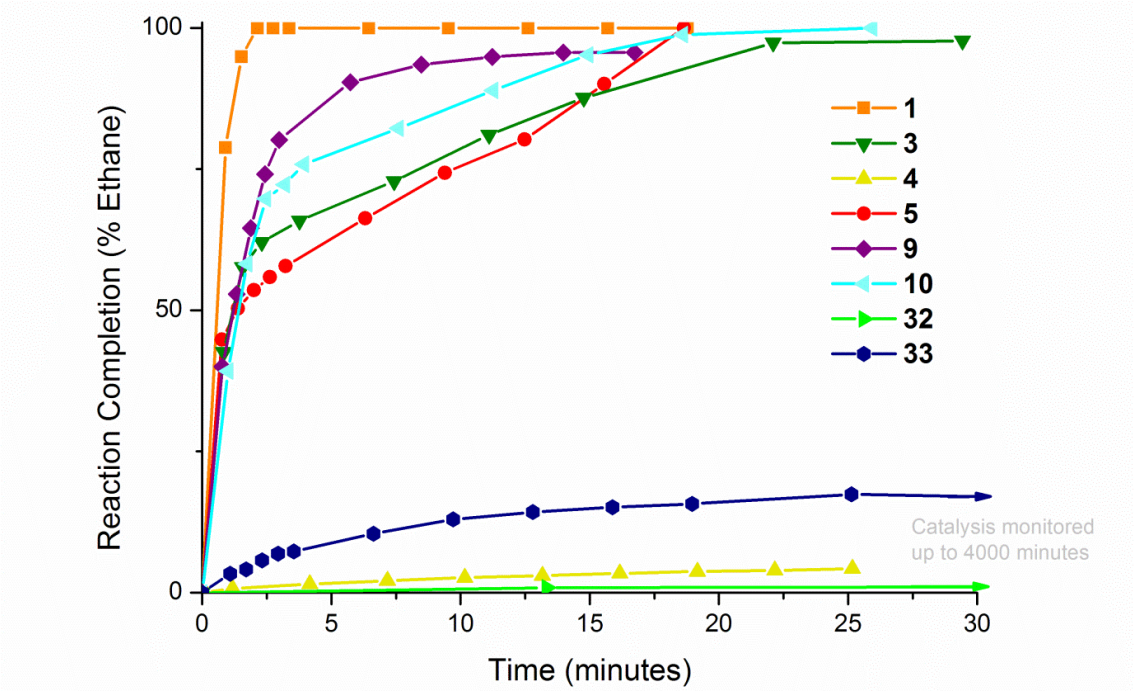

Figure 4.17. Graph displaying hydrogenation of ethene to ethane using a variety of solid-state catalysts. % Ethane calculated from integrals of ethane and ethene signals in gas phase NMR spectroscopy.

Entry	Precatalyst	Conversion at completion (%)	Time to completion (minutes)	Conversion after 4 minutes (%)	Organometallic species after completion (by $^{31}P\{^{1}H\}$ NMR spectroscopy (CD_2Cl_2)
1	**1**	100	2	100	**4**
2	**3**	98	30	66	**3***
3	**4**	100	2880	0.5	**4**
4	**5**	100	18	60	**4**
5	**9**	96	9	90	**4**
6	**10**	100	25	76	**4**
7	**32**	75 (after 4110 minutes)	>4110	1	**32**
8	**33**	100	4000	7	**33**

Table 4.3. Results of hydrogenation of ethene (hydrogen in excess) using a variety of solid-state catalysts. Conversion calculated from integrals of ethane and ethene signals in gas phase NMR spectroscopy. *Due to the fact that **3** forms an equilibrium with **4** in CD_2Cl_2 the total composition of the final product can only be estimated.

Precatalysts containing alkene ligands (**1**, **9** and **10**, [Table 4.3 entries *1*, *5* & *6*]) all catalyse the reaction rapidly (**1** requires less than 2 minutes). Initially hydrogenation of the ligand(s) must occur (at least on the most available surface sites), releasing NBA (as a non volatile liquid), butane or ethane (both gases) this generates an active metal centre which can coordinate ethene and continue to

catalyse the reaction. Once the concentration of ethene drops (hydrogen remains) the alkene complexes will begin to convert to **4** as previously discussed (*see Chapter 2*).

Zwitterionic complex **4** is a slow catalyst [Table 4.3 entry *3*] even though the metal centre is bound to the poorly coordinating anion $[BAr^{F}_{4}]^{-}$. This suggests the rearrangement to allow release of the anion or η^6- to η^2-ring slippage of the anion is a kinetically disfavoured process in the solid-state {*N.B.* in solution **4** forms **10** under an atmosphere of ethene and hydrogenation catalysis is then rapid (upon mixing, < 2 minutes)}. This also indicates that the resting state of catalysis for the faster catalysts cannot be **4** and the conversion to form this (which occurs with a loss of crystallinity) only occurs when the concentration of ethene drops. It is therefore possible that crystallinity is maintained for the catalysts formed from **9** and **10** (which release gases upon initial hydrogenation) until the concentration of ethene diminishes.

σ-alkane complex **5** reacts with ethene (*see Section 4.2.iii*) to form **10** alongside one equivalent of non-volatile liquid NBA. Therefore on initial addition of ethene to freshly prepared **5** the ethene complex **10** will form before subsequent addition of hydrogen. The hydrogenation reaction proceeds quickly at first with this catalyst but then slows [Table 4.3 entry *4*], this reaction has been repeated several times with similar results. It is expected that some conversion to **4** occurs under these experimental conditions and the reaction begins to adopt a slower rate (akin to **4**) after a certain period. Perhaps **5** is not as effective as a precatalyst as **1** because the unstable σ-alkane complex is formed prior to the experiment rather than *in situ*.

3 is an ideal precursor for a solution reaction, since the 1,2-$C_6H_4F_2$ ligand is weakly bound. In the solid-state it is a fairly fast catalyst requiring 30 minutes to reach completion [Table 4.3 entry *2*]. However, it should be noted that solid **3** becomes oily under a pressure of ethene, suggesting that the weakly bound 1,2-$C_6H_4F_2$ may be at least partially replaced by ethene in the solid-state. In keeping with this observation the rate using **3** is fairly similar to **10**.

It is noteworthy that in the case of precatalysts **5**, **3** and **10** (all with weakly bound ligands) the rate of hydrogenation drops to a fairly similar rate after around two minutes [Figure 4.17]. This secondary rate is similar to the initial rate using precatalyst **4** and may be indicative of transformation of the organometallic species into **4**.

32 and **33** are slow catalysts [Table 4.3 entries *7* & *8*], presumably as their strongly bound carbonyl and ammine ligands are difficult to displace. The organometallic species after completion of catalysis is the same as the starting material (by subsequent solution $^{31}P\{^{1}H\}$ NMR spectroscopy).

It is noteworthy that this simple hydrogenation reaction can occur rapidly at ambient temperature (~5 atm total pressure). Previous reports of the catalytic hydrogenation of ethene using solid-state organometallic catalysts typically require longer timescales and/or higher temperatures (albeit with lower pressure reaction conditions) [Table 4.4].[7, 49, 50]

Catalyst	Amount of catalyst (μmol)	Pressure (atm) (*ethene : H_2 ratio*)	Time to completion (minutes)	Temperature (K)
1	2.2	~5 (*1 : 4*)	2	295
(POCOP)Ir(N_2)[7]	1.2*	2.3 (*1.2 : 2*)	30	348
Ir(CO)Cl(PPh_3)[49]	"filled NMR tube"	1 (*1:2*)	10080	298
[(triphos)Ir($H)_2$(C_2H_4)][BPh_4][50]	1.9	1** (*1:5*)	780	343

Table 4.4. Reported examples for the hydrogenation of ethene using solid-state organometallic catalysts (POCOP = C_6H_3[OP(C_6H_2(CF_3)$_3$-2,4,6)$_2$]$_2$-1,3), triphos = ($Ph_2PCH_2CH_2$)$_2$PPh).*Single crystals used as catalyst. **Includes 0.75 atm argon.

The kinetics of the hydrogenation reaction were followed using **4** as a (slow) solid-state catalyst, the consumption of ethene shows a close to zero order profile up to 50% consumption (hydrogen is in a ~3 fold excess) [Figure 4.18]. A rate which is zero order in ethene may be expected if the rate determining step in the catalytic cycle is dissociative displacement of the anion (or ring slippage) from **4**. The kinetics of solid-state reactions are often difficult to predict and interpret because surface and interior sites may operate in different ways.[6]

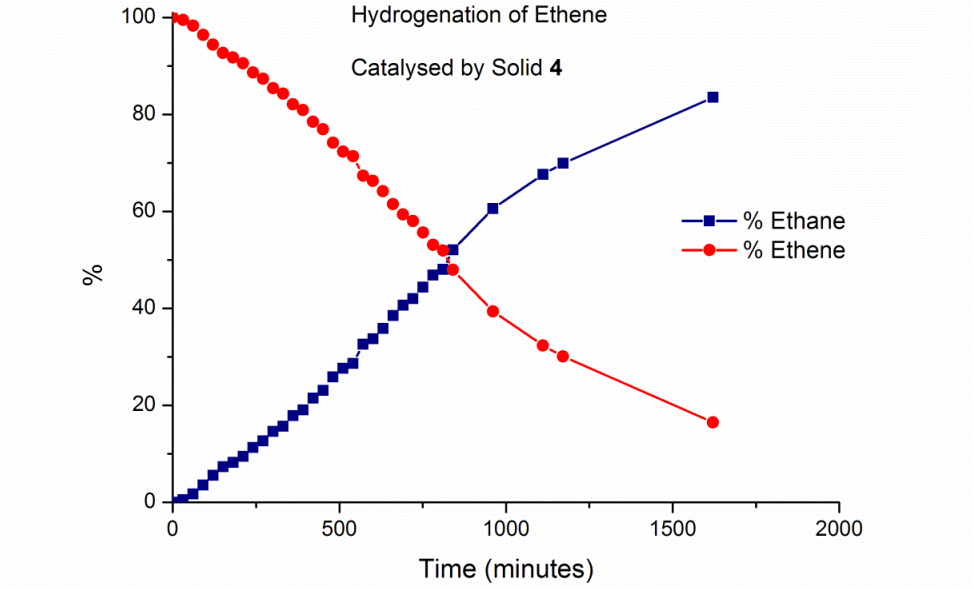

Figure 4.18. Hydrogenation of ethene using solid **4** as a catalyst (starting conditions: 295 K, H_2 3.9 atm, Ethene 1 atm).

More complex kinetic profiles are observed if using **1**, **5** or **9**, possibly because gradually these active species convert into **4** which is a far slower catalyst. Therefore it is possible that multiple active species are present in the solid-state catalysts which act with different turnover rates [Figure 4.19].

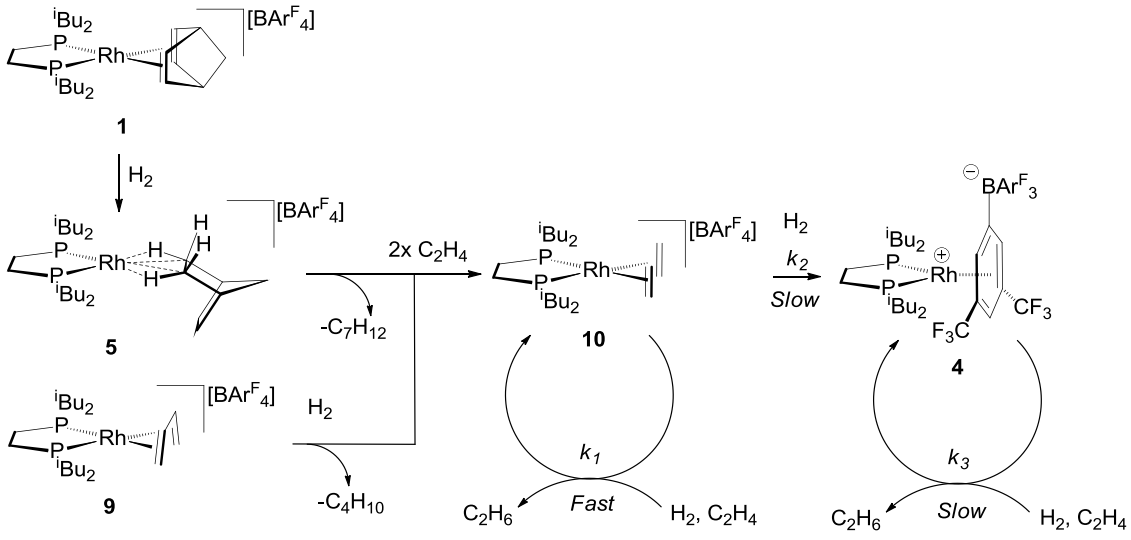

Figure 4.19. Proposed mechanism for the hydrogenation of ethene $k_1 >> k_2$ and k_3.

Surface area of a solid catalyst is likely to be important for the rate of reaction. Therefore sample of **1** was ground down and separated into different particle size fractions (d < 50 μm, 50 < d < 71 μm, 71 <

d < 150 μm, d > 150 μm) using a set of Endecotts test sieves. These different size particles were used for the hydrogenation of ethene using the standard conditions previously defined [Figure 4.20].

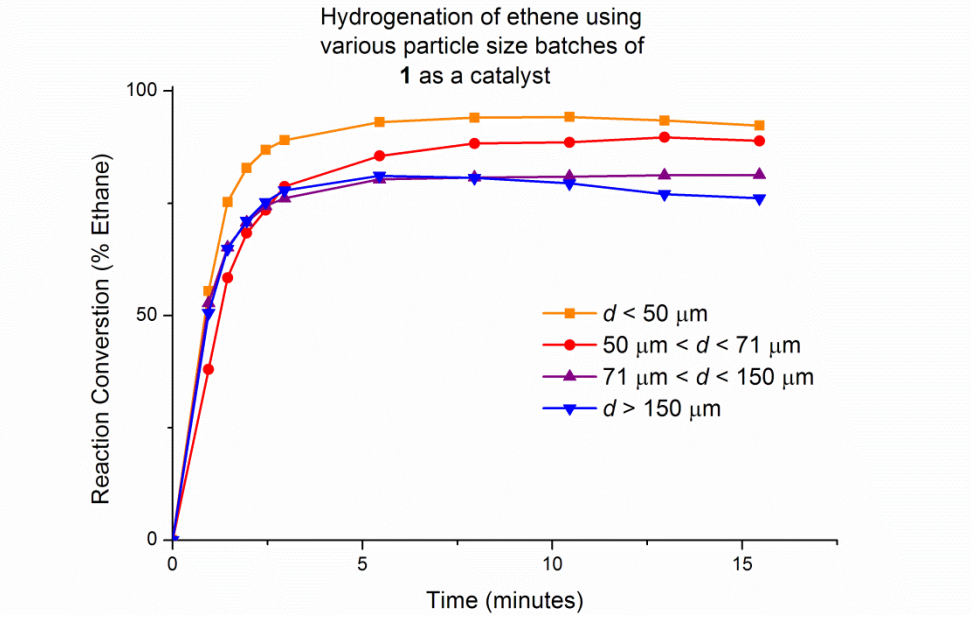

Figure 4.20. Hydrogenation of ethene using various particle size batches of solid **1** as a catalyst (starting conditions: 295 K, H_2 3.9 atm, Ethene 1 atm). *N.B.* these plots do not fit a first order kinetic profile.

All the different size particles rapidly hydrogenate ethene at a similar initial rate, however, as the concentration of ethene drops, reaction of the catalyst with hydrogen to form **4** may occur and the rate of catalysis slows significantly (*N.B.* all experiments had reached 100% completion after 16 hours). The larger particle sizes appear to adopt this slower rate at a lower reaction % conversion. It is interesting to note that catalysis may be a surface dominated process, since the greater surface area of the smaller particles could allow a greater % conversion, before conversion of the active sites to less active **4**.

4.7.ii. Isomerisation of 1-butene

The isomerisation of 1-butene is another simple gas phase reaction which can be monitored *in situ* by gas phase NMR spectroscopy [Scheme 4.25].

Scheme 4.25. Isomerisation of 1-butene using a solid-state catalyst.

The gaseous product of the isomerisation of 1-butene (using **5** as a precatalyst) is 2-butene by analysis of the ^{1}H gas phase NMR spectra [δ 1.58 (integral 6H), 5.43 (integral 2H)], however, it was not clear whether *cis* or *trans* 2-butene was present by NMR analysis. Gas phase IR spectroscopy was undertaken to determine which isomer was present. The IR spectrum gave evidence suggesting the *trans*-isomer (thermodynamic product) is preferred although also some of the *cis*-isomer is also present [Scheme 4.25 & Figure 4.21].[46] The key markers found only for *trans* isomer are located at 2748.21, 1310.46 & 962.73. The peak observed at 671.68 cm^{-1} is indicative of the presence of a smaller amount of *cis*-2-butene.[46]

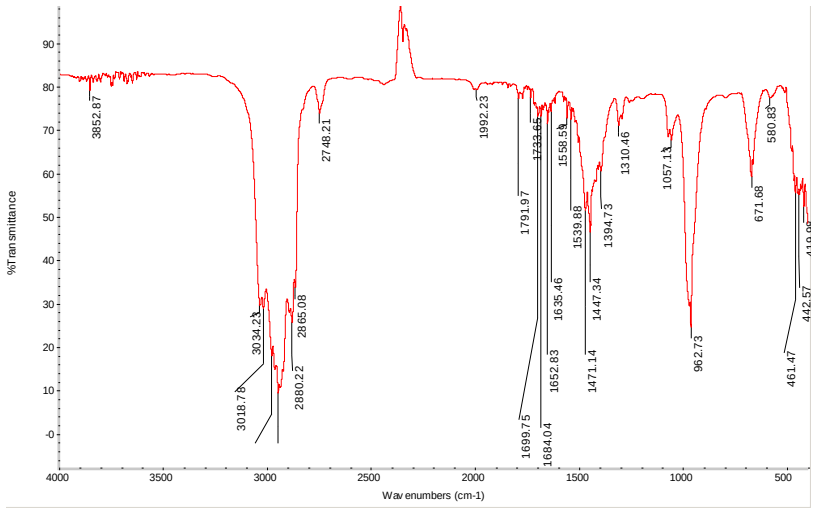

Figure 4.21. Gas phase IR spectrum collected after isomerisation of 1-butene to 2-butene (after two days) using **5** as a precatalyst.

The effects of T_1 time upon the gas phase spectra of 1-butene and the 2-butenes produced were compared and were sufficiently similar to allow comparison of the integrals directly. A variety of complexes (**1**, **3**, **4**, **5**, **9**, **10**, **32** and **33**) were then tested for their catalytic ability. A high pressure NMR tube was charged with 3 (± 0.3) mg of powdered microcrystalline catalyst and placed under 1 atm 1-butene [Figure 4.22 & Table 4.5]. The isomerisation process is generally slow (in comparison to the hydrogenation of ethene).

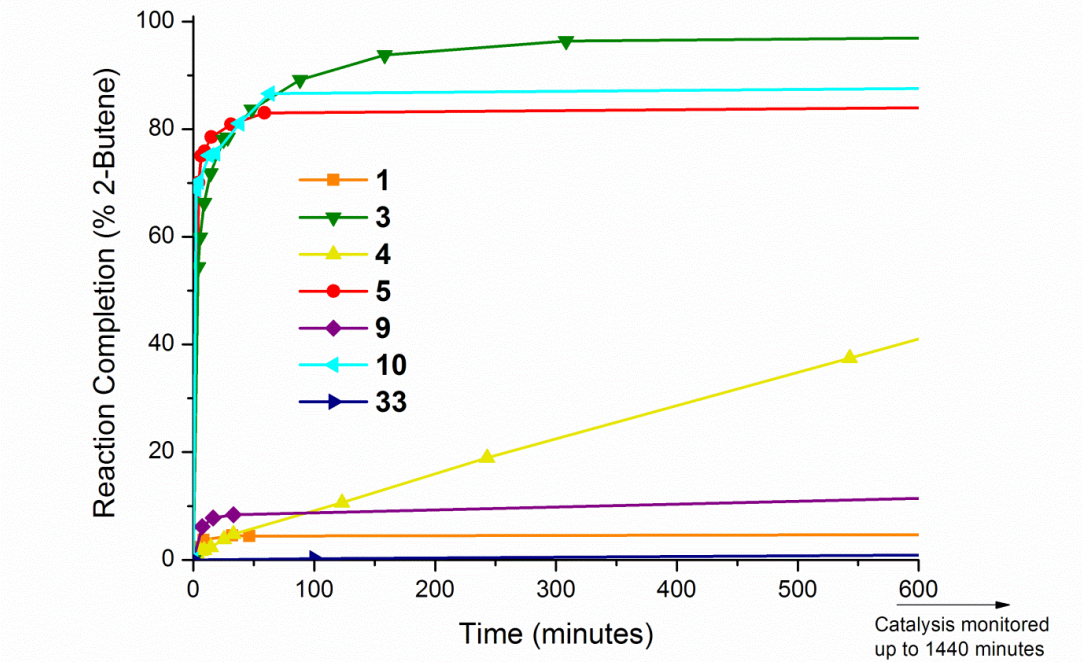

Figure 4.22. Progress of the isomerisation of 1-butene over time using a variety of solid-state complexes. Reaction completion determined by integration of ^{1}H gas phase NMR spectra.

Entry	Precatalyst	Conversion at end of reaction (%)	Reaction time (minutes)	Conversion after 20 minutes (%)	Organometallic species after completion (by $^{31}P\{^{1}H\}$ NMR spectroscopy (CD_2Cl_2)
1	**1**	5	1440	3	**1**
2	**3**	97	860	75	**3****
3	**4**	74	1440	4	**4**
4	**5**	85	1440	80	**34*** & **9**
5	**9**	16	1440	8	**9**
6	**10**	90	1440	76	**10*** & **9**
7	**32**	0	1440	0	**32**
8	**33**	2	960	0	**33**

Table 4.5. Results of isomerisation of 1-butene using a variety of solid-state catalysts. Conversion calculated from integrals of butene signals in gas phase NMR spectroscopy. *Decomposition of weakly bound species in solution produces **4** in CD_2Cl_2.**Due to the fact that **3** forms an equilibrium with **4** in CD_2Cl_2 the total composition of the final product can only be estimated.

5 is a reactive precursor and a colour change from claret to orange/brown is observed on the addition of 1-butene consistent with the formation of proposed butene complex **34** (*see Section 4.5*). Prolonged exposure to butenes results in the production of **9** by transfer hydrogenation (*as previously discussed, see Section 4.5*), with traces of butane observed in the gas phase spectra. Catalysis occurs readily with **5** [Table 4.5, entry *4*] but does not quite reach completion probably due to conversion to less active **9** *vide infra*.

Isomerisation using **3** also occurs readily and approaches completion [Table 4.5, entry *2*], no evidence of the formation of **9** is observed by $^{31}P\{^{1}H\}$ NMR spectroscopy after solvation of the products after catalysis. The organometallic products after catalysis dissolve in CH_2Cl_2 to give an equilibrium mixture of **4** and **3** (*see Sections 2.2.ii and 5.2.iii*) consistent with **3** being present at the end of catalysis.

Ethene complex **10** is also an active catalyst [Table 4.5, entry *6*], the ethene ligands may exchange with butene allowing isomerisation to occur. Free ethene gas is observed by gas phase ^{1}H NMR spectroscopy in the headspace during catalysis supporting solid-state ligand exchange. The final organometallic product was dissolved in CD_2Cl_2 and $^{31}P\ \{^{1}H\}$ NMR spectroscopy showed that it contains ~23% butadiene complex **9** (alongside decomposition product **4** which forms upon room temperature solvation of **10**).

Isomerisation using **4** is quite slow [Table 4.5, entry *3*] and reaches 74% after 24 hours which is a similar rate to the hydrogenation of ethene using **4**. The reaction profile shows a close to zero-order profile (up to 50% isomerisation). Perhaps a similar rate determining step may apply (for example η^6- to η^2- slippage) in both processes. The final organometallic species is observed by $^{31}P\{^{1}H\}$ as **4** only, suggesting that 1-butene cannot displace the anion and form other complexes easily.

The isomerisation using other precursors is slow [Table 4.5, entries *1*,*5*,*7* & *8*], with **32** totally inactive (over 24 hours), presumably because the ligand(s) need to decoordinate to allow access to the metal centre.

Due to the lack of hydride ligands upon the precatalysts we propose the isomerisation proceeds through the "allyl mechanism" [Scheme 4.26].[22] This mechanism requires two vacant sites upon the metal and passes through a Rh(III) intermediate, it is therefore possible that a three coordinate (14 electron) Rh species would allow initial coordination of 1-butene, which could then pass through an five coordinate (18 electron) Rh(III) species before ejecting 2-butene. This would thus require decoordination of at least one site in the square planar precursors.

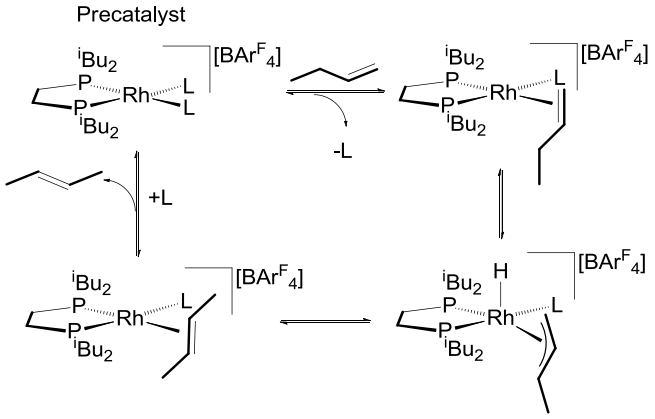

Scheme 4.26. Proposed mechanism of 1-butene hydrogenation, when L = bound ligand e.g. C_2H_4, NH_3. In the case of a bidentate ligand such as η^4-1,3-C_4H_6, partial decoordination may take place.

4.7.iii. Hydrogenation of butadiene

Butadiene gas can also be hydrogenated using **1** as a solid-state catalyst [Scheme 4.27]. The experiment was undertaken using the same conditions as for the hydrogenation of ethene (using an excess of hydrogen). The reaction was again monitored by gas phase NMR spectroscopy and showed intermediate species corresponding to 1-butene and 2-butenes [Figure 4.23]. It appears that a stepwise mechanism occurs in which the first hydrogenation reaction generates 1-butene which can dissociate and is observed in the gas phase. 1-butene isomerises to 2-butene which is again observed as a gaseous species before finally a second hydrogenation to form butane. The final organometallic species is **4**. A short induction period is observed in this reaction, possibly as the precatalyst is hydrogenated to form an active species.

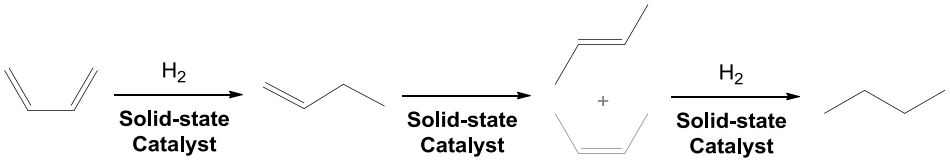

Scheme 4.27. Double hydrogenation (including isomerisation) of butadiene, using **1** as the solid-state precatalyst.

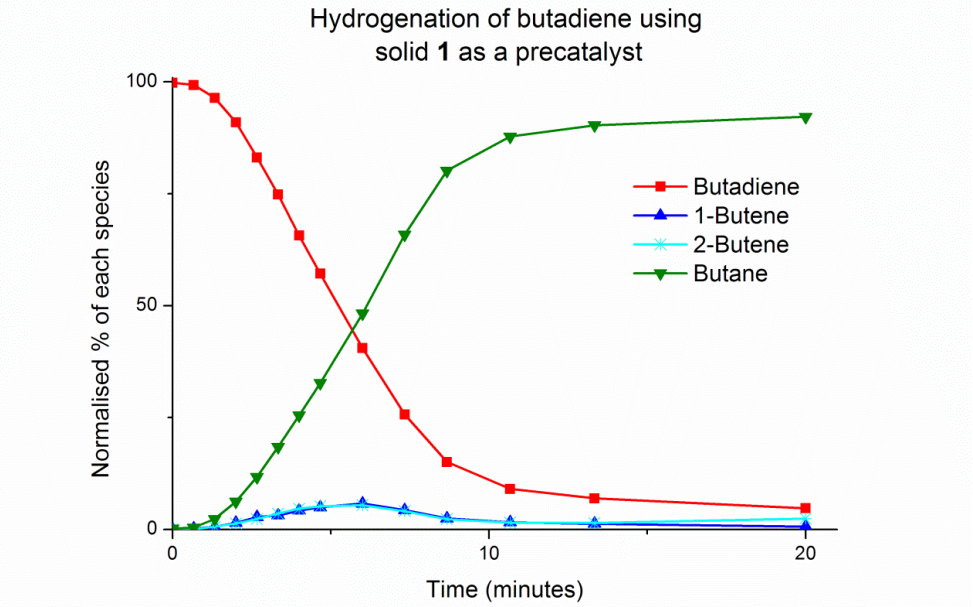

Figure 4.23. Hydrogenation of butadiene gas using **1** as a catalyst. Normalised % of each species calculated by integration of gas phase ^{1}H NMR spectra with consideration of the number of protons in each species (*N.B.* only alkene signals of 1-butene used for calculation). 1-butene and 2-butene concentration profiles appear coincidentally to be very similar.

4.7.iv. Catalysis using surface passivated crystals

Whilst it is likely that reaction occurs fastest upon surface sites of solid-state complexes, it is also possible that the metal centres located inside the interior of a crystal are also active. SC-SC transitions have been discussed and support the possibility of gases diffusing through the crystalline lattice to reach interior sites. Passivated crystals were produced by exposing single crystals of **9** to CO gas for three hours (*see Section 4.2.iv.Figure 4.5*). These crystals were tested for their catalytic ability in comparison to similar size single crystals of **9** and **32**.

32 catalyses the hydrogenation of ethene slowly whilst **9** catalyses the reaction rapidly, therefore the surface passivated crystals **Passivated-9** will give an indication of the ability of interior metal centres to react. In order to maintain the single crystallinity of the diene complexes (**9**, and the interior of **Passivated-9**) it is important to keep ethene in excess (in contrast to previously discussed reactions in which hydrogen is in excess) because formation of any **4** (which is driven by hydrogen) will destroy the crystal. A high pressure NMR tube containing (3 ± 0.3) mg of crystalline catalyst was evacuated and refilled with ~1 atm of ethene. This tube was then cooled to 195 K reducing the pressure inside to ~0.66 atm. The cold tube was then opened to a stream of hydrogen (1 atm) and then sealed and

warmed to room temperature. The resulting atmosphere is then composed of ~1 atm ethene and ~0.5 atm H_2 (although in practice slightly less than 0.5 atm H_2 is observed by gas phase NMR).

Single crystals of **32** are very poor catalysts for the hydrogenation of ethene under these conditions and only 3% conversion occurs within one hour and little further progress is observed over the next 24 hours.

Dark claret single crystals of **9** hydrogenate ethene until all hydrogen is used up in ~9 minutes (29% of ethene hydrogenated) [Figure 4.24]. The crystals retain their apparent crystallinity and their ability to rotate polarised light. A second pressurisation of hydrogen can be applied using the same method and the catalysis is observed to begin again and continue until the hydrogen is used up a second time (42% of ethene hydrogenated). The hydrogenation experiment was repeated (initial conditions 1 atm ethene, ~0.25 atm H_2) and the NMR tube evacuated after the hydrogen had been totally consumed (left for two hours, 25% of headspace converted to ethane). The NMR tube was then frozen in liquid nitrogen and CD_2Cl_2 was distilled onto the crystals. The sample was then directly characterised by NMR spectroscopy at low temperature (220 K). Only **9** was observed by $^{31}P\{^1H\}$ NMR spectroscopy suggesting that catalysis occurs without significant hydogenation of the bulk crystal (when ethene is in excess), although presumably a small number of sites (probably on the surface) are initially hydrogenated in order to create active sites for catalysis.

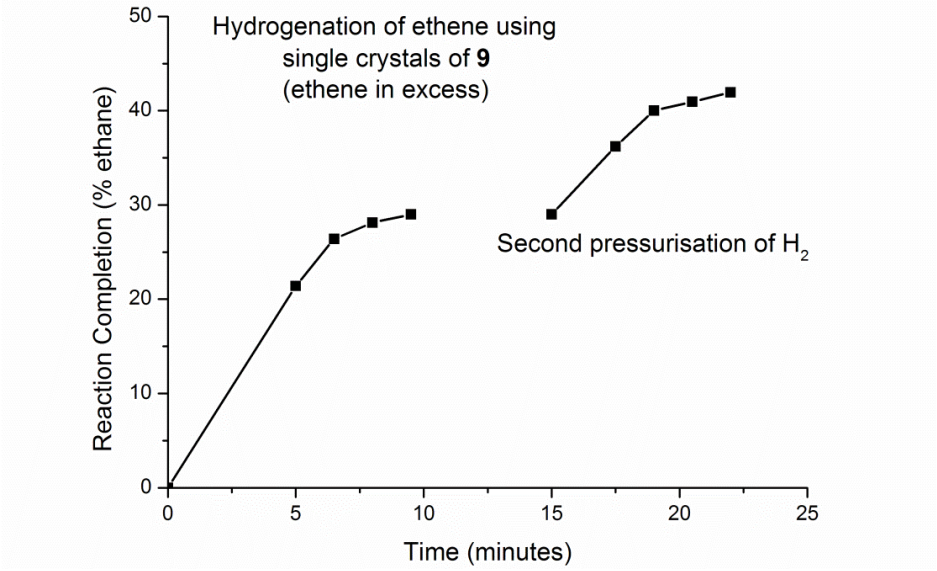

Figure 4.24. Hydrogenation of ethene using single crystals of **9** as a precatalyst. Ethene was added at 1 atm, hydrogen was added at less than 1 atm (~0.3 atm) and added a second time after 15 minutes (~0.2 atm).

Passivated-9 also catalyses the hydrogenation of ethene but at a slower rate than pure **9**; 55% of the hydrogen has been used up after 33 minutes and the reaction goes to completion after 12 hours. After catalysis the crystals appear intact and in good condition [Figure 4.25]. A second amount of hydrogen can be subsequently added and catalysis re-starts [Figure 4.26]. A small trace of butane grows in to the gas phase spectrum over the course of catalysis [integral = 1% of ethane peak], suggesting that some interior sites have been hydrogenated, perhaps hydrogen can access sites within the crystal more readily than ethene. Low temperature NMR spectroscopy analysis (220 K, solvent distilled onto sample at low temperature) of these crystals resolved only **9** and **32**.

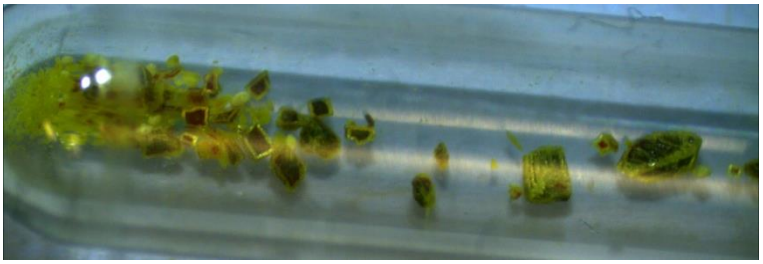

Figure 4.25. Well defined crystals of **Passivated-9** after catalysis has completed (hydrogen has been used up). Little colour or shape change has occurred.

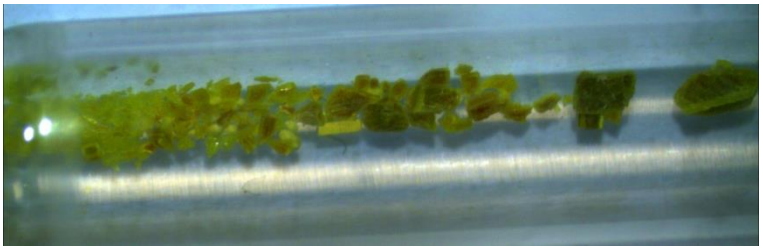

Figure 4.26. Crystals of **Passivated-9** after a second injection of hydrogen and subsequent second catalytic run has completed (hydrogen has been used up). Crystals are beginning to lose some definition (the interior may be beginning to convert into **4**) but general shape remains.

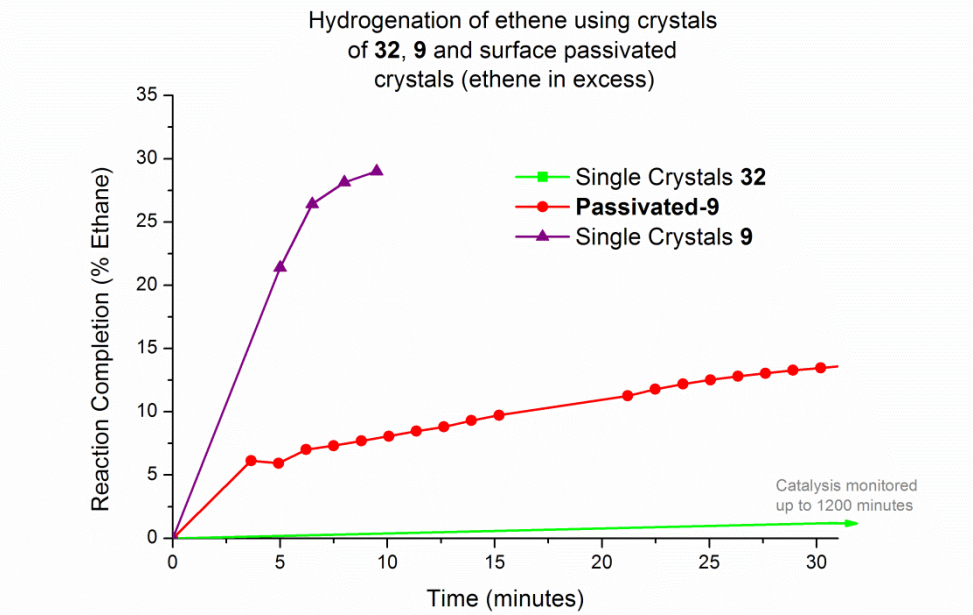

Figure 4.27. Hydrogenation of ethene using crystalline precatalysts. Ethene added at 1 atm, hydrogen added at less than 1 atm (~0.3 atm).

The comparative rates of catalysis [Figure 4.27] suggest that penetration of ethene and hydrogen can occur to access active interior sites of a crystal which can then catalyse the reaction from inside the crystalline lattice. However we cannot conclusively discount the possibility of crystal cracking occurring (due to reaction with hydrogen) which may expose the interior of the crystals to the atmosphere.

Crystals of **Passivated-9** do not catalyse the isomerisation of 1-butene; even over an 8 day period there is no evidence of 2-butenes. This lack of isomerising ability is akin to **32**, however, single crystals of **9** do isomerise 1-butene, albeit very slowly (5% isomerisation after 1 day, by integration of gas phase NMR spectra). Therefore it appears that 1-butene cannot penetrate the surface of the passivated crystals or that the mechanism of isomerisation is only possible upon the surface, perhaps because more space is required.

It is noteworthy that by changing the size of the gaseous reagent some reactivity can be blocked by passivation of the surface sites (*i.e.* selectivity can be enhanced by passivation).

Unfortunately, the remarkable selective hydrogenation of ethene in the presence of propene, demonstrated by Brookhart and co-workers using passivated single crystals, was not able to be reproduced with crystals of **Passivated-9**.[7] Using a mixture of ethene, butene and hydrogen

(approximate 2 : 2 : 1 ratio) a fairly equal ratio of butane and ethane was produced with crystalline catalysts of **9**, **Passivated-9** and **32**.

4.8. Conclusions

Various solid-state reactions of organometallic complexes with gases are reported. The σ-alkane complex **5** is a useful synthon – allowing for the addition of gases such as ammonia and ethene. In particular the formation of *bis*-ammonia complex **33** is noteworthy because it was only successful by using solid-state techniques, although it is stable in solution (1,2-$C_6H_4F_2$) after formation. **33** can undergo solid-state H/D exchange upon its ammine ligands. Whilst the mechanism of this reaction is as yet undetermined, the activation of N–H bonds is of interest with the potential for the functionalisation of ammonia to generate greater value products.

It appears that SC-SC transitions are possible in some of these complexes (diffraction patterns can be collected of the products), such as the displacement of ethene or butadiene ligands by CO gas (*N.B. Chapter 2 describes another SC-SC transition:* ***1*** *to* ***5***). The crystal packing environments, which incorporate large $[BAr^F_4]^-$ anions, may allow for subtle rearrangements in the solid-state without disruption of the crystallinity. The approximate solid-state structures also show some interconnected voids which may allow movement of small gases throughout the crystals.

The solid-state complexes were used as precatalysts for the hydrogenation of ethene and isomerisation of 1-butene to 2-butenes. These reactions show the ability of solid-state organometallic complexes to act as active heterogeneous catalysts at room temperature. Particle size experiments infer that surface area is influential upon catalysis, suggesting that molecules on the surface act as the most active sites for catalysis. Passivation of the surface sites of single crystals of **9**, by reaction with CO gas, resulted in a two-colour crystal (**Passivated-9**). These surface passivated crystals were faster catalysts for the hydrogenation of ethene than the pure crystals of carbonyl complex **32** (but slower than pure **9**), suggesting that the interior sites of a crystal may also be active for catalysis.

4.9. References

1. A. R. Steynberg and M. Dry, *Fischer-Tropsch Technology*, Elsevier Science, 2004.
2. P. J. Perez, *Alkane C-H Activation by Single-Site Metal Catalysis*, Springer, 2012.
3. R. A. Meyers, *Handbook of Petroleum Refining Processes*, 3rd edn., McGraw-Hill Education, 1997.
4. J. Foster, 2013, p. www.platts.com/IM.Platts.Content/InsightAnalysis/IndustrySolutionPapers/ ShaleGasReport13.pdf.
5. R. W. True, *Oil Gas J.*, 2012, **110**.
6. N. J. Coville and L. Cheng, *J. Organomet. Chem.*, 1998, **571**, 149-169.
7. Z. Huang, P. S. White and M. Brookhart, *Nature*, 2010, **465**, 598-601.
8. O. V. Zenkina, E. C. Keske, R. Wang and C. M. Crudden, *Angew. Chem. Int. Ed.*, 2011, **50**, 8100-8104.
9. J. F. Hartwig, *OrganoTransition Metal Chemistry*, University Science Books, 2010.
10. A. Bollmann, K. Blann, J. T. Dixon, F. M. Hess, E. Killian, H. Maumela, D. S. McGuinness, D. H. Morgan, A. Neveling, S. Otto, M. Overett, A. M. Z. Slawin, P. Wasserscheid and S. Kuhlmann, *J. Am. Chem. Soc.*, 2004, **126**, 14712-14713.
11. M. J. Overett, K. Blann, A. Bollmann, J. T. Dixon, D. Haasbroek, E. Killian, H. Maumela, D. S. McGuinness and D. H. Morgan, *J. Am. Chem. Soc.*, 2005, **127**, 10723-10730.
12. M. J. Overett, K. Blann, A. Bollmann, R. de Villiers, J. T. Dixon, E. Killian, M. C. Maumela, H. Maumela, D. S. McGuinness, D. H. Morgan, A. Rucklidge and A. M. Z. Slawin, *J. Mol. Catal. A: Chem.*, 2008, **283**, 114-119.
13. D. S. McGuinness, A. J. Rucklidge, R. P. Tooze and A. M. Z. Slawin, *Organometallics*, 2007, **26**, 2561-2569.
14. T. Agapie, S. J. Schofer, J. A. Labinger and J. E. Bercaw, *J. Am. Chem. Soc.*, 2004, **126**, 1304-1305.
15. J. Zhao, A. S. Goldman and J. F. Hartwig, *Science*, 2005, **307**, 1080-1082.
16. E. Morgan, D. F. MacLean, R. McDonald and L. Turculet, *J. Am. Chem. Soc.*, 2009, **131**, 14234-14236.
17. I. Mena, M. A. Casado, P. García-Orduña, V. Polo, F. J. Lahoz, A. Fazal and L. A. Oro, *Angew. Chem. Int. Ed.*, 2011, **50**, 11735-11738.
18. J. I. van der Vlugt, *Chem. Soc. Rev.*, 2010, **39**, 2302-2322.
19. H. M. Senn, P. E. Blöchl and A. Togni, *J. Am. Chem. Soc.*, 2000, **122**, 4098-4107.
20. T. Nagano and S. Kobayashi, *J. Am. Chem. Soc.*, 2009, **131**, 4200.
21. S. D. Pike, Exploring New Hydroacylation Catlaysts Based on Rhodium Phosphine Systems, MChem Thesis, University of Oxford, 2010.
22. R. H. Crabtree, *The Organometallic Chemistry Of The Transition Metals*, 4 edn., John Wiley & Sons, Inc., 2005.
23. P. Atkins, T. Overton, J. Rourke, M. Weller and F. Armstrong, *Inorganic Chemistry*, 4th edn., Oxford University Press, 2006.
24. T. M. Douglas, A. B. Chaplin and A. S. Weller, *Organometallics*, 2008, **27**, 2918-2921.
25. O. R. Gilliam, C. M. Johnson and W. Gordy, *Physical Review*, 1950, **78**, 140-144.
26. T. A. Betley and J. C. Peters, *Angew. Chem. Int. Ed.*, 2003, **42**, 2385-2389.
27. C. Bianchini, W. Oberhauser, A. Orlandini, C. Giannelli and P. Frediani, *Organometallics*, 2005, **24**, 3692-3702.
28. R. A. Baber, M. F. Haddow, A. J. Middleton, A. G. Orpen, P. G. Pringle, A. Haynes, G. L. Williams and R. Papp, *Organometallics*, 2006, **26**, 713-725.
29. O. Nürnberg and H. Werner, *J. Organomet. Chem.*, 1993, **460**, 163-175.
30. M. Bosch and H. Werner, *Organometallics*, 2010, **29**, 5646-5660.
31. http://sdbs.db.aist.go.jp, National Institute of Advanced Industrial Science and Technology, 2014.
32. P. H. M. Budzelaar, N. N. P. Moonen, R. Gelder, J. M. M. Smits and A. W. Gal, *Eur. J. Inorg. Chem.*, 2000, 753-769.
33. W. Leitner, J. M. Brown and H. Brunner, *J. Am. Chem. Soc.*, 1993, **115**, 152-159.
34. A. D. Burrows, D. Michael, P. Mingos, S. E. Lawrence, A. J. P. White and D. J. Williams, *J. Chem. Soc. Dalton Trans.*, 1997, 1295-1300.
35. A. Spek, *J. Appl. Crystallogr.*, 2003, **36**, 7-13.
36. H. M. Colquhoun, S. M. Doughty, J. F. Stoddart and D. J. Williams, *Angew. Chem. Int. Ed.*, 1984, **23**, 235-236.
37. L. A. Bengtsson, B. T. Heaton, J. A. Iggo, C. Jacob, G. L. Monks, J. Ratnam and A. K. Smith, *J. Chem. Soc. Dalton Trans.*, 1994, 1857-1865.
38. T. Zuschneid, H. Fischer, T. Handel, K. Albert and G. Häfelinger, *Zeitschrift für Naturforschung B*, 2004, **59b**, 1153-1176.
39. S. K. Wolff, D. J. Grimwood, J. J. McKinnon, M. J. Turner, D. Jayatilaka and M. A. Spackman, *Crystal Explorer (v3.1)*, (2012) University of Western Australia.
40. M. J. Turner, J. J. McKinnon, D. Jayatilaka and M. A. Spackman, *CrystEngComm*, 2011, **13**, 1804-1813.
41. G. Kaupp_in:, J. L. Atwood, J. E. D. Davies, D. D. MacNicol and F. Votgle, *Comprehensive Supramolecular Chemistry*, Pergamon, New York, 1996.
42. M. Oliván, A. V. Marchenko, J. N. Coalter and K. G. Caulton, *J. Am. Chem. Soc.*, 1997, **119**, 8389-8390.
43. M. Paneque, P. J. Pérez, A. Pizzano, M. L. Poveda, S. Taboada, M. Trujillo and E. Carmona, *Organometallics*, 1999, **18**, 4304-4310.
44. M. C. Nicasio, M. Paneque, P. J. Pérez, A. Pizzano, M. L. Poveda, L. Rey, S. Sirol, S. Taboada, M. Trujillo, A. Monge, C. Ruiz and E. Carmona, *Inorg. Chem.*, 1999, **39**, 180-188.
45. Y. Alvarado, O. Boutry, E. Gutiérrez, A. Monge, M. C. Nicasio, M. L. Poveda, P. J. Pérez, C. Ruíz, C. Bianchini and E. Carmona, *Chemistry – A European Journal*, 1997, **3**, 860-873.
46. http://webbook.nist.gov/chemistry, NIST Chemistry Webbook.
47. S. A. Cohen, P. R. Auburn and J. E. Bercaw, *J. Am. Chem. Soc.*, 1983, **105**, 1136-1143.
48. A.-K. Jungton, C. Herwig, T. Braun and C. Limberg, *Chem. Eur. J.*, 2012, **18**, 10009-10013.
49. J. Matthes, T. Pery, S. Gründemann, G. Buntkowsky, S. Sabo-Etienne, B. Chaudret and H.-H. Limbach, *J. Am. Chem. Soc.*, 2004, **126**, 8366-8367.
50. C. Bianchini, E. Farnetti, M. Graziani, J. Kaspar and F. Vizza, *J. Am. Chem. Soc.*, 1993, **115**, 1753-1759.

CHAPTER 5
BINDING AFFINITIES OF η^6-FLUOROBENZENE COMPLEXES

5.1. Introduction

5.1.i. η^6-coordination of fluorobenzenes

Fluorobenzenes are used as labile ligands with late transition metal complexes as they are ideal for stabilising a low coordinate (12 electron) metal centre by acting as a six electron (η^6) ligand (to form an 18 electron complex). Such complexes have been targeted by Weller and co-workers as precatalysts for hydroacylation,[1, 2] Suzuki type C–C coupling *via* C–S activation,[3] and the dehydrogenation of amine boranes.[4] Upon solvation of these precatalysts the fluorobenzene ligand becomes labile and is easily displaced by reagents or solvent molecules. Understanding the coordinating abilities of fluorobenzenes is key to the design of stable and yet active precatalysts. Fluorobenzene complexes are also potentially useful for the synthesis of many organometallic complexes, and are used extensively as precursors in Weller group research. We therefore set out to synthesise and study a range of fluoro-arene complexes in order to rationalise the binding strengths of the fluoro-arene ligands to rhodium fragments.

In particular we are interested in the comparison of η^6-fluoro-arene complexes with η^6-arene anion bound complexes (such as **4**, which forms from σ-alkane complex **5** in the solid-state). Such comparisons could lead to greater insight into the coordination chemistry of weakly coordinating anions.

Typically an η^6-coordination mode is anticipated for fluoro-arene binding to a metal centre, however in some cases preferential fluorine (κ_F) coordination may occur [Figure 5.1]. In the case of a 16 electron fragment an η^2-coordination mode may be observed (since η^6 coordination is not possible).[5, 6] Fluorine (κ_F) coordination is more likely when less than six electrons are required to reach electronic

saturation and for more electropositive transition metals to the left hand side of the periodic table.[7, 8] There are also examples of complexes which coordinate chlorobenzene through the chlorine atom.[9, 10]

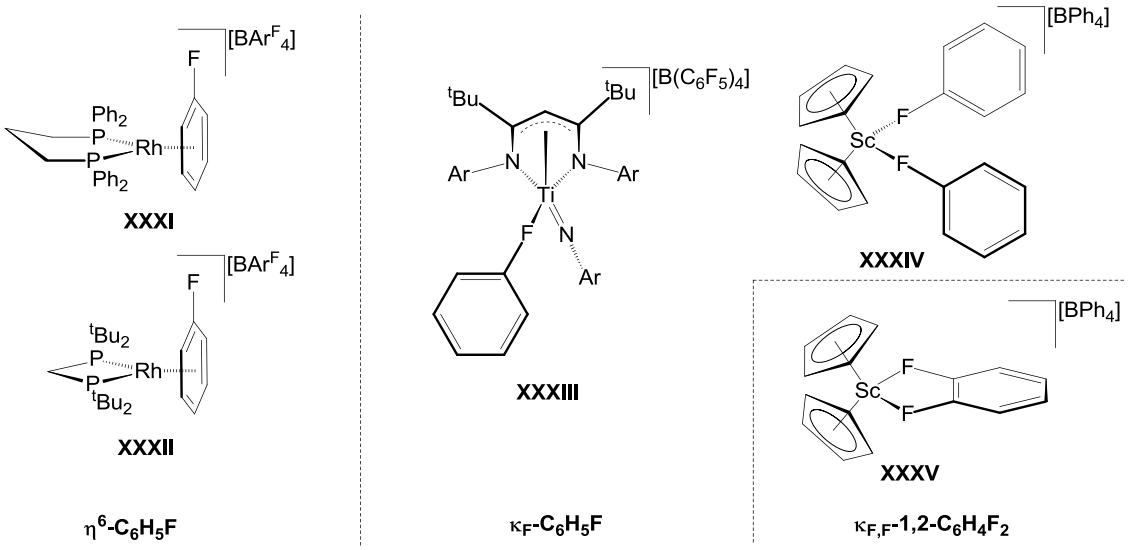

Figure 5.1. Examples of η^6- and κ_F binding in transition metal fluorobenzene complexes.[1, 2, 7, 8]

During the 1970s studies upon sandwich compounds $Cr(C_6H_{6-n}F_n)_2$, synthesised by metal atom condensation, noted the instability of complexes when n > 2.[11] The authors commented that the low π-basicity [12] of arenes with a multitude of electron withdrawing substituents inhibits formation of stable complexes. To a reasonable approximation the stability of these complexes to oxidation is governed by the sum of the inductive parameters of the substituents, with relative ring positions less important (*i.e.* 1,3-trifluoromethylbenzene behaves similarly to 1,4-trifluoromethylbenzene).[13] Unsymmetrical sandwich complexes $Cr(C_6H_6)(C_6H_{6-n}F_nH)_2$ have been prepared with n = 4-6, suggesting that if the strongly binding benzene ligand is used a less strongly binding arene can take the second site.[14, 15] Hammett parameters (which relate the acidity of a substituted benzoic acid with the inductive and mesomeric effects of the substituent)[16, 17] were used to rationalise the stability of $Cr(C_6H_{6-n}F_nH)_2$ and $Cr(C_6H_6)(C_6H_{6-n}F_nH)_2$ complexes.[11]

The substituents upon an arene will affect the frontier molecular orbitals. It is known that for alkene ligands electron donating substituents stabilise an interaction with an electron poor metal fragment (optimising the alkene to metal donor interaction) and conversely electron withdrawing groups stabilise interactions with electron rich metal centres (optimising the metal to π* back-bonding interaction).[18] The same effects will occur with arene ligands. For electron poor metal centres (e.g.

cationic systems) the addition of electron withdrawing substituents to the arene ligand will worsen the energy match for the arene to metal donor interactions and the electron poor metal can contribute little backbonding to compensate, overall reducing the binding affinity. For elctron rich complexes, capable of greater degrees of backbonding, the addition of electron withdrawing groups to an arene may have a lesser or different effect.

Perutz and co-workers have investigated the effect of fluorine substituents upon $CpRe(CO)_2(\eta^2\text{-}C_6H_{6-n}F_n)$ (n= 1-5) complexes.[6] A clear preference for coordination to HC=CH sites is calculated in preference to HC=CF and FC=CF. However, greater back-bonding is predicted in the fluorinated coordinated double bonds; as would be expected by the lowering of the available C=C π^* orbitals upon addition of electron withdrawing substituents. Addition of fluorines to the other (non coordinating) positions of the arene ring has little effect on the η^2 binding affinity, displaying that only the π orbitals in direct combination with the metal centre are important for the binding affinity in the η^2 case.

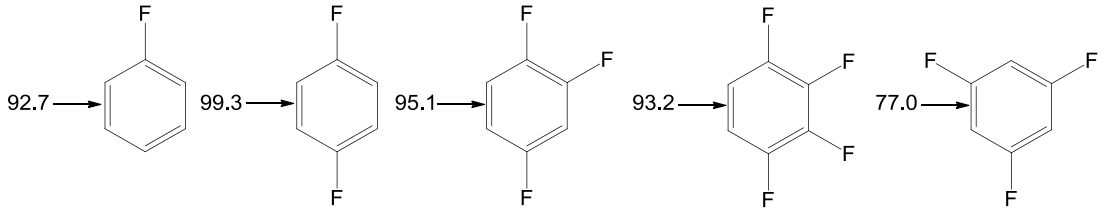

Figure 5.2. Binding energy (kJ/mol) of $CpRe(CO)_2$ to $C_6H_{6-n}F_n$ in an η^2 fashion to the preferred coordination site (HC=CH favoured over HC=CF).

More recently a variety of small bite angle chelating phosphine ligands (P_2) have been used to form $[Rh(P_2)(\eta^6\text{-}C_6H_5F)][BAr^F{}_4]$ by Weller and co-workers {P_2 = $^iPr_2P(CH_2)_nP^iPr_2$ (n=1-3) and $(^iPr_2P)_2NCH_3$}.[2] They observed that for the smallest bite angle ligands the fluorobenzene complexes exhibit an equilibrium in acetone solution with the analogous acetone complexes, $[Rh(P_2)(acetone)_2][BAr^F{}_4]$. However, for wider bite angle phosphines complete loss of fluorobenzene occurs leaving only the related acetone complex, $[Rh(P_2)(acetone)_2][BAr^F{}_4]$, behind. This suggests that bite angle affects the binding affinity of fluorobenzene (η^6-) relative to acetone (2x κ_O-) [Scheme 5.1]. The structural metrics of the solid state structures of fluorobenzene complexes were examined,

however the rhodium–arene distance has little variation [*average*-Rh–$C_{(arene)}$ 2.31 to 2.34 Å] across these complexes.

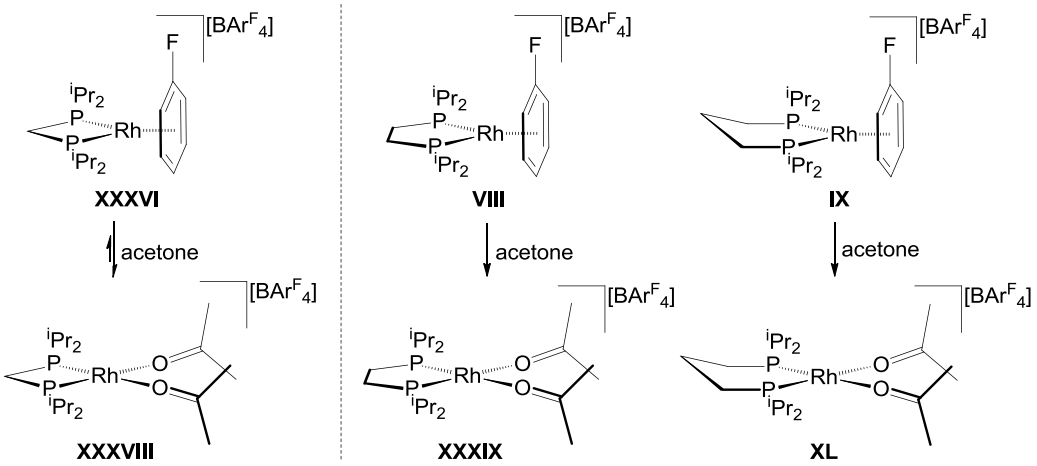

Scheme 5.1. Displacement of the labile fluorobenzene ligand in acetone. Small bite angle phosphine complexes in equilibrium whilst larger bite angles phosphine complexes are fully displaced.

5.1.ii. Mass spectrometry experiments for measuring binding affinity

Mass spectrometry techniques have been previously used to study the binding affinities of fluorobenzenes to metal ions.

A thorough study into the coordination of fluorobenzenes with Cr^+ ions has been reported by Klippenstein, Dunbar and co-workers.[19] Cr^+ ions were generated by laser desorption ionisation and selectively separated by mass spectrometry. The Cr^+ ions were then allowed to coordinate with previously injected fluorobenzenes ($C_6F_nH_{6-n}$) in a low pressure environment. The temporal evolution of these products was recorded by mass spectrometry. This allows the rate of radiative association to be determined (at low pressure association of two species generates an excited state that decays radiatively into a product). Using these rates of radiative association (k_{ra}) the binding strength energetics could be modelled, which also compared well with computational results. Computational calculations suggest that in most cases the fluorobenzene binds through its π system to the Cr^+ ion however when two fluorine substituents are located *ortho* to each other a chelating *bis*-fluorine coordination mode is preferred in these systems [Figure 5.3].

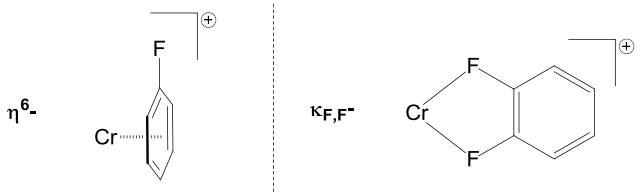

Figure 5.3. Preferred binding mode of fluorobenzene and 1,2-difluorobenzene to Cr^+ ions from computational calculations.

The experimental and computational results show that increasing fluorination results in weaker η^6- (π) binding affinity. Previous studies have suggested that coordination to the π system of arenes by transition metals is primarily electrostatic, although some covalent interaction is also important.[20, 21] Covalency through d-orbitals is shown to be influential by the comparison of the binding affinity of benzene with Na^+ (28 kcal/mol) and Cr^+ (~40 kcal/mol) ions.[20, 22] Considering the importance of electrostatic contributions it is noted that additional fluorine substituents reduce the negative charge located across the π region and in the case of hexafluorobenzene the π region has a partial positive charge. Theoretical calculations predict hexafluorobenzene to have π-acidic properties (*i.e.* a favourable interaction with NH_3)[12] and it has even been observed to coordinate to a negatively charged Au^- anion.[16] The study by Klippenstein, Dunbar and co-workers shows that for every fluorine added to the arene the η^6- binding affinity reduces by around 5 kcal/mol [Table 5.1]. In the case of *ortho* fluorine substituents the alternative chelating *bis*-fluorine geometry is preferred, which also becomes less strongly bound with additional fluorination (although this effect is less pronounced).

Ligand	Binding Affinity (computational calculations) (kcal/mol)		Binding Affinity (radiative association kinetics modeling) (kcal/mol)
	π face (η^6-)	Chelating F,F ($\kappa_{F,F}$)	
C_6H_6	**38.9**	-	**44.5**
C_6H_5F	**34.0**	-	**39.1**
1,2-$C_6H_4F_2$	30.2	**31.0**	**32.9**
1,3-$C_6H_4F_2$	**29.6**	-	**32.0**
1,4-$C_6H_4F_2$	**28.3**	-	**29.0**
1,2,3-$C_6H_3F_3$	26.3	**27.9**	**29.3**
1,3,5-$C_6H_3F_3$	**23.5**	-	**26.3**
1,2,3,4-$C_6H_2F_4$	22.9	**25.5**	**25.4**
C_6HF_5	17.8	**23.1**	**23.6**
C_6F_6	10.1	**20.4**	**19.0**

Table 5.1. Binding affinities of fluorobenzenes to Cr^+ ions (Where a chelating *bis*-fluorine coordination is preferred the results are shown in grey).

A similar study upon Au^+ cations indicated the binding affinity of benzene (70 kcal/mol) to be significantly larger than that of C_6F_6 (31 kcal/mol) which is in turn larger than that of C_6F_6 to Au^- (~24 kcal/mol).[23-25] Calculations predict two possible structures for $[Au(C_6F_6)]^+$ the most stable being an η^3- coordination mode with the gold located above one carbon atom and a slightly less stable coordination mode operating through one fluorine atom [Figure 5.4(a)].[25] A neutral Ni(0) C_6F_6 complex has also been synthesised, **XXXVI**, and characterised by X-ray crystallography displaying an η^2-binding mode. Ring whizzing of the arene is observed in its NMR spectra [Figure 5.4(b)].[26] A neutral W(0) *bis*-C_6F_6 sandwich complex, **XXXVII**, $W(C_6F_6)_2$, displays both arenes in an η^6-geometry [Figure 5.4(b)].[27] In comparison to Cr^+ ions these structures highlight greater tendency for π coordination with late or third row transition metals, which are capable of greater covalency.

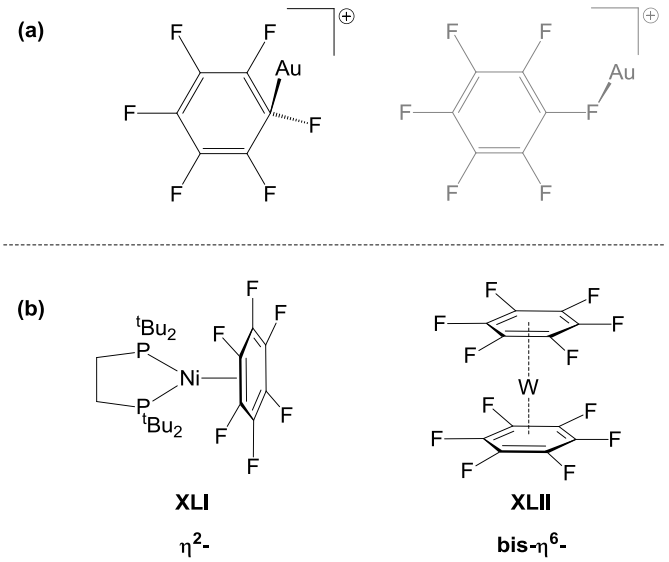

Figure 5.4. (a) Calculated ground state of $[Au(C_6F_6)]^+$ and a low energy excited state (shown in grey). **(b)** An η^2-C_6F_6 complex with nickel and *bis* η^6-C_6F_6 with tungsten.

Other, less involved, mass spectrometry techniques can be used for determining binding strengths, for example ESI-MS/MS (electrospray ionisation mass spectrometry/mass spectrometry) can selectively fragment an ion and determine the energetics of that dissociation. ESI-MS is a useful technique for characterising charged particles in polar solvents, it is a "soft" ionisation technique and allows the parent ion to be observed with little or no fragmentation.[28, 29] This is particularly useful for studying weakly bound organometallic complexes and can be coupled to a glove-box in order to study air sensitive complexes.[30] The ions generated by ESI-MS can be separated and then exposed to an inert collision gas (such as Argon), this process (ESI-MS/MS) allows controlled fragmentation of a chosen

ion. By varying the collision voltage the degree of fragmentation changes and the binding strengths can then be correlated to collision voltage.

McIndoe and co-workers have presented the fragmentation of X_3^- ions to $X_2 + X^-$ by ESI-MS/MS (X = Cl, Br, I), they record the collision voltage values at 50% fragmentation and adjust the data for a centre of mass correction ($E_{COM} = E_{LAB}(m / (m + M))$, where m is the mass of the collision gas and M the mass of X_3^-).[31] Techniques similar to this will be presented in this chapter to determine the comparative binding strengths of fluoroarenes, allowing for rationalisation of the effect of arene substituents upon binding affinity.

5.2. Synthesis and Characterisation of [Rh(^{i}Bu$_2$PCH$_2$CH$_2$P^{i}Bu$_2$)(η^6-fluoro-arene)][BAr$^F_4$] complexes

5.2.i. Synthesis of new complexes

A variety of new rhodium η^6-arene complexes using the phosphine (^{i}Bu$_2$PCH$_2$CH$_2$P^{i}Bu$_2$) have been synthesised alongside **2**, **3** and **24**, which have been discussed in previous chapters. The general synthetic route to these species is the hydrogenation of **1** in the presence of the desired arene (either as the solvent or as a reagent dissolved in CH_2Cl_2). In most cases the product can then be crystallised by layering the reaction mixture directly with pentane. In order to investigate the binding affinities of a range of arene complexes, [Rh(^{i}Bu$_2$PCH$_2$CH$_2$P^{i}Bu$_2$)(η^6-arene)][BAr$^F_4$] {arene = C_6H_6 (**35**), C_6H_5F (**2**), 1,2-$C_6H_4F_2$ (**3**), 1,3-$C_6H_4F_2$ (**36**), 1,4-$C_6H_4F_2$ (**37**), 1,2,3-$C_6H_3F_3$ (**38**), $C_6H_5CH_3$ (**39**), $C_6H_5CF_3$ (**40**) & C_6H_5Cl (**24**)}, were synthesised alongside zwitterionic **4** and **12** [Figure 5.5]. Understanding the effects that the arene substituents have upon η^6-binding affinity allows rationalisation of the formation of η^6-anion bound complexes such as **4** and **12**.

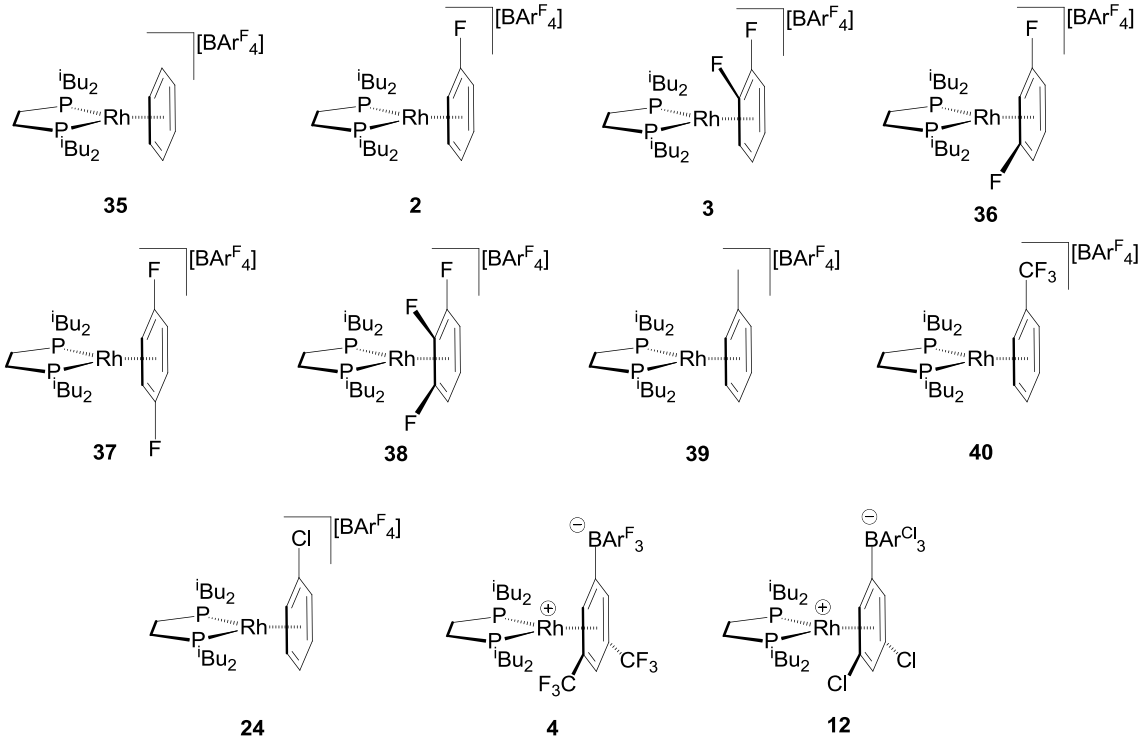

Figure 5.5. η^6-arene complexes with the ^{i}Bu$_2$PCH$_2$CH$_2$P^{i}Bu$_2$ phosphine.

5.2.ii. Characterisation and comparison of [Rh(^{i}Bu$_2$PCH$_2$CH$_2$P^{i}Bu$_2$)(η^6-fluoro-arene)][BAr$^F_4$] complexes

All the [Rh(^{i}Bu$_2$PCH$_2$CH$_2$P^{i}Bu$_2$)(η^6-arene)][BAr$^F_4$] complexes exhibit a large coupling constant (J_{RhP}) in their ^{31}P{^{1}H} NMR spectra [Table 5.2], this appears to be indicative of η^6- coordination and is consistent with similar reported examples.[2, 4] It should however be noted that some square planar complexes, such as 1,2-C$_2$H$_4$Cl$_2$ complexes like **20** [J_{RhP} 190 Hz] (*see Section 2.6.vii*), also exhibit large coupling constants if weakly bound ligands are present. The ^{1}H NMR spectra of the arene complexes are unremarkable and comparable to previously published η^6-arene complexes.[2] Signals for the coordinated arenes are located upfield of the reported signals for free arene, indicative of η^6-arene coordination [Table 5.2]. No evidence of a fluorine coordination mode is observed even with *ortho* fluorine substituents, and the solid state structures confirm η^6-coordination (*vide infra*). It is likely that a greater covalent contribution is present in the bonding of these rhodium complexes compared to the naked Cr$^+$ ions mentioned in *Section 5.1.ii*.

Complex	Arene Ligand	$^{31}P\{^{1}H\}$ NMR		^{1}H NMR η^6-arene region
		δ (CD_2Cl_2 solvent)	J_{RhP} (Hz)	δ (CD_2Cl_2 solvent unless specified)
35	C_6H_6	73.2	201	6.47
2	C_6H_5F	73.3	201	5.47, 6.19, 6.25 (C_6H_5F)
3	1,2-$C_6H_4F_2$	73.3	200	6.18, 6.83 (1,2-$C_6H_4F_2$)
36	1,3-$C_6H_4F_2$	73.2	200	6.19, 7.01, *
37	1,4-$C_6H_4F_2$	73.1	201	6.81
38	1,2,3-$C_6H_3F_3$	73.3	201	*
39	$C_6H_5CH_3$	73.0	202	6.30, 6.45
40	$C_6H_5CF_3$	72.9	200	6.46, 6.64, 6.94
24	C_6H_5Cl	73.2	201	6.15, 6.57, 6.75
4	$Ar^F(BAr^F_3)$	68.8	199	6.57, 7.27
12	$Ar^{Cl}(BAr^{Cl}_3)$	67.8	202	6.15, 7.10

Table 5.2. $^{31}P\{^{1}H\}$ and ^{1}H NMR spectroscopy data. **resonance(s) not located due to coincidence with another signal.*

38 is a rare example of a solution phase trifluorobenzene complex. It was synthesised by hydrogenation of **1** in 1,2,3-$C_6H_3F_3$ and the ^{1}H, $^{19}F\{^{1}H\}$ and $^{31}P\{^{1}H\}$ NMR spectrum recorded in 1,2,3-$C_6H_3F_3$ [Table 5.2, Scheme 5.2]. The $^{19}F\{^{1}H\}$ NMR spectrum displays two signals [δ −167.95 & −147.52], upfield of the respective solvent peaks, with a 1:2 ratio (doublet and triplet respectively) these peaks have integral values of 1 and 2 compared to the free $[BAr^F_4]^-$ signal (integral = 24), no **4** is observed. The $^{31}P\{^{1}H\}$ NMR spectrum contains one doublet signal only [Table 5.2]. Unfortunately the solvent obscures the arene region of the ^{1}H NMR spectrum. It appears that **38** is only stable in the presence of an excess of 1,2,3-$C_6H_3F_3$. As when a solution of **38** is dried under vacuum and re-dissolved in CD_2Cl_2 **4** is observed as the major product, although a small signal for **38** is retained, presumably due to an equilibrium with **4** (*vide infra*). Very small single crystals were grown from a 1,2,3-$C_6H_3F_3$ solution of **38** layered with pentane, but X-ray diffraction data was not of high enough quality for reliable refinement. ESI-MS was undertaken using 1,2,3-$C_6H_3F_3$ as the solvent. At the required concentrations for ESI-MS ($1x10^{-6}$ mol cm^{-3}) small amounts of solvent impurities such as benzene and fluorobenzene can displace a significant proportion of the weakly bound 1,2,3-$C_6H_3F_3$ ligands and so, although **38** is observed in the mass spectrum [$\{M^+\}$ m/z = 553.19, $\{M^+\}$ calc = 553.18], it is only a minor peak (major peaks for the cations of **35** and **2**).

Hydrogenation of **1** in 1,2,3,4-$C_6H_2F_4$, C_6HF_5 or C_6F_6 forms **4** directly, in these cases the fluorobenzenes now act as non-coordinating solvents [Scheme 5.2].

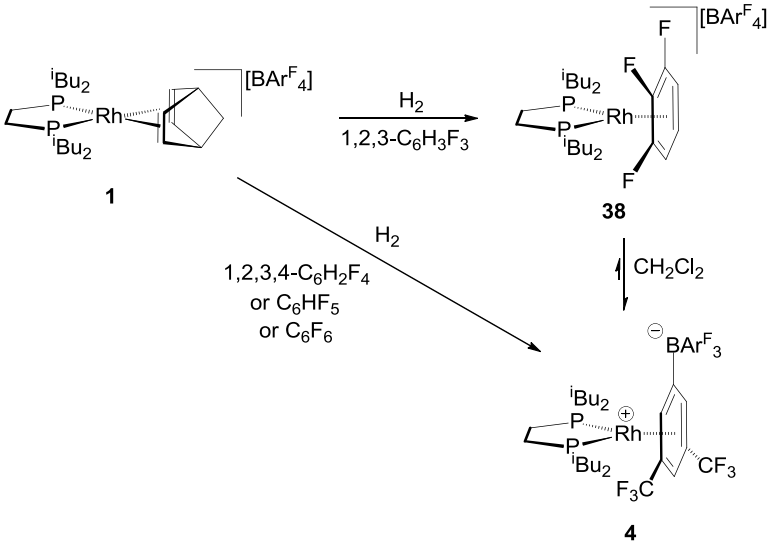

Scheme 5.2. Hydrogenation of **1** in fluorobenzenes $C_6H_nF_{6-n}$ (n = 0-3).

Most of the above mentioned η^6-arene complexes were crystallised and their solid state structures investigated by X-ray crystallography. All the [Rh(^{i}Bu$_2$PCH$_2$CH$_2$P^{i}Bu$_2$)(η^6-arene)][BAr$^F_4$] complexes display a *pseudo*-octahedron of anions surrounding the cations (*see Chapter 2 for examples*) sometimes allowing for multiple conformations of the cation within this pocket, which is observed as structural disorder. Many of the arene complexes exhibit cation disorder either of the phosphine {**24** (*Section 3.3.i*), **36** and **40** (*vide infra*)}, the arene {**3** (*Section 2.2.ii*)} or entire cation {**2** (*Section 2.2.ii*)}, this is proposed to be a consequence of the solid-state packing geometry in which six bulky anions form a pocket around the cation, allowing multiple configurations of the cation. The disordered cations are in contrast to the well ordered zwitterionic **4**. The structures of **39** and **37**, while consistent with the proposed structure, were of low quality and too disordered for accurate refinement. An X-ray diffraction dataset was collected for a high quality crystal of benzene complex **35**; however, the dataset could not be solved. The high symmetry of **35** may allow several orientations of the cation {as seen in the solid-structure of **9** (*see Section 4.2.ii*)} within the lattice structure of [BAr$^F_4$]$^-$ anions.

X-ray diffraction data for **36** were collected and analysed to confirm the expected geometry. Disorder of the anion, phosphine and arene were all observed and a low quality structure was produced by restraining the disorder components to behave similarly (R = 16%) [Figure 5.6]. The two phosphine disorder components occur approximately perpendicular to each other and refine to give a 64 : 36 ratio.

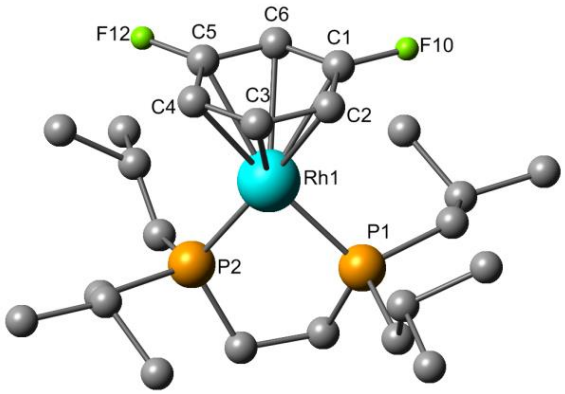

Figure 5.6. Ball and stick plot of complex **36** in the solid-state. Major disorder component shown only. Hydrogen atoms and anions omitted for clarity.

The structure of **40** with its bulkier $C_6H_5CF_3$ ligand does allow accurate refinement despite phosphine disorder over two positions (major component 60% refined occupancy) [Figure 5.7]. The two phosphine ligand disorder components occur approximately parallel and perpendicular to the C(1)-CF_3 vector [angle between planes Rh(1)P(1)P(2) – Rh(1)C(1)C(7), 88.9°; Rh(1)P(3)P(4) – Rh(1)C(1)C(7) 4.0°]. The structural metrics are typical of an η^6-arene complex with Rh–$C_{(arene)}$ bond lengths ranging 2.301(5) to 2.350(6).[2, 32]

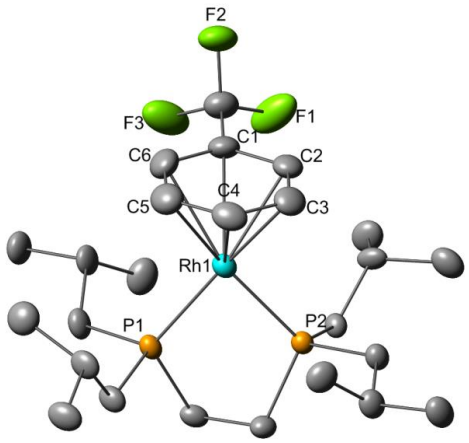

Figure 5.7. Displacement ellipsoid plots (30% probability) of complex **40** in the solid state. Major disorder component shown only. Hydrogen atoms and anions omitted for clarity. Selected bond length (Å) and angle (°) data: Rh(1)–C(6), 2.350(6); Rh(1)–C(3), 2.301(5); Rh(1)–P(1), 2.2726(16); Rh(1)–P(2), 2.2788(17); P(1)-Rh(1)-P(2), 81.88(6). Minor component: Rh(1)–P(3), 2.194(3); Rh(1)–P(4), 2.184(3); P(3)-Rh(1)-P(4), 85.84(12).

The two most reliable solid-state structures of η^6-arene complexes (**40** and **3**) are compared. The major disorder component of **40** shows similar Rh–C and Rh–P bond distances to **3** [Table 5.3], but the minor disorder component of **40** [minor component occupancy 40%] displays a shorter Rh–P distance and a wider bite angle. This variation is also located between the two disorder components of the less reliable structures of **24** (disorder components 50% each) and **36** (major disorder component 64%). Perhaps the chelating phosphine $^{i}Bu_2PCH_2CH_2P^{i}Bu_2$ is slightly flexible and can subtly adapt its bite angle to fit within different steric environments within a crystal lattice. The bite angle of other complexes described in this thesis with $^{i}Bu_2PCH_2CH_2P^{i}Bu_2$ varies from 82.68(14)° (complex **1-[BAr$^{Cl}_4$]**) to 87.23(6)° (complex **26**).

Complex	Average Rh–$C_{(arene)}$ distance (Å)	Average Rh–P distance (Å)		Bite angle (°)	
		Major Disorder Component	Minor Disorder Component	Major Disorder Component	Minor Disorder Component
40	2.33(1)	2.28(1)	2.19(1)	81.88(6)	85.84(12)
3	2.31(1)	2.242(2)	N/A	82.79(12)	N/A
24*	2.33(1)	2.31(1)	2.17(1)	80.12(18)	86.5(2)
36*	2.35(1)	2.27(1)	2.22(1)	81.76(19)	86.6(5)

Table 5.3. Comparison of the key bond lengths and angles of solid state structures of [Rh($^{i}Bu_2PCH_2CH_2P^{i}Bu_2$)($\eta^6$-arene)][BAr$^F_4$] complexes (arene = **40**, $C_6H_5CF_3$; **3**, 1,2-$C_6H_4F_2$; **24**, C_6H_5Cl; **36**, 1,3-$C_6H_4F_2$). **The structures of **24** and **36** were not of high quality but data is consistent with the other structures*.*

5.2.iii. Comparison of binding strength with the [BAr$^F_4$]$^-$ anion

As the number of fluorine substituents increases, [BAr$^F_4$]$^-$ becomes a competitive ligand for coordination. The arene 1,3-$C_6H_4(CF_3)_2$ presents an interesting comparison with [BAr$^F_4$]$^-$ since the influence of the anionic (BAr$^F_3$)$^-$ group can be tested. Hydrogenation of **1** in 1,3-$C_6H_4(CF_3)_2$ results in a yellow solution. The $^{31}P\{^1H\}$ NMR spectrum contains a major signal attributed to **4** with two smaller signals (~25% of total signal) [δ 72.8 & 72.5, J_{RhP} 200 & 198 Hz respectively], these smaller signals are likely to be [Rh($^{i}Bu_2PCH_2CH_2P^{i}Bu_2$)($\eta^6$-1,3-$C_6H_4(CF_3)_2$)][BAr$^F_4$], **41**, or complexes formed with more strongly binding impurities in the solvent (such as **40**) [Scheme 5.3]. ESI-MS analysis of this solution displays **40** as the major peak (*N.B.* impurities are emphasised at the high dilutions required for ESI-MS). A small peak confirming the presence of some **41** is located [m/z = 635.20, calc = 635.19] (*N.B.* neutral **4** is not observed by ESI-MS).

Therefore even in the presence of a great excess of 1,3-$C_6H_4(CF_3)_2$ the anionic $[BAr^F_4]^-$ species acts as a better ligand despite its greater steric profile. It appears that the electron donating properties of the $(BAr^F_3)^-$ substituent increases the binding affinity of an arene, this is consistent with the relatively strong binding affinity of $[BAr^{Cl}_4]^-$ which has been shown to displace η^6-C_6H_5F arene ligands.[33] It is also noteworthy that coordination of an anion to a cation results in charge balancing which is likely to be entropically favoured as less order is then imposed on the surrounding solvent.

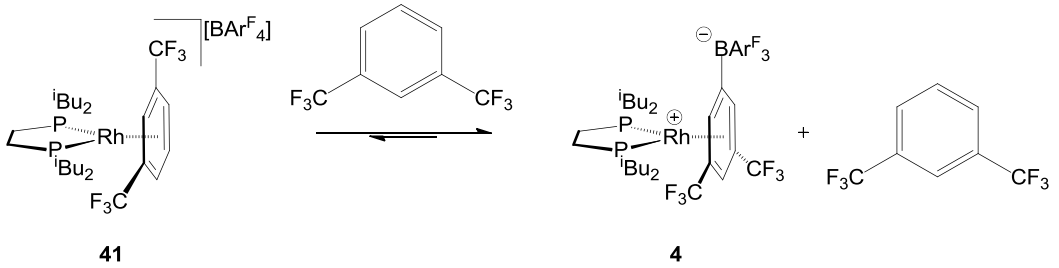

Scheme 5.3. Equilibrium between **41** and **4** in 1,3-$C_6H_4(CF_3)_2$

Some of the fluorobenzene complexes are also in equilibrium with **4** when solvated in CH_2Cl_2 [Scheme 5.4]. The $^{31}P\{^1H\}$ NMR spectroscopy chemical shifts of the $[Rh(^iBu_2PCH_2CH_2P^iBu_2)(\eta^6\text{-arene})][BAr^F_4]$ complexes are all slightly downfield of the signal for **4**, and this makes comparison by $^{31}P\{^1H\}$ NMR possible in the case of an equilibrium. Whilst **4** decomposes over ~1 hour in neat CH_2Cl_2, it appears to have a prolonged lifetime when formed from an arene complex under equilibrium conditions (one equivalent of arene present in the CH_2Cl_2 solution). For example, a CH_2Cl_2 solution of **3** undergoes ~50% decomposition in two days (by analysis of $^{31}P\{^1H\}$ and $^{19}F\{^1H\}$ NMR spectra). Therefore, to a good approximation, integration analysis of the $^{31}P\{^1H\}$ NMR spectra may be undertaken upon freshly solvated samples without the complications of decomposition.

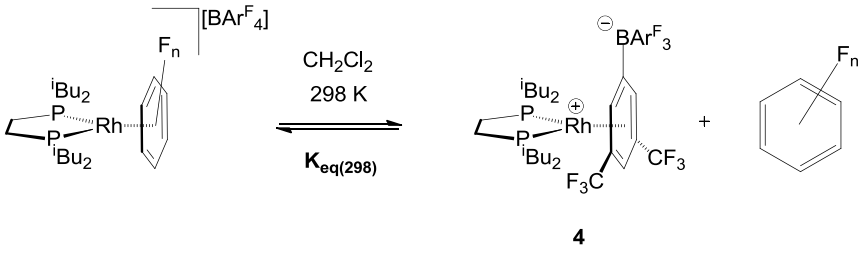

Scheme 5.4. Equilibrium established between a coordinated arene complex and **4** + free arene in CH_2Cl_2. $^{31}P\{^1H\}$ NMR Data used for equilibrium constants.

The equilibrium constant is determined in terms of concentration of all free species (*i.e.* cation and anion treated separately) [Table 5.4]. There are equal numbers of cations and anions and also an equal number of arene ligands present in a crystalline sample. Therefore the equilibrium constant equation simplifies so that it can be determined directly by the ratio of the squares of the integrals of respective $^{31}P\{^{1}H\}$ NMR signals [Equation 5.1].

$$K_{eq} = \frac{[\{Rh(^{i}Bu_2PCH_2CH_2P^{i}Bu_2)(\eta^6\text{-}Ar^F(BAr^F{}_3)\}] \times [\text{arene}]}{[\{Rh(^{i}Bu_2PCH_2CH_2P^{i}Bu_2)(\eta^6\text{-arene})\}^+] \times [\{BAr^F{}_4\}^-]} = \frac{[\{Rh(^{i}Bu_2PCH_2CH_2P^{i}Bu_2)(\eta^6\text{-}Ar^F(BAr^F{}_3)\}]^2}{[\{Rh(^{i}Bu_2PCH_2CH_2P^{i}Bu_2)(\eta^6\text{-arene})^+\}]^2}$$

Equation 5.1. Equilibrium constant for displacement of η^6-arene ligand by $[BAr^F{}_4]^-$ [Scheme 5.4]

The Gibbs free energy of the reaction at 298 K can be calculated from $\Delta G_{(298)} = -RT\ln\{K_{eq(298)}\}$ [Table 5.4].

Complex	Arene	$K_{eq(298)}$ (2 s. f)	$\Delta G_{(298)}$ (kJ/mol, 2 s. f.)
2	C_6H_5F	0.0030 (± 0.0014)	14 (± 1)
3	1,2-$C_6H_4F_2$	3.2 (± 0.3)	−2.9 (± 0.2)
36	1,3-$C_6H_4F_2$	12* (± 0.2)	−6.1* (± 0.3)
37	1,4-$C_6H_4F_2$	2.8* (± 0.3)	−2.5* (± 0.2)
38	1,2,3-$C_6H_3F_3$	260 (± 125)	−14 (± 1)
40	$C_6H_5CF_3$	0.23 (± 0.22)	3.6 (± 0.2)
24	C_6H_5Cl	0.00061 (± 0.00064)	18 (± 3)

Table 5.4. The equilibrium constants ($K_{eq(298)}$) [Equation 5.1] of arene complexes ↔ **4** at 298 K in CH_2Cl_2, and the Gibbs free energy associated with the reactions at 298 K [Scheme 5.4]. Errors calculated from a ±1% inaccuracy of the ratio of species determined by integration of the $^{31}P\{^{1}H\}$ NMR spectra .* *~15% **2** present from impurities in the solvent (supplied by Fluorochem).*

These equilibrium experiments show that by increasing the amount of electronegative substituents upon an arene the binding affinity of the arene decreases relative to $[BAr^F{}_4]^-$. The difluorobenzenes have an equilibrium constant which is close to 1 showing that there is little preference between the arene complex and zwitterionic anion coordinated species (+ free arene) [Scheme 5.4].

It is noteworthy that these η^6-arene complexes are cationic and any back-bonding interactions may be relatively small. Addition of fluorine substituents may lower the arene π orbital energies making the donor orbitals less accessible but the empty accepting orbitals more accessible. In a neutral or anionic complex greater degrees of backbonding may occur in the fluorinated arenes and the trends could be different.

5.3. Estimation of binding affinities of [Rh(^{i}Bu$_2$PCH$_2$CH$_2$P^{i}Bu$_2$)(η^6-fluoro-arene)] complexes using ESI-MS techniques

Rhodium phosphine complexes with the phosphine ^{i}Bu$_2$PCH$_2$CH$_2$P^{i}Bu$_2$ are ideal for gas-phase ESI-MS fragmentation studies because the phosphine is not susceptible to dehydrogenation or decomposition – which may complicate the experiment. Controlled fragmentation experiments were achieved by combined glove box ESI-MS.[30] The exit voltage (or cone voltage), which accelerates the ions, (relative to residual, neutral solvent or gas molecules), in the intermediate-pressure region of the spectrometer, determines the degree of cationic fragmentation by collision-induced dissociation processes.[28] By varying the exit voltage, the ratio of η^6-arene coordinated cation, [Rh(^{i}Bu$_2$PCH$_2$CH$_2$P^{i}Bu$_2$)(η^6-arene)]$^+$, to the fragmented rhodium phosphine fragment, [Rh(^{i}Bu$_2$PCH$_2$CH$_2$P^{i}Bu$_2$)]$^+$, is altered [Scheme 5.5]. The results are plotted as the percentage of arene bound cations against exit voltage.

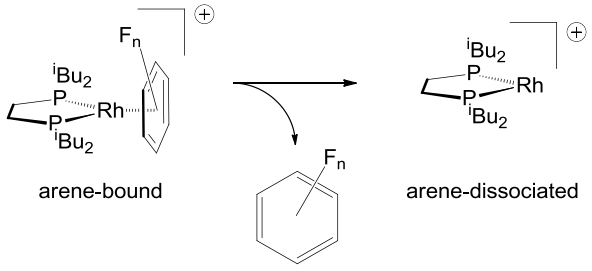

Scheme 5.5. Fragmentation process observed during ESI-MS, which can be increased by using higher exit voltages.

In preparation for the experiment the arene complex was diluted to a concentration of ~1 x10^{-6} M, using the same arene as the coordinated ligand as the solvent (*N.B.* all solvents were dried over CaH_2 and distilled before use). The ESI-mass spectrum was then recorded over a range of exit voltage values until > 95% fragmentation was occurring [Figure 5.8]. The workable range for the exit voltage which resulted in a strong signal without decomposition was 50 V - 250 V. The spectra were analysed by recording the intensity of the largest isotope peak for the two signals [Rh(^{i}Bu$_2$PCH$_2$CH$_2$P^{i}Bu$_2$)(η^6-arene)]$^+$ and [Rh(^{i}Bu$_2$PCH$_2$CH$_2$P^{i}Bu$_2$)]$^+$. In order to compensate for differing isotopic distributions the intensity was then normalised (by division by the fractional proportion of the isotopic distribution in the largest isotope peak). Since this experiment measures fragmentation by cone voltage induced

dissociation only (ESI-MS) and not by secondary collisions using a specific inert gas (ESI-MS/MS) a centre of mass correction was not applied to the results.

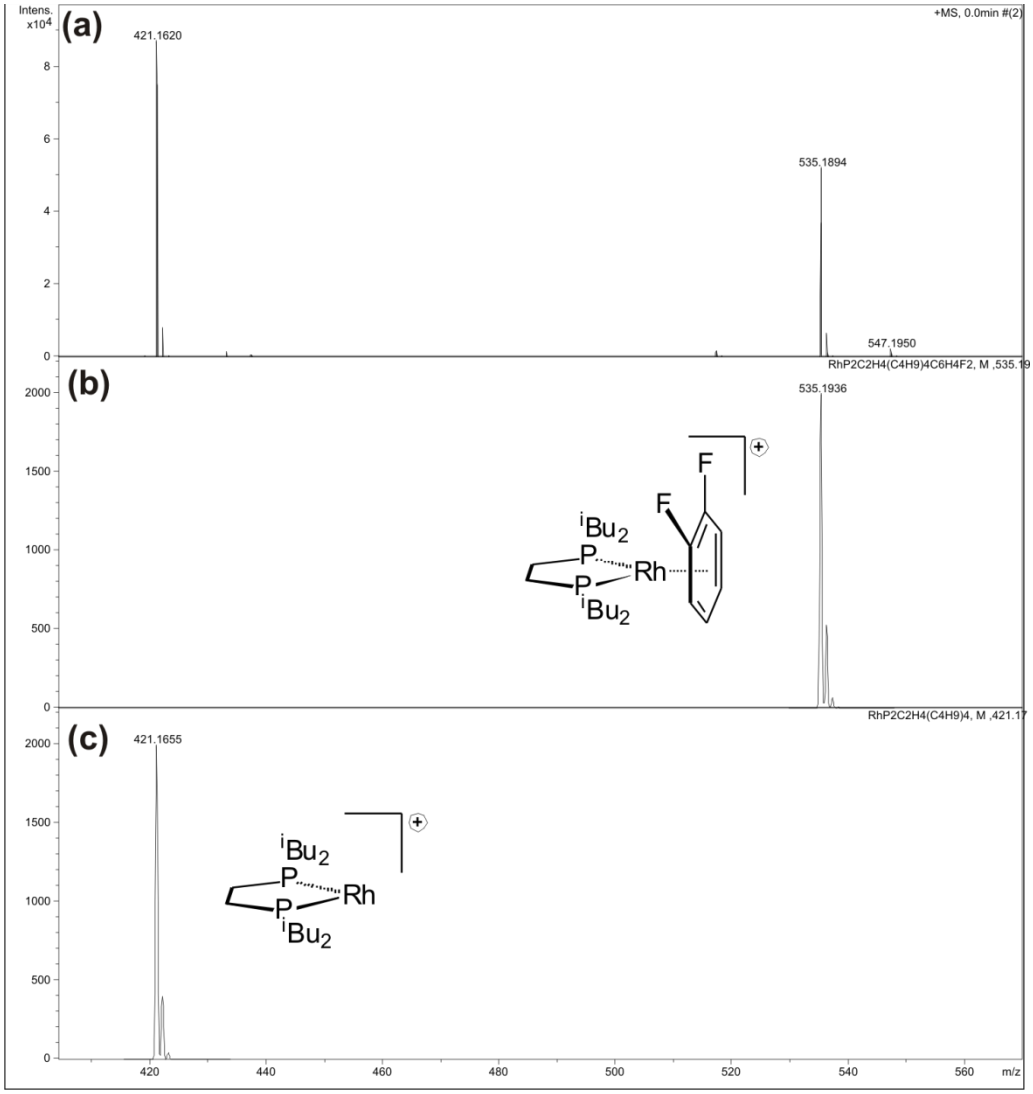

Figure 5.8. (a) Example of a mass spectrum (complex **3** in 1,2-$C_6H_4F_2$, exit voltage = 130 V). **(b and c)** calculated peaks for $[Rh(^iBu_2PCH_2CH_2P^iBu_2)(\eta^6\text{-}1,2\text{-}C_6H_4F_2)]^+$ and $[Rh(^iBu_2PCH_2CH_2P^iBu_2)]^+$

All the cationic arene complexes aforementioned in this chapter were tested in this manner so that the binding affinity of the arene could be compared directly. The point at which 50% fragmentation occurs was taken as a suitable value for comparison.[31] These values are representative of the gas-phase dissociation energy of η^6-arene from the $\{RhP_2\}^+$ fragment. They can be compared to the equilibrium measurements (between arene complex and **4**) previously mentioned, although it is important to note the distinction between these measurements, since the equilibrium reaction occurs in the solution phase and creates a different set of products [Scheme 5.6].

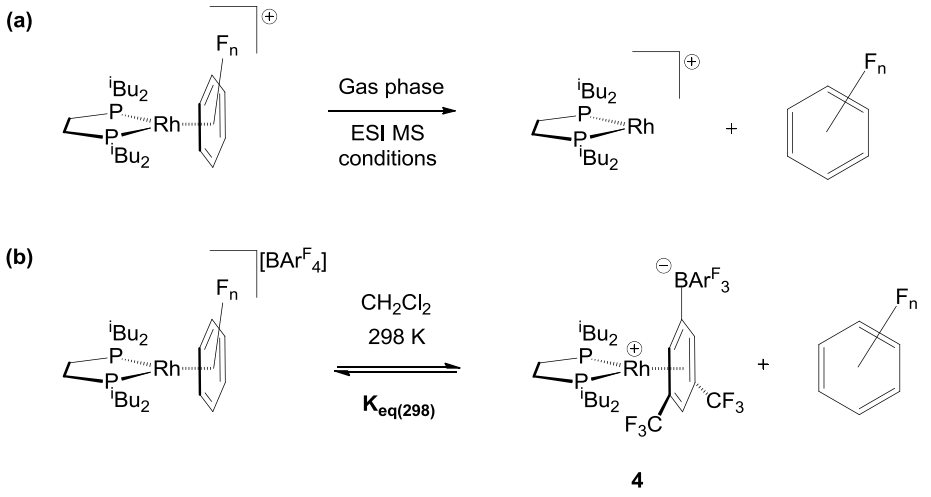

Scheme 5.6. (a) ESI-MS fragmentation reaction in the gas phsae. **(b)** Comparison with the solution phase equilibrium experiments aforementioned in which **4** forms as the product.

The effects of increasing the number of fluorine substituents are displayed in Figure 5.9.

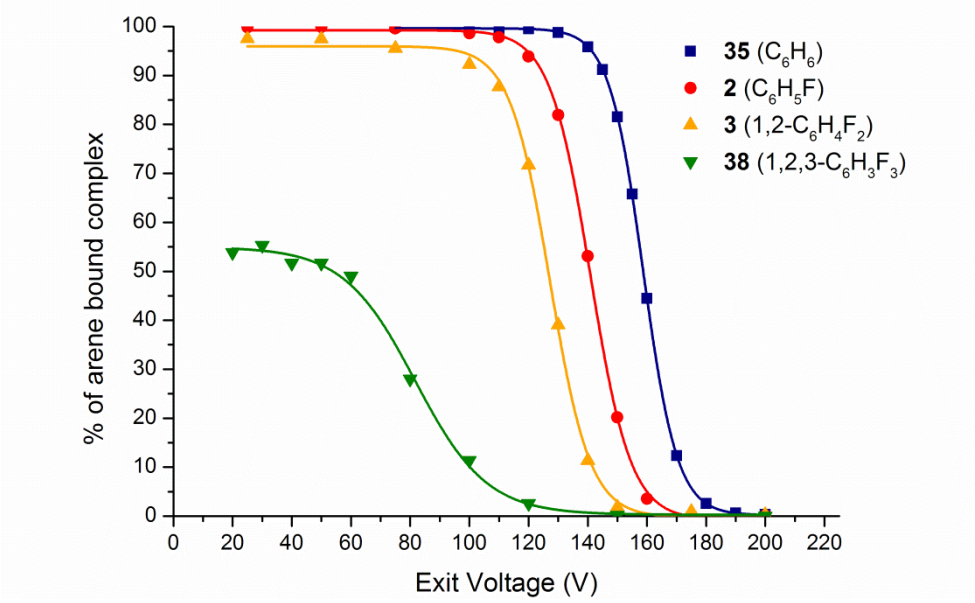

Figure 5.9. Fragmentation of $[Rh(^{i}Bu_2PCH_2CH_2P^{i}Bu_2)(\eta^6\text{-}C_6H_{6-n}F_n)]^+$ (n = 0-3) cations in ESI-MS over a range of exit voltage values. More strongly bound species shown on the right hand side of the graph.

The fragmentation profiles in Figure 5.9 clearly show that as extra fluorine substituents are added to the arene the binding affinity of the arene drops, consistent with previous reports and calculations.[11, 13-15, 19] The fragmentation profile of **38**, whilst broadly the same line-shape as the other complexes, is distorted due to a large signal for the fragmented species $[Rh(^{i}Bu_2PCH_2CH_2P^{i}Bu_2)]^+$, even at low exit voltage. This is because the signal for $[Rh(^{i}Bu_2PCH_2CH_2P^{i}Bu_2)(\eta^6\text{-}C_6H_3F_3)]^+$ is a minor peak at the

concentrations used in ESI-MS alongside solvent impurity species which contribute to the fragmented $[Rh(^{i}Bu_2PCH_2CH_2P^{i}Bu_2)]^+$ peak intensity. Because of this an estimate of the 50% fragmentation point is recorded at half of the maximum percentage ratio, *i.e.* 0.5 x 54% = 27% arene bound complex. A similar effect is present for **3** but to a much smaller extent and in this case the same result (127 V), to within 1 V, is generated regardless of whether the 50% fragmentation point is amended or not. The 50% fragmentation points drop with increasing fluorine incorporation [Table 5.5]. This trend is consistent with the $K_{eq(298)}$ values of **2**, **3** and **38** in equilibrium with **4** in CH_2Cl_2 (*see Table 5.4*).

$[Rh(^{i}Bu_2PCH_2CH_2P^{i}Bu_2)(\eta^6\text{-arene})]^+ \rightarrow [Rh(^{i}Bu_2PCH_2CH_2P^{i}Bu_2)]^+ + \text{arene}$		
Complex	Arene	50% dissociation (V)
35	C_6H_6	158
2	C_6H_5F	141
3	1,2-$C_6H_4F_2$	127
38	1,2,3-$C_6H_3F_3$	~83*

Table 5.5. Exit voltage at which 50% arene dissociation occurs.**approximate result based upon when half of the maximum % value is reached (< 50%) in the case of weakly bound **38** which occurs with impurities.*

The three structurally isomeric difluorobenzene complexes **3**, **36** and **37** were investigated to see whether the electronic effect of fluorine substituents could be considered additive or whether position around the ring was also important [Figure 5.10].

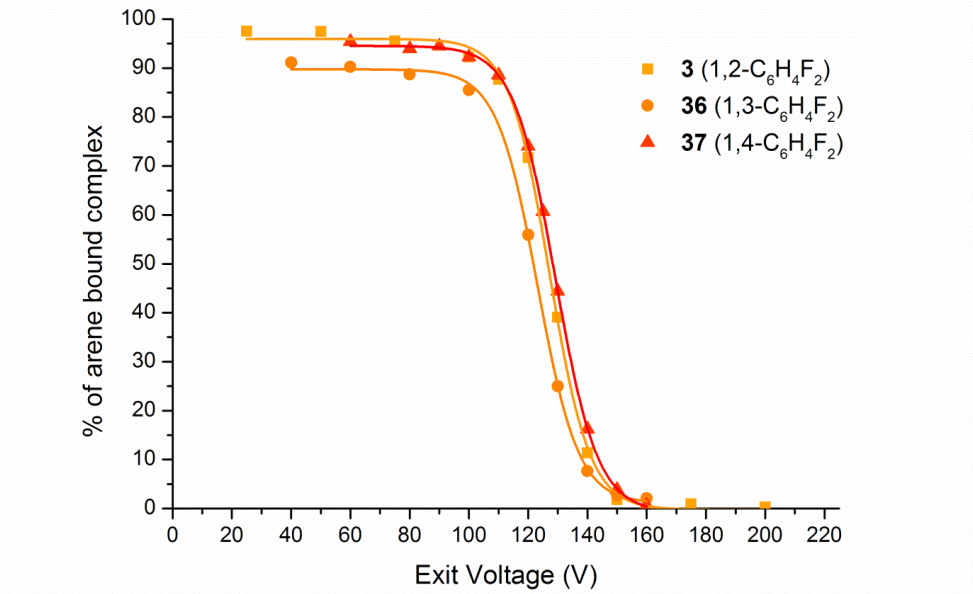

Figure 5.10. Fragmentation of $[Rh(^{i}Bu_2PCH_2CH_2P^{i}Bu_2)(\eta^6\text{-1,n-}C_6H_4F_2)]^+$ (n = 2,3,4) cations in ESI-MS over a range of exit voltage values.

Unfortunately some minor impurities affected these experiments which resulted in a slight distortion of the fragmentation profile (by an artificially increased concentration of the fragment species $[Rh(^{i}Bu_2PCH_2CH_2P^{i}Bu_2)]^+$, as explained above for **38**). Amendment of the 50% fragmentation point (to 50% of the maximum recorded percentage of bound species) changes the 50% fragmentation value for **36** from 122 V to 124 V, and the value of **37** from 128 V to 129 V, the other value remains the same to the nearest 1 volt. The range of amended 50% fragmentation voltages is therefore 124 - 129 V which indicates very similar binding affinities for the three difluorobenzenes and suggests substituent positioning is not very influential on the overall binding affinity as previously reported.[13] A comparison can be made with equilibrium that forms between the difluorobenzene complexes and **4** when dissolved in CH_2Cl_2 (*see Table 5.4*). The $K_{eq(298K)}$ values are similar for the three complexes [$K_{eq(298K)}$: **3**, 3.2 (±0.3); **36**, 12 (±0.2); **37**, 2.8 (±0.3)] but show that **36** favours the displacement of difluorobenzene by the anion slightly more so than for **3** and **37**. Whilst a small difference this is consistent with the slightly lower 50% fragmentation voltage observed for **36**.

The 50% fragmentation point of the various arene ($C_6H_{6-n}F_n$) complexes can be plotted against the number of fluorine substituents present (n) displaying a roughly linear trend, although the estimated value of **38** falls slightly off of the general trend [Figure 5.11].

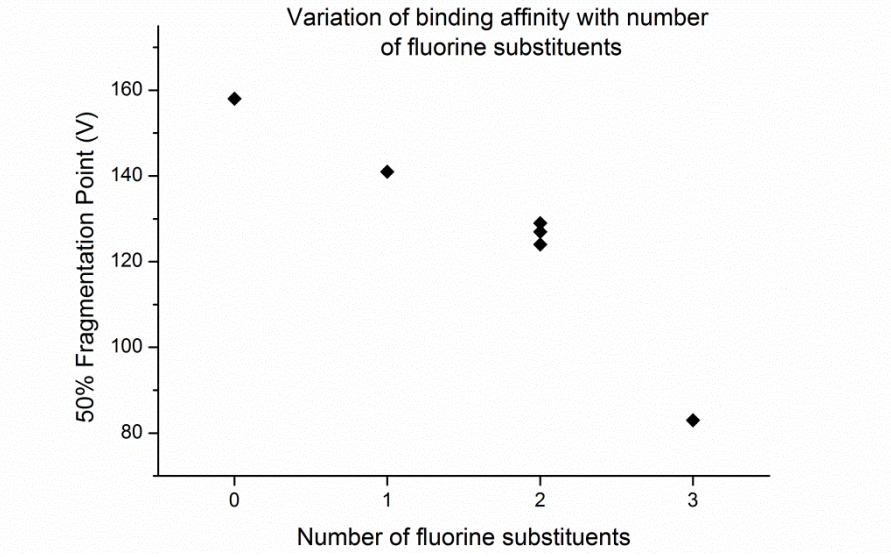

Figure 5.11. Comparison of the 50% fragmentation point of $[Rh(^{i}Bu_2PCH_2CH_2P^{i}Bu_2)(\eta^6\text{-}C_6H_{6-n}F_n)]^+$ with number of fluorine substituents (n).

The $\Delta G_{(298)}$ values previously calculated (from the equilibrium of η^6-arene complex with **4** [Scheme 5.4]) can also be plotted against the number of fluorine substituents and again show a nearly linear trend [Figure 5.12]. No equilibrium was measured for the benzene complex since **4** was not observed in CH_2Cl_2 solutions of **35**.

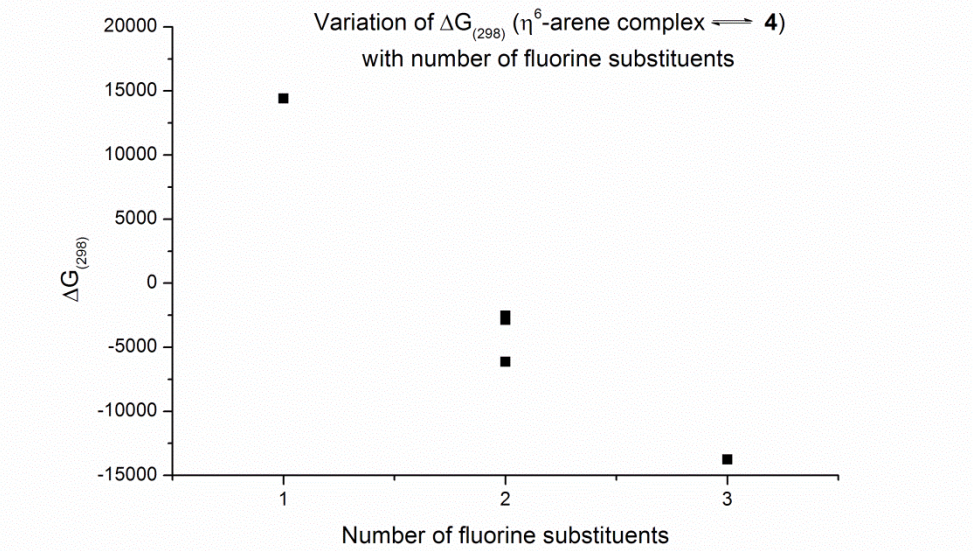

Figure 5.12. Comparison of the $\Delta G_{(298)}$ value for $[Rh(^{i}Bu_2PCH_2CH_2P^{i}Bu_2)(\eta^6\text{-}C_6H_{6-n}F_n)]^+ \rightarrow$ **4** with number of fluorine substituents (n).

A comparison between C_6H_5F and C_6H_5Cl was undertaken [Figure 5.13]. Both **2** and **24** display very similar fragmentation profiles and exhibit 50% fragmentation values of 141 V and 143 V respectively.

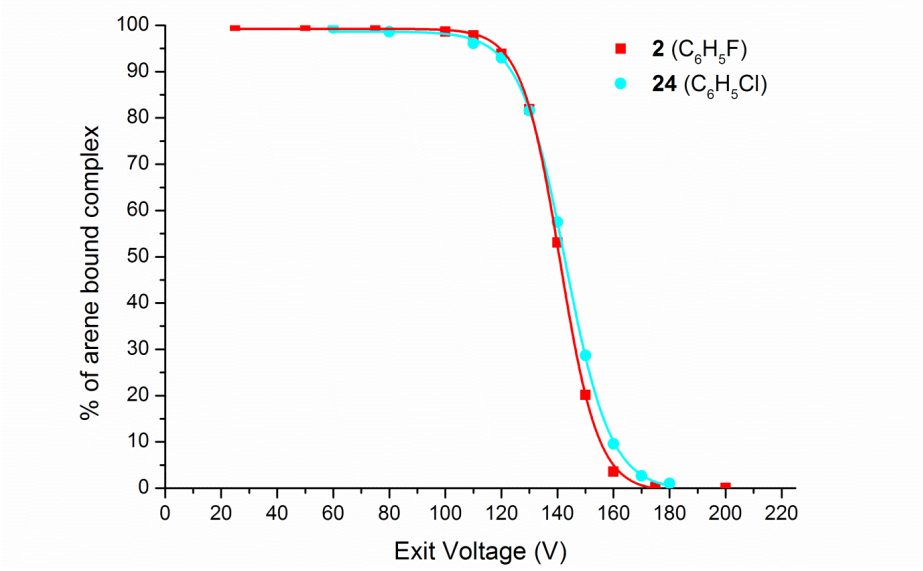

Figure 5.13. Fragmentation of $[Rh(^{i}Bu_2PCH_2CH_2P^{i}Bu_2)(\eta^6\text{-}C_6H_5X)]^+$ (X = F, Cl) cations in ESI-MS over a range of exit voltage values.

The $K_{eq(298)}$ values of **2** and **24** in equilibrium with **4** in CH_2Cl_2 are 3.0 (±1.4) $x10^{-3}$ and 6.1 (±6.4) $x10^{-4}$ ($\Delta G_{(298)}$ 14 (±1) & 18 (±3) kJ/mol respectively) which also indicate a similar binding affinity for both arenes. These results suggest the electronic effect of a fluorine substituent is very similar to a chlorine substituent. This is possibly due to a combination of inductive and mesomeric effects.[34]

Toluene was compared to benzene to investigate the effect of adding electron donating alkyl substituents [Figure 5.14]. Very little change was observed; the toluene complex **39** displayed a 50% fragmentation point at 160 V, just 2 V higher than that for **35**.

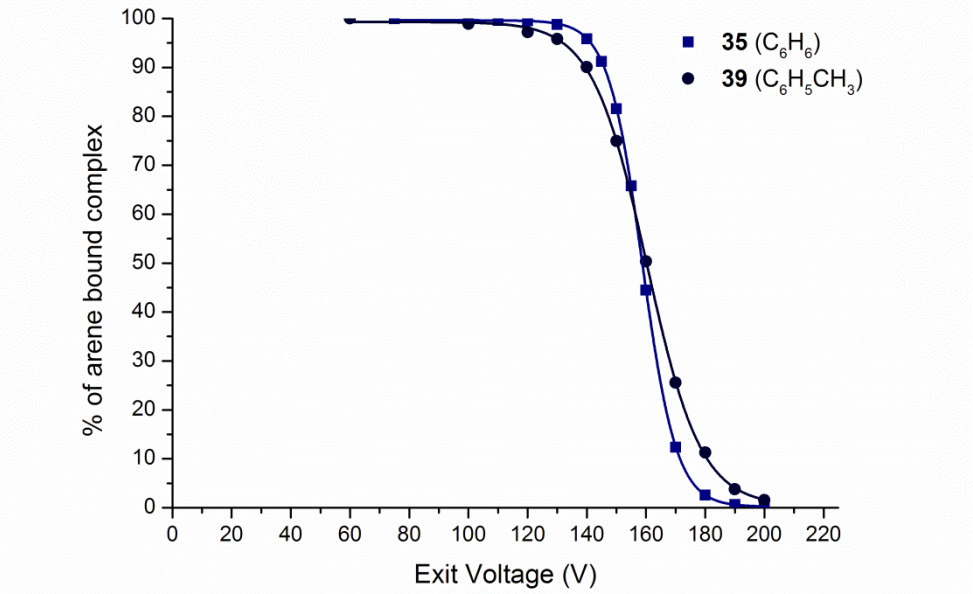

Figure 5.14. Fragmentation of $[Rh(^{i}Bu_2PCH_2CH_2P^{i}Bu_2)(\eta^6\text{-}C_6H_5R)]^+$ (R = H, CH_3) cations in ESI-MS over a range of exit voltage values.

CF_3 groups are often used as electron withdrawing groups and are also present in the anion $[BAr^F_4]^-$ therefore the binding affinity of $C_6H_5CF_3$ is of interest {*N.B.* $C_6H_4(CF_3)_2$ binds very weakly in **41** and is displaced by impurities (mainly $C_6H_5CF_3$) making it unsuitable for variable exit voltage ESI-MS} [Figure 5.15]. The 50% fragmentation point for **40** occurs at 136 V which is less than for **2** but greater than the difluorobenzene complexes. This suggests that the CF_3 group has a greater destabilising effect than a single fluorine but less than two fluorines. The $K_{eq(298)}$ value for the equilibrium between arene complex and **4** is also found for **40** to sit in between the values of **2** and the difluorobenzene complexes (**3**, **36** and **37**).

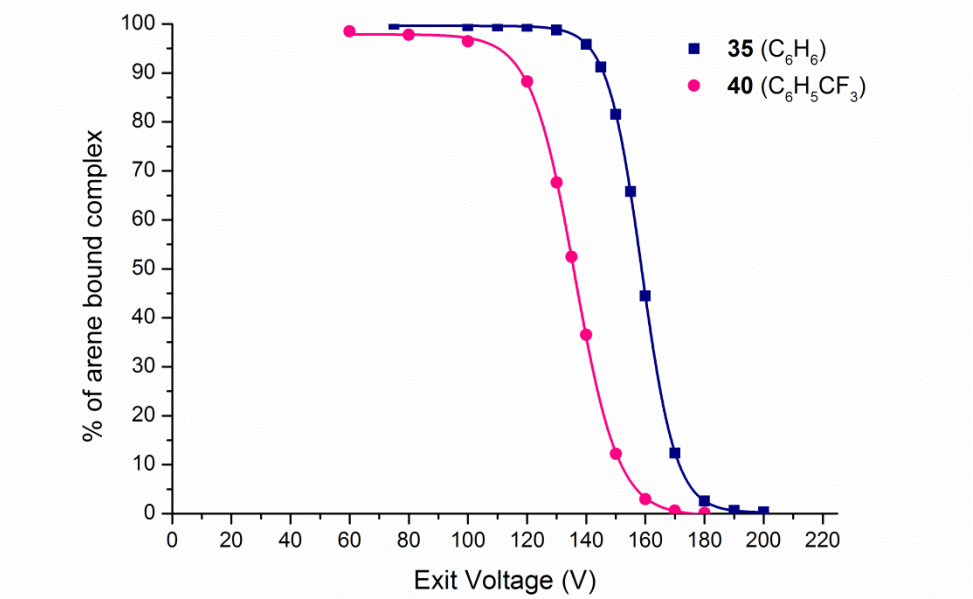

Figure 5.15. Fragmentation of $[Rh(^{i}Bu_2PCH_2CH_2P^{i}Bu_2)(\eta^6\text{-}C_6H_{6-n}(CF_3)_n)]^+$ (n = 0-2) cations in ESI-MS over a range of exit voltage values.

The ESI-MS experimental results are compiled in Table 5.6, and show that addition of electron withdrawing substituents decreases the binding affinity of arenes to the $[Rh(^{i}Bu_2PCH_2CH_2P^{i}Bu_2)]^+$ fragment in the gas-phase, with CF_3 groups having a greater effect than single fluorine substituents.

$[Rh(^{i}Bu_2PCH_2CH_2P^{i}Bu_2)(\eta^6\text{-arene})]^+ \rightarrow [Rh(^{i}Bu_2PCH_2CH_2P^{i}Bu_2)]^+ +$ arene		
Complex	Arene	50% dissociation (V)
39	$C_6H_5CH_3$	160
35	C_6H_6	158
24	C_6H_5Cl	143
2	C_6H_5F	141
40	$C_6H_5CF_3$	136
37	1,4-$C_6H_4F_2$	129*
3	1,2-$C_6H_4F_2$	127
36	1,3-$C_6H_4F_2$	~124*
38	1,2,3-$C_6H_3F_3$	~83*

Table 5.6. Exit voltage at which 50% arene dissociation occurs.**approximate results based upon when half of the maximum % value is reached (< 50%) in the cases of weakly bound species which occur with impurities.*

5.4. Estimation of binding affinities of [Rh(P_2)(η^6-C_6H_5F)][BAr^F_4] complexes (P_2 = chelating phosphine) using ESI-MS techniques

5.4.i. Electronic influence upon binding affinity

Whilst the chelating ligands $^iBu_2PCH_2CH_2P^iBu_2$ and $(O^iPr)_2PCH_2CH_2P(O^iPr)_2$ are sterically very similar, the addition of an oxygen atom in the latter has an electronic effect. Phosphites are more electron withdrawing than phosphines and will not donate as much electron density to a metal centre.[18] Therefore the metal centre might be expected to bind more strongly to other ligands that are coordinated.

The phosphite complexes [Rh{$(O^iPr)_2PCH_2CH_2P(O^iPr)_2$}($\eta^6$-$C_6H_6$)][$BAr^F_4$] **42**, [Rh{$(O^iPr)_2PCH_2CH_2P(O^iPr)_2$}($\eta^6$-$C_6H_5F$)][$BAr^F_4$] **43** and [Rh{$(O^iPr)_2PCH_2CH_2P(O^iPr)_2$}($\eta^6$-$C_6H_4F_2$)][$BAr^F_4$] **44** were prepared by hydrogenation of **21** in the appropriate arene solvent. The phosphite complexes were investigated by variable exit voltage ESI-MS in comparison with the analogous $^iBu_2PCH_2CH_2P^iBu_2$ phosphine complexes (**35**, **2** and **3**) [Figure 5.16]. It is noteworthy that the product of fragmentation is now different to the previous ESI-MS experiments (as a different P_2 ligand is used). The stability of the final $\{RhP_2\}^+$ species, [Rh{$(O^iPr)_2PCH_2CH_2P(O^iPr)_2$}]$^+$ in this case, may influence the gas-phase dissociation process.

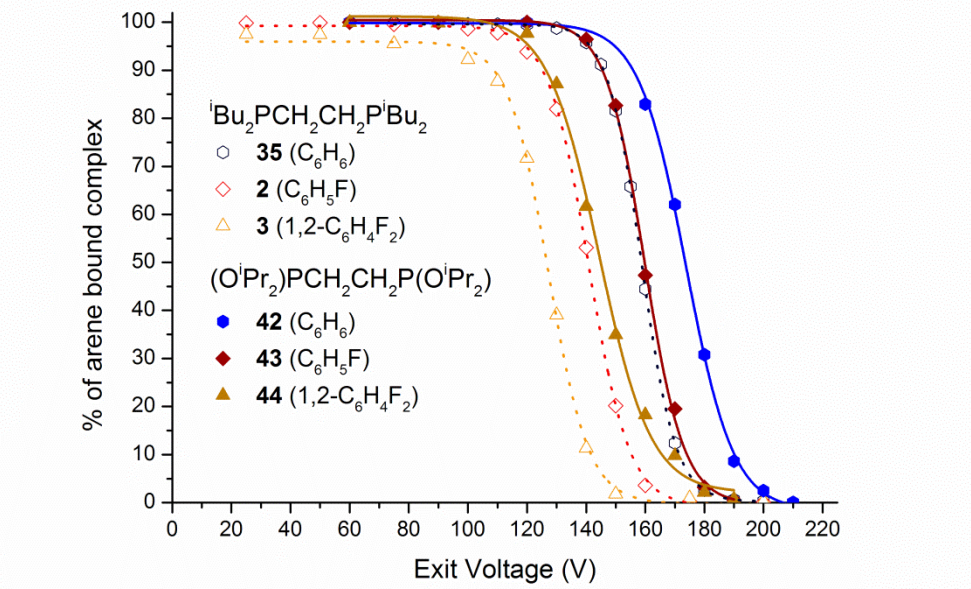

Figure 5.16. Fragmentation of [Rh{$(O^iPr)_2PCH_2CH_2P(O^iPr)_2$}($\eta^6$-$C_6H_{6-n}F_n$)]$^+$ (n = 0-2) cations in ESI-MS over a range of exit voltage values (comparison with [Rh($^iBu_2PCH_2CH_2P^iBu_2$)(η^6-$C_6H_{6-n}F_n$)]$^+$ (n = 0-2) cations displayed in dotted lines).

The fragmentation profiles of the phosphite complexes are all shifted to the right of the analogous phosphine complexes indicating a greater gas-phase binding affinity of the arene. The 50% fragmentation points are all 17 ±1 V greater than the respective phosphine complexes [**42**, 174 V; **43**, 159 V; **44** 144 V]. Coincidentally the fragmentation profiles of the phosphite complexes match well with the phosphine complexes with one less fluorine substituent.

A crystal structure of **43** was collected to confirm the expected structure, which was analogous to the phosphine analogue **2** [Figure 5.17]. The structure solved well but disorder was located in the ^{i}Pr groups, and the fluorine atom was disordered across three positions of the arene. Unlike **2**, the anions do not form a well defined octahedron surrounding the cation (linear 1-D chains of cations are located), indicating that different effects dictate the packing in this phosphite complex.

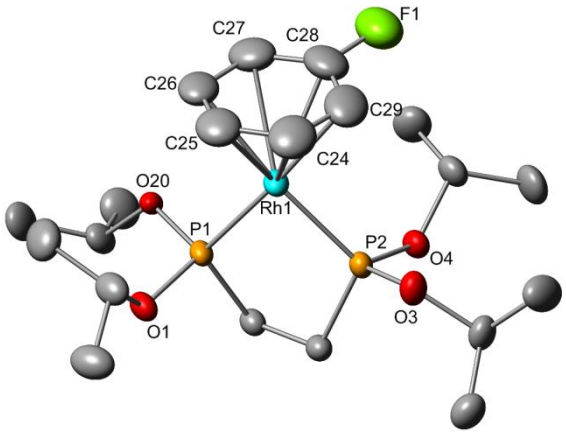

Figure 5.17. Displacement ellipsoid plots (30% probability) of complex **43** in the solid state. Major disorder component shown only. Hydrogen atoms and anions omitted for clarity. Selected bond length (Å) and angle (°) data: Rh(1)–C(28), 2.345(6); Rh(1)–C(26), 2.297(5); Rh(1)–P(1), 2.2042(12); Rh(1)–P(2), 2.2091(12); P(1)-Rh(1)-P(2), 82.83(4).

The Rh–$C_{(arene)}$ bond lengths in **43** are all similar [range 2.345(6)-2.297(5) Å] and typical of η^6-C_6H_5F complexes.[2, 35] The Rh–P distances are a little shorter in comparison with phosphine complexes such as **40**.

The ^{1}H NMR spectra of **42**, **43** and **44** show that the η^6-arene protons are shifted upfield with respect to the value for free arene (similarly to the analogous phosphine complexes **35**, **2** & **3**). However, the displacements of these chemical shifts from their analogous free arene values, do not correlate with the gas-phase binding affinity results.

5.4.ii. The effect of bite angle upon binding affinity

Previous studies by Weller and co-workers have indicated a greater preference for square planar 16 electron geometries (such as [Rh(*P*$_2$)(acetone)$_2$][BAr$^F_4$]) compared to 18 electron η^6- coordination ([Rh(*P*$_2$)(η^6-C_6H_5F)][BAr$^F_4$]) when using large bite angle ligands.[2] Understanding the effect of bite angle upon the stability of η^6-arene complexes is also of interest with respect to the binding of [BAr$^F_4$]$^-$ anions to metal complexes and utilisation of [BAr$^F_4$]$^-$ as a truly non-coordinating anion for specific systems. An investigation of different bite angle [Rh(^{i}Pr-phosphine)(η^6-C_6H_5F)][BAr$^F_4$] complexes was undertaken by ESI-MS methods [Figure 5.19]. Complexes [Rh{(^{i}Pr$_2$P)$_2$NCH$_3$}(η^6-C_6H_5F)][BAr$^F_4$], **XXXVII**, [Rh{^{i}Pr$_2$P(CH$_2$)$_n$P^{i}Pr$_2$}(η^6-C_6H_5F)][BAr$^F_4$] (n=1, **XXXVI**; n=2, **VIII**; n=3, **IX**) were prepared by Indrek Pernik (D.Phil student, Prof. A. Weller group) who kindly donated samples for ESI-MS experiments. The bite angles of these complexes had been previously reported by analysis of their solid state structures [Figure 5.18].

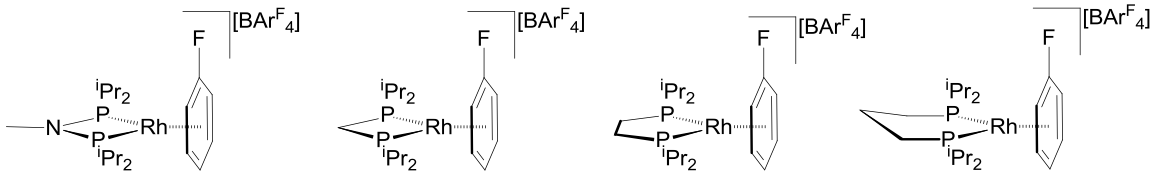

Figure 5.18. [Rh(^{i}Pr-phosphine)(η^6-C_6H_5F)]$^+$ {^{i}Pr-phosphine = (^{i}Pr$_2$P)$_2$NCH$_3$ or ^{i}Pr$_2$P(CH$_2$)$_n$P^{i}Pr$_2$ (n = 1,2,3)} complexes and their bite angles.

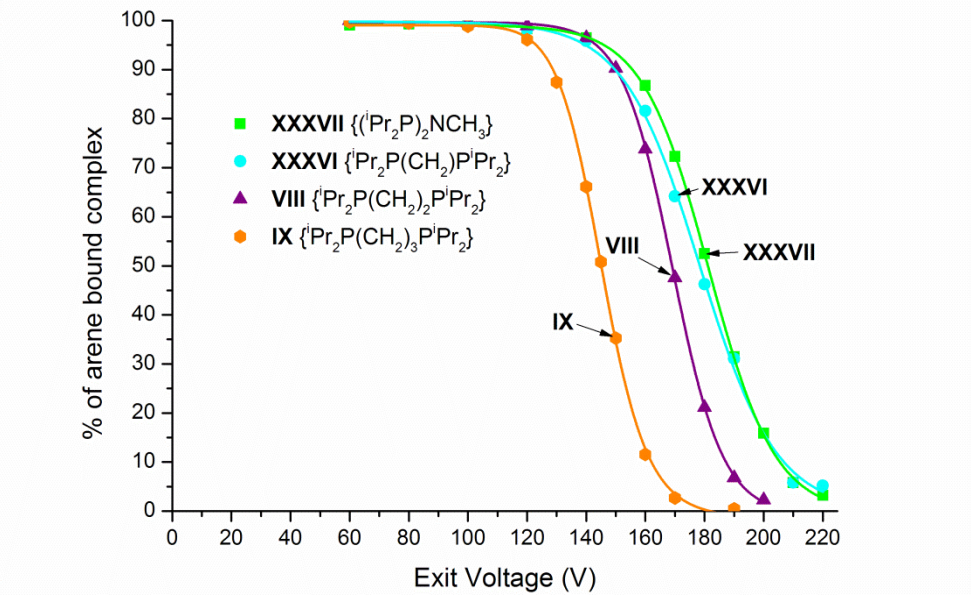

Figure 5.19. Fragmentation of [Rh(^{i}Pr-phosphine)(η^6-C_6H_5F)]$^+$ {^{i}Pr-phosphine = ($^{i}Pr_2P)_2NCH_3$ or $^{i}Pr_2P(CH_2)_nP^{i}Pr_2$ (n = 1,2,3)} cations in ESI-MS over a range of exit voltage values.

These data clearly show that as bite angle increases the binding affinity drops. This could be a steric effect from the phosphine, however, evidence of the electronic influence of the bite angle has been previously reported.[4] The 50% fragmentation points can be plotted against bite angle and display an approximate linear trend [Figure 5.20].

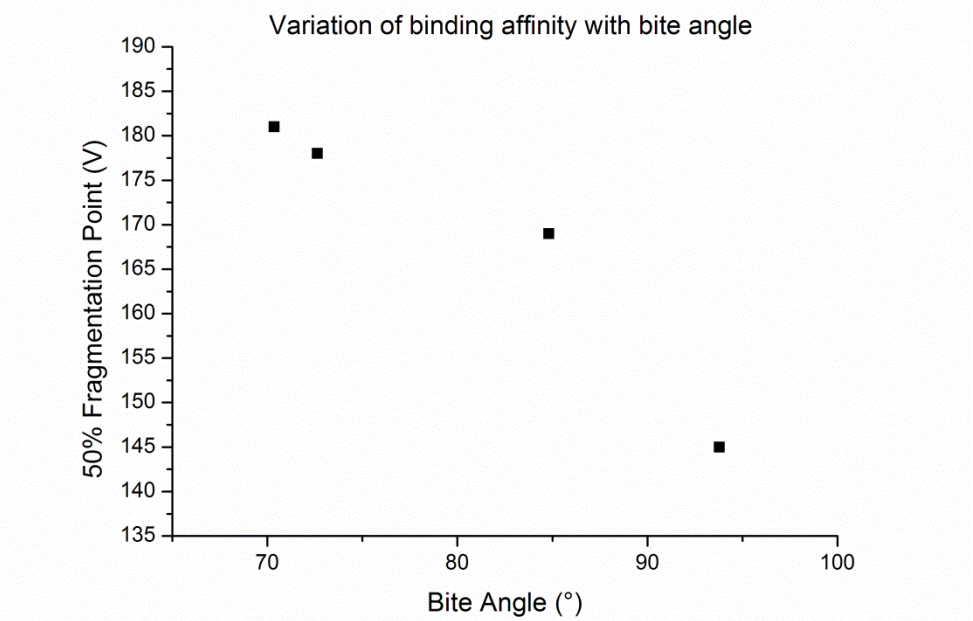

Figure 5.20. Comparison of 50% fragmentation point of [Rh(^{i}Pr-phosphine)(η^6-C_6H_5F)]$^+$ {^{i}Pr-phosphine = ($^{i}Pr_2P)_2NCH_3$ or $^{i}Pr_2P(CH_2)_nP^{i}Pr_2$ (n = 1,2,3)} cations from ESI-MS experiments with bite angle.

The steric influence can be investigated by analysis of the space filling diagrams of the previously published solid state structures [Figure 5.21]. Visual inspection indicates little steric pressure occurs towards the arene in the small bite angle ligands and only a small contact area is observed with **IX** – suggesting that sterics may not have a large influence upon fragmentation.

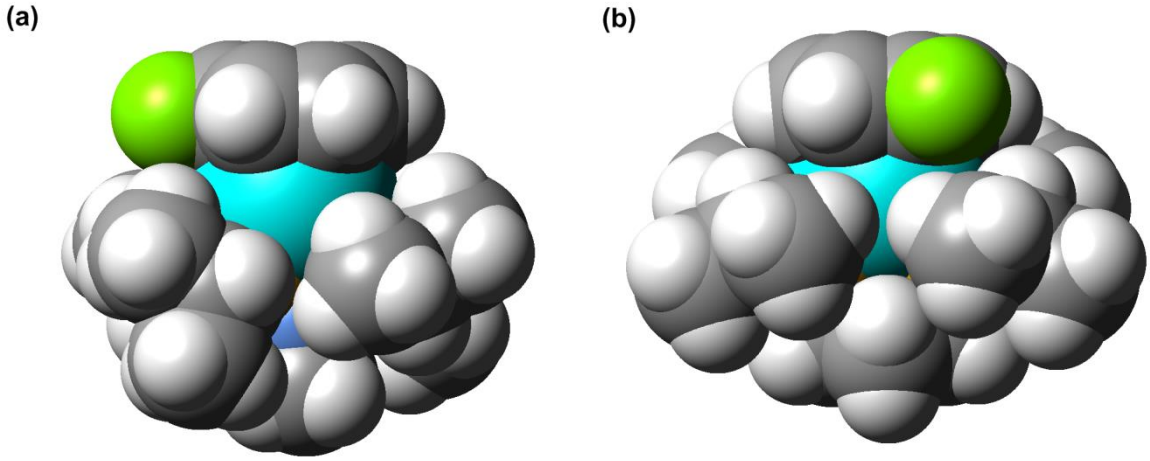

Figure 5.21. Space filling diagrams using Van-der-Waals radii of **(a) XXXVII** and **(b) IX**.[2]

The stability of the $[Rh(P_2)]^+$ fragment, which is produced upon fragmentation, may influence the overall binding affinity. It can be assumed that fragmentation is an endothermic process and the activation energy required for dissociation may be correlated to the stability of the final product formed [Figure 5.22].

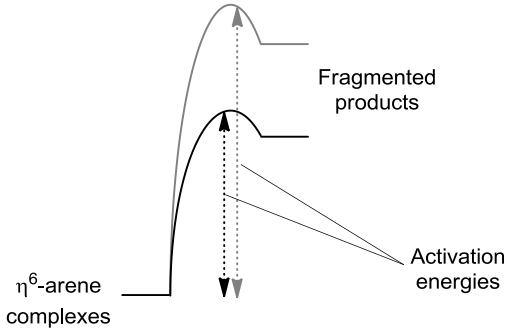

Figure 5.22. Diagram displaying the fragmentation of an η^6-arene complex and correlation between activation energy and stability of the fragment formed.

Agostic interactions are the most likely possibility for stabilising the gas-phase fragments generated by ESI-MS. As bite angle increases the strain upon an agostic interaction will diminish and the fragment will be more stable [Figure 5.23].

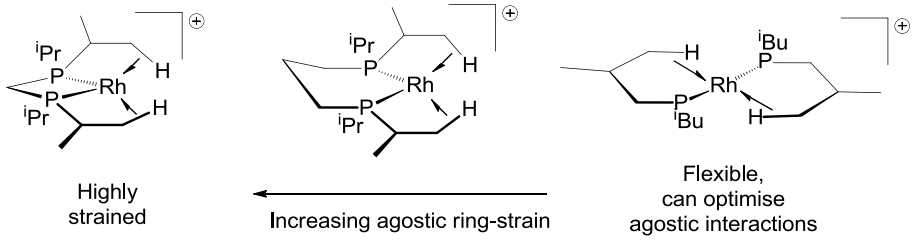

Figure 5.23. Potential agostic interactions stabilising the fragmented cations.

The cationic fragment $[Rh(P^iBu_3)_2]^+$ has been previously reported to be stabilised by agostic interactions [Figure 5.23], and so the binding affinity of a C_6H_5F ligand to this fragment was investigated.[35, 36] $[Rh(P^iBu_3)_2(\eta^6\text{-}C_6H_5F)][BAr^F{}_4]$, **VI**, was investigated by ESI-MS and at even the lowest exit voltages the complex was observed only as fragmented $[Rh(P^iBu_3)_2]^+$. This indicates that dissociation of the arene occurs very readily for this complex even at low exit voltages. A wide P-Rh-P angle [95.31(5)°] has been reported from the solid state structure of **VI**, however, upon fragmentation the monodentate phosphines could adopt positions *trans* to each other.[35] The ^{1}H NMR chemical shifts of the η^6-C_6H_5F ligand in **VI** are upfield of free C_6H_5F as expected (and similar to **2**), indicating a notable interaction with the metal centre. It would therefore seem that the ease of arene dissociation in **VI** may be related to the ability of the complex to form a product stabilised by agostic interactions.

5.4.iii. The effect of phosphine substituents upon binding affinity

With a view towards the stability of η^6-coordinated $[BAr^F{}_4]^-$ complexes, the effect of phosphine substituent upon the binding affinity of fluorobenzenes was investigated. A range of alkyl substituents upon small bite angle phosphine complexes ($[Rh(R_2PCH_2PR_2)(\eta^6\text{-}C_6H_5F)][BAr^F{}_4]$, R = ^{i}Pr, ^{i}Bu, Cy, ^{t}Bu) were tested by ESI-MS experiments [Figure 5.25]. $[Rh(^iPr_2PCH_2P^iPr_2)(\eta^6\text{-}C_6H_5F)][BAr^F{}_4]$ **XXXVI**, $[Rh(Cy_2PCH_2PCy_2)(\eta^6\text{-}C_6H_5F)][BAr^F{}_4]$ **XLIII** and $[Rh(^tBu_2PCH_2P^tBu_2)(\eta^6\text{-}C_6H_5F)][BAr^F{}_4]$ **XXXII,** were prepared by Indrek Pernik & Dr. Rowan Young (DPhil student & PDRA, Prof. A. Weller group) who kindly donated samples for ESI-MS experiments [Figure 5.24].[1, 2] $[Rh(^iBu_2PCH_2P^iBu_2)(\eta^6\text{-}C_6H_5F)][BAr^F{}_4]$, **XLIV**, was synthesised in collaboration with Mark Scott (MChem student Prof. A. Weller group) who also performed the ESI-MS experiment on this complex [Figure 5.24].[37]

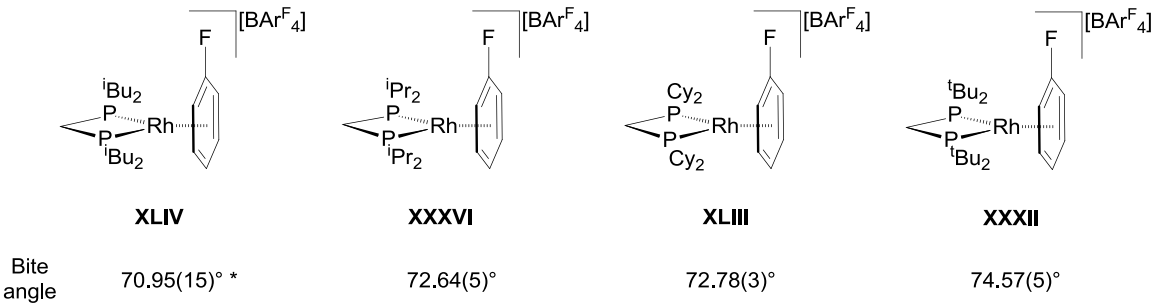

	XLIV	XXXVI	XLIII	XXXII
Bite angle	70.95(15)° *	72.64(5)°	72.78(3)°	74.57(5)°

*approximate value from low quality solid-state structure

Figure 5.24. Small bite angle η^6-C_6H_5F complexes with different phosphine substituents.

A wide range of 50% fragmentation points is displayed in Figure 5.25 [**XXXII**, 210; **XLIII**, 197; **XXXVI** 178; **XLIV**, 167] indicating a large dependence of binding affinity upon phosphine substituent.

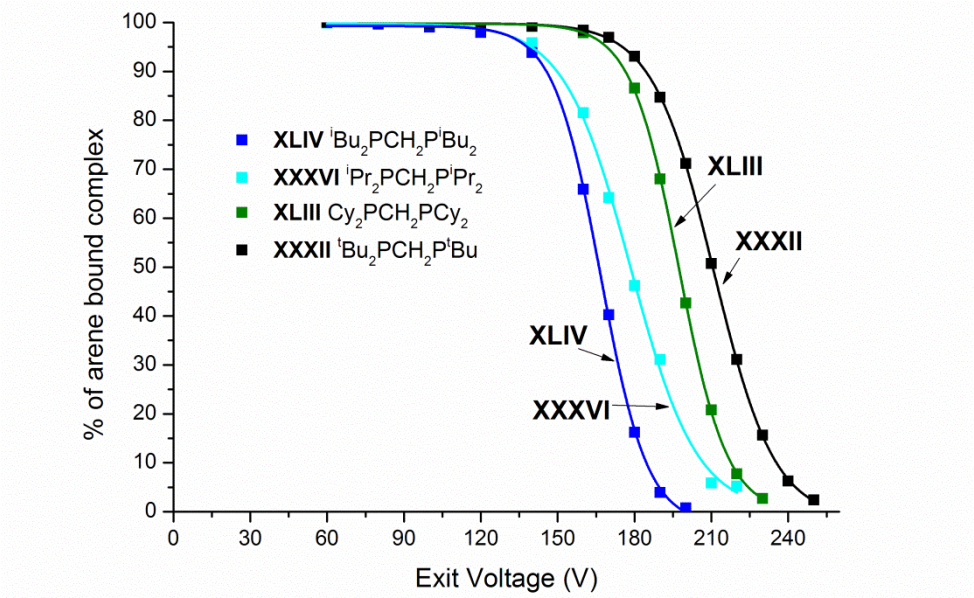

Figure 5.25. Fragmentation of [Rh($R_2PCH_2PR_2$)(η^6-C_6H_5F)]$^+$ (R = ^{i}Pr, ^{i}Bu, Cy or ^{t}Bu) cations in ESI-MS over a range of exit voltage values.

In such small bite angle complexes it is likely that sterics may not be very influential, in fact, the most strongly bound fluorobenzene complex is **XXXII** with the bulkiest substituent (^{t}Bu). The bite angles of all four complexes are similar with that of **XLIV** the smallest and **XXXII** the largest.[1, 2, 37] These bite angle variations would suggest the opposite trend (*see Section 5.4.ii*) in binding affinities to that which is observed. The four alkyl substituents should have similar electronic behaviour and the ^{1}H NMR spectra of all four complexes display similar signals for the bound η^6-C_6H_5F ligands, upfield of

the free arene resonances. The binding affinity may be influenced by the stabilisation of the $[Rh(P_2)]^+$ fragment which forms upon dissociation (*i.e.* agostic interactions or similar) [Figure 5.22]. Agostic interactions are likely to stabilise the gas-phase fragments generated by ESI-MS and it is possible that the most flexible ^{i}Bu groups have the greatest tendency to form such interactions (δ-agostics possible), even though the small bite angle will induce strain upon such an interaction. ^{i}Pr groups will have to stretch even further to form a γ-agostic interactions and the bulky Cy and ^{t}Bu groups may be even more restricted.

5.4.iv. Attempts to form a stable 1,2,3-$C_6H_3F_3$ complex

Previously described 1,2,3-$C_6H_3F_3$ complex **38**, which was not stable in CH_2Cl_2, included the phosphine $^{i}Bu_2PCH_2CH_2P^{i}Bu_2$. The η^6-C_6H_5F complex **2** also used this same phosphine and has been shown to bind C_6H_5F much less strongly than small bite angle phosphine complexes (in the gas-phase by ESI-MS experiments) [50% dissociation: **2**, 141 V; **XLIII**, 197 V]. We were interested to determine if formation of a 1,2,3-$C_6H_3F_3$ complex stable in CH_2Cl_2 may be achievable with a small bite angle ligand that binds arenes strongly (albeit in the gas-phase). The complex $[Rh(Cy_2PCH_2PCy_2)(\eta^6\text{-}1,2,3\text{-}C_6H_3F_3)]$, **45**, was synthesised by hydrogenation of $[Rh(Cy_2PCH_2PCy_2)(\eta^2\eta^2\text{-NBD})]$ in 1,2,3-$C_6H_3F_3$ [Scheme 5.7]. **45** displays clean NMR spectra in 1,2,3-$C_6H_3F_3$ with two $^{19}F\{^1H\}$ NMR signals [d −167.2 and −146.8] for the coordinated arene similar to **38**. The $^{31}P\{^1H\}$ NMR contains a doublet [δ −11.3, J_{RhP} 167 Hz] which is similar to that of **XLIII**.[1] ESI-MS experiments confirm the cationic composition of **45** and a 50% fragmentation value of 168 V is recorded (29 V lower than for **XLIII**). However attempts to crystallise **45** by slow dilution of the solution with pentane resulted in single crystals of zwitterionic complex $Rh(Cy_2PCH_2PCy_2)(\eta^6\text{-}C_6H_3(CF_3)_2(BAr^F{}_3)$ **46** [Scheme 5.7].

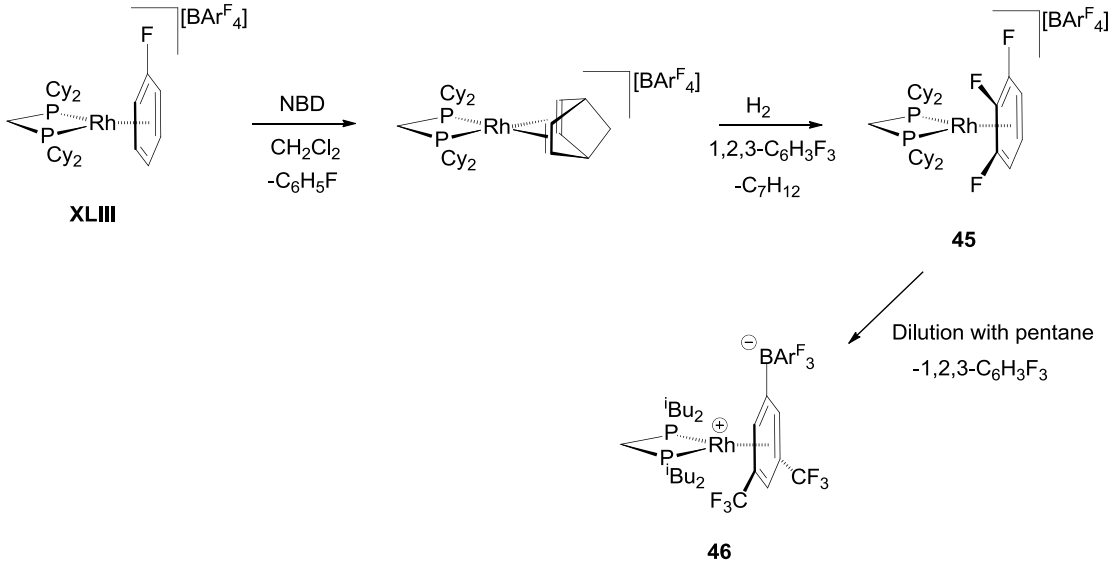

Scheme 5.7. Formation of **45** and subsequent arene dissociation to form zwitterionic **46**

It appears that, as the concentration of 1,2,3-$C_6H_3F_3$ drops, the η^6-1,2,3-$C_6H_3F_3$ dissociates and the anion $[BAr^F_4]^-$ binds preferentially. It is interesting to note that even though in the gas-phase 1,2,3-$C_6H_3F_3$ binds much more strongly in **45** than C_6H_5F does in **2** (168 V compared to 141 V) it is the comparative binding strength of the $[BAr^F_4]^-$ anion to each system specifically that determines the complex's stability in solution. It therefore appears that the binding affinity of $[BAr^F_4]^-$ (which cannot be determined by ESI-MS experiments due to the neutral nature of its coordination complexes) follows similar trends to the binding strength of fluorobenzenes. It also appears that $[BAr^F_4]^-$ binds more strongly than 1,2,3-$C_6H_3F_3$ but less strongly than C_6H_5F. $[BAr^F_4]^-$ contains two strongly electron withdrawing CF_3 groups but also an electron donating anionic $(BAr^F_3)^-$ substituent. This combination results in an arene group with a similar binding affinity to 1,2-$C_6H_4F_2$.

The $^{31}P\{^1H\}$ NMR spectrum of **46** contains a doublet [δ −16.3, J_{RhP} 172 Hz] similar to **XLIII** and **45**. The ^1H and $^{19}F\{^1H\}$ NMR spectra confirm the coordination of one arene group of $[BAr^F_4]^-$ whilst the other arene groups appear equivalent by free rotation, these spectra are similar to those of **4**. A solid-state structure was determined and confirmed the expected geometry [Figure 5.26]. Whilst an approximate η^6-coordination of the arene occurs, the arene does not sit flat above the metal centre [angle between η^6-arene plane and Rh(1)P(1)P(2), 82.9°]. The Rh–C bonds to two adjacent carbons are quite long in comparison to the other four bonds [Rh(1)–C(31), 2.487(3); Rh(1)–C(32), 2.407(3); other four bonds range: 2.269(3) - 2.312(3)]. This is probably due to steric interactions between the

bulky $[BAr^F_4]^-$ ligand and the cyclohexyl groups. The arene could be considered to be η^5-coordinated as the longest Rh···C bond is at the limit of reported Rh–C_{arene} bonding distances.[32] These Rh–C_{arene} bond lengths fall within the range of Rh–C_{arene} bond lengths for other coordinated $[BAr^F_4]^-$ complex such as **4**, **14** and **19**. The distance between Rh(1) and the plane defined by the six coordinated arene carbons is 1.862 Å which is similar to the equivalent distance for **4**.

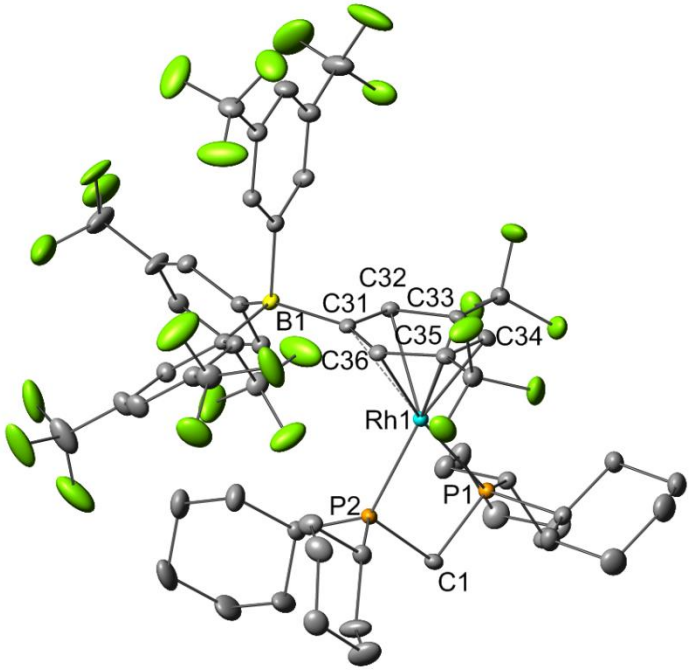

Figure 5.26. Displacement ellipsoid plot (30% probability) of complex **46** in the solid state. Hydrogen atoms and minor CF_3 disorder components omitted for clarity. Selected bond length (Å) and angle (º) data: Rh(1)–P(1), 2.2419(7); Rh(1)–P(2), 2.2682(8); Rh(1)–C(31), 2.487(3); Rh(1)–C(32), 2.407(3); Rh(1)–C(33), 2.269(3); P(1)-Rh(1)-P(2), 72.35(3).

An additional observation in the ESI-MS experiments of cyclohexylphosphine complexes **XLIII** and **45** is the dehydrogenation of one cyclohexyl substituent in the $[Rh(Cy_2PCH_2PCy_2)]^+$ fragment to form a cyclohexenyl moiety; similar reactivity with cyclohexylphosphines has been previously reported.[38, 39] Dehydrogenation initially requires the approach of a C–H bond to the metal centre. This is additional evidence that the gas-phase fragmented cations are stabilised by agostic interactions [Scheme 5.8]. This secondary reaction occurs at high exit voltages and forms the cationic fragment $[Rh\{Cy_2PCH_2PCy(C_6H_9)\}]^+$ [m/z = 509.20] in which the C=C bond can presumably coordinate to the metal centre.

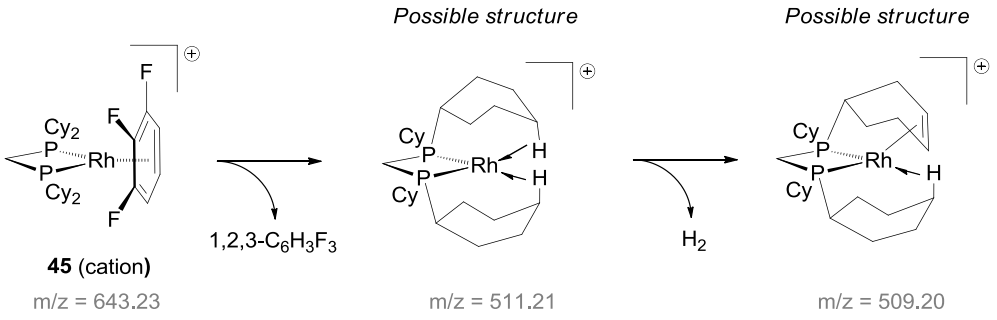

Scheme 5.8. Fragmentation of the cationic fragment of **45** (gas-phase) to form a cation which may be stabilised by agostic interactions and subsequent dehydrogenation of one cyclohexyl group at high exit voltages as observed by ESI-MS (m/z values shown in grey).

5.5. Comparisons with ESI-MS/MS data (in collaboration with Prof. Scott McIndoe)

In order to test the reliability of the variable exit voltage ESI-MS experiments some of the flurorobenzene compounds were sent to the laboratory of Prof. J. Scott McIndoe (University of Victoria, British Columbia). Here the compounds were screened using ESI-MS/MS techniques where the fragmentation of a selected mass species is controlled by the altering the collision voltage. Neutral inert gas molecules cause the collisions and a centre of mass correction is applied.[28, 31] The results agree well with the simple variable exit voltage ESI-MS data we collected, and display the same order of binding strengths. A good linear correlation relates the data sets ($R^2 = 0.95$) if the result for **XXXII** is discounted ($R^2 = 0.85$ for a linear fit to all data) [Figure 5.27]. Perhaps that result (with the highest 50% fragmentation point) is prone to error in one of the two experiments (both experiments were repeated with **XXXII** and gave the same results). It is also possible that a non-linear relationship is present. Approximate 50% fragmentation points are displayed in Table 5.7 along with all of the ESI-MS data collected for the various fluorobenzene complexes.

$[Rh(P_2)(\eta^6\text{-}C_6H_5F)]^+ \rightarrow [Rh(P_2)]^+ + \text{arene}$ (P_2 = chelating phosphine)				
P_2	Atoms in backbone	Substituents	50% dissociation (V) (ESI-MS)	50% dissociation, mass normalised collision voltage (V) (ESI-MS/MS)
^{t}Bu$_2$PCH$_2$P^{t}Bu$_2$	1	^{t}Bu	210	2.27
(Cy$_2$P)$_2$NCH$_3$	1 (N)	Cy	204	N/A
Cy$_2$PCH$_2$PCy$_2$	1	Cy	197	N/A
(^{i}Pr$_2$P)$_2$NCH$_3$	1 (N)	^{i}Pr	181	2.08
^{i}Pr$_2$PCH$_2$P^{i}Pr$_2$	1	^{i}Pr	178	2.04
^{i}Pr$_2$P(CH$_2$)$_2$P^{i}Pr$_2$	2	^{i}Pr	169	1.90
^{i}Bu$_2$PCH$_2$P^{i}Bu$_2$	1	^{i}Bu	167	N/A
(O^{i}Pr)$_2$P(CH$_2$)$_2$P(O^{i}Pr)$_2$	2	O^{i}Pr	159	1.46
^{i}Pr$_2$P(CH$_2$)$_3$P^{i}Pr$_2$	3	^{i}Pr	145	1.36
^{i}Bu$_2$P(CH$_2$)$_2$P^{i}Bu$_2$	2	^{i}Bu	141	1.04

Table 5.7. Overview of all η^6-C_6H_5F complexes tested in variable exit voltage ESI-MS.

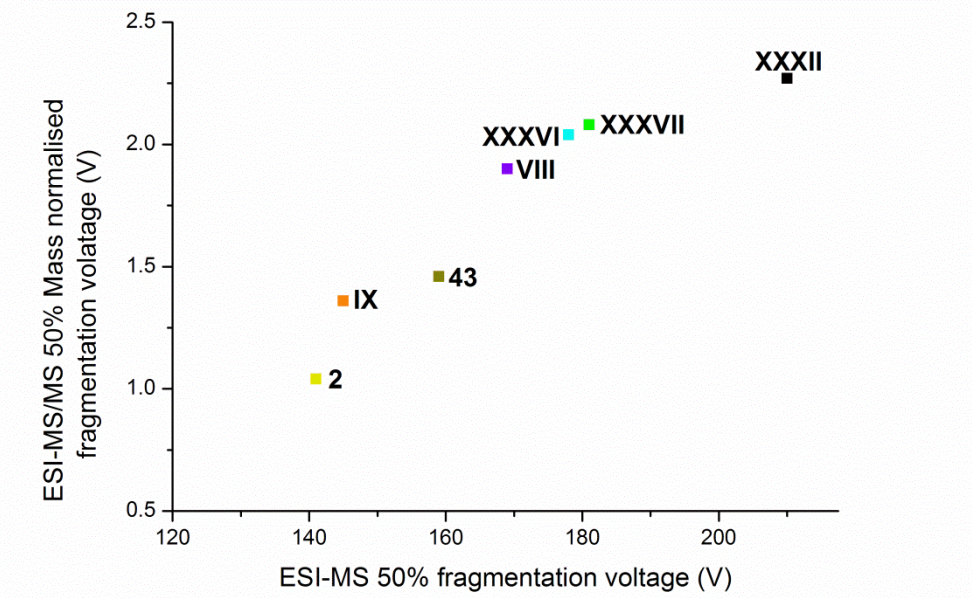

Figure 5.27. Correlation between ESI-MS experiments (Oxford) and ESI-MS/MS experiments (Victoria). Approximate linear relationship if point for **XXXII** is excluded.

5.6. Conclusions

A set of variable exit voltage (cone voltage) ESI-MS experiments have been undertaken which show the dissociation of an arene from a variety of η^6-arene complexes. These experiments show that increasing the number of electron withdrawing substituents reduces the binding affinity of the arene. The results are in agreement with equilibrium measurements in solution where the $[BAr^F{}_4]^-$ anion can

displace the coordinated arene (possibly *via* a short lived low coordinate transition state, *i.e*. by a dissociative mechanism). The gas-phase binding affinity of η^6-C_6H_5F is also much greater in conjunction with small bite angle phosphine ligands or more electron withdrawing phosphites. The phosphine substituents also influence the gas-phase binding affinity of η^6-C_6H_5F, with ^{t}Bu groups associated with the greatest binding affinities and ^{i}Bu groups with the least of those tested. The ease of fragmentation may be correlated with the stability of the $\{RhP_2\}^+$ fragment that forms, with agostic interactions likely to be influential.

It appears that $[BAr^F_4]^-$ binds more strongly than 1,2,3-$C_6H_3F_3$, less than C_6H_5F and is similar to difluorobenzenes. It is likely that the binding affinity of $[BAr^F_4]^-$ follows similar trends with respect to bite angle and phosphine substituents to those observed for C_6H_5F, however additional steric factors may be important for the bulkier anion.

It is interesting to note that the two systems which form characterisable σ-alkane complexes use phosphines ^{i}Bu$_2$PCH$_2$CH$_2$P^{i}Bu$_2$ and ^{i}Pr$_2$PCH$_2$CH$_2$CH$_2$P^{i}Pr$_2$ and that η^6-C_6H_5F complexes with these phosphines have the lowest gas-phase binding affinities of C_6H_5F out of all the P_2 ligands tested [Table 5.8]. This could suggest that formation of a coordinated $[BAr^F_4]^-$ complex is also not highly favoured for these systems. It should, however, be noted that the low gas-phase binding affinities may be partially accounted for by stabilisation of the $\{RhP_2\}^+$ dissociation fragments by agostic interactions in the gas-phase (which may be more favoured in relation to the other phosphines). Steric effects in coordinated $[BAr^F_4]^-$ complexes are also not well accounted for in these η^6-C_6H_5F complexes.

P_2	Atoms in backbone	Substituents	50% dissociation (V) of $[Rh(P_2)(\eta^6\text{-}C_6H_5F)]^+$ (ESI-MS, gas-phase)	Observation of a solid-state σ-alkane complex $[Rh(P_2)(\eta^4\text{-}C_7H_{12})][BAr^F_4]$
^{i}Pr$_2$P(CH$_2$)$_2$P^{i}Pr$_2$	2	^{i}Pr	169	Yes (very short lived)
^{i}Bu$_2$PCH$_2$P^{i}Bu$_2$	1	^{i}Bu	167	No (*study by Mark Scott*)[37]
(O^{i}Pr)$_2$P(CH$_2$)$_2$P(O^{i}Pr)$_2$	2	O^{i}Pr	159	No
^{i}Pr$_2$P(CH$_2$)$_3$P^{i}Pr$_2$	**3**	**^{i}Pr**	**145**	**Yes**
^{i}Bu$_2$P(CH$_2$)$_2$P^{i}Bu$_2$	**2**	**^{i}Bu**	**141**	**Yes**

Table 5.8. Comparison of binding affinity of C_6H_5F with the observation of a stable σ-alkane complex with different phosphines.

This simple variable exit voltage ESI-MS process, which can be performed quickly and without any extra modifications to normal ESI-MS, is a useful process for comparing the binding affinities of reactive complexes, although no quantitative assessment can be obtained from the values. The technique is found to agree well with ESI-MS/MS experiments.

5.7. References

1. A. B. Chaplin, J. F. Hooper, A. S. Weller and M. C. Willis, *J. Am. Chem. Soc.*, 2012, **134**, 4885-4897.
2. I. Pernik, J. F. Hooper, A. B. Chaplin, A. S. Weller and M. C. Willis, *ACS Catalysis*, 2012, **2**, 2779-2786.
3. J. F. Hooper, R. D. Young, I. Pernik, A. S. Weller and M. C. Willis, *Chem. Sci.*, 2013, **4**, 1568-1572.
4. R. Dallanegra, A. P. M. Robertson, A. B. Chaplin, I. Manners and A. S. Weller, *Chem. Commun.*, 2011, **47**, 3763-3765.
5. C. L. Higgitt, A. Hugo Klahn, M. H. Moore, B. Oelckers, M. G. Partridge and R. N. Perutz, *J. Chem. Soc., Dalton Trans.*, 1997, 1269-1280.
6. E. Clot, B. Oelckers, A. H. Klahn, O. Eisenstein and R. N. Perutz, *Dalton Transactions*, 2003, 4065-4074.
7. F. Basuli, H. Aneetha, J. C. Huffman and D. J. Mindiola, *J. Am. Chem. Soc.*, 2005, **127**, 17992-17993.
8. M. W. Bouwkamp, P. H. M. Budzelaar, J. Gercama, I. Del Hierro Morales, J. de Wolf, A. Meetsma, S. I. Troyanov, J. H. Teuben and B. Hessen, *J. Am. Chem. Soc.*, 2005, **127**, 14310-14319.
9. A. V. Korolev, F. Delpech, S. Dagorne, I. A. Guzei and R. F. Jordan, *Organometallics*, 2001, **20**, 3367-3369.
10. X.-Y. Liu, K. Venkatesan, H. W. Schmalle and H. Berke, *Organometallics*, 2004, **23**, 3153-3163.
11. N. Hao and M. J. McGlinchey, *J. Organomet. Chem.*, 1978, **161**, 381-390.
12. S. Kawahara, S. Tsuzuki and T. Uchimaru, *Chem. Eur. J.*, 2005, **11**, 4458-4464.
13. K. J. Klabunde and H. F. Efner, *Inorg. Chem.*, 1975, **14**, 789-791.
14. A. Agarwal, M. J. McGlinchey and T.-S. Tan, *J. Organomet. Chem.*, 1977, **141**, 85-97.
15. N. Hao and M. J. McGlinchey, *J. Organomet. Chem.*, 1979, **165**, 225-231.
16. L. P. Hammett, *Chem. Rev.*, 1935, **17**, 125-136.
17. L. P. Hammett, *J. Am. Chem. Soc.*, 1937, **59**, 96-103.
18. J. F. Hartwig, *OrganoTransition Metal Chemistry*, University Science Books, 2010.
19. V. Ryzhov, C.-N. Yang, S. J. Klippenstein and R. C. Dunbar, *Int. J. Mass spectrom.*, 1999, **185-187**, 913-923.
20. F. Meyer, F. A. Khan and P. B. Armentrout, *J. Am. Chem. Soc.*, 1995, **117**, 9740-9748.
21. C. W. Bauschlicher Jr and H. Partridge, *Chem. Phys. Lett.*, 1991, **181**, 129-133.
22. B. C. Guo, J. W. Purnell and A. W. Castleman Jr, *Chem. Phys. Lett.*, 1990, **168**, 155-160.
23. D. Schroeder, J. Hrusak, R. H. Hertwig, W. Koch, P. Schwerdtfeger and H. Schwarz, *Organometallics*, 1995, **14**, 312-316.
24. Y.-P. Ho and R. C. Dunbar, *Int. J. Mass spectrom.*, 1999, **182**, 175-184.
25. D. Schröder, H. Schwarz, J. Hrušák and P. Pyykkö, *Inorg. Chem.*, 1998, **37**, 624-632.
26. I. Bach, K.-R. Pörschke, R. Goddard, C. Kopiske, C. Krüger, A. Rufińska and K. Seevogel, *Organometallics*, 1996, **15**, 4959-4966.
27. J. J. Barker, A. G. Orpen, A. J. Seeley and P. L. Timms, *J. Chem. Soc. Dalton Trans.*, 1993, 3097-3102.
28. W. Henderson and J. S. McIndoe, *Mass Spectrometry of Inorganic and Organometallic Compounds: Tools - Techniques - Tips*, Wiley, 2005.
29. J. B. Fenn, M. Mann, C. K. Meng, S. F. Wong and C. M. Whitehouse, *Mass Spectrom. Rev.*, 1990, **9**, 37-70.
30. A. T. Lubben, J. S. McIndoe and A. S. Weller, *Organometallics*, 2008, **27**, 3303-3306.
31. E. Crawford, J. S. McIndoe and D. G. Tuck, *Can. J. Chem.*, 2006, **84**, 1607-1613.
32. A. Woolf, A. B. Chaplin, J. E. McGrady, M. A. M. Alibadi, N. Rees, S. Draper, F. Murphy and A. S. Weller, *Eur. J. Inorg. Chem.*, 2011, 1614-1625.
33. A. B. Chaplin and A. S. Weller, *Eur. J. Inorg. Chem.*, 2010, 5124-5128.
34. D. G. Streets and G. P. Ceasar, *Mol. Phys.*, 1973, **26**, 1037-1052.
35. T. M. Douglas, A. B. Chaplin and A. S. Weller, *Organometallics*, 2008, **27**, 2918-2921.
36. T. M. Douglas, Chemistry of Cationic Rhodium Alkyl Phosphine Complexes, DPhil Thesis, University of Oxford, 2009.
37. M. Scott, Exploring the synthesis of transition metal alkane complexes, MChem Thesis, University of Oxford, 2013.
38. S. Hietkamp, D. J. Stufkens and K. Vrieze, *J. Organomet. Chem.*, 1978, **152**, 347-357.
39. M. L. Christ, S. Sabo-Etienne and B. Chaudret, *Organometallics*, 1995, **14**, 1082-1084.

CHAPTER 6

EXPERIMENTAL

6.1. Experimental Techniques

6.1.i. General

All manipulations, unless otherwise stated, were performed under an atmosphere of argon, using standard Schlenk-line and glovebox techniques. Glassware was oven-dried at 403 K overnight and flamed under vacuum prior to use. CH_2Cl_2, Et_2O, hexane and pentane were dried using a Grubbs-type solvent purification system (MBraun SPS-800) and degassed by successive freeze-pump-thaw cycles.[1] CD_2Cl_2, C_6H_5Cl, C_6H_5F, 1,2-$C_6H_4F_2$, 1,3-$C_6H_4F_2$, 1,4-$C_6H_4F_2$, 1,2,3-$C_6H_3F_3$, 1,2,3,4-$C_6H_2F_4$, C_6HF_5 and C_6F_6 were distilled under vacuum from CaH_2 and stored over 3 Å molecular sieves. $CDCl_3$ used in the preparation of $CDCl_2F$ was degassed by successive freeze-pump-thaw cycles and stored over 3 Å molecular sieves prior to reaction. The solvent $CDCl_2F$ was prepared by literature methods.[2]

6.1.ii. Nuclear Magnetic Resonance (NMR) Spectroscopy

Solution & gas-phase NMR spectra were recorded on Varian Unity 500 MHz, Bruker AVC 500 MHz, Bruker AVD 500 MHz, Bruker Ascend 400 MHz or Varian Mercury 300 MHz spectrometers at room temperature unless otherwise stated. Non-Deuterated Solvents were locked to a standard CD_2Cl_2 or C_6D_6 solution. Residual protio solvent was used as reference for ^{1}H, ^{2}H and ^{13}C NMR spectra in deuterated solvent samples. In 1,2-$C_6H_4F_2$ and C_6H_5F ^{1}H NMR spectra were referenced to the centre of the downfield solvent multiplet (δ 7.07 and δ 7.11 respectively). ^{11}B, ^{19}F and ^{31}P NMR spectra were externally referenced to $BF_3.OEt_2$, CCl_3F and 85% H_3PO_4 respectively. All chemical shifts (δ) are quoted in ppm and coupling constants in Hz. Gas-phase samples were separately referenced to the reported values for hydrogen, ethane, ethene and butadiene (all data were fully consistent with reported values).[3, 4]

Solid-state NMR spectra were recorded at the EPSRC National Solid-State NMR service centre (Durham University – with assistance from Dr. David Apperley and Fraser Markwell) on a Varian

VNMRS 400 MHz spectrometer, using the cross-polarisation pulse sequence (contact time 3-10 ms and recycle delay 1-2 s), with TPPM decoupling. Cross-polarisation experiments were employed in order to avoid the long relaxation delays associated with direct excitation which would have been problematic for investigating short lived intermediates. A spinning rate of 10 kHz was employed. Experiments were undertaken at temperatures from 213 K to 323 K. Spectral referencing is with respect to external neat tetramethylsilane for ^{13}C and ^{2}H and to 85% H_3PO_4 for ^{31}P. Spinning was carried out using dry nitrogen. Powdered microcrystalline material was used in all cases which had been ground by the back of a spatula thoroughly before use. The samples were loaded into 4 mm rotors in a N_2 filled glovebox. In order to undertake hydrogenation reactions the filled rotors were exposed to an atmosphere of hydrogen (1 atm) with one end left open, using normal Schlenk line apparatus, and the rotors then capped within the glovebox.

$^{13}C\{^1H\}$ NMR spectroscopy *$[BAr^F{}_4]^-$ resonances*

Solution: *118.2-117.9 (m, 2C), 125.2 (q (CF_3), $^1J_{FC}$ = 272 Hz, 2C), 129.4 (qq, $^2J_{FC}$ = 31 Hz, $^3J_{BC}$ = 3 Hz, 2C), 135.4 (s, 1C), 162.3 (q, $^1J_{BC}$ = 50 Hz, 1C)*

Solid-state: *117.3 (m, 2C), 124.5 (br, 2C), 130.6 (br, 2C), 134.9 (br, 1C), 164.3 (br, 1C)*

6.1.iii. Gas-phase NMR spectroscopy integration

In order to determine the progress of ethene hydrogenation reactions by gas-phase NMR spectroscopy, accurate comparison of the integrals of ethene and ethane is required. In order for this to be reliable the T_1 times of the signals in question should be similar. The effect of d_1 (relaxation delay) upon the ^1H NMR spectra of ethene and ethane in the gas phase (1 atm, 295 K) was compared and the spectra of both species were found to react similarly (*N.B.* the default ^1H NMR spectroscopy relaxation delay is 1 second) [Figure 6.1]. The null point (τ_{null}) is between 0.25 and 0.5 s for both, therefore the T_1 time is approximately located in the range of 0.36-0.72 s for both species ($T_1 \sim \tau_{null}$ x 1.44). This indicates that direct comparison of the integrals is appropriate. The signal for H_2 is broad in the gas phase and so is not so useful for integration analysis. Similar analysis was conducted upon gas-phase samples of 1-butene and 2-butene and a null point between 1 and 2 seconds was observed for both these species. Therefore it can be concluded that direct comparison of the integration values from signals for 1-butene and 2-butene should be reliable, but that care should be taken comparing the signals of butenes with that of ethene or ethane.

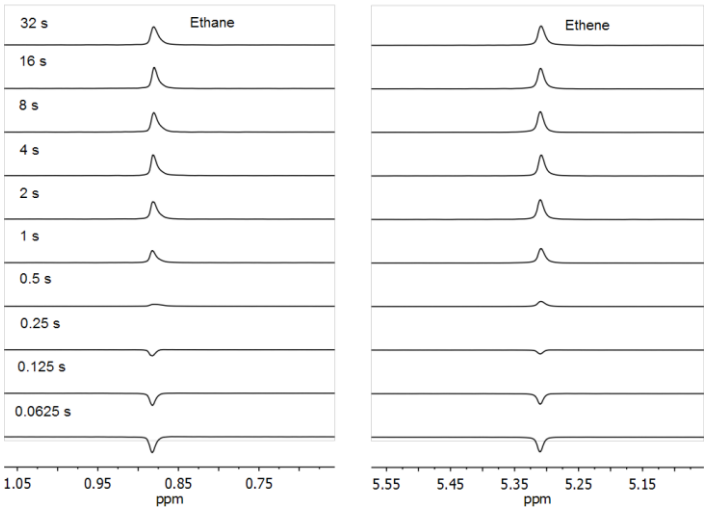

Figure 6.1. Gas phase NMR spectra of ethene and ethane at various relaxation delay times. Spectra display a null point (τ_{null}) at a similar delay in both cases (delay ~0.4 s).

6.1.iv. Mass Spectroscopy (ESI-MS)

Electrospray Ionisation Mass Spectrometry (ESI-MS) was recorded using a Bruker MicrOTOF-Q instrument directly connected to a modified Innovative Technology glovebox.[5] Typical acquisition parameters were as follows: sample flow rate [4 μL/min], nebuliser gas pressure [0.4 bar], drying gas [argon at 333 K, flowing at 4 L/min], capillary voltage [4.5 kV], exit voltage [60 V (variable exit voltage studies 50– 250 V)]. The spectrometer was calibrated using a mixture of tetralkyl ammonium bromides $[N(C_nH_{2n+1})_4]Br$ (n = 2-8, 12, 16 & 18). Samples were diluted to a concentration of 1×10^{-6} M in the appropriate solvent before running.

Variable exit voltage experiments were measured for ~10 s per voltage step, and the intensity of the largest isotope peak of the fragmented and non-fragmented signals were recorded. Subsequently the intensities were normalised to account for the varying isotopic distributions.[6] In arene dissociation experiments where multiple fragmentation products were formed (see below)* the intensities of the fragmented products were summed and compared to the non-fragmented intensity None of the secondary fragments coordinate arene ligands and so are presumed to form after initial arene dissociation.

* $[Rh\{(O^iPr)_2PCH_2CH_2P(O^iPr)_2\}]^+$ fragments undergo partial $^iPr/H$ exchange at > 150 V exit voltage, similarly $[Rh(^tBu_2P(CH_2)P^tBu_2)]^+$ undergoes $^tBu/H$ exchange at > 200 V exit voltage and $[Rh(Cy_2P(CH_2)PCy_2)]^+$ undergoes partial dehydrogenation to form $[Rh\{Cy_2P(CH_2)PCy(C_6H_9)\}]^+$ which begins at exit voltages > 100 V.

6.1.v. Single Crystal X-ray Crystallography

Single crystal X-ray diffraction data were collected either using an Enraf Nonius Kappa CCD diffractometer (Mo Kα radiation, λ = 0.71073 Å), an Agilent SuperNova (Cu Kα radiation, λ = 1.54180 Å), or using I19 (EH1) at the Diamond Light Source,[7] with the use of low temperature devices. Data were reduced using the instrument manufacturer software, DENZO-SMN,[8] CrysAlisPro,[9] and CrystalClear. All structures were solved *ab initio* using SIR92,[10] or SuperFlip,[11] and the structures were refined using CRYSTALS[12, 13] {or SHELX in structures solved by Dr. Adrian Chaplin (**3** and **31**)}[14], dihedral were angles and hydrogen bonds were calculated using PLATON.[15] Electron density maps were plotted using MCE.[16] Crystal void surfaces were located using CrystalExplorer[17, 18] at the point where the sum of the promolecule density (sum of spherically-averaged atomic charge densities at their respective crystallographic coordinates) in the unit cell is less than 0.002 e au^{-3} (electron density, default program value). The fully disordered crystal structures were used so that all space potentially filled by an atom is discounted. It should however be noted that any disorder present may represent some flexibility in the crystal lattice, aiding passage of small molecules by limited molecular motion.

6.1.vi. Preparation of single crystals of 5 for X-ray diffraction and special refinement details

Single crystals of **1** were exposed to 1 atm hydrogen for 11 minutes. The tube was then evacuated and refilled with argon. Under a positive pressure of argon, perfluoropolyalkylether was dripped onto the crystals and the tube sealed and frozen in liquid nitrogen. The whole process was completed within 12.5 minutes, as delay was found to encourage the formation of final product **4**. A small single crystal (< 0.1 mm^3) was selected quickly and placed in the flow of an Oxford CryoSystems CryoStream at 100 K which was mounted on the diffractometer. A diffraction pattern was collected and the data refined in collaboration with Dr. Amber Thompson. The NBA ligand sits upon the 2-fold

crystallographic axis and so is disordered equally over two positions. No restraints were necessary in the refinement but constraints were placed upon bridgehead carbons C(3) and C(6) to enforce the crystallographic symmetry.

6.1.vii. Powder X-ray Crystallography at the Diamond light source

Powder X-ray diffraction data was collected at the Diamond light source on beamline I12 with the assistance of Dr. Michael Hart (beamline scientist). A large sample (400 mg) of **1** was ground down and separated into batches of defined particle size using a set of Endecotts test sieves. The finest powder batch (particle diameter < 50 μm) was used for powder X-ray diffraction. The powder was loaded into a glass capillary tube within a glovebox. The tube was then attached to a Swagelock fitting with an air tight valve. Once the valve was closed the sample tube was removed from the glovebox and connected to a gas exchange manifold inside the beam-line experimental hutch (*for diagram see Section 2.2xiv*). The manifold comprised of a H_2/He (10% H_2) feed and a connection to a turbo vacuum pump. The sample could then be evacuated and maintained under a static vacuum whilst the hutch was evacuated and locked. A background X-ray diffraction pattern was collected by directing the beam through the tube above the sample. After alignment of the sample, the collection of continual powder X-ray diffraction datasets was started (~10 s per diffraction experiment) and H_2/He then added *in situ*. A Pixium detector located ~2510 mm from the sample was used to record the diffraction pattern. The wavelength of the synchrotron beam was 0.02378 nm.

6.1.viii. Miscellaneous

Fourier Transform Infrared (IR) Spectroscopy was carried out upon a Thermo-Scientific Nicolet iS5 with iD3 ATR and iD1 transmission attachments.

Elemental micro-analysis carried out upon crystalline samples dried under dynamic vacuum (1 $x10^{-2}$ Torr) overnight, by Stephen Boyer at London Metropolitan University.

For computational details (carried out at Heriot-Watt University, Edinburgh) see supporting information of *Science*, 2012, **337**, 1648-1651.[19]

Van der Waals radii recently calculated by Alvarez were used for comparison to bond lengths.[20] In the case of the $CH_{3/2}$ groups it is accepted that a CH_3 group as a whole has an assigned van der Waals radius of 2.0 Å and (according to Pauling) a CH_2 group can be considered to have the same value.[21]

6.2. Synthesis and Characterisation

6.2.i. Starting Materials

$Na[BAr^F{}_4]$,[22] $Na[BAr^{Cl}{}_4]$,[23] $(O^iPr)_2PCH_2CH_2P(O^iPr)_2$,[24, 25] $[Rh(\eta^2,\eta^2\text{-COD})_2][BAr^F{}_4]$,[26] and $[(\eta^2,\eta^2\text{-NBD})RhCl]_2$ [27] were prepared by the literature Procedures. $[(\eta^2,\eta^2\text{-COD})RhCl]_2$ was prepared by altering the preparation for the analogous Iridium complex.[28]

Previous publications using $^iBu_2PCH_2CH_2P^iBu_2$ follow the synthesis of $Et_2PCH_2CH_2PEt_2$.[29, 30] We present a modified synthesis similar to that used in the formation of $^iPr_2PCH_2CH_2P^iPr_2$.[31] Under argon, 0.5 ml (3.31 mmol) of 1,2-$C_2H_4(PCl_2)_2$ was dissolved in 23ml Et_2O. 9.1 ml of 2.0 M (18.21 mmol, 5.5 eq.) ^{i}BuMgCl in Et_2O was added to a 2 neck round bottom flask with a stirrer bar. This was cooled to 273 K with an ice bath. The phosphine solution was added dropwise to the Grignard solution over half an hour. The reaction mixture was left to stir overnight at room temperature. A saturated aqueous solution of $[NH_4]Cl$ was prepared and degassed by bubbling argon through. 75 ml of the $[NH_4]Cl$ solution was added to the reaction mixture and the ethereal layer extracted. 23 ml Et_2O was added to the aqueous layer and extracted a further 3 times. The product solution was dried with $Na_2[SO_4]$, filtered and reduced by vacuum to 20 ml. 20 ml of degassed methanol was added before removing the rest of the Et_2O by vacuum. The methanol solution was left at 253 K for 24 hours. The methanol layer was decanted to leave behind the liquid phosphine, with any remaining solvent removed by vacuum. 0.55 g of colourless liquid product was obtained (52% yield).

All other chemicals were used as received from Sigma-Aldrich, Acros, Fisher, Fluorochem, and Strem Chemicals.

6.2.ii. New Compounds

All chemical shifts (δ) quoted in ppm. Elemental microanalysis results quoted in %. All reported ESI-MS signals display the expected isotope pattern.

1. [Rh(^{i}Bu$_2$PCH$_2$CH$_2$P^{i}Bu$_2$)($\eta^2\eta^2$-NBD)][BAr$^F_4$]

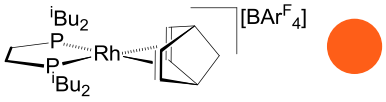

---

❶ **Synthesis:** 150 mg (325 mmol) of [(NBD)RhCl]$_2$ was added to a Schlenk tube with a stirrer bar and dissolved in 13 ml of fluorobenzene. To this 4.23 ml of a 0.154 M (650 mmol, 2 eq.) pentane solution of ^{i}Bu$_2$PCH$_2$CH$_2$P^{i}Bu$_2$ was added and the mixture stirred for 5 minutes. This mixture was added to a Schlenk flask containing 576.8 mg (650 mmol) Na[BAr$^F_4$] and a moving stirrer bar by cannula transfer. After 10 minutes of stirring, the solution was left to allow the solid product to precipitate. The dark yellow solution was decanted off and is likely to contain the by-product [Rh(^{i}Bu$_2$PCH$_2$CH$_2$P^{i}Bu$_2$)$_2$][BAr$^F_4$]. The remaining solid was dissolved in 20 ml CH_2Cl_2 and solid NaCl was then removed by filter cannula. 4 ml pentane was added and the solution left at 253 K overnight to grow crystalline product. The first crop of 520 mg orange crystalline product was isolated in a 58% yield

---

❷ **NMR Spectroscopy:**

^{1}H NMR (500 MHz CD_2Cl_2): δ 1.07 (d (^{i}Bu CH$_3$), J_{HH} = 6 Hz, 12H), 1.16 (d (^{i}Bu CH$_3$), J_{HH} = 6 Hz, 12H), 1.62 (m (^{i}Bu CH$_2$), 8H), 1.78 (m (PCH$_2$CH$_2$P, ^{i}Bu CH, NBD CH$_2$), 10H), 4.09 (s (NBD bridgehead, 2H), 5.31 (s (NBD CH=CH), 4H), 7.55 (s (BAr$^F_4$), 4H), 7.70 (s (BAr$^F_4$), 8H)

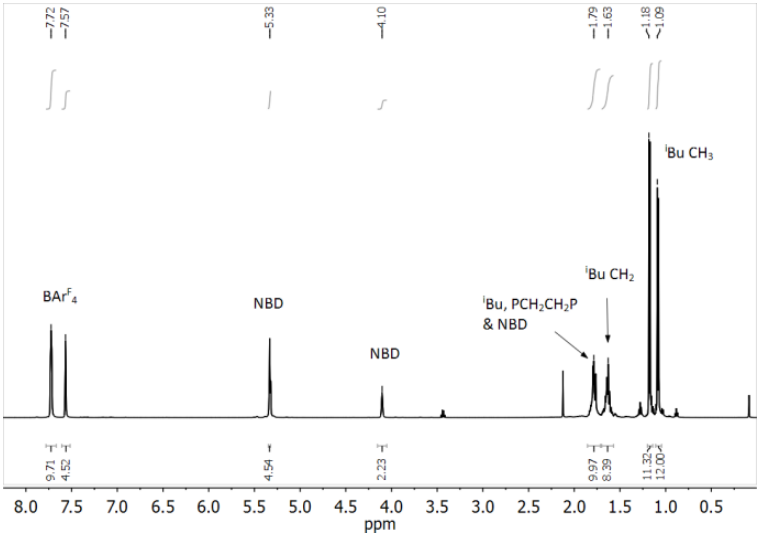

^{31}P{^{1}H} NMR (202 MHz CD_2Cl_2): δ 50.04 (d, J_{RhP} = 158 Hz 2P)

^{31}P{^{1}H} NMR (162 MHz Solid-state *10 kHz spin rate*): δ 48.50 (br, 2P)

^{13}C{^{1}H} NMR (126 MHz CD_2Cl_2): δ 24.7 (vt (^{i}Bu CH$_3$), J_{PC} = 3 Hz, 4C), 25.5 (vt (^{i}Bu CH$_3$), J_{PC} = 4 Hz, 4C), 25.7 (m (NBD CH$_2$), C), 26.0 (s (^{i}Bu CH, 4C), 37.1 (m (^{i}Bu CH$_2$), 4C), 55.9 (s (NBD bridgehead), 2C), 71.4 (m (PCH$_2$CH$_2$P), 2C), 86.4 (m (NBD C=C), 4C), *+[BAr$^F_4$] resonances*

^{13}C{^{1}H} NMR (101 MHz Solid-state *10 kHz spin rate*): δ 22.5 – 27.0 (br (^{i}Bu CH$_3$ & CH), 12C) 31.8 (br (NBD CH$_2$), 1C), 38.3 (br (^{i}Bu CH$_2$), 4C), 54.7 (s (NBD bridgehead), 2C), 64.75 & 68.4 (2x br (PCH2CH2P), 2x 1C), 86.7, 87.5 (2x s (NBD C=C), 2x 2C), *+[BAr$^F_4$] resonances as defined in 6.1.ii*

---

❸ **ESI-MS:** [M$^+$] m/z = 513.23, [M$^+$] calc = 513.23.

Exit voltage at 50% fragmentation to form [Rh(^{i}Bu$_2$PCH$_2$CH$_2$P^{i}Bu$_2$)]$^+$ = 208 V

---

❹ **Elemental Micro-Analysis:** $C_{57}H_{60}BF_{24}P_2Rh$ C, 49.73 H, 4.39 found C, 49.82 H, 4.50

---

❺ **X-ray Crystallography:** Crystals suitable for X-ray diffraction were grown from CH_2Cl_2/pentane. They also form directly out of a fluorobenzene solution at room temperature.

Internal crystal void volume percentage = 7%

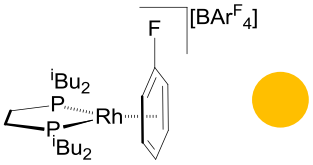

2. [Rh(^{i}Bu$_2$PCH$_2$CH$_2$P^{i}Bu$_2$)(η^6-C$_6$H$_5$F][BAr$^F_4$]

---

❶ **Synthesis:** Complex **1** (50 mg, 0.036 mmol) was suspended in C_6H_5F (~10 ml) in a J. Young's flask (poor solubility) and this solution/suspension hydrogenated at 1 atm H_2. The solution changes to a yellow colour and was stirred for 15 minutes. The flask was placed under vacuum to remove H_2 and excess solvent. Pentane was then added to crystallise a yellow solid which was then washed with pentane to give a 71% yield of **2**.

---

❷ **NMR Spectroscopy:**

^{1}H NMR (500 MHz C$_6$H$_5$F): δ 0.89 (d (^{i}Bu CH$_3$), J_{HH} = 7 Hz, 12H), 0.95 (d (^{i}Bu CH$_3$), J_{HH} = 7 Hz, 12H), 1.36 (m (^{i}Bu CH$_2$), 8H), 1.44 (d (PCH$_2$CH$_2$P), J_{PH} = 17 Hz, 4H), 1.65 (m (^{i}Bu CH), 4H), 5.47 (t (C$_6$H$_5$F), J_{HH} = 6 Hz, 1H), 6.19 (m (C$_6$H$_5$F), 2H), 6.25 (m (C$_6$H$_5$F), 2H), 7.66 (s (BAr$^F_4$), 4H), 8.35 (s (BAr$^F_4$), 8H)

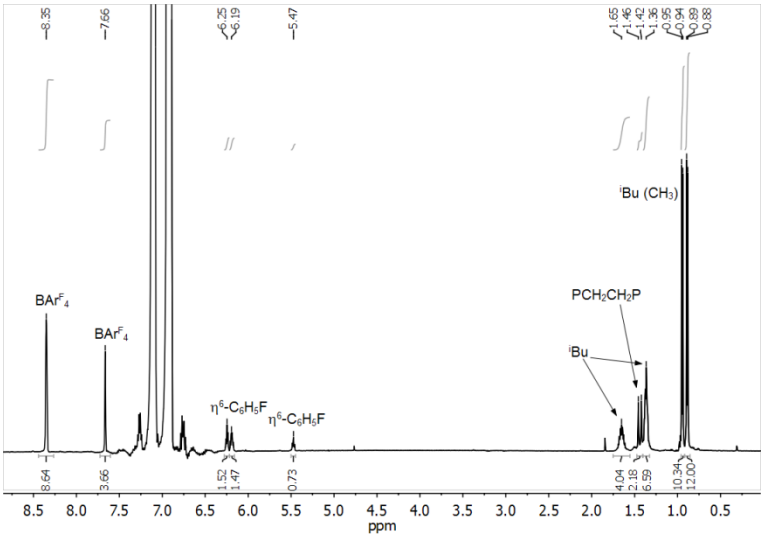

^{19}F{^{1}H} NMR (282 MHz C$_6$H$_5$F): δ -126.59 (s (C$_6$H$_5$F), F), -64.16 (s (BAr$^F_4$), 24F)

^{31}P{^{1}H} NMR (202 MHz C$_6$H$_5$F): δ 74.54 (d, J_{RhP} = 206 Hz, 2P)

---

❸ **ESI-MS:** [M$^+$] m/z = 517.21, [M$^+$] calc = 517.20.

Exit voltage at 50% fragmentation to form [Rh(^{i}Bu$_2$PCH$_2$CH$_2$P^{i}Bu$_2$)]$^+$ = 141 V

---

❹ **Elemental Micro-Analysis:** $C_{56}H_{57}BF_{25}P_2Rh$ C, 48.72 H, 4.16 found C, 48.68 H, 4.24

---

❺ **X-ray Crystallography:** Crystals were grown from C_6H_5F/pentane and a diffraction pattern collected. The solution showed the cation to be disordered and only a very rough structure was produced, this was consistent with the proposed connectivity.

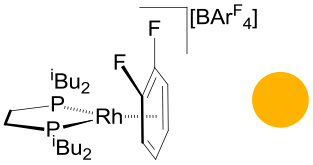

3. [Rh(^{i}Bu$_2$PCH$_2$CH$_2$P^{i}Bu$_2$)(η^6-1,2-C$_6$H$_4$F$_2$][BAr$^F_4$]

---

❶ **Synthesis:** **1** (250 mg, 0.179 mmol) was dissolved in difluorobenzene (5 ml) in a J. Young's flask (good solubility) and this solution hydrogenated at 1 atm H_2. The solution changes to an amber colour and was stirred for 15 minutes. The flask was placed under vacuum to remove H_2 and excess solvent, pentane was then added to crystallise a yellow/orange solid. This was then washed with pentane to give a 76% yield.

---

❷ **NMR Spectroscopy:**

^{1}H NMR (500 MHz C$_6$H$_4$F$_2$): δ 1.07 (d, J_{HH} = 7 Hz, 12H), 1.15 (d, J_{HH} = 7 Hz, 12H), 1.72 (m, 8H), 1.86 (d (PCH2CH2P), J_{PH} = 17 Hz, 4H), 1.95 (m, 4H), 6.18 (br (C$_6$H$_4$F$_2$), 2H), 6.83 (m (C$_6$H$_4$F$_2$), 2H), 7.68 (s (BAr$^F_4$), 4H), 8.33 (s (BAr$^F_4$), 8H)

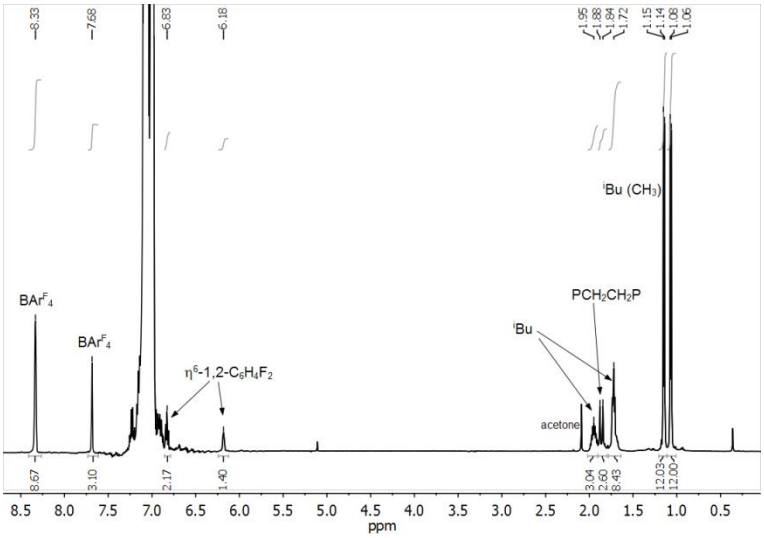

^{19}F{^{1}H} NMR (282 MHz C$_6$H$_4$F$_2$): δ -150.12 (s (C$_6$H$_4$F$_2$), F), -64.77 (s (BAr$^F_4$), 24F)

^{31}P{^{1}H} NMR (202 MHz C$_6$H$_4$F$_2$): δ 74.70 (d, J_{RhP} = 204 Hz, 2P)

---

❸ **ESI-MS:** [M$^+$] m/z = 535.18, [M$^+$] calc = 535.19.

Exit voltage at 50% fragmentation to form [Rh(^{i}Bu$_2$PCH$_2$CH$_2$P^{i}Bu$_2$)]$^+$ = 127 V

---

❹ **Elemental Micro-Analysis:** C$_{56}$H$_{56}$BF$_{26}$P$_2$Rh C, 48.09 H, 4.04 found C, 48.19 H, 3.96

---

❺ **X-ray Crystallography:** Crystals suitable for X-ray diffraction were grown from a difluorobenzene solution layered with pentane.

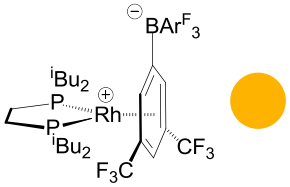

4. Rh(^{i}Bu$_2$PCH$_2$CH$_2$P^{i}Bu$_2$){η^6-C$_6$H$_3$(CF$_3$)$_2$}BAr$^F_3$

---

❶ **Synthesis:** Method 1; 60 mg (0.044 mmol) of solid **1** was placed into a J. Young's flask and hydrogenated under 1 atm H_2 for 30 mins, the orange crystals of starting material at first turn claret as they react with hydrogen to form the NBA bound intermediate **5**. This is left under argon for at least 5 hours at which point the material has turned to amber. To the final solid product 30 ml of hexane is added and after 1 hour of sonication a yellow solution of **4** has formed. The solution was filtered by filter cannula methods whilst warmed in a 308 K water bath. Then the solution was left at 275 K for 4 hours and then at 253 K overnight to yield amber crystals of **4**. The hexane/NBA supernatant was decanted and the resulting crystalline material dried under vacuum. 32 mg of large amber crystals were obtained (yield 58%) (*N.B.* a white layer of possibly NBA forms on the sides of the flask but the crystals can be easily separated).

Method 2; Complex **1** was dissolved in a non-coordinating arene (C_6F_6 or C_6F_5H) in a J. Young's flask and this saturated solution hydrogenated at 1 atm H_2 to give a yellow solution of **4**.

---

❷ **NMR Spectroscopy:**

^{1}H NMR (500 MHz C_6F_6 *(referenced to. C_6HF_5 impurity. 6.82)*): δ 0.91 (d (^{i}Bu CH_3), J_{HH} = 7 Hz, 12H), 0.97 (d (^{i}Bu CH_3), J_{HH} = 7 Hz, 12H), 1.52 (m (inequivalent ^{i}Bu CH_2), 4H), 1.64 (m (inequivalent ^{i}Bu CH_2), 4H), 1.89 (m (^{i}Bu CH), 4H), 2.01 (d (PCH_2CH_2P), J_{PH} = 17 Hz, 4H), 6.74 (s ((BAr$^F_3$)C$_6$**H$_3$**(CF$_3$)$_2$), 2H), 7.36 (s ((BAr$^F_3$)C$_6$**H$_3$**(CF$_3$)$_2$), H), 7.41 (s ((B**Ar$^F_3$**)C$_6$H$_3$(CF$_3$)$_2$), 3H), 7.62 (s ((B**Ar$^F_3$**)C$_6$H$_3$(CF$_3$)$_2$), 6H)

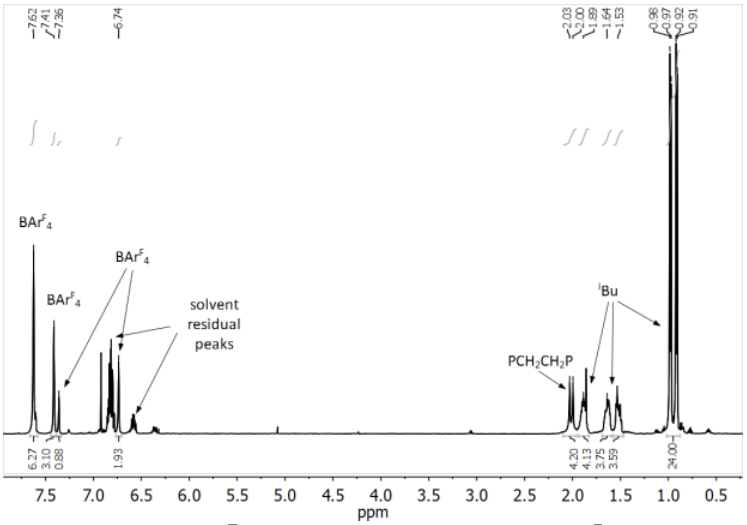

^{19}F{^{1}H} NMR (282 MHz C_6F_6 *(ref. C_6F_6 -168.35)*): δ -67.43 (s ((B**Ar$^F_3$**)C$_6$H$_3$(CF$_3$)$_2$), 18F), -64.93 (s ((BAr$^F_3$)C$_6$H$_3$(C**F$_3$**)$_2$), 6F)

^{31}P{^{1}H} NMR (202 MHz C_6F_6): δ 70.15 (d, J_{RhP} = 204 Hz, 2P)

^{31}P{^{1}H} NMR (162 MHz Solid-state *10 kHz spin rate*): 1:1 ratio of two independent molecules in the unit cell δ 63.78 (d, J_{RhP} = 197 Hz, 0.5P), 69.47 (d, J_{RhP} = 197 Hz, 0.5P) and 67.86 (d, J_{RhP} = 194 Hz, 0.5P), 71.14 (d, J_{RhP} = 194 Hz, 0.5P)

^{13}C{^{1}H} NMR (101 MHz Solid-state *10 kHz spin rate*): 1:1 ratio of two independent molecules in the unit cell δ 20.5 – 31.6 (m (^{i}Bu), 8C), 36.6 & 38.1 (2x s (^{i}Bu), 4C), 40.8 - 46.5 (m (^{i}Bu), 4C), 59.6 (br (PCH_2CH_2P), 2C), *BAr$^F_4$ peaks (92.3, 94.1, 95.1, 96.4, 100.0, 105.8, 112.7, 118.9, 124.9, 129.7, 135.5, 145.4, 155.2, 159.2)*

^{11}B NMR (160 MHz C_6F_6): δ -7.64 (s, 1B)

---

❸ **ESI-MS:** Complex **4** is neutral and not suitable for ESI-MS techniques

---

❹ **Elemental Micro-Analysis:** $C_{50}H_{52}BF_{24}P_2Rh$ C, 46.75 H, 4.08 found C, 46.61 H, 4.17

---

❺ **X-ray Crystallography:** Crystals suitable for X-ray diffraction were grown from a saturated pentane solution at 277 K.

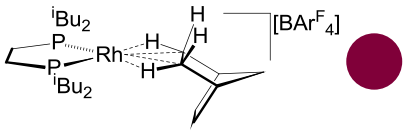

5. [Rh(^{i}Bu$_2$PCH$_2$CH$_2$P^{i}Bu$_2$)($\eta^2_{CH}\eta^2_{CH}$-NBA][BAr$^{F}_4$]

---

❶ **Synthesis:** Solid **1** was placed in a J. Young's flask and exposed to an atmosphere of hydrogen (1 atm). A colour change is observed from orange to claret within 1 minute. However as followed by SSNMR spectroscopy and X-ray crystallography, complete conversion requires approximately 5 minutes (microcrystalline) or longer (e.g. 12 minutes) for larger crystalline samples. This complex is stable in the solid-state at 253 K but reacts further to give **4** at ambient temperatures (> 293 K). Single crystals of **1** retain crystallinity upon reaction to give **3**, allowing X-ray diffraction data for **3** to be collected.

Solvation in CD_2Cl_2 at temperatures above 253 K results in direct formation of **4** and free NBA, while solvation in $CDCl_2F$ at 163 K results in loss of NBA and formation of a low coordinate organometallic species likely to be stabilised by agostic or solvent interactions that forms **4** upon warming.

---

❷ **NMR Spectroscopy:**

^{31}P{^{1}H} NMR (162 MHz Solid-state *10 kHz spin rate*): δ tightly coupled ABX system (modelled by gNMR but broad lineshape made accurate analysis of coupling constants difficult) 77.6 (d, J_{RhP} ~ 183 Hz, 1P), 78.9 (d, J_{RhP} ~ 180 Hz, 1P).

^{13}C{^{1}H} NMR (101 MHz Solid-state *10 kHz spin rate*): δ 21-32.5 (br (^{i}Bu CH_3 & NBA), 12C + 7C), 36-41 (d (^{i}Bu CH_2), 4C), *+[BAr$^{F}_4$] resonances as defined in 6.1.ii*

---

❸ **ESI-MS:** The complex was not solution stable for ESI-MS characterisation

---

❹ **Elemental Micro-Analysis:** The complex was too air sensitive for micro-analysis characterisation

---

❺ **X-ray Crystallography:** Crystals suitable for X-ray diffraction were generated by SC-SC reaction of **1** with H_2.

---

❻ **IR spectroscopy:**

Solid-state: No significant peaks were observed to grow in across the appropriate C-H (Rh···C-H) stretching region (calculated at 2429 and 2461 cm^{-1} for **5**) by *in situ* analysis of the reaction of hydrogenation of **1** in the solid-state.

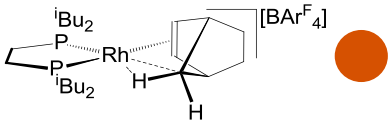

6. [Rh(^{i}Bu$_2$PCH$_2$CH$_2$P^{i}Bu$_2$)($\eta^2_{CC}\eta^2_{CH}$-NBE][BAr$^F_4$]

---

❶ **Synthesis:** 150 mg (0.107 mmol) of **3** was loaded into a Schlenk tube with 100 mg of solid NBE (1.06 mmol). To this was added 5 ml of CH_2Cl_2 and the solution stirred for 30 minutes during which a colour change from yellow to red occurs. Pentane was added whilst stirring to give a fine red precipitate, which was washed with pentane and isolated in a 95% yield. Very air sensitive crystals were grown by recrystallisation in CH_2Cl_2 layered with pentane at 277 K (**6** is not stable in CH_2Cl_2 at room temperature for a prolonged time (~30 minutes) and reacts to give undefined products).

---

❷ **NMR Spectroscopy:**

^{1}H NMR (500 MHz CD_2Cl_2): δ -3.67 (br (Rh···H-CH'), 1H), 1.09 (d (NBE CH_2), J_{HH} = 7 Hz, 2H), 1.14 (d (^{i}Bu CH_3), J_{HH} = 7 Hz, 12H), 1.24 (d (^{i}Bu CH_3), J_{HH} = 7 Hz, 12H), 1.45 (m (NBE H'CH), 1H), 1.50 (d (NBE CH_2), J_{HH} = 7 Hz, 2H), 1.66 (m (^{i}Bu CH_2), 8H), 1.74 (m (PCH_2CH_2P), 4H), 1.89 (m (^{i}Bu CH), 4H), 3.49 (s (NBE Bridgehead), 2H), 4.89 (s (NBE CH=CH), 2H), 7.56 (s (BAr$^F_4$), 4H), 7.72 (s (BAr$^F_4$), 8H)

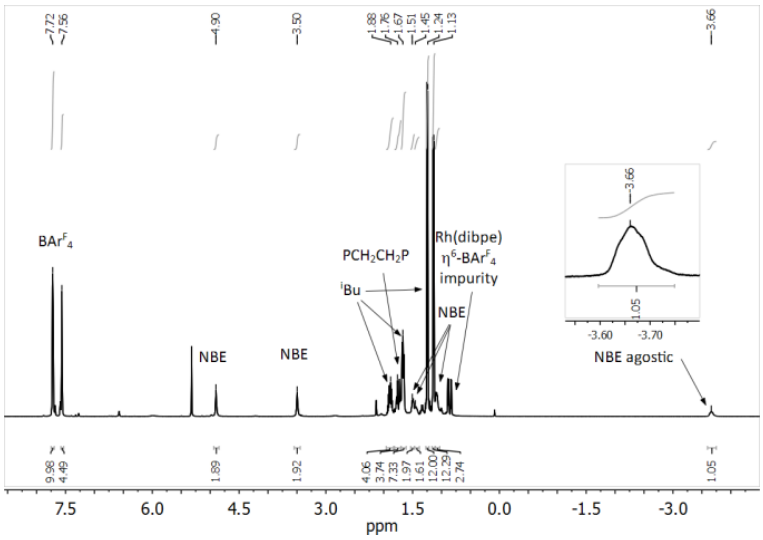

^{31}P{^{1}H} NMR (202 MHz CD_2Cl_2 *225 K*): δ 50.79 (d, J_{RhP} = 149 Hz, 1P), 79.36 (d (P *trans* to the agostic), J_{RhP} = 210 Hz, 1P)

^{31}P{^{1}H} NMR (162 MHz Solid-state *10 kHz spin rate*): δ 55.71 (br, 1P), 75.73 (br, 1P)

^{13}C{^{1}H} NMR (126 MHz CD_2Cl_2): δ 25.4 (d (^{i}Bu CH_3), J_{PC} = 7 Hz, 4C), 25.8 (d (^{i}Bu CH_3), J_{PC} = 9 Hz, 4C), 26.7 (s (^{i}Bu CH, 4C), 28.6 (s (NBE CH_2), 2C), 31.6 (s (NBE Rh···H-CH'), 1C)*, 39.5(d (^{i}Bu CH_2), J_{PC} = 25 Hz, 4C), 48.7 (s (NBE bridgehead), 2C), 92.9 (br (NBE C=C), 2C), *+[BAr$^F_4$] resonances. PCH_2CH_2P (2C) ^{13}C resonance not located.*

* *The agostic Rh···HC signal was assigned by a correlation in the HSQC NMR spectrum with ^{1}H NMR signal at* δ 1.45 (m (NBE H'CH), 1H) *which in turn correlates in a ^{1}H/^{1}H COSY NMR spectrum with the agostic Rh···HC signal* {-3.67 (br (Rh···H-CH'), 1H)}. *The signal is also consistent in chemical shift with the calculated value of 38.9 ppm.*

^{13}C{^{1}H} NMR (101 MHz Solid-state *10 kHz spin rate*): δ 25.0 (s (^{i}Bu CH_3), 8C), 26.4 (br (^{i}Bu CH, 4C & NBE, 2C), 31.4 (m (NBE), 1C), 39.3 (d (^{i}Bu CH_2), 4C), 47.3 (s (NBE), 2C), 64.2 (br (PCH_2CH_2P), 2C), 93.9 (br (NBE), 2C), *+[BAr$^F_4$] resonances as defined in 6.1.ii*

---

❸ **ESI-MS:** The complex was too unstable for ESI-MS characterisation

---

❹ **Elemental Micro-Analysis:** $C_{57}H_{62}BF_{24}P_2Rh$ C, 49.66, H, 4.53 found C, 49.50, H, 4.60

---

❺ **X-ray Crystallography:** Crystals suitable for X-ray diffraction were grown from CH_2Cl_2/pentane.

7. [Rh(^{i}Bu$_2$PCH$_2$CH$_2$P^{i}Bu$_2$)($\eta^2\eta^2$-COD)][BAr$^F_4$]

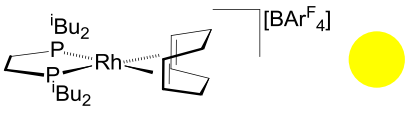

❶ **Synthesis:** 80 mg (0.057 mmol) of **3** was dissolved in 1 ml of 1,2-difluorobenzene, to this was added 36 µl (0.42 mmol), an excess of 1,5-cyclooctadiene (COD). The tube was shaken and left to react for 10 minutes. The product was crystallised by layering the mixture with pentane. Large yellow crystals formed which were washed with pentane. 80% yield.

❷ **NMR Spectroscopy:**

^{1}H NMR (500 MHz CD_2Cl_2): δ 1.07 (d (^{i}Bu CH_3), J_{HH} = 7 Hz, 12H), 1.16 (d (^{i}Bu CH_3), J_{HH} = 7 Hz, 12H), 1.73 (m (^{i}Bu CH_2), 8H), 1.88 (m (^{i}Bu CH and PCH_2CH_2P), 8H), 2.32 (m, (COD), 4H), 2.40 (m, (COD), 4H), 5.14 (br (COD), 4H), 7.58 (s (BAr$^F_4$), 4H), 7.74 (s (BAr$^F_4$), 8H)

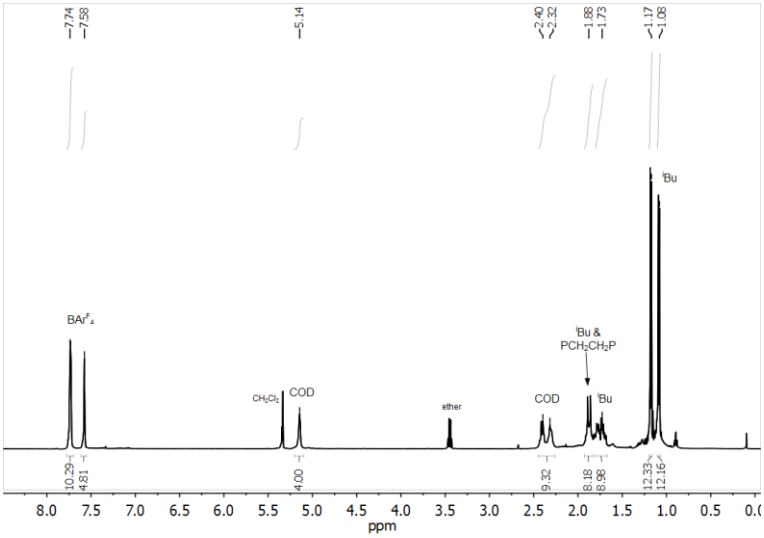

^{31}P{^{1}H} NMR (202 MHz CD_2Cl_2): δ 50.27 (d, J_{RhP} = 150 Hz, 2P)

❸ **ESI-MS:** [M^+] m/z = 529.28, [M^+] calc = 529.26.

❹ **Elemental Micro-Analysis:** $C_{58}H_{64}BF_{24}P_2Rh$ C, 50.02, H, 4.63 found C, 50.19 H, 4.74

❺ **X-ray Crystallography:** Yellow crystals were grown from CH_2Cl_2/pentane. Significant disorder hindered an accurate refinement, but the connectivity of the atoms could be confirmed.

8. [Rh(^{i}Bu$_2$PCH$_2$CH$_2$P^{i}Bu$_2$)(η^4-C$_6$H$_8$)][BAr$^F_4$]

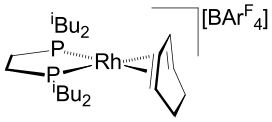

---

❶ **Synthesis:** 80 mg (0.058 mmol) of **3** was placed in a small schlenk and to this solid an excess of cyclohexene (59 µl, 0.58 mmol) was directly added before solvation of the mixture in CH_2Cl_2. Upon solvation a strong colour change from yellow to deep red was observed, however heating at 313 K for 30 minutes was required to complete the reaction. The cyclohexene is reduced to cyclohexadiene (C_6H_8) in the presence of rhodium, presumably by a transfer hydrogenation process releasing one equivalent of cyclohexane in the process.[32] large deep red crystals of the compound were grown by directly layering the mixture with pentane, these were then washed with pentane. 71% Yield.

---

❷ **NMR Spectroscopy:**

^{1}H NMR (500 MHz CD_2Cl_2): δ 0.95 (dd (^{i}Bu CH_3), J_{HH} = 6 Hz & 12 Hz, 12H), 1.10 (dd (^{i}Bu CH=3), J_{HH} = 6 Hz & 13 Hz, 12H), 1.70 (m (^{i}Bu CH_2), 8H), 1.84 (m (C_6H_8), 4H), 1.95 (m, (^{i}Bu CH and PCH_2CH_2P) 8H), 5.10 (br (C_6H_8), 2H), 5.31 (br d (C_6H_8), J_{HH} = 6 Hz, 2H), 7.56 (s (BAr$^F_4$), 4H), 7.72 (s (BAr$^F_4$), 8H)

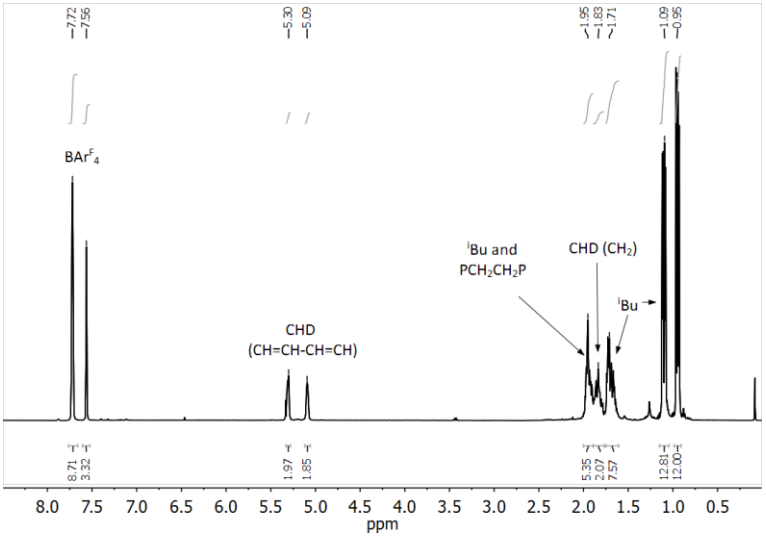

^{31}P{^{1}H} NMR (202 MHz CD_2Cl_2): δ 53.05 (d, J_{RhP} = 176 Hz, 2P)

^{31}P{^{1}H} NMR (162 MHz Solid-state *10 kHz spin rate*): δ 48.04 (d, J_{RhP} = 172 Hz, 1P), 52.95 (d, J_{RhP} = 165 Hz, 1P)

^{13}C{^{1}H} NMR (101 MHz Solid-state *10 kHz spin rate*): δ 18.34 – 27.62 (br (^{i}Bu & C_6H_8), 14C), 39.76 (br (^{i}Bu), 4C), 64.77 (br (PCH_2CH_2P), 2C), 80.39 & 84.17 (2x s (C_6H_8), 2x 1C), 95.56 (s (C_6H_8), 2C) *+[BAr$^F_4$] resonances*

---

❸ **ESI-MS:** [M$^+$] m/z = 501.25, [M$^+$] calc = 501.23.

---

❹ **Elemental Micro-Analysis:** $C_{56}H_{60}BF_{24}P_2Rh$ C, 49.29 H, 4.43 found C, 49.18 H, 4.34

---

❺ **X-ray Crystallography:** Red crystals were grown from CH_2Cl_2/pentane.

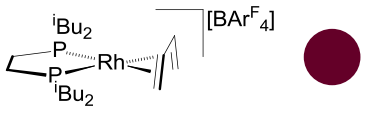

9. [Rh(^{i}Bu$_2$PCH$_2$CH$_2$P^{i}Bu$_2$)(η^4-C$_4$H$_6$)][BAr$^F_4$]

---

❶ **Synthesis:** 250 mg (0.179 mmol) **3** was dissolved in 1,2-$C_6H_4F_2$ and the solution frozen and placed under vacuum. Butadiene gas was used to refill the flask and upon warmng a colour change to a dark claret solution occurs, the flask was left sealed for 2 hours. Since reducing the pressure inside the flask drives the backwards reaction, releasing butadiene gas, the complex was crystallised by adding pentane via syringe directly to the solution under an atmosphere of butadiene. Dark claret crystalline material forms, 66% yield. Solid **9** is vacuum stable.

---

❷ **NMR Spectroscopy:**

^{1}H NMR (300 MHz CD_2Cl_2): δ 0.94 (vt (^{i}Bu CH_3), J_{HH} = 7 Hz, 12H), 1.07 (d (^{i}Bu CH_3), J_{HH} = 7 Hz, 6H), 1.09 (d (^{i}Bu CH_3), J_{HH} = 7 Hz, 6H), 1.64 (m (^{i}Bu CH or CH_2), 4H), 1.74 (m (PCH_2CH_2P), 4H), 1.80-2.04 (m, (^{i}Bu CH or CH_2), 8H), 2.86 (d J_{HH} = 14 Hz (C_4H_6), 2H), 4.27 (d J_{HH} = 7 Hz (C_4H_6), 2H), 5.45 (m, (C_4H_6), 2H) 7.56 (s (BAr$^F_4$), 4H), 7.72 (s (BAr$^F_4$), 8H)

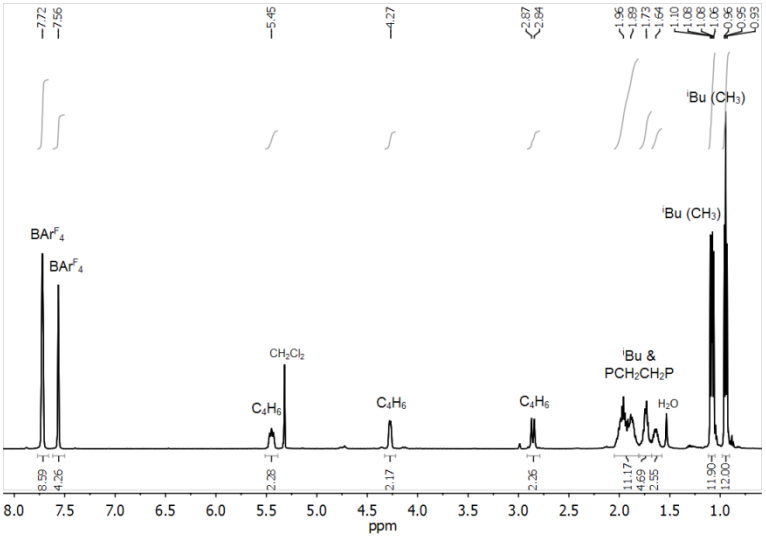

^{31}P{^{1}H} NMR (122 MHz CD_2Cl_2): δ 54.64 (d, J_{RhP} = 170 Hz, 2P)

^{31}P{^{1}H} NMR (162 MHz Solid-state *10 kHz spin rate*): δ 52.07 (br, major peak), 59.84 (br, minor peak), 62.25 (br, minor peak)

---

❸ **ESI-MS:** [M^+] m/z = 475.21, [M^+] calc = 475.21.

Exit voltage at 50% fragmentation to form [Rh(^{i}Bu$_2$PCH$_2$CH$_2$P^{i}Bu$_2$)]$^+$ = 154 V

---

❹ **Elemental Micro-Analysis:** $C_{54}H_{58}BF_{24}P_2Rh$ C, 48.45 H, 4.37 found C, 48.57 H, 4.43

---

❺ **X-ray Crystallography:** Dark claret crystals grow from CH_2Cl_2/pentane, whilst the crystals diffract well and the anions can be well refined, the cation shows significant disorder over four positions (rotated 90°, inverted, rotated 90° and inverted). Therefore only a rough model can be generated.

Internal crystal void volume percentage = 7%

10. [Rh(^{i}Bu$_2$PCH$_2$CH$_2$P^{i}Bu$_2$)(C$_2$H$_4$)$_2$][BAr$^{F}_4$]

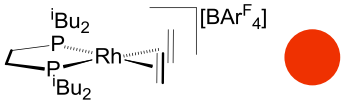

---

❶ **Synthesis:** 26 mg (0.019 mmol) of solid **1** was placed in a crystallisation tube with a Young's tap and exposed to hydrogen (1 atm) for ten minutes to form **5**. The flask was evacuated and ethene (1 atm) was immediately added. With the flask under a pressure of ethene, CH_2Cl_2 was added by syringe through a Suba-Seal to dissolve the compound forming a vermillion solution. Pentane was also added by syringe to form a layer over the CH_2Cl_2 and the flask was sealed under 1.5 atm of ethene. Vermillion crystals formed over 48 hours which could be isolated and appear vacuum stable (25% yield). The complex is not stable in solution (or when suspended in pentane) at room temperature in the absence of an ethene atmosphere, as decomposition to **4** occurs.

---

❷ **NMR Spectroscopy:**

^{1}H NMR (500 MHz CD_2Cl_2 240 K): δ 0.96 (d (^{i}Bu CH_3), J_{HH} = 6 Hz, 12H), 1.03 (d (^{i}Bu CH_3), J_{HH} = 6 Hz, 12H), 1.5-2.0 (br (^{i}Bu CH, ^{i}Bu CH_2 & PCH_2CH_2P), 16H), 3.98 (s (C_2H_4), 8H), 7.53 (s (BAr^{F}_4), 4H), 7.71 (s (BAr^{F}_4), 8H)

^{31}P{^{1}H} NMR (202 MHz CD_2Cl_2 240 K): δ 54.74 (d, J_{RhP} = 144 Hz, 2P)

^{1}H NMR (500 MHz CD_2Cl_2 4 atm C_2H_4): δ 1.06 (d (^{i}Bu CH_3), J_{HH} = 6 Hz, 12H), 1.11 (d (^{i}Bu CH_3), J_{HH} = 6 Hz, 12H), 1.78 (m (^{i}Bu CH_2), 8H), 1.94 (dd (PCH_2CH_2P), J_{PH} = 17 Hz, 4H), 1.8-2.2 (br (^{i}Bu CH), 4H), 5.31 (br (C_2H_4) (in exchange with atmosphere)), 7.57 (s (BAr^{F}_4), 4H), 7.72 (s (BAr^{F}_4), 8H)

^{31}P{^{1}H} NMR (202 MHz CD_2Cl_2 4 atm C_2H_4): δ 55.9 (d, J_{RhP} = 145 Hz, 2P)

---

❸ **ESI-MS:** The complex is not stable in solution at room temperature.

---

❹ **Elemental Micro-Analysis:** $C_{54}H_{60}BF_{24}P_2Rh$ C, 48.38, H, 4.51 found C, 48.52, H, 4.41

---

❺ **X-ray Crystallography:** Vermillion crystals were grown from CH_2Cl_2/pentane under 1.5 atm of ethene. The refinement displays significant cation disorder with approximately 1/3 of the cations occupying a position rotated at 90° from the major component.

Internal crystal void volume percentage = 9%

11. [Rh(^{i}Bu$_2$PCH$_2$CH$_2$P^{i}Bu$_2$)(η^4-2,3-C$_4$H$_4$Me$_2$)][BAr$^F_4$]

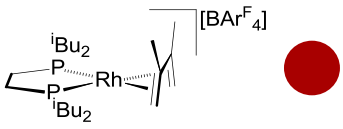

---

❶ **Synthesis:** 10 mg (0.007 mmol) of **3** was placed in a small Schlenk and to this solid an excess of 2,3-dimethylbutadiene (η^4-2,3-C$_4$H$_4$Me$_2$) (8 µl, 0.07 mmol) was directly added before solvation of the mixture in CH_2Cl_2. Upon solvation a strong colour change from yellow to red was observed. Deep red crystalline material was obtained by adding pentane.

---

❷ **NMR Spectroscopy:**

^{1}H NMR (300 MHz CD_2Cl_2): δ 0.98 (dd (^{i}Bu CH$_3$), J_{HH} = 6 Hz, 12H), 1.07 (vt (^{i}Bu CH$_3$), J_{HH} = 7 Hz, 12H), 1.6-2 (m, PCH$_2$CH$_2$P, ^{i}Bu CH, ^{i}Bu CH$_2$), 16H), 2.12 (s (2,3-C$_4$H$_4$Me$_2$ Me), 6H), 2.64 (s (2,3-C$_4$H$_4$Me$_2$), 2H), 4.04 (d, J_{HH} = 3 Hz, (2,3-C$_4$H$_4$Me$_2$), 2H) 7.56 (s (BAr$^F_4$), 4H), 7.71 (s (BAr$^F_4$), 8H)

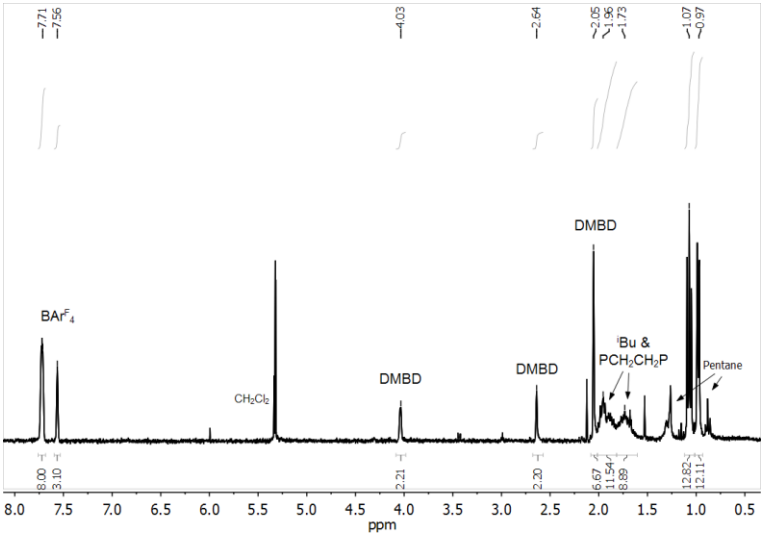

^{31}P{^{1}H} NMR (122 MHz CD_2Cl_2): δ 53.22 (d, J_{RhP} = 167 Hz, 2P)

---

❸ **ESI-MS:** [M$^+$] m/z = 503.24, [M$^+$] calc = 503.26.

---

❹ **Elemental Micro-Analysis:** $C_{56}H_{62}BF_{24}P_2Rh$ C, 49.21 H, 4.57 found C, 49.18 H, 4.66

---

❺ **X-ray Crystallography:** Deep red crystals were grown from CH_2Cl_2/pentane.

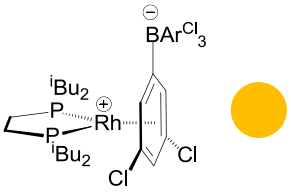

12. Rh(^{i}Bu$_2$PCH$_2$CH$_2$P^{i}Bu$_2$){(η^6-C$_6$H$_3$Cl$_2$)BAr$^{Cl}_3$}

---

❶ **Synthesis:** A microcrystalline sample of **1-[BAr$^{Cl}_4$]** was exposed to one atmosphere of H_2, either in the solid-state or in a CH_2Cl_2 solution, for 30 minutes to give a yellow solid/solution. Relatively rapid recrystallisation from CH_2Cl_2/pentane (277 K, 24 hours) yields yellow crystalline **12** (10 mg (9.0 x10^{-3} mmol) scale, ~60% yield).

---

❷ **NMR Spectroscopy:**

^{1}H NMR (500 MHz CD$_2$Cl$_2$): δ 0.93 (d (^{i}Bu CH$_3$), J_{HH} = 7 Hz, 12H), 0.98 (d (^{i}Bu CH$_3$), J_{HH} = 7 Hz, 12H), 1.52 (m (^{i}Bu CH$_2$), 8H), 1.82 (m (^{i}Bu CH, PCH$_2$CH$_2$P), 8H), 6.15 (s ((BAr$^{Cl}_3$)C$_6$**H$_3$**Cl$_2$), 2H), 7.02 (s ((B**Ar$^{Cl}_3$**)C$_6$H$_3$Cl$_2$), 6H), 7.06 (s ((BAr$^{Cl}_3$)C$_6$**H$_3$**Cl$_2$), H), 7.10 (s ((B**Ar$^{Cl}_3$**)C$_6$H$_3$Cl$_2$), 3H).

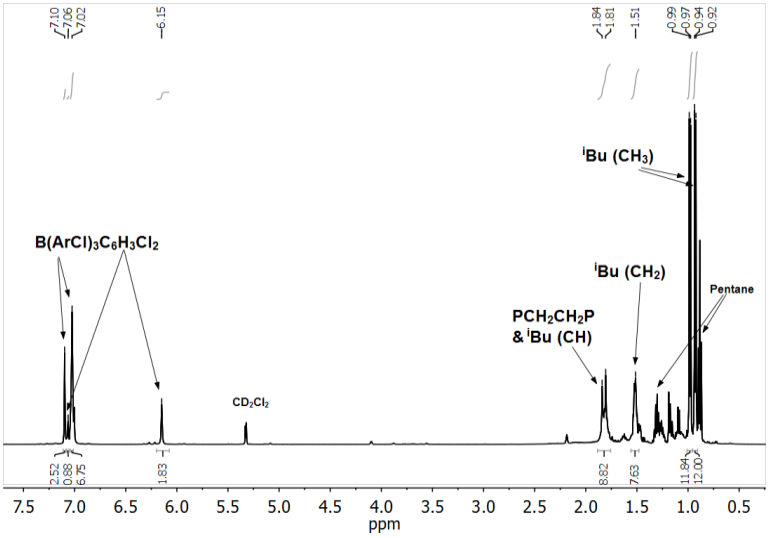

^{31}P{^{1}H} NMR (202 MHz CD$_2$Cl$_2$): δ 67.84 (d, J_{RhP} = 202 Hz, 2P).

^{11}B{^{1}H} NMR (160 MHz CD$_2$Cl$_2$): δ -8.30 (s, 1B).

---

❸ **ESI-MS:** The complex is neutral and not suitable for ESI-MS.

---

❹ **Elemental Micro-Analysis:** over time **12** slowly converts to **23** in the solid-state, therefore microanalysis was recorded only for **23** (*vide infra*)**.**

---

❺ **X-ray Crystallography:** Yellow crystals were grown relatively quickly from CH_2Cl_2/Pentane.

13. [Rh(^{i}Pr$_2$PCH$_2$CH$_2$P^{i}Pr$_2$)NBD][BAr$^{F}_4$]

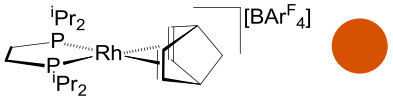

❶ **Synthesis:** 44 µl (0.44 mmol) of NBD was added directly to 117 mg (0.089 mmol) of solid [Rh(^{i}Pr$_2$PCH$_2$CH$_2$P^{i}Pr$_2$)(C$_6$H$_5$F)][BAr$^{F}_4$], **VIII**, [33] and the combination dissolved in 3 ml of CH_2Cl_2. A colour change from yellow to vermillion occurred as the solution was stirred for five minutes, the flask was heated to 313 K for 35 minutes. Pentane was added to form a vermillion precipitate, this was further washed with pentane before drying under vacuum. 95 mg of product was obtained, 81% yield.

❷ **NMR Spectroscopy:**

^{1}H NMR (300 MHz CD_2Cl_2): δ 1.19 (m (^{i}Pr CH_3), 24H), 1.74 (d (PCH_2CH_2P), J_{PH} = 12 Hz, 4H), 1.84 (s (NBD CH_2), 2H), 2.14 (m (^{i}Pr CH), 4H), 4.20 (br (NBD bridgehead), 2H), 5.62 (m (NBD C=C), 4H), 7.56 (s (BAr$^{F}_4$), 4H), 7.72 (s (BAr$^{F}_4$), 8H)

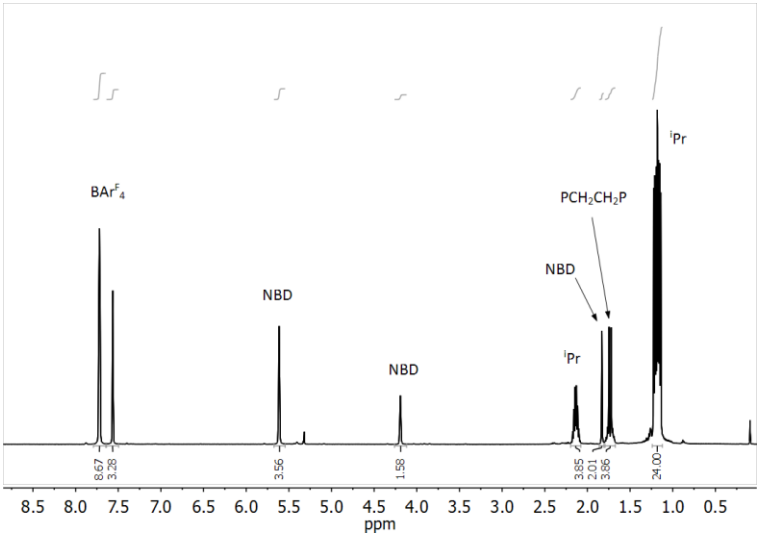

^{31}P{^{1}H} NMR (122 MHz CD_2Cl_2): δ 78.05 (d, J_{RhP} = 155 Hz, 2P)

^{31}P{^{1}H} NMR (162 MHz Solid-state *10 kHz spin rate*): δ 77.32 (d, J_{RhP} = 155 Hz, 1P), 79.84 (d, J_{RhP} = 154 Hz, 1P)

^{13}C{^{1}H} NMR (101 MHz Solid-state *10 kHz spin rate*): δ 13.50 – 20.72 (br (^{i}Pr), 8C) 24.18 (br (NBD CH_2), 1C), 28.58 (br (^{i}Pr), 4C), 55.44 (s (NBD), 2C), 72.24 (br (PCH_2CH_2P), 2C), 85.40 - 87.97 (4x s (NBD), 4x 1C), *+[BAr$^{F}_4$] resonances as defined in 6.1.ii*

❸ **ESI-MS:** [M^{+}] m/z = 457.17, [M^{+}] calc = 457.17.

❹ **Elemental Micro-Analysis:** $C_{53}H_{52}BF_{24}P_2Rh$ C, 48.20, H, 3.97 found C, 48.06 H, 3.89

❺ **X-ray Crystallography:** Vermillion crystals were grown from CH_2Cl_2/pentane.

Internal crystal void volume percentage = 16%

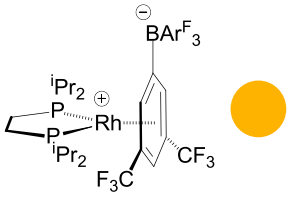

14. Rh(^{i}Pr$_2$PCH$_2$CH$_2$P^{i}Pr$_2$)(η^6-C$_6$H$_3$(CF$_3$)$_2$)BAr$^F_3$]

---

❶ **Synthesis:** 33 mg of **13** was hydrogenated in the solid-state at 1 atmosphere, a colour change from vermillion to amber occurs over 5 minutes. After 2 hours under hydrogen the sample was degassed and placed under and an argon atmosphere. The product was recrystallised by solvation in hexafluorobenzene layered with pentane and left at 277 K. Crystals can also be grown directly out of pentane (slight solubility) at low temperature.

---

❷ **NMR Spectroscopy:**

^{1}H NMR (500 MHz C$_6$F$_6$ *(ref. C$_6$HF$_5$ impurity. 6.82)*): δ 1.06 – 1.14 (m (^{i}Pr CH$_3$), 24H), 1.83 (d (PCH$_2$CH$_2$P), J_{PH} = 14 Hz, 4H), 1.90 (m (^{i}Pr CH), 4H), 7.21 (s ((BAr$^F_3$)C$_6$**H$_3$**(CF$_3$)$_2$), H), 7.22 (s ((BAr$^F_3$)C$_6$**H$_3$**(CF$_3$)$_2$), 2H), 7.39 (s ((B**Ar$^F_3$**)C$_6$H$_3$(CF$_3$)$_2$), 3H), 7.50 (s ((B**Ar$^F_3$**)C$_6$H$_3$(CF$_3$)$_2$), 6H)

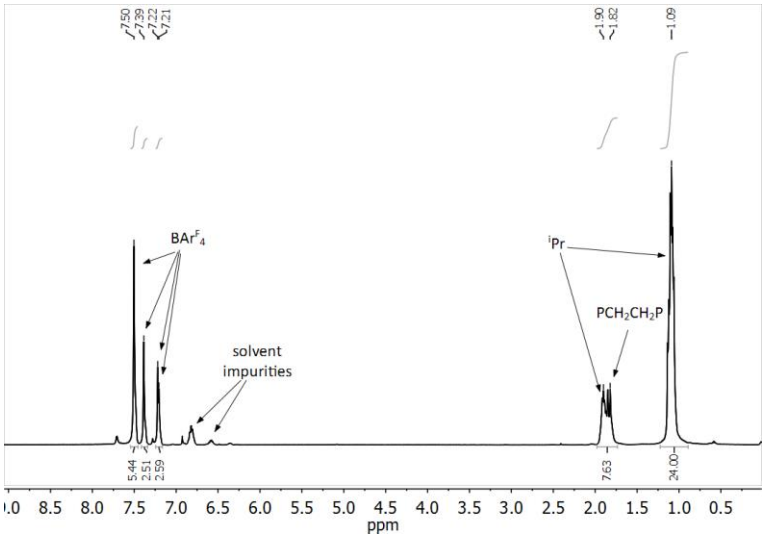

^{31}P{^{1}H} NMR (202 MHz C$_6$F$_6$): δ 102.13 (d, J_{RhP} = 206 Hz, 2P)

^{31}P{^{1}H} NMR (162 MHz Solid-state *10 kHz spin rate*): δ 101.87 (d, J_{RhP} = 205 Hz, 1P), 104.05 (d, J_{RhP} = 198 Hz, 1P)

^{19}F{^{1}H} NMR (169 MHz CD$_2$Cl$_2$): δ -61.06 (s ((B**Ar$^F_3$**)C$_6$H$_3$(CF$_3$)$_2$), 18F), -58.83 (s ((BAr$^F_3$)C$_6$H$_3$(C**F$_3$**)$_2$), 6F)

^{11}B NMR (160 MHz C$_6$F$_6$): δ -6.89 (s, 1B)

^{13}C{^{1}H} NMR (101 MHz Solid-state *10 kHz spin rate*): δ 13.40 – 23.40 (br (^{i}Pr), 8C) 28.43 (br (^{i}Pr), 4C), 55.44 (s (NBD), 2C), *BAr$^F_4$ peaks (95.94, 97.53, 99.39, 102.57, 118.34, 123.10, 124.91, 128.80, 130.39, 135.42, 153.66, 156.67, 162.37) (PCH$_2$CH$_2$P, 2C, unidentified)*

---

❸ **ESI-MS:** The complex is neutral and not suitable for ESI-MS techniques

---

❹ **Elemental Micro-Analysis:** C$_{46}$H$_{44}$BF$_{24}$P$_2$Rh C, 44.97, H, 3.61 found C, 44.86 H, 3.71

---

❺ **X-ray Crystallography:** Yellow crystals were grown directly from pentane at 277 K.

15. [Rh(^{i}Pr$_2$PCH$_2$CH$_2$CH$_2$P^{i}Pr$_2$)NBD][BAr$^{F}_4$]

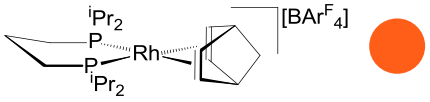

---

❶ **Synthesis:** *Synthetic method developed by **Mark Scott**, a Masters student supervised by Seb Pike.*[34]

266 mg (0.225 mmol) of [Rh(COD)$_2$][BAr$^{F}_4$] was dissolved in 3 ml of C_6H_5F. 62.2 mg (0.225 mmol) of ^{i}Pr$_2$PCH$_2$CH$_2$CH$_2$P^{i}Pr$_2$ was dissolved in 2 ml of C_6H_5F and this was added dropwise to the stirring [Rh(COD)$_2$][BAr$^{F}_4$] solution. The solution was stirred for 1 hour and then placed under 4 atm of H_2 before being left to stir for a further 2 hours. This solution was dried under vacuum, then washed with hexane (with sonication) to give an orange solid, [Rh(^{i}Pr$_2$PCH$_2$CH$_2$CH$_2$P^{i}Pr$_2$)(η^6-C$_6$H$_5$F)][BAr$^{F}_4$], **IX**.[33] The solid was dried and excess NBD (80 µl, 0.787 mmol) added, followed by 5 ml of CH_2Cl_2. The solution was stirred for 30 minutes before a layer of pentane was added and the solution left to crystallise at room temperature overnight. Orange crystalline material forms (80% yield).

---

❷ **NMR Spectroscopy:** *Solution NMR recorded by **Mark Scott**, Solid-state NMR recorded in collaboration with **Mark Scott**.*

^{1}H NMR (300 MHz CD$_2$Cl$_2$): δ 1.15 (dd (^{i}Pr CH$_3$), J_{HH} = 7 Hz, 12H), 1.31 (dd (^{i}Pr CH$_3$), J_{HH} = 7 Hz, 12H), 1.49 (m (PC**H$_2$**CH$_2$C**H$_2$**P), 4H), 1.77 (s (NBD CH$_2$), 2H), 1.92 (m (PCH$_2$C**H$_2$**CH$_2$P), 2H), 2.05 (m (^{i}Pr CH), 4H), 4.11 (s (NBD bridgehead), 2H), 5.25 (m (NBD C=C), 4H), 7.56 (s (BAr$^{F}_4$), 4H), 7.71 (s (BAr$^{F}_4$), 8H)

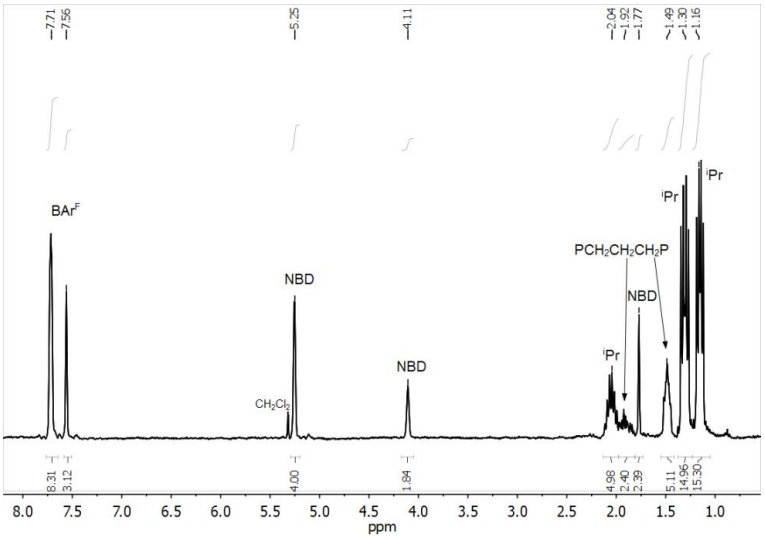

^{31}P{^{1}H} NMR (122 MHz CD$_2$Cl$_2$): δ 22.25 (d, J_{RhP} = 148 Hz, 2P)

^{31}P{^{1}H} NMR (162 MHz Solid-state *10 kHz spin rate*): δ 21.40 (d, J_{RhP} = 141 Hz, 2x $^{2}/_{3}$P), ~19.3 (br, $^{2}/_{3}$P) due to modulated solid-state structure.

^{13}C{^{1}H} NMR (101 MHz Solid-state *10 kHz spin rate*): δ 11.8 – 35.4 (br (^{i}Pr, NBD and backbone region), 34C), 50-80 (very weak, br (NBD), 4C), 72.24 (br (PCH$_2$CH$_2$P), 2C), *+[BAr$^{F}_4$] resonances as defined in 6.1.ii*

---

❸ **ESI-MS:** *recorded by **Mark Scott***

[M$^+$] m/z = 471.18, [M$^+$] calc = 471.18.

Exit voltage at 50% fragmentation to form [Rh(^{i}Pr$_2$PCH$_2$CH$_2$CH$_2$P^{i}Pr$_2$)]$^+$ = 188 V

---

❹ **Elemental Micro-Analysis:** $C_{54}H_{54}BF_{24}P_2Rh$ C, 48.60, H, 4.08 found C, 48.61 H, 3.90

---

❺ **X-ray Crystallography:** Orange crystals were grown from CH_2Cl_2/pentane. The structure shows commensurate modulation in one direction, such that the asymmetric unit contains 1.5 molecules.

Internal crystal void volume percentage = 13%

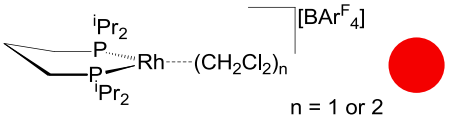

16. [Rh(^{i}Pr$_2$PCH$_2$CH$_2$CH$_2$P^{i}Pr$_2$)(CH$_2$Cl$_2$)$_n$][BAr$^F_4$] (n = 1 or 2)

---

❶ **Synthesis:** *Synthetic method developed by **Mark Scott**, a Masters student supervised by Seb Pike.*[34]

8 mg microcrystalline solid **15** was hydrogenated at 1 atm for 10 minutes in a high pressure NMR tube. The hydrogen atmosphere was removed and the tube was frozen at 77 K. CH_2Cl_2 was distilled onto the frozen solid and the mixture warmed to 188 K resulting in a red solution which was analysed by NMR spectroscopy immediately. The complex decomposes at elevated temperatures.

---

❷ **NMR Spectroscopy:**

^{31}P {^{1}H} NMR (202 MHz CD_2Cl_2): δ 51.01 (d, J_{RhP} = 199 Hz, 2P).

---

❸ **ESI-MS:** The complex is not stable at room temperature.

---

❹ **Elemental Micro-Analysis:** The complex is too unstable for micro analysis.

---

❺ **X-ray Crystallography:** The complex is not stable at room temperature.

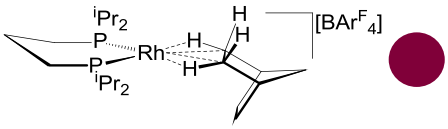

17. [Rh(^{i}Pr$_2$PCH$_2$CH$_2$CH$_2$P^{i}Pr$_2$)(η^4-NBA)][BAr$^F_4$]

---

❶ **Synthesis:** *Synthetic method developed by **Mark Scott**, a Masters student supervised by Seb Pike.*[34]

Microcrystalline solid material of **15** was hydrogenated at 1 atm for 10 minutes and then the hydrogen was removed. The complex is unstable and decomposes over time to form **19**, however **17** appears to remain stable at temperatures ~233 K.

---

❷ **NMR Spectroscopy:**

^{31}P{^{1}H} NMR (162 MHz Solid-state *10 kHz spin rate*): δ 57.83 (d, J_{RhP} = 191 Hz, 2P).

---

❸ **ESI-MS:** The complex is not stable in solution

---

❹ **Elemental Micro-Analysis:** The complex is too unstable for micro analysis

---

❺ **X-ray Crystallography:** Orange single crystals of **15** were placed under an atmosphere of hydrogen for 45 minutes over which time they turn claret. These crystals were taken to the Diamond Light Source (beamline I12) (kept at 77 K in transit). Incommensurate modulation in two directions was observed and the dataset requires analysis by a professional crystallographer (Dr. Kirsten Kristensen, Uni. Oxford).

18. $[Rh(^{i}Pr_2PCH_2CH_2CH_2P^{i}Pr_2)(H)(\mu\text{-}H)]_2[BAr^{F}_4]_2$

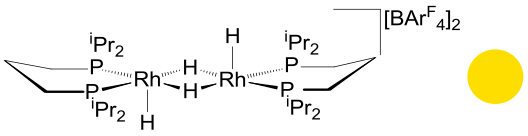

---

❶ **Synthesis:** 15 mg of (0.010 mmol) of **15** was exposed to 4 atm of hydrogen for one hour. A yellow solid forms which can be dissolved in 1,2-$C_6H_4F_2$. Recrystallisation can be achieved by layering the solution with pentane and leaving at 277 K, the solid product is a microcrystalline material not suitable for X-ray diffraction.

---

❷ **NMR Spectroscopy:**

^{1}H NMR (500 MHz 1,2-$C_6H_4F_2$): δ -25.59 (br (terminal hydrides), 2H) -4.57 (br (bridginh hydrides), 2H) 1.34 (m (^{i}Pr CH_3), 24H), 1.41 (m (^{i}Pr CH_3), 24H), 1.5 – 2.4 (multiple peaks (^{i}Pr CH & $PCH_2CH_2CH_2P$), 20H), 7.68 (s (BAr^{F}_4), 8H), 8.31 (s (BAr^{F}_4), 16H).

^{31}P{^{1}H} NMR (202 MHz 1,2-$C_6H_4F_2$): δ 61.50 (d, J_{RhP} = 103 Hz, 2P)

^{2}H{^{1}H} NMR (62 MHz Solid-state *10 kHz spin rate* d_4-18: δ -25.8 (s, 2H) -5.06 (s, 2H)

^{31}P{^{1}H} NMR (162 MHz Solid-state *10 kHz spin rate*): δ 58.8 (br, 2P), 63.2 (br, 2P)

---

❸ **ESI-MS:** $[M^{2+}]$ m/z = 381.13, $[M^{2+}]$ calc = 381.13 (with an expected isotope splitting pattern of ½ integral steps).

---

❹ **Elemental Micro-Analysis:** $C_{94}H_{96}B_2F_{48}P_4Rh2$ C, 45.36 H, 3.89 found C, 45.53 H, 3.99

---

❺ **X-ray Crystallography:** Single crystals could not be formed although microcrystalline material was grown from 1,2-$C_6H_4F_2$/pentane.

19. $Rh(^{i}Pr_2PCH_2CH_2CH_2P^{i}Pr_2)(\eta^4\text{-}C_6H_3(CF_3)_2)BAr^F{}_3$

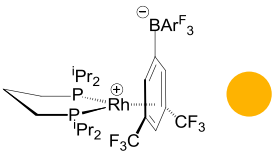

---

❶ **Synthesis:** 10 mg of (0.007 mmol) of **15** was hydrogenated (1 atm) in the solid-state for 20 minutes. After removing the hydrogen atmosphere, hexane is added and the suspension heated to 313 K for 1 hour with periodic sonication. This yields a yellow solution of **19** which can be crystallised by allowing the solution to cool at room temperature, to yield very small yellow crystals.

---

❷ **NMR Spectroscopy:**

$^{31}P\{^{1}H\}$ NMR (202 MHz C_5H_{12}): δ 41.47 (d, J_{RhP} = 196 Hz, 2P)

$^{31}P\{^{1}H\}$ NMR (162 MHz Solid-state *10 kHz spin rate*): δ 39.64 (d, J_{RhP} = 195 Hz, P), 43.72 (d, J_{RhP} = 195 Hz, P)

$^{19}F\{^{1}H\}$ NMR (169 MHz C_5H_{12}): δ -63.30 (s ((B**Ar$^F{}_3$**)$C_6H_3(CF_3)_2$), 18F), -60.30 (s ((B$Ar^F{}_3$)C_6H_3(C**F$_3$**)$_2$), 6F)

$^{13}C\{^{1}H\}$ NMR (101 MHz Solid-state *10 kHz spin rate*): δ 11.8-35.4 (^{i}Pr and backbone region, 34 C) 90.34, 94.88, 98.17 (all br (η^4-**$C_6H_3(CF_3)_2$**)B$Ar^F{}_3$)), 116-120, 124.45, 130.62, 135.06, 162.27 (all br (η^4-$C_6H_3(CF_3)_2$)B$Ar^F{}_3$)), 153.16, 157.95, 162.27 (all br (η^4-$C_6H_3(CF_3)_2$)B$Ar^F{}_3$) (*ipso C region*))

---

❹ **Elemental Micro-Analysis:** Only very small amounts of material were produced and micro-analysis was not conducted.

---

❺ **X-ray Crystallography:** Small yellow crystals form directly out of pentane at room temperature.

20. $[Rh(^{i}Pr_2PCH_2CH_2CH_2P^{i}Pr_2)(\eta^4\text{-}1,2\text{-}C_2H_4Cl_2)][BAr^F{}_4]$

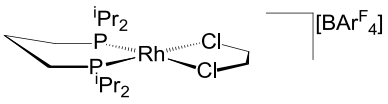

---

❶ **Synthesis:** 15 mg (0.011 mmol) of **15** was dissolved in 1,2-$C_2H_4Cl_2$ and hydrogenated (1 atm) for 10 minutes to form a red solution. The hydrogen atmosphere was then removed and the complex was crystallised by layering with pentane.

---

❷ **NMR Spectroscopy:**

^{1}H NMR (500 MHz 1,2-$C_2H_4Cl_2$ 240 K): δ 1.11 (m (^{i}Pr CH_3), 12H), 1.21 (m (^{i}Pr CH_3), 12H), 1.36 - 1.41 (m (PC**H$_2$**CH_2C**H$_2$**P), 4H), 1.89 (m (^{i}Pr CH & PCH_2C**H$_2$**CH_2P), 6H), 7.52 (s ($BAr^F{}_4$), 4H), 7.70 (s ($BAr^F{}_4$), 8H). *N.B. coordinated $C_2H_4Cl_2$ is in exchange with solvent molecules and the large solvent peak is observed only.*

$^{31}P\{^{1}H\}$ NMR (202 MHz): δ 50.22 (d, J_{RhP} = 190 Hz, 2P)

---

❸ **ESI-MS:** ESI-MS was attempted but was not successful, presumably due to the instability of the complex.

---

❹ **Elemental Micro-Analysis:** The complex is highly sensitive and therefore no micro-analysis was undertaken.

---

❺ **X-ray Crystallography:** Red crystals were grown from 1,2-$C_2H_4Cl_2$/pentane.

21. [Rh{(O^iPr_2)$PCH_2CH_2P(O^iPr_2)$}NBD][BAr^F_4]

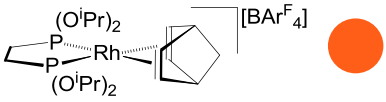

❶ **Synthesis:** 90 mg (195 mmol) of $[(NBD)RhCl]_2$ was added to a Schlenk tube with a stirrer bar and dissolved in 5 ml of C_6H_5F. To this, 3 ml of a 0.131 M (393 mmol, 2 eq.) of a pentane solution of (O^iPr_2)$PCH_2CH_2P(O^iPr_2)$ was added and the mixture stirred for 5 minutes, a slight darkening of the yellow solution is observed. This mixture was added to a Schlenk flask containing 346.2 mg (391 mmol) $Na[BAr^F_4]$ and a moving stirrer bar by cannula transfer to give an orange solution. The solvent was reduced by vacuum to 1 ml and then 10 ml of pentane was added. A stream of argon bubbles was then passed through the mixture to aid crystallisation. The product is then dissolved in CH_2Cl_2 and NaCl removed by filter cannula methods. Finally recrystallisation can be achieved by layering with pentane (*N.B.* an oily product is typical, although slow crystallisation occurs over time at 277 K).

❷ **NMR Spectroscopy:**

^{1}H NMR (300 MHz CD_2Cl_2): δ 1.29 (d (^{i}Pr CH_3), J_{HH} = 6 Hz, 12H), 1.33 (d (^{i}Pr CH_3), J_{HH} = 6 Hz, 12H), 1.86 (d (PCH_2CH_2P), J_{PH} = 22 Hz, 4H), 1.88 (m (NBD CH_2), 2H), 4.17 (s (NBD bridgehead), 2H), 4.42 (m ($OCHMe_2$), 4H), 5.91 (s (NBD C=C), 4H), 7.56 (s (BAr^F_4), 4H), 7.72 (s (BAr^F_4), 8H)

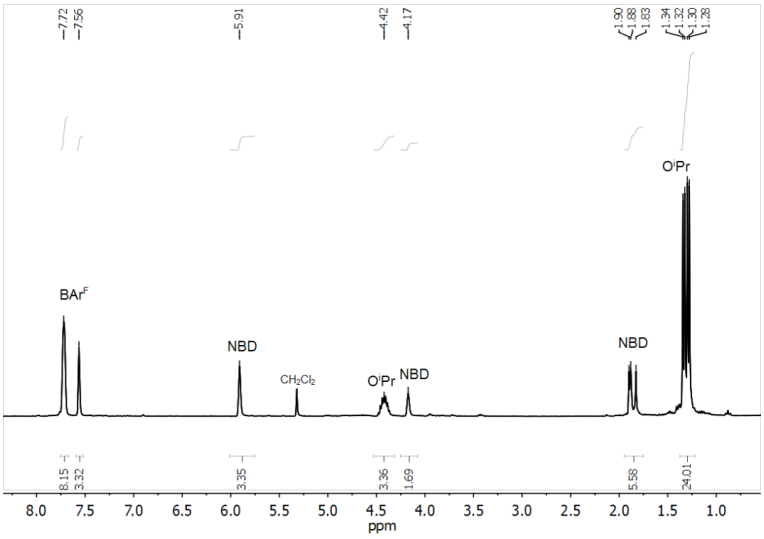

^{31}P{^{1}H} NMR (122 MHz CD_2Cl_2): δ 167.30 (d, J_{RhP} = 217 Hz, 2P)

❸ **ESI-MS:** $[M^+]$ m/z = 537.15, $[M^+]$ calc = 537.14

❹ **Elemental Micro-Analysis:** $C_{53}H_{52}BO_4F_{24}P_2Rh$ C, 45.97 H, 3.79 found C, 45.95 H, 3.81

❺ **X-ray Crystallography:** Crystals suitable for X-ray diffraction were grown from CH_2Cl_2/pentane. The cation was highly disordered.

Internal crystal void volume percentage = 10%

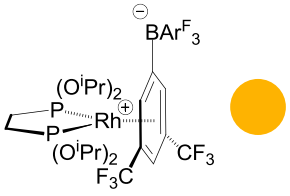

22. Rh{(O^{i}Pr$_2$)PCH$_2$CH$_2$P(O^{i}Pr$_2$)}{η^6-C$_6$H$_3$(CF$_3$)$_2$}BAr$^F_3$

---

❶ **Synthesis:** 10 mg of (0.007 mmol) of **21** was hydrogenated (1 atm) in the solid state for 20 minutes. After removing the hydrogen atmosphere, pentane is added to form a suspension, which is then sonicated. This yields a pale yellow solution of **22** which can be crystallised by allowing the solution to cool to 277 K, to yield very small yellow crystals.

---

❷ **NMR Spectroscopy:**

^{31}P{^{1}H} NMR (122 MHz CD$_2$Cl$_2$): δ 176.74 (d, J_{RhP} = 265 Hz, 2P)

---

❸ **ESI-MS:** The complex is neutral and therefore not suitable for ESI-MS.

---

❹ **Elemental Micro-Analysis:** Only a small amount of crystalline material was produced and micro-analysis was not conducted

---

❺ **X-ray Crystallography:** Crystals suitable for X-ray diffraction were grown from pentane at 277K.

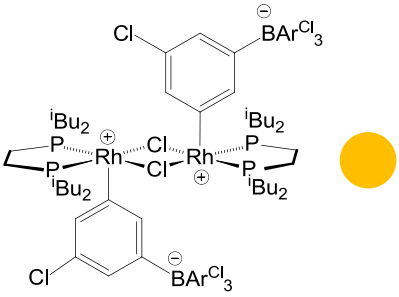

23-*syn* [Rh(*i*Bu$_2$PCH$_2$CH$_2$P*i*Bu$_2$){C$_6$H$_3$Cl(BAr$^{Cl}_3$)}Cl]$_2$

---

❶ **Synthesis:** **23** forms from **12** in the solid-state over 2 weeks, approximately 50% of the product forms as the *syn* isomer.

---

❷ **NMR Spectroscopy:** NMR spectroscopy data taken from spectra of both isomers mixed (approximately 50% of *syn* isomer)

^{1}H NMR (500 MHz CD$_2$Cl$_2$ sparingly soluble): δ 0.64 (d (^{i}Bu CH$_3$), J_{HH} = 6 Hz, 6H), 0.72 (d (^{i}Bu CH$_3$), J_{HH} = 6 Hz, 6H), ~0.86 (obscured by pentane (^{i}Bu CH$_3$), 6H), 0.93 (d (^{i}Bu CH$_3$), J_{HH} = 6 Hz, 6H), 0.98 (d (^{i}Bu CH$_3$), J_{HH} = 6 Hz, 6H), 1.10 (d (^{i}Bu CH$_3$), J_{HH} = 6 Hz, 6H), 1.15 (d (^{i}Bu CH$_3$), J_{HH} = 6 Hz, 6H), 1.18 (d (^{i}Bu CH$_3$), J_{HH} = 6 Hz, 6H), 1.4-2.4 (m (^{i}Bu CH, ^{i}Bu CH$_2$ & PCH$_2$CH$_2$P), 32H), 5.88 (s (C$_6$**H**$_3$Cl(BAr$^{Cl}_3$)), 1+1H coincidence), 5.95 (s (C$_6$**H**$_3$Cl(BAr$^{Cl}_3$)), 1+1H coincidence), 7.00 (s ((C$_6$H$_3$Cl(B**Ar**$^{Cl}_3$)), 12H), 7.08 (s ((C$_6$H$_3$Cl(B**Ar**$^{Cl}_3$)), 6H), 7.17 (s (C$_6$**H**$_3$Cl(BAr$^{Cl}_3$)), 1H), 7.35 (s (C$_6$**H**$_3$Cl(BAr$^{Cl}_3$)), 1H)

^{31}P{^{1}H} NMR (122 MHz CD$_2$Cl$_2$): δ 86.88 (d, J_{RhP} = 139 Hz, 2P), 89.09 (d, J_{RhP} = 140 Hz, 2P)

^{11}B{^{1}H} NMR (160 MHz CD$_2$Cl$_2$): δ -6.65 (s, 1B), -6.41 (s, 1B)

---

❹ **Elemental Micro-Analysis:** $C_{84}H_{104}B_2P_4Cl_{16}Rh_2$ C, 49.64 H, 5.16 found C, 49.53 H, 5.23 (for mixture of two isomers)

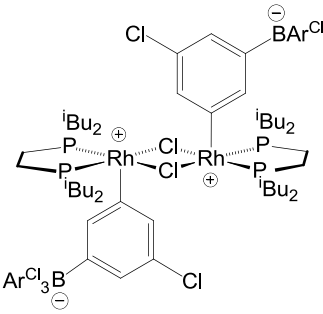

23-*anti* [Rh(^{i}Bu$_2$PCH$_2$CH$_2$P^{i}Bu$_2$){C$_6$H$_3$Cl(BAr$^{Cl}_3$)}Cl]$_2$

---

❶ **Synthesis:** Compound **23** forms directly from a CH_2Cl_2 solution of **12** as the *anti* isomer. Crystalline material precipitates directly out of CH_2Cl_2 solutions composed of **23**.(4½ CH_2Cl_2). The complex can also be synthesised using microcrystalline **12** via a solid-state route, although a mixture of both *syn* and *anti* isomers forms as the final solid product.

---

❷ **NMR Spectroscopy:**

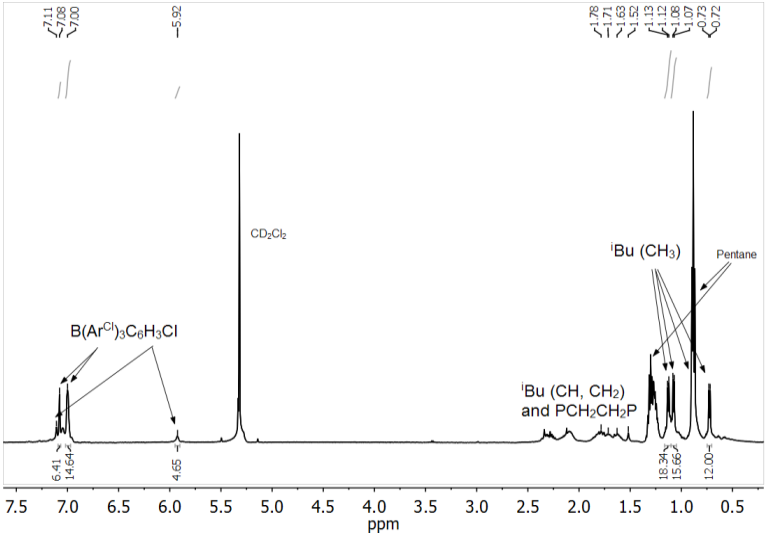

^{1}H NMR (500 MHz CD_2Cl_2 sparingly soluble): δ 0.72 (d (^{i}Bu CH_3), J_{HH} = 6 Hz, 12H), 0.89 (d (^{i}Bu CH_3), J_{HH} = 6 Hz, 12H), 1.08 (d (^{i}Bu CH_3), J_{HH} = 6 Hz, 12H), 1.13 (d (^{i}Bu CH_3), J_{HH} = 6 Hz, 12H), 1.6-2.4 (m (^{i}Bu CH, ^{i}Bu CH_2 & PCH_2CH_2P), 32H, *by ^{1}H COSY analysis ^{i}Bu CH_2 occur at 1.71 & 2.08*), 5.92 (s (C$_6$**H**$_3$Cl(BAr$^{Cl}_3$)), 2+2H coincidence), 7.00 (s ((C$_6$H$_3$Cl(B**Ar**$^{Cl}_3$)), 12H), 7.08 (s ((C$_6$H$_3$Cl(B**Ar**$^{Cl}_3$)), 6H), 7.11 (s (C$_6$**H**$_3$Cl(BAr$^{Cl}_3$)), 2H). *Small peak at 7.03 ppm is likely to be due to a small amount of non-coordinated [BAr$^{Cl}_4$], presumably through a small amount of cation decomposition, a small peak is also seen at the appropriate shift for free [BAr$^{Cl}_4$] in the ^{11}B{^{1}H} NMR spectrum*

^{31}P{^{1}H} NMR (202 MHz CD_2Cl_2): δ 88.00 (d, J_{RhP} = 140 Hz, 4P).

^{11}B{^{1}H} NMR (160 MHz CD_2Cl_2): δ -6.65 (s, 2B).

---

❸ **ESI-MS:** The complex is neutral and not suitable for ESI-MS.

---

❹ **Elemental Micro-Analysis:** $C_{84}H_{104}B_2P_4Cl_{16}Rh_2$ C, 49.64 H, 5.16 found C, 49.53 H, 5.23 (for mixture of two isomers)

---

❺ **X-ray Crystallography:** Yellow crystals were grown directly from CH_2Cl_2 solutions of **23-*anti*** over several days. The crystals were very delicate and collapsed when removed from the solvent, this is attributed to the high amount of CH_2Cl_2 located in the structure.

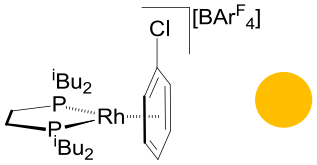

24. [Rh(^{i}Bu$_2$PCH$_2$CH$_2$P^{i}Bu$_2$)(η^6-C$_6$H$_5$Cl)][BAr$^F_4$]

❶ **Synthesis:** 40 mg (0.029 mmol) of **1** was dissolved in a mixture of chlorobenzene (0.5 ml) and CH_2Cl_2 (2 ml) in a Young's flask and this solution exposed to 1 atm H_2. The solution changes to a yellow colour and was left to react for 15 minutes before the tube was degassed. The product was precipitated by adding pentane, with a yield of 64%. The resulting solid can be recrystallised from CH_2Cl_2/pentane.

❷ **NMR Spectroscopy:**

^{1}H NMR (500 MHz CD_2Cl_2): δ 1.01 (d (^{i}Bu CH_3), J_{HH} = 7 Hz, 12H), 1.09 (d (^{i}Bu CH_3), J_{HH} = 7 Hz, 12H), 1.68 (m (^{i}Bu CH_2), 8H), 1.79 (d (PCH_2CH_2P), J_{PH} = 17 Hz, 4H), 1.87 (m (^{i}Bu CH), 4H), 6.15 (t (C_6H_5Cl), J_{HH} = 6 Hz, H), 6.57 (t (C_6H_5Cl), J_{HH} = 6 Hz, 2H), 6.75 (d (C_6H_5Cl), J_{HH} = 6 Hz, 2H), 7.52 (s (BAr$^F_4$), 4H), 7.72 (s (BAr$^F_4$), 8H).

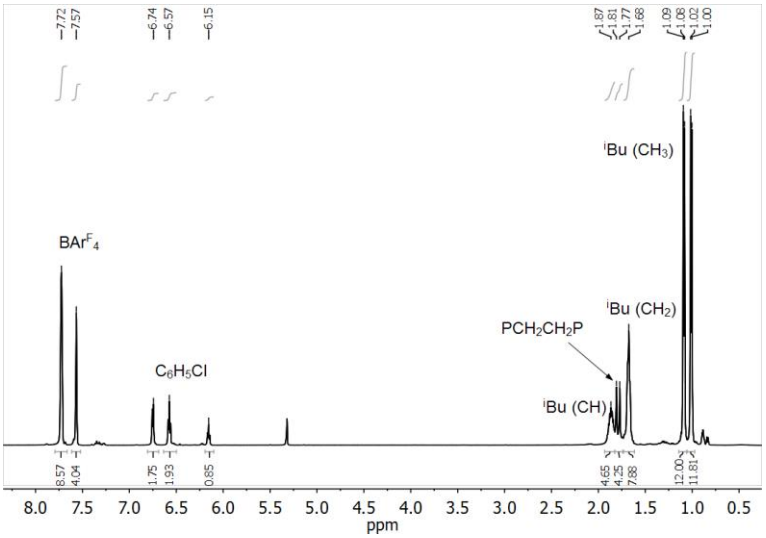

^{31}P{^{1}H} NMR (202 MHz CD_2Cl_2): δ 73.24 (d, J_{RhP} = 201 Hz, 2P).

❸ **ESI-MS:** [M^+] m/z = 533.17, [M^+] calc = 533.17.

Exit voltage at 50% fragmentation to form [Rh(^{i}Bu$_2$PCH$_2$CH$_2$P^{i}Bu$_2$)]$^+$ = 143 V

❹ **Elemental Micro-Analysis:** $C_{56}H_{57}BClF_{24}P_2Rh$ C, 48.14 H, 4.11 found C, 48.08 H, 4.14

❺ **X-ray Crystallography:** X-ray quality crystals were grown from CH_2Cl_2/pentane. The X-ray diffraction pattern of **24** was collected and the space group was determined as C2/c, it appears that a large amount of disorder is present within the structure especially in the phosphine unit which is disordered fairly equally over two positions. Whilst the expected bond connectivity is consistent with the structure, the solution was not of publication quality.

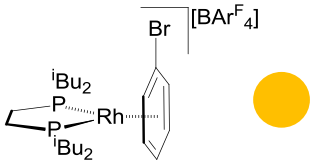

25. [Rh(^{i}Bu$_2$PCH$_2$CH$_2$P^{i}Bu$_2$)(η^6-C$_6$H$_5$Br)][BAr$^F_4$]

---

❶ **Synthesis:** 15 mg (0.011 mmol) **1** was dissolved in CH_2Cl_2 in a high pressure NMR tube and 10 equivalents of bromobenzene (11.5µl, 0.11 mmol) added. The tube was charged with 1 atm H_2. A yellow solution forms. **25** rapidly converts into **26** via a first order process. Due to its short lifetime ($t_{1/2}$ = 9 min 28 sec) a clean ^{1}H NMR spectrum free of **25** was not recorded.

---

❷ **NMR Spectroscopy:**

^{31}P{^{1}H} NMR (202 MHz CD_2Cl_2): δ 73.19 (d, J_{RhP} = 201 Hz, 2P)

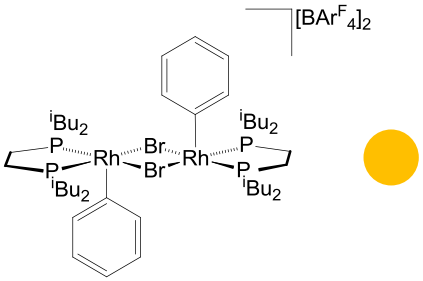

26. [Rh(^{i}Bu$_2$PCH$_2$CH$_2$P^{i}Bu$_2$)(C$_6$H$_5$)Br]$_2$[BAr$^F_4$]$_2$

---

❶ **Synthesis:** A CH_2Cl_2 solution of 2**5** (see above) forms 2**6** directly, after 5 hours pentane was added to precipitate the product and the solid recrystallised in CH_2Cl_2/pentane.

---

❷ **NMR Spectroscopy:**

^{1}H NMR (500 MHz CD_2Cl_2): δ 0.73 (d (^{i}Bu CH_3), J_{HH} = 6 Hz, 12H), 0.94 (d (^{i}Bu CH_3), J_{HH} = 6 Hz, 12H), 1.07 (d (^{i}Bu CH_3), J_{HH} = 6 Hz, 12H), 1.15 (d (^{i}Bu CH_3), J_{HH} = 6 Hz, 12H), 1.75 (m (^{i}Bu CH), 4H), 1.82 (m (^{i}Bu CH_2), 4H), 2.02 (m (^{i}Bu CH_2), 4H), 2.13 (m (^{i}Bu CH), 4H), 2.20 (m (^{i}Bu CH_2), 4H), 2.44 (m (^{i}Bu CH_2 & PCH_2CH_2P), 12H), 7.07 (m (C_6H_5), 8H), 7.17 (t (C_6H_5), J_{HH} = 6 Hz, 2H), 7.57 (s (BAr$^F_4$), 8H), 7.72 (s (BAr$^F_4$), 16H).

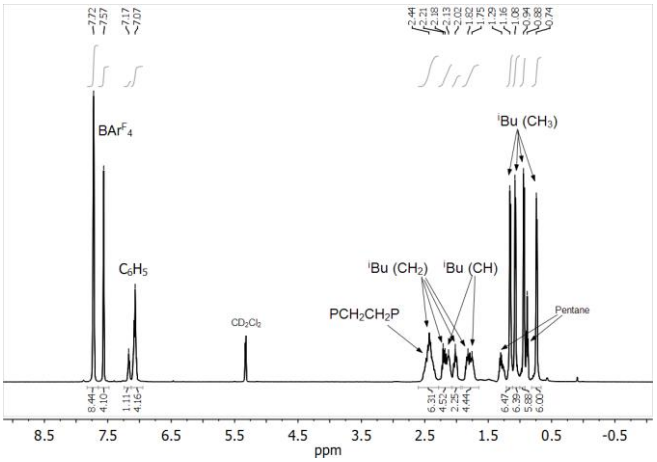

^{31}P{^{1}H} NMR (202 MHz CD_2Cl_2): δ 91.78 (d, J_{RhP} = 137 Hz, 4P)

---

❸ **ESI-MS:** $[M^{2+} + Br^-]^+$ m/z =1237.12, $[M^{2+} + Br^-]$ calc = 1237.16.

---

❹ **Elemental Micro-Analysis:** $C_{112}H_{114}B_2Br_2F_{48}O_2P_4Rh_2$ C, 46.66 H, 3.99 found C, 46.58 H, 4.06

---

❺ **X-ray Crystallography:** Yellow crystals were grown from CH_2Cl_2/pentane.

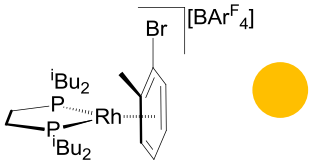

27. [Rh(^{i}Bu$_2$PCH$_2$CH$_2$P^{i}Bu$_2$)(η^6-o-C$_6$H$_4$CH$_3$Br)][BAr$^F_4$]

---

❶ **Synthesis:** 15 mg (0.011 mmol) of **1** was dissolved in CH_2Cl_2 in a high pressure NMR tube and 20 equivalents of ortho-bromotoluene (25 µl, 0.21 mmol) added. The tube was charged with 1 atm H_2. A yellow solution forms. **27** converts into **30** via a first order process. Due to its short lifetime ($t_{1/2}$ = 40 min) a clean ^{1}H NMR spectrum free of **27** was not recorded.

---

❷ **NMR Spectroscopy:**

^{31}P{^{1}H} NMR (202 MHz CD_2Cl_2): δ 72.5 (d, J_{RhP} = 201 Hz, 2P).

---

❸ **ESI-MS:** The complex was too short lived.

---

❹ **Elemental Micro-Analysis:** The complex was too short lived.

---

❺ **X-ray Crystallography:** The complex was too short lived.

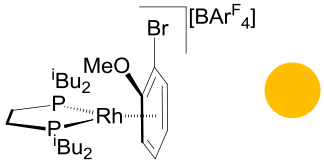

28. [Rh(^{i}Bu$_2$PCH$_2$CH$_2$P^{i}Bu$_2$)(η^6-o-C$_6$H$_4$(OMe)Br)][BAr$^F_4$]

---

❶ **Synthesis:** 10 mg (0.007 mmol) of **1** was dissolved in CH_2Cl_2 in a high pressure NMR tube and ~20 equivalents of ortho-bromoanisole (15 µl, 0.12 mmol) added. The tube was charged with 1 atm H_2. A yellow solution forms. **28** converts into **31** via a first order process. Due to its short lifetime ($t_{1/2}$ = 10.5 min) a clean ^{1}H NMR spectrum free of **28** was not recorded.

---

❷ **NMR Spectroscopy:**

^{31}P{^{1}H} NMR (202 MHz CD_2Cl_2): δ 73.4 (d, J_{RhP} = 202 Hz, 2P).

---

❸ **ESI-MS:** The complex was too short lived.

---

❹ **Elemental Micro-Analysis:** The complex was too short lived.

---

❺ **X-ray Crystallography:** The complex was too short lived.

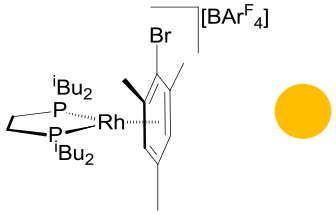

29. [Rh(^{i}Bu$_2$PCH$_2$CH$_2$P^{i}Bu$_2$)(η^6-1,3,5-(Me)$_3$C$_6$H$_2$Br)][BAr$^F_4$]

---

❶ **Synthesis:** 8 mg (0.006 mmol) **1** was dissolved in CH_2Cl_2 in a high pressure NMR tube and ~20 equivalents of ortho-bromoanisole (18 µl, 0.12 mmol) added. The tube was charged with 1 atm H_2. A yellow solution of **29** forms. The hydrogen gas was removed and pentane added to crystallise the product directly from the solution.

---

❷ **NMR Spectroscopy:**

^{1}H NMR (500 MHz CD_2Cl_2): δ 1.00 (d (^{i}Bu CH_3), J_{HH} = 6 Hz, 12H), 1.10 (d (^{i}Bu CH_3), J_{HH} = 7 Hz, 12H), 1.57-1.77 (m (^{i}Bu CH_2), 8H), 1.80 (d (PCH_2CH_2P), J_{PH} = 17 Hz, 4H), 1.84 (m (^{i}Bu CH), 4H), 2.28 (s (Me), 3H), 2.41 (s (Me), 6H), 6.13 (s ($C_6H_2Me_3Br$), 2H), 7.56 (s (BAr$^F_4$), 4H), 7.72 (s (BAr$^F_4$), 8H).

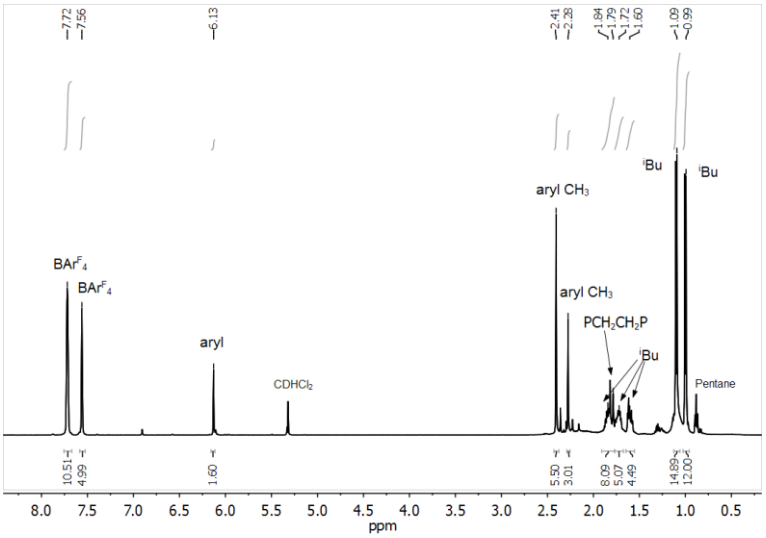

^{31}P{^{1}H} NMR (202 MHz CD_2Cl_2): δ 71.0 (d, J_{RhP} = 202 Hz, 2P)

---

❸ **ESI-MS:** [M^+] m/z = 619.16, [M^+] calc = 619.17

---

❹ **Elemental Micro-Analysis:** The complex was not analysed by micro-analysis

---

❺ **X-ray Crystallography:** Single crystals were formed from CH_2Cl_2/Pentane. The crystals exhibit very large unit cells with three molecules per asymmetric unit. Because of the large number of atoms computational refinement was very slow and therefore disorder was not modeled. An approximate structure (R = 12%) was recorded.

30. $[Rh(^{i}Bu_2PCH_2CH_2P^{i}Bu_2)(C_6H_4CH_3)Br]_2[BAr^{F}_4]_2$

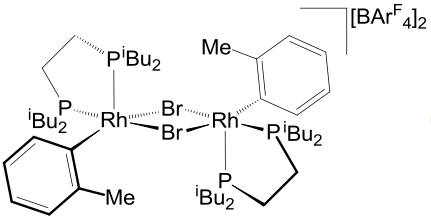

---

❶ **Synthesis:** A CH_2Cl_2 solution of **30** forms **27** directly, with a slight colour change from yellow to amber. After 24 the solvent was removed by vacuum and the product washed with pentane. Crystalline material could not be generated.

---

❷ **NMR Spectroscopy:**

^{1}H NMR (500 MHz CD_2Cl_2): δ 0.98 (broad (^{i}Bu CH_3), 24H), 1.10 (d (^{i}Bu CH_3), J_{HH} = 7 Hz, 12H), 1.15 (d (^{i}Bu CH_3), J_{HH} = 7 Hz, 12H), 1.95 (m (^{i}Bu CH_2), 16H), 2.17 (s (tolyl CH_3), 6H), 2.15-2.35 (m (PCH_2CH_2P), 8H), 2.49 (m (^{i}Bu CH), 8H), 6.71 (d (tolyl), J_{HH} = 7 Hz, 2H), 6.83 (d (tolyl), J_{HH} = 7 Hz, 2H), 7.12 ((m (tolyl), 4H), 7.55 (s (BAr^{F}_4), 8H), 7.71 (s (BAr^{F}_4), 16H)

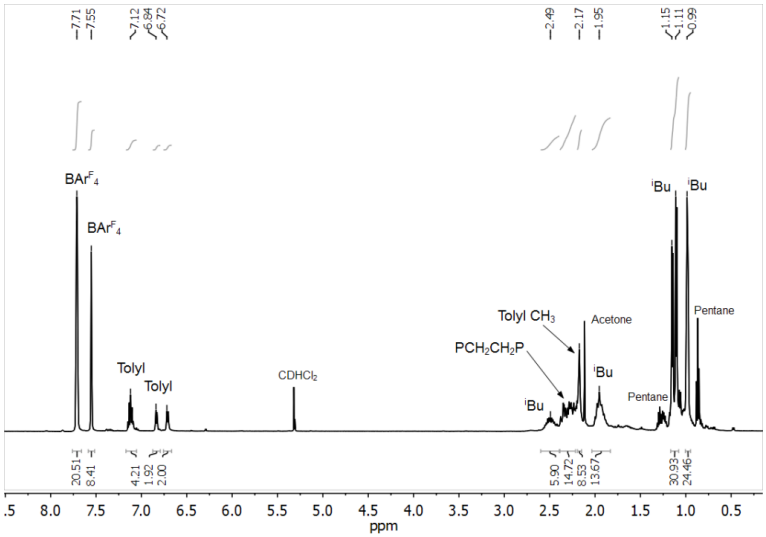

^{31}P{^{1}H} NMR (202 MHz CD_2Cl_2): δ 95 (d (broad), 4P)

^{31}P{^{1}H} NMR (202 MHz CD_2Cl_2 *193 K*): δ 74.5 (broad, 2P), 113.44 (broad, 2P)

---

❸ **ESI-MS:** [M^+ monomer] m/z = 591.14, [M^+ + monomer] calc = 591.14, fragmentation presumably occurs during ESI-MS experiment.

---

❹ **Elemental Micro-Analysis:** No crystalline material could be produced.

---

❺ **X-ray Crystallography:** No crystalline material could be produced.

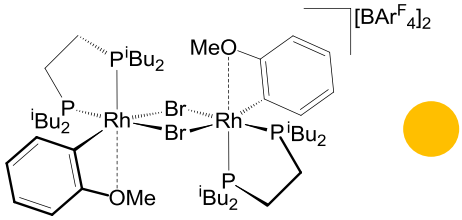

31. $[Rh(^{i}Bu_2PCH_2CH_2P^{i}Bu_2)(C_6H_4(OMe))Br]_2[BAr^F{}_4]_2$

---

❶ **Synthesis:** A CH_2Cl_2 solution of **31** forms **28** directly, after 24 hours pentane was added to precipitate the product and the solid recrystallised in CH_2Cl_2/pentane.

---

❷ **NMR Spectroscopy:**

^{1}H NMR (500 MHz CD_2Cl_2): δ 0.92 (broad (^{i}Bu CH_3), 12H), 0.94 (d (^{i}Bu CH_3), J_{HH} = 6 Hz, 12H), 1.04 (d (^{i}Bu CH_3), J_{HH} = 6 Hz, 12H), 1.12 (d (^{i}Bu CH_3), J_{HH} = 6 Hz, 12H), 1.8-2.5 (m (^{i}Bu CH, ^{i}Bu CH_2 and PCH_2CH_2P) 32H), 4.01 (s (OMe), 6H), 6.68 (d (anisoyl), J_{HH} = 8 Hz, 2H), 6.89 (d (anisolyl), J_{HH} = 7 Hz, 2H), 6.99 (t (anisolyl), J_{HH} = 8 Hz, 2H), 7.24 (t (anisoyl), J_{HH} = 8 Hz, 2H), 7.57 (s ($BAr^F{}_4$), 8H), 7.73 (s ($BAr^F{}_4$), 16H).

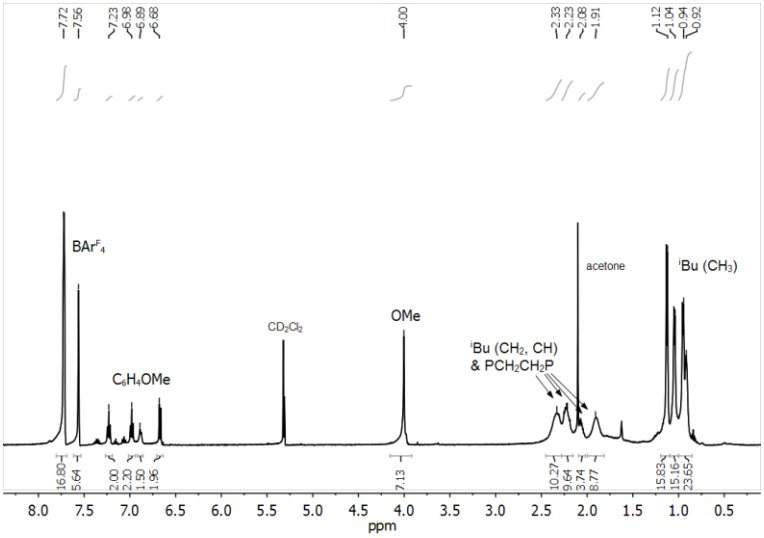

^{31}P{^{1}H} NMR (202 MHz CD_2Cl_2): δ 90.25 ((broad), 4P)

^{31}P{^{1}H} NMR (202 MHz CD_2Cl_2 *225 K*): δ 75.75 (d, J_{RhP} = 135 Hz, 2P), 100.64 (d, J_{RhP} = 152 Hz, 2P)

---

❸ **ESI-MS:** $[M^{2+} + Br^-]^+$ m/z = 1297.10, $[M^{2+} + Br^-]^+$ calc = 1297.18

---

❹ **Elemental Micro-Analysis:** $C_{114}H_{118}B_2Br_2F_{48}O_2P_4Rh_2.(0.5C_6H_5F)$ C, 46.98 H, 4.06 found C, 46.99 H, 4.00

---

❺ **X-ray Crystallography:** Single crystals were grown from C_6H_5F/Pentane and the crystal structure contains one equivalent of co-crystallised C_6H_5F.

32. [Rh(^{i}Bu$_2$PCH$_2$CH$_2$P^{i}Bu$_2$)(CO)$_2$][BAr$^{F}_4$]

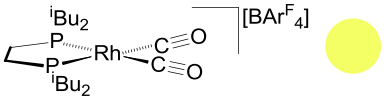

❶ **Synthesis:** 30 mg (0.022 mmol) **3** was dissolved in CH_2Cl_2 and the solution frozen and placed under vacuum. CO gas was used to refill the flask, and upon warming a slight colour change from amber to bright yellow occurs, the flask was left sealed for 2 hours. The solution was then degassed and crystallised by adding pentane. Bright yellow crystalline material forms.

The $^{31}P\{^{1}H\}$ NMR spectrum of **32**, prepared as above, displays a small minor species (6%) which is observed in separately prepared samples. Two double doublet signals are observed [δ 55.34, J_{RhP} 116 Hz, J_{PP} 23 & δ 67.92, J_{RhP} 117 Hz, J_{PP} 23)], one of which is very similar to the signal for **32**. It is possible that a minor species [Rh(^{i}Bu$_2$PCH$_2$CH$_2$P^{i}Bu$_2$)(CO)L][BAr$^{F}_4$] (L = solution impurity) forms alongside **32**.

❷ **NMR Spectroscopy:**

^{1}H NMR (300 MHz CD_2Cl_2): δ 1.12 (d (^{i}Bu CH_3), J_{HH} = 6 Hz, 12H), 1.16 (d (^{i}Bu CH_3), J_{HH} = 6 Hz, 12H), 1.89 (m (^{i}Bu CH), 4H), 1.96 (m (^{i}Bu CH_2), 8H) 2.10 (d, PCH_2CH_2P, J_{PH} = 18 Hz, 4H), 7.57 (s (BAr$^{F}_4$), 4H), 7.72 (s (BAr$^{F}_4$), 8H)

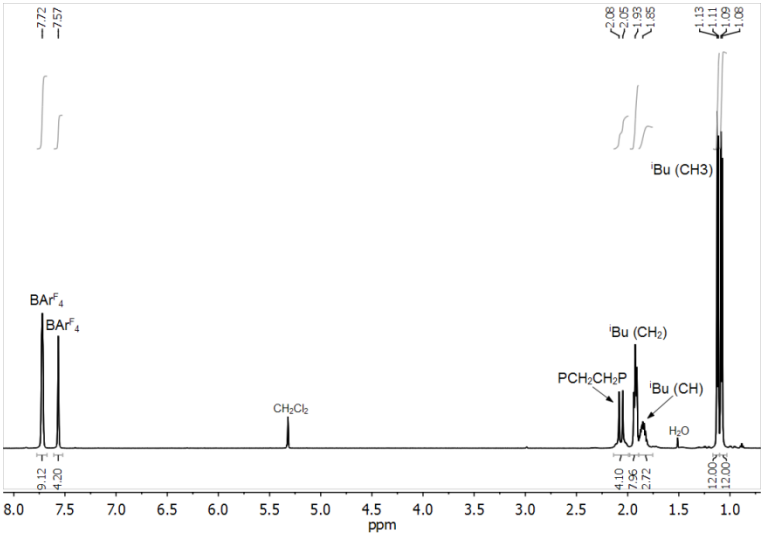

$^{31}P\{^{1}H\}$ NMR (122 MHz CD_2Cl_2): δ 56.10 (d, J_{RhP} = 116 Hz, 2P)

$^{31}P\{^{1}H\}$ NMR (162 MHz Solid-state *10 kHz spin rate*): δ 54.17 (br, 2P)

❸ **ESI-MS:** [M^+] m/z = 477.16, [M^+] calc = 477.16

Exit voltage at 50% fragmentation to form [Rh(^{i}Bu$_2$PCH$_2$CH$_2$P^{i}Bu$_2$)CO]$^+$ or [Rh(^{i}Bu$_2$PCH$_2$CH$_2$P^{i}Bu$_2$)]$^+$ = 144 V

❹ **Elemental Micro-Analysis:** $C_{52}H_{52}BO_2P_2F_{24}Rh$ C, 46.59 H, 3.91 found C, 46.67 H, 3.82

❺ **X-ray Crystallography:** Bright yellow crystals grow from CH_2Cl_2/pentane, whilst the crystals diffract well and the anions can be well refined, the cation shows disorder over two positions (with one position rotated 90° and upside down relative to the first). High quality data lead to a reliable structural model incorporating this disorder.

Internal crystal void volume percentage = 8%

❻ **IR spectroscopy:**

(CH_2Cl_2 solution): CO stretches 2093.4 & 2049.1 cm^{-1}

(Solid-state): CO stretches 2099.0 & 2056.9 cm^{-1}

33. [Rh(^{i}Bu$_2$PCH$_2$CH$_2$P^{i}Bu$_2$)(NH$_3$)$_2$][BAr$^{F}_4$]

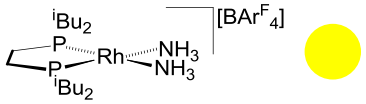

---

❶ **Synthesis:** 50mg (0.036 mmol) solid **1** was placed in a youngs flask. The flask was degassed and placed under 1 atm NH_3 gas. The flask was then frozen in a liquid N_2 bath and opened to 1 atm pressure of H_2 whilst at low temperature. The flask was then sealed and warmed; this generated roughly 1 atm NH_3 and 3 atm H_2. The solid quickly turned a bright yellow colour. The flask was left for 3 hours to make sure of total conversion. The product was washed twice with pentane to remove NBA. Crystals can be grown from 1,2-$C_6H_4F_2$/pentane. 35 mg (0.027 mmol) produced; 73% yield. The complex is not stable in CH_2Cl_2.

The solution $^{31}P\{^{1}H\}$ NMR spectrum of freshly prepared **33** displays a small minor species (~5%) which is observed in separately prepared samples. Two double doublet signals are observed [δ 65.18 (dd, J_{RhP} 180 Hz, J_{PP} 38) & δ 75.67 (dd, J_{RhP} 177 Hz, J_{PP} 38)], one of which is very similar to the signal for **33**. It is possible that a minor species [Rh(^{i}Bu$_2$PCH$_2$CH$_2$P^{i}Bu$_2$)(NH$_3$)L][BAr$^{F}_4$] (L = solvent impurity) is forming alongside **33** in 1,2-$C_6H_4F_2$ solution.

---

❷ **NMR Spectroscopy:**

^{1}H NMR (500 MHz 1,2-$C_6H_4F_2$): δ 1.18 (d (^{i}Bu CH$_3$), J_{HH} = 6 Hz, 12H), 1.33 (d (^{i}Bu CH$_3$), J_{HH} = 6 Hz, 12H), 1.51 (d (PCH$_2$CH$_2$P), J_{PH} = 14 Hz, 4H), 1.57 (m (^{i}Bu CH$_2$), 8H), 1.91 (m (^{i}Bu CH), 4H), 1.93 (s, NH$_3$, 6H), 7.68 (s (BAr$^{F}_4$), 4H), 8.32 (s (BAr$^{F}_4$), 8H)

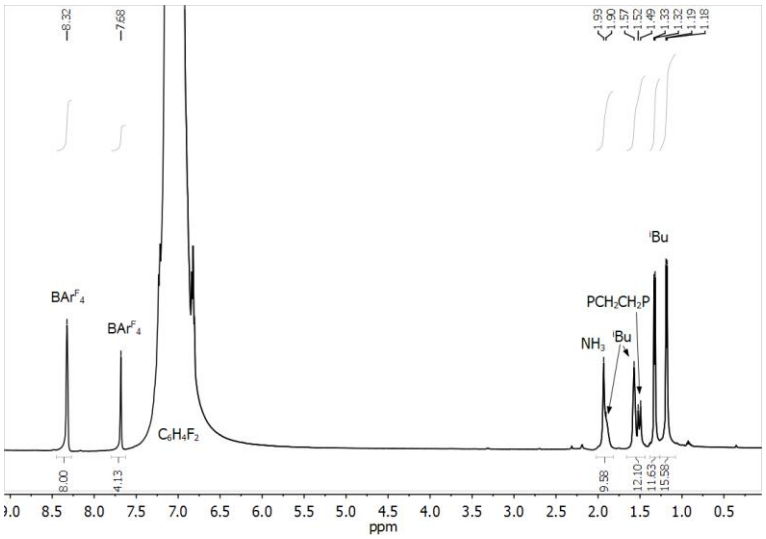

$^{31}P\{^{1}H\}$ NMR (202 MHz 1,2-$C_6H_4F_2$): δ 65.45 (d, J_{RhP} = 177 Hz, 2P)

---

❸ **ESI-MS:** The complex did not appear to be stable in the mass spectrometry process.

---

❹ **Elemental Micro-Analysis:** $C_{50}H_{58}BP_2N_2F_{24}Rh$ C 45.54, H 4.43, N 2.12, found C 45.69, H 4.43 N 1.95

---

❺ **X-ray Crystallography:** Bright yellow crystals grow from 1,2-$C_6H_4F_2$/pentane

---

❻ **IR spectroscopy:** No N-H stretches were located in the solid-state

35. [Rh(^{i}Bu$_2$PCH$_2$CH$_2$P^{i}Bu$_2$)(η^6-C$_6$H$_6$)][BAr$^F_4$]

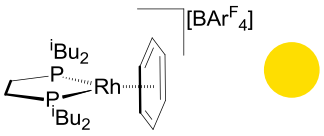

❶ **Synthesis:** 15 mg (0.011 mmol) of **1** was dissolved in CH_2Cl_2 (0.4 ml) in a high pressure NMR tube and 0.05 ml of benzene was added. The tube was charged with 1 atm H_2 and left for 24 hours. A yellow solution of **XY5.1** forms. The hydrogen gas was removed and pentane added to crystallise the product directly from the solution.

❷ **NMR Spectroscopy:**

^{1}H NMR (500 MHz CD_2Cl_2): δ 1.00 (d (^{i}Bu CH_3), J_{HH} = 7 Hz, 12H), 1.07 (d (^{i}Bu CH_3), J_{HH} = 7 Hz, 12H), 1.63 (m (^{i}Bu CH_2), 8H), 1.73 (d (PCH_2CH_2P), J_{PH} 17 Hz, 4H), 1.85 (m (^{i}Bu CH), 4H), 6.47 (s (C_6H_6), 6H), 7.56 (s (BAr^F_4), 4H), 7.72 (s (BAr^F_4), 8H)

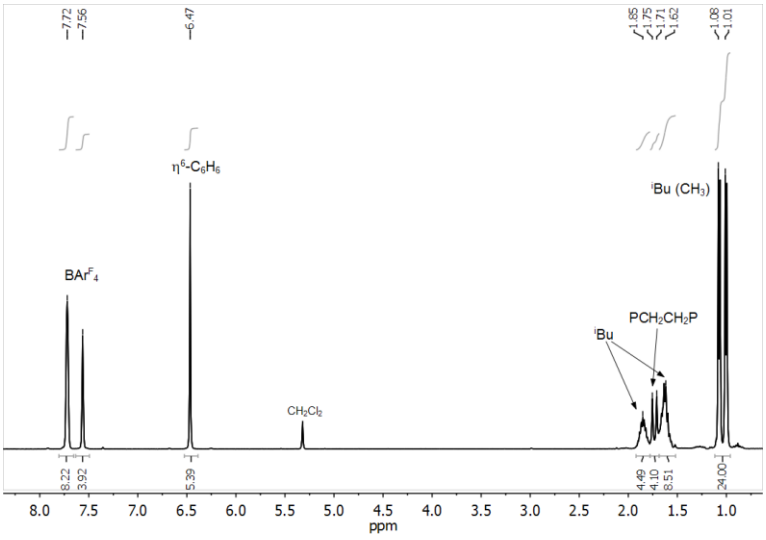

^{31}P{^{1}H} NMR (202 MHz CD_2Cl_2): δ 73.4 (d, J_{RhP} = 201 Hz)

❸ **ESI-MS:** [M^+] m/z = 499.23, [M^+] calc = 499.21

Exit voltage at 50% fragmentation to form [Rh(^{i}Bu$_2$PCH$_2$CH$_2$P^{i}Bu$_2$)]$^+$ = 158 V

❹ **Elemental Micro-Analysis:** $C_{56}H_{58}BF_{24}P_2Rh$ C, 49.36 H, 4.29 found C, 49.44 H, 4.44

❺ **X-ray Crystallography:** Single crystals were formed from CH_2Cl_2/Pentane. A clean diffraction pattern was collected however the data could not be solved, we expect the small cation to be heavily disordered within a pocket defined by the anions.

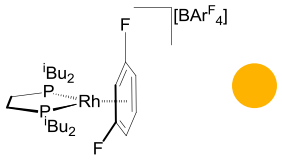

36. [Rh(^{i}Bu$_2$PCH$_2$CH$_2$P^{i}Bu$_2$)(η^6-1,3-C$_6$H$_4$F$_2$)][BAr$^F_4$]

---

❶ **Synthesis:** 18 mg (0.013 mmol) of **1** was dissolved in 1,3-C$_6$H$_4$F$_2$ in a high pressure NMR tube. The tube was charged with 1 atm H$_2$. A yellow solution of **36** forms upon shaking. The hydrogen gas was removed and pentane added to crystallise the product directly from the solution.

---

❷ **NMR Spectroscopy:**

^{1}H NMR (500 MHz 1,3-C$_6$H$_4$F$_2$ *ref upfield solvent signal* δ*7.16*): δ 1.03 (d (^{i}Bu CH$_3$), J_{HH} = 6 Hz, 12H), 1.11 (d (^{i}Bu CH$_3$), J_{HH} = 6 Hz, 12H), 1.66 (m (^{i}Bu CH$_2$), 8H), 1.78 (d (PCH$_2$CH$_2$P), J_{PH} = 17 Hz, 4H), 1.88 (m (^{i}Bu CH), 4H), 6.07 (s (1,3-C$_6$H$_4$F$_2$), 2H), 7.68 (s (BAr$^F_4$), 4H), 8.28 (s (BAr$^F_4$), 8H). *Two aryl protons unaccounted for, likely to be obscured by the solvent.*

^{31}P{^{1}H} NMR (202 MHz 1,3-C$_6$H$_4$F$_2$): δ 72.8 (d, J_{RhP} = 200 Hz, 2P)

---

❸ **ESI-MS:** [M$^+$] m/z = 535.19, [M$^+$] calc = 535.19. Exit voltage at 50% fragmentation to form [Rh(P_2)]$^+$ = 124 V

---

❹ **Elemental Micro-Analysis:** C$_{56}$H$_{56}$BF$_{26}$P$_2$Rh C, 47.97 H, 3.84 found C, 48.09 H, 4.04

---

❺ **X-ray Crystallography:** Single crystals were formed from 1,3-C$_6$H$_4$F$_2$/Pentane. Cation disorder resulted in a low quality refinement.

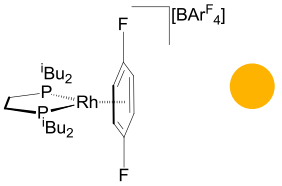

37. [Rh(^{i}Bu$_2$PCH$_2$CH$_2$P^{i}Bu$_2$)(η^6-1,4-C$_6$H$_4$F$_2$)][BAr$^F_4$]

---

❶ **Synthesis:** 18 mg (0.013 mmol) of **1** was dissolved in CH$_2$Cl$_2$ (0.4 ml) in a high pressure NMR tube and 0.05 ml of 1,4-C$_6$H$_4$F$_2$ was added. The tube was charged with 1 atm H$_2$. A yellow solution of **37** forms upon shaking. The hydrogen gas was removed and pentane added to crystallise the product directly from the solution. *N.B.* **1** and **37** are virtually insoluble in neat 1,4-C$_6$H$_4$F$_2$.

---

❷ **NMR Spectroscopy:**

^{1}H NMR (500 MHz CD$_2$Cl$_2$): {*N.B.* minor species (20%) in CD$_2$Cl$_2$ solution as is in equilibrium with **4** δ 1.02 (d (^{i}Bu CH$_3$), J_{HH} = 7 Hz, 12H), 1.09 (d (^{i}Bu CH$_3$), J_{HH} = 7 Hz, 12H), 1.2-1.9 (m (PCH$_2$CH$_2$P, ^{i}Bu CH & ^{i}Bu$_2$), 16H), 6.81 (t (1,4-C$_6$H$_4$F$_2$), J_{FH} = 3 Hz, 4H), 7.56 (s (BAr$^F_4$), 4H), 7.72 (s (BAr$^F_4$), 8H)

^{31}P{^{1}H} NMR (202 MHz CD$_2$Cl$_2$): δ 73.2 (d, J_{RhP} = 200 Hz)

^{19}F{^{1}H} NMR (169 MHz CD$_2$Cl$_2$): δ -132.2 (s (1,4-C$_6$H$_4$F$_2$), 2F), -62.87 (s (BAr$^F_4$), 24F)

---

❸ **ESI-MS:** [M$^+$] m/z = 535.19, [M$^+$] calc = 535.19. Exit voltage at 50% fragmentation to form [Rh(P_2)]$^+$= 129 V

---

❺ **X-ray Crystallography:** Single crystals were formed from CH$_2$Cl$_2$/Pentane. Extensive cation disorder inhibited refinement of a X-ray crystal structure, although the rough connectivity could be observed.

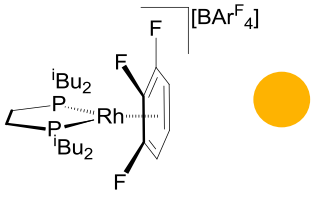

38. [Rh(^{i}Bu$_2$PCH$_2$CH$_2$P^{i}Bu$_2$)(η^6-1,2,3-C$_6$H$_3$F$_3$)][BAr$^F_4$]

---

❶ **Synthesis:** 8 mg (0.006 mmol) of **1** was dissolved in 1,2,3-$C_6H_3F_3$ in a high pressure NMR tube. The tube was charged with 1 atm H_2. A yellow solution of **38** forms upon shaking.

---

❷ **NMR Spectroscopy:**

^{1}H NMR (500 MHz 1,2,3-C$_6$H$_3$F$_3$ *(referenced to left central peak of solvent quartet at δ 6.80)*): δ 0.95 (d (^{i}Bu CH$_3$), J_{HH} = 7 Hz, 12H), 1.03 (d (^{i}Bu CH$_3$), J_{HH} = 7 Hz, 12H), 1.72 (m (^{i}Bu CH$_2$), 8H), 1.88 (m (PCH$_2$CH$_2$P and ^{i}Bu CH), 8H), 7.37 (s (BAr$^F_4$), 4H), 7.97 (s (BAr$^F_4$), 8H).

The ^{1}H NMR resonances of the bound trifluorobenzene are likely to be obscured by the free solvent resonances.

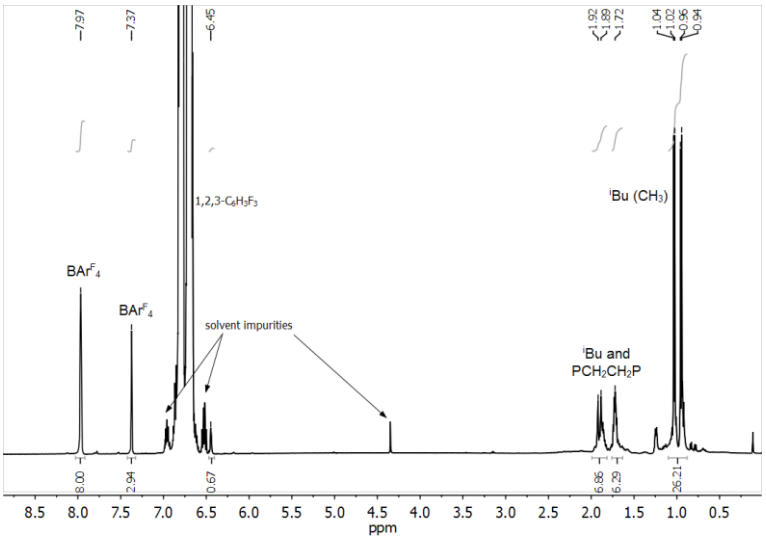

^{31}P{^{1}H} NMR (202 MHz 1,2,3-C$_6$H$_3$F$_3$): δ 75.05 (d, J_{RhP} = 203 Hz, 2P)

^{19}F{^{1}H} NMR (282 MHz 1,2,3-C$_6$H$_3$F$_3$): δ -167.95 (t (C$_6$H$_3$F$_3$), J_{FF} = 30 Hz, F), -147.52 (d (C$_6$H$_3$F$_3$), J_{FF} = 30 Hz, 2F), -64.09 (s (BAr$^F_4$), 24F)

---

❸ **ESI-MS:** [M$^+$] m/z = 553.19, [M$^+$] calc = 553.18

Exit voltage at 50% fragmentation to form [Rh(^{i}Bu$_2$PCH$_2$CH$_2$P^{i}Bu$_2$)]$^+$ = 83 V

---

❹ **Elemental Micro-Analysis:** No crystalline material suitable for micro-analysis was obtained.

---

❺ **X-ray Crystallography:** Small crystals were formed by adding pentane to a 1,2,3-$C_6H_3F_3$ solution of **38**. A diffraction pattern was collected but no reliable solution was obtained possibly due to disorder or impurities.

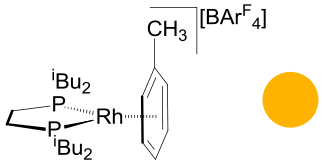

39. [Rh(^{i}Bu$_2$PCH$_2$CH$_2$P^{i}Bu$_2$)(η^6-C$_6$H$_5$CH$_3$)][BAr$^F_4$]

---

❶ **Synthesis:** 11 mg (0.008 mmol) of **1** was suspended in toluene in a high pressure NMR tube. The tube was charged with 1 atm H_2. The material is not very soluble, but over the course of 24 hours a sparingly dissolved yellow compound, **39**, forms. The solvent and hydrogen was removed by vacuum and the material dissolved in CD_2Cl_2 for analysis. Pentane could be added to a CH_2Cl_2 solution to form a crystalline product.

---

❷ **NMR Spectroscopy:**

^{1}H NMR (300 MHz CD_2Cl_2): δ 0.99 (d (^{i}Bu CH_3), J_{HH} = 7 Hz, 12H), 1.07 (d (^{i}Bu CH_3), J_{HH} = 7 Hz, 12H), 1.62 (m (^{i}Bu CH_2), 8H), 1.73 (d (PCH_2CH_2P), J_{PH} = 17 Hz, 4H), 1.84 (m (^{i}Bu CH), 4H), 2.35 (s ($C_6H_5CH_3$), 3H), 6.30 (d ($C_6H_5CH_3$), J_{HH} = 4 Hz, 4H), 6.45 (quintet ($C_6H_5CH_3$), J_{HH} = 4 Hz, 1H), 7.56 (s (BAr^F_4), 4H), 7.72 (s (BAr^F_4), 8H)

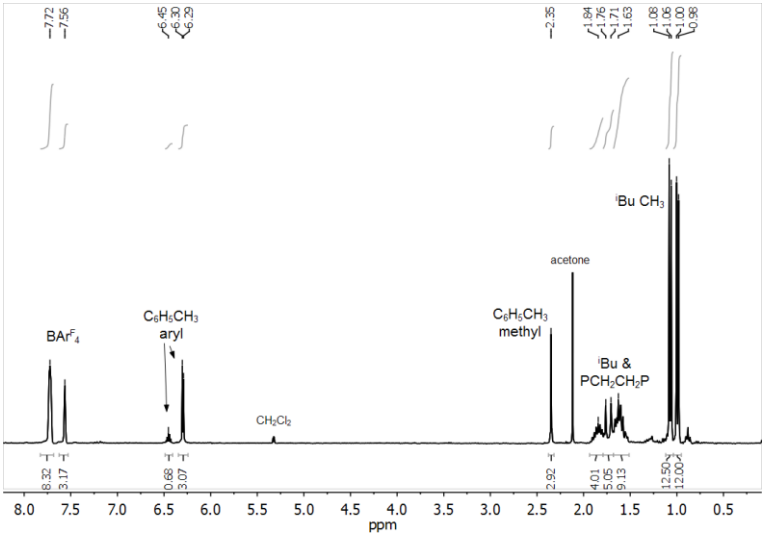

^{31}P{^{1}H} NMR (121 MHz CD_2Cl_2): δ 73.02 (d, J_{RhP} = 202 Hz, 2P)

---

❸ **ESI-MS:** [M^+] m/z = 513.23, [M^+] calc = 513.23

Exit voltage at 50% fragmentation to form [Rh(^{i}Bu$_2$PCH$_2$CH$_2$P^{i}Bu$_2$)]$^+$ = 160 V

---

❹ **Elemental Micro-Analysis:** $C_{57}H_{60}BF_{24}P_2Rh$ C, 49.73 H, 4.39 found C, 49.76 H, 4.25

---

❺ **X-ray Crystallography:** Crystals were formed from CH_2Cl_2/pentane and a diffraction pattern was collected. A disordered solution was obtained which was consistent with the general connectivity but not of high enough quality for accurate refinement.

40. [Rh(^{i}Bu$_2$PCH$_2$CH$_2$P^{i}Bu$_2$)(η^6-C$_6$H$_5$CF$_3$)][BAr$^F_4$]

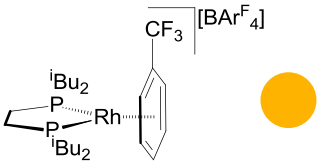

---

❶ **Synthesis:** 11 mg (0.008 mmol) **1** was dissolved in $C_6H_5CF_3$ in a high pressure NMR tube. The tube was charged with 1 atm H_2. A yellow solution of **40** forms upon shaking. The hydrogen was removed and pentane added to crystallise the product directly from the solution.

---

❷ **NMR Spectroscopy:**

^{1}H NMR (300 MHz CD_2Cl_2): {*N.B.* major species (66%) in CD_2Cl_2 solution as is in equilibrium with **4** δ 1.02 (d (^{i}Bu CH_3), J_{HH} = 7 Hz, 12H), 1.08 (d (^{i}Bu CH_3), J_{HH} = 7 Hz, 12H), 1.6-1.9 (m (PCH_2CH_2P, ^{i}Bu CH & ^{i}Bu CH_2), 16H), 6.46 (t ($C_6H_5CF_3$), J_{HH} = 6 Hz, 2H), 6.64 (d ($C_6H_5CF_3$), J_{HH} = 6 Hz, 2H), 6.94 (t ($C_6H_5CF_3$), J_{HH} = 6 Hz, 1H), 7.56 (s (BAr$^F_4$), 4H), 7.72 (s (BAr$^F_4$), 8H)

^{31}P{^{1}H} NMR (121 MHz CD_2Cl_2): δ 72.09 (d, J_{RhP} = 200 Hz, 2P)

^{19}F{^{1}H} NMR (282 MHz CD_2Cl_2): δ -61.36 or -61.01* (s ($C_6H_5CF_3$), 3F), -62.84 (s (BAr$^F_4$), 24F)

ambiguous to which peak is **40 and which is from **4***

---

❸ **ESI-MS:** [M^+] m/z = 567.21, [M^+] calc = 567.20

Exit voltage at 50% fragmentation to form [Rh(^{i}Bu$_2$PCH$_2$CH$_2$P^{i}Bu$_2$)]$^+$ = 136 V

---

❹ **Elemental Micro-Analysis:** $C_{57}H_{57}BF_{27}P_2Rh$ C, 47.85 H, 4.02 found C, 47.90 H, 3.95

---

❺ **X-ray Crystallography:** Crystals were formed from $C_6H_5CF_3$/pentane.

42. [Rh{(O^iPr_2)$PCH_2CH_2P(O^iPr_2)$}(η^6-C_6H_6)][BAr^F_4]

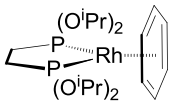

---

❶ **Synthesis:** 4 mg (0.003 mmol) of **21** was dissolved in CH_2Cl_2 in a high pressure NMR tube and ~25 µl of benzene was added. The tube was charged with 1 atm H_2. A pale yellow solution of **42** forms upon shaking. The NMR tube was evacuated to dryness and the product solvated in CD_2Cl_2. The complex was characterised in solution only, by NMR spectroscopy and ESI-MS.

---

❷ **NMR Spectroscopy:**

^{1}H NMR (500 MHz CD_2Cl_2): δ 1.25 (d (^{i}Pr CH_3), J_{HH} = 6 Hz, 12H), 1.29 (d (^{i}Pr CH_3), J_{HH} = 6 Hz, 12H), 1.77 (d (PCH_2CH_2P), J_{PH} = 24 Hz, 4H), 4.415 (m ($OCHMe_2$), 4H), 6.62 (s (C_6H_6), 6H), 7.56 (s (BAr^F_4), 4H), 7.72 (s (BAr^F_4), 8H)

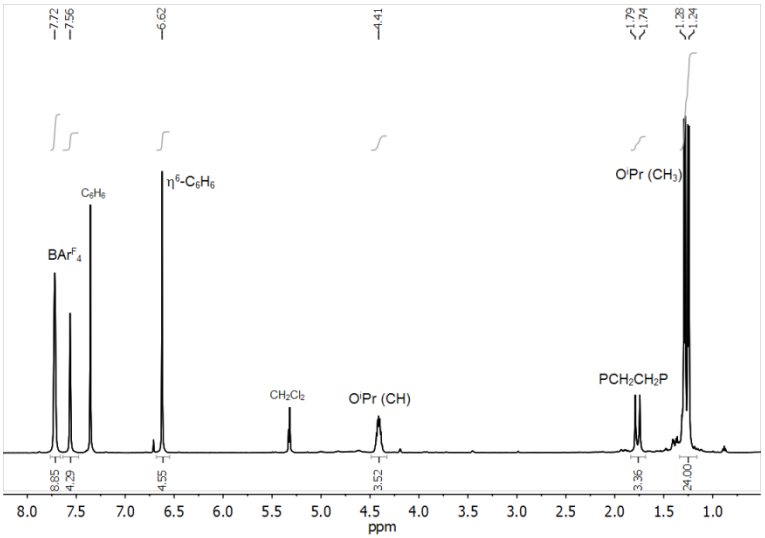

^{31}P{^{1}H} NMR (202 MHz 1,2-$C_6H_4F_2$): δ 181.63 (d, J_{RhP} = 263 Hz, 2P)

---

❸ **ESI-MS:** ([M^+] m/z = 507.13, [M^+] calc = 507.13)

Exit voltage at 50% fragmentation to form [Rh(^{i}$Bu_2PCH_2CH_2P^iBu_2$)]$^+$ = 174 V

---

❹ **Elemental Micro-Analysis:** The complex was only formed on a NMR tube scale in solution.

---

❺ **X-ray Crystallography:** The complex was only formed on a NMR tube scale in solution.

43. [Rh{(O^iPr_2)$PCH_2CH_2P(O^iPr_2)$}(η^6-C_6H_5F)][BAr^F_4]

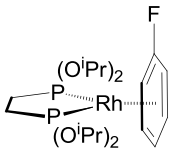

❶ **Synthesis:** 25 mg (0.018 mmol) **21** was dissolved in C_6H_5F in a high pressure NMR tube. The tube was charged with 1 atm H_2. A pale yellow solution of **43** forms upon shaking. After 2.5 hours the hydrogen was removed and pentane added to crystallise the product directly from the solution.

❷ **NMR Spectroscopy:**

^{1}H NMR (500 MHz C_6H_5F): δ 1.13 (d (^{i}Pr CH_3), J_{HH} = 4 Hz, 12H), 1.14 (d (^{i}Pr CH_3), J_{HH} = 4 Hz, 12H), 1.55 (d (PCH_2CH_2P), J_{PH} = 24 Hz, 4H), 4.25 (m ($OCHMe_2$), 4H), 5.78 (t (C_6H_5F), J_{HH} = 6 Hz, 1H), 6.29 (m (C_6H_5F), 2H), 6.36 (t (C_6H_5F), J_{HH} = 6 Hz, 2H), 7.66 (s (BAr^F_4), 4H), 8.33 (s (BAr^F_4), 8H)

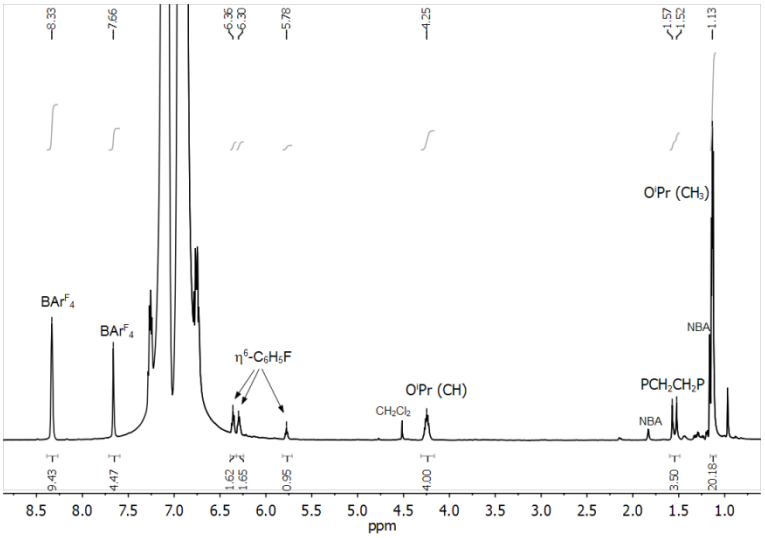

^{31}P{^{1}H} NMR (202 MHz C_6H_5F): δ 179.45 (d, J_{RhP} = 263 Hz, 2P)

^{19}F{^{1}H} NMR (282 MHz C_6H_5F): δ -120.5 (s (C_6H_5F), F), -62.5 (s (BAr^F_4), 24F)

❸ **ESI-MS:** [M^+] m/z = 525.12, [M^+] calc = 525.12

Exit voltage at 50% fragmentation to form [Rh(^{i}$Bu_2PCH_2CH_2P^iBu_2$)]$^+$ = 159 V

❹ **Elemental Micro-Analysis:** $C_{52}H_{49}BF_{25}O_4P_2Rh$ C, 44.98 H, 3.56 found C, 44.80 H, 3.84

❺ **X-ray Crystallography:** Crystals were formed from C_6H_5F/pentane.

44. [Rh{(O^iPr_2)$PCH_2CH_2P(O^iPr_2)$}(η^6-1,2-$C_6H_4F_2$)][BAr^F_4]

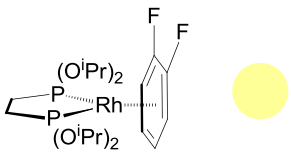

---

❶ **Synthesis:** 6 mg (0.004 mmol) **21** was dissolved in 1,2-$C_6H_4F_2$ in a high pressure NMR tube. The tube was charged with 1 atm H_2. A pale yellow solution of **44** forms upon shaking. The complex was characterised in solution only, by NMR spectroscopy and ESI-MS.

A minor species is observed in the $^{31}P\{^1H\}$ and ^{19}F NMR spectra, this was attributed to a minor impurity of C_6H_5F complex **43**.

---

❷ **NMR Spectroscopy:**

^{1}H NMR (500 MHz 1,2-$C_6H_4F_2$): δ 1.35 (m (^{i}Pr CH_3), 24H), 1.88 (d (PCH_2CH_2P), J_{PH} = 21 Hz, 4H), 4.54 (m ($OCHMe_2$), 4H), 6.39 (s (1,2-$C_6H_4F_2$), 2H), 7.69 (s (BAr^F_4), 4H), 8.33 (s (BAr^F_4), 8H)

One aryl resonance for coordinated 1,2-$C_6H_4F_2$ was not located and is probably obscured by the free solvent

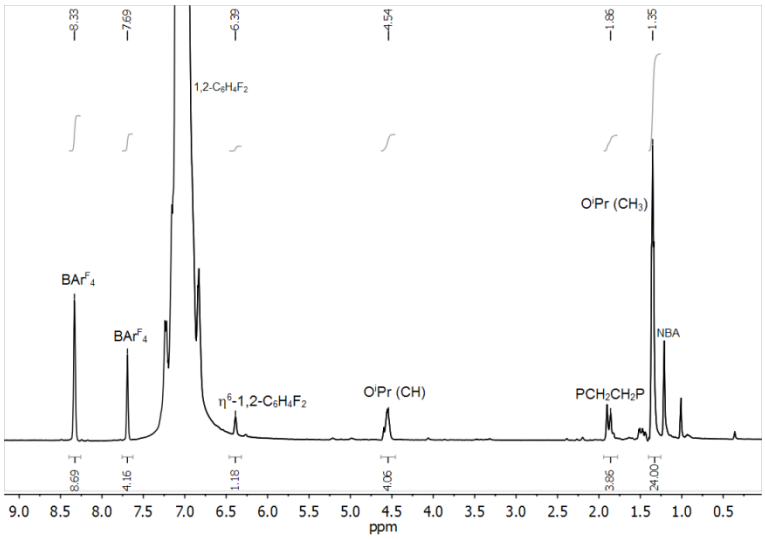

$^{31}P\{^1H\}$ NMR (202 MHz 1,2-$C_6H_4F_2$): δ 177.99 (d, J_{RhP} = 262 Hz, 2P)

$^{19}F\{^1H\}$ NMR (282 MHz 1,2-$C_6H_4F_2$): δ -144.5 (s (C_6H_5F), F), -63.2 (s (BAr^F_4), 24F)

---

❸ **ESI-MS:** [M^+] m/z = 543.11, [M^+] calc = 543.11

Exit voltage at 50% fragmentation to form [Rh(^{i}$Bu_2$$PCH_2CH_2P^{i}Bu_2$)]$^+$ = 144 V

---

❹ **Elemental Micro-Analysis:** The complex was only formed on a NMR tube scale in solution.

---

❺ **X-ray Crystallography:** The complex was only formed on a NMR tube scale in solution.

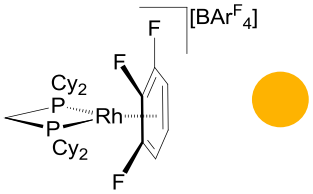

45. [Rh($Cy_2PCH_2PCy_2$)(η^6-1,2,3-$C_6H_3F_3$)][BAr^F_4]

---

❶ **Synthesis:** 23mg (0.016 mmol) [Rh($Cy_2PCH_2PCy_2$)(η^6-C_6H_5F)][BAr^F_4], **XLIII**,[33] was placed in a high pressure NMR tube and to this 5 µl (0.049 mmol) of NBD was added before 0.4 ml of CH_2Cl_2. The tube was then heated to 313 K for 2 hours during which time a colour change from yellow to orange was observed. Pentane was added to precipitate the product (presumed to be [Rh($Cy_2PCH_2PCy_2$)(η^2,η^2-NBD)][BAr^F_4], but uncharacterised) which was further washed with pentane and dried under vacuum. 0.4 ml of 1,2,3-$C_6H_3F_3$ was then added to the product and the resulting solution exposed to one atmosphere of hydrogen for 10 minutes. A colour change back to yellow is observed and the complex was characterised in 1,2,3-$C_6H_3F_3$ solution. **45** decomposed to **46** when diluted with pentane in an attempt at recrystallisation.

---

❷ **NMR Spectroscopy:**

$^{31}P\{^1H\}$ NMR (202 MHz 1,2,3-$C_6H_3F_3$): δ -11.30 (d, J_{RhP} = 167 Hz, 2P)

$^{19}F\{^1H\}$ NMR (282 MHz 1,2,3-$C_6H_3F_3$): δ -167.19 (t ($C_6H_3F_3$), J_{FF} = 30 Hz, 1F), -146.82 (d ($C_6H_3F_3$), J_{FF} = 30 Hz, 1F), -63.74 (s (BAr^F_4), 24F)

---

❸ **ESI-MS:** [M^+] m/z = 643.23, [M^+] calc = 643.23

Exit voltage at 50% fragmentation to form [Rh($^iBu_2PCH_2CH_2P^iBu_2$)]$^+$ = 168 V

---

❹ **Elemental Micro-Analysis:** Crystalline material could not be formed.

---

❺ **X-ray Crystallography:** Crystalline material could not be formed.

46. Rh($Cy_2PCH_2PCy_2$)(η^6-$C_6H_3(CF_3)_2$)BAr^F_3

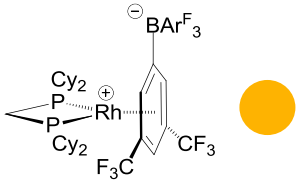

---

❶ **Synthesis:** A 1,2,3-$C_6H_3F_3$ solution of **45** was diluted with pentane, this resulted in the formation of **46**. Crystalline material formed directly from this solution.

---

❷ **NMR Spectroscopy:**

^{1}H NMR (300 MHz CD_2Cl_2): δ 0.93-1.90 (m, Cy, 44H), 2.10 (td (J_{PH} = 10 Hz), PCH_2P, 2H), 6.88 (s ((BAr^F_3)C_6**H_3**$(CF_3)_2$), 1H), 7.03 (s ((BAr^F_3)C_6**H_3**$(CF_3)_2$), 2H), 7.55 (s ((B**Ar^F_3**)$C_6H_3(CF_3)_2$), 6H), 7.65 (s ((B**Ar^F_3**)$C_6H_3(CF_3)_2$), 3H)

^{31}P{^{1}H} NMR (121 MHz CD_2Cl_2): δ -16.26 (d, J_{RhP} = 172 Hz, 2P)

^{19}F{^{1}H} NMR (282 MHz CD_2Cl_2): δ -62.94 (s ((B**Ar^F_3**)$C_6H_3(CF_3)_2$), 18F), -61.12 (s ((BAr^F_3)$C_6H_3(C$**F_3**$)_2$), 6F)

---

❸ **ESI-MS:** The complex is neutral and therefore is not suitable for ESI-MS.

---

❹ **Elemental Micro-Analysis:** Only very small amounts of crystalline material were produced, and micro-analysis was not conducted.

---

❺ **X-ray Crystallography:** Small yellow crystals form directly out of 1,2,3-$C_6H_3F_3$/pentane.

1-[BAr^{Cl}_4]. [Rh(^{i}$Bu_2PCH_2CH_2P^i$$Bu_2$)NBD][$BAr^{Cl}_4$]

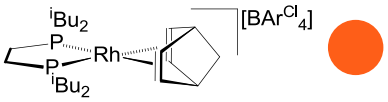

---

❶ **Synthesis:** Prepared as for **1** except using Na[BAr^{Cl}_4] used instead of Na[BAr^F_4]. Cationic portions of NMR spectra and ESI-MS data consistent with **1**.

---

❷ **NMR Spectroscopy:**

^{1}H NMR (300 MHz CD_2Cl_2): δ 1.07 (d (^{i}Bu CH_3), J_{HH} = 6 Hz, 12H), 1.16 (d (^{i}Bu CH_3), J_{HH} = 6 Hz, 12H), 1.62 (m (^{i}Bu CH_2), 8H), 1.78 (m (PCH_2CH_2P, ^{i}Bu CH, NBD CH_2), 10H), 4.09 (s (NBD bridgehead), 2H), 5.31 (s (NBD C=C), 4H), 7.03 (m (BAr^{Cl}_4), 12H)

^{31}P{^{1}H} NMR (122 MHz CD_2Cl_2): δ 48.88 (d, J_{RhP} = 155 Hz 2P)

^{11}B{^{1}H} NMR (160 MHz CD_2Cl_2): δ -6.95 (s, 1B)

---

❸ **ESI-MS:** [M^+] m/z = 513.23, [M^+] calc = 513.23

---

❹ **Elemental Micro-Analysis:** $C_{49}H_{60}BP_2Cl_8Rh$ C, 53.10 H, 5.46 found C, 52.97 H, 5.37

---

❺ **X-ray Crystallography:** Crystals suitable for X-ray diffraction were grown from CH_2Cl_2/pentane.

Internal crystal void volume percentage = 11%

1-[B(C$_6$F$_5$)$_4$]. [Rh(^{i}Bu$_2$PCH$_2$CH$_2$P^{i}Bu$_2$)(η^2,η^2-NBD)][B(C$_6$F$_5$)$_4$]

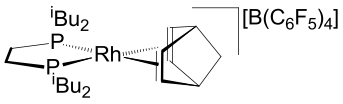

---

❶ **Synthesis:** 44 mg (0.044 mmol) of [Rh($\eta^2\eta^2$-COD)$_2$][B(C$_6$F$_5$)$_4$] (prepared by exchanging K[B(C$_6$F$_5$)$_4$] for Na[BAr$^F{}_4$] in the reported synthesis of the [BAr$^F{}_4$]$^-$ analogue [Rh($\eta^2\eta^2$-COD)$_2$][BAr$^F{}_4$])[26] was dissolved in C$_6$H$_5$F and 277 µl of a 0.159 mmol/ml (0.044 mmol) solution of ^{i}Bu$_2$PCH$_2$CH$_2$P^{i}Bu$_2$ was added. This solution was evacuated to dryness and recrystallised in CH$_2$Cl$_2$/pentane (forms solid material of [Rh(^{i}Bu$_2$PCH$_2$CH$_2$P^{i}Bu$_2$)(η^2,η^2-COD)][B(C$_6$F$_5$)$_4$] after one week). This product was dissolved in C$_6$H$_5$F and exposed to 4 atm of hydrogen for two hours to form [Rh(^{i}Bu$_2$PCH$_2$CH$_2$P^{i}Bu$_2$)(η^6-C$_6$H$_5$F)][B(C$_6$F$_5$)$_4$]. The solution was evacuated to dryness and an excess of NBD was added before solvation of the mixture in CH$_2$Cl$_2$. The final product is **1-[B(C$_6$H$_5$)$_4$]** but this could not be recrystallised and only oily solids could be produced.

---

❷ **NMR Spectroscopy:**

^{1}H NMR (500 MHz CD$_2$Cl$_2$): δ 1.07 (d (^{i}Bu CH$_3$), J_{HH} = 6 Hz, 12H), 1.17 (d (^{i}Bu CH$_3$), J_{HH} = 6 Hz, 12H), 1.62 (m (^{i}Bu CH$_2$), 8H), 1.78 (m (PCH$_2$CH$_2$P, ^{i}Bu CH & NBD CH$_2$), 10H), 4.09 (s (NBD bridgehead), 2H), 5.32 (s (NBD C=C), 4H)

^{31}P{^{1}H} NMR (202 MHz CD$_2$Cl$_2$): δ 48.88 (d, J_{RhP} = 154 Hz, 2P)

^{19}F{^{1}H} NMR (169 MHz CD$_2$Cl$_2$): δ -167.5 (m (C$_6$F$_5$ 3,5-F), 2F), -163.7 (t (C$_6$F$_5$ 4-F), J_{FF} = 20 Hz, 1F), -133.1 (br (C$_6$F$_5$ 2,6-F), 2F)

---

❹ **Elemental Micro-Analysis:** No crystalline material could be formed

---

❺ **X-ray Crystallography:** No crystalline material could be formed

7-[Al{OC(CF$_3$)$_3$}$_4$]. [Rh(^{i}Bu$_2$PCH$_2$CH$_2$P^{i}Bu$_2$)(η^2,η^2-COD)][Al{OC(CF$_3$)$_3$}$_4$]

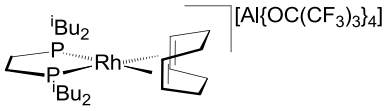

---

❶ **Synthesis:** 16 mg (0.012 mmol) of [Rh($\eta^2\eta^2$-COD)$_2$][B(C$_6$F$_5$)$_4$] (prepared by exchanging Li[Al{OC(CF$_3$)$_3$}$_4$] for Na[BAr$^F{}_4$] in the reported synthesis of the [BAr$^F{}_4$]$^-$ analogue [Rh($\eta^2\eta^2$-COD)$_2$][BAr$^F{}_4$])[26] was dissolved in C$_6$H$_5$F and 71 µl of a 0.170 mmol/ml (0.012 mmol) solution of ^{i}Bu$_2$PCH$_2$CH$_2$P^{i}Bu$_2$ was added. Pentane was layered on to this solution and crystalline material of **7-[Al{OC(CF$_3$)$_3$}$_4$]** formed.

---

❷ **NMR Spectroscopy:**

^{1}H NMR (500 MHz CD$_2$Cl$_2$): δ 1.10 (d (^{i}Bu CH$_3$), J_{HH} = 7 Hz, 12H), 1.19 (d (^{i}Bu CH$_3$), J_{HH} = 7 Hz, 12H), 1.75 (m (^{i}Bu CH$_2$), 8H), 1.88 (m (^{i}Bu CH and PCH$_2$CH$_2$P), 8H), 2.36 (m, (COD), 4H), 2.56 (m, (COD), 4H), 5.16 (br (COD C=C), 4H)

^{31}P{^{1}H} NMR (202 MHz CD$_2$Cl$_2$): δ 49.12 (d, J_{RhP} = 146 Hz, 2P)

^{19}F{^{1}H} NMR (169 MHz CD$_2$Cl$_2$): δ -75.8 (s, 36F)

---

❹ **Elemental Micro-Analysis:** Only very small amounts of crystalline material were produced, not enough for micro-analysis.

---

❺ **X-ray Crystallography:** Crystals were formed from C$_6$H$_5$F/pentane. Internal crystal void volume = 16%

1-[Al{OC(CF$_3$)$_3$}$_4$]. [Rh(^{i}Bu$_2$PCH$_2$CH$_2$P^{i}Bu$_2$)(η^2,η^2-NBD)][Al{OC(CF$_3$)$_3$}$_4$]

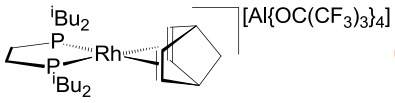

---

❶ **Synthesis:** 255 mg (0.198 mmol) of [Rh($\eta^2\eta^2$-COD)$_2$][B(C$_6$F$_5$)$_4$] (prepared by exchanging Li[Al{OC(CF$_3$)$_3$}$_4$] for Na[BAr$^F{}_4$] in the reported synthesis of the [BAr$^F{}_4$]$^-$ analogue [Rh($\eta^2\eta^2$-COD)$_2$][BAr$^F{}_4$])[26] was dissolved in C$_6$H$_5$F (1 ml) and 1.73 ml of a 0.109 mmol/ml (0.189 mmol) solution of ^{i}Bu$_2$PCH$_2$CH$_2$P^{i}Bu$_2$ was added to form **7-[Al{OC(CF$_3$)$_3$}$_4$]**. This solution was exposed to 4 atm hydrogen for 2.5 hours to form [Rh(^{i}Bu$_2$PCH$_2$CH$_2$P^{i}Bu$_2$)(η^6-C$_6$H$_5$F)][Al{OC(CF$_3$)$_3$}$_4$]. The solution was then evacuated to dryness and 100 µl of NBD added before solvation of the mixture in CH$_2$Cl$_2$. **1-[Al{OC(CF$_3$)$_3$}$_4$]** forms as the final product but could not be crystallised. Only oily solids could be produced.

---

❷ **NMR Spectroscopy:**

^{1}H NMR (500 MHz CD$_2$Cl$_2$): δ 1.07 (d (^{i}Bu CH$_3$), J_{HH} = 6 Hz, 12H), 1.17 (d (^{i}Bu CH$_3$), J_{HH} = 6 Hz, 12H), 1.62 (m (^{i}Bu CH$_2$), 8H), 1.78 (m (PCH$_2$CH$_2$P, ^{i}Bu CH, NBD CH$_2$), 10H), 4.10 (s (NBD bridgehead), 2H), 5.32 (s (NBD C=C), 4H)

^{31}P{^{1}H} NMR (202 MHz CD$_2$Cl$_2$): δ 49.12 (d, J_{RhP} = 146 Hz, 2P)

---

❹ **Elemental Micro-Analysis:** No crystalline material could be formed

---

❺ **X-ray Crystallography:** No crystalline material could be formed

6.2.iii. Crystallographic Data

Compound	**1**	**3**	**4**	**5**	**6**	**8**	**10**	**11**
CCDC No.	892326	-	892329	892328	892327	-	-	-
Formula	$C_{57}H_{60}B_1F_{24}P_2Rh_1$	$C_{56}H_{56}B_1F_{26}P_2Rh_1$	$C_{50}H_{52}B_1F_{24}P_2Rh_1$	$C_{57}H_{64}B_1F_{24}P_2Rh_1$	$C_{57}H_{62}B_1F_{24}P_2Rh_1$	$C_{56}H_{59}B_1F_{24}P_2Rh_1$	$C_{54}H_{60}B_1F_{24}P_2Rh_1$	$C_{54}H_{62}B_1F_{24}P_2Rh_1$
M	1376.72	1398.67	1284.58	1380.75	1378.73	1363.71	1340.69	1366.72
Crystal System	Monoclinic	Tetragonal	Triclinic	Monoclinic	Monoclinic	Monoclinic	Monoclinic	Monoclinic
Space group	*C* 2/c	*P* -4	*P* -1	*C* 2/c	*C* 2/c	*C* 2/c	*C* 2/c	*C* 2/c
T [K]	100(2)	150(2)	100(2)	100(2)	100(2)	150(2)	150(2)	150(2)
a [Å]	18.7785(3)	13.3654(2)	13.5523(4)	18.4711(7)	18.5660(3)	19.3446(2)	19.1357(2)	19.3625(2)
b [Å]	17.0624(3)	13.3654(2)	16.8383(7)	17.5963(5)	17.4669(2)	16.7255(2)	16.3613(2)	16.8990(2)
c [Å]	18.5960(4)	17.0416(3)	24.2031(8)	18.6026(5)	18.5304(2)	37.3570(3)	38.2121(5)	37.1703(4)
α [deg]	90	90	89.350(3)	90	90	90	90	90
β [deg]	90.8634(17)	90	89.235(3)	91.528(3)	90.5620(13)	90.5287(4)	91.7612(9)	90.3569(4)
γ [deg]	90	90	79.452(3)	90	90	90	90	90
V [Å^3]	5957.62(19)	3044.21(8)	5429.1(3)	6044.1(3)	6008.93(15)	12086.3(2)	11958.0(2)	12162.1(2)
Z	4	2	4	4	4	8	8	8
Density [gcm^{-3}]	1.535	1.526	1.572	1.517	1.524	1.499	1.489	1.493
μ (mm^{-1})	3.842	0.449	4.169	3.787	3.809	0.446	3.81	0.443
θ range [deg]	$3.5 \le \theta \le 76.876$	$5.097 \le \theta \le 27.485$	$3.221 \le \theta \le 77.052$	$3.470 \le \theta \le 77.345$	$3.474 \le \theta \le 77.206$	$5.113 \le \theta \le 29.135$	$3.555 \le \theta \le 76.209$	$5.102 \le \theta \le 28.715$
Reflns collected	27887	5755	67547	49730	47446	28345	62859	47577
R_{int}	0.038	0.0063	0.029	0.066	0.038	0.038	0.04	0.048
No. of data/restr/param	6182 / 1104 / 592	5748 / 952 / 608	22526 / 0 / 1405	6336 / 564 / 491	6248 / 671 / 500	11074 / 1248 / 910	9565 / 9565 / 1124	13688 / 1248 / 934
R_1 [I > 2σ(I)]	0.0884	0.0773	0.0331	0.078	0.0819	0.0602	0.1163	0.0557
wR_2 [all data]	0.2325	0.2116	0.079	0.222	0.231	0.1567	0.4307	0.1578
GoF	1.0024	1.036	0.9982	0.9839	0.9908	1.0109	2.272	0.8027
Largest diff. pk and hole [eÅ^{-3}]	1.86, -2.17	5.362, -0.791	1.30, -0.72	1.94, -1.33	2.14, -1.31	0.89, -0.68	2.77, -1.57	1.14, -1.24

* Averaged structure not accounting for modulation

Compound	**12**	**13**	**14**	**15**	**17***	**19**	**20**	**21**
CCDC No.	945336	-	-	-	-	-	-	-
Formula	$C_{42}H_{52}B_1Cl_8P_2Rh_1$	$C_{53}H_{52}B_1F_{24}P_2Rh_1$	$C_{46}H_{44}B_1F_{24}P_2Rh_1$	$C_{54}H_{54}B_1F_{24}P_2Rh_1$	$C_{54}H_{58}B_1F_{24}P_2Rh_1$	$C_{47}H_{46}B_1F_{24}P_2Rh_1$	$C_{49}H_{50}B_1Cl_2F_{24}P_2Rh_1$	$C_{53}H_{52}B_1O_4F_{24}P_2Rh_1$
M	1016.16	1320.61	1228.47	1334.47	1338.67	1242.5	1341.46	1384.61
Crystal System	Triclinic	Monoclinic	Triclinic	Monoclinic	Triclinic	Triclinic	Tetragonal	Monoclinic
Space group	*P* -1	*C* 2/c	*P* -1	*C* 2/c	*P* -1	*P* -1	*P* $4_1 2_1 2$	*C* 2/c
T [K]	150(2)	150(2)	150(2)	150(2)	150(2)	150(2)	150(2)	150(2)
a [Å]	12.6148(3)	36.6257(4)	12.6227(2)	17.8334(5)	12.4723(18)	12.9936(4)	12.90210(10)	19.6865(3)
b [Å]	12.7474(3)	12.85990(10)	14.0591(2)	17.5483(4)	12.7523(18)	13.0852(4)	12.90210(10)	16.9449(3)
c [Å]	16.1361(3)	24.1810(3)	16.1221(3)	55.0406(15)	18.258(2)	16.0745(5)	67.9669(10)	18.0112(3)
α [deg]	101.9704(18)	90	67.8471(8)	90	91.084(11)	109.669(3)	90	90
β [deg]	102.9988(19)	100.0884(5)	72.8930(7)	90.957(2)	93.445(11)	96.825(3)	90	95.0310(7)
γ [deg]	106.980(2)	90	68.3387(8)	90	92.378(11)	91.997(2)	90	90
V [Å^3]	2311.91(10)	11213.2(2)	2422.52(7)	17222.3(8)	2895.5(7)	2547.15(15)	11314.1(2)	5985.13(17)
Z	2	8	2	12	2	2	8	4
Density [gcm^{-3}]	1.46	1.564	1.684	1.544	1.535	1.62	1.575	1.537
μ (mm^{-1})	8.117	0.478	0.546	3.968	3.933	4.421	4.877	0.456
θ range [deg]	$3.79 \le \theta \le 76.31$	$5.109 \le \theta \le 27.448$	$5.091 \le \theta \le 27.433$	$3.534 \le \theta \le 76.545$	$3.553 \le \theta \le 78.193$	$3.437 \le \theta \le 76.436$	$3.487 \le \theta \le 77.046$	$5.157 \le \theta \le 27.484$
Reflns collected	23606	22737	19043	17822	15647	26194	65822	13253
R_{int}	0.027	0.032	0.034	0.233	0.103	0.032	0.105	0.025
No. of data/restr/param	9509 / 108 / 523	12695 / 0 / 730	10921 / 228 / 695	12965 / 2334 / 1422	6755 / 3526 / 963	10485 / 684 / 758	9742 / 2050 / 945	6770 / 1162 / 593
R_1 [$I > 2\sigma(I)$]	0.0386	0.0465	0.04	0.1039	0.2481	0.0439	0.119	0.132
wR_2 [all data]	0.105	0.1099	0.0864	0.3009	0.5832	0.1174	0.2775	0.4463
GoF	1.0037	0.9358	0.9848	0.9819	2.1556	0.9599	1.1053	2.0355
Largest diff. pk and hole [eÅ^{-3}]	2.06, -0.80	1.09, -0.98	0.85 / -1.07	2.36, -1.80	2.97, -1.61	1.71, -1.08	1, -1.40	1.78, -2.73

Compound	**22**	**23-*anti***	**24**	**26**	**29**	**31**	**32**	**33**
CCDC No.	-	945337	-	945334	-	-	-	-
Formula	$C_{46}H_{44}B_1O_4F_{24}P_2Rh_1$	$C_{84}H_{104}B_2Cl_2P_4Rh_2.3.1(CH_2Cl_2)$	$C_{56}H_{57}B_1Cl_1F_{24}P_2Rh_1$	$0.5(C_{112}H_{114}B_2Br_2F_{48}P_4Rh_2).1.44(CH_2Cl_2)$	$C_{59}H_{63}B_1Br_1F_{24}P_2Rh_1$	$C_{114}H_{118}B_2Br_2O_2F_{48}P_4Rh_2.2(C_6H_5F)$	$C_{52}H_{52}B_1F_{24}O_2P_2Rh_1$	$C_{50}H_{58}B_1F_{24}N_2P_2Rh_1$
M	1328.55	2295.84	1397.14	1537.98	1483.66	3135.42	1340.6	1318.64
Crystal System	Triclinic	Triclinic	Monoclinic	Triclinic	Monoclinic	Triclinic	Monoclinic	Monoclinic
Space group	*P* -1	*P* -1	*C* 2/c	*P* -1	*C* 2/c	*P* -1	*C* 2	*C* 2/c
T [K]	150(2)	150(2)	150(2)	150(2)	150(2)	150(2)	150(2)	150(2)
a [Å]	12.9279(3)	13.2301(3)	19.3373(3)	13.4344(4)	41.5250(8)	13.3182(2)	19.2382(17)	18.9702(2)
b [Å]	20.8343(4)	17.4742(5)	16.6016(3)	16.2486(5)	18.6257(2)	16.4382(2)	16.0729(5)	16.3804(2)
c [Å]	21.8302(5)	23.2939(5)	37.9999(7)	16.3500(5)	55.0866(10)	17.2470(3)	13.6017(12)	18.7908(2)
α [deg]	88.0127(10)	78.048(2)	90	73.8487(16)	90	114.7417(6)	90	90
β [deg]	86.0539(10)	88.4952(19)	91.5102(6)	88.5368(15)	115.327(2)	94.2689(6)	134.960(16)	91.5496(8)
γ [deg]	73.0587(10)	77.569(2)	90	87.5505(11)	90	94.2088(9)	90	90
V [Å^3]	5610.7(2)	5144.0(2)	12194.9(4)	3424.70(18)	38510.5(13)	3396.86(9)	2976.0(9)	5836.91(11)
Z	4	2	8	2	24	1	2	4
Density [gcm^{-3}]	1.573	1.482	1.522	1.491	1.535	1.533	1.496	1.5
μ (mm^{-1})	0.483	8.813	0.486	1.068	4.313	0.995	3.855	3.902
θ range [deg]	$5.099 \le \theta \le 25.012$	$3.42 \le \theta \le 76.67$	$5.105 \le \theta \le 27.458$	$5.120 \le \theta \le 27.507$	$2.949 \le \theta \le 76.511$	$5.10 \le \theta \le 26.37$	$4.256 \le \theta \le 76.358$	$3.565 \le \theta \le 76.217$
Reflns collected	32121	54944	36050	27223	215322	13736	15564	16679
R_{int}	0.061	0.028	0.056	0.066	0.075	0.0244	0.018	0.024
No. of data/restr/param	19471 / 1508 / 1624	21268 / 170 / 1110	8001 / 1892 / 1115	10296 / 569 / 886	40017 / 648 / 2377	13736 / 1112 / 1713	5856 / 1949 / 596	6008 / 970 / 529
R_1 [I > 2σ(I)]	0.0618	0.0524	0.0966	0.0606	0.0956	0.0519	0.0654	0.0669
wR_2 [all data]	0.1441	0.1381	0.2683	0.1498	0.2703	0.1378	0.1742	0.1715
GoF	0.9524	0.9822	0.9409	0.9485	0.9638	1.023	1.0456	0.9992
Largest diff. pk and hole [eÅ^{-3}]	1.36, -1.19	3.17, -1.75	2.28, -1.09	0.91, -1.08	5.36, -1.85	1.066, -0.752	0.61, -0.95	2.00, -1.12
						R = $C(CF_3)_3$	Incomplete refinements	
Compound	**36**	**40**	**43**	**46**	**1-[BArCl$_4$]**	**7-[Al(OR)$_4$]**	**2**	**9**
CCDC No.	-	-	-	-	945335	-	-	-
Formula	$C_{56}H_{56}B_1F_{26}P_2Rh_1$	$C_{57}H_{57}B_1F_{27}P_2Rh_1$	$C_{52}H_{49}B_1F_{25}O_4P_2Rh_1$	$C_{57}H_{58}B_1F_{24}P_2Rh_1$	$C_{49}H_{60}B_1Cl_8P_2Rh_1$	$C_{52}H_{49}B_1F_{25}O_4P_2Rh_1$		
M	1398.67	1430.69	1388.57	1374.7	1108.3	1496.63		
Crystal System	Monoclinic	Monoclinic	Monoclinic	Monoclinic	Triclinic	Triclinic	Tetragonal	Monoclinic
Space group	*C* 2/c	*C* 2/c	*P* 2_1/c	*P* 2_1/n	*P* -1	*P* -1	*P* -4	*C* 2
T [K]	150(2)	150(2)	150(2)	150(2)	150(2)	150(2)	150(2)	150(2)
a [Å]	19.1196(10)	19.4111(5)	19.3327(2)	14.03670(10)	12.0494(3)	12.4950(5)	13.36990(10)	19.0002(4)
b [Å]	16.6624(11)	16.6829(5)	16.14680(10)	24.1160(2)	12.4222(3)	13.6136(5)	13.36990(10)	16.61810(10)
c [Å]	38.1252(18)	37.9754(11)	18.7394(2)	18.0407(2)	17.4694(4)	17.6947(8)	16.96640(10)	13.4375(3)
α [deg]	90	90	90	90	88.3937(9)	100.459(2)	90	90
β [deg]	91.356(5)	91.343(3)	97.4533(8)	104.4969(9)	89.8872(9)	101.030(2)	90	135.006(4)
γ [deg]	90	90	90	90	86.3926(9)	94.6594(14)	90	90
V [Å^3]	12142.5(12)	12294.3(6)	5800.29(9)	5912.50(10)	2608.61(11)	2884.2(2)	3032.82(4)	2999.8(2)
Z	8	8	4	4	2	2	2	2
Density [gcm^{-3}]	1.53	1.546	1.59	1.544	1.411	1.723		
μ (mm^{-1})	3.829	3.82	4.033	3.871	0.831	0.523		
θ range [deg]	$3.519 \le \theta \le 77.298$	$3.666 \le \theta \le 76.829$	$3.579 \le \theta \le 76.361$	$3.124 \le \theta \le 76.552$	$5.10 \le \theta \le 27.47$	$5.145 \le \theta \le 27.663$		
Reflns collected	60580	34986	68258	35747	20032	12942		
R_{int}	0.106	0.029	0.028	0.03	0.038	0.158		
No. of data/restr/param	9159 / 3937 / 1126	12685 / 3135 / 1108	10987 / 1629 / 961	12247 / 684 / 847	10747 / 1312 / 650	7821 / 0 / 775		
R_1 [$I > 2\sigma(I)$]	0.1574	0.0702	0.0716	0.0452	0.0628	0.1388		
wR_2 [all data]	0.4789	0.1761	0.1983	0.1089	0.1563	0.4214		
GoF	1.9701	0.9292	1.0047	1.105	1.009	1.4477		
Largest diff. pk and hole [eÅ^{-3}]	3.45, -1.69	1.18 , -0.92	1.58, -1.33	2.38, -1.69	1.34, -1.29	5.66, -2.07		

6.3. References

1. A. B. Pangborn, M. A. Giardello, R. H. Grubbs, R. K. Rosen and F. J. Timmers, *Organometallics*, 1996, **15**, 1518-1520.
2. J. S. Siegel and F. A. L. Anet, *J. Org. Chem.*, 1988, **53**, 2629-2630.
3. T. Zuschneid, H. Fischer, T. Handel, K. Albert and G. Häfelinger, *Zeitschrift für Naturforschung B*, 2004, **59b**, 1153-1176.
4. J. Matthes, T. Pery, S. Gründemann, G. Buntkowsky, S. Sabo-Etienne, B. Chaudret and H.-H. Limbach, *J. Am. Chem. Soc.*, 2004, **126**, 8366-8367.
5. A. T. Lubben, J. S. McIndoe and A. S. Weller, *Organometallics*, 2008, **27**, 3303-3306.
6. http://fluorine.ch.man.ac.uk/research/mstool.php, Mass Spectrum isotope pattern calculator, University of Machester.
7. H. Nowell, S. A. Barnett, K. E. Christensen, S. J. Teat and D. R. Allan, *J. Synch. Rad.*, 2012, **19**, 435-441.
8. Z. Otwinowski, W. Minor and Charles W. Carter, Jr., in *Methods Enzymol.*, Academic Press, 1997, vol. Volume 276, pp. 307-326.
9. *Crysalis Pro.*, (2011) Oxford Diffraction Ltd, Abingdon, England.
10. A. Altomare, G. Cascarano, C. Giacovazzo, A. Guagliardi, M. C. Burla, G. Polidori and M. Camalli, *J. Appl. Crystallogr.*, 1994, **27**, 435-436.
11. L. Palatinus and G. Chapuis, *J. Appl. Crystallogr.*, 2007, **40**, 786-790.
12. P. W. Betteridge, J. R. Carruthers, R. I. Cooper, K. Prout and D. J. Watkin, *J. Appl. Crystallogr.*, 2003, **36**, 1487.
13. R. I. Cooper, A. L. Thompson and D. J. Watkin, *J. Appl. Crystallogr.*, 2010, **43**, 1100-1107.
14. G. M. Sheldrick, *Acta Crystallogr. Sect. A*, 2008, **64**, 112-122.
15. A. Spek, *J. Appl. Crystallogr.*, 2003, **36**, 7-13.
16. J. Rohlicek and M. Husak, *J. Appl. Crystallogr.*, 2007, **40**, 600-601.
17. S. K. Wolff, D. J. Grimwood, J. J. McKinnon, M. J. Turner, D. Jayatilaka and M. A. Spackman, *Crystal Explorer (v3.1)*, (2012) University of Western Australia.
18. M. J. Turner, J. J. McKinnon, D. Jayatilaka and M. A. Spackman, *CrystEngComm*, 2011, **13**, 1804-1813.
19. S. D. Pike, A. L. Thompson, A. s. G. Algarra, D. C. Apperley, S. A. Macgregor and A. S. Weller, *Science*, 2012, **337**, 1648-1651.
20. S. Alvarez, *Dalton Trans.*, 2013, **42**, 8617-8636.
21. L. Pauling, *The Nature of the Chemical Bond*, 3rd edn., Cornell University Press, 1960.
22. W. E. Buschmann and J. S. Miller, *Inorg. Synth.*, 2002, **33**, 83-91.
23. R. Anulewicz-Ostrowska, T. Klis, D. Krajewski, B. Lewandowski and J. Serwatowski, *Tetrahedron Lett.*, 2003, **44**, 7329-7331.
24. M. D. Fryzuk, *Can. J. Chem.*, 1983, **61**, 1347-1351.
25. R. B. King and W. M. Rhee, *Inorg. Chem.*, 1978, **17**, 2961-2963.
26. B. Guzel, M. A. Omary, J. P. Fackler Jr and A. Akgerman, *Inorg. Chim. Acta*, 2001, **325**, 45-50.
27. M. Kranenburg, Y. E. M. van der Burgt, P. C. J. Kamer, P. W. N. M. van Leeuwen, K. Goubitz and J. Fraanje, *Organometallics*, 1995, **14**, 3081-3089.
28. J. L. Herde, J. C. Lambert, C. V. Senoff and M. A. Cushing, in *Inorg. Synth.*, John Wiley & Sons, Inc., 2007, pp. 18-20.
29. R. J. Burt, J. Chatt, W. Hussain and G. J. Leigh, *J. Organomet. Chem.*, 1979, **182**, 203-206.
30. X.-L. Luo, G. J. Kubas, C. J. Burns, R. J. Butcher and J. C. Bryan, *Inorg. Chem.*, 1995, **34**, 6538-6545.
31. M. D. Fryzuk, T. Jones and F. W. B. Einstein, *Organometallics*, 1984, **3**, 185-191.
32. A. Rifat, M. F. Mahon and A. S. Weller, *J. Organomet. Chem.*, 2003, **667**, 1-4.
33. I. Pernik, J. F. Hooper, A. B. Chaplin, A. S. Weller and M. C. Willis, *ACS Catalysis*, 2012, **2**, 2779-2786.
34. M. Scott, Exploring the synthesis of transition metal alkane complexes, MChem Thesis, University of Oxford, 2013.

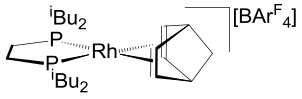

1

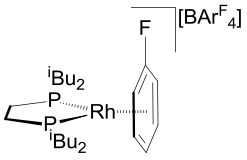

2

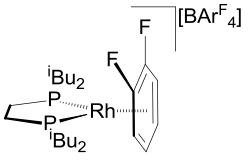

3

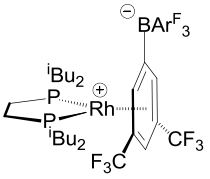

4

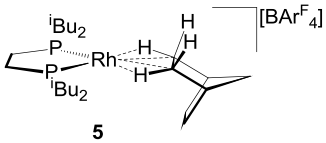

5

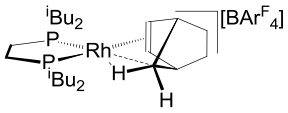

6

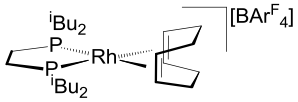

7

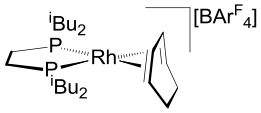

8

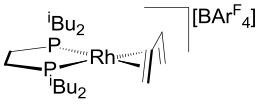

9

10

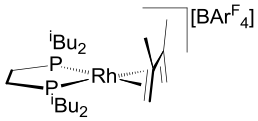

11

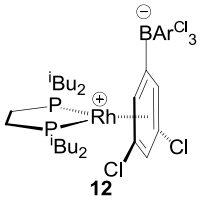

12

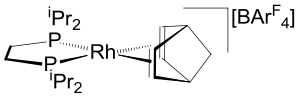

13

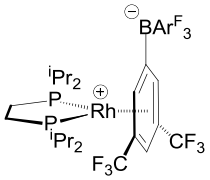

14

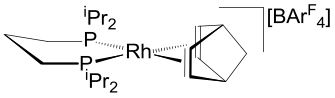

15

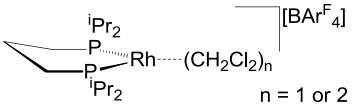

16

n = 1 or 2

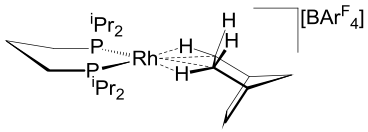

17

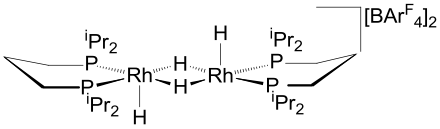

18

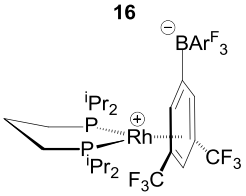

19

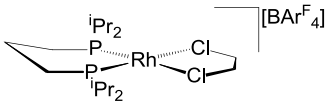

20

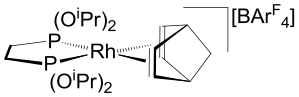

21

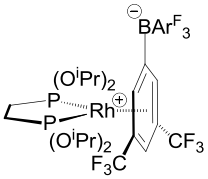

22

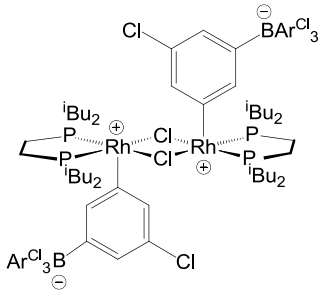

23-*anti*

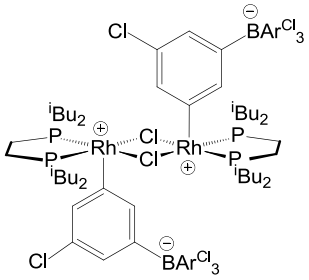

23-*syn*

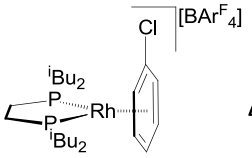

24

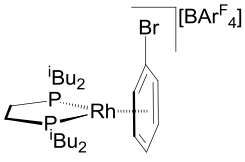

25

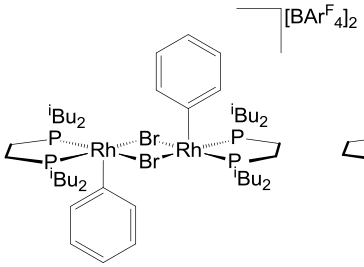

26

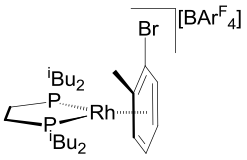

27

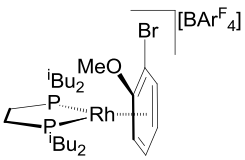

28

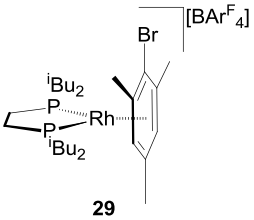

29

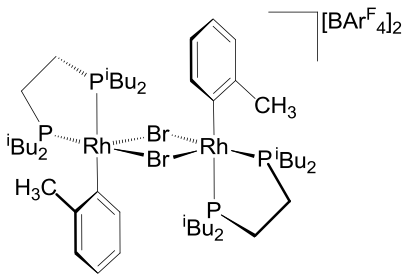

30

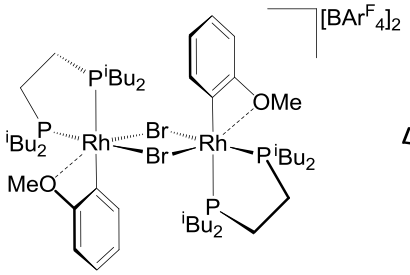

31

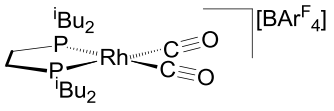

32

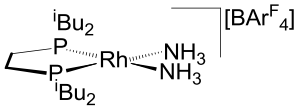

33

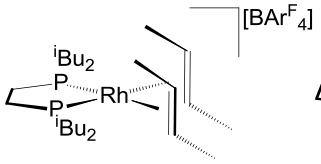

34
proposed structure

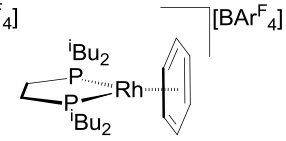

35

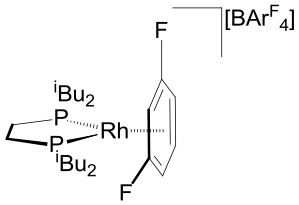

36

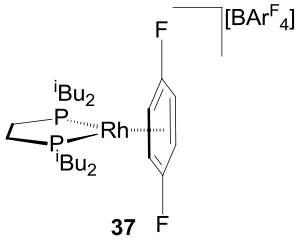

37

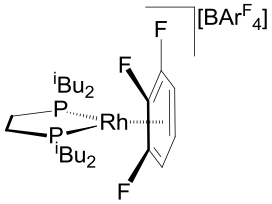

38

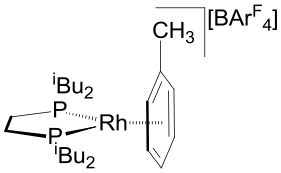

39

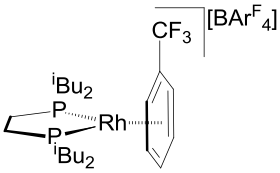

40

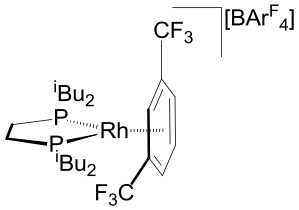

41

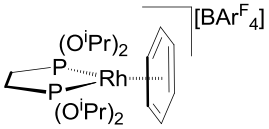

42

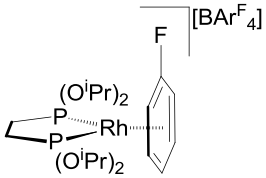

43

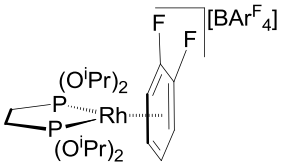

44

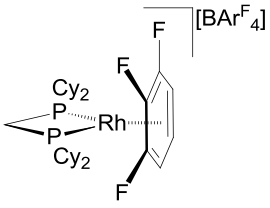

45

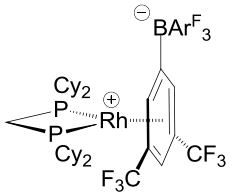

46